ADVANCES IN MULTIAXIAL FATIGUE

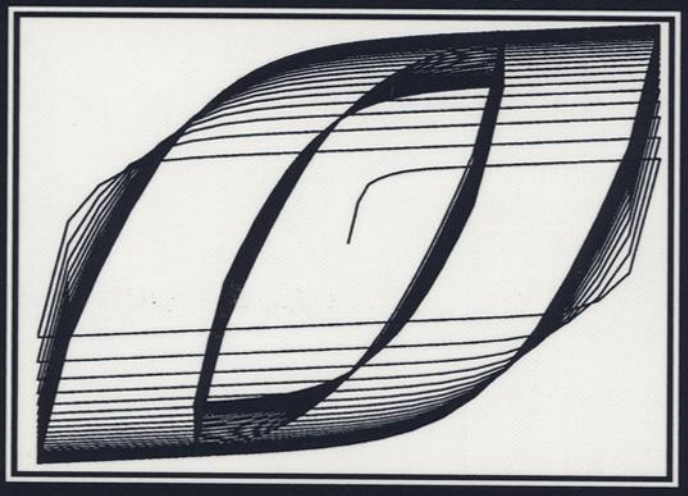

McDowell/Ellis, editors

ASTM STP 1191

STP 1191

Advances in Multiaxial Fatigue

David L. McDowell and Rod Ellis, editors

ASTM Publication Code Number (PCN)
04-011910-30

ASTM
1916 Race Street
Philadelphia, PA 19103

Library of Congress Cataloging in Publication Data
Advances in multiaxial fatigue/David L. McDowell and Rod Ellis, editors.
p. cm. — (STP ; 1191)
Includes bibliographical references and index.
ISBN 0-8031-1862-7
1. Metals—Fatigue—Congresses. I. McDowell, David L., 1956– . II. Ellis, Rod, 1939– . III. Series: ASTM special technical publication; 1191.
TA460.A26 1993
620.1'66—dc20 93-11048
CIP

Peer Review Policy

Each paper published in this volume was evaluated by three peer reviewers. The authors addressed all of the reviewers' comments to the satisfaction of both the technical editor(s) and the ASTM Committee on Publications.

The quality of the papers in this publication reflects not only the obvious efforts of the authors and the technical editor(s), but also the work of these peer reviewers. The ASTM Committee on Publications acknowledges with appreciation their dedication and contribution to time and effort on behalf of ASTM.

Printed in Ann Arbor, MI
September 1993

Foreword

This publication, *Advances in Multiaxial Fatigue,* contains papers presented at the Symposium on Multiaxial Fatigue, which was held in San Diego, California, 14–16 Oct. 1991. The symposium was sponsored by ASTM Committee E-9 on Fatigue. David L. McDowell, Georgia Institute of Technology, and Rod Ellis, NASA Lewis Research Center, presided as symposium co-chairmen and were editors of this publication.

Contents

Multiaxial Stress-Strain Behavior

Multiaxial Micro/Macro Crack Growth Studies

Multiaxial Fatigue of Notched Components

Overview

The effect of the multiaxial stress state on cyclic deformation and fatigue life has emerged over the last two decades as one of the most rapidly developing areas of fatigue research. The intense focus on this subject may be attributed to the general recognition of its importance in the fatigue design of components as well as the relatively recent widespread availability of high-quality multiaxial testing equipment. Marked advances in understanding the influence of both material structure and multiaxiality of loading have been made in the past two decades. This is the second symposium of its type sponsored by ASTM since 1980. The first, the Symposium on Multiaxial Fatigue, was held in San Francisco 15–17 Dec. 1982, with a resulting ASTM special technical publication *(Multiaxial Fatigue, ASTM STP 853).* The results of the more recent Symposium on Multiaxial Fatigue, held in San Diego 14–15 Nov. 1991, forms the basis for this special technical publication.

This symposium was conceived and planned within ASTM Subcommittee E09.01 on Fatigue Research, a subcommittee of ASTM Committee E09 on Fatigue. The purpose of the symposium was to communicate the most recent international advances in multiaxial cyclic deformation and fatigue research as well as applications to component analysis and design. Reflective of the continuing yet incomplete development of the subject, this volume will be of considerable interest to researchers and industrial practitioners of fatigue design. The papers herein predominately reflect a concern with stress state effects on cyclic deformation and fatigue of a wide range of monolithic metals, with applications ranging from power plant pressure vessel components to hot section jet engine components to automotive assemblies. The understanding of multiaxial loading effects on fatigue life has proven to be a very challenging and somewhat elusive pursuit; this volume provides insight into some important advances of our understanding during the last ten years.

The collection of 24 papers published in this volume has been grouped into five categories. Each category reflects the most fundamental area of contribution of its papers, although a certain degree of overlap is unavoidable. These categories are multiaxial fatigue life models, experimental multiaxial fatigue studies, multiaxial stress-strain behavior, multiaxial micro/macro crack growth studies, and multiaxial fatigue of notched components.

Multiaxial Fatigue Life Models

Prior to the 1960s, most multiaxial fatigue life prediction schemes concentrated on high-cycle fatigue applications. Effective stress, maximum shear stress, or modified schemes involving tensile mean stress and/or hydrostatic stress were most applicable in the HCF regime. With increasing concern for low-cycle fatigue applications following the 1960s, multiaxial fatigue approaches adopted strain-based methodologies. The decade of the 1970s witnessed the introduction of so-called critical plane approaches which made connections between fatigue crack initiation on specific planes at the surface of the material and the maximum shear strain range and/or normal strains on these planes. The first paper in this volume reviews these approaches and offers significant experimental insight into the relative role of microcrack nucleation and propagation in multiaxial fatigue. Extensive data sets including microcrack sizes and shapes

over a wide range of stress states are considered. The key conclusions are (1) each material has a potentially distinct mode of resistance to fatigue crack initiation, and (2) the critical plane model selected should always reflect the actual physics of microcracking, either shear-based or normal stress/strain-based. The second paper provides an application of these critical plane principles to constant and variable amplitude fatigue of SAE notched shaft specimens; a novel computational scheme for multi-surface plasticity theory is used to predict the stress-strain histories which are essential for fatigue life analyses. The third and fourth papers in this section deal with promising hysteretic energy-based approaches with provision for mean stress effects. The fifth paper employs a triaxiality factor to correlate fatigue data over a range of stress states.

The final two papers in this section employ incremental damage approaches to the multiaxial fatigue problem, permitting consideration of quite arbitrary loading histories. The first of these two papers uses a thermoviscoplasticity theory to determine incremental inelastic strains; then creep and fatigue damage increments are determined and summed to assess total damage. The last paper considers the prediction of the high-cycle fatigue response using micromechanical techniques and a shakedown approach to assess the possibility of persistent cyclic plastic strains.

Experimental Multiaxial Fatigue Studies

Much of our collective knowledge regarding multiaxial fatigue has developed by virtue of experimental studies of various materials. In this section, the papers consider, among other things, effects of complex loading and material anisotropy. The first paper presents a high-temperature tension-torsion experimental study of the in-phase and out-of-phase fatigue behavior of a superalloy. Several fatigue theories are examined in terms of their correlative capability.

In the second paper, the effects of anisotropy of initially cold-worked Al-6061-T6 on tension-torsion fatigue behavior are studied and correlated using an anisotropic generalization of a critical plane theory. The third papers reports results of high-temperature fatigue tests consisting of sequences of uniaxial and torsional loading of tubular specimens; strongly nonlinear interaction effects are observed for tension-torsion loading and are attributed to oxide-induced cracking and differences of microcrack initiation and growth between uniaxial and torsional cyclic loading. The last paper presents a unique, relatively low-cost test method which may achieve a wide range of biaxiality ratios using only uniaxial testing equipment.

Continued experimental examination of microcracking and effects of complex multiaxial loading paths, as reported in this section, will prove to be an essential tool in further advancing our understanding of the fatigue process.

Multiaxial Stress-Strain Behavior

It is increasingly evident that any successful multiaxial fatigue life prediction methodology invariably relies on accurate multiaxial cyclic stress-strain relations for input. In turn, development of constitutive equations for cyclic inelastic material behavior depend on carefully conducted combined stress state experiments. The first two papers in this section deal with such experimental studies on advanced metallic alloys. The first paper considers the appropriateness of using a J_2-based constitutive model to correlate both uniaxial and pure torsional thermomechanical test results. The second paper reports the behavior of a single crystal superalloy under tension-torsion loading of thin-walled tubular specimens.

The next two papers in this section study the performance of cyclic inelasticity theories. In the third paper, the concept of an irreversible component of cyclic inelastic strain is introduced

to model the path-dependent cyclic hardening behavior of an austenitic stainless steel. The fourth paper examines the predictive capability of two rate-independent multisurface plasticity models for nonproportional loading paths and introduces a modified integration scheme for near neutral loading conditions.

The final paper in this section addresses the problem of predicting cycle-dependent plastic strain accumulation for nonproportional loading paths typical of pressure vessel and piping components with steady primary stresses and alternating secondary stresses. Using a multisurface plasticity theory, the author introduces a ratchet assessment diagram as a graphical presentation of results and discusses these results in terms of ASME code considerations.

Multiaxial Micro/Macro Crack Growth Studies

There has been a growing emphasis during the 1980s on applying fracture mechanics principles to fatigue, including growth of very short cracks which have conventionally fit within the so-called "fatigue crack initiation" regime. Numerous recent studies have considered the details of crack growth for microstructurally short cracks and the transition to long crack behavior. The first two papers in this section examine experimentally the propagation behavior of microcracks in low-cycle fatigue under tension-torsion loading of thin-walled tubular specimens. Results are correlated using critical plane concepts as a basis for microcrack propagation laws.

The last two papers in this section consider macrocrack propagation under mixed mode conditions in a biaxial stress field. The third paper examines self-similar crack propagation as a function of mode mixity for a high-strength steel; several mixed mode theories are unsuccessful at correlating mixed mode results based on constants determined using Mode I data. The final paper deals with curvature of the growth of initially longitudinal cracks in thin pressurized and independently axially loaded cylinders.

Multiaxial Fatigue of Notched Components

The preceding sections of this volume present much of the latest research regarding multiaxial cyclic deformation and fatigue. Ultimately, the application of these concepts to life prediction of notched structural components is the primary driving force for this research. In this section, four papers are included which represent a variety of applications.

The first paper presents a method of estimating the local cyclic strains given the autofrettage history of pressurized components and compares the results with finite element analyses. The second paper presents a method to estimate notch root stresses and inelastic strains, including plastic and creep strains, based on two linear finite element analyses per point on the load versus notch root strain curve.

The third paper compares the ASME Boiler and Pressure Vessel Code multiaxial low-cycle fatigue approach with a local stain approach and the Japanese MITI Code, including a study of a pressure vessel component. The final paper in this section presents a methodology for correlating the fatigue life of composite hip prothesis components with the progressive degradation of stiffness.

The papers briefly outlined in this overview should provide a glimpse into the advances made in the subject of multiaxial fatigue from the 1982 ASTM symposium to the present. We should also acknowledge the very dynamic and important activities and symposia elsewhere on this subject which have contributed so greatly to this volume and the state of the art in multiaxial fatigue. The editors of this volume gratefully acknowledge the extremely dedicated

efforts of the authors, reviewers, and ASTM personnel who have made this publication possible.

D. L. McDowell

George M. Woodruff School of Mechanical Engineering, Georgia Institute of Technology, Atlanta, GA 30332-0405; symposium co-chairman and editor

J. R. Ellis

NASA Lewis Research Center, MS 49/7, 21000 Brookpark Road, Cleveland, OH 44135; symposium co-chairman and editor

Multiaxial Fatigue Life Models

Darrell Socie[1]

Critical Plane Approaches for Multiaxial Fatigue Damage Assessment

REFERENCE: Socie, D., **"Critical Plane Approaches for Multiaxial Fatigue Damage Assessment,"** *Advances in Multiaxial Fatigue, ASTM STP 1191,* D. L. McDowell and R. Ellis, Eds., American Society for Testing and Materials, Philadelphia, 1993, pp. 7–36.

ABSTRACT: This paper reviews the evolution of the critical plane damage models and traces their origins from the early work such as that of Guest. Physical justification in the form of detailed observations of crack nucleation and early growth are provided for the models. A common feature of all successful models is that they consider both cyclic stresses and strains. Material-dependent failure models are needed to account for the differences in crack nucleation and early growth. Shear strain–based models are appropriate for materials that have substantial Mode II growth. Tensile strain–based models are needed for materials that have predominantly Mode I growth. Problems and inconsistencies in interpreting the damage models for variable amplitude nonproportional loading are discussed. Critical experiments for evaluating and discriminating between proposed damage models are suggested.

KEY WORDS: fatigue, multiaxial, biaxial, damage models, cyclic deformation, critical planes

Fatigue damage is best described as the nucleation and growth of cracks to final failure. In 1903 Ewing and Humfrey [*1*], motivated by the work of Wohler and Bauschinger, published their classic paper, "The Fracture of Metals under Repeated Alternations of Stress." Their description of the fatigue process follows:

> The course of the breakdown was as follows: The first examination, made after a few reversals of stress, showed slip-lines on some of the crystals, ... the slip-lines were quite similar in appearance to those which are seen when a simple tensile stress exceeding the elastic limit is applied. . . . After more reversals of stress additional slip-lines appeared. . . . After many reversals they changed into comparatively wide bands with rather hazily defined edges, ... As the number of reversals increased this process of broadening continued, and some parts of the surface became almost covered with dark markings. . . . When this stage was reached it was found that some of the crystals had cracked. The cracks occurred along broadened slip-bands: in some instances they were first seen on a single crystal, but soon they joined up from crystal to crystal, until finally a long continuous crack was developed across the surface of the specimen. When this happened a few more reversals brought about fracture.

These authors also noted that: "Once an incipient crack begins to form across a certain set of crystals, the effect of further reversals is mainly confined to the neighborhood of the crack." Later work using the electron microscope, X-ray, and other powerful tools has confirmed these concepts of the basic cause of fatigue crack nucleation and early growth. Fine [*2*] provides an excellent review of the fatigue damage process.

These slip lines, more commonly called persistent slip bands, are caused by the movement of dislocations. The crystals are individual grains in the material. Sometimes features called

[1] Professor, University of Illinois, Urbana, IL 61801.

intrusions and extrusions are formed on the surface. Slip occurs more readily along certain crystal directions and planes than along others. Dislocations move only on their crystallographic slip planes under an applied shear stress. In a FCC metal such as aluminum there are four slip planes and three slip directions for a total of twelve slip systems. When the critical resolved shear stress in a grain is exceeded, the dislocations move and result in plastic shear strains. During tensile loading, shear stresses are produced on planes that are oriented at 45° to the tensile axis. Grains whose crystallographic slip planes and directions are also oriented at 45° to the tensile axis will have the highest critical resolved shear stress and plastic strains and will be the first to form slip bands and cracks. A dislocation model proposed by Fine and Ritchie [*3*] is shown in Fig. 1*a*. Paired dislocation pileups against an obstacle on a metal surface are imagined to grow with cyclic straining until they reach a critical size. An avalanche then occurs, giving an intrusion or extrusion depending on the sign of the dislocation.

Given this description of the process, it is clear that the macroscopic cyclic shear stress and strain are the driving forces for crack nucleation and should be the appropriate parameters for correlating test data for various states of stress such as tension/compression and torsion. Equal cyclic shear stress or strains should result in equivalent fatigue damage. Unfortunately, this is not always observed. A more complete understanding requires consideration of how small cracks grow from the slip band that forms in a single grain. In some materials and loading conditions, the majority of the fatigue life is consumed in growing small cracks from the order of the grain size to a length of a few millimeters. Hence, their growth is more important than their nucleation. A mechanism for crack extension in metals has been described by Laird [*4*]

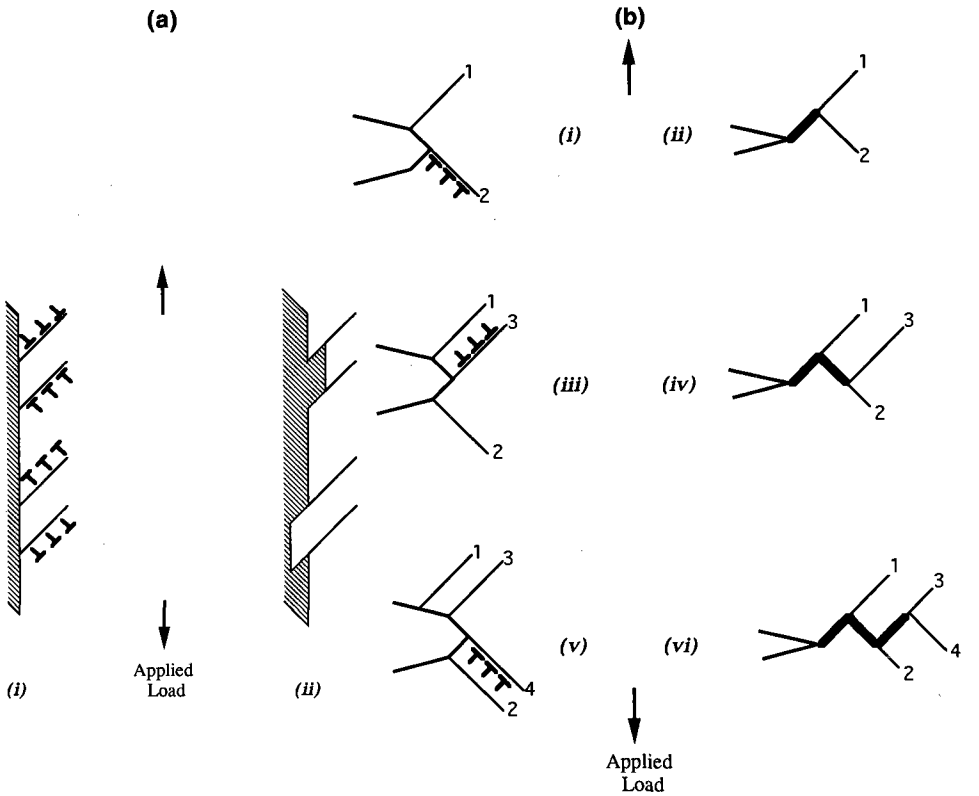

FIG. 1—*Dislocation Fatigue Models:* (a) *crack initiation;* (b) *crack growth.*

that is consistent with Ewing and Humfrey's observations that after a dominant crack forms, damage is confined to the region surrounding the crack tip. An illustration is given in Fig. 1*b*. Growth occurs by local shear processes at the crack tip. Slip acts on two intersecting slip planes at the crack tip. Unloading or compressive loading relaxes the stresses or dislocations on the slip planes. This process continues with an increment of crack extension on each loading cycle that is often related to the formation of striations. This model suggests that macroscopic crack growth will occur on a plane perpendicular to the maximum principal stress even though the local growth at the crack tip is a shear strain–controlled process. Viewed on a macroscale that is on a scale larger than the grain size, tensile stresses are responsible for the growth of fatigue damage and should be an appropriate damage parameter.

Early multiaxial fatigue researchers such as Gough et al. [*5*] proposed empirical relationships that reduce to shear stress for ductile materials and principal stress for brittle materials. Gough's ellipse quadrant is often cited and given here as an example.

$$(\tau_a/\tau_f)^2 + (\sigma_a/\sigma_f)^2(\sigma_f/\tau_f - 1) + \sigma_a/\sigma_f(2 - \sigma_a/\tau_a) = 1 \tag{1}$$

The applied tension and shear stresses are given by σ_a and τ_a. Fatigue limits in tension and torsion are denoted σ_f and τ_f in Eq 1. No physical interpretation was ascribed to this equation. When the ratio of fatigue limits in torsion and bending equals 0.5, the expression reduces to the maximum shear stress criterion. Similarly, the maximum principal stress criterion is obtained when the ratio is equal to 1.

Stulen and Cummings [*6*] proposed a model that considered the interaction of the ranges of maximum shear stress and normal stress on the maximum shear stress plane

$$(\sigma_1 - \sigma_3)/2 + g((\sigma_1 + \sigma_3)/2) = \text{constant} \tag{2}$$

where σ_1 and σ_3 are the maximum values of the largest and smallest nominal principal stress during a loading cycle. Constant fatigue lives are a function of the maximum shear stress range modified by the normal stress range on the maximum shear stress plane. The effect of the normal stress is included through the constant g. If the constant g was selected to be equal to 0, the criterion will be the maximum shear stress. Similarly, $g = 1$ will give the maximum principal stress. Here again a single criteria can be made to fit both cracking modes described above by a suitable choice of an adjustable constant. It is not surprising that these theories consistently fit the data.

Based on physical observations of the orientation of initial fatigue cracks in steel and aluminum, Findley [*7*] discussed the influence of normal stress acting on the maximum shear stress plane. A critical plane model was introduced [*8*]

$$\tau_a + k\sigma_{n,\max} = \text{constant} \tag{3}$$

For a constant fatigue life, the allowable alternating shear stress, τ_a, decreases with an increase in the maximum normal stress, $\sigma_{n,\max}$, on the plane of the critical alternating shear stress. Here, the maximum normal stress was formulated as the sum of the normal stress resulting from the amplitude and mean stress. A constant k is used to fit the experimental data. These shear criteria could be made into a principal stress theory by setting the constant to 1.

McDiarmid [*9*] conducted an extensive literature survey on multiaxial fatigue in the high-cycle regime in 1972. He showed that the ellipse quadrant proposed by Gough can be divided into components of maximum shear stress amplitude and the normal stress acting on the plane of maximum shear stress amplitude similar to Findley's model. McDiarmid argued that his proposed model is based on physical observations on the effect of normal stress on the maxi-

mum shear stress orientation, whereas the Gough ellipse quadrant is empirical. The most recent formulation of his work [*10*] results in the following model

$$\begin{aligned} &\text{Case A } \tau_a/\tau_{f,A} + \sigma_{n,\max}/2\sigma_u = 1 \\ &\text{Case B } \tau_a/\tau_{f,B} + \sigma_{n,\max}/2\sigma_u = 1 \end{aligned} \tag{4}$$

This failure criterion is also based on the shear stress amplitude and the maximum normal stress on the plane of maximum shear stress amplitude. The model considers two types of shear cracking modes. Case A cracks growing along the surface have a shear fatigue limit, $\tau_{f,A}$, and Case B cracks growing into the surface have fatigue limit $\tau_{f,B}$. Case A cracks are found in torsion loading, and Case B cracks occur under biaxial tension loading. The tensile strength is denoted σ_u.

Brown and Miller [*11*] provide a comprehensive review of the literature in terms of strain. They considered the nucleation and growth of fatigue cracks and suggested the terms Case A and Case B cracks. Case A cracks are illustrated in Fig. 2*a* for torsion loading. The shear stress acts on the free surface in a direction parallel to the length of the crack. There is no shear stress acting perpendicular to the free surface along the crack depth. As a result, these types of cracks tend to be shallow and have a large aspect ratio. In biaxial tension (Case B), the shear stress acts to cause the cracks to grow into the depth as shown in Fig. 2*b*. These types of cracks will always intersect the surface at an angle of 45°. Case B cracks are the type described by the intrusion extrusion model. Tension loading has the same shear stress for both Case A and Case B and can display either mode of cracking. Combined tension/torsion loading always has Case A cracks. Brown and Miller then proposed a separate criterion for each type of cracking

$$\begin{aligned} &\text{Case A } \varepsilon_1 - \varepsilon_3 = f(\varepsilon_1 + \varepsilon_3) \\ &\text{Case B } \varepsilon_1 - \varepsilon_3 = \text{constant} \end{aligned} \tag{5}$$

Here, f represents a function of the principal strains, which are denoted ϵ_1 and ϵ_3. They present test data to show that the fatigue life depends on both shear and normal strain amplitudes for Case A cracks.

Much work has been done during the last 15 years and will not be referenced here. Three international symposia have been held [*12-14*]. The critical plane approaches evolved from considering how cracks nucleate and grow. Details of the damage models continue to be improved but the focus remains the same: The nucleation and subsequent growth of cracks. This paper focuses on detailed observations of the nucleation and growth of small cracks ($<$ 1 mm) under multiaxial loading. Appropriate damage models are then suggested based on these observations.

Many investigators have contributed to the literature describing the nucleation and growth of cracks. In this paper, the author makes extensive use of his own students' work because he is more familiar with it and has a more complete understanding of the experiments. Detailed crack observations have been made on three materials, AISI 304 stainless steel, Inconel 718, and normalized SAE 1045 steel. These materials exhibit different regions of cracking behavior and represent extremes in the behavior observed in initally isotopic metals during tensile and torsional fatigue testing. Experimental data and observations can be found in earlier papers by Hua and Socie [*15*], by Socie et al. [*16*], and by Bannantine and Socie [*17*].

The behavior of the three materials subjected to tension and torsion is summarized in Figs. 3–5. In these figures, the vertical axis is in terms of the life fraction N/N_f, and the horizontal scale is presented in terms of fatigue life N_f in cycles. The solid line represents the first observation of a surface crack length of 100 μm and serves as a demarcation between crack nucle-

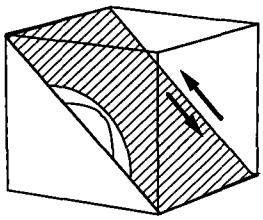

(a) Case A

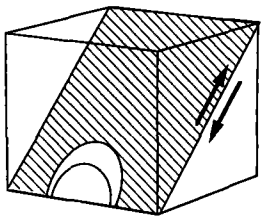

(b) Case B

FIG. 2—*Crack nucleation and growth planes:* (a) *Case A;* (b) *Case B.*

ation and growth. It could be argued that nucleation occurs much earlier, say for example 10 μm long. This would simply shift the line downward without changing the qualitative phenomena represented by the plots. The broken line represents the demarcation between crack growth on planes of maximum shear strain amplitude and crack growth on planes of maximum principal strain amplitude. Cracking behavior is categorized into three general regions: Regions A, B, and C. Region A denotes a failure mode that is dominated by shear crack growth. In Region B, shear crack nucleation is followed by crack growth on planes of maximum principal strain (Stage II growth planes). The fatigue life represented in Region C is dominated by crack nucleation. Materials may exhibit cracking behavior that is representative of one, two, or all three of these regions. The cracking behavior of each of the three materials is discussed below in detail.

AISI 304 stainless steel (yield strength, 325 MPa) was tested in tension and torsion. The type of cracking behavior exhibited is summarized in Fig. 3*a* for the stainless steel tested in torsion. Cracking behavior could be categorized into two regions: Regions A and B. Region A behavior was observed at short lives. Microcracks initiated on shear planes. Once initiated, the cracks became more distinct but showed no significant increase in length. At failure, a large density of small, coarse cracks dominated the surface of the specimen. A small amount of branching onto tensile planes (Stage II planes) was observed. Failure cracks grew on either shear planes (Stage I planes) or tensile planes (Stage II planes) by a slow linking of previously initiated shear cracks. Region B is characterized by shear crack nucleation followed by crack growth on planes of maximum principal strain amplitude (Stage II planes). Shear crack growth consumes a small fraction of the fatigue life. Region C behavior was observed at the longest lives in torsion. The fraction of life spent growing the crack on shear planes was reduced, as was the crack density. A small number of cracks initiated on shear planes but quickly branched to Stage II planes. Growth on these planes occurred by the propagation of the main crack rather than by a linking process.

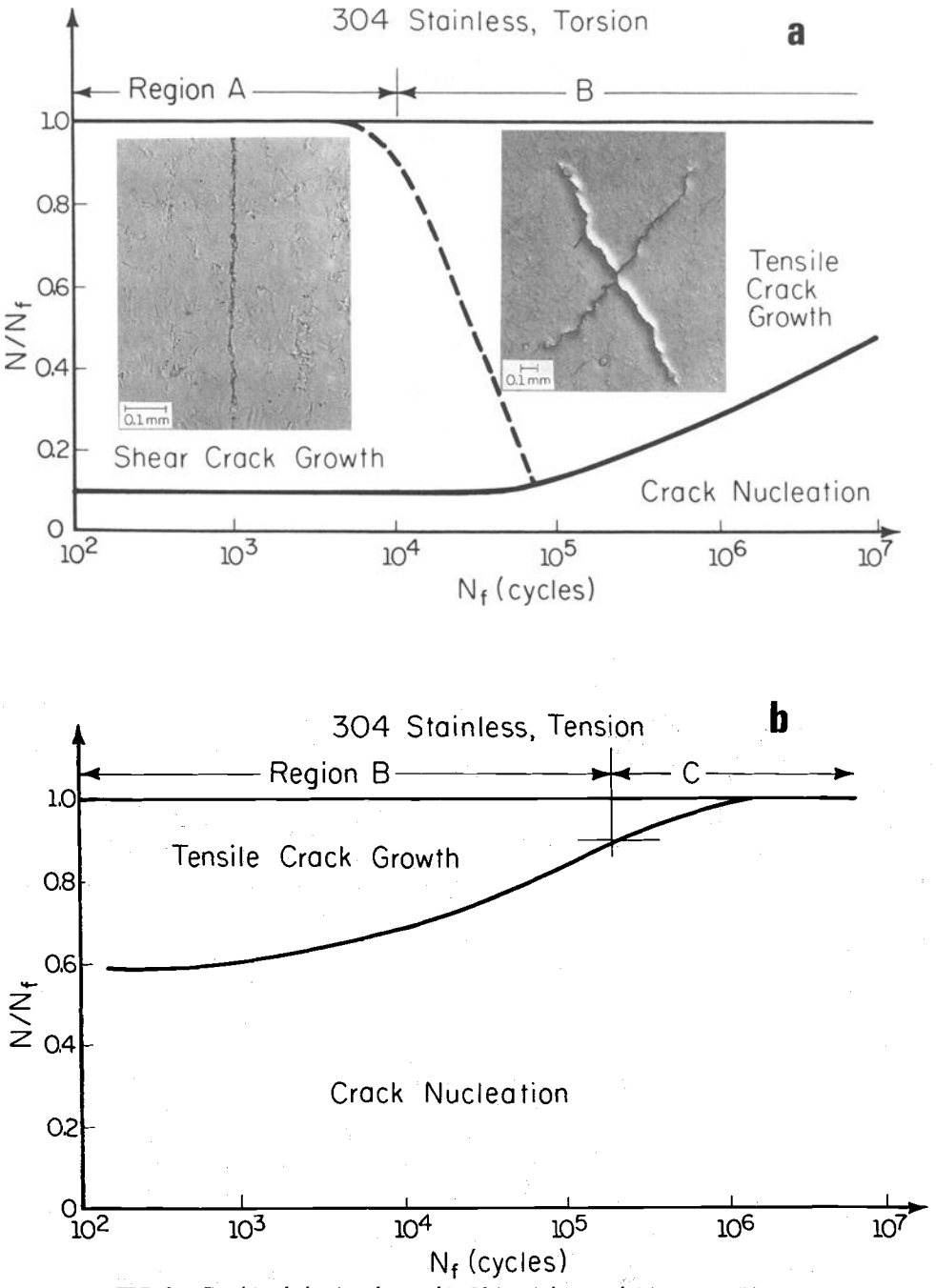

FIG. 3—*Cracking behavior observed in 304 stainless steel:* (a) *torsion;* (b) *tension.*

Surface replicas and scanning electron examination of fracture surfaces of AISI 304 stainless steel specimens tested in tension showed no perceptible evidence of Stage I growth. As a result, no Region A behavior is shown in Fig. 3*b*. The fracture surfaces appeared to be almost entirely dominated by Stage II growth. Plumbridge [*18*] also reported that, at low strain amplitudes, up to 90% of the fatigue life may be taken up in initiation and Stage I growth while at high-strain amplitudes a similar fraction may be spent in Stage II crack growth.

The behavior of Inconel 718 (yield strength, 1160 MPa) is summarized in Fig. 4. The behavior of Inconel 718 tested in torsion is presented in Fig. 4*a*. Unlike the stainless steel that displayed a mixed behavior, the results of the Inconel 718 torsion tests showed that cracks initiated and remained on the maximum shear planes (Region A behavior) at all values of the shear strain investigated. Even at the lowest strain amplitude, in which the normal stress-strain response was essentially elastic, cracks initiated and remained on shear planes throughout the life. The crack density decreased with increasing fatigue life as it did in AISI 304 stainless steel, but no branching onto tensile planes was observed.

Under tensile loading, cracks remained on shear planes for the majority of the fatigue life, and a large zone of Region A behavior was observed (Fig. 4*b*). Final failure in all tension tests was in a macroscopic tensile direction consisting of large portions of microscopic shear growth. Large amounts of shear growth were observed at failure for short and intermediate fatigue lives. Growth on Stage II planes occurred only late in life.

Damage accumulation in Inconel 718 appears to be shear dominated. This is attributed to localized shear deformation bands developed during cyclic loading. Reversed movement of dislocations progressively shears precipitates in these bands. Crack propagation then occurs along the bands with extensive shear crack growth exhibited throughout the fatigue life.

Two types of cracking system have been observed in the hot-rolled and normalized SAE 1045 (yield strength, 380 MPa). A high density of microcracks are observed at high strain amplitudes, with the final failure occurring by a very rapid linking of these cracks. This type of damage has been termed the R system by Marco and Starkey [*19*]. Alternatively, the S system, which dominated crack behavior at low strain amplitudes, exhibited one dominant crack that grew until failure.

In torsion, at high amplitudes, the R system crack behavior was characteristic of Region A as shown in Fig. 5*a*. Two common features were observed. First, the number of microcracks increased with increasing number of loading cycles. Second, the surface length of microcracks which appeared in the early stages remained almost unchanged during the fatigue life. Darkness and clarity of the microcracks substantially increased with progress of fatigue cycles. These observations indicate that the crack opening and hence the crack depth increased. Cracks initiated on the surface and propagated into the surface, while the surface crack length remained nearly constant. Also, crack orientations were developed equally on both planes of maximum shear. These multimicrocracks were almost uniformly distributed over the entire gage length. The failure was similar to that observed in the stainless steels at high amplitudes except that the linking of microcracks and final failure in SAE 1045 steel occurred over a very few cycles, while the growth of the Region A failure crack in stainless steels occurred progressively throughout the fatigue life. At lower amplitudes, progressive growth of a single crack occurred by a linking process on the shear plane.

Region B behavior was observed only at long lives. At the lowest strain amplitude 0.26%, the crack branched and growth occurred on the tensile plane by a linking of previously initiated shear cracks. After a period of tensile growth, the crack linked with a large shear crack which had been developing simultaneously. Final failure occurred by a mixture of Region A and Region B behavior.

In tension (Fig. 5*b*), failure occurred in both the R and the S systems on Stage II planes.

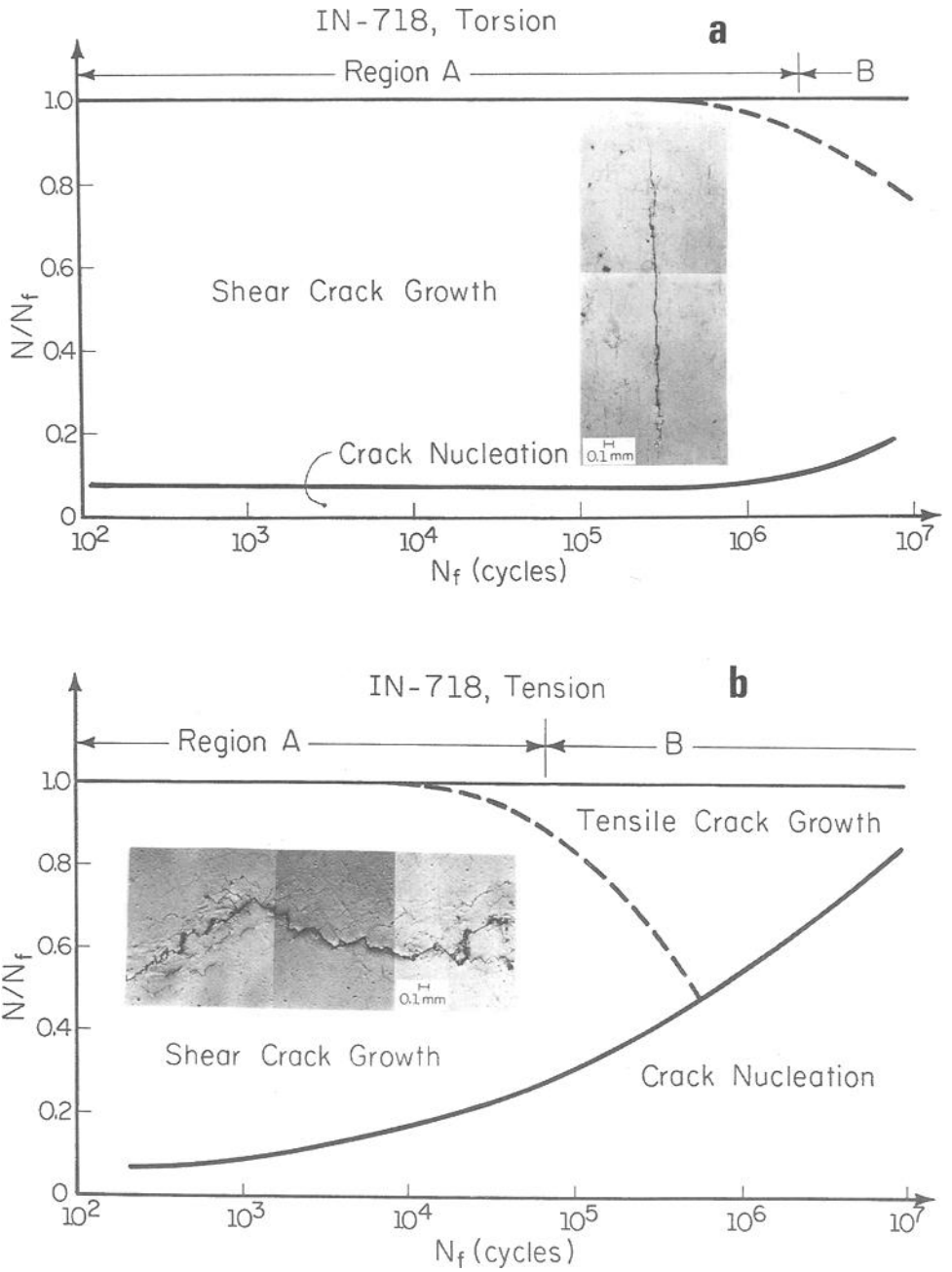

FIG. 4—*Cracking behavior observed in Inconel 718:* (a) *torsion;* (b) *tension.*

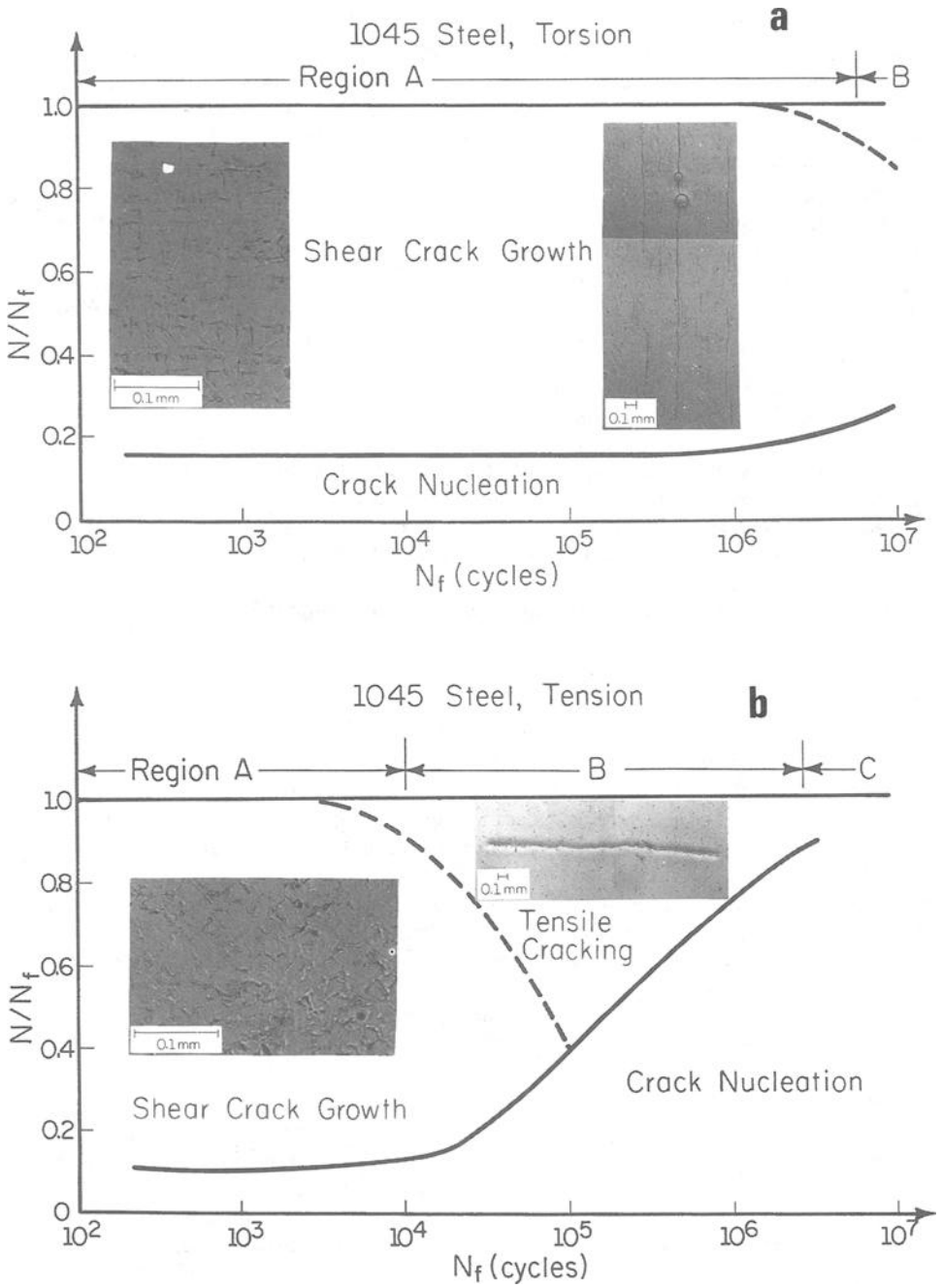

FIG. 5—*Cracking behavior observed in normalized 1045 steel:* (a) *torsion;* (b) *tension.*

Microcracks initiated on shear planes at high amplitudes in a manner representative of the R crack system. A very rapid linking of these microcracks occurred immediately prior to failure such that the failure crack was on tensile (Stage II) planes. At low strain amplitudes, cracks initiated on shear planes but progressive growth occurred on Stage II planes.

In Region C, crack nucleation plays the dominant role. This region has been extensively studied by others. Nisitani [*20*] and Nisitani and Kawano [*21*] made extensive observations of long-life fatigue failure in low-carbon steels. They concluded that, at the fatigue limit, cracks formed within single grains but were unable to propagate into neighboring grains because of the differences in crystallographic orientation. This long-life region should be controlled by cyclic shear stress. Tensile crack growth consumes a small portion of the total fatigue life. For low-ductility materials containing flaws, nonpropagating cracks should be considered and the maximum principal stress and flaw size are the controlling parameters.

Fatigue Models

Once the failure mode has been identified, an appropriate life estimation model can be selected. Each region requires a separate damage model based on the observed failure mode. The following damage models are proposed, although it is important to note that alternative models could have been chosen. The models selected, however, must incorporate the dominant or controlling parameters for each region, as those below do, such as shear strain for Region A, tensile strain for Region B, and shear stress or strain for Region C.

Region A

This region is dominated by plastic shear strains. Shear strains alone will not correlate the results from tension and torsion tests. Torsion tests have longer lives when compared to tension tests cycled with the same shear strain. The conceptual basis for a damage model is shown schematically in Fig. 6. During shear loading, the irregularly shaped crack surface results in frictional forces that will reduce crack tip stresses, thus hindering crack growth and increasing the fatigue life. Normal stresses and strains will separate the crack surfaces and reduce frictional forces. Fractographic evidence for this behavior is shown in Fig. 7 from tests on Inconel 718. The torsion test fractograph shows extensive rubbing and is featureless in contrast to the tension test fractograph where individual slip bands are observed on the fracture surface. The following damage model may be interpreted as the cyclic shear strain modified by the normal stress to include the crack closure effects described above.

$$\gamma(1 + k\sigma_{n,\max}/\sigma_y) = \tau_f'/G(2N)^b + \gamma_f'(2N)^c \tag{6}$$

This model was first proposed by Fatemi and Socie [*22*]. The right-hand side is the description of the strain-life curve generated from torsion testing with the following nomenclature: γ_f' is the shear fatigue ductility coefficient, c the fatigue ductility exponent, τ_f' the shear fatigue strength coefficient, b the fatigue strength exponent, G the shear modulus, and $2N$ the reversals to the formation of a surface crack 1 mm long. The terms on the left-hand side represent the loading parameters defined on the plane experiencing the largest range of cycle shear strain and have the following definitions: γ is the maximum shear strain amplitude, $\sigma_{n,\max}$ the maximum tensile stress perpendicular to plane of the maximum shear strain amplitude normalized by σ_y, the yield strength, to preserve the dimensionless features of strain; constant k is usually equal to unity.

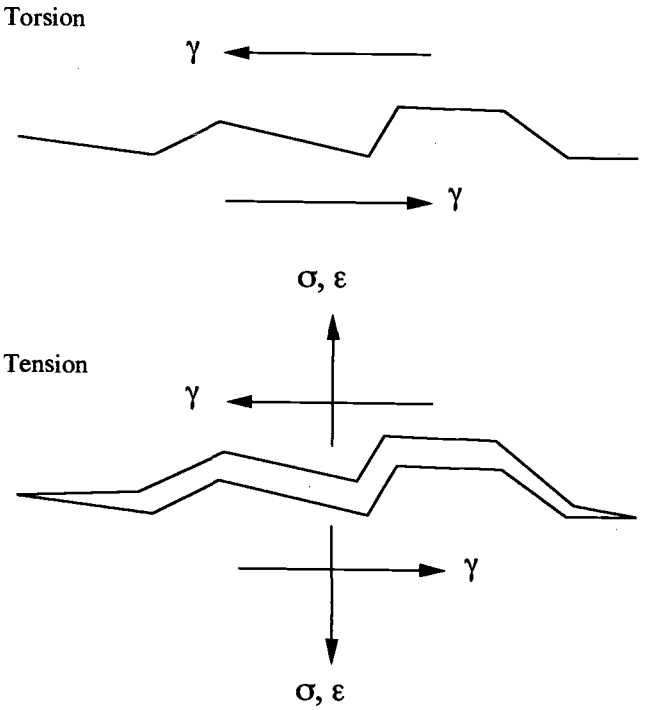

FIG. 6—*Schematic illustration of the effect of normal stress on shear cracks.*

Region B

Cracks nucleate in shear and then grow on a plane perpendicular to the maximum principal stress and strain. Many models have been proposed for this type of behavior. A model such as the one originally proposed by Smith et al. [*23*] for mean stress effects during uniaxial loading is appropriate. It has subsequently been successfully used for multiaxial loading by Socie [*24*], i.e.

$$\sigma_{\max}\varepsilon = \sigma_f'^2/E(2N)^{2b} + \varepsilon_f'(2N)^{b+c} \tag{7}$$

The right-hand side is a description of the uniaxial strain-life curve generated from uniaxial testing with the following nomenclature: ε_f' is the tensile fatigue ductility coefficient, c the fatigue ductility coefficient, σ_f' the tensile fatigue strength coefficient, b the fatigue strength exponent, E the elastic modulus, and $2N$ the reversals to the formation of a surface crack 1 mm long. The terms on the left-hand side represent the loading parameters and have the following definitions: ε is the maximum principal strain amplitude and $\sigma_{\max}$ the maximum stress on the maximum principal strain plane.

Region C

This region is typically called high-cycle fatigue. The majority of the fatigue life is consumed in crack nucleation on planes of maximum shear stress or strain for ductile materials. Findley's model can be combined easily with a description of the materials fatigue resistance to describe

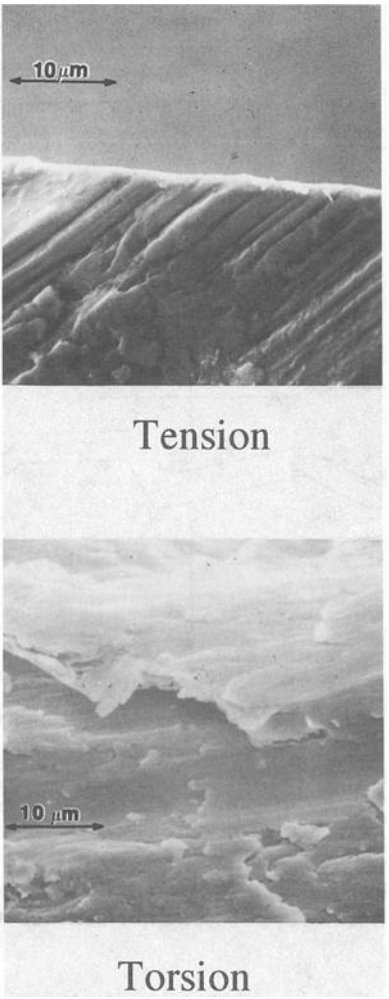

FIG. 7—*Comparison of fracture surfaces in tension and torsion.*

fatigue damage in the finite life region. McDiarmid's model could also be formulated for the finite life region.

$$\tau_a + k\sigma_{n,\max} = \tau'_f(2N)^b \tag{8}$$

The right-hand side of the equation is the elastic portion of the strain-life curve with the nomenclature the same as that given for Eq 6. The terms on the left-hand side of the equation represent the loading parameters defined on the plane experiencing the largest range of cyclic shear stress and have the following definitions: τ_a is the maximum shear stress amplitude and $\sigma_{n,\max}$ the maximum normal stress on the plane of maximum shear stress amplitude.

For low-ductility materials such as grey cast iron that are dominated by flaws, a shear model is inappropriate and consideration of the principal stress and flaw size is needed. Fracture

mechanics approaches are suggested. This will require consideration of small crack effects and fatigue-crack-growth threshold stress intensities.

A common feature of these damage models is that they are evaluated on a critical plane for crack nucleation and growth. They can easily be extended to complex nonproportional loading by evaluating the damage parameter on all planes to determine the plane experiencing the greatest fatigue damage and shortest expected fatigue life.

Influence of Mean Stress

Several sets of test data are reviewed to demonstrate the effect of mean stress. Inconel 718 specimens were tested with six loading histories that are shown in Fig. 8. The loading histories are shown in terms of the applied shear and axial strains on tubular specimens. Details of the testing are given in Ref *25*. They were designed to have the same maximum shear strain amplitudes. Histories D, E, and F have cyclic proportional straining with a static mean strain and would not be classified as nonproportional straining for purposes of fatigue analysis. The experiments resulted in nearly the same maximum shear stress amplitudes, equivalent stress and strain amplitudes, and plastic work. The major difference between the loading histories is the normal stresses and strains across the plane of maximum shear strain. Observations of the specimens showed that all of the tests had cracks on the plane of maximum shear strain amplitude. Mohr's circle of strain, Fig. 9, shows that two perpendicular planes experience the same maximum shear strain amplitude. The maximum principal strain is observed on only one plane. If fatigue damage was determined by shear strain alone, the two maximum shear strain planes would be damaged equally since the strain state is the same. Recall that the sign of the shear strain has no physical meaning and is used only as a sign convention. Figure 10 shows the cracks that are formed for these histories. The orientation of the crack pictures is the same as the shear planes shown in Fig. 9. Except for loading history C, cracks form on only one of the two maximum shear strain planes. History C represents compression loading where cracks

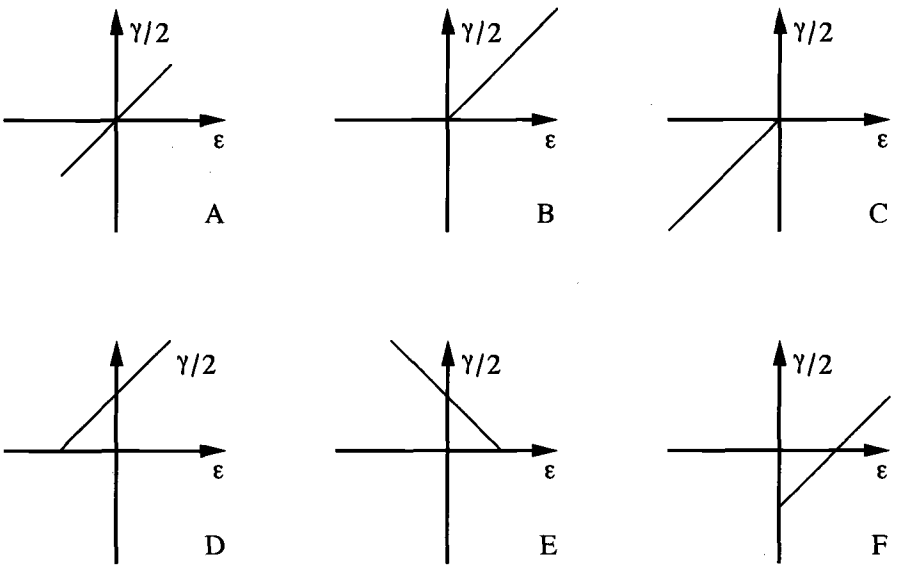

FIG. 8—*Loading histories for mean stress tests.*

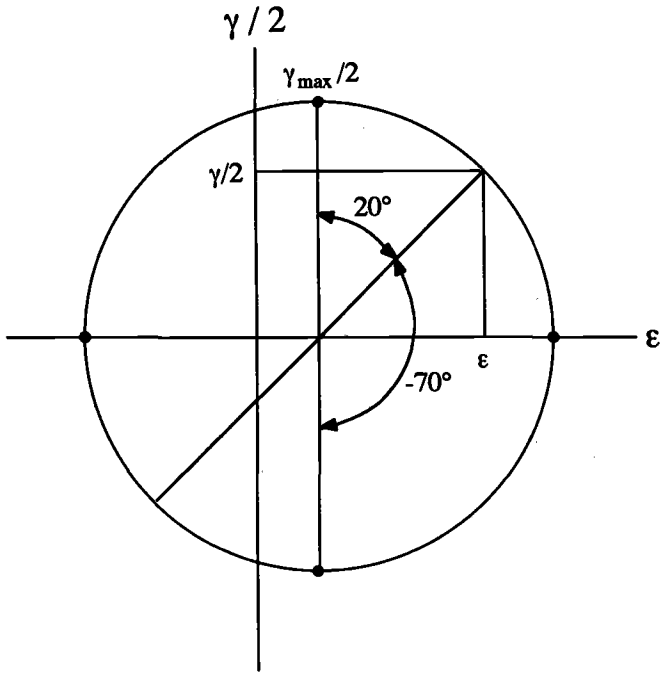

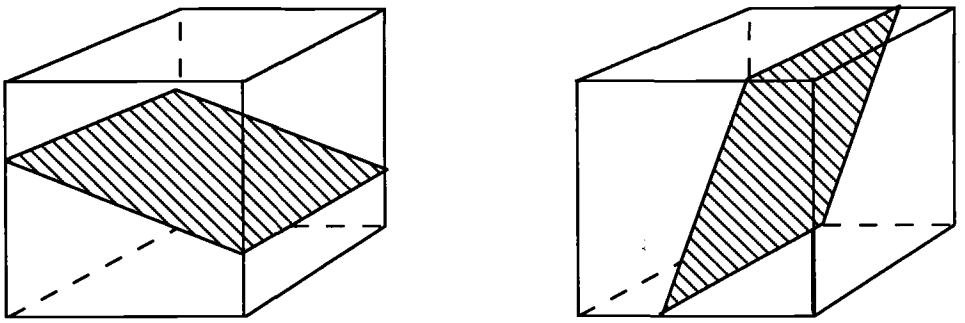

FIG. 9—*Mohr's circle of strain.*

form on both shear planes. The compressive normal stress inhibits growth of the initial cracks, which allows more time for cracks to form on the second shear plane. The shear plane for History E is $-20°$ rather than $20°$ because the loading direction is reversed from the other histories. Fatigue lives are given in Fig. 11. Even in a proportionally strained test, the stresses do not pass through zero at the same time since the principal axes of stress and strain are not coincident. Thus, mean stresses on the two shear planes are not equal. The open symbols in Fig. 11 represent the maximum normal stress on the shear plane, and the solid symbols rep-

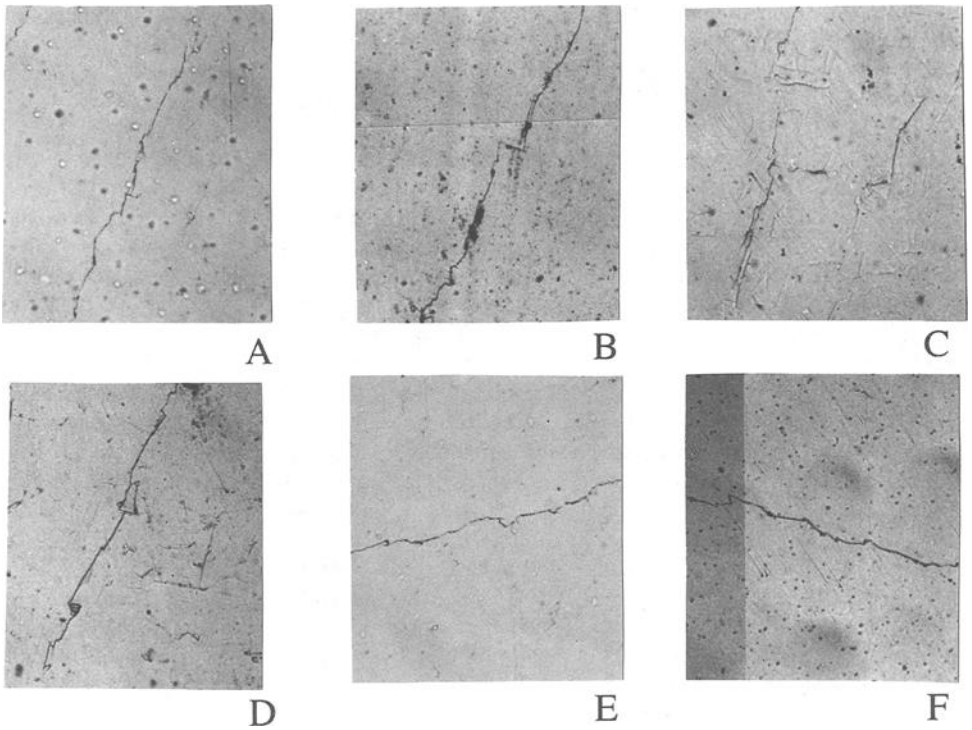

FIG. 10—*Crack observations for the histories in Fig. 8.*

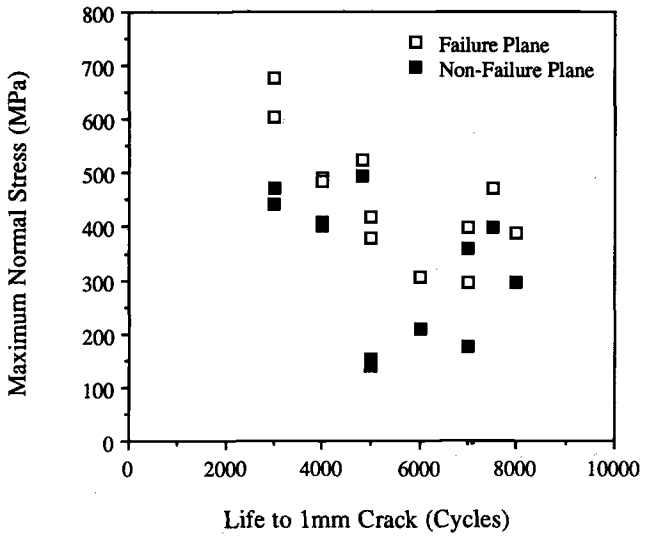

FIG. 11—*Mean stress on the maximum shear strain amplitude planes and fatigue life.*

resent the lower normal stress on the other shear plane. Pairs of symbols at the same lives correspond to perpendicular planes for the same test. These data clearly show that, for materials that crack in Mode II, the normal stresses determine the preferred maximum shear strain amplitude plane for crack nucleation and early growth as well as the fatigue life and distribution of cracks.

The results of monitoring the failure crack lengths for two decades of length are shown in Fig. 12. The effect of normal stress across the plane of the crack is evident from the differing rates of growth for the tests with positive and negative mean stress. Crack surfaces are irregularly shaped (see Fig. 6) as the crack grows through adjacent grains. This mechanical interlocking allows the crack surface to transmit shear loads. Tensile mean stresses reduce this effect and result in a higher growth rate.

Mean stress affects not only the growth rate but also the distribution of cracks. Two tests, zero to tension (see Figs. 8*b* and 10*b*) and zero to compression (see Figs. 8*c* and 10*c*), are considered here. In the compression test, the normal mean stress on both shear planes is compressive. Multiple cracking is observed on both shear planes. Many cracks nucleate but have difficulty growing. Fatigue lives are greater so that more cracks have an opportunity to nucleate in grains that have crystallographic slip planes oriented near the maximum shear plane. Finally, a dominate crack forms on the shear plane that has the lowest compressive mean stress and grows to failure. In the tension loading case, cracks are observed on only one of the two shear planes. The first cracks to nucleate can easily grow to failure. Little secondary cracking is observed. Extensive observations have been made for these tests. Mean stresses have a lesser influence on the initiation of a crack if crack initiation is defined on the order of 10 μm, which is the size of the smaller grains in the material.

The stress and strain ranges as well as the equivalent stress and strain ranges are the same for all six loading histories. Mean stress effects have been demonstrated even in the life regime controlled by plastic strain. Energy-based approaches such as plastic work and strain approaches that do not consider mean stresses predict that all the loading histories will have the same fatigue life. This is clearly not the case, and the use of these approaches must be restricted. Hydrostatic stress corrections for the strain theories have been proposed. Hydro-

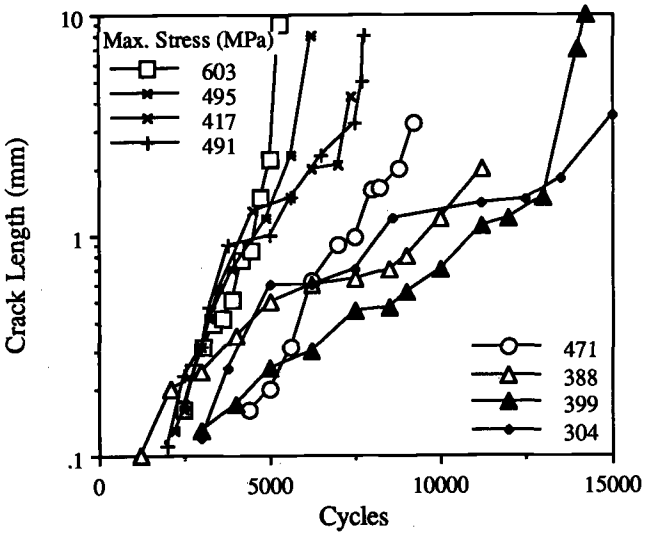

FIG. 12—*Crack growth data showing mean stress influence.*

static stress represents the average mean stress on the shear planes. This implies that the effects of a tensile mean stress on one shear plane could be eliminated by a compressive mean stress of the same magnitude on the other shear plane. The photographs in Fig. 10 show a clear preference for cracks to nucleate and grow on one of the two shear planes. This is the plane with the maximum tensile mean stress. An additional discussion of this topic will be given in the next section of the paper.

Two loading cases that result in the same shear and normal stresses and strains are shown in Fig. 13. On the top left, consider a tubular specimen loaded in strain control from zero to some maximum tensile strain denoted Case T. This type of loading results in a mean axial stress of σ_0 denoted with a single-ended arrow and a cyclic strain, $\Delta\epsilon/2$, that is denoted by a double-ended arrow. Now consider a second test, not shown in Fig. 13, that is loaded with the same axial strain amplitude as the first but in completely reversed loading, Case R. No mean stress is present in the axial direction. This test will have a longer life than the test with the mean stress, Case T. A third test is then performed, Case H, where the axial strains are again completely reversed. The mean stress observed in the first test is now applied as a hoop stress to the tubular specimen. Both Case T and Case H result in the same shear damage parameter even though in one case the mean stress and cyclic stress are in the same direction and in the other the mean stress is oriented 90° from the cyclic stress. Tensile damage parameters for the two tests are shown in the bottom half of the figure. The maximum stress in Case T is higher than Case H. The mean stress for Case H would not influence the fatigue life in a tensile damage model. Results for these tests are given in Table 1. At higher strains, the fatigue lives for Case T and Case H are nearly the same and differ significantly from Case R, indicating that mean stresses applied in the hoop direction are just as damaging as mean stresses in the loading direction. This is consistent with the shear damage model where both the tension and hoop mean stress have the same resolved normal stress on the shear plane. The tensile mean stress is more damaging than the hoop mean stress at lower strain amplitudes. The fatigue lives for Case H are nearly the same as Case R. This behavior may be expected if the fatigue damage map shown in Fig. 4 is considered. A transition from shear-dominated behavior to tensile-dominated behavior occurs at about 10^6 cycles in tension loading. The failure crack is shown in Fig. 14 where the arrow indicates the start of the crack. The transition suggested by the fatigue damage map is observed from shear to tensile cracking.

With this background, we are now in a position to suggest a series of critical or descriminating tests to clearly establish the influence of mean stresses. Consider a tubular specimen that can be loaded in tension, torsion, and internal pressure. The baseline test will be torsion. Materials that exhibit extensive Mode II shear cracking are expected to have a distribution of damage as shown in Fig. 15. The cyclic strains are shown as double-ended arrows. Both shear and tensile strain planes are indicated by dashed lines. Expected cracking directions are also indicated. Adding static tension would introduce a tensile stress on only one of the two shear

TABLE 1—*Mean stress results.*

		Fatigue Life, cycles		
$\Delta\epsilon/2$	σ_0, Mpa	Case T, $R_\epsilon = 0$	Case H, $R_\epsilon = -1 + \sigma_0$	Case R, $R_\epsilon = -1$
0.005	270	4 425	6 735	14 420
		9 768	7 221	17 430
0.0025	517	47 530	142 100	187 791
		65 960	165 100	237 702

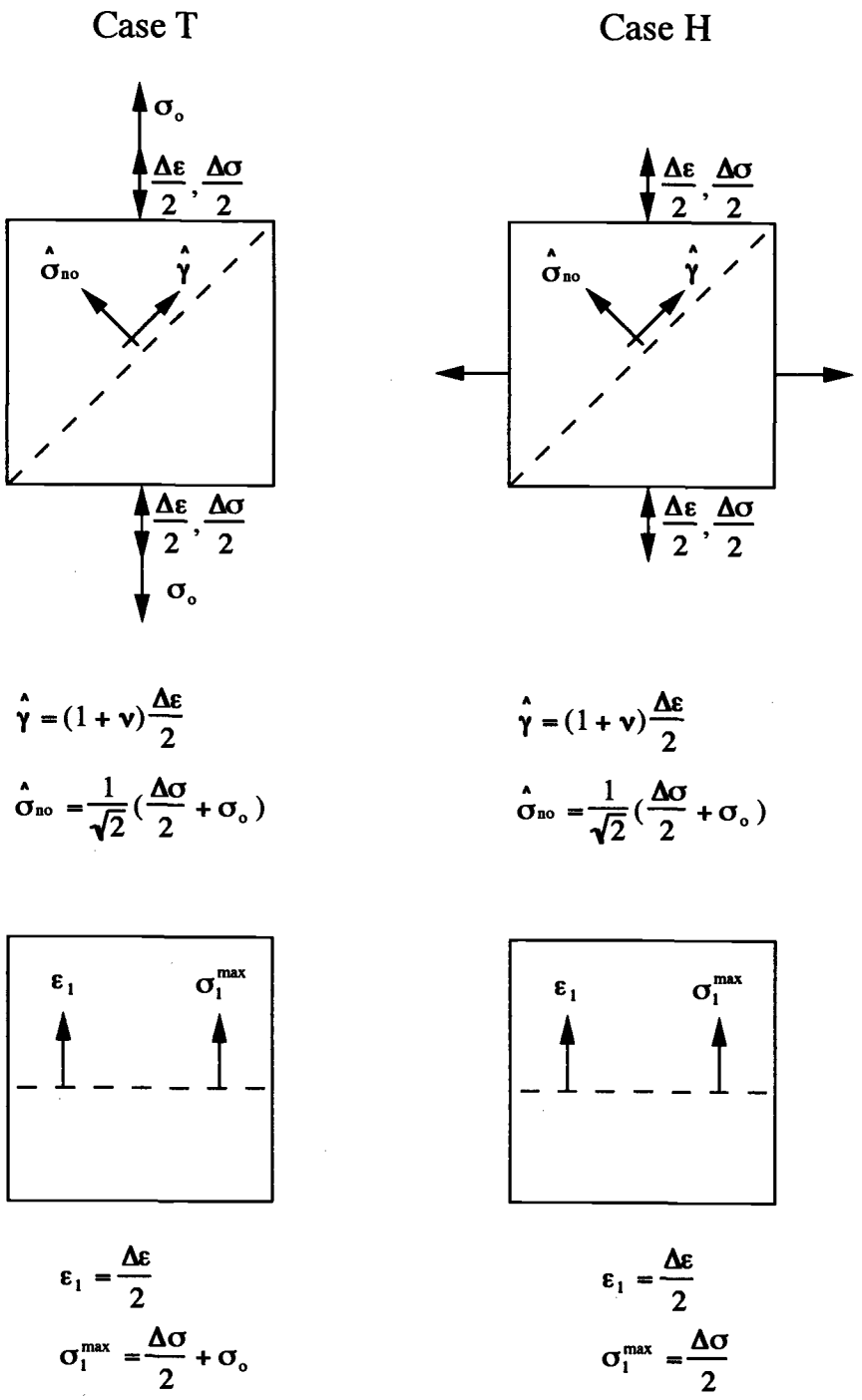

FIG. 13—*Mean stress illustration.*

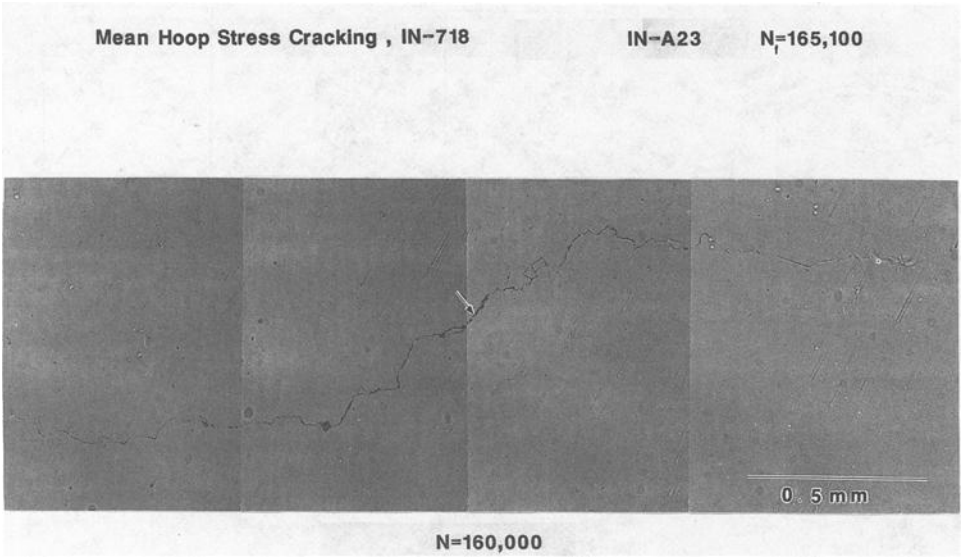

FIG. 14—*Failure crack for mean stress test.*

planes indicated by a single-ended arrow in Fig. 16 and be expected to reduce the fatigue life from the case of torsion alone. Static tension will not influence the stress on the vertical shear plane, and no damage is expected on this plane. Static tension will result in increased stresses on both tension planes. The addition of static tension will be detrimental for both materials that fail in shear and for materials that fail in tension. Now consider the case of static compression with cyclic torsion given in Fig. 17. The horizontal shear plane will have a compres-

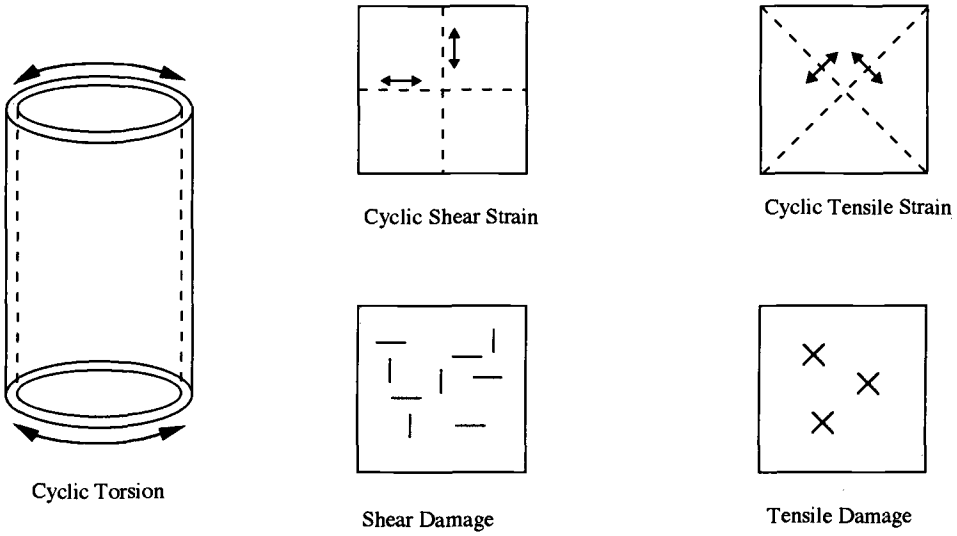

FIG. 15—*Torsion loading example.*

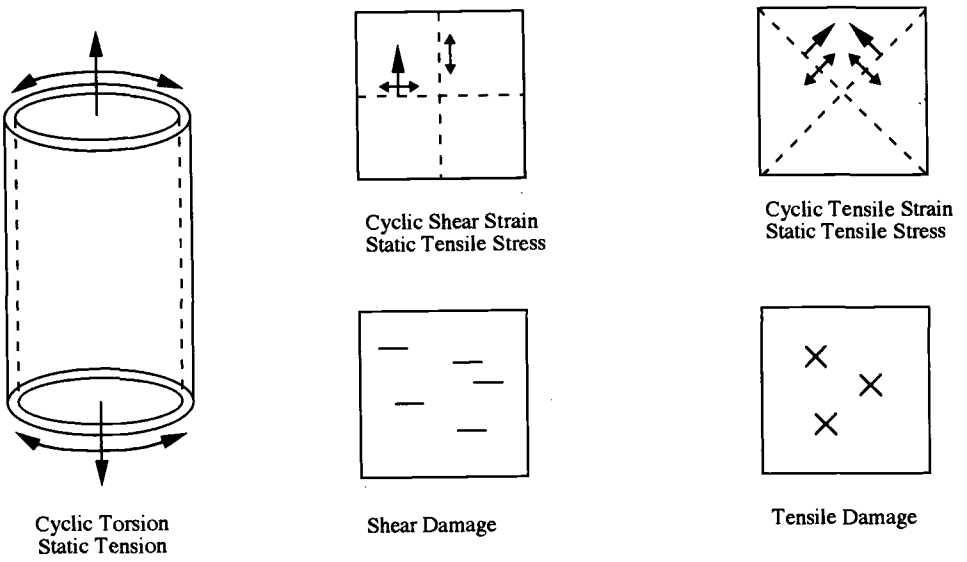

FIG. 16—*Torsion with static tension.*

sive stress, but this beneficial compressive stress will not increase the fatigue life because the material will fail on the vertical shear plane. Both tensile planes will see the beneficial effect of the compressive stress. This critical test suggests that the compressive stress will not have an influence on the fatigue life for materials that fail in shear and have a large influence for materials that fail in tension. Finally, the fourth test case is presented in Fig. 18. Internal pressure is added to produce a hoop tension stress and a compression stress generated by the axial load.

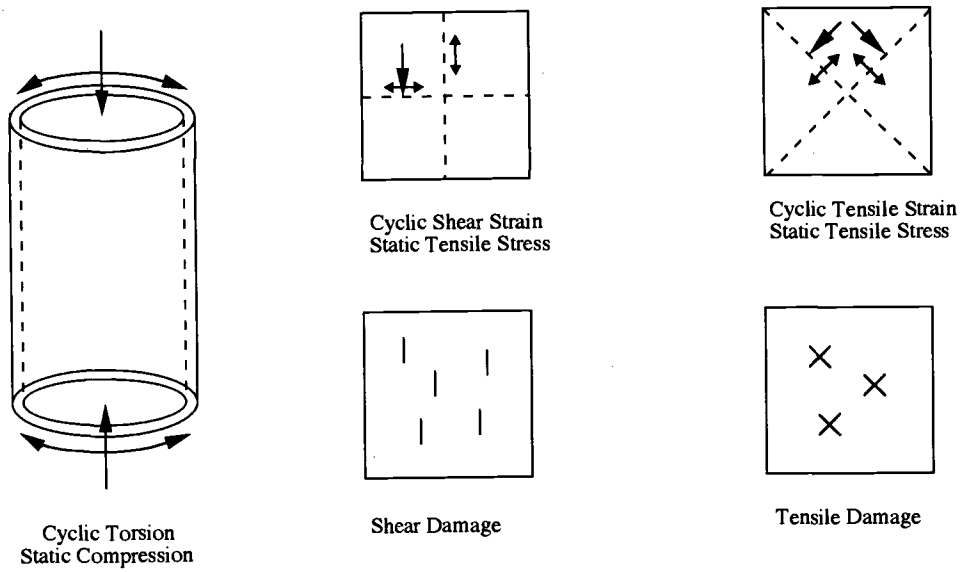

FIG. 17—*Torsion with static compression.*

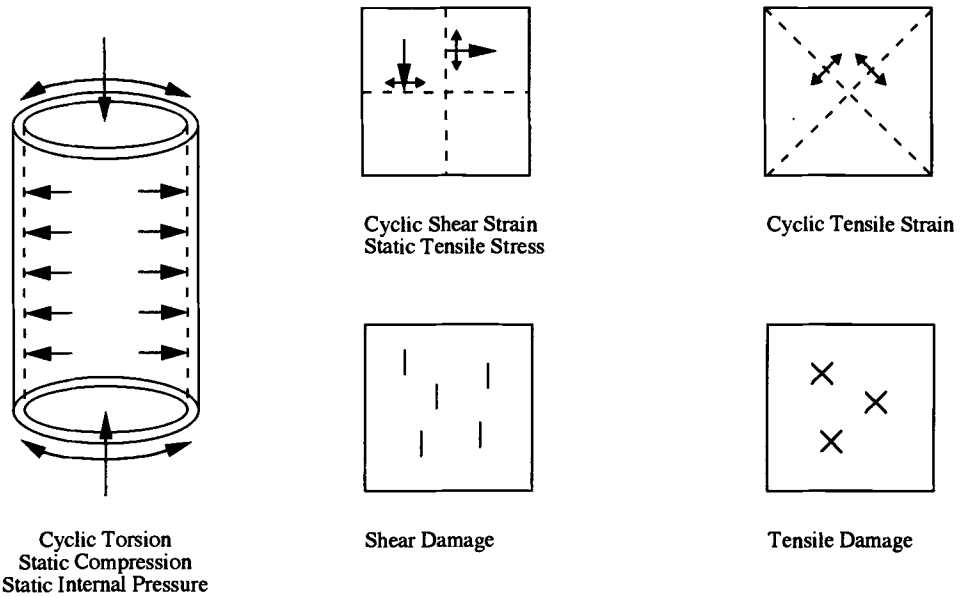

FIG. 18—*Torsion with static compression and internal pressure.*

In this case the tensile stress on the vertical shear plane is detrimental and the compressive stress on the horizontal plane is beneficial. Naturally the expected fatigue life will be reduced and failure will be on the vertical plane. The two stresses will combine and cancel each other on the tension plane. In this critical test, the shear damage material is expected to show a large influence of the static stresses and the tensile material should be unaffected. This is exactly opposite to the loading case presented in Fig. 16. Fatigue models must be able to distinguish between these two loading cases and materials. Results for tests conducted on Inconel 718 are given in Table 2 and confirm the discussion above for materials that fail in shear. Unfortunately, no test data are yet available for materials such as cast iron that fail in tension.

A series of mean stress tests has been reported by Ei-Magd and Mielke [*26*] for a low-carbon St 60 steel with a tensile strength of 765 MPa. Tests were conducted on tubular specimens subjected to tension and static internal pressure to introduce a tensile mean hoop stress. Results are shown in Fig. 19. Tests were conducted to establish the influence of mean stress on the fatigue limit. The vertical scale is presented as the alternating axial stress, σ_A, normalized by the fatigue strength, σ_w. The horizontal scale is the hoop mean stress, σ_{Hm}, normalized by the ultimate strength. Data are presented for axial mean stresses, σ_{Am}, normalized by the tensile

TABLE 2—*Torsion with static mean stresses.*

Load Case	$\Delta\gamma/2$	σ_{hoop}, MPa	σ_{axial}, MPa	N_f, cycles
Figure 15	0.0054	0	0	41 400
	0.0054	0	0	45 200
Figure 16	0.0054	450	0	10 300
Figure 17	0.0054	0	−500	50 000
Figure 18	0.0054	450	−500	11 200

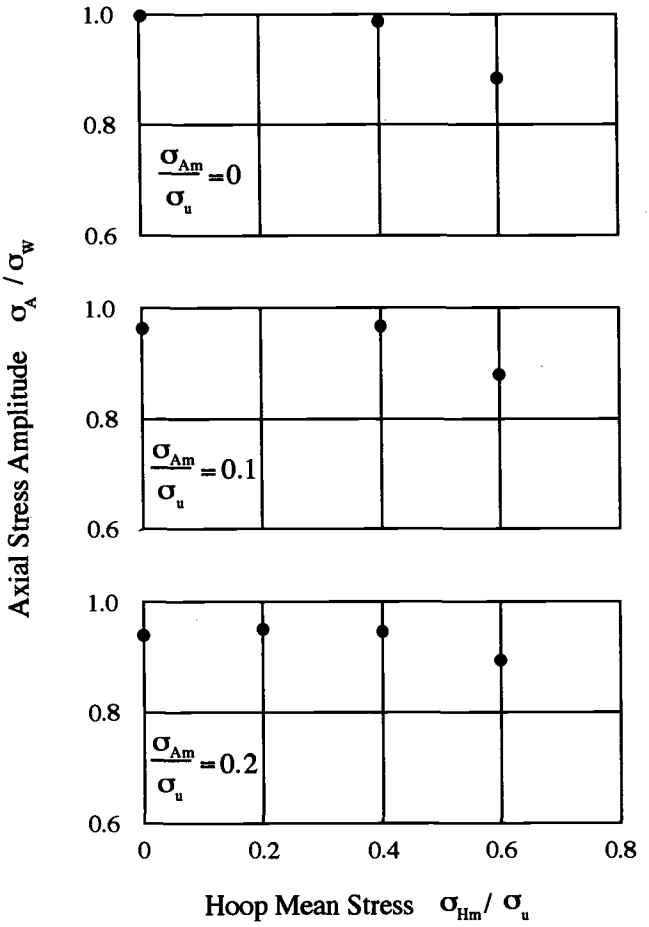

FIG. 19—*Fatigue strength with a hoop mean stress.*

strength of 0, 0.1, and 0.2. The test data show that there is a decrease in the fatigue limit or alternating stress with increasing tensile mean stresses. The test data show little influence of the hoop mean stress until the stresses exceed the monotonic yield strength of the material. In this case, plastic deformation occurs in the hoop direction in these stress-controlled tests, and cyclic ratcheting must be considered. The damage map given in Fig. 5 suggests that a tensile failure mode is likely in this material so that these test results would be expected to be the same as those for Inconel 718 at long lives.

Nonproportional Loading

It has been reported [*27*] that in-phase loading is more damaging at low-strain amplitudes and out-of-phase loading is more damaging at high-strain amplitudes. Strain histories for these two cases are given in Fig. 20. These statements are usually made by comparing the amplitude of the applied torsion and tension or bending strains. Both maximum shear strain range and maximum principal strain range are proportional to the diameter of the circle for 90° out-of-

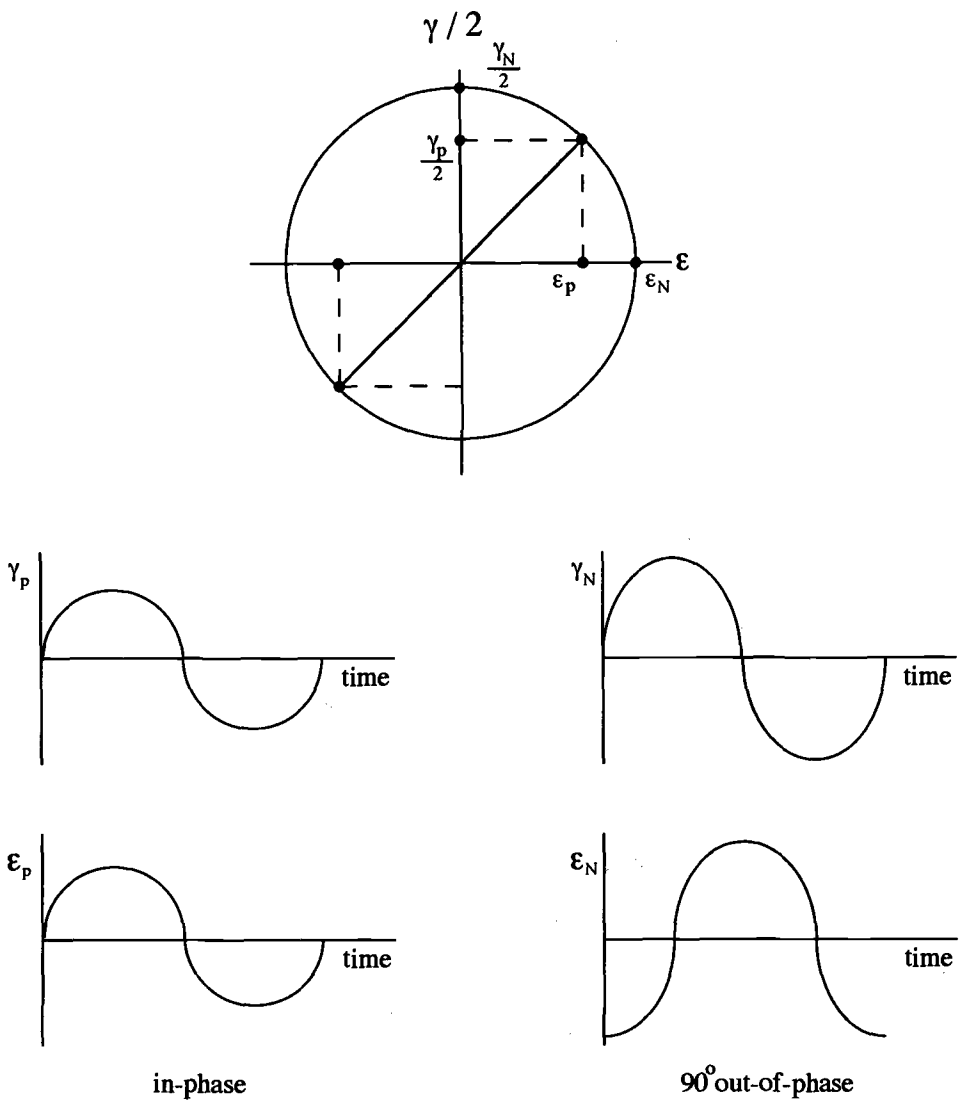

FIG. 20—*In-phase and out-of-phase loading examples.*

phase loading and to the length of the line for in-phase loading. To achieve the same strain range, the applied tension and torsion strains for nonproportional loading, ϵ_N and γ_N, must be increased relative to the proportional loading case, ϵ_P and γ_P. Out-of-phase loading is expected to be less damaging if the comparison is based on applied strains because the maximum strains are smaller. Comparisons should be based on the basis of the same maximum strain rather than on the basis of the applied strains. This will show that out-of-phase loading is always equally or more damaging. For higher strains where plastic strains are large, out-of-phase loading is more damaging than in-phase loading even if the comparison is made on the basis of maximum strain. Results for 304 stainless steel are given in Table 3 for in-phase and out-of-

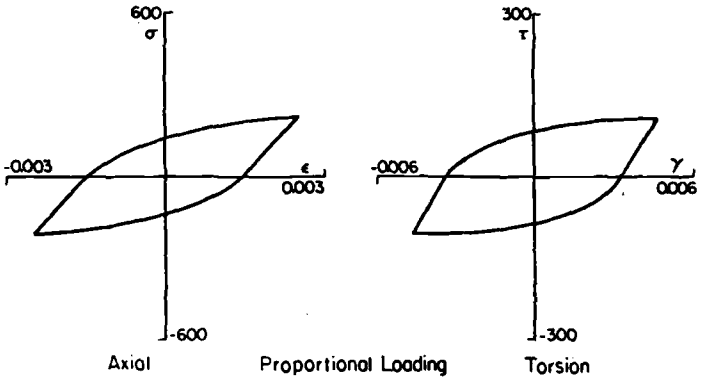

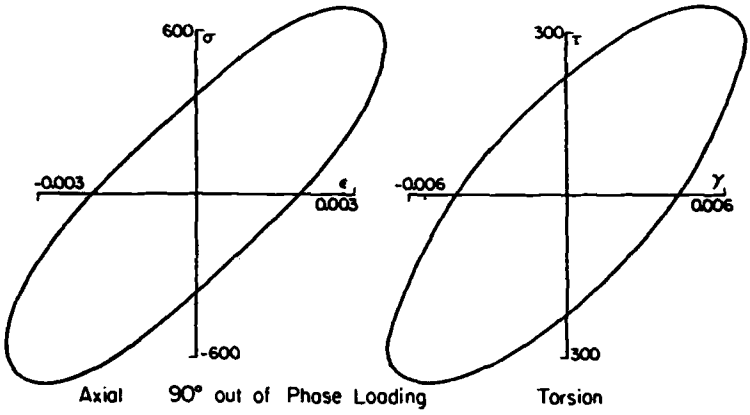

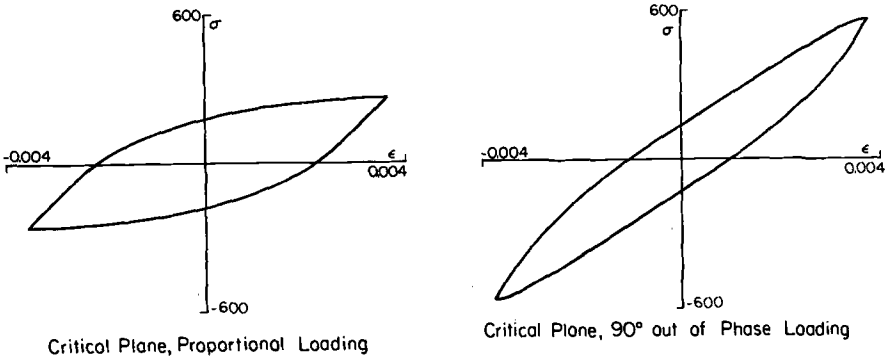

FIG. 21—*Axial and torsional stress strain response for in-phase and out-of-phase loading.*

TABLE 3—*In-phase and out-of-phase results.*

Load Case	$\Delta\epsilon/2$	$\Delta\gamma/2$	$\Delta\sigma/2$, MPa	$\Delta\tau/2$, MPa	N_f, cycles
Proportional	0.002 5	0.0043	184	109	53 000
	0.002 5	0.0043	176	101	52 900
	0.001 45	0.0023	161	89	440 000
	0.001 45	0.0023	157	90	356 000
90° out of phase	0.003 5	0.0061	477	267	3 560
	0.003 5	0.0061	457	256	3 730
	0.002 0	0.0035	300	168	50 000
	0.002 0	0.0035	307	176	45 000

phase loading. Out-of-phase loading reduces the fatigue lives by more than a factor of ten. Axial and torsional stress strain response for these two tests are shown in Fig. 21. The stabilized stress for the out-of-phase loading is increased by about a factor of two as shown in the von Mises effective stress strain curves in Fig. 22 for the two loading cases. Note that the in-phase loading test has the larger plastic strain as indicated by the width of the hysteresis loop than the out-of-phase test. It also has a longer fatigue life which conflicts with the widely held notion that plastic strain alone is responsible for fatigue damage. Cyclic stress amplitude plays an important role and cannot be neglected. These test data have been successfully correlated with Eq 7 [*24*]. The cracking behavior observed for this material, Fig. 3, indicates that a tensile strain damage model is appropriate. Nonproportional hardening is included in the damage model by means of the maximum stress term. The nucleation and early growth of small cracks will be enhanced when the cyclic stresses are doubled.

The variation in strain amplitude on each plane is shown in Fig. 23 for the 90° out-of-phase loading history. The 0° plane is perpendicular to the axis of the specimen. Note that the tensile strain range is nearly the same for all planes in the material. The damage parameter is nearly

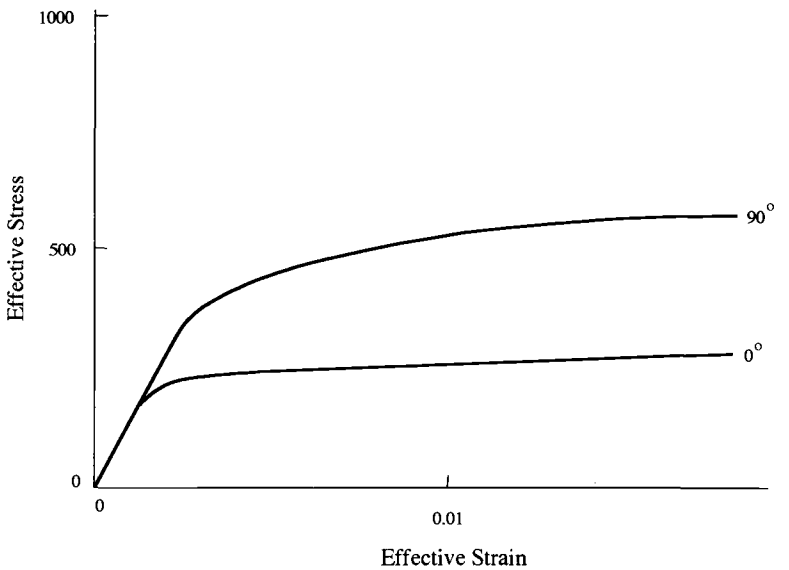

FIG. 22—*Effective stress-strain curve.*

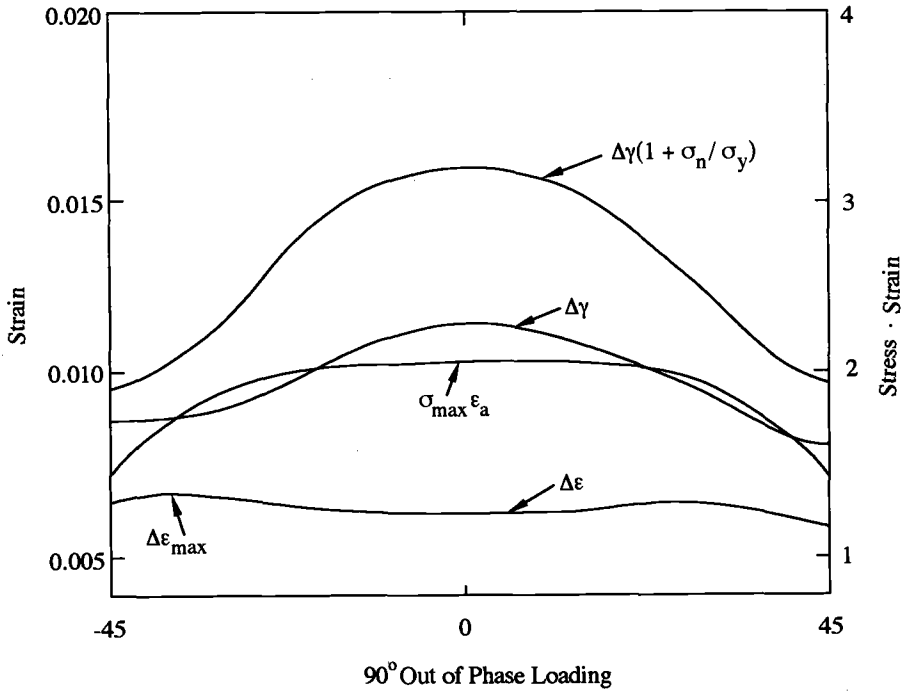

FIG. 23—*Variation of strain amplitude and damage parameter.*

constant for all planes ranging from −20 to +20° and reaches a maximum on the 0° plane. Cracks would be expected to form on any of these planes.

Materials such as the 300 series stainless steels show a large amount of nonproportional cyclic hardening. The flow stress can increase by a factor of two. Low-carbon steel such as the 1045 steel reported here has nonproportional hardening of about 20%. Aluminum alloys have not exhibited the additional cyclic hardening found in the other materials. This behavior is related to the slip characteristics of the deformation [*28*]. Nonproportional softening has not been observed in any material.

A second type of nonproportional loading involves cases where the cyclic strains are proportional with static stresses and/or strains in a different direction. An example would be the torsion tests with static axial strain shown in Fig. 16. The strain history is plotted in Fig. 24. The maximum shear strain direction changes from +22.5° at the maximum applied torque to −22.5° at the minimum applied torque. A plot of the cyclic shear strain, however, shows that the maximum range occurs on the 0 and 90° planes. These planes have the greatest fatigue damage. This loading history may be considered proportional cyclic straining. Additional cyclic hardening is not observed. Therefore, these types of loading histories should be treated as proportional straining for purposes of fatigue analysis.

Variable Amplitude Loading

Variable amplitude multiaxial loading is essentially an issue of how cycles will be identified and damage computed for a complex loading history. Stress strain behavior can be modeled for variable amplitude loading with existing nonproportional cyclic plasticity models. Inter-

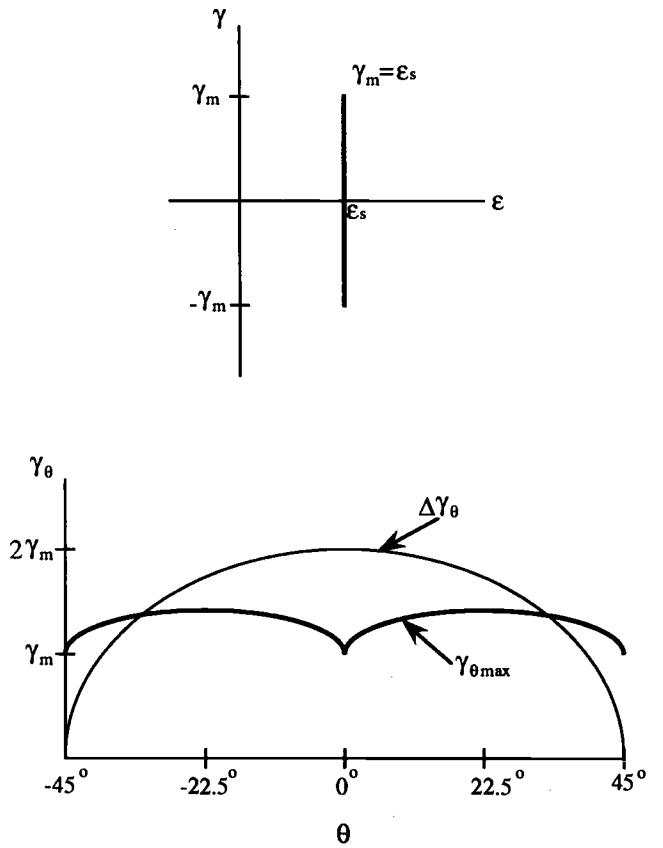

FIG. 24—*Difference between maximum shear strain and maximum shear strain amplitude direction.*

pretation of the damage parameter for complex loadings poses some problems. For simple short loading histories such as the out-of-phase tests, the maximum value of the tensile strain amplitude and the damage parameter are usually on the same plane. Similarly, the maximum shear strain amplitude and damage parameter are also on the same plane. For complex loading the maximum shear strain amplitude and maximum value of the damage parameter may be on different planes. Should damage be calculated on the planes that experience the maximum strain amplitudes or should it be computed on the basis of the maximum value of the damage parameter? A simple example shows the need to compute damage based on the maximum value of the damage parameter. Consider a few large torsion cycles applied to a tubular specimen followed by a large number of tension cycles at a smaller strain range. The plane experiencing the largest range of strain would be at 0 and 90° from the torsion cycles. Failure, however, would be expected to occur on the 45° planes from all of the tension cycles.

While this interpretation is useful and leads to reasonable life estimates, it is inconsistent with some of the experimental observations. Consider the case of simple torsion loading and the shear damage parameter given in Eq 6. The critical plane is predicted to be 10° rather than 0 and 90° as expected. Mohr's circle for this loading is given in Fig. 25. The shear strain on the 10° plane is 6% less than the maximum. The normal stress on the 10° plane is increased from 0 to 35% of the maximum stress. As a result the damage parameter reaches a maximum on

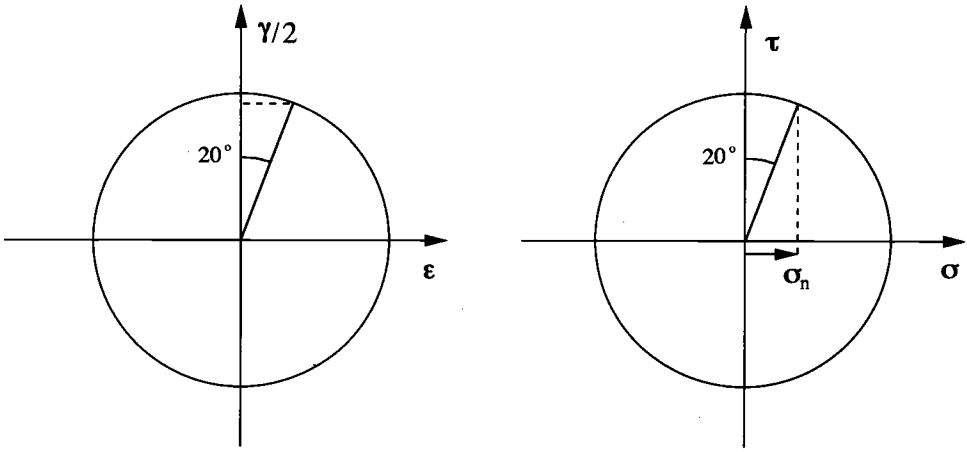

FIG. 25—*Mohr's circle for torsion.*

the 10° plane. Experimental observations show that cracks form on the 0 and 90° planes in torsional loading. Perhaps the exact form of the damage parameter needs to be modified to account for this difference.

Hayhurst et al. [*29*] and McDowell et al. [*30*] have conducted these experiments with alternating tension and torsion loading. Tests were conducted on 304 stainless steel. Forty cycles of axial strain were followed by 40 cycles of shear strain of the same equivalent strain amplitude. At failure, two distinct crack systems were observed, one for the axial strains and one for the shear strains. The fatigue life for this combined test was the same as that for an axial strain only test. No interaction between the damage systems was observed. This suggests each plane accumulates damage independently from the others. This leads to the conclusion that damage should be tracked on each plane by considering the maximum value of the damage parameter.

Two-level tension and torsion testing has been conducted by Robillard and Cailletaud [*31*]. Torsion cycles followed by tension cycling to failure followed a linear damage summation. Shear cracks nucleate on planes parallel and perpendicular to the specimen axis. These cracks can then grow in Mode I when the tension cycles are applied. Tension cycles followed by torsion cycling resulted in damage summations that are greater than one. Here, the cracks that nucleated on 45° planes during the tension cycling do not propagate during the subsequent torsion loading. Damage should be tracked on each potential failure plane. These experiments clearly demonstrate that the interaction and growth of the damage systems must be tracked on each potential failure plane. Few models exist for tracking the growth of damage.

Summary

Observations have been presented to support the hypothesis that cracks nucleate and grow on critical planes in materials. Depending on the material, these critical planes may be planes of either shear strain or tensile strain. Stresses play an important role and cannot be ignored. Tensile mean stresses normal to the critical plane enhance crack growth and reduce fatigue life. Additional cyclic hardening during nonproportional loading increases the stress amplitude during strain-controlled testing and reduces the fatigue life. This work has identified and quantified the important loading variables. Damage models for multiaxial fatigue have been developed for simple loading histories. Future work should be directed towards developing models for the growth and interaction of damage.

Acknowledgments

The author would like to thank all the graduate students who participated in this research work. Without their contributions, this work would not have been possible. This work was completed over a ten-year period with funding provided by General Electric, Allison Gas Turbine, National Science Foundation, NASA, and the Department of Energy.

References

[1] Ewing, J. A. and Humfrey, J. C. W., "The Fracture of Metals under Repeated Alternations of Stress," *Philosophical Transactions of the Royal Society,* Vol. 210, 1903, pp. 241–253.

[2] Fine, M. E., "Fatigue Resistance of Metals," *Metallurgical Transactions A,* Vol. 11A, 1980, pp. 365–379.

[3] Fine, M. E. and Ritchie, R. O., "Fatigue Crack Initiation and Near Threshold Crack Growth," *Fatigue and Microstructure,* American Society for Metals, Metals Park, OH, 1979, p. 245.

[4] Laird, C., "The Influence of Microstructure on the Mechanisms of Fatigue Crack Propagation," *Fatigue Crack Propagation, ASTM STP 415,* 1967, pp. 131–180.

[5] Gough, H. J., Pollard, H. V., and Clenshaw, W. J., "Some Experiments on the Resistance of Metals Under Combined Stress," Ministry of Supply, Aeronatical Research Council Reports and Memoranda No. 2522, HMSO, London, 1951.

[6] Stulen, F. B. and Cummings, H. N., "A Failure Criterion for Multiaxial Fatigue Stresses," *Proceedings,* ASTM, Vol. 54, 1954, pp. 822–835.

[7] Findley, W. N., Coleman, J. J., and Handley, B. C., "Theory for Combined Bending and Torsion Fatigue with Data for 4340 Steel," *Proceedings* International Conference on Fatigue of Metals, The Institution of Mechanical Engineers, New York, 1956, pp. 150–157.

[8] Findley, W. N., "A Theory for the Effect of Mean Stress on Fatigue of Metals Under Combined Torsion and Axial Load or Bending," *Journal of Engineering for Industry,* 1959, pp. 301–306.

[9] McDiarmid, D. L., "Failure Criteria and Cumulative Damage in Fatigue Under Multiaxial Stress Conditions," Ph.D. thesis, Department of Mechanical Engineering, The City University, London, 1972.

[10] McDiarmid, D. L., "A General Criterion for High Cycle Multiaxial Fatigue Failure," *Fatigue and Fracture of Engineering Materials and Structures,* Vol. 14, No. 4, 1990, pp. 429–454.

[11] Brown, M. W. and Miller, K. J., "A Theory for Fatigue Failure Under Multiaxial Stress Strain Conditions," *Proceedings,* Institute of Mechanical Engineers, Vol. 187, No. 65, 1973, pp. 745–755.

[12] *Multiaxial Fatigue, ASTM STP 853,* K. J. Miller and M. W. Brown, Eds., ASTM, Philadelphia, 1985.

[13] *Biaxial and Multiaxial Fatigue,* EGF3, M. W. Brown and K. J. Miller, Eds., Mechanical Engineering Publications, London, 1989.

[14] Kussmaul, K. F., McDiarmid, D. L., and Socie, D. F., *Fatigue under Biaxial and Multiaxial Loading,* ESIS 10, Mechanical Engineering Publications, London, 1991.

[15] Hua, C. T. and Socie, D. F., "Fatigue Damage in 1045 Steel Under Variable Amplitude Loading," *Fatigue and Fracture of Engineering Materials and Structures,* Vol. 8, No. 2, 1985, pp. 101–114.

[16] Socie, D. F., Kurath, P., and Koch, J. L., "A Multiaxial Fatigue Damage Parameter," *Biaxial and Multiaxial Fatigue,* EGF3, Mechanical Engineering Publications, London, 1989, pp. 535–550.

[17] Bannantine, J. A. and Socie, D. F., "Observations of Cracking Behavior in Tension and Torsion Low Cycle Fatigue," *Low Cycle Fatigue, ASTM STP 942,* 1985, pp. 899–921.

[18] Plumbridge, W. J., "Review: Fatigue Crack Propagation in Metallic and Polymeric Materials," *Journal of Materials Science,* Vol. 7, 1972, pp. 939–962.

[19] Marco, A. M. and Starkey, W. L., "A Concept of Fatigue Damage," *Transactions of ASME,* Vol. 76, 1954, pp. 627–632.

[20] Nisitani, H., *Bulletin of JSME,* Vol. 11, No. 48, 1968, pp. 947–957.

[21] Nisitani, H. and Kawano, K., *JSME,* Japanese Society of Mechanical Engineers, Vol. 15, No. 82, 1972, pp. 433–438.

[22] Fatemi, A. and Socie, D. F., "A Critical Plane Approach to Multiaxial Fatigue Damage Including Out-of-Phase Loading," *Fatigue and Fracture of Engineering Materials and Structures,* Vol. 11, 1988, pp. 149–165.

[23] Smith, R. N., Watson, P., and Topper, T. H., "A Stress-Strain Parameter for the Fatigue of Metals," *Journal of Materials,* Vol. 5, No. 4, 1970, pp. 767–778.

[24] Socie, D. F., "Multiaxial Fatigue Damage Models," *Journal of Engineering Materials and Technology,* Vol. 109, 1987, pp. 293–298.

[25] Socie, D. F. and Shield, T. W., "Mean Stress Effects in Biaxial Fatigue of Inconel 718," *Journal of Engineering Materials and Technology,* Vol. 106, 1984, pp. 227–232.
[26] El-Magd, E. and Mielke, S., "Dauerfestigkeit bei uberlangerter zweiachsiger statischer Beanspruchung," *Konstruktion,* Vol. 26, 1977, pp. 253–257.
[27] Garud, Y. S., "A New Approach to the Evaluation of Fatigue under Multiaxial Loadings," *Methods for Predicting Material Life,* ASME, New York, 1979, pp. 247–263.
[28] Doong, S. H., Socie, D. F., and Robertson, I. M., "Dislocation Substructures and Nonproportional Hardening," *Journal of Engineering Materials and Technology,* Vol. 112, 1990, pp. 456–464.
[29] Hayhurst, D. R., Leckie, F. A., and McDowell, D. L., "Damage Growth under Nonproportional Loading," *Multiaxial Fatigue, ASTM STP 853,* 1985, pp. 688–699.
[30] McDowell, D. L., Stahl, D. R., Stock, S. R., and Antolovich, S. D., "Biaxial Path Dependence of Deformation Substructure of Type 304 Stainless Steel," *Metallurgical Transactions A,* 1988, pp. 1277–1293.
[31] Robillard, M. and Cailletaud, G., "Directionally Defined Damage in Multiaxial Low Cycle Fatigue: Experimental Evidence and Tentative Modeling," ESIS 10, Mechanical Engineering Publications, London, 1991, pp. 103–130.

DISCUSSION

Y. S. Garud[1] *(written discussion)*—One of the main conclusions of this presentation was that the maximum normal stress, and not the hydrostatic (or volumetric) stress, on the critical plane of fatigue damage (or cracking) affects the fatigue life. Since this is in direct contrast to the observations, also based on a set of systematic and critical experiments, made by Prof. Sines,[2] it would be of interest if the author can offer some comparative comments or thoughts.

For the test material of 6061-T6 (61S-T6) aluminum alloy, Sines observed that "the formation of a longitudinal crack was delayed by a longitudinal compressive stress, although it has no component on the plane of the crack"; the delay was consistently of the order of 2 to 3.5 times the life without compression. These and other prior observations led him to conclude with his "support to the criterion which states that it is the sum of the orthogonal components of the normal static stress that is effective." It is apparent that the hydrostatic stress can be an influencing factor in determining the fatigue response.

D. Socie (author's closure)—The observations that a longitudinal compressive stress would increase the fatigue life in torsion is consistent with the tensile damage given in Fig. 17. In this case, both hydrostatic stress and critical plane stress predict an increase in life. This is in contrast to the data given in Table 2 for Inconel 718, which fails in shear where the compressive stress does not increase the life. This shows the importance of describing the failure mode in reporting the experimental data.

[1] S. Levy Inc., 3425 S. Bascom Avenue, Campbell, CA 95008-7006.
[2] Sines, G., Failure of Materials under Combined Repeated Stresses with Superimposed Static Stresses, *NACA TN-3495,* 1954.

Chin-Chan Chu,[1] *F. Albrecht Conle,*[1] *and John J. F. Bonnen*[1]

Multiaxial Stress-Strain Modeling and Fatigue Life Prediction of SAE Axle Shafts

REFERENCE: Chu, C.-C., Conle, F. A., and Bonnen, J. J. F., **Multiaxial Stress-Strain Modeling and Fatigue Life Prediction of SAE Axle Shafts,"** *Advances in Multiaxial Fatigue, ASTM STP 1191,* D. L. McDowell and R. Ellis, Eds., American Society for Testing and Materials, Philadelphia, 1993, pp. 37–54.

ABSTRACT: A three-dimensional stress-strain model with an isotropic-kinematic hardening rule has been successfully applied to obtain estimated stress histories from the rosette strain histories. The strains are measured on surface elements near the notch root of SAE axle shafts subjected to variable-amplitude multiaxial service loading conditions. The critical plane approach is adopted to predict fatigue lives by examining the detailed stress and strain states on all potential critical planes of an element. Several commonly used damage criteria as well as a work-based criterion proposed here are evaluated by comparing the predicted and experimentally observed fatigue lives for a wide range of tests. The encouraging results demonstrate the current model's capability of simulating complex tests and predicting fatigue lives.

KEY WORDS: multiaxial stress-strain model, isotropic-kinematic hardening, critical plane approach, damage criteria, variable amplitude test, proportional loading, fatigue life prediction

One of the major obstacles in the area of multiaxial fatigue analysis has been the unavailability of reliable material models that can predict the complex elastic-plastic stress-strain behavior occurring in many cyclically loaded elements. The last few years have seen the development and application of new stress-strain models that can simulate multiaxial cyclic behavior. For example, Refs *1* and *2* used a model based on a two-surface theory. Chu [*3*] generalized from Mróz's discrete yield surface field concept [*4*] a model using a continuous field of work-hardening moduli. There are also theories such as kinematic hardening rules and endochronic theories which have not been widely used because of various difficulties involved in their implementation. Since Chu's model, like Mróz's, is a superset of earlier successful one-dimensional models used in uniaxial fatigue analysis [*5*] and has been shown to efficiently reproduce many important features of experimentally observed biaxial cyclic stress-strain behavior [*6*], it will be used in this analysis.

With the new multiaxial stress-strain model it is now possible to simulate the three-dimensional stress-strain behavior of a critical element in components subjected to variable-amplitude multiaxial fatigue loading. This capability offers a unique opportunity to examine old and new multiaxial fatigue damage criteria in great detail.

Damage criteria for materials subjected to multiaxial loading generally utilize parameters which transform the multiaxial stress and strain states into equivalent uniaxial quantities directly related to the standard uniaxial fatigue characterization curves. These equivalent parameters can be categorized into two types: criteria based on general stress (strain) state variables, such as the equivalent stress and the major principal stress; and criteria based on stress

[1] Research staff, Ford Motor Company, Scientific Research Laboratories, Dearborn, MI 48121-2053.

(strain) acting on specific critical planes. Comprehensive reviews can be found in, for example, Ref *7*.

In this paper a variety of fatigue criteria are evaluated by applying the multiaxial plasticity model of Ref *3* in conjunction with the critical plane approach to predict the fatigue lives of the extensive SAE constant amplitude [*8*] and multiaxial variable amplitude [*9,10*] test of shafts under bending and/or torsion.

Analysis

Multiaxial Stress-Strain Analysis

Although the method presented here is general enough to be applied to any three-dimensional problem, the equations are specifically derived for surface elements in which plane stress conditions prevail and where surface strains are given by strain gage measurements. As sketched in Fig. 1, for an element on the top surface of an axle shaft adopting the *x-y-z* coordinate system, the plane stress conditions are

$$\sigma_{iz} \equiv 0 \qquad i = x, y, z$$
$$\epsilon_{\alpha z} \equiv 0 \qquad \alpha = x, y$$

Given a time history of rosette strains, $e_1(t)$, $e_2(t)$, $e_3(t)$, the history of surface strains can be derived by

$$\epsilon_{xx}(t) = e_2(t)$$
$$\epsilon_{xy}(t) = \tfrac{1}{2}[-e_1(t) + e_3(t)]$$
$$\epsilon_{yy}(t) = e_1(t) - e_2(t) + e_3(t)$$

An isotropic-kinematic hardening model generalized from Mróz's yield surface field concept [*3,6*] is adopted to follow the strain history and calculate the corresponding stress history. The material model, utilizing two commonly adopted assumptions that (a) during an elastic-plastic deformation the total strain increment is the sum of the elastic and the plastic increment and (b) the plastic strain increment obeys the normality rule, can be summarized here by the following set of equations describing the incremental stress-incremental strain relationship.

$$d\sigma_{ij} = L_{ijkl}\, d\epsilon_{kl} = \frac{E}{1+\nu}\left(d\epsilon_{ij} + \frac{\nu}{1-2\nu}\,\delta_{ij}\, d\epsilon_{kk} - H\frac{r_{ij}r_{kl}}{\bar{\sigma}^2}\, d\epsilon_{kl}\right) \tag{1a}$$

with

$$r_{ij} = s_{ij} - \alpha_{ij} = (\sigma_{ij} - \tfrac{1}{3}\,\delta_{ij}\,\sigma_{kk}) - \alpha_{ij} \tag{1b}$$

$$\bar{\sigma}^2 = \tfrac{3}{2}\, r_{ij} r_{ij} \tag{1c}$$

$$H = \begin{cases} 0 & \text{if } \bar{\sigma} \le \bar{\sigma}_y \\ \dfrac{3}{2}\left(\dfrac{2(1+\nu)}{3(E/E_t(\bar{\sigma}) - 1)} + 1\right)^{-1} & \text{if } \bar{\sigma} > \bar{\sigma}_y \end{cases} \tag{1d}$$

In Eqs 1a through 1d, L is used to denote the instantaneous modulus matrix, E is Young's modulus, ν is Poisson's ratio, δ is the Kronecker delta, $E_t(\bar{\sigma})$ is the instantaneous tangent mod-

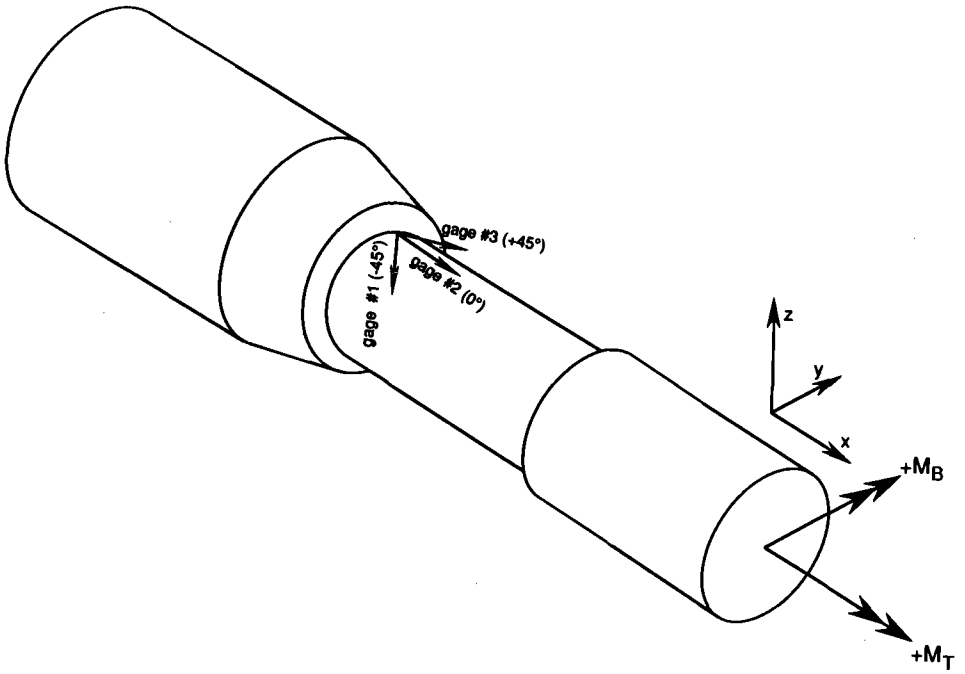

FIG. 1—*SAE biaxial specimen and strain rosette placement.*

ulus at equivalent stress level $\bar{\sigma}$, and $\bar{\sigma}_y$ denotes the initial yield stress which is a material constant. The center of the active yield surface in the deviatoric stress (s_{ij}) space is denoted by α, which during a plastic loading process moves in a direction toward the center of the previously active yield surface at the last load reversal. In the above equations and hereafter, Roman subscripts i through l take values that range from x to z and Greek subscripts α through δ take values that range from x to y. Repetition of these subscripts implies summation.

The plane stress conditions mentioned earlier can be expressed by

$$d\sigma_{iz} = L_{iz\alpha\beta}\, d\epsilon_{\alpha\beta} + L_{izzz}\, d\epsilon_{zz} \equiv 0$$

which can be used with Eq 1 to give the incremental stress-strain relationship on the x-y plane

$$\begin{aligned} d\sigma_{\alpha\beta} &= L_{\alpha\beta\gamma\delta}\, d\epsilon_{\gamma\delta} + L_{\alpha\beta zz}\, d\epsilon_{zz} \\ &= \left(L_{\alpha\beta\gamma\delta} - \frac{L_{\alpha\beta zz} L_{zz\gamma\delta}}{L_{zzzz}} \right) d\epsilon_{\gamma\delta} \end{aligned} \tag{2}$$

The basic equivalent stress-strain equation of the material used in this analysis is a modified power law type

$$\bar{\epsilon} = \begin{cases} \bar{\sigma}/E \; (= \bar{\epsilon}_y \bar{\sigma}/\bar{\sigma}_y) & \text{if } \bar{\sigma} \leq \bar{\sigma}_y \\ \bar{\epsilon}_y (n'(\bar{\sigma}/\bar{\sigma}_y)^{1/n'} - n' + 1) & \text{if } \bar{\sigma} > \bar{\sigma}_y \end{cases} \tag{3}$$

The function of tangent modulus used in Eq 1, $E/E_t(\bar{\sigma})$, is then obtained as

$$\frac{E}{E_t} = \frac{E}{d\bar{\sigma}/d\bar{\epsilon}} = \begin{cases} 1 & \text{if } \bar{\sigma} \leq \bar{\sigma}_y \\ (\bar{\sigma}/\bar{\sigma}_y)^{1/n'-1} & \text{if } \bar{\sigma} > \bar{\sigma}_y \end{cases}$$

Here n' is the strain-hardening exponent of the material. It is important to note that the material constants, n' and $\bar{\sigma}_y$, should be determined from fitting the above stress-strain relation to the cyclically stabilized stress-strain data instead of the initial monotonic curve. The present initial yield stress, $\bar{\sigma}_y$, corresponds more to a cyclic proportional limit than the 0.2% offset yield stress of the material. The modified power law, Eq 3, is used mainly to give a smooth curve with continuous slope change at the yield point, $\bar{\sigma} = \bar{\sigma}_y$.

The Critical Plane Approach

Most of the fatigue analyses performed to date were in either uniaxial or multiaxial proportional loading cases. For proportional loadings, i.e. where the input loads are related by scalar constants, even if the amplitude variation is random and complex, the most critical plane, for example the plane on which shear or normal stress are maximized, remains fixed relative to the loading axis throughout the history. The critical plane is thus relatively easy to define. For a general multiaxial cyclic problem, however, the principal axes of the stress and strain matrices vary with time, and features such as the maximum shear plane assume an instantaneous rather than a constant definition. In consequence it becomes necessary to individually study a set of potentially critical planes that will locate the eventual fatigue crack. This so-called "critical plane approach" is adopted here.

As sketched in Fig. 2, the potentially critical planes examined are defined by two angles, θ and ϕ. Angle θ is between the plane-surface intersection and the x-axis, and it has the physical significance that it indicates the orientation of the eventual surface crack. Angle ϕ is the rotation of the plane's normal from the z-axis, and it indicates the inclination of the plane the fatigue crack will propagate on.

The stress and strain matrix on the new x'-y'-z' coordinate system based on the potentially critical plane, with z'-axis in the plane's normal direction, can be obtained by the following matrix transformation

$$\sigma'_{ij} = F_{ki}\sigma_{kl}F_{lj}, \quad \epsilon'_{ij} = F_{ki}\epsilon_{kl}F_{lj}$$

with

$$\{F_{kl}\} = \begin{pmatrix} \cos\theta & -\cos\phi\sin\theta & -\sin\phi\sin\theta \\ \sin\theta & \cos\phi\cos\theta & \sin\phi\cos\theta \\ 0 & -\sin\phi & \cos\phi \end{pmatrix}$$

The normal and shear components of the traction acting on such a potentially critical plane are then defined as

$$\sigma_n = \sigma'_{z'z'}, \; \tau_{\text{III}} = \sigma'_{x'z'}, \quad \text{and} \quad \tau_{\text{II}} = \sigma'_{y'z'}$$

Here notations τ_{III} and τ_{II} are respectively used for the shear stress parallel and perpendicular to the x'-axis because they contribute to Modes III and II types of crack openings on the critical plane in the linear elastic fracture mechanics sense.

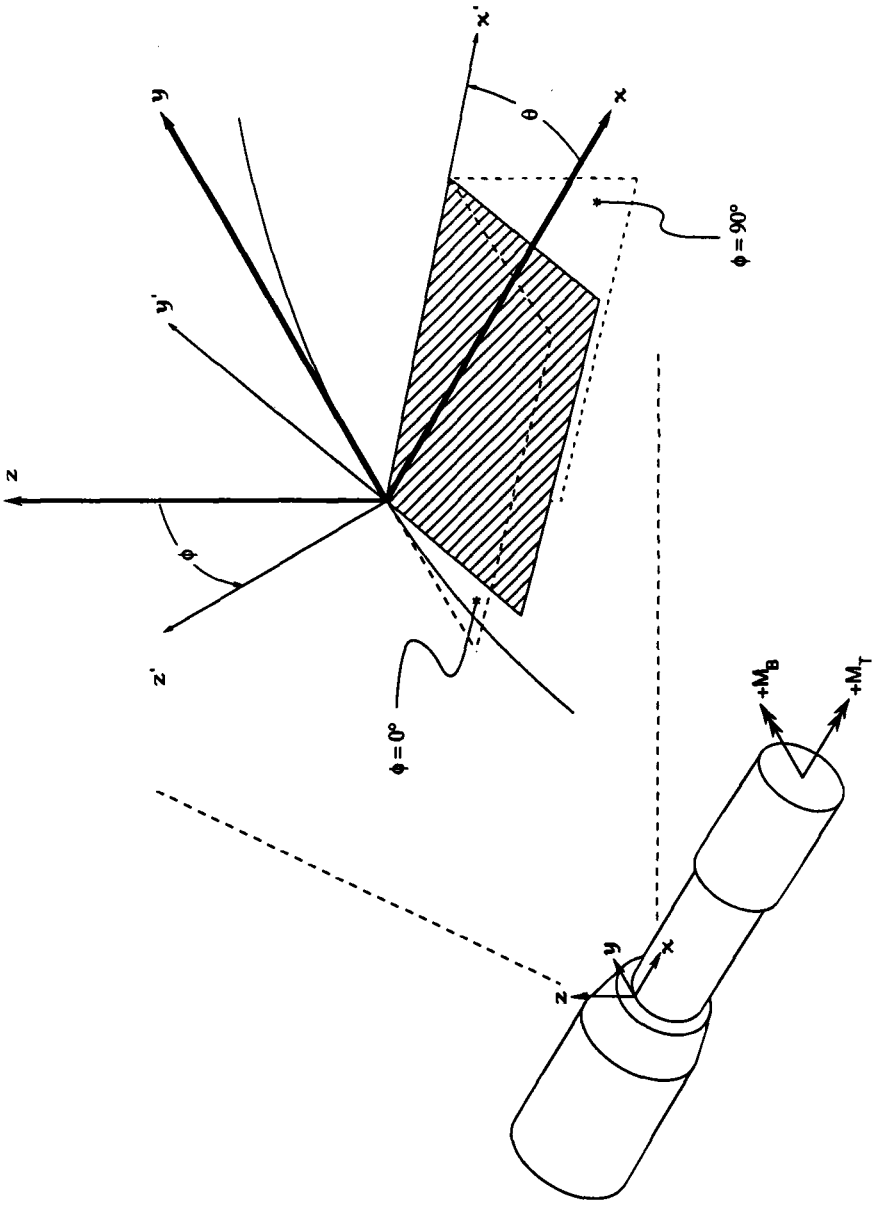

FIG. 2—*Candidate critical planes.*

The search for the most critical plane in specimens subjected to a general multiaxial history can be very time consuming. Fortunately, for the surface elements of concern here, it can be shown that the plane stress conditions make the planes with $\phi = 90°$ always the worst ones for the Mode I or Mode III type damage criteria, and the planes with $\phi = 45°$ the worst if the Mode II shear component is used as the damage parameter. Therefore, only planes of various θ (with two specific angles of ϕ mentioned above) need to be examined. In cases where the loading does not allow such simplified determinations, the calculations will take more time, usually in equal proportion to the number of planes specified for examination.

Damage Criteria

The objective of multiaxial fatigue research is to find a key parameter which will unify fatigue results from multiaxial tests with those from uniaxial tests. The latter tests are generally used to characterize the deformation and fatigue behavior of the material. The applicability of a number of damage criteria that have been proposed in the literature will be evaluated in this study. In this section and in the Appendix the stabilized stress-strain relation, Eq 3, and the fatigue stress-life equation are used with the critical plane approach to derive the various parameter-life relationships.

First, it is assumed that the fully reversed tension/compression test is the baseline test and that the material's fatigue behavior is characterized by the Basquin's stress-life relationship [*11*]

$$\sigma_a = \sigma_f'(2N_f)^b \tag{4}$$

where σ_a is the stress amplitude of a hysteresis loop, σ_f' and b are both material constants, and N_f is the number of closed hysteresis loops, or cycles, to failure.

The amplitude of the stress and strain matrices for the baseline uniaxial test conditions are

$$\{\sigma_{ij}\}_a = \begin{pmatrix} \sigma_a & 0 & 0 \\ 0 & 0 & 0 \\ 0 & 0 & 0 \end{pmatrix} \quad \text{and} \quad \{\epsilon_{ij}\}_a = \begin{pmatrix} \epsilon_a & 0 & 0 \\ 0 & (\epsilon_2)_a & 0 \\ 0 & 0 & (\epsilon_3)_a \end{pmatrix},$$

where

$$\epsilon_a = \frac{\sigma_a}{E} + (\epsilon_p)_a \tag{5}$$

$$(\epsilon_2)_a = (\epsilon_3)_a = -\frac{\nu\sigma_a}{E} - \frac{1}{2}(\epsilon_p)_a$$

Using Eq 3, $(\epsilon_p)_a = 0$ for $\bar{\sigma} \leq \bar{\sigma}_y$ and $(\epsilon_p)_a = \bar{\epsilon}_y(n'(\sigma_a/\bar{\sigma}_y)^{1/n'} - n' + 1) - \sigma_a/E$ for $\bar{\sigma} \geq \bar{\sigma}_y$.

To adopt the critical plane approach here, let us consider a plane whose normal makes an angle of ψ with the loading axis. The normal stress and the Mode II or III shear stress can be found to be

$$(\sigma_n)_a = \frac{\sigma_a}{2} + \frac{\sigma_a}{2}\cos 2\psi \quad \text{and} \quad (\tau_{II})_a = (\tau_{III})_a = \frac{\sigma_a}{2}\sin 2\psi \tag{6}$$

Similarly, the normal and shear strains are

$$(\epsilon_n)_a = (\epsilon_m)_a + (\epsilon_d)_a \cos 2\psi \quad \text{and} \quad (\gamma_{II})_a = (\gamma_{III})_a = (\epsilon_d)_a \sin 2\psi, \tag{7}$$

with

$$(\epsilon_m)_a = \tfrac{1}{2}(\epsilon_a + (\epsilon_2)_a) \quad \text{and} \quad (\epsilon_d)_a = \tfrac{1}{2}(\epsilon_a - (\epsilon_2)_a)$$

If the normal strain on a potentially critical plane is assumed to be the damage parameter, then from Eq 7 it can be seen that the most critical plane will be $\psi = 0°$, a plane where the normal strain, and hence the fatigue damage parameterized by it, is maximized. Combining Eqs 4, 5, and 7, the parameter-life equation can therefore be obtained as

$$\begin{aligned}(P)_{\epsilon_n} &= (\epsilon_n)_a \\ &= \begin{cases} \bar{\epsilon}_y \sigma_f''(2N_f)^b & \text{if } (P)_{\epsilon_n} \le \bar{\epsilon}_y \\ \bar{\epsilon}_y[n'(\sigma_f'')^{1/n'}(2N_f)^{b/n'} - n' + 1] & \text{if } (P)_{\epsilon_n} > \bar{\epsilon}_y \end{cases}\end{aligned} \tag{8}$$

where

$$\sigma_f'' = \sigma_f'/\bar{\sigma}_y.$$

Note that here and below $(P)_{\text{criterion}}$, followed by the definition of the parameter, is simply used for convenient referencing purpose.

If the Smith-Watson-Topper criterion [*12*] is applied to the normal stress and normal strain, the most critical plane is again found to be of $\psi = 0°$ where the parameter $[(\sigma_n)_{\max}(\epsilon_n)_a]$ is maximized. The parameter-life equation is then derived as

$$\begin{aligned}(P)_{SWT} &= (\sigma_n)_{\max}(\epsilon_n)_a \\ &= \begin{cases} \bar{\sigma}_y\bar{\epsilon}_y(\sigma_f'')^2(2N_f)^{2b} & \text{if } (P)_{SWT} \le \bar{\sigma}_y\bar{\epsilon}_y \\ \bar{\sigma}_y\bar{\epsilon}_y[n'(\sigma_f'')^{1+1/n'}(2N_f)^{b/n'+b} + (1 - n')\sigma_f''(2N_f)^b] & \text{if } (P)_{SWT} > \bar{\sigma}_y\bar{\epsilon}_y \end{cases}\end{aligned} \tag{9}$$

Note that $(\ )_{\max}$ here and below denotes the maximum value of a quantity during a hysteresis loop. For the fully reversed tension/compression test considered here $(\ )_{\max}$ is of the same value as $(\ )_a$.

If the shear strain based criterion proposed by Brown and Miller [*13*] is used, then the parameter on a potentially critical plane of angle ψ is

$$\begin{aligned}(P)_{BM} &= \gamma_a + K(\epsilon_n)_a \\ &= (\epsilon_d)_a \sin 2\psi + K(\epsilon_m)_a + K(\epsilon_d)_a \cos 2\psi\end{aligned}$$

where K was proposed a material constant. A value of $K = 0.5$ has been used in earlier studies for SAE1045 steels. (Note that the shear strain used here is the tensoral shear strain, which is half the more commonly used engineering shear strain. Therefore, the material constant, K, here is also half the previously proposed value.) By differentiating the above equation with respect to angle ψ, the most critical plane in the completely reversed uniaxial tension/compression test is found to be of $2\psi = \tan^{-1}(1/K)$. Applying Eqs 3 and 4 to the most critical plane, the parameter-life relationship is derived as

$$\begin{aligned}(P)_{BM} &= \sqrt{K^2 + 1}\,(\epsilon_d)_a + K(\epsilon_m)_a \\ &= \begin{cases} C_1\bar{\epsilon}_y\sigma_f''(2N_f)^b & \text{if } (P)_{BM} \le C_1\bar{\epsilon}_y \\ \tfrac{1}{2}\bar{\epsilon}_y(C_2(n'(\sigma_f'')^{1/n'}(2N_f)^{b/n'} - n' + 1) + C_3\sigma_f''(2N_f)^b) & \text{if } (P)_{BM} > C_1\bar{\epsilon}_y \end{cases}\end{aligned} \tag{10}$$

with

$$C_1 = K\left(\frac{1-\nu}{2}\right) + \sqrt{K^2+1}\left(\frac{1+\nu}{2}\right)$$
$$C_2 = \tfrac{1}{2}(K + 3\sqrt{K^2+1})$$
$$C_3 = (\tfrac{1}{2} - \nu)(K - \sqrt{K^2+1})$$

It is worth pointing out that in the last example the most critical plane obtained by maximizing the parameter $(P)_{BM}$ is different from the originally proposed "maximum shear plane" of $\psi = 45°$ for simple tension/compression test conditions. When the critical plane approach is adopted it should be consistently applied to both the complicated multiaxial analyses and the simple uniaxial baseline tests. Therefore it is the "maximum-parameter plane" in the baseline test on which the material's parameter-life curve should be calculated with the critical plane approach.

Besides the above three criteria, this paper also includes the following parameters in the investigation to study their applicability to multiaxial fatigue problems: normal stress $[(P)_{\sigma_n} = (\sigma_n)_a]$ with Morrow's mean stress correction [*14*]; shear strain $[(P)_\gamma = \gamma_a]$; Lohr and Ellison's parameter [*15*] $[(P)_{LE} = (\gamma_{II})_a + 0.2(\epsilon_n)_a]$; Socie, Waill, and Dittmer's parameter [*16*] $[(P)_{SO} = \gamma_a + 0.5(\epsilon_n)_a + (\sigma_n)_0/E]$; Fatemi and Kurath's parameter [*17*] $[(P)_{FK} = \gamma_a(1 + 0.6(\sigma_n)_a/\bar{\sigma}_y)]$; plastic work $[(P)_{W_p} = \oint_{\text{hysteresis loop}} dW]$. Finally, one new parameter, $(P)_{C_{swt}} = 2\tau_{\max}\gamma_a + (\sigma_n)_{\max}(\epsilon_n)_a$, is proposed here. The parameter-life equations for these criteria can be derived as illustrated above, and a summary of them are included in the Appendix.

Computation Procedures

In the present case strain histories taken from rosette gages on the component were first translated into parallel stress histories by the three-dimensional stress-strain model. Both the stress and strain histories are transformed to create histories of the normal and shear stress and strain components on each of the candidate critical planes specified by the user for examination. Each plane's stress and strain component history is then scanned to delineate the closed hysteresis loops using a rainflow-type counting procedure. It is worth pointing out here that for a general multiaxial problem the normal and shear strain components are often out-of-phase. If a combined normal and shear type of criterion is adopted, using $(P)_{BM}$ as an example, while counting the hysteresis loops of the primary variable, γ, the variable, ϵ_n, which was proposed to have an adverse effect on shear damage and hence named as the secondary variable below, may see many more (or less) reversals than the primary variable does. As a result, the mean value and the amplitude of the secondary variable, required by some parameters, may be difficult to determine. In the current study, the mean and maximum of the secondary component are monitored throughout the occurrence of each primary variable hysteresis loop and the amplitude is taken to be the difference between the mean and the maximum.

It is assumed that each individual force-deformation hysteresis loop delineated on a plane is a damaging event, and the amount of damage that it contributes to the whole can be obtained from the parameter-life relationship. By summing up the damage caused by each hysteresis loop within the loading block, the block life can then be predicted.

After damage on all the potentially critical planes are calculated, the most critical plane can be determined as the one which gives the maximum damage and thus the lowest fatigue life.

Results

Some recently published biaxial tests of variable amplitude on SAE1045 steel axle shafts are the major focus of the current analysis. They include two sets of biaxial histories from the Society of Automotive Engineers Fatigue Design and Evaluation (SAE FD&E) Committee:

the cable log skidder history and a phase-shifted transmission history. Detailed description of the testing procedures can be found in Refs *9* and *10*. The rosette strains measured at the notch root and recorded for a stabilized block are used as the history input to the analysis. Only six material constants are used in the analyses: $E = 204\,000$ MPa, $\nu = 0.33$, $n' = 0.329$, $\bar{\sigma}_y = 165.4$ MPa, $\sigma_f' = 3553.4$ MPa, and $b = -0.1416$. (Here E, n', and $\bar{\sigma}_y$ are obtained from fitting Eq 3 to the observed cyclic stress-strain curve, and σ_f' and b are obtained by fitting Eq 4 to the observed stress amplitude-life curve.)

The intermediate stress and strain results for two biaxial tests, Test 1 of Ref *10* and Test DP55 of Ref *9*, and one essentially proportional bending-only test, Test 2 of Ref *10*, are shown in Figs. 3 through 5. Plots *a* through *d* in these figures show the input strain history and the corresponding stress history obtained from the multiaxial stress analysis. The circumferential strain and stress were not influential and hence omitted. Plots *e* and *f* are the same results presented in stress-strain coordinates for bending and torsional component. Figure 4*e* illustrates the convergence of the current multiaxial model to uniaxial stress-strain behavior when applied to proportional loadings, in this case a bending-only shaft history. Figures 3*e* and 3*f* and 5*e* and 5*f*, on the other hand, show complexities attributable to interactions between bending and torsion. Plot *g* in Figs. 3 through 5 is yet another way to look at the loading history. Taking advantage of the current condition that $\sigma_{yy} \approx 0$, it can be shown that the major principal stress axis of any stress state in Plot *g* makes an angle $\varphi = \frac{1}{2} \tan^{-1} (2\sigma_{xy}/\sigma_{xx})$ with the loading x-axis, as demonstrated in Fig. 3*g* for one peak loading state as an example. Unfortunately, the instantaneous major principal axis easily visualized here does not generally correlate with the critical direction determined in the fatigue analysis except in cases of proportional loading. Nevertheless Plot *g* in Figs. 3 through 5 does show the degree of multiaxiality of the tests.

Illustrated in Fig. 6 is an example of the computer's printout of the life predictions for the most severe biaxial tests, Test 1 of Ref *10*. The predicted lives expressed in base 10 logarithms are arranged in columns by damage criteria and in rows by the planar angle, θ. Note that the planar angle is arbitrarily chosen 15° apart here. The planar angle which gives the lowest life prediction of each column defines the most critical plane. The last row repeats the lowest life found by each criterion.

The complete results on all eight tests with variable amplitude histories reported in Refs *9* and *10* are summarized in Fig. 7 where the predicted life is plotted against the observed initiation life: Fig. 7*a* groups the results from uniaxial type of criteria, and Fig. 7*b* groups the results from combined normal and shear type of criteria. These figures clearly indicate that damage parameters accounting for both shear and normal contributions do better than those with only a shear or normal term.

The fatigue analysis results for the constant amplitude bending/torsion shaft tests, for which the strain data are available from Ref *8*, are graphically compared in Figs. 8*a* and 8*b*. These comparisons suggest that all but $(P)_{\sigma_n}$ with Morrow's mean stress correction seem reasonable (within a factor of 3 except for very long lives). For the very long-life constant amplitude tests, all criteria underestimate fatigue life significantly. These conservative predictions were also found by Tipton and Fash [*8*] and require further research.

Discussion

The study shows that the advent of good multiaxial plastic deformation models has provided a tool for detailed estimation of the stress and strain states at a critical location at all instances of time in a complex multiaxial strain or stress history. In developing a complete multiaxial fatigue program to analyze the extensive test data sets provided by the SAE Fatigue Design and Evaluation Committee, this study also emphasizes how the critical plane approach

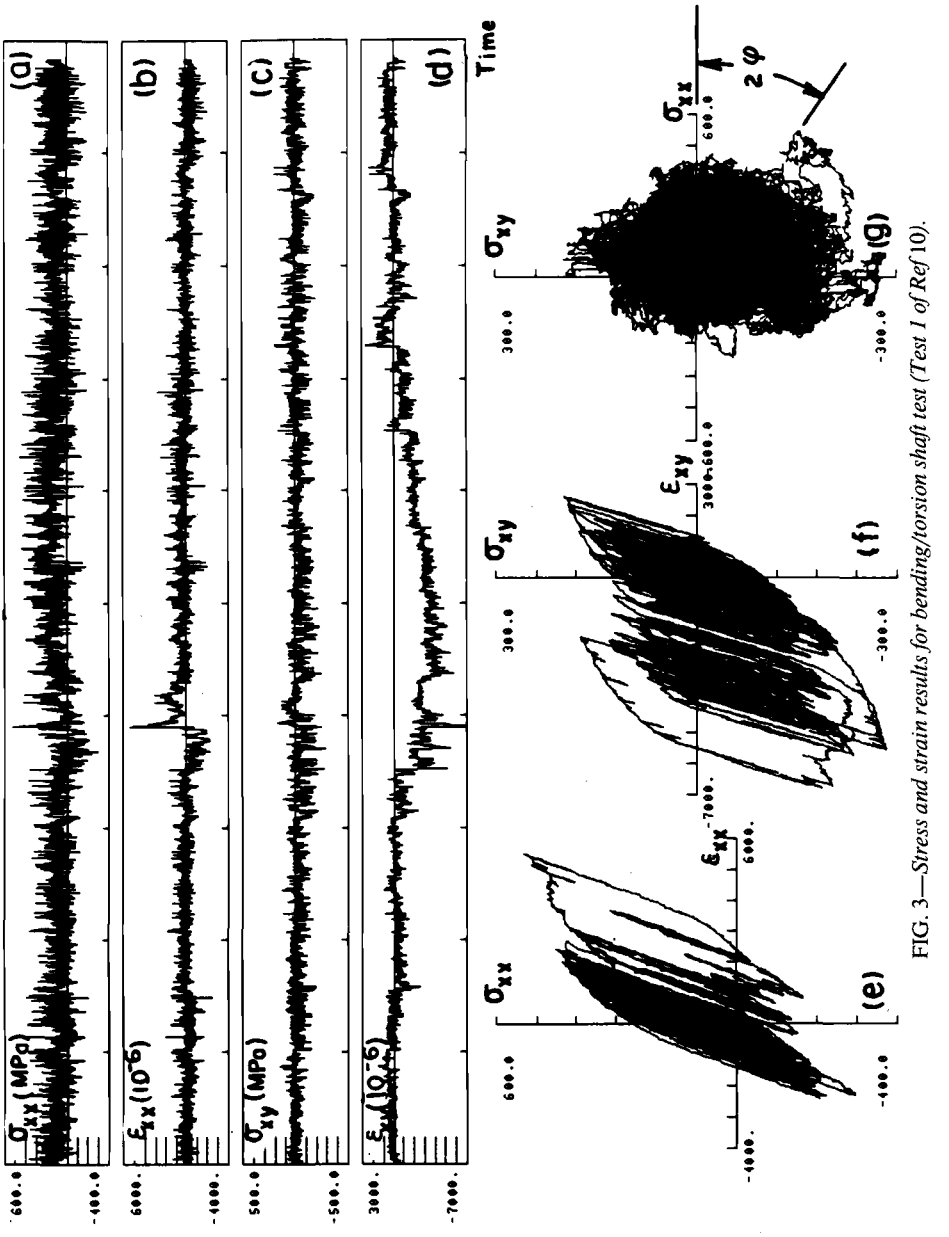

FIG. 3—*Stress and strain results for bending/torsion shaft test (Test 1 of Ref* 10).

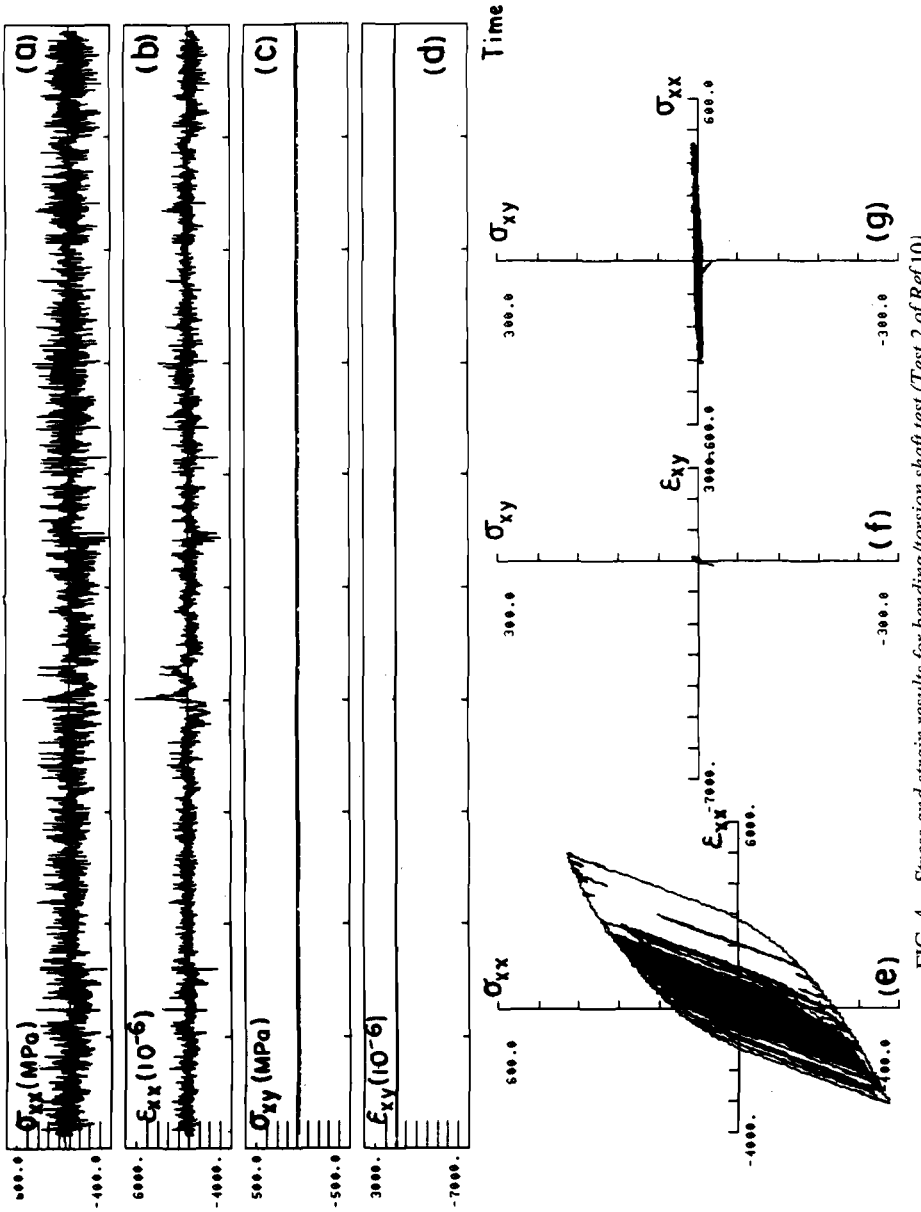

FIG. 4—*Stress and strain results for bending/torsion shaft test (Test 2 of Ref 10).*

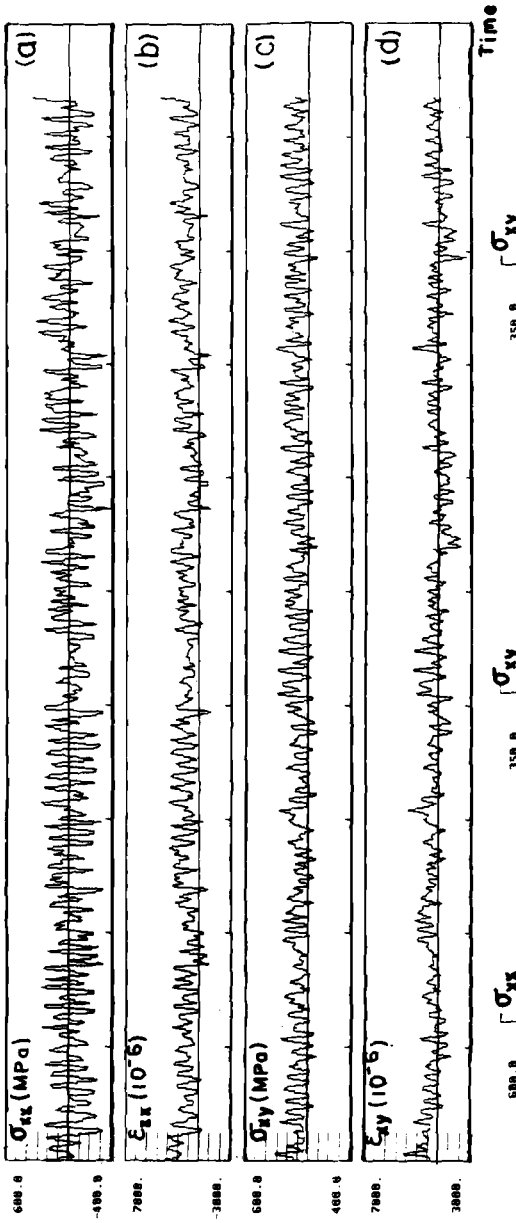

FIG. 5—*Stress and strain results for bending/torsion shaft test (Test DP55 of Ref 9).*

TEST ID: Test 1

θ	P_{ϵ_n}	P_{SWT}	P_{σ_n}	P_{LE}	P_γ	P_{BM}	P_{So}	P_{FK}	P_{CSWT}	P_W
90	3.52	3.06	3.21	3.51	3.20	3.13	2.66	3.17	2.70	
75	3.42	3.01	3.17	3.48	3.35	3.22	2.53	3.21	2.76	
60	3.41	3.12	3.50	3.51	3.60	3.00	2.51	3.21	2.57	
45	3.51	3.38	3.99	3.65	3.61	3.32	2.79	3.47	2.91	
30	3.84	3.96	5.00	3.93	3.41	3.35	3.11	3.46	3.06	
15	4.61	5.00	6.46	4.52	3.23	3.32	3.24	3.45	3.16	
0	5.61	7.15	7.85	6.20	3.21	3.38	3.34	3.57	3.31	
-15	4.45	5.50	7.01	5.02	3.35	3.32	3.34	3.41	3.37	
-30	3.90	4.42	5.46	4.14	3.60	3.44	3.45	3.46	3.35	
-45	3.71	3.91	4.55	3.84	3.61	3.41	3.17	3.55	3.13	
-60	3.66	3.52	3.91	3.67	3.41	3.15	2.83	3.33	2.81	
-75	3.63	3.22	3.47	3.58	3.23	3.11	2.68	3.20	2.69	
	3.41	3.01	3.17	3.48	3.20	3.00	2.51	3.17	2.57	1.95

FIG. 6—*Predicted fatigue lives (in base 10 logarithms) for Test 1 of Ref* 10).

can be consistently applied both to the baseline test in the derivation of parameter-life relationships and to the other tests analyzed.

Critical planes have been determined for a variety of damage parameters, and fatigue damage has been calculated for the prediction of test life. Constant amplitude bending/torsion test life prediction comparisons show that most of the parameters evaluated in this paper seem reasonable except for very long lives. Simulations of most recent variable amplitude service histories reduce the list of more promising parameters to those with combined normal and shear effects. The new energy-based parameter, introduced in this study (in the Appendix), appears to be very promising for life prediction. It also offers the advantage of simplicity and is an extension of concepts that have worked well for uniaxial predictions.

While the fatigue life predictions from this study appear very encouraging, it has implicitly adopted the following assumptions whose validity warrant further research.

1. The rosette strains from the various test histories were assumed to be representative of the strains at the critical location. For the SAE axle shafts tested in Ref *10,* however, it was observed that the failures occurred slightly away from the rosette, further up the radius. Without careful analysis it is not clear how to account for both the potential stress-strain amplification due to possible notch factor and stress-strain attenuation due to section size increase, and, in consequence, strain histories were used without modification in this study.
2. The damage caused by each hysteresis loop is assumed to accumulate linearly. There have been many uniaxial studies of phenomena such as sequence effects and large-small cycle interaction effects which call this assumption into question.

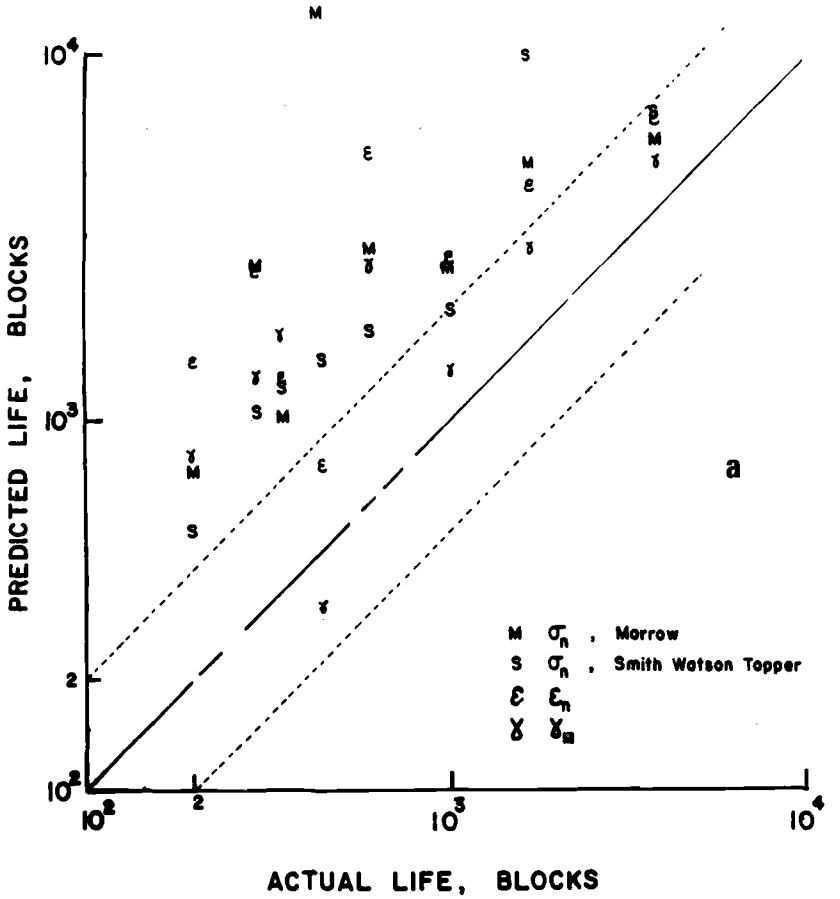

FIG. 7—*Comparison between predicted and observed fatigue lives for variable amplitude tests:* (a) *according to uniaxial type of criteria, and* (b) *according to combined normal and shear type of criteria.*

3. The rainflow counting scheme used in this analysis is the same as those applied to the uniaxial fatigue analysis. As mentioned earlier, when the normal and shear components on a specific plane are not cycling in phase, cycle or event counting becomes difficult and needs clarification.

APPENDIX

Equivalent Damage Parameter-Life Relationships

Normal stress amplitude—Normal stress amplitude as the damage parameter but with Morrow's mean stress correction is calculated as follows

$$(\sigma_n)_a = (\sigma_f' - (\sigma_n)_0)(2N_f)^b$$

where $(\sigma_n)_0$ is the mean value of the σ_n cycle.

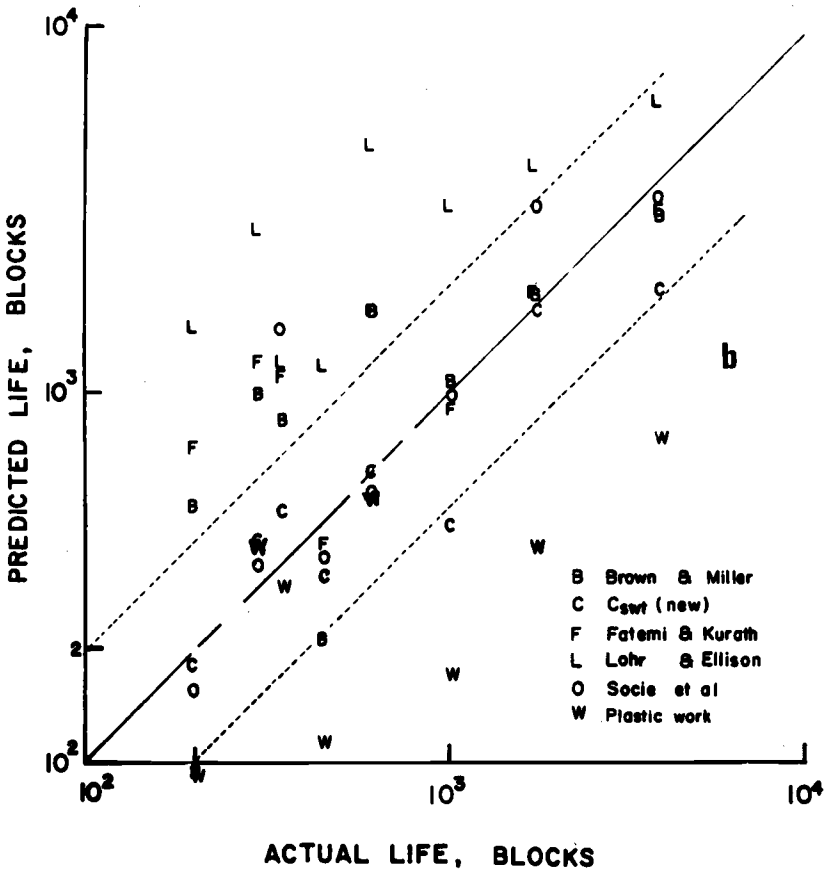

FIG. 7—*Continued.*

Shear strain amplitude—Shear strain amplitude as the damage parameter is calculated as follows

$$(P)_\gamma = \gamma_a = \begin{cases} \dfrac{1+\nu}{2}\bar{\epsilon}_y\sigma_f''(2N_f)^b & \text{if } \gamma_a \le \dfrac{1+\nu}{2}\bar{\epsilon}_y \\ \dfrac{1}{2}\bar{\epsilon}_y\left[\left(\dfrac{1}{2}+\nu\right)\sigma_f''(2N_f)^b + \dfrac{1}{2}(1-n') + \dfrac{n'}{2}(\sigma_f'')^{1/n'}(2N_f)^{b/n'}\right] & \text{if } \gamma_a > \dfrac{1+\nu}{2}\bar{\epsilon}_y \end{cases}$$

Lohr and Ellison's criterion—This criterion has the same form as that of $(P)_{BM}$ in the text except that $K = 0.2$. This is because Mode II and Mode III shear strains in a uniaxial tension test are identical.

Fatemi and Kurath's parameter—Fatemi and Kurath's parameter as the damage criterion is calculated as follows

$$(P)_{FK} = \gamma_a\left(1 + k\frac{(\sigma_n)_a}{\bar{\sigma}_y}\right).$$

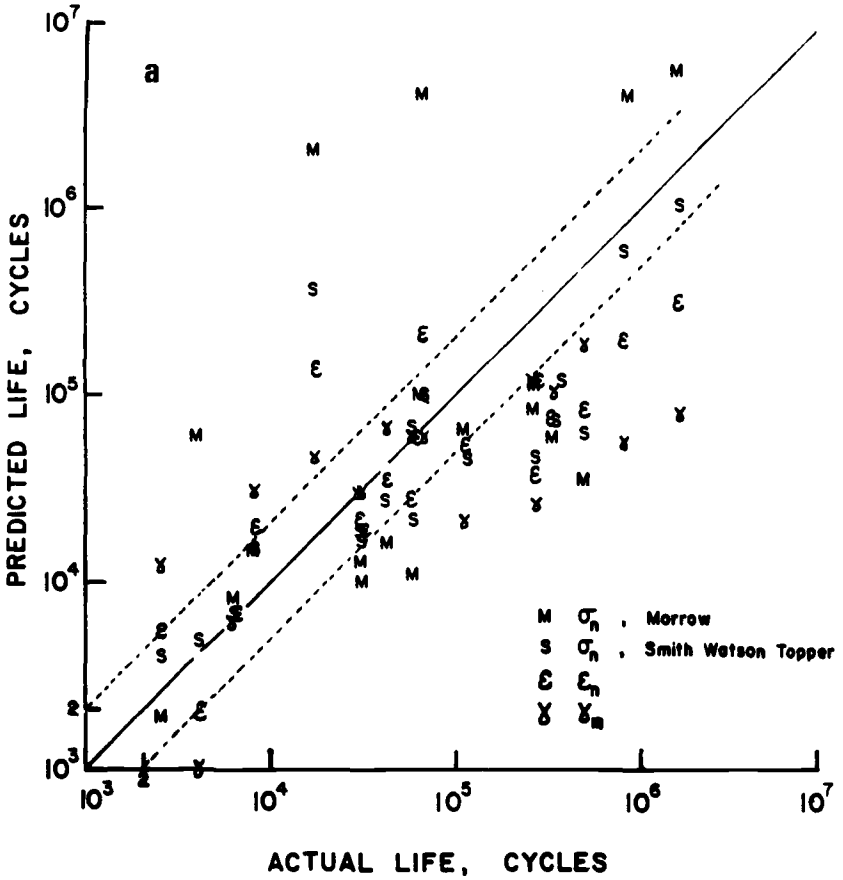

FIG. 8—*Comparison between predicted and observed fatigue lives for constant amplitude tests:* (a) *according to uniaxial type of criteria, and* (b) *according to combined normal and shear type of criteria.*

The parameter-life equation for this criterion is extremely complicated and hence omitted here.

Socie, Waill, and Dittmer's parameter as the damage criterion—This parameter is Brown and Miller's parameter with an additional term accounting for the mean stress effect due to the normal stress component. Since there is no mean stress in the fully reversed uniaxial test, the right-hand side of the parameter-life equation is the same as that for $(P)_{BM}$ in the text

$$(P)_{SO} = \gamma_a + (\epsilon_n)_a + (\sigma_n)_0/E = \text{(the right hand side of } (P)_{BM}).$$

Plastic work—Plastic work as the damage parameter is calculated as follows

$$(P)_W = W = 4\frac{1-n'}{1+n'}\bar{\sigma}_y\bar{\epsilon}_y[1 + n'(\sigma_f'')^{1/n'+1}(2N_f)^{b/n'+b} - (1+n')\sigma_f''(2N_f)^b]$$

There are two major difficulties associated with the application of this work criterion: (1) it is a scalar and thus shows no preference for any plane on which final failure may occur, and (2)

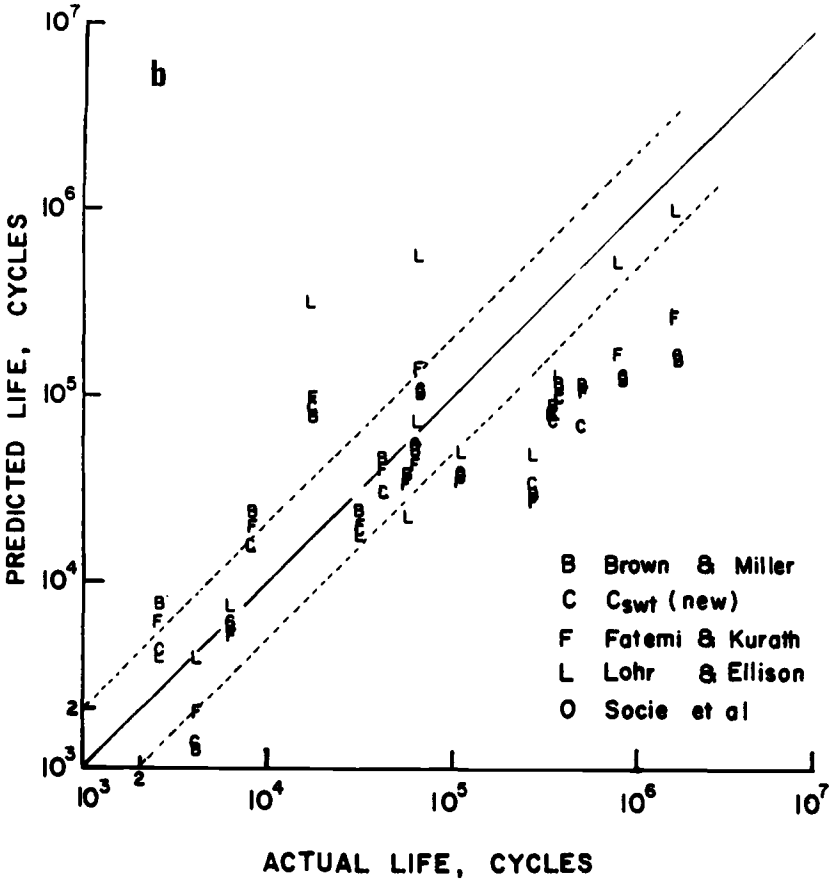

FIG. 8—*Continued.*

the criterion seems to be more prone to error in the long-life region because of the increased difficulty of decomposing the total strain into its elastic and plastic portions.

A work-based new criterion—This criterion in concept parallels that of the combined shear and normal criterion, but instead of using strain amplitude as the parameter form, it uses the Smith-Watson-Topper type of work form.

$$(P)_{C_{swt}} = 2\tau_{max}\gamma_a + (\sigma_n)_{max}(\epsilon_n)_a$$

$$= \begin{cases} \dfrac{1+\nu}{4}\bar{\sigma}_y\bar{\epsilon}_y(\sigma_f'')^2(2N_f)^{2b} & \text{if } (P)_{C_{swt}} \le \dfrac{1+\nu}{4}\bar{\sigma}_y\bar{\epsilon}_y \\ \dfrac{1}{4}\bar{\sigma}_y\bar{\epsilon}_y\left[\left(\dfrac{1}{2}+\nu\right)(\sigma_f'')^2(2N_f)^{2b}\right. & \\ \left. + \dfrac{n'}{2}(\sigma_f'')^{1/n'+1}(2N_f)^{b/n'+b} + \dfrac{1-n'}{2}\sigma_f''(2N_f)^b\right] & \text{if } (P)_{C_{swt}} > \dfrac{1+\nu}{4}\bar{\sigma}_y\bar{\epsilon}_y \end{cases}$$

Note that the work form is proposed here because the summation of work terms has more physical significance than the summation of strain amplitudes in two different directions does. The factor of 2 used in the shear portion of the parameter is to put the contributions from simple shear and simple tension on an equal basis.

Reference

[1] McDowell, D. L., "A Two-Surface Model for Transient Nonproportional Cyclic Plasticity," *Journal of Applied Mechanics,* Vol. 52, 1985, pp. 298–308.

[2] Bannantine, J. A., "A Variable Amplitude Multiaxial Fatigue Life Prediction Method," Report No. 151/UILU-ENG 89-3605, University of Illinois, Urbana, IL, October 1989.

[3] Chu, C.-C., "A Three-Dimensional Model of Anisotropic Hardening in Metals and Its Application to the Analysis of Sheet Metal Formability," *Journal of the Mechanics and Physics of Solids,* Vol. 32, 1984, pp. 197–212.

[4] Mróz, Z., "On the Description of Anisotropic Work-Hardening," *Journal of the Mechanics and Physics of Solids,* Vol. 15, 1967, pp. 163–175.

[5] Conle, A., Oxland, T. R., and Topper, T. H., "Computer-Based Prediction of Cyclic Deformation and Fatigue Behavior," *Low Cycle Fatigue, ASTM STP 942,*. H. Solomon, G. Halford, L. Kaisand, and B. Leis, Eds., American Society for Testing and Materials, Philadelphia, 1988, pp. 1218–1236.

[6] Chu, C.-C., "The Analysis of Multiaxial Cyclic Problems with An Anisotropic Hardening Model," *International Journal of Solids and Structures,* Vol. 23, No. 5, 1987, pp. 569–579.

[7] Garud, Y. S., "Multiaxial Fatigue: A Survey of the State of the Art," *Journal of Testing and Evaluation,* Vol. 9, No. 3, 1981, pp. 165–178.

[8] *Multiaxial Fatigue: Analysis and Experiments, SAE AE-14,* G. E. Leese and D. Socie, Eds., Society of Automative Engineers, Warrendale, PA, 1989.

[9] Dindinger, P., communication to SAE Fatigue Design and Evaluation Committee, 1989.

[10] Bonnen, J. J. F., Conle, F. A., and Chu, C.-C., "Biaxial Torsion-Bending Fatigue of SAE Axle Shafts," SAE Paper No. 910164, Society of Automotive Engineers, Warrendale, PA, 1991.

[11] Basquin, O. H., "The Exponential Law of Endurance Test," *Proceedings,* American Society for Testing and Materials, Philadelphia, Vol. 10, 1919, pp. 625–630.

[12] Smith, R. N., Watson, P., and Topper, T. H., "A Stress Strain Function for the Fatigue of Metals," *Journal of Materials,* JMLSA, Vol. 5, No. 4, 1970, pp. 767–778.

[13] Brown, M. W. and Miller, K. J., "A Theory for Fatigue under Multiaxial Stress-Strain Conditions," *Proceedings,* The Institution of Mechanical Engineers, Vol. 187, No. 65, 1973, pp. 745–755.

[14] Morrow, J., *Fatigue Design Handbook, SAE AE-6,* Society of Automotive Engineers, Warrendale, PA, 1968, pp. 21–30.

[15] Lohr, R. D. and Ellison, E. G., "A Simple Theory for Low Cycle Multiaxial Fatigue," *Fatigue of Engineering Materials and Structures,* Vol. 3, 1980, pp. 1–17.

[16] Socie, D. F., Waill, L. A., and Dittmer, D. F., "Biaxial Fatigue of Inconel 718 Including Mean Stress Effects," *Multiaxial Fatigue, ASTM STP 853,* K. J. Miller and M. W. Brown, Eds., American Society for Testing and Materials, Philadelphia, 1985, pp. 463–481.

[17] Fatemi, A. and Kurath, P., "Multiaxial Fatigue Life Predictions under the Influence of Mean Stresses," *Journal of Engineering Materials and Technology,* Transactions of the American Society of Mechanical Engineers, New York, Vol. 110, 1988, pp. 380–388.

Fernand Ellyin[1] *and Daniel Kujawski*[2]

A Multiaxial Fatigue Criterion Including Mean-Stress Effect

REFERENCE: Ellyin, F. and Kujawski, D., **"A Multiaxial Fatigue Criterion Including Mean-Stress Effect,"** *Advances in Multiaxial Fatigue, ASTM STP 1191,* D. L. McDowell and R. Ellis, Eds., American Society for Testing and Materials, Philadelphia, 1993, pp. 55–66.

ABSTRACT: An energy-based criterion for multiaxial fatigue which includes the influence of mean stress in an explicit form is presented. The criterion is applicable to fatigue lives up to initiation of a small size crack and could be classified as a criterion for the initiation of macroscopic cracks. The appropriate fatigue damage variable is defined as a function of the mechanical input of the distortion energy per reversal of loading, the level of tensile mean stress, and the nature of the imposed constraint. A fatigue failure criterion is obtained by plotting the damage variable versus number of reversals to failure to produce a "master" life curve. The effect of mean stress on fatigue life is described in a consistent manner for both high- and low-cycle fatigue. The predictions of the proposed criterion are compared with experimental data, and the agreement is found to be good.

KEY WORDS: biaxial and multiaxial fatigue, distortion strain energy, principal strain ratio, mean stress, constraint factor, in-phase cyclic loading

Most engineering components/structures are subjected to multiaxial stress states during their service life. This multiaxial stress state complicates the manner of assessing the accumulation of fatigue damage during a component life. The search for a continuum damage variable which could describe the damage process under multiaxial loading condition is still under active investigation.

Experimental observations have confirmed the significant role that plastic deformation plays in the fatigue damage process. However, in contrast to the yield criterion (e.g., von Mises), the fatigue process is sensitive to superimposed tensile mean (hydrostatic) stress in both the high-cycle fatigue [*1–4*] and low-cycle fatigue [*5–6*] regimes.

The fatigue failure is generally a multi-stage process involving initiation of cracks and their subsequent propagation. Ideally a separate multiaxial criterion has to be developed for both of these phases. However, the demarcation between crack initiation stage and that of propagation is not easily defined. Instead the life to achieve a crack of a certain length, e.g. of the order of a millimetre, is taken to represent the "fatigue life" of a smooth specimen. Sometimes this is also referred to as the life-to-crack initiation in the case of large components.

It is the objective of this paper to present an energy-based criterion for multiaxial fatigue which includes the influence of mean stress in an explicit form. The proposed criterion is applicable to fatigue lives defined in terms of a crack length of a small size. It is thus a criterion for the initiation of macroscopic cracks. The crack propagation beyond this phase will not be dealt with herein.

[1] Professor and [2]research associate, Department of Mechanical Engineering, University of Alberta, Edmonton, Alberta, Canada T6G 2G8. Daniel Kujawski is on leave from the Institute of Machine Design Fundamentals, Warsaw Technical University, Narbutta 84, 02-524 Warsaw, Poland.

Previous Investigations

A large number of theories of multiaxial fatigue have been proposed in the past and many are reviewed in the literature, for example see Refs *7–12*. These theories may be divided into four categories, viz: equivalent-stress and -strain, energy-based criteria, and the critical plane approaches.

The equivalent-stress and -strain approaches (e.g., extensions of the static von Mises yield criterion to fatigue) are insensitive to the hydrostatic pressure and fail to account for the path dependency of the cyclic plastic deformation. This essential interaction between stress path and plastic strain is inherently included in the energy approach [*13*]. However, most of the energy criteria are based on the plastic part of the strain energy and thus are also insensitive to the hydrostatic pressure effect.

The critical plane theories are claimed to be motivated by a physical interpretation of the fatigue damage mechanism. This is based on the assumption that the maximum shear stress (strain) amplitude and the mean or maximum normal stress (strain) on the critical plane are the controlling fatigue damage variables.

It should be noted, however, that any fatigue criterion which is insensitive to the tensile mean stress would be of limited use. Let us now discuss more specifically some multiaxial criteria which have bearing on the particular aspect of the mean stress effect.

The Mean Stress Effect

Sines [*14*] proposed a criterion in the form

$$\tau_{a,oct} + \alpha p_m = \beta \tag{1}$$

where $\tau_{a,oct}$ is a shear stress amplitude, and p_m is a corresponding normal mean stress given by

$$p_m = \frac{\sigma_1^m + \sigma_2^m + \sigma_3^m}{3} \tag{2a}$$

in which σ_i^m is the mean value of principal stresses ($i = 1,2,3$), and α and β are parameters.

Crossland [*1*] has suggested a criterion similar to that of Sines except the maximum value of hydrostatic pressure

$$p_{\max} = \frac{\sigma_1^{\max} + \sigma_2^{\max} + \sigma_3^{\max}}{3} \tag{2b}$$

is considered instead of the mean value p_m.

Dang Van [*15*] has put forward a criterion which uses local variables based on the cyclic steady state material response for a constant amplitude test; these variables are the shear stress amplitude acting on the plane of maximum shear, $\tau_{a,\max}$, and the maximum hydrostatic pressure $p_{\max}$.

Using the $p_{\max}$ instead of the p_m provides a means to differentiate between fully reversed torsional and axial (or bending) fatigue tests, i.e., $p_{\max} = 0$ and $p_{\max} = \sigma_{\max}/3$ in pure alternating torsion and axial (or bending) loading, respectively. It can be seen from Eq 2a that the mean value of pressure, p_m, would be equal to zero in both cases.

An interesting concept of differentiating between different cracking systems, observed experimentally, i.e. Case A—cracks propagate along the surface, and Case B—cracks propagate away from the surface, was suggested by Brown and Miller [*7*]. According to them, failure

under multiaxial fatigue is governed by the maximum amplitude of shear strain, $\gamma_{a,\max}$, and the amplitude of normal strain, ε_n, acting on the plane where the former occurs. The criterion of multiaxial fatigue failure proposed in Ref *7* is given by

$$f(\gamma_{a,\max}, \varepsilon_n) = \text{constant} \tag{3}$$

In Eq 3 a specific functional form for Case A and Case B cracking have to be found. In a uniaxial loading, the two separate contours corresponding to Case A and Case B coincide. The criterion expressed mathematically by Eq 3 is represented graphically by contours called "Γ-plots" in coordinates $\gamma_{a,\max} - \varepsilon_n$. Unfortunately, the functional relationship, f, is difficult to specify since it may vary with life and because the shape of the Γ-plots is dependent on the Poisson's ratio.

Most of the above criteria, however, are applicable only to low- or to high-cycle fatigue regimes, separately. Moreover, experimental results [*16–19*] indicate different ratios of tension-to-torsion fatigue strength from the ones predicted by most of the classical approaches. For example, the von Mises criterion predicts a single ratio equal to $\sqrt{3}$ which is independent of the fatigue life.

An extensive experimental and analytical program was carried out by Grubisic and Simbürger [*20*] which indicated that irrespective of the change of direction of the principal axes (proportional or nonproportional loading) slipping on all planes (not only the critical plane) influences fatigue failure.

More general representation of the multiaxial failure criteria as a surface in six-dimensional stress (or strain) space for constant life was proposed by Krempl [*21*]. For an isotropic material and in-phase constant amplitude loading (proportional loading), the surface may be represented by a quadratic form of the stress (strain) tensor, T_{ij}, i.e.

$$aT_{ii} + b_1(T_{ii})^2 + b_2 T_{ij} T_{ji} = 1 \tag{4}$$

where a, b_1, and b_2 are constants.

It has been shown that Eq 4 contains von Mises, Sines, and Gough criteria as special cases and indicates that the axial-torsion ratio must be less than 2. Krempl points out that when permanent changes of plastic deformation occur (e.g., due to strain hardening, strain softening, or mean-stress) the fatigue failure surface cannot be constructed on the basis of the controlling variable alone. In such cases the surface must be modified according to the history that the material has undergone.

In order to treat in a coherent way the history that the material has experienced during multiaxial loading, we propose to utilize the strain energy input per reversal, ΔW, as an essential variable which controls fatigue damage. The severity of the input energy depends on the level of tensile mean stress and the nature of the imposed constraint. This new damage variable is motivated by experimental observations which indicate that for the same input energy a particular cracking system and the rate of fatigue damage are influenced by a state of multiaxial strain and mean stress.

Ellyin's result in Ref *22* and more recent extension of the work in Refs *23* and *24* has led to the development of a criterion which will be described in the next section.

A New Damage Variable

In general, the fatigue damage process, associated with dissipation of strain energy, takes place as a localized phenomenon on a scale of a material's microstructure. Thus, the fatigue crack initiation criterion should be written in terms of the current microscopic stress and strain

variables in an idealized situation. However, at this microscopic scale, the local material response can differ significantly from the macroscopic values due to inhomogeneity and anisotropy of individual grains. For this reason a direct approach based on the current microscopic variables would be a difficult task. Therefore, a phenomenological approach based on experimental observations of macroscopic variables (bulk stress and strain) will be used in this development.

It was pointed out in the last part of the previous section that an appropriate damage function, ψ, would have the following form

$$\psi = \psi(\Delta W, \bar{\rho}, \sigma_m) \tag{5a}$$

where ΔW is the strain energy input per reversal, and σ_m is a measure of tensile mean stress given by

$$\sigma_m = \sigma_1^m + \sigma_2^m + \sigma_3^m \tag{5b}$$

where $\sigma_1^m, \sigma_2^m, \sigma_3^m$ are the principal static stresses, and $\bar{\rho}$ is a measure of the multiaxial constraint. The $\bar{\rho}$ and σ_m provide indices of equal damage for different multiaxial stress/strain conditions.

Earlier it was mentioned that the fatigue damage is governed by the plastic deformation. For an elastic-plastic isotropic material, the von Mises yield condition is equivalent to a constant value of the distortional component of the strain energy density, i.e.

$$W_d = \int s_{ij}\, de_{ij} = \text{constant} \tag{6}$$

where

$$s_{ij} = \sigma_{ij} - \sigma_{kk}\, \delta_{ij}/3 \tag{7a}$$

and

$$e_{ij} = \varepsilon_{ij} - \varepsilon_{kk}\, \delta_{ij}/3$$

are the deviatoric stress and strain tensors, respectively.

Thus, Eq 5a can be written as

$$\psi = \psi(\Delta W_d, \bar{\rho}, \sigma_m) \tag{8}$$

where ΔW_d stands for the distortional component of the strain energy density "range" per reversal of loading (Fig. 1). The form of Eq 8 reflects experimental observations that fatigue cracks are closely aligned with the plane where shear is predominant. Therefore, the distortion component of the strain energy range per reversal, ΔW_d, is the principal input quantity which governs the crack initiation in ductile materials. Consequently, the process of fatigue crack initiation will take place at a critical location with the highest density of "total," i.e. dissipated and nondissipated distortion energy.

In the early stage of fatigue process, i.e. crack initiation and growth of a small engineering crack, the localized dissipation may be neglected at the level of macro-scale. Therefore, the damage variable, ψ, defined by Eq 8 in terms of the bulk (macroscopic) material response, can be used to correlate fatigue life. A fatigue failure criterion is obtained by plotting the damage variable, ψ, versus number of reversals to failure, $2N_f$, to produce a "master" life curve. In

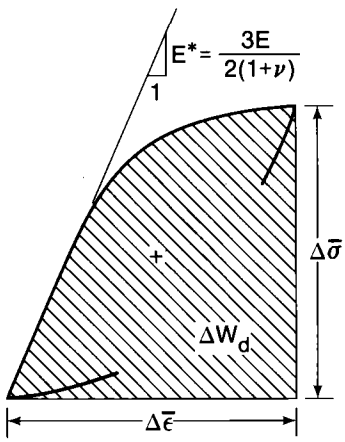

FIG. 1—*Definition of* ΔW_d *and ranges of equivalent stress and equivalent total strain.*

doing this, it is assumed that the material degradation does not affect appreciably the material response before failure.

Ellyin [*22*] has shown that for the proportional loading, the total distortion energy input, ΔW_d^T, may be calculated from the following relation

$$\Delta W_d^T = \zeta \Delta\bar{\epsilon} \Delta\bar{\sigma} + \Delta\bar{\epsilon}\,\bar{\sigma}_m \tag{9}$$

where $\zeta\ \Delta\bar{\epsilon}\ \Delta\bar{\sigma} = \Delta W_d$ is the distortion strain energy range, with the coefficient ζ depending on the stress level when material response is inelastic (for an explicit relationship, see Ref *22*, e.g. for a uniaxial loading and Masing type of behavior, $\zeta = \dfrac{1 - n'}{2(1 + n')}\left(1 - \dfrac{\Delta\sigma}{E\Delta\varepsilon}\right)$), and

$$\Delta\bar{\epsilon} = (\tfrac{2}{3}\Delta e_{ij}\Delta e_{ij})^{1/2} \tag{10a}$$

$$\Delta\bar{\sigma} = (\tfrac{3}{2}\Delta s_{ij}\Delta s_{ij})^{1/2} \tag{10b}$$

are equivalent total strain and stress ranges, respectively. The prefix symbol, Δ, means that $\Delta\bar{\epsilon}$ (or $\Delta\bar{\sigma}$) represents "peak-to-peak" change in equivalent strain (or stress). The $\bar{\sigma}_m$ stands for equivalent mean stress

$$\bar{\sigma}_m = (\bar{\sigma}_U + \bar{\sigma}_L)/2 \tag{10c}$$

where $\bar{\sigma}_U$ and $\bar{\sigma}_L$ are the upper and lower limits of effective stress, respectively.

The essential step in the determination of the controlling damage variable, ψ, is the specification of Eq 8. In general, a particular form of it may be deduced from the experimental data, or a postulate can be put forward.

Let us assume the following form of Eq 8

$$\psi = \frac{\Delta W_d\left(1 + \alpha \dfrac{\sigma_m}{\bar{\sigma}}\right)}{f(\bar{\rho})} \tag{11}$$

in which $\bar{\sigma} = \Delta\bar{\sigma}/2$ is the effective stress amplitude, the coefficient α characterized the material sensitivity to mean stress, and $f(\bar{\rho})$ is a multiaxial constraint function (MCF) to be specified later on. Note that for $\alpha = \frac{1}{2}\zeta$ and $f(\bar{\rho}) = 1$, Eq 11 is similar to Eq 9, which was put forward by Ellyin in 1974.

Specification of the Multiaxial Constraint Function (MCF)

The MCF reduces the multiaxial fatigue life data for various combinations of the imposed strain ratios on a unique (master) life curve. However, before specifying MCF, the constraint factor $\bar{\rho}$ has to be defined.

The definition proposed in Ref *24* will be adopted here, i.e.

$$\bar{\rho} = (1 + \bar{\nu}) \frac{\hat{\varepsilon}_{max}}{\hat{\gamma}_{max}} \tag{12}$$

with

$$\hat{\varepsilon}_{max} = \max[\varepsilon_a \quad \text{or} \quad \varepsilon_t],$$
$$\hat{\gamma}_{max} = \max[|\varepsilon_a - \varepsilon_r| \quad \text{or} \quad |\varepsilon_t - \varepsilon_r|],$$

and $\bar{\nu}$, the effective Poisson's ratio, is calculated from[3]

$$\bar{\nu} = \frac{\nu_p(1 - \nu_e)(\varepsilon_a + \varepsilon_t) + (\nu_e - \nu_p)(\varepsilon_a^e + \varepsilon_t^e)}{(1 - \nu_e)(\varepsilon_a + \varepsilon_t) + (\nu_e - \nu_p)(\varepsilon_a^e + \varepsilon_t^e)}; \varepsilon_a \neq -\varepsilon_t \tag{13}$$

In the above the peak values of ε_a and ε_t are principal in-plane strains (axial and transversal) parallel to the "free" surface, subscripts (or superscripts) e and p stand for elastic and plastic values, respectively, and ε_r is radial strain (perpendicular to the "free" surface) given by

$$\varepsilon_r = \frac{-\bar{\nu}}{1 - \bar{\nu}} (\varepsilon_a + \varepsilon_t) \tag{14}$$

Equations 13 and 14 were obtained assuming that the radial stress, σ_r, perpendicular to the "free" surface, is negligible in comparison with the in-plane principal stresses, σ_a and σ_t.

The multiaxial constraint factor, $\bar{\rho}$, defined by Eq 12, demonstrates the importance of the orientation of the "free" surface with respect to the imposed principal strains. Note that in this context a "free" surface may be the surface of a smooth specimen as well as the new surface created by a crack or even the internal surface of a defect or porosity.

A further examination of Eq 12 reveals that $\bar{\rho}$ has an important physical interpretation regarding the fatigue damage process. Using the $\bar{\rho}$ provides a means to differentiate between fully reversed torsion ($\varepsilon_a = -\varepsilon_t$) with $\bar{\rho} = 1 + \bar{\nu}$ and equibiaxial loading ($\varepsilon_a = \varepsilon_t$) with $\bar{\rho} = 1 - \bar{\nu}$, i.e. in the terminology of Brown and Miller [*7*] between Case A and Case B loading, respectively. The factor $(1 + \bar{\nu})$ in Eq 12 is included so that for an isotropic material under a uniaxial stress condition, $\bar{\rho} = 1$ since $\varepsilon_r = \varepsilon_t = -\bar{\nu}\varepsilon_a$. This denotes the transition from Case A to Case B loading.

Since Case B loading gives lower fatigue strength than Case A, then $1/\bar{\rho}$ indicates the severity of a particular multiaxial loading with reference to the uniaxial stress condition. The actual

[3] For fully reversed torsion ($\varepsilon_a = -\varepsilon_t$) Eq 13 becomes indeterminate since both the numerator and denominator are equal to zero. In this case a limit calculation must be performed.

"driving force" of a fatigue damage accumulation is accounted through an appropriate form of the multiaxial constraint function f. A simple functional form would be a power law form, i.e.

$$f(\bar{\rho}) = (\bar{\rho})^n \tag{15}$$

where $n \geq 0$ is a parameter.

Substituting Eq 15 into Eq 11 we get

$$\psi = \frac{\Delta W_d \left(1 + \alpha \frac{\sigma_m}{\bar{\sigma}}\right)}{(\bar{\rho})^n} \tag{16}$$

For test conditions with $\sigma_m = 0$, Eq 16 reduces to

$$\psi = \frac{\Delta W_d}{(\bar{\rho})^n} = (\Delta W_d)_{\text{uniaxial}} \tag{17}$$

In the case of a high-cycle fatigue regime when bulk material response is essentially elastic, Eq 17 can be written in terms of amplitudes of the stress components σ_a and σ_t. A convenient way to present the predictions of Eq 17 is to plot the amplitudes of alternating principal stresses (e.g. σ_a and σ_t) which cause fatigue failure after a certain number of reversals. The predictions of Eq 17 are compared in Fig. 2 with biaxial experimental data of the fatigue limit (i.e. $2N_f \geq 5 \times 10^6$ reversals) for three different steels. The results are shown in terms of a normalized stress amplitude through division of the fatigue strength for alternating push-pull or bending loading, σ_{-1}, where subscript -1 refers to $R = \sigma_{\min}/\sigma_{\max} = -1$.

Figure 2 indicates the effect of the exponent n on the shape of the criterion. The values of the exponent n ranging from 0 to 1 result in a fair correlation with experimental data. Note that for $n = 0$ the damage parameter given by Eq 17 will be independent of $\bar{\rho}$ and equivalent to the distortion strain energy parameter. For the sake of convenience in the subsequent calculation, $n = 1$ will be used.

Note that the shape of the proposed criterion (Eq 16) depends on the multiaxial constraint function, $(\bar{\rho})^n$. This then indicates that the tension-torsion fatigue strength ratios are not constant but depend on the applied strain levels since the $\bar{\rho}$ (see Eq 12) is a function of the effective Poisson's ratio $\bar{\nu}$ (Eq 13).

Comparison with Experimental Results

Consider first the correlation of mean-stress data obtained from tests of uniaxial smooth specimen in high-cycle regime. In the case of uniaxial loading $\bar{\rho} = 1$, Eq 16 can be written in terms of the normalized stress amplitude, σ_a/σ_{-1}, versus normalized mean stress, σ_m/σ_a. For a particular life and with $\alpha = \frac{1}{2}$, Eq 16 reduces to

$$\frac{\sigma_a}{\sigma_{-1}} = \frac{1}{\left(1 + \frac{1}{2}\frac{\sigma_m}{\sigma_a}\right)^{1/2}} \quad \text{for } \sigma_{\max} \leq \sigma_u, \quad \text{and} \quad |\sigma_{\min}| \leq |\sigma_c| \tag{18}$$

where $\sigma_{\max} = \sigma_m + \sigma_a$ and $\sigma_{\min} = \sigma_m - \sigma_a$ are maximum and minimum stresses, respectively, and σ_u (or σ_c) is the ultimate tensile strength (or a critical buckling or crushing stress). Obvi-

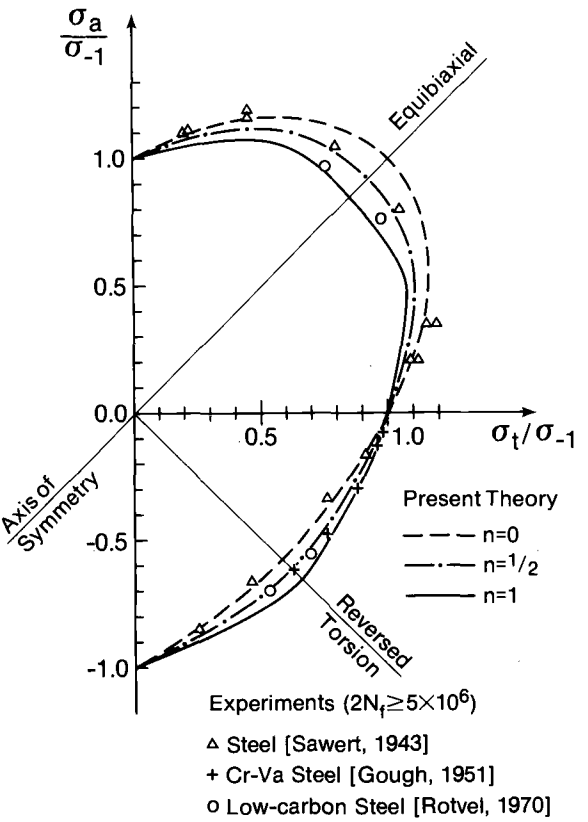

FIG. 2—*Comparison of multiaxial experimental data with proposed failure criterion for the fatigue limit ($2N_f \geq 5 \times 10^6$ reversals).*

ously the σ_{max} (or σ_{min}) cannot exceed the σ_u (or σ_c), otherwise a "failure" will occur at the first reversal of loading.

For most engineering alloys the ratio σ_{-1}/σ_u is the range of ⅓ ~ ½. Assuming that $|\sigma_c| = \sigma_u \approx 3\sigma_{-1}$ will limit the applicability of the Eq 18 to the following range $-1.06 \leq \sigma_m/\sigma_a \leq 4.4$. Since σ_m/σ_a could not reach a ratio of -2, therefore σ_a/σ_{-1} in Eq 18 cannot exhibit a singular behavior.

The graphical interpretation of Eq 18 is shown in Fig. 3 together with experimental results taken from the literature [*14,26,27*] for several steels and aluminum alloys. It is interesting to note that a good fit to experimental results is obtained with $\alpha = ½$.

Next, consider the use of Eq 16 to correlate low-cycle biaxial fatigue data with zero mean stress obtained from a cruciform specimen by Pascoe and de Villiers [*28*]. Figure 4 shows experimental data for three different strain ratios of a mild steel in coordinates of log $(\Delta W_d/\bar{\rho})$ versus log $2N_f$. It is evident from Fig. 4 that the variable $\Delta W_d/\bar{\rho}$ provides a fairly good correlation independent of experimentally applied biaxial strain ratio $\rho = \Delta\epsilon_t/\Delta\epsilon_a$.

In the case of multiaxial loading, the calculations of ΔW_d and $\bar{\rho}$ were done using a recently developed rate-independent constitutive model [*29*]. The stable cyclic stress-strain response of the relevant steel was approximated by the Ramberg-Osgood type of relation

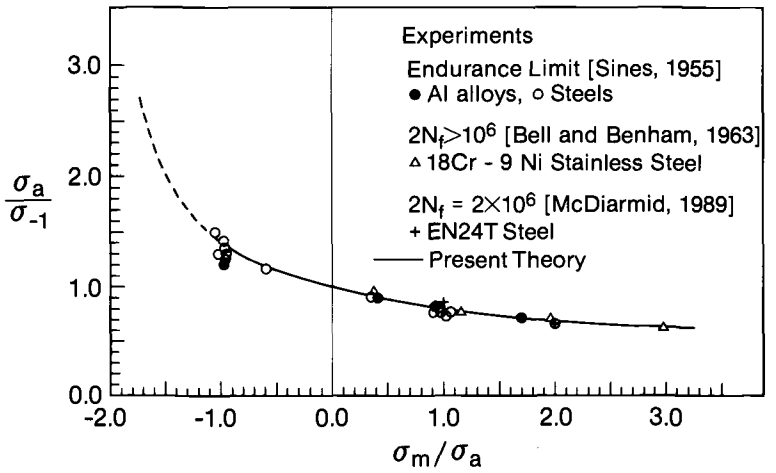

FIG. 3—*Compressive and tensile mean stress effect in high-cycle regime.*

$$\frac{\Delta\epsilon}{2} = \frac{\Delta\sigma}{2E} + \left(\frac{\Delta\sigma}{2K'}\right)^{1/n'} \tag{19}$$

The data used in the calculation were: $E = 200$ GPa, $K' = 1008$ MPa, $n' = 0.2$, and Poisson's ratio $\nu = 0.265$.

A further correlation between experimental results and predictions of Eq 16 is shown in Fig. 5. In this figure $\Delta W_d/\bar{\rho}$ is calculated using the constitutive model in Ref *29*. The number of

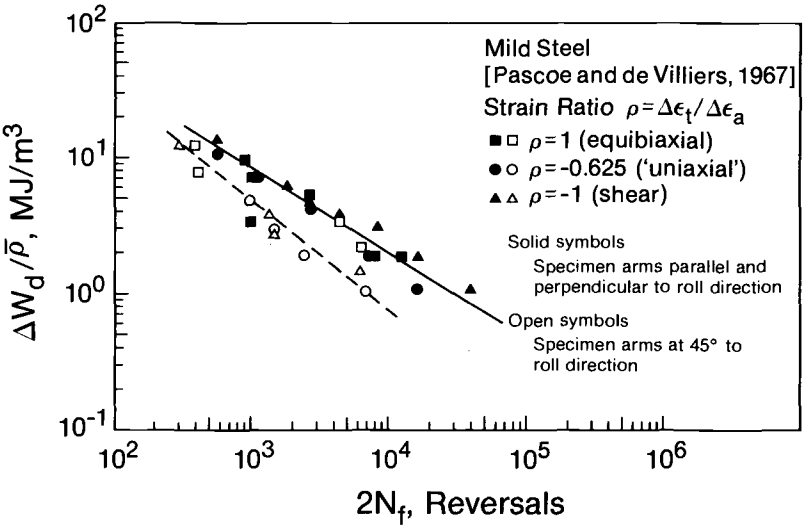

FIG. 4—*Correlation of multiaxial experimental data in low-cycle regime using the proposed energy criterion.*

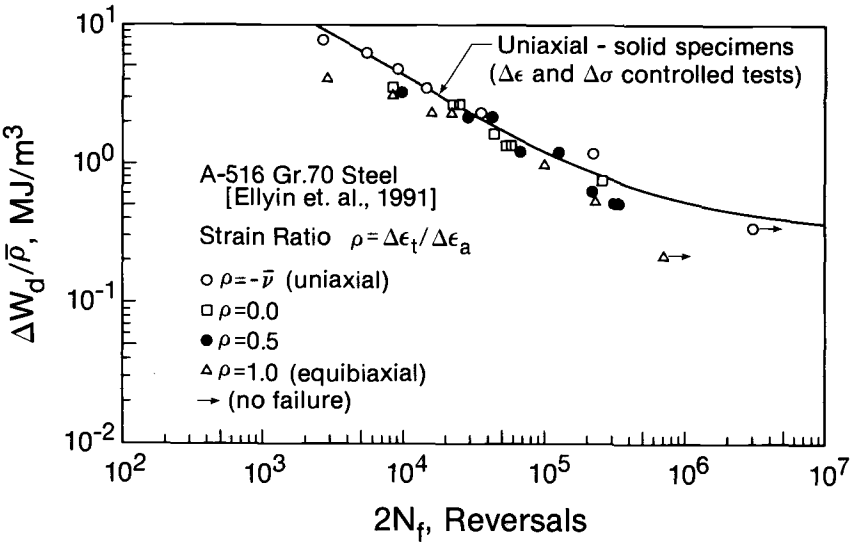

FIG. 5—*Correlation between the proposed criterion and multiaxial data of ASTM A-516 Gr. 70 carbon steel* [24].

reversals to failure are taken from Table 3 of Ref *24*, and the cyclic stress-strain coefficient of Eq 19 were taken from Table 1 of the same reference.

Note that despite the material anisotropy of data (in terms of fatigue lives) used in Fig. 4 and the inevitable bending stresses due to misalignment of both loading systems of Refs *24* and *28*, the scatter band in Figs. 4 and 5 is well within the acceptable range.

Conclusions

A fatigue damage variable is introduced based on the governing physical phenomenon. The following general form for the damage variable, ψ, is suggested

$$\psi = \frac{\Delta W_d h(\sigma_m)}{f(\bar{\rho})} \tag{20}$$

where ΔW_d is the distortion strain energy range and $f(\bar{\rho})$ and $h(\sigma_m)$ are appropriate functions of multiaxial constraint and tensile mean stress measures, respectively. Explicit functional forms of f and h are given in Eq 16. It is shown that the present phenomenological approach unifies both the high- and low-cycle regimes.

The proposed criterion is based on the premise that the damage caused by cyclic loading is a function of the mechanical input of the distortion energy into the material at each reversal of loading. The proposed criterion includes the effect of mean stress and imposed multiaxial constraint. It indicates that the ratio of axial-torsional fatigue strengths is not constant but changes with the applied strain levels.

The predictions of the proposed criterion are compared with the experimental results, and the agreement is found to be fairly good. The constitutive relations used in the present analysis are time independent, and thus phenomena such as strain-rate sensitivity and creep are excluded.

The method developed herein is limited, however, to predicting lives defined in terms of the initiation of macroscopic cracks, i.e. those cases where the life associated with the crack propagation stage is negligible. When the crack propagation stage cannot be neglected, this approach is to be supplemented by a crack growth law, e.g. such as that given in Ref *30*.

An extension of the present approach to the out-of-phase loading will be described in the forthcoming paper [*31*].

Acknowledgment

The work reported here is part of a general investigation into material behavior under multiaxial states of stress and adverse environments. The research is supported, in part, by the Natural Science and Engineering Research Council of Canada (NSERC Grant No. A-3808).

The authors would like to thank Z. Xia for his help in providing computer predictions for Figs. 4 and 5.

References

[*1*] Crossland, B., "Effect of Large Hydrostatic Pressures on the Torsional Fatigue Strength of an Alloy Steel," *Proceedings,* International Conference on Fatigue of Metals, Institution of Mechanical Engineers, London, 1956, pp. 138–149.

[*2*] White, D. J., Crossland, B., and Morrison, J. L. M., "Effect of Hydrostatic Pressure on the Direct-Stress Fatigue Strength of an Alloy Steel," *Journal of Mechanical Engineering Science,* Vol. 1, No. 1, 1959, pp. 39–49.

[*3*] Welter, G. and Choquet, J. A., "Triaxial Tensile Stress Fatigue Testing," Welding Research Supplement, American Welding Society, Miami, FL, 1963, pp. 565s–570s.

[*4*] Burns, D. J. and Parry, J. S., "Effect of Large Hydrostatic Pressures on the Torsional Fatigue Strength of Two Steels," *Journal of Mechanical Engineering Science,* Vol. 6, No. 3, 1964, pp. 293–305.

[*5*] Libertiny, G. Z., "Short-Life Fatigue under Combined Stresses," *Journal of Strain Analysis,* Vol. 2, No. 2, 1967, pp. 91–95.

[*6*] Ludsford, G., Pense, A. W., Venkatesan, P. S., and McIntosh, M. J., "The Effect of Hydrostatic Pressure Environment on the Low Cycle Fatigue Properties of a Maraging Steel," *ASME Journal of Engineering Materials and Technology,* July 1973, pp. 157–160.

[*7*] Brown, M. W. and Miller, K. J., "The Theory of Fatigue Failure under Multiaxial Stress-Strain Conditions," *Proceedings of the Institution of Mechanical Engineering,* Vol. 187, 1973, pp. 745–755.

[*8*] Krempl, E., in *The Influence of State of Stress on Low Cycle Fatigue of Structural Materials, ASTM STP 549,* American Society for Testing and Materials, Philadelphia, 1974.

[*9*] Garud, Y. S., "Multiaxial Fatigue: A Survey of the State of the Art," *Journal of Testing and Evaluation,* JTEVA, Vol. 9, No. 3, May 1981, pp. 165–178.

[*10*] Jordan, E. H., "Fatigue-Multiaxial Aspects," *Journal of Pressure Vessel and Piping: A Decade of Progress,* American Society for Mechanical Engineers, New York, 1982, pp. 507–520.

[*11*] Ellyin, F. and Valaire, B., "Development of Fatigue Failure Theories for Multiaxial High-Strain Conditions," *SM Archives,* Vol. 10, 1985, pp. 45–85.

[*12*] Ellyin, F., "Recent Development in Predicting Multiaxial Fatigue Failure," *RES Mechanica,* Vol. 25, 1988, pp. 1–23.

[*13*] Garud, Y. S., "A New Approach to the Evaluation of Fatigue under Multiaxial Loading," *Proceedings,* Symposium of Methods Predicting Material Life in Fatigue, W. J. Ostergen and J. R. Whitehead, Eds., ASME, New York, 1979, pp. 247–264.

[*14*] Sines, G., "Failure of Materials under Combined Repeated Stresses with Superimposed Static Stresses," NACA TN 3495, National Advisory Committee for Aeronautics, Washington, DC, November 1955.

[*15*] Dang Van, K., "Sur la Résistance à la Fatigue des Métaux," *Sciences Techniques Armament,* Vol. 47, 1973, pp. 641–722.

[*16*] Sines, G. and Ohgi, G., "Fatigue Criteria Under Combined Stresses or Strains," *ASME Journal of Engineering Materials and Technology,* Vol. 103, April 1981, pp. 82–90.

[*17*] Gough, H. J., "Some Experiments on the Resistance of Metals to Fatigue under Combined Stresses," Ministry of Supply, Aeronautical Research Council, Reports and Memorandum, No. 2522, London, 1951.

[18] Rotvel, F., "Biaxial Fatigue Tests with Zero Mean Stresses using Tubular Specimens," *International Journal of Mechanical Sciences,* Vol. 12, 1970, pp. 597–613.
[19] McDiarmid, D. L., "A General Criterion for High Cycle Multiaxial Fatigue Failure," *Fatigue Fracture of Engineering Materials and Structures,* Vol. 14, No. 4, 1991, pp. 429–453.
[20] Grubisic, V. and Simbürger, A., "Fatigue under Combined Out-of-Phase Multiaxial Stresses," *International Conference on Fatigue Testing and Design,* Society of Environmental Engineers, London, 1976, pp. 27.1–27.8.
[21] Krempl, E., "Multiaxial Fatigue. Present and Future Methods of Correlation," *AGARD Conference Proceedings,* No. 155, NATO, Advisory Group for R&D, Neuilly sur Seine, France, 1974, pp. 5.1–5.12.
[22] Ellyin, F., "A Criterion for Fatigue under Multiaxial States of Stress," *Mechanics Research Communication,* Vol. 1, 1974, pp. 219–224.
[23] Ellyin, F., and Golos, K., "Multiaxial Fatigue Damage Criterion," *ASME Journal of Engineering Materials and Technology,* Vol. 110, 1988, pp. 63–68.
[24] Ellyin, F., Golos, K., and Xia, Z., "In-Phase and Out-of-Phase Multiaxial Fatigue," *ASME Journal of Engineering Materials and Technology,* Vol. 113, 1991, pp. 112–118.
[25] Sawert, W., "Verhalten der Baustaehle bei wechselnder mhrachsiger Beanspruchung," *Zeitschrift Verein Deutscher Ingenieuve,* Vol. 87, No. 39/40, 1943, pp. 609–615.
[26] Bell, W. J. and Benham, P. P., "The Effect of Mean Stress on Fatigue Strength of Plane and Notched Stainless Steel Sheet in the Range from 10 to 10^7 Cycles," *Symposium on Fatigue of Aircraft Structures: Low-Cycle, Full-Scale, and Helicopter, STP 338,* American Society for Testing and Materials, Philadelphia, 1963, pp. 25–46.
[27] McDiarmid, D. L., "The Effects of Mean Stress on Biaxial Fatigue Where the Stresses are Out-of-Phase and at Different Frequencies," *Biaxial and Multiaxial Fatigue, EGF3,* M. W. Brown and K. J. Miller, Eds., 1989, Mechanical Engineering Publications, London, pp. 605–619.
[28] Pascoe, K. J. and de Villiers, J. W. R., "Low Cycle Fatigue of Steels under Biaxial Straining," *Journal of Strain Analysis,* Vol. 2, No. 2, 1967, pp. 117–126.
[29] Ellyin, F. and Xia, Z., "A Rate-Independent Constitutive Model for Transient Non-Proportional Loading," *Journal Mechanics, Physics and Solids,* Vol. 37, No. 1, 1989, pp. 71–91.
[30] Kujawski, D. and Ellyin, F., "A Fatigue Crack Growth Model with Load Ratio Effects," *Engineering Fracture Mechanics,* Vol. 28, No. 4, 1987, pp. 367–378.
[31] Ellyin, F. and Z. Xia, "A General Theory of Fatigue with Application of Out-of-Phase Cyclic Loading," to be published in *ASME Journal of Engineering Materials and Technology.*

K. C. Liu[1]

A Method Based on Virtual Strain-Energy Parameters for Multiaxial Fatigue Life Prediction

REFERENCE: Liu, K. C., **"A Method Based on Virtual Strain-Energy Parameters for Multiaxial Fatigue Life Prediction,"** *Advances in Multiaxial Fatigue, ASTM STP 1191,* D. L. McDowell and R. Ellis, Eds., American Society for Testing and Materials, Philadelphia, 1993, pp. 67–84.

ABSTRACT: A new method is proposed for multiaxial fatigue life prediction using correlation parameters based on virtual strain energy as a measure of fatigue damage on critical planes of fracture. The virtual strain-energy parameters are physically associated with two different modes of fatigue fracture planes. The critical plane leading to Mode I fracture is driven by the principal stress and strain, and the other, leading to Mode II fracture, is driven by the maximum shear stress and strain. The mode of crack initiation and propagation depends on material, temperature, strain range, and stress and strain histories, but not on the relative magnitude of the virtual strain-energy parameters. Biaxial fatigue data obtained from the literature were analyzed for Type 304 stainless steel tested at room and elevated temperatures and for SAE 1045 steel tested at room temperature under in-phase and 90° out-of-phase loading conditions. Comparisons are made between experimental data and theoretical predictions to show the effectiveness of the proposed method.

KEY WORDS: multiaxial fatigue, cyclic fatigue, life prediction, stress, strain, virtual strain energy, fatigue fracture, in-phase loading, out-of-phase loading

Fatigue is an important consideration in the design of structural components subjected to cyclic loading. To understand fatigue behavior, a wealth of uniaxial cyclic fatigue data have been generated for many structural materials. One approach used to characterize fatigue behavior is to establish the relationship between applied stress (or strain) and fatigue life in terms of number of cycles to failure (Fig. 1). Manson [*1*] and Coffin [*2*] have independently proposed the life relation expressed in a two-term power law equation

$$\Delta\varepsilon = \Delta\varepsilon_p + \Delta\varepsilon_e = AN_f^{-\alpha} + BN_f^{-\beta}, \tag{1}$$

in which

$$\Delta\varepsilon_p = AN_f^{-\alpha}, \tag{2}$$
$$\Delta\varepsilon_e = BN_f^{-\beta} \tag{3}$$

where

$\Delta\varepsilon$ = total strain range per cycle,
$\Delta\varepsilon_e$ = elastic component of $\Delta\varepsilon$,

[1] Metals and Ceramics Division, Oak Ridge National Laboratory, Oak Ridge, TN 37831-6155.

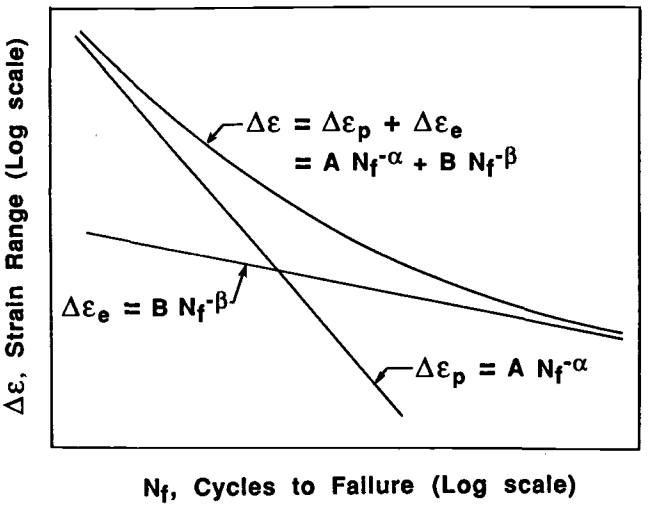

FIG. 1—*Schematic of uniaxial fatigue behavior represented by the two-term power law relationship in a log-log plot of* $\Delta\varepsilon$ *versus* N_f.

$\Delta\varepsilon_p$ = plastic component of $\Delta\varepsilon$,
N_f = fatigue life, cycles to failure, and
A, B, α, β = material constants.

Fatigue behavior of many structural metal alloys has been shown to obey the two-term power law equation.

Since the state of stresses in structural components is usually complex during service lifetime, it is apparent that an extension to multiaxiality is necessary if the method is to be used in practical design. Accounting for the multiaxiality in Eq 1 is usually accomplished by substituting the uniaxial strain with an equivalent strain inferred from von Mises' strain formulation. This subtle scheme is based on the observation that the von Mises equivalent strain reduces to uniaxial strain under uniaxial loading. However, this approach often fails to bring test data into the single curve represented by Eq 1. Another deficiency is that the von Mises equivalent strain cannot be rationally divided into elastic and plastic equivalent strain components for identification with the terms given in the right-hand side of Eq 1. This is not a serious deficiency if Eqs 2 and 3 are not mandatory requirements.

A dozen or more methods for multiaxial fatigue life prediction have been proposed to date. Some are based on philosophical approaches, such as that discussed above, while others are based on physical approaches [*3–6*], which have shown some success. However, no single approach has demonstrated to be superior to the others when applied to general situations. Excellent survey studies on multiaxial fatigue have been made, and results are reported elsewhere [*7,8*]. In general, fatigue life predictive methods are based on stress, strain, or energy as a correlating parameter.

Fatigue criteria based on the concept of damage in terms of energy have been proposed and evaluated with experimental fatigue data generated under uniaxial as well as biaxial loading conditions [*9–12*]. Most of the energy-based methods utilize plastic energy of stress-strain hysteresis loops as a correlating parameter. Limited success has been made in predicting fatigue life in low-cycle fatigue regime where the plastic energy of the hysteresis loops is well defined. However, it is difficult to estimate the plastic hysteresis energy in high-cycle fatigue regime

where the stress-strain behavior is practically elastic. Failure to adequately predict high-cycle fatigue life is an obvious shortcoming of the plastic energy-based method.

Although not following the same concept of energy in the classical sense, two parameters expressed in terms of virtual strain-energy (VSE) are introduced here as a measure of fatigue damage and have shown to be effective in correlating with multiaxial cyclic fatigue life. The VSE parameters are physically associated with two different modes of fatigue fracture occurring on respective critical planes; one is associated with the maximum vector product of normal stress and strain and the other with that of shear stress and strain. The mode of fatigue fracture varies depending on material, temperature, strain range, and loading history. Based on observations of crack formulation for a number of materials tested in biaxial modes [*13*], Socie [*5*] presented a shear strain model and a tensile strain model based on the critical plane for crack nucleation and growth. The former uses a strain-based correlation parameter consisting of three strain components, and the latter uses the Smith-Watson-Topper (SWT) parameter [*14*].

Biaxial fatigue data were analyzed for Type 304 stainless steel [*5,15–18*] and SAE 1045 steel [*19–21*] subjected to in-phase and 90° out-of-phase tension/torsion loading at room and elevated temperatures. Comparisons were made between the experimental data and theoretical predictions to show the effectiveness of the new approach.

Preliminaries and Concept

The proposed method is a straightforward generalization of the uniaxial fatigue life prediction method based on Eq 1, which has been widely studied and accepted. The total strain range of a typical cyclic stress-strain hysteresis loop is divisible into two parts, $\Delta\varepsilon_e$ and $\Delta\varepsilon_p$ (Fig. 2). A virtual strain-energy quantity, ΔW, can be defined as the product of $\Delta\varepsilon$ and $\Delta\sigma$ as

$$\Delta W = \Delta\sigma \cdot \Delta\varepsilon = E\Delta\varepsilon_e \cdot (\Delta\varepsilon_p + \Delta\varepsilon_e) \tag{4}$$

where

$$\Delta\sigma = E\Delta\varepsilon_e \tag{5}$$

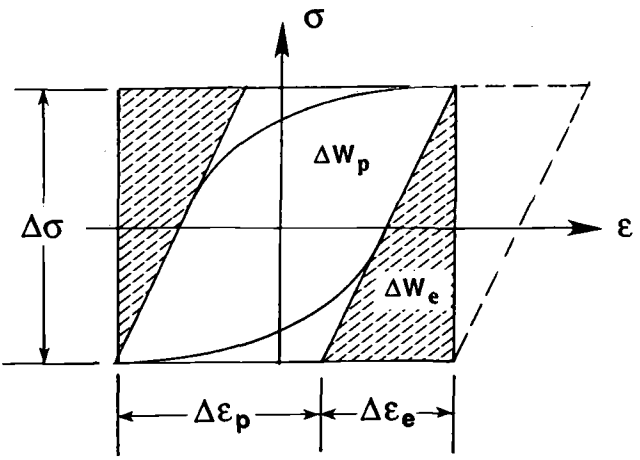

FIG. 2—*Definitions of* ΔW, ΔW_p, *and* ΔW_e.

where E = Young's modulus. Equation 4 is equivalent to the SWT parameter. Substituting Eqs 2 and 3 into Eq 4, one obtains

$$\Delta W = \Delta W_p + \Delta W_e = EAB N_f^{-(\alpha+\beta)} + EB^2 N_f^{-2\beta} \tag{6}$$

Figure 2 shows that ΔW_p is slightly greater than the actual plastic hysteresis energy, and ΔW_e is the sum of the two shaded wedges representing the virtual elastic strain energy. It should be noted that Eq 6 retains the characteristics of the two-term power-law expression. As the cyclic strain range decreases and ΔW_p decreases to a negligible quantity, ΔW_e becomes the dominant factor in Eq 6. This explains why a fatigue damage parameter, which lacks the key ingredient equivalent to the elastic component of the VSE, correlates poorly with fatigue data in the high-cycle fatigue regime.

Since biaxial loading in tension and torsion is usually performed using a tubular specimen, cylindrical coordinates are employed, using subscripts, r, θ, and z, to indicate the radial, circumferential, and longitudinal directions, respectively, as shown in Fig. 3*a*. The numerical subscripts of σ_i and ε_i (i = 1, 2, and 3) represent the three principal direct stress and strain axes, as shown in Fig. 3*b*. The stress-free surfaces are perpendicular to axes "r" and "2" as indicated.

To facilitate discussions on the VSE parameters under multiaxial loading conditions, a Mohr representation of biaxial stress (Points P and Q) and strain states (P′ and Q′) is illustrated in Fig. 4*a*, in which σ, τ, ε, and γ are normal stress, shear stress, normal strain, and engineering shear strain, respectively.

Uniaxial loading is a special case of biaxial loading in the absence of torsion, represented by the strain biaxiality ratio, $\lambda = \gamma/\varepsilon$, being equal to zero. The Mohr representation of uniaxial loading is shown in Fig. 4*b*. In the absence of axial loading on the other extreme, the condition of pure torsion is arrived at with $\lambda = \infty$, as shown in Fig. 4*c*. Any axial/torsional combined loading is shown in Fig. 4*a*. Note that the principal stress and strain directions are determined by angles Φ_σ and Φ_ε, respectively, and generally are not the same unless $\lambda = 0$ or ∞. Φ_n and Φ_s are the angles between the z-axis and the vectors normal to the critical planes associated with Stress Points A and B (Fig. 4*a*), respectively.

Modes of Failure

A tubular specimen subjected to tension-torsion loading is considered here. To facilitate general understanding, a method of presentation similar to those of Brown and Miller [*3*] and Lohr and Ellison [*4*] will be employed. The crack driven along the surface of the specimen (Fig. 3*a*) is defined as Type A, and the crack acting through the thickness of the specimen is defined as Type B (Fig. 3*b*). The crack that propagates in the tension-dominated critical plane, indicated as I_a-plane (sanded as shown in Fig. 3*a*) is defined as Mode I fracture. With the aid of Fig. 4*a*, the VSE parameter for Mode I fracture, ΔW_I, can be calculated as follows

$$\Delta W_I = \{2(\mathbf{OA}) \cdot 2(\mathbf{O'A'})\}_{max} \tag{7}$$

or decomposed in two vector products as

$$\Delta W_I = (\Delta W_n)_{max} + \Delta W_s \tag{8}$$

where the tensile components, ΔW_n, is maximized. The vector, n_a, normal to the I_a-plane makes the angle, Φ_n, with the z-axis.

In contrast to Mode I fracture, the crack that propagates in a shear-dominated critical plane (hatched as shown in Fig. 3*a*) is defined as Mode II fracture. The VSE parameter for Type A/

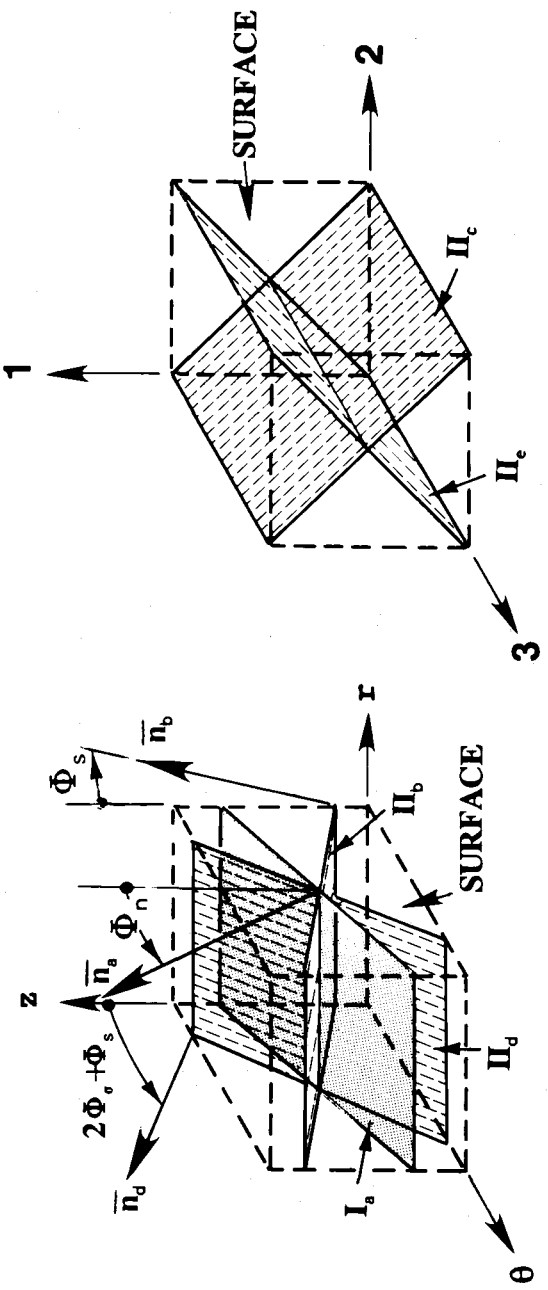

FIG. 3—*Descriptions of:* (a) *Type A fracture in Modes I and II and* (b) *Type B fracture in Mode II.*

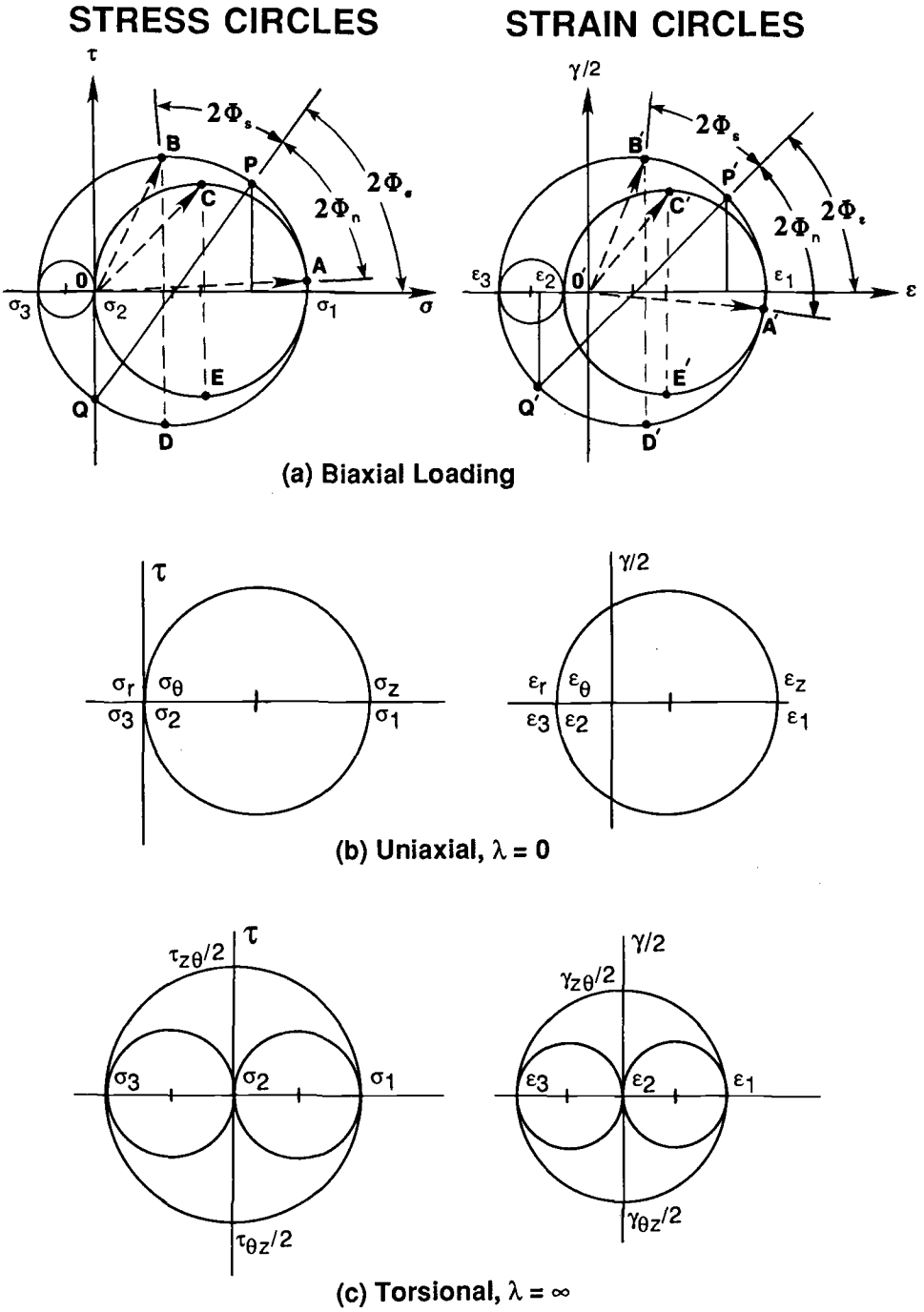

FIG. 4—*Mohr's stress and strain circles:* (a) *biaxial loading,* (b) *uniaxial loading, and* (c) *pure torsion.*

Mode II fracture, $\Delta W_{II,A}$ (simplified as ΔW_{II} since the discussion here is focused on Type A fracture), can be calculated as

$$\Delta W_{II} = 2(\mathbf{OB}) \cdot 2(\mathbf{O'B'}) = \Delta W_n + (\Delta W_s)_{max} \tag{9}$$

where the shear component of ΔW_{II} is maximized as indicated by $(\Delta W_s)_{max}$, and ΔW_n is the associated tensile component of ΔW_{II}. The vector, n_b, normal to the shear-dominated critical plane, indicated as II_b-plane in Fig. 3*a*, makes the angle, Φ_s, with the z-axis. A second Mode II fracture plane, which is about 90° apart from the II_b-plane, can be inferred from the symmetry of Mohr circles with respect to the axes, σ and ϵ. Stress Points D, E, D', and E' are the mirror images of Stress Points B, C, B', and C', respectively. The vector, n_d, normal to the second shear-dominated critical plane, indicated as II_d-plane in Fig. 3*a*, makes an angle of $\Phi_s + 2\Phi_\sigma$ with the z-axis.

The VSE parameter for Mode II fracture in Type B critical planes (II_c- and II_e-planes as shown in Fig. 3*b*) can be calculated with the aid of Fig. 4*a* as

$$\Delta W_{II,B} = 2(\mathbf{OC}) \cdot 2(\mathbf{O'C'}) = \Delta W_n + (\Delta W_s)_{max} \tag{10}$$

where the shear component, ΔW_s, is maximized.

It is important to note that $\Delta W_{II,B}$ is equal to $\Delta W_{II,A}$ under uniaxial loading ($\lambda = 0$) or just slightly lower than $\Delta W_{II,A}$ under biaxial loading with a low biaxiality ratio ($\lambda \leq 1.7$). The reason is that a specimen under biaxial loading with a low value of λ may have actually initiated microcracking in Type B/Mode II but appears to have fractured in Type A/Mode I due to the synergistic effect of both failure modes.

Under uniaxial loading, the maximum VSE occurs in the plane normal to the uniaxial loading axis. This leads to $\Phi_\sigma = \Phi_\epsilon = \Phi_n = 0$ and $\Phi_s = \pi/4$. In the absence of ΔW_s in Eq 8, ΔW_I becomes

$$\Delta W_I = \Delta W_n = (2\sigma_z) \cdot (2\varepsilon_z) = (2\sigma_1) \cdot (2\varepsilon_1) \tag{11}$$

When a tubular specimen is subjected to pure torsion (Fig. 4*c*), the values of ΔW_I and ΔW_{II} are the same.

Evaluations of Proposed Method

Evaluations Based on In-Phase Biaxial Fatigue Data of Type 304 Stainless Steel

Zamrik [*15*] conducted in-phase tension-torsion fatigue tests on Type 304 stainless steel at 538°C and showed that the von Mises equivalent strain range, $\Delta\varepsilon_{eq}$, correlated poorly with the fatigue data obtained (Fig. 5). The curve shown in Fig. 5 represents the best fit of the uniaxial data. Test data for the same type of material, but obtained from a different supplier, from tests at room temperature (RT) and 650°C by Ogata et al. [*16*], and from tests at 550°C by Nitta et al. [*17*] showed about the same degree of scatter from the uniaxial data (Figs. 6 through 8). In all cases, fatigue life was shown to be a function of biaxial strain ratio. Out-of-phase (90°) data were shown to have fallen far below the in-phase data, indicating a serious deficiency in using $\Delta\epsilon_{eq}$ as a correlating parameter to predict multiaxial fatigue behavior.

The use of ΔW_I and ΔW_{II} as correlating parameters was studied with existing data reported in the open literature. Effectiveness of correlating ΔW_I to Zamrik's data into a single curve is well illustrated (Fig. 9). Numbers attached to the data points indicate $\Delta\varepsilon_{eq}$ in percent of strain. The curve represents the two-term power law expression determined by the least-squares-fit method.

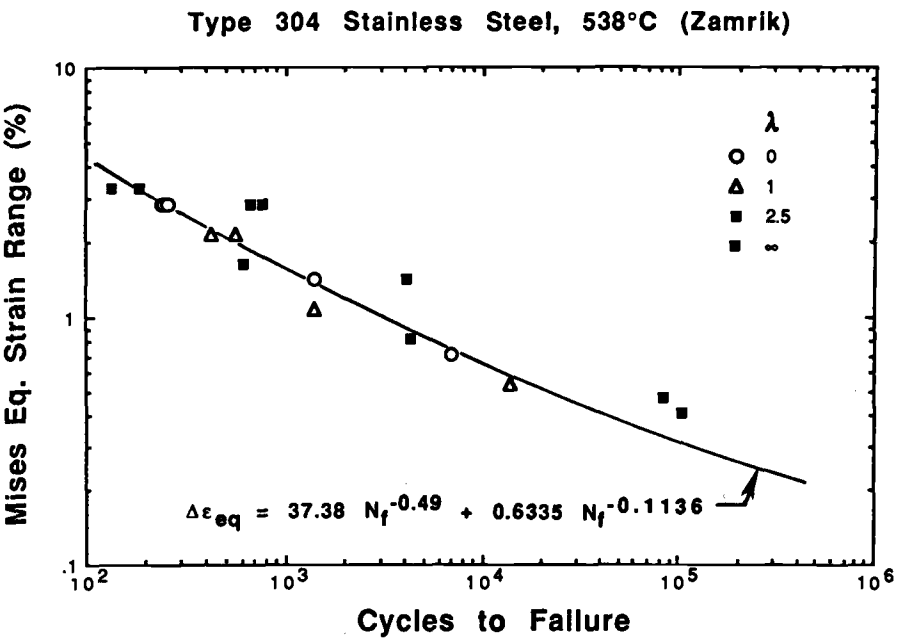

FIG. 5—*A fatigue life correlation based on von Mises equivalent strain range for Type 304 stainless steel tested at 538°C* [15].

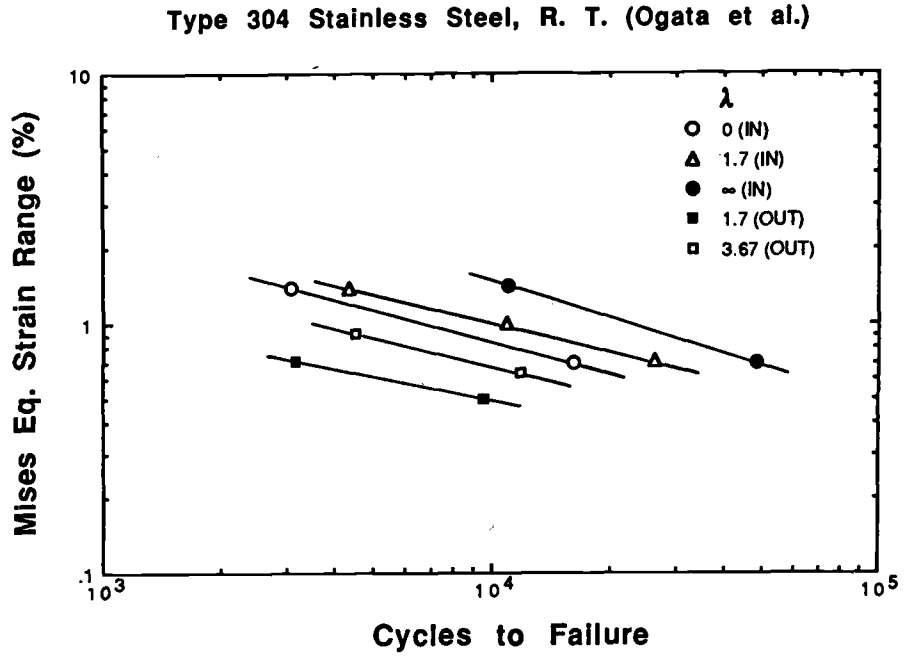

FIG. 6—*A fatigue life correlation based on von Mises equivalent strain range for Type 304 stainless steel tested at room temperature* [16].

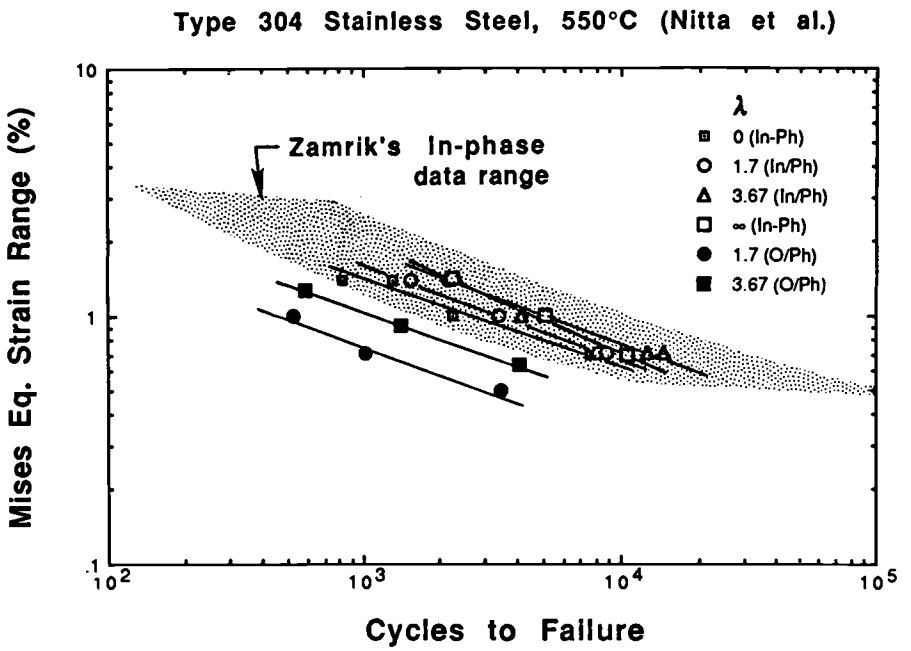

FIG. 7—*A fatigue life correlation based on von Mises equivalent strain range for Type 304 stainless steel tested at 550°C* [17].

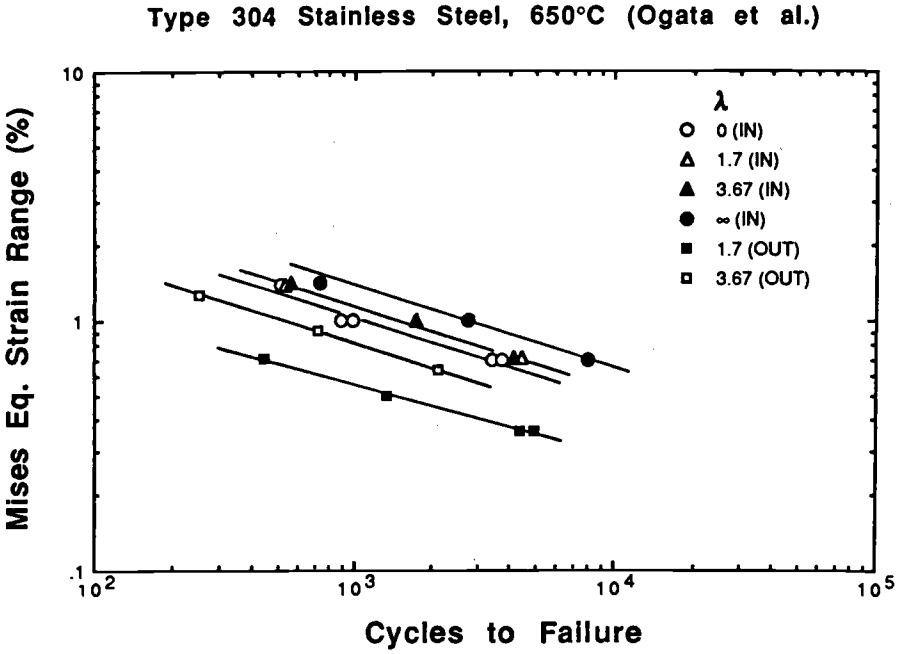

FIG. 8—*A fatigue life correlation based on von Mises equivalent strain range for Type 304 stainless steel tested at 650°C* [16].

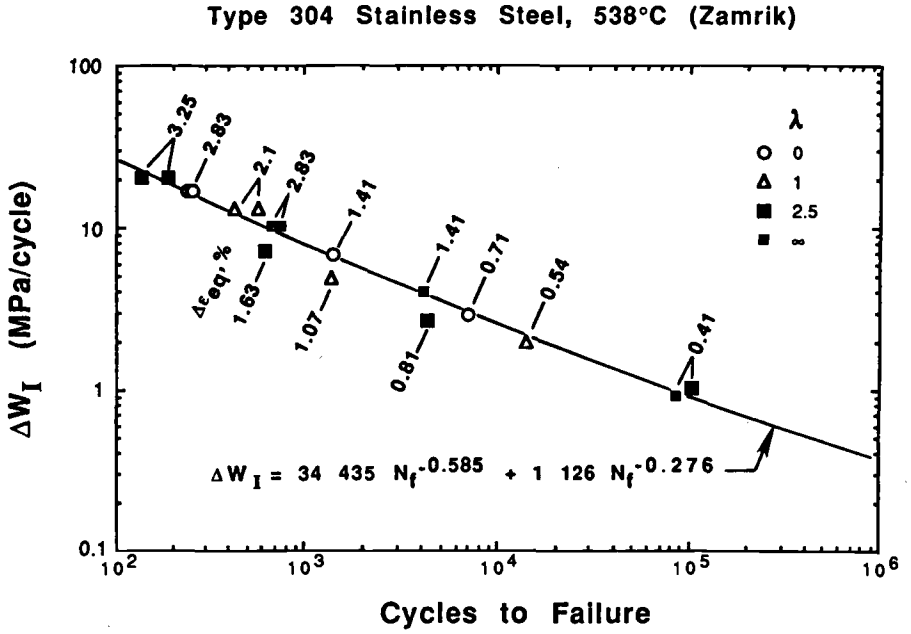

FIG. 9—*A fatigue life correlation based on* ΔW_I *for Type 304 stainless steel tested at 538°C* [15].

Data obtained by Ogata et al. [*16*] show that ΔW_I correlates well with RT fatigue life data, and ΔW_{II} does well with those obtained at 650°C (Fig. 10). They reported that all specimens tested at RT initiated crack in Mode I independent of strain ratio and strain range. The mode of fracture at 650°C was more complex due to surface oxidation. However, observations showed that the microcracking in the grain boundary region occurred on the maximum shear plane for specimens tested at 650°C. These findings explain why ΔW_I and ΔW_{II} correlate well with RT and 650°C data, respectively.

Figure 10 also shows that ΔW_I correlates well with RT test data obtained by Socie [*5*] as an independent set of test data by itself. Fatigue life data obtained in low-cycle regime (below 10^4 cycles) by Ogata et al. [*16*] and those by Socie are in good agreement. However, in high-cycle regime, Socie's data will probably fall above those of Ogata et al. Some discrepancies in fatigue lives at different levels of cyclic strain ranges are expected due to the differences in supply sources, batch variation, stress and strain measurements, the definition of fatigue failure, and other factors. Socie reported that Mode II shear failures were observed at high strain amplitudes, and Mode I failures were observed at low strain amplitudes for specimens tested in torsion. Despite the change in failure mode, the above correlation between ΔW_I and Socie's torsion data remained effective because the value of ΔW_{II} and that of ΔW_I are the same under pure torsion, as mentioned previously.

A study shows that in-phase biaxial fatigue data obtained at 550°C by Nitta et al. [*17*] and Takahashi [*18*] correlate well with ΔW_{II} (Fig. 11), but correlate poorly with ΔW_I. The opposite was observed in Zamrik's case, although Zamrik's tests were performed just 12°C lower than the test temperature used by Nitta et al. They reported that initial cracks occurred on the maximum shear plane under in-phase tests at 550°C with $\lambda > 1.7$. However, tests under $\lambda \leq 1.7$ showed Mode I fracture. A plausible reason is that when a specimen is subjected to biaxial loading with a low value of λ, fracture may be facilitated by synergistic damage due to Type

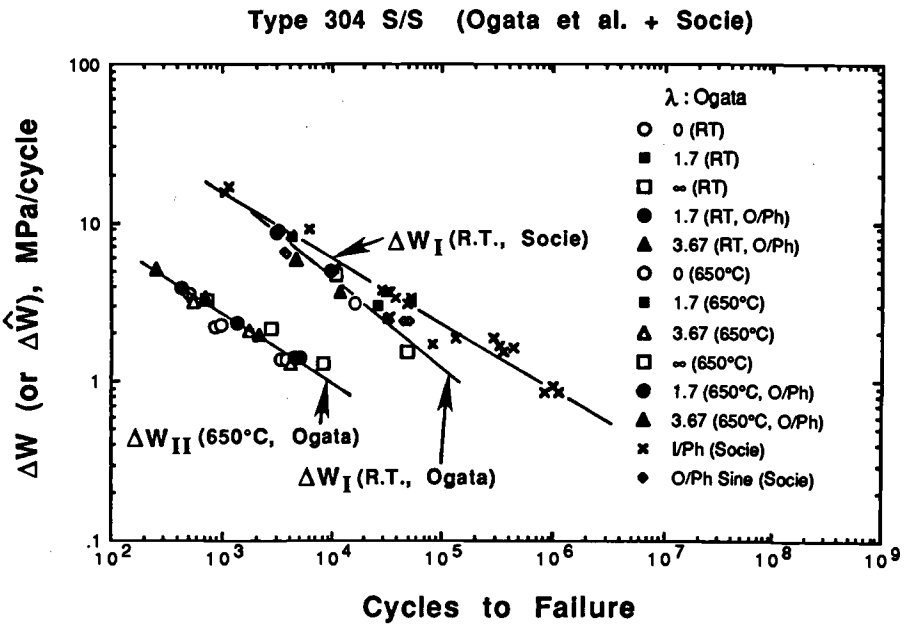

FIG. 10—*A fatigue life correlation based on the proposed method for Type 304 stainless steel tested at room and elevated temperatures* [5,16].

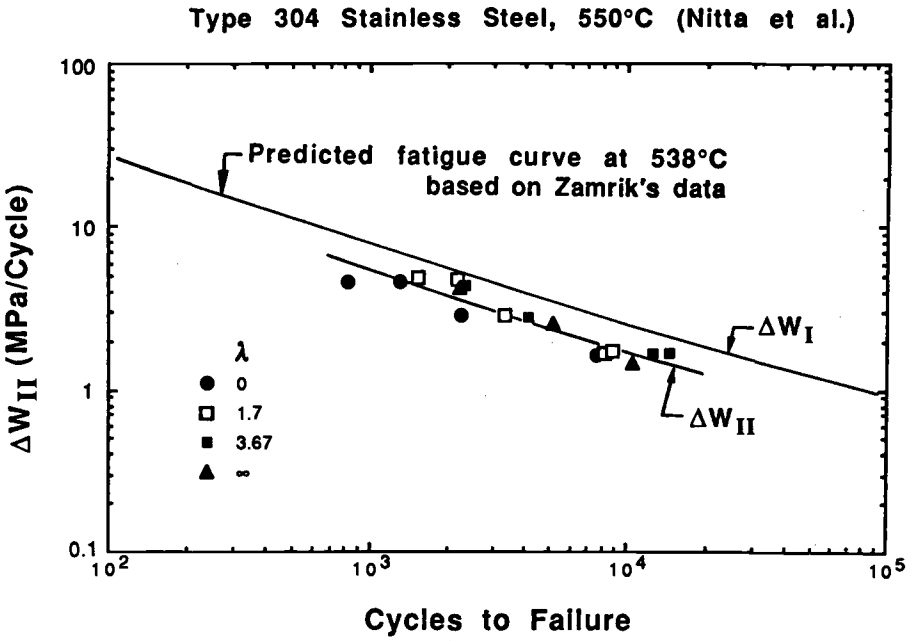

FIG. 11—*A fatigue life correlation based on the proposed method for Type 304 stainless steel tested at 550°C* [17].

B/Mode II fatigue coupled with Type A/Mode I fatigue. Based on the reported observations [*17*], it appeared that initial cracks were actually initiated in Type B/Mode II, but the final failure occurred on the plane in Type A/Mode I fracture.

Agreement between data obtained by Zamrik [*15*] and those by Nitta et al. [*17*] is respectable (Fig. 11) despite the fact that two different batches of the material were used. Generally, Nitta's data fell slightly below Zamrik's. It is logical to assume that less energy was required to fatigue the material at higher temperature. These two sets of data further hinted that the crossover of fracture mode from Mode I to Mode II occurred at temperatures in the range from 538 to 550°C.

Evaluations Based on In-Phase Biaxial Fatigue Data of SAE 1045 Steel

Biaxial fatigue data obtained by Kurath et al. [*19*] and Fatemi and Stephens [*20,21*] for SAE 1045 steel were used to evaluate the proposed model. Results (Fig. 12) illustrate that the von Mises equivalent strain range correlates well with both sets of in-phase fatigue data, which interestingly are in good mutual agreement also. Reasons for the good correlation will be cited later. However, most of the out-of-phase data fell below the in-phase data as a whole.

The quality of correlation between ΔW_I and 1045 steel data are poor. Results of the analysis show strong dependency to biaxiality ratio. However, ΔW_{II} correlates superbly with all 1045 steel data combined (Fig. 13). Comparisons between predicted and observed lives (Fig. 14) showed that only few data points fell slightly outside the upper and lower limit bounds of factor two. Results of the good correlation demonstrated in Fig. 13 are not fortuitous. Studies [*22*] revealed that 1045 steel was sensitive to crack initiation on the maximum shear strain plane under biaxial loading. Since the von Mises strain range $\Delta\epsilon_{eq}$ is equivalent to the octahedral

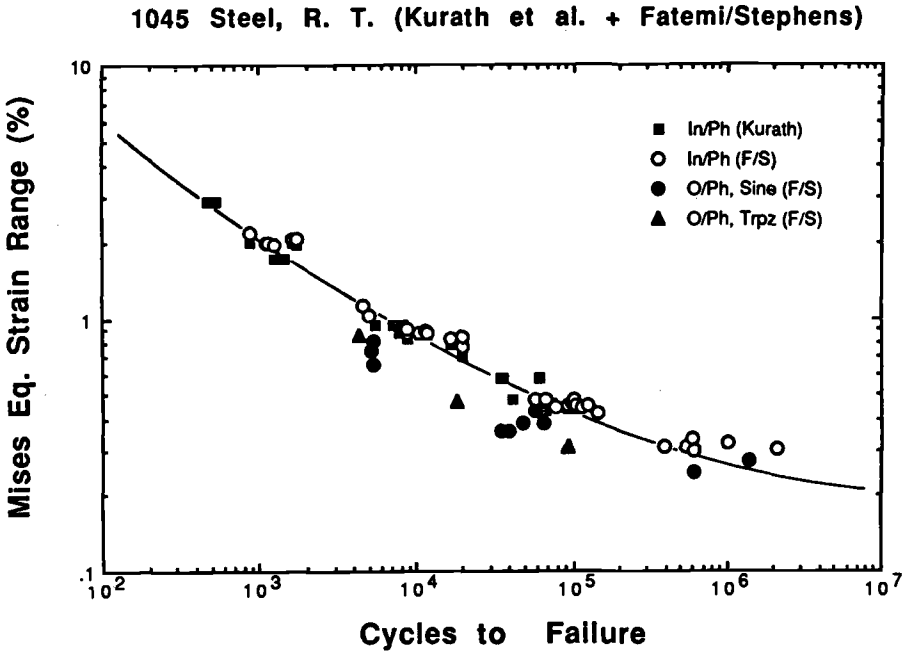

FIG. 12—*A fatigue life correlation based on von Mises equivalent strain range for SAE 1045 steel tested at room temperature* [19,20].

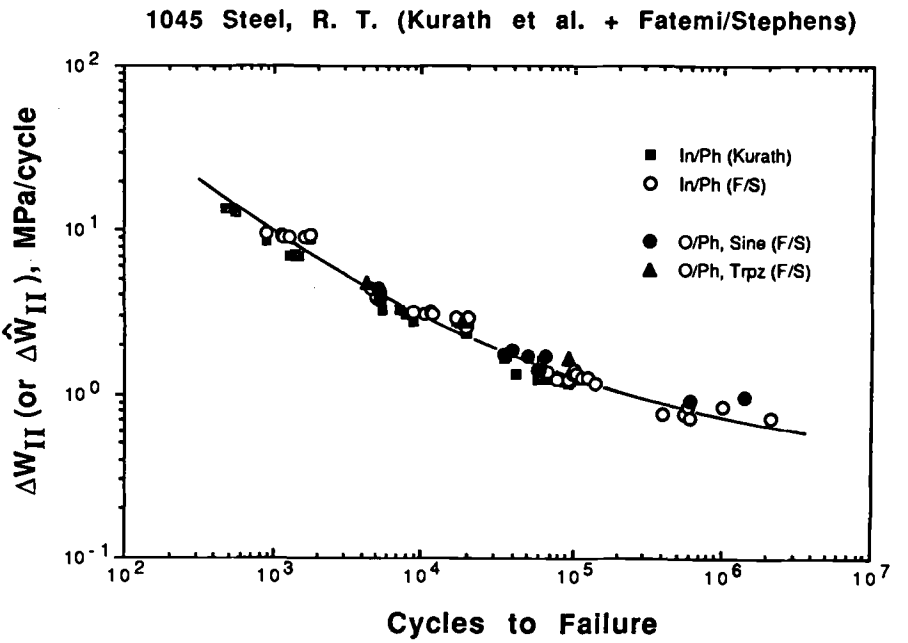

FIG. 13—*A fatigue life correlation based on the proposed method for SAE 1045 steel tested under in-phase and out-of-phase loading conditions at room temperature* [20].

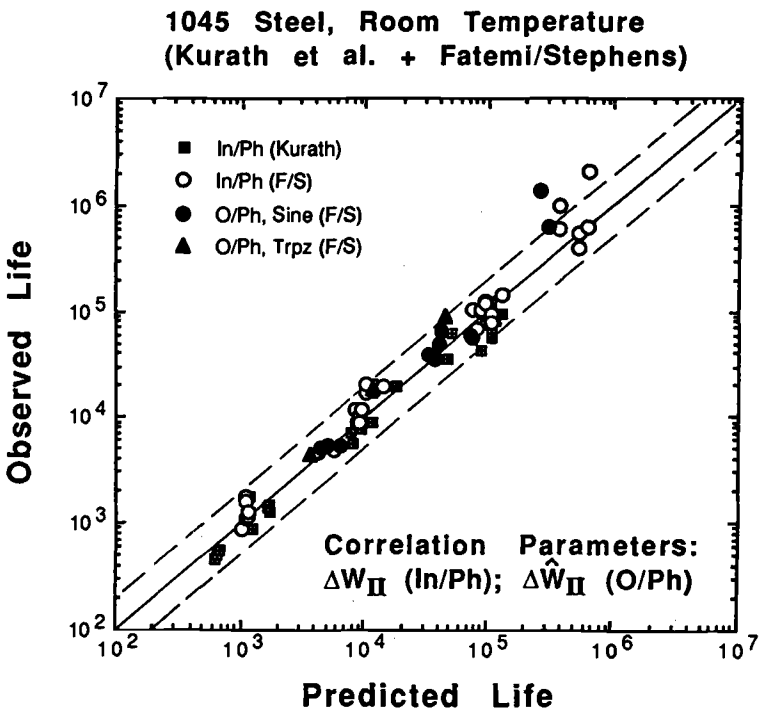

FIG. 14—*Comparison of predicted and observed fatigue lives of SAE 1045 steel* [19,20].

shear strain and ΔW_{II} is related to the VSE on the maximum shear plane, both parameters should correlate well with the in-phase 1045 steel data.

Evaluation Based on 90° Out-of-Phase Fatigue Data

Stress and strain histories are usually more complex for specimens tested under out-of-phase (O/Ph) loading conditions (nonproportional loading) compared to those observed under in-phase loading conditions (proportional loading) [*21*]. The situations are further complicated by loading waveforms, control mode (stress or strain), and the phase differential between the maximum stress and strain states. In what follows, the discussion will be limited only to the cases dealing with 90°-O/Ph loading conditions due to the complexity of the problems.

As stated earlier, both ΔW_I and ΔW_{II} are virtual quantities. Although the physical meaning of the VSE can be explained rationally, discussions will be deferred to the future paper since the subject is beyond the scope of this paper. A direct application of the two VSE parameters to correlation in O/Ph loading situations is difficult since the stress and strain paths for in-phase loading are linear in their respective coordinate systems, whereas those for O/Ph loadings are complex. To simplify the matter, an independent set of VSE parameters $\Delta \hat{W}_I$ and $\Delta \hat{W}_{II}$ will be introduced here and used to correlate with O/Ph multiaxial fatigue life data. The relationship between both sets of the VSE parameters has not been fully explored and remains weak at this time. However, a summary of analysis results based on in-phase data combined with O/Ph data strongly hints that both sets of the VSE parameters appear to be related.

When a specimen is subjected to 90°-O/Ph sinusoidal strain histories in biaxial loading with λ other than 0 or ∞, the stress and strain loci are elliptical (Fig. 15*a*). As λ approaches null, both of the elliptical loci will be flattened into a line which represents a uniaxial cyclic loading path. Analogously, as λ approaches the other extreme, both loci will be compressed again into a vertical line which represents a torsional cyclic loading path. Therefore, it is not unreasonable to postulate that completing a cycle of the elliptical strain path in the biaxial strain space is equivalent to the sum of completing a cycle each of fictitious uniaxial and pure shear loading along the major and minor diameters of the elliptical strain locus, as shown in Fig. 15*a*. The VSE parameter $\Delta \hat{W}_I$ for Mode I fracture on the critical plane is assumed to be the sum of the ΔW_I due to the fictitious uniaxial loading path and the VSE on the same critical plane due to the torsional loading path. The VSE parameter $\Delta \hat{W}_{II}$ for Mode II fracture is assumed to be the maximum sum of ΔW_{II}*s* on the critical plane due to both of the fictitious loading paths. In the case of uniaxial loading or pure torsion, $\Delta \hat{W}_I$ and $\Delta \hat{W}_{II}$ reduce to ΔW_I and ΔW_{II}, respectively.

When a specimen is subjected to O/Ph sinusoidal strain histories in biaxial loading with a phase lag other than 90°, the stress and strain loci will be tilted from the axial coordinate axis with an angle (Fig. 15*b*). The loci will remain elliptical when sinusoidal strain histories are employed. It is postulated analogously that completing a cycle of the elliptical strain path is equivalent to the sum of completing a cycle each of two fictitious loading paths along the major and minor diameters of the elliptical strain locus. The VSE parameters, $\Delta \hat{W}_I$ and $\Delta \hat{W}_{II}$, for this loading condition can be computed analogously as the case discussed above for the 90°-O/Ph loading conditions. When the phase lag between the axial and torsional loading paths decreases to null, i.e., in-phase loading, $\Delta \hat{W}_I$ and $\Delta \hat{W}_{II}$, reduce to ΔW_I and ΔW_{II}, respectively. Testing under O/Ph loading with a phase lag other than 90° has been reported [*17*]. However, incomplete information precludes effective evaluations of the proposed method for general O/Ph biaxial loading conditions.

When a specimen is subjected to 90° O/Ph trapezoidal strain histories, the stress locus in the biaxial stress space is usually neither symmetric with respect to the stress axes nor rectangular in shape (Fig. 15*c*). Because the peak stress and strain states are also out of phase in this situation, the method of VSE calculation employed in the previous cases appears to be somewhat

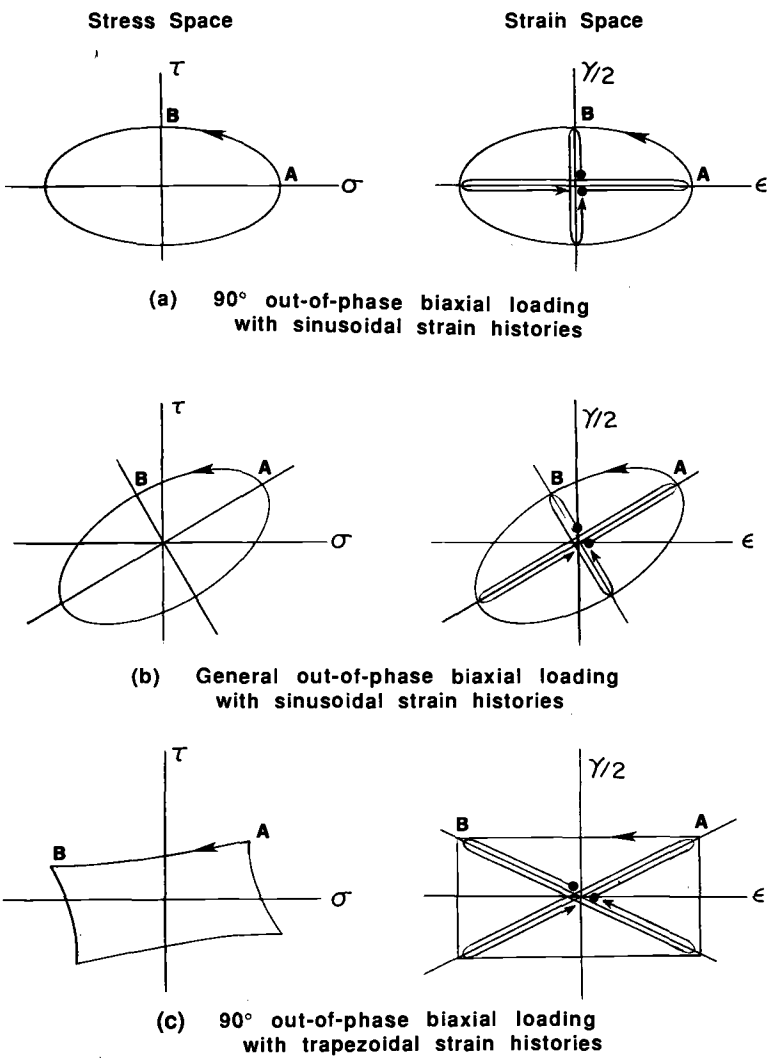

FIG. 15—*Methods used in estimating* $\Delta\hat{W}_I$ *and* $\Delta\hat{W}_{II}$ *under out-of-phase cyclic loading conditions.*

inappropriate. Therefore, an ad hoc rule is used to estimate the values of the VSE parameters. It is assumed that completing a cycle of rectangular strain path is equivalent to the sum of completing a cycle each of fictitious loading paths along the two fictitious diagonal strain paths (Fig. 15*c*). The VSE parameters, $\Delta\hat{W}_I$ and $\Delta\hat{W}_{II}$, for this loading situation were then computed analogously as described above. In the absence of either of the fictitious loading paths, $\Delta\hat{W}_I$ and $\Delta\hat{W}_{II}$ also reduce to ΔW_I and ΔW_{II}, respectively.

Ninety-degree-O/Ph fatigue data obtained by Ogata et al. [*16*] for Type 304 stainless steel tested at RT and 650°C were analyzed. By fortuity, both the RT and high temperature O/Ph data correlate well not only with $\Delta\hat{W}_I$ and $\Delta\hat{W}_{II}$, respectively, but also blend well with the family of in-phase fatigue data based on ΔW_I and ΔW_{II}, as shown in Fig. 10. A limited number of O/Ph test data obtained by Socie [*5*] were also analyzed and compared with in-phase data in

Fig. 10. Good agreement between the two families of data was again demonstrated. These observations hint that there may exist a close relationship between the two sets of the VSE parameters. It should be noted that the fatigue curve shown in Fig. 10 was determined from the in-phase data but represented the O/Ph lifetimes as well. Comparisons are made between observed and predicted lives (Fig. 16). The information published by Nitta et al. [*17*] and Socie [*5*] was insufficient for predicting fatigue lifetimes of Type 304 stainless steel tested under other types of O/Ph loading conditions.

Out-of-phase fatigue data obtained by Fatemi and Stephens [*20*] were analyzed and compared with the in-phase data, as shown in Fig. 13. Good correlations among the data as a whole illustrated in Fig. 13 further suggest that both sets of the VSE parameters may be closely related. Predicted and observed lifetime data of 1045 steel tested under O/Ph loading conditions are included in Fig. 14, which further illustrates the effectiveness of the proposed method.

Conclusions

1. The proposed VSE-based method for multiaxial fatigue life prediction is a rational extension of the well established power-law fatigue criterion that has successfully predicted the uniaxial fatigue behavior of many materials tested under various temperatures.

2. The concept of the proposed method is physically based. Results of careful analyses combined with reported information concerning fatigue fracture modes indicate that multiaxial fatigue life correlates well with either ΔW_{I} (and $\Delta \hat{W}_{\mathrm{I}}$) or ΔW_{II} (and $\Delta \hat{W}_{\mathrm{II}}$), depending on the

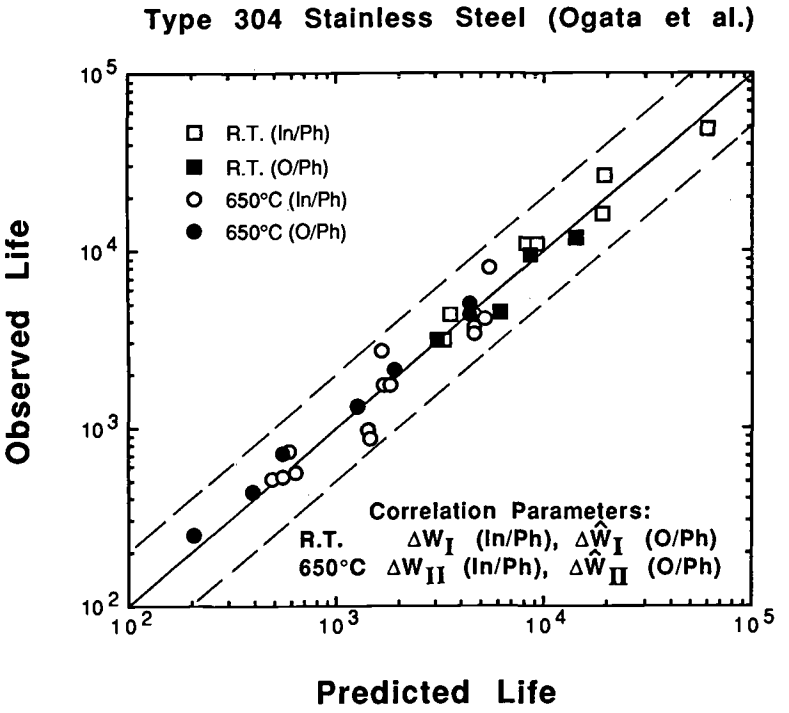

FIG. 16—*Comparison of predicted and observed fatigue lives of Type 304 stainless steel tested at room and elevated temperatures* [16].

critical plane along which the crack propagates in Mode I or Mode II fracture. The mode of crack initiation and propagation depends on the material and temperature.

3. Successful correlations between the VSE parameters and biaxial fatigue lives have been demonstrated for Type 304 stainless steel at RT and elevated temperatures and for SAE 1045 steel at RT under both in-phased as well as out-of-phase loading conditions.

4. Comparisons between predicted and observed fatigue lives indicate the proposed method is highly effective for multiaxial fatigue life predictions.

5. Results of correlation analyses suggest that the VSE parameters ΔW_I and ΔW_{II} for in-phase multiaxial fatigue and $\Delta \hat{W}_I$ and ΔW_{II} for 90°-O/Ph multiaxial fatigue are closely related. In particular situations, $\Delta \hat{W}_I$ and $\Delta \hat{W}_{II}$ also reduce to ΔW_I and ΔW_{II}, respectively. Further studies are needed to clarify their relationship and expand the concept to establish a set of unified VSE parameters for general loading conditions.

Acknowledgment

This research was sponsored by the Division of Materials Science, the U.S. Department of Energy, under contract DE-AC05-84OR21400 with Martin Marietta Energy Systems, Inc. The author wishes to thank Drs. H. Pih and O. M. Jadaan for reviewing and L. A. Starkey for preparing the manuscript.

References

[1] Manson, S. S., Heat Transfer Symposium, University of Michigan, 27–28 June 1952, University of Michigan Press, also in NACA-TN-2933, July 1953.

[2] Coffin, L. F., Jr., *Transactions, American Society of Mechanical Engineers,* Vol. 76, 1954, pp. 931–950.

[3] Brown, M. W. and Miller, K. J., *Proceedings, Institute of Mechanical Engineers,* Vol. 187, 1973, pp. 745–755.

[4] Lohr, R. D. and Ellison, E. G., *Fatigue of Engineering Materials and Structures,* Vol. 3, No. 1, 1980, pp. 1–17.

[5] Socie, D., *Transactions, American Society of Mechanical Engineers, Journal of Engineering Materials and Technology,* Vol. 109, 1987, pp. 293–298.

[6] Fatemi, A. and Socie, D., *Fatigue and Fracture of Engineering Materials and Structures,* Vol. 11, No. 3, 1988, pp. 145–165.

[7] Tipton, S. M. and Fash, J. W. in *Multiaxial Fatigue: Analysis and Experiments,* SAE AE-14, Society of Automotive Engineers, Warrendale, PA, 1989, pp. 67–80.

[8] Garud, Y. S., *Journal of Testing and Evaluation,* Vol. 9, No. 3, May 1981, pp. 165–178.

[9] Martin, D. E., *Transactions, American Society of Mechanical Engineers, Journal of Basic Engineering,* Vol. 83, December 1961, pp. 565–571.

[10] Morrow, J. in *Internal Friction, Damping and Cyclic Plasticity, ASTM STP 378,* American Society for Testing and Materials, Philadelphia, 1965, pp. 45–87.

[11] Garud, Y. S., *Journal of Engineering Materials and Technology, Transactions, American Society of Mechanical Engineers,* Vol. 103, 1981, pp. 118–125.

[12] Ellyin, F. and Golos, K., *Transactions, American Society of Mechanical Engineers, Journal of Engineering Materials and Technology,* Vol. 110, 1988, pp. 63–68.

[13] Bannantine, J. and Socie, D. in *Low Cyclic Fatigue, ASTM STP 942,* American Society for Testing and Materials, Philadelphia, 1988, pp. 899–921.

[14] Smith, R. N., Watson, P., and Topper, T. H., *Journal of Materials,* Vol. 5, No. 4, 1970, pp. 767–778.

[15] Zamrik, S. Y., "The Effect of Biaxiality in Creep-Fatigue at Elevated Temperatures," Annual Report, ORNL/Sub-3649-3, Pennsylvania State University, University Park, PA, March 1975.

[16] Ogata, T., Nitta, A., and Kuwabara, K. in *Proceedings,* Third International Conference on Biaxial/Multiaxial Fatigue, MPA, University of Stuttgart, Stuttgart, Germany, 3–6 April 1989, Vol. 2, pp. 56. 1–56.17.

[17] Nitta, A., Ogata, T., and Kuwabara, K., *Fatigue and Fracture of Engineering Materials and Structures,* Vol. 12, No. 2, 1989, pp. 77–92.

[*18*] Takahashi, Y., Ogata, T., and Nitta, A. in *Transactions,* Tenth International Conference on Structural Mechanics in Reactor Technology, 14–18 Aug. 1989, American Association for Structural Mechanics in Reactor Technology, Vol. L, 1989, pp. 49–54.

[*19*] Kurath, P., Downing, S. D., and Galliart, D. R. in *Multiaxial Fatigue: Analysis and Experiments,* SAE AE-14, Society of Automotive Engineers, Warrendale, PA, 1989, pp. 13–32.

[*20*] Fatemi, A. and Stephens, R. I. in *Multiaxial Fatigue: Analysis and Experiments,* SAE AE-14, Society of Automotive Engineers, Warrendale, PA, 1989, pp. 121–138.

[*21*] Fatemi, A. and Stephens, R. I. in *Multiaxial Fatigue: Analysis and Experiments,* SAE AE-14, Society of Automotive Engineers, Warrendale, PA, 1989, pp. 139–148.

[*22*] Hua, C. T. and Socie, D. F., *Fatigue of Engineering Materials and Structures,* Vol. 2, No. 3, 1984, pp. 165–179.

S. Y. Zamrik,[1] *M. Mirdamadi,*[2] *and D. C. Davis*[3]

A Proposed Model for Biaxial Fatigue Analysis Using the Triaxiality Factor Concept

REFERENCE: Zamrik, S. Y., Mirdamadi, M., and Davis, D. C., **"A Proposed Model for Biaxial Fatigue Analysis Using the Triaxiality Factor Concept,"** *Advances in Multiaxial Fatigue, ASTM STP 1191,* D. L. McDowell and R. Ellis, Eds., American Society for Testing and Materials, Philadelphia, 1993, pp. 85–106.

ABSTRACT: A biaxial fatigue model for axial-torsion strain cycling is proposed which includes elastic and plastic strain life regimes at elevated temperatures. The biaxial fatigue model is based on the concept that the transition from the plastic strain region to the elastic strain region on the bilinear fatigue life curve occurs at a cycle at which the elastic and plastic strain components of the total applied strain are equal. This transition corresponds to the intersection of the elastic and plastic strain lifelines of either a uniaxial or a torsional strain cycling condition. The transition point can combine the fatigue strength and fracture ductility coefficients of the material. The von Mises yield criterion was modified by using the Davis and Connelly triaxiality factor (TF) to account for the effects of the stress state and strain rate on the fracture ductility at elevated temperatures, which decreases as TF increases. Experimental data by the authors as well other available data were analyzed on the basis of the proposed model.

KEY WORDS: biaxial fatigue, triaxiality factor, transition cycle, *Z*-parameter

Nomenclature

B	Elastic fatigue strength material constant
b	Axial fatigue strength exponent
b_0	Torsional fatigue strength exponent
C	Plastic fatigue strength material constant
c	Axial fatigue ductility exponent
c_0	Torsional fatigue ductility exponent
C_{TF}	Triaxiality constant
E	Young's modulus of elasticity
G	Shear modulus
I_1	Hydrostatic stress
MF	Multiaxiality factor
N_f	Number of cycles to failure (continuous cycling)
N_T	Fatigue transition cycle
TF	Triaxiality factor
Z	*Z*-parameter
x, y, z	Reference axes, x is along specimen's longitudinal axis
$\Delta\varepsilon$	Axial strain range
$\Delta^*\varepsilon$	Modified axial strain range

[1] Professor and [3]associate professor, respectively, The Pennsylvania State University, Dept. of Engineering Science and Mechanics, University Park, PA 16802.
[2] Resident research associate, NASA-Langley Research Center, Hampton, VA 23665.

$\Delta\gamma$ Shear strain range
$\Delta\sigma$ Axial stress range
$\Delta\tau$ Torsional shear stress range
ε Axial strain
ε_{f0} Tensile ductility (tensile elongation)
ε_f Effective ductility
ε_f Axial fatigue ductility coefficient
γ Shear strain
γ_f Torsional fatigue ductility coefficient
Λ Ductility parameter
λ Biaxiality strain ratio ($\Delta\gamma^t/\Delta\varepsilon^t$)
ν Poisson's ratio
ϕ Principal strain ratio (smaller/larger)
σ Normal stress component
σ_a Normal stress amplitude
σ_f Axial fatigue stength coefficient
τ Torsional stress component
τ_f Torsional fatigue strength coefficient

Superscripts

e Elastic component
in Inelastic compontent
p Plastic component
t Total

Subscripts

eq von Mises equivalent
x, y, z Axes components
1, 2, 3 Principal direction ($1 > 2 > 3$)

Life prediction of engineering components experiencing multiaxial loading conditions requires a multiaxial fatigue theory that indicates which stress or strain parameter(s) best measure the severity of the fatigue damage. The validity of the multiaxial fatigue theory can only be assessed relative to its agreement with experimental data. It is highly desirable for the theory to make life prediction possible with a minimum of test data. Due to the complexity of multiaxial fatigue testing under a triaxial state of stress, multiaxial fatigue theories are commonly developed by conducting biaxial fatigue tests, where stresses or strains are measured and controlled in two principal directions.

Multiaxial fatigue analysis can be carried out by defining an equivalent strain, such as the von Mises yield criterion, which has frequently been used to determine the equivalent strain. There is considerable experimental evidence suggesting that, at room temperature, the von Mises (octahedral shear strain) theory is valid over a wide variety of materials and stress states [*1–4*]. However, experimental results show that the greatest shortcomings of the von Mises theory when used for fatigue analysis occur in correlating torsional fatigue data with test data obtained at other stress states [*5–9*]. Blass and Zamrik [*6*] showed that the biaxial (axial-torsion) fatigue data on Type 304 stainless steel, when correlated using von Mises equivalent strain range, were lower bounded by the uniaxial fatigue data and upper bounded by the pure torsion fatigue data. The pure torsion fatigue life was greater by a factor of two, and the difference was attributed to the effect of the stress state on ductility.

The Triaxiality Factor Concept

A number of investigators have used the triaxiality factor (TF) concept to show the effect of stress state on ductility. The early development of the concept is due to Davis and Connelly [*10*], who showed that the ductility decreases as a result of triaxial tension. They proposed that an effective ductility, $\bar{\varepsilon}_f$, under multiaxial loading conditions may be obtained by

$$\bar{\varepsilon}_f = \frac{\varepsilon_{f0}}{\mathrm{TF}} \tag{1}$$

where ε_{f0} is the tensile ductility (tensile elongation), and

$$\mathrm{TF} = \frac{(\sigma_1 + \sigma_2 + \sigma_3)}{\frac{1}{\sqrt{2}}[(\sigma_1 - \sigma_2)^2 + (\sigma_2 - \sigma_3)^2 + (\sigma_3 - \sigma_1)^2]^{1/2}} = \frac{I_1}{\sigma_{eq}} \tag{2}$$

The triaxiality factor (TF) is equal to one for the uniaxial case, zero for pure torsion, and two for the biaxial case. Their view was that the effective ductility decreases as TF increases. Manson and Halford [*11*] analyzed the test results of Blass and Zamrik [*6*] on Type 304 stainless steel at room temperature and at 1100°F (593°C) and 1200°F (650°C) and showed that the octahedral shear strain theory could not correlate the experimental fatigue results. Blass and Zamrik showed that pure torsional fatigue life was consistently greater than uniaxial fatigue life at both room and elevated temperatures for the same equivalent octahedral strain range. In fact, the pure torsional data were less damaging by a factor of two in comparison with the uniaxial data. Based on this observation, Manson and Halford proposed a modified von Mises equivalent plastic strain range ($\Delta\varepsilon^p_{eq}$) by introducing a multiaxial factor (MF) such that

$$\Delta^*\varepsilon^p_{eq} = \mathrm{MF}\ \Delta\varepsilon^p_{eq} \tag{3}$$

where

$$\mathrm{MF} = \mathrm{TF} \qquad \text{for TF} \geq 1 \tag{4}$$

$$\mathrm{MF} = \frac{1}{2 - \mathrm{TF}} \qquad \text{for TF} \leq 1 \tag{5}$$

Manson and Halford correlated the data of Blass and Zamrik for the uniaxial case (MF = 1) and the pure torsion case (MF = ½). Using the MF procedure, an excellent correlation was obtained between axial and torsional fatigue data when plotted versus cyclic life (N_f). Blass and Zamrik, in reply, showed that on a specific set of data for TF $\leq$ 1, a good correlation exists using the MF factor. However, for TF $>$ 1, the MF procedure does not predict a good correlation between axial and torsional fatigue data.

Manjoine [*12*] and Marloff [*13*] have applied the concept of triaxiality factor to explain the effect of stress state on ductility at elevated temperatures under monotonic loading. The measured reduction in ductility for a number of materials versus triaxiality factor is shown in Fig. 1. Manjoine's experimental results indicated that for a given temperature and strain rate, ductility decreases as triaxiality factor increases. The data correlated well with a triaxiality constant (C_{TF}) when expressed as

$$C_{\mathrm{TF}} = 2^{1-\mathrm{TF}} \tag{6}$$

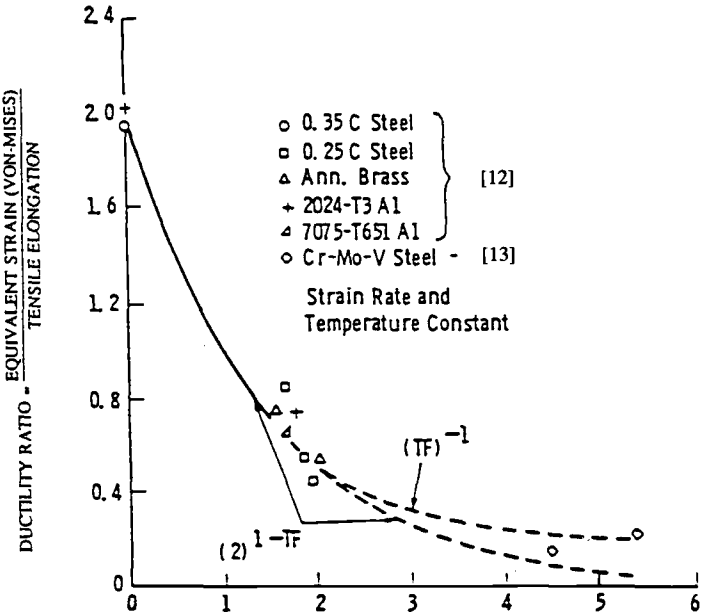

FIG. 1—*Triaxiality factor, TF* = I_1/σ_{eq}.

Marloff et al. [*14*] proposed that in multiaxial low cycle fatigue a strain life equation, similar to the Coffin-Manson relation, may be expressed in terms of von Mises equivalent total strain range as

$$\Delta\varepsilon_{eq}^{t} = BN_f^{-b} + 2^{1-TF}CN_f^{-c} \tag{7}$$

The plastic strain component is modified by a triaxiality factor and the constants B and C are found from uniaxial fatigue data. The TF can be expressed as a function of Poisson's ratio

$$TF = \frac{1+\nu}{(1-\nu+\nu^2)^{1/2}} \tag{8}$$

where for the plastic condition ($\nu = 0.5$), TF = 1.732. Using the TF concept, they reported good agreement using Eq 7 with the experimental results.

Marloff et al. [*14*] also examined published biaxial fatigue data on Cr-Mo-V steel conducted at room temperature by Lohr and Ellison [*15*] and Liddle and Miller [*16*] and at room temperature and 1050°F (565°C) by Brown and Miller [*17*]. The Brown and Miller data were from combined axial-torsion tests conducted at fixed ratios of shear to axial strain ranges. Such stress states produced triaxiality factors between 0 and 1. The materials used in these investigations were similar in chemical composition and tensile properties to materials used by Marloff et al.

The predicted life was based on Eq 7 using the appropriate uniaxial constants. The Lohr and Ellison [*15*] data were from biaxial fatigue tests on tubular specimens subjected to the combined axial loading and internal pressure at a fixed ratio ϕ (ratio of surface principal strains, smaller/larger). Four different stress states resulted in triaxiality factors of TF = 1 for the uniaxial case, TF = 1.73 for the plane strain case, TF = 2 for the equal biaxial case, and TF = 0 for the pure torsion case. The worst case of $\phi = 1$ (equal biaxial case) predicted the life to be 65% of the actual experimentally observed fatigue life. Life prediction of room temperature

test results by Lohr and Ellison [*15*], Liddle and Miller [*16*], and Brown and Miller [*17*], were within the factor of ± 1.5 in life. The correlation of the elevated temperature test results in terms of measured versus predicted life was within a factor of ± 2 in life. Since Marloff et al. [*13*] modified the von Mises equivalent plastic strain by a triaxiality factor, they suggested a factor of $2^{(TF-1)}$ for $-1 \leq TF \leq +3$, and Marloff noted that the multiaxiality factor (MF) defined by Manson and Halford and $2^{(TF-1)}$ differ very little from each other. From a practical standpoint, this range of TF covers most of the loading conditions of interest so that either factor may be employed. For much larger values of the TF, however, the two factors differ significantly.

Bonacuse and Kalluri [*18*] conducted a series of strain-controlled, in-phase combined axial-torsion fatigue tests on Type 304 stainless steel at room temperature. Three multiaxial fatigue life prediction models were examined by using Type 304 stainless steel uniaxial fatigue material constants reported by Bannantine and Socie [*19*].The Socie [*20*] and Smith, Watson, and Topper (SWT) [*21*] and Manson and Halford [*11*] models were used for comparison. The predictions by the Manson-Halford model and the SWT model were closer to the experimental results than those obtained by the Socie shear strain model [*20*]. This difference was attributed to the tensile mode of cracking exhibited by Type 304 stainless steel at room temperature.

Proposed Fatigue Model Using the Triaxiality Factor Concept

Inclusion of the triaxiality factor (TF) in the von Mises criterion is significant in that it recognizes the effect of hydrostatic pressure via the parameter I_1. This allows the proposed model to distinguish between fatigue life under multiaxial tension ($I_1 > 0$) and compression ($I_1 < 0$), thus reflecting proper fatigue behavior of material under superimposed hydrostatic pressure. Ideally, triaxiality factor (TF) can vary from $+\infty$ (under pure hydrostatic tension), where materials become brittle, to $-\infty$ (under pure hydrostatic pressure), where most brittle materials become ductile. Practically, however, the triaxiality factor has been limited to experimentally attainable values which are within the range $0 \leq TF < +6$, as shown in Fig. 1.

The proposed biaxial fatigue model, to be discussed in the sections that follow, was initially developed for LCF using the triaxiality factor and was based on the Coffin-Manson relationship. However at a later date, by examining the strain transition from low cycle fatigue (LCF) to high cycle fatigue (HCF), the model was extended to cover the total strain range region by using a modified von Mises equivalent strain.

Fatigue Transition Cycle

The strain transition from LCF to HCF could be considered to occur at a cycle where the elastic and plastic components of the total strain are equal. The transition cycle corresponds to the intersection of the elastic and plastic strain life lines. This transition point may be used to relate the fatigue strength and ductility coefficients of the material. This relation will be discussed under uniaxial and pure torsion cycling for the purpose of correlating fatigue data obtained under the following loading conditions: uniaxial, pure torsion, and combined axial-torsion (biaxial).

Uniaxial

Under uniaxial total strain range cycling, the fatigue transition cycle ($2N_T$) occurs when the elastic and plastic components of the total strain range are equal. It follows that

$$\frac{\sigma_f'}{E}(2N_T)^b_{\text{axial}} = \varepsilon_f'(2N_T)^c_{\text{axial}} \tag{9}$$

and the ratios of N_T become

$$(2N_T)^{c-b}_{\text{axial}} = \frac{\sigma'_f/E}{\varepsilon'_f} \tag{10}$$

The right-hand side of Eq 10 represents the ratio of the elastic and plastic strain life intercepts at $2N_f = 1$.

Pure Torsion

Under pure torsion loading, the total shear strain-life relationship is analogous to the uniaxial case and can be written as

$$\frac{1}{2}\Delta\gamma^t_{xy} = \frac{1}{2}\Delta\gamma^e_{xy} + \frac{1}{2}\Delta\gamma^p_{xy} = \frac{\tau'_f}{G}(2N_f)^{b_0} + \gamma'_f(2N_f)^{c_0} \tag{11}$$

By equating the two shear strain components at the transition cycle, the transition cycle ratio is

$$(2N_T)^{c_0-b_0}_{\text{torsion}} = \frac{\tau'_f/G}{\gamma'_f} \tag{12}$$

where γ'_f is the torsional fatigue ductility coefficient defined by the strain intercept at one load reversal ($2N_f = 1$), b_0 is the torsional fatigue strength exponent, and c_0 is the torsional fatigue ductility exponent.

Combined Axial-Torsion (Biaxial)

In order to make a comparison between uniaxial and pure torsion loading, the von Mises equivalent strain is used. Under combined axial-torsion loading, the state of strain is as follows

$$\begin{aligned} \varepsilon_x &\neq 0 \\ \varepsilon_y &= \varepsilon_z = -\nu\varepsilon_x \\ \gamma_{xy} &\neq 0 \\ \gamma_{yz} &= \gamma_{zx} = 0 \end{aligned} \tag{13}$$

The von Mises criterion reduces to

$$\varepsilon_{eq} = \left[\varepsilon_x^2 + \frac{3}{4(1+\nu)^2}\gamma_{xy}^2\right]^{1/2} \tag{14}$$

where ν is the Poisson's ratio. For the pure torsion case, the von Mises equivalent elastic strain is

$$\left(\frac{1}{2}\Delta\varepsilon^e_{eq}\right)_{\text{torsion}} = \frac{\sqrt{3}}{2(1+\nu^e)}\left(\frac{1}{2}\Delta\gamma^e_{xy}\right) \tag{15}$$

or in terms of cycles

$$\left(\frac{1}{2}\Delta\varepsilon^e_{eq}\right)_{\text{torsion}} = \frac{\sqrt{3}}{2(1+\nu^e)}\frac{\tau'_f}{G}(2N_f)^{b_0} \tag{16}$$

and the plastic shear strain component is

$$\left(\frac{1}{2}\Delta\varepsilon^p_{eq}\right)_{torsion} = \frac{\gamma'_f}{\sqrt{3}}(2N_f)^{c_0} \tag{17}$$

At the fatigue transition cycle

$$\frac{\sqrt{3}}{2(1+\nu^e)}\frac{\tau'_f}{G}(2N_T)^{b_0} = \frac{\gamma'_f}{\sqrt{3}}(2N_T)^{c_0} \tag{18}$$

Hence, the transition cycle ratio is given by

$$(2N_T)^{c_0-b_0}_{torsion} = \frac{3}{2(1+\nu^e)}\frac{\tau'_f/G}{\gamma'_f} \tag{19}$$

The right-hand side of Eq 19 represents the ratio of the elastic and plastic strain life intercepts at $2N_f = 1$.

Figure 2 is a schematic representation of the von Mises equivalent elastic, plastic, and total strain versus fatigue life for uniaxial and pure torsion. From Fig. 2, the pure torsional and uniaxial fatigue ductility coefficients, $\gamma'_f/\sqrt{3}$ and ε'_f, respectively, are located at the intercept of Lines (1) and (2) with $2N_f = 1$. Subsequently, the normalized pure torsion and uniaxial fatigue strength coefficients, $\left(\frac{\sqrt{3}\,\tau'_f/G}{2(1+\nu^e)}, \sigma'_f/E\right)$, respectively, are located at the intercept of Lines (3) and (4) with $2N_f = 1$. The fatigue transition cycle for pure torsional strain cycling is located at the intercept of Lines (1) and (3) and is identified by Line (5) in Fig. 2. Similarly, the fatigue transition cycle for uniaxial strain cycling is located at the intercept of Lines (2) and (4) and is identified by Line (6). Although it has been shown experimentally [*9,22,23*] that the stress state has a minor effect on the fatigue exponents of the Coffin-Manson relationship, there is a definite effect on the fatigue ductility and fatigue strength coefficients. This can be seen in Fig. 2 by the nearly parallel lines of the elastic component of the uniaxial and pure torsion cases, and the plastic component of the uniaxial and torsion curves. Depending on the state of stress, the transition fatigue cycle will shift to the right of the uniaxial transition point, indicating higher life for the same equivalent strain, or to the left, indicating lower life for the same equivalent strain. Therefore, if the equivalent strain, based on the von Mises yield criterion, correlates the fatigue data regardless of stress state, the torsional transition cycle should coincide with the uniaxial transition cycle and should also be stationary. However, if the von Mises criterion cannot correlate the fatigue data under different stress states, then it is assumed that a shift in the transition cycle is caused by the state of stress.

The proposed biaxial fatigue model is based on the relationship between the fatigue transition cycle in uniaxial and pure torsion. This is derived by dividing Eq 19 by Eq 10, which results in

$$\frac{(2N_T)^{c_0-b_0}_{torsion}}{(2N_T)^{c-b}_{axial}} = \frac{3}{2(1+\nu^e)}\frac{\tau'_f/G}{\sigma'_f/E}\frac{\varepsilon'_f}{\gamma'_f} \tag{20}$$

The right-hand side of Eq 20 is a constant determined by the fatigue properties under uniaxial and pure torsion conditions and is defined as the "Z-parameter" expressed as

$$Z = \frac{3}{2(1+\nu^e)}\frac{\tau'_f/G}{\sigma'_f/E}\frac{\varepsilon'_f}{\gamma'_f} \tag{21}$$

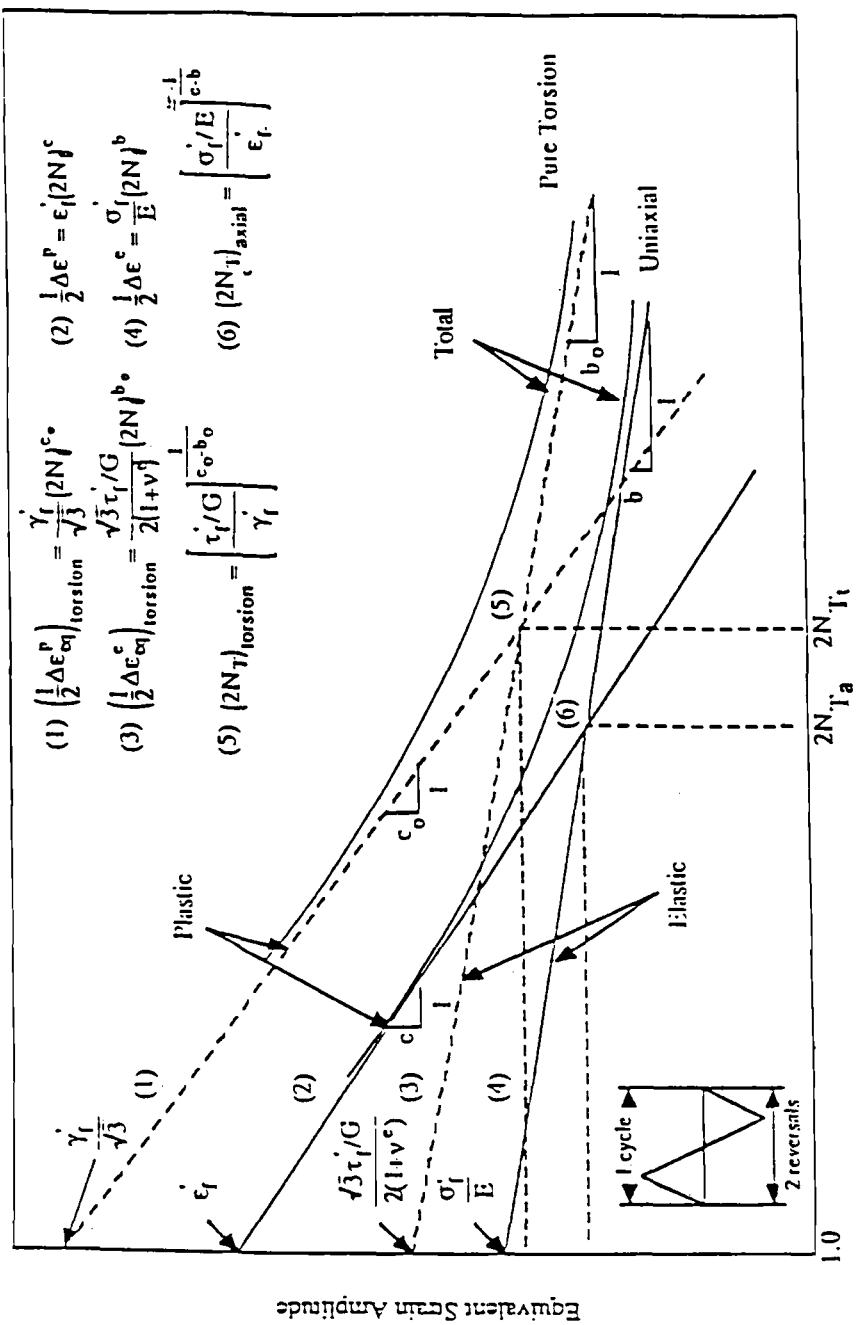

FIG. 2—*Total strain range as the sum of equivalent plastic and elastic components versus reversals to failure on logarithmic coordinates.*

The Z-parameter will now be used to modify the Coffin-Manson strain-life relationship to develop a criterion for biaxial fatigue life prediction.

It is proposed that the Coffin-Manson strain-life relationship can be extended to the multiaxial in-phase strain control conditions by using the von Mises equivalent elastic and equivalent plastic strain-life relationship as

$$\begin{aligned}\frac{1}{2}\Delta\varepsilon'_{eq} &= \frac{1}{2}\Delta\varepsilon^{e}_{eq} + \frac{1}{2}\Delta\varepsilon^{p}_{eq} \\ &= B(2N_f)^{-b} + C(2N_f)^{-c}\end{aligned} \tag{22}$$

where B and C are material constants which are a function of the metallurgical state, strain rate, temperature, and stress state $\{f(M_s, \dot{\varepsilon}, T, \sigma_{ij})\}$. Under multiaxial stress conditions, C is related to the uniaxial fatigue ductility coefficient (ε'_f) and with the state of stress (σ_{ij}) through the triaxiality factor (TF) as

$$C = (\Lambda^{1-TF})\varepsilon'_f \tag{23}$$

where Λ is a ductility parameter. Based on experimental data [*22*], Λ was found to be 1.8; hence, the value of 2 was chosen. It should be noted that Λ may change from material to material depending of the ductility of the material being tested. This is the reason why Eq 23 specifically was chosen to reflect the variation of the fatigue ductility coefficient. The fatigue ductility coefficient has been shown to be an effective parameter for describing ductility under multiaxial stress conditions [*12*] and has been used to correlate multiaxial fatigue data when the applied strain is well within the plastic regime [*13,11,18*]. Similarly, it is assumed that the material constant, B, is a function of the stress state at a given temperature and its variation with the state of stress can be expressed through the Z-parameter and TF as

$$B = (Z^{1-TF})\frac{\sigma'_f}{E} \tag{24}$$

Therefore Eq 22 becomes

$$\frac{1}{2}\Delta\varepsilon'_{eq} = \frac{1}{2}\Delta\varepsilon^{e}_{eq} + \frac{1}{2}\Delta\varepsilon^{in}_{eq} = Z^{1-TF}\frac{\sigma'_f}{E}(2N_f)^{b} + \Lambda^{1-TF}\varepsilon'_f(2N_f)^{c} \tag{25}$$

Equation 25 can be rewritten in terms of a modified von Mises equivalent strain, $\Delta^*\varepsilon_{eq}$, by rearranging the elastic component to the following form

$$\frac{1}{2}\Delta\varepsilon^{e}_{eq}\, Z^{TF-1} = \frac{\sigma'_f}{E}(2N_f)^{b} \tag{26}$$

The left-hand side of Eq 26 can now be expressed as a modified von Mises equivalent elastic strain component as

$$\frac{1}{2}\Delta^*\varepsilon^{e}_{eq} = Z^{TF-1}\frac{1}{2}\Delta\varepsilon^{e}_{eq} = \frac{\sigma'_f}{E}(2N_f)^{b} \tag{27}$$

Similarly, for the plastic strain component, the modified von Mises equivalent plastic strain component can be expressed as [*14*]

$$\frac{1}{2}\Delta^*\varepsilon^{p}_{eq} = \Lambda^{TF-1}\frac{1}{2}\Delta\varepsilon^{p}_{eq} = \varepsilon'_f(2N_f)^{c} \tag{28}$$

Therefore, the modified von Mises equivalent total strain can be written as

$$\frac{1}{2}\Delta^*\varepsilon^t_{eq} = (Z^{TF-1})\frac{1}{2}\Delta\varepsilon^e_{eq} + (\Lambda^{TF-1})\frac{1}{2}\Delta\varepsilon^p_{eq} \tag{29}$$

When TF = 1, the modified von Mises equivalent strain reduces to the simple uniaxial strain case given by

$$\left(\frac{1}{2}\Delta^*\varepsilon^t_{eq}\right)_{axial} = \frac{1}{2}\Delta\varepsilon^t = \frac{\sigma'_f}{E}(2N_f)^b + \varepsilon'_f(2N_f)^c \tag{30}$$

Analysis of Fatigue Test Results

Fatigue tests were conducted on thin-walled, tubular annealed Type 316 stainless steel (Heat 8092297) specimens at an elevated temperature of 1150°F (621°C) under continuous cycling at a frequency of ten cycles per minute to minimize the creep effect. The tests were conducted under uniaxial, pure torsion, and combined in-phase axial-torsion (biaxial) strain cycling. The following four aspects of the experimental results are discussed:

1. Uniaxial continuous cycling fatigue data using the Coffin-Manson strain-life relationship.
2. Pure torsion continuous cycling fatigue data using the Coffin-Manson strain-life relationship.
3. Analysis of uniaxial, pure torsion, and combined axial-torsion continuous cycling fatigue data using von Mises equivalent strain.
4. Analysis of uniaxial, pure torsion, and combined axial-torsion fatigue data using von Mises equivalent strain modified by the proposed Z-parameter.

Uniaxial Continuous Cycling Fatigue Data

The Coffin-Manson strain-life relationship was used to analyze the uniaxial fatigue data. The plastic and elastic components of the total strain range were measured at mid-life from a stabilized hysteresis loop and were fitted to the plastic strain-life relationship. Failure was defined as a 10% drop in the applied load from the stabilized cycle load range identified from the strip chart record. Uniaxial fatigue data of Wareing [*24*] on similar Type 316 stainless steel at 1150°F (621°C) were included in the regression analysis. The magnitude of uniaxial fatigue constants at the applied temperature were determined from regression analysis and are given in Table 1. On the basis of total strain amplitude, in unit percent, the uniaxial fatigue data is described by the following equation

$$\begin{aligned}\frac{1}{2}\Delta\varepsilon^t &= \frac{1}{2}\Delta\varepsilon^e + \frac{1}{2}\Delta\varepsilon^p \\ &= 0.53(2N_f)^{-0.13} + 37.77(2N_f)^{-0.63}\end{aligned} \tag{31}$$

The fatigue lives are plotted as a function of strain amplitude in Fig. 3.

Pure Torsion Continuous Cycling Fatigue Data

Similar to the uniaxial fatigue data expressed by Eq 31, pure torsion fatigue data were analyzed using the following total shear strain-life relation

$$\frac{1}{2}\Delta\gamma^t = \frac{\tau'_f}{G}(2N_f)^{b_0} + \gamma'_f(2N_f)^{c_0} \tag{32}$$

TABLE 1—*Fatigue data at 1150°F (621°C).*

Fatigue Data	
Axial fatigue strength coefficient, σ_f'	104.70 ksi (721.9 MPa)
Young's modulus, E, (mid-life cycle)	19 750 ksi (136.2 GPa)
Ratio of σ_f'/E	0.0053
Axial fatigue strength exponent, b	−0.13
Axial fatigue ductility coefficient, ϵ_f'	0.3773
Axial fatigue ductility exponent, c	−0.63
Uniaxial fatigue transition reversals, $2N_T$	5079 cycles
Torsional fatigue strength coefficient, (τ_f')	73.37 ksi (505.9 MPa)
Shear modulus, G, (mid-life cycle)	6670 ksi (45.99 GPa)
Ratio of τ_f'/G	0.011
Torsional fatigue strength exponent, b_0	−0.13
Torsional fatigue ductility coefficient, γ_f'	0.6381
Torsional fatigue ductility exponent, c_0	−0.563
Torsional fatigue transition reversals, $2N_T$	11 820 cycles

The failure in pure torsion fatigue was also defined by a 10% load (torque) drop from the stabilized cycle load range. The pure torsion fatigue constants in Eq 32 at the applied temperature of 1150°F (621°C) were also determined from the regression analysis and are given in Table 1. It should be noted that the value for G in Table 1 determined by the regression analysis is less than that which would be calculated using the E value in Table 1 and a Poisson's ratio ν^e = 0.3. However, the discrepancy is small and should not affect the proposed concept and for simplicity the value of ν^e = 0.3 was used. The coefficients are numerical numbers fitted to the data and are used to illustrate the computational scheme. Substituting the coefficients given

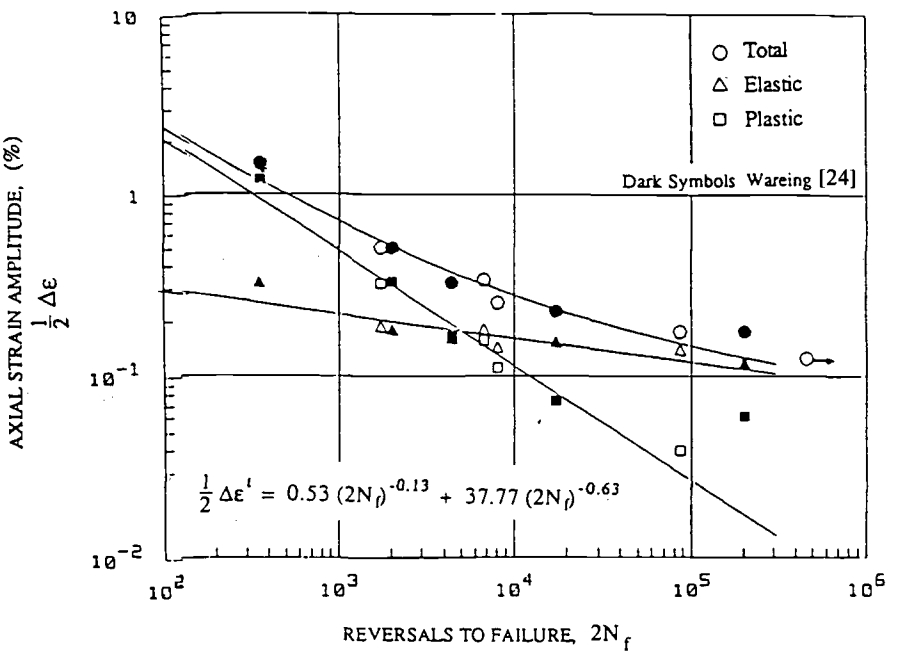

FIG. 3—*Axial strain amplitude versus number of reversals to failure in uniaxial fatigue at cyclic frequency of 10 cpm. Annealed Type 316 stainless steel material (Heat 8092297) tested at 1150°F (621°C).*

in Table 1 into Eq 32, the pure torsional fatigue data are described by the following

$$\frac{1}{2}\Delta\gamma' = 1.1(2N_f)^{-0.13} + 63.81(2N_f)^{-0.563} \tag{33}$$

Fatigue cycles as a function of shear strain amplitude are shown in Fig. 4 up to 1×10^5 reversals.

Combined In-Phase Axial-Torsion Strain

Biaxial fatigue experiments using Type 316 stainless steel were conducted under combined in-phase axial-torsion strain using a frequency of 10 cpm and at 1150°F (621°C). In these combined tests, the strain biaxiality ratio, ($\lambda = \Delta_{xy}\gamma'/\Delta\varepsilon_x'$), is defined as the ratio of the total shear strain range to the total axial strain range. However, in all these combined tests $'\Delta\varepsilon_x$ was kept at a constant value of approximately 0.4 to 0.5%. The fatigue data were analyzed by measuring both the elastic and plastic shear and axial strains from their respective stabilized hysteresis loops recorded at mid-life. The failure criterion was also defined by a 10% load drop of either the axial or torsional load from their respective stabilized cycle load range level.

Analysis of Fatigue Data Using the von Mises Equivalent Strain Criterion

Fatigue data under uniaxial, pure torsion, and combined axial-torsion (biaxial) tests were analyzed using von Mises equivalent strain defined by

$$\varepsilon_{eq} = \left[\varepsilon_x^2 + \frac{3}{4(1+\nu)^2}\gamma_{xy}^2\right]^{1/2} \tag{14}$$

The von Mises total equivalent strain was then calculated by summing the von Mises equivalent elastic and plastic strain components. Comparison of the fatigue data on the basis of elastic, plastic, and total von Mises equivalent strains versus $2N_f$ are shown in Figs. 5, 6, and 7, respectively. As can be seen, the von Mises equivalent strain cannot correlate the torsion and the combined axial-torsion fatigue data to that of the uniaxial data. Moreover, the fatigue life in torsion is considerably greater than in the uniaxial case for the same equivalent strain. The results also indicate that combined axial-torsion fatigue data are somewhat bounded between uniaxial and pure torsion.

Analysis of Fatigue Data Using a "Modified" von Mises Equivalent Strain Criterion

The concept of triaxiality factor (TF) and the proposed Z-parameter are used to modify the von Mises equivalent strain to analyze fatigue data under continuous strain cycling. The Z-parameter value was determined by substituting uniaxial and pure torsional fatigue constants into the Eq 21, which resulted in a value of 1.42. Using this value for the Z-parameter, the data obtained from all fatigue tests can be reanalyzed on the basis of the modified von Mises equivalent strain as shown in Fig. 8. The von Mises equivalent plastic strain-life relationship, when modified by (Λ^{TF-1}) [*14*], yields

$$\frac{1}{2}\Delta\varepsilon_{eq}^p\Lambda^{TF-1} = \varepsilon_f'(2N_f)^c \tag{28}$$

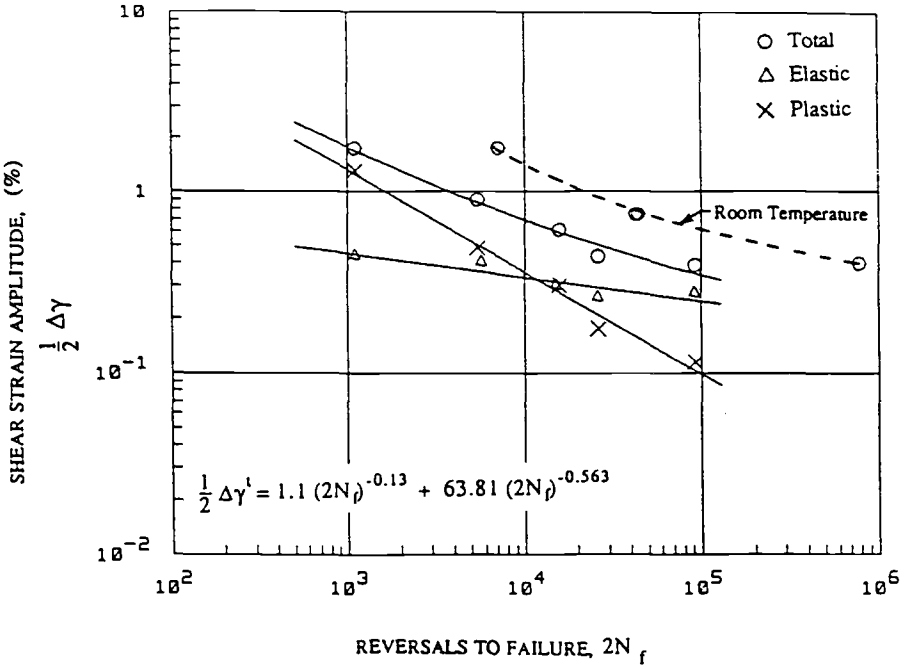

FIG. 4—*Shear strain amplitude versus number of reversals to failure in pure torsion fatigue at cyclic frequency of 10 cpm. Annealed Type 316 stainless steel material (Heat 8092297) tested at 1150°F (621°C).*

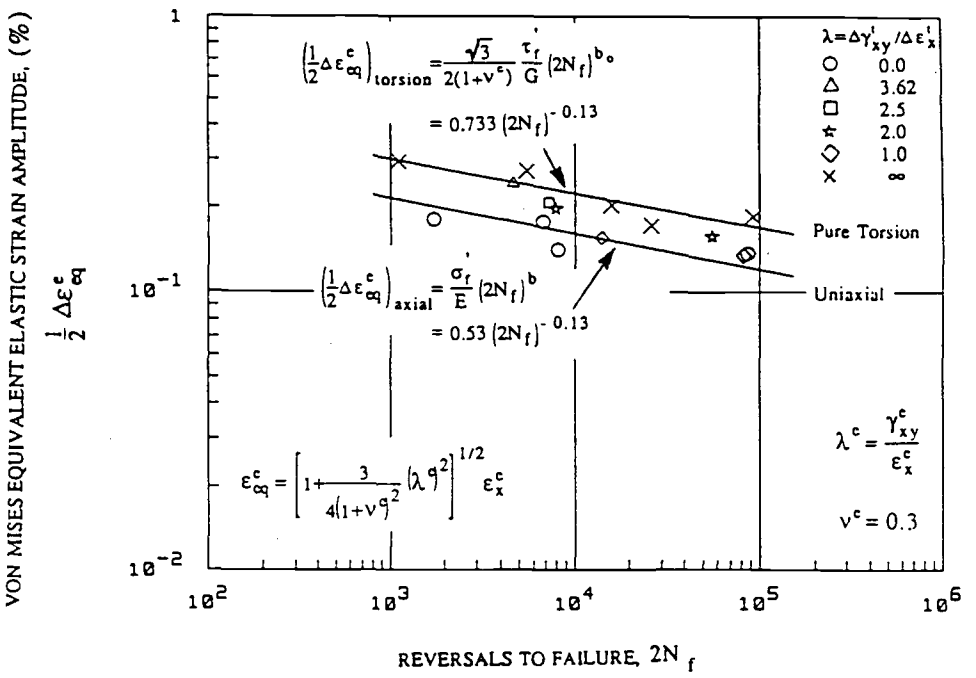

FIG. 5—*von Mises equivalent elastic strain amplitude versus number of reversals to failure in uniaxial, pure torsion, and combined axial-torsion fatigue at cyclic frequency of 10 cpm. Annealed Type 316 stainless steel material (Heat 8092297) tested at 1150°F (621°C).*

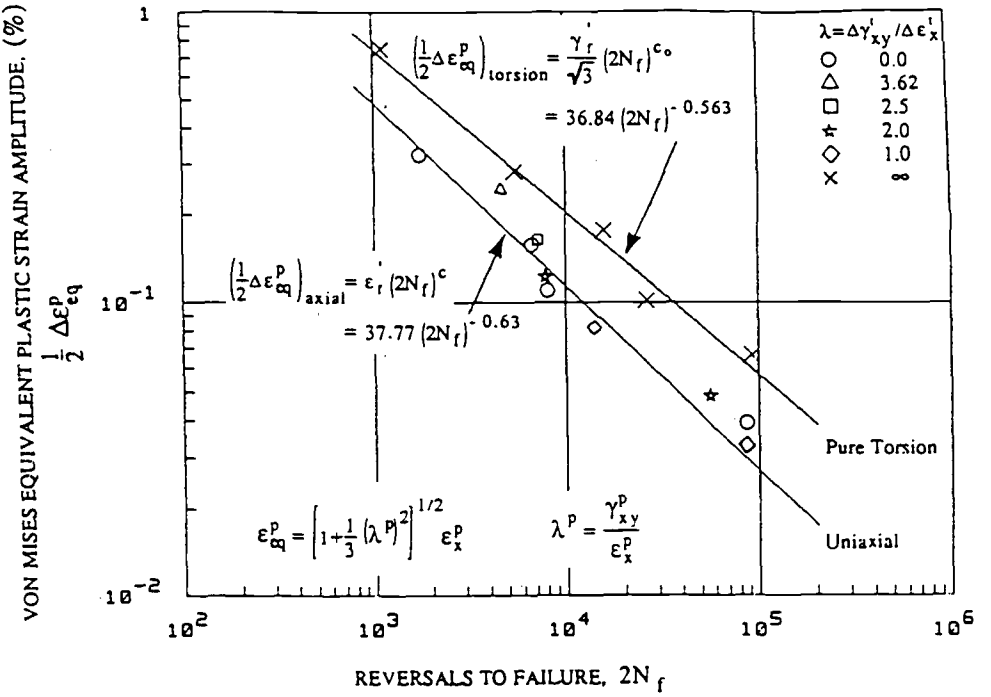

FIG. 6—*von Mises equivalent plastic strain amplitude versus number of reversals to failure in uniaxial, pure torsion, and combined axial-torsion fatigue at cyclic frequency of 10 cpm. Annealed Type 316 stainless steel material (Heat 8092297) tested at 1150°F (621°C).*

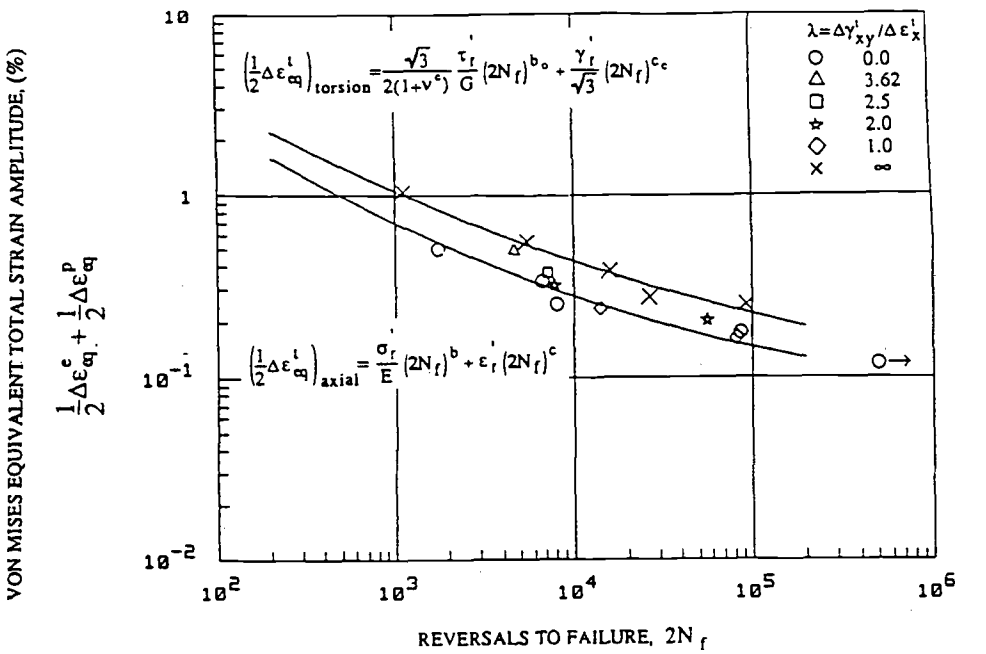

FIG. 7—*von Mises equivalent total strain amplitude versus number of reversals to failure in uniaxial, pure torsion, and combined axial-torsion fatigue at cyclic frequency of 10 cpm. Annealed Type 316 stainless steel material (Heat 8092297) tested at 1150°F (621°C).*

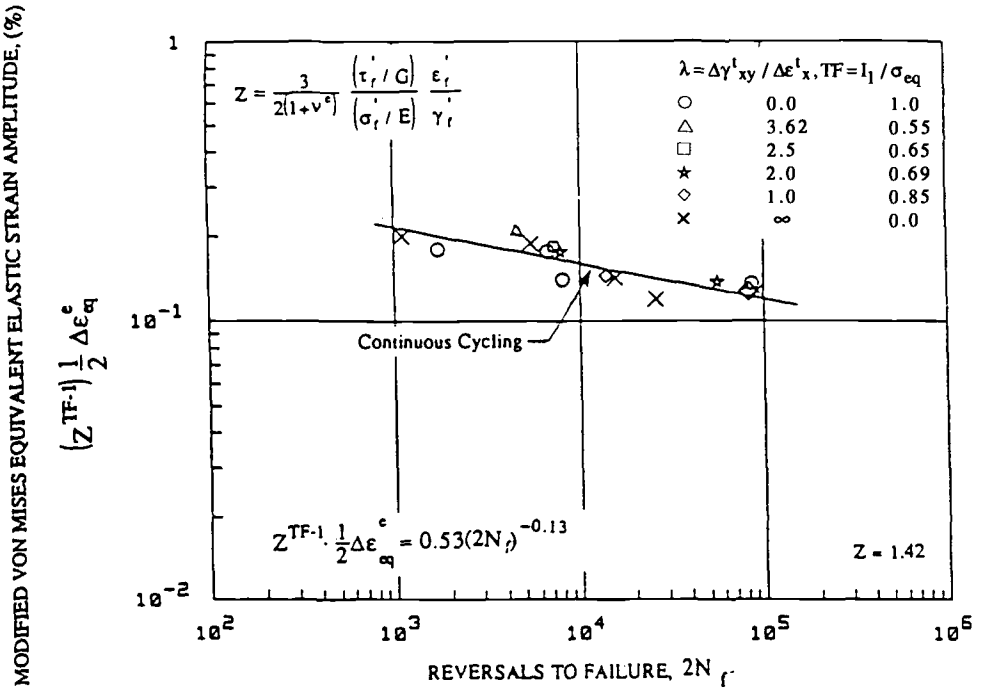

FIG. 8—*Analysis of uniaxial, pure torsion, and combined axial-torsion fatigue data at cyclic frequency of 10 cpm using von Mises equivalent elastic strain modified by proposed Z-parameter. Annealed Type 316 stainless steel material (Heat 8092297) tested at 1150°F (621°C).*

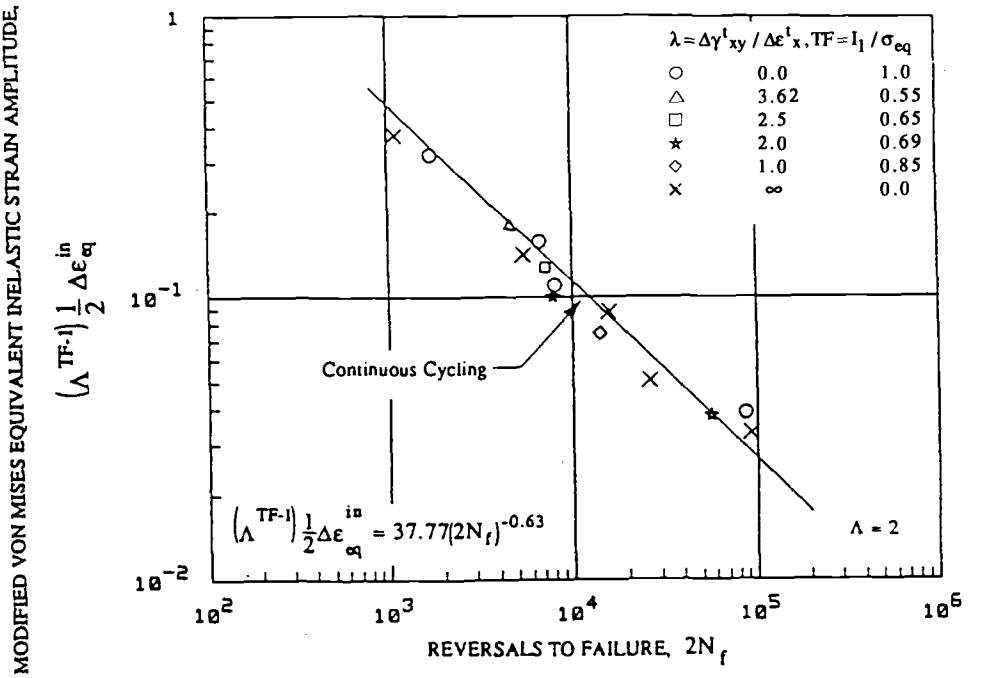

FIG. 9—*Analysis of uniaxial, pure torsion, and combined axial-torsion fatigue data at cyclic frequency of 10 cpm using von Mises equivalent inelastic strain modified by triaxiality factor, TF. Annealed Type 316 stainless steel material (Heat 8092297) tested at 1150°F (621°C).*

which, as shown in Fig. 9, is in good agreement with the experimental results. Therefore, the modified von Mises equivalent total strain-life relationship can be written as

$$(Z^{TF-1})\frac{1}{2}\Delta\varepsilon^{e}_{eq} + (\Lambda^{TF-1})\frac{1}{2}\Delta\varepsilon^{p}_{eq} = \frac{\sigma'_f}{E}(2N_f)^b + \varepsilon'_f(2N_f)^c \tag{29}$$

Discussion

The correlation of pure torsion and combined axial-torsion from uniaxial fatigue based on the modified von Mises equivalent total strain amplitude is shown in Fig. 10. As can be seen, excellent agreement is achieved using the proposed criterion where data from individual tests collapse to the uniaxial fatigue curve. Based on the proposed model, any TF value can be used to predict fatigue life from the uniaxial fatigue curve as illustrated in Fig. 11. The success of the proposed model is in the incorporation of stated material properties, which are essential factors in fatigue analysis.

The proposed biaxial fatigue model is based on the concept of the fatigue transition cycle, which corresponds to the intersection of the elastic and plastic strain life lines. This point of intersection can be used to combine the elastic and plastic material fatigue constants. The proposed Z-parameter is based on the ratio of the torsional fatigue transition cycle properties to that of the uniaxial fatigue transition cycle properties. If the value of the proposed Z-parameter based on the von Mises yield criterion is unity, then the fatigue transition cycle is stationary.

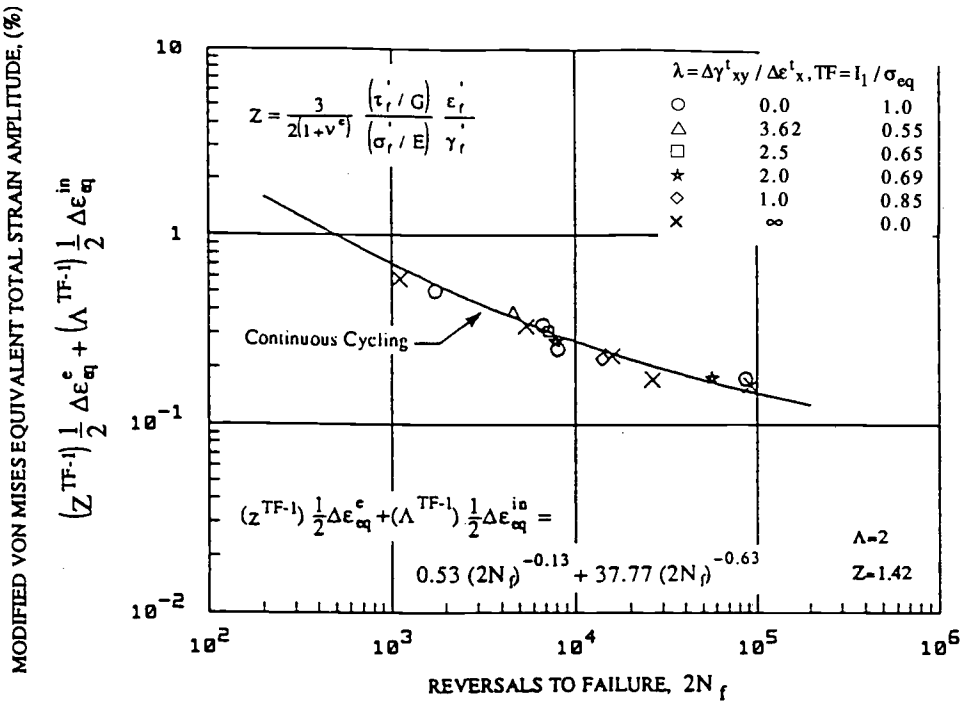

FIG. 10—*Analysis of uniaxial, pure torsion, and combined axial-torsion fatigue data at cyclic frequency of 10 cpm using von Mises equivalent elastic strain modified by triaxiality factor, TF, and proposed Z-parameter. Annealed Type 316 stainless steel material (Heat 8092297) tested at 1150°F (621°C).*

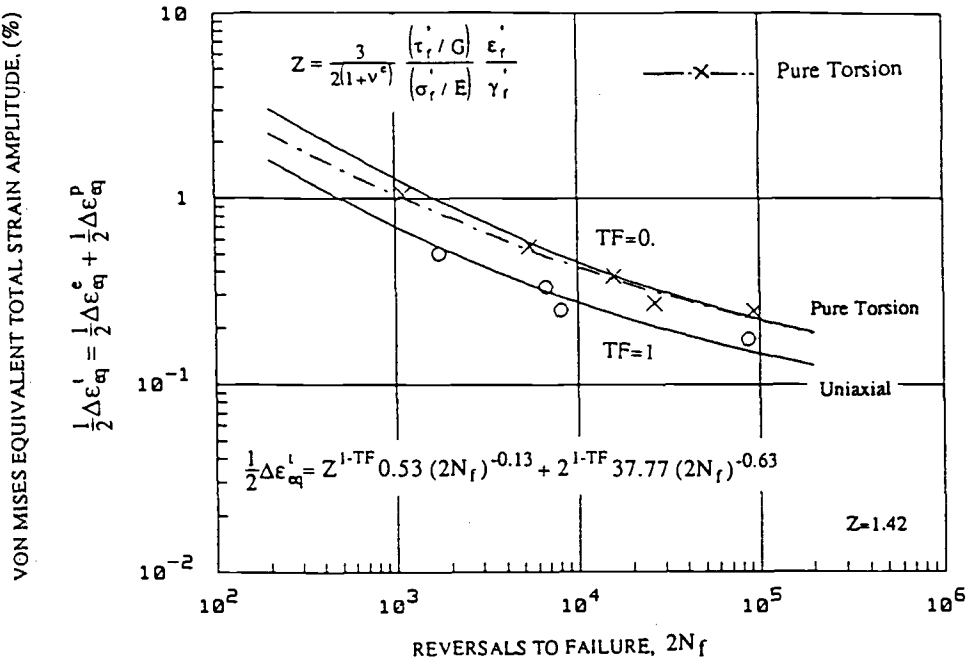

FIG. 11—*Effect of stress state on fatigue behavior of Type 316 stainless steel material (Heat 8092297) tested at 1150°F (621°C) using von Mises equivalent total strain modified by triaxiality factor, TF, and proposed Z-parameter. Solid line represents torsional correlation using uniaxial fatigue properties.*

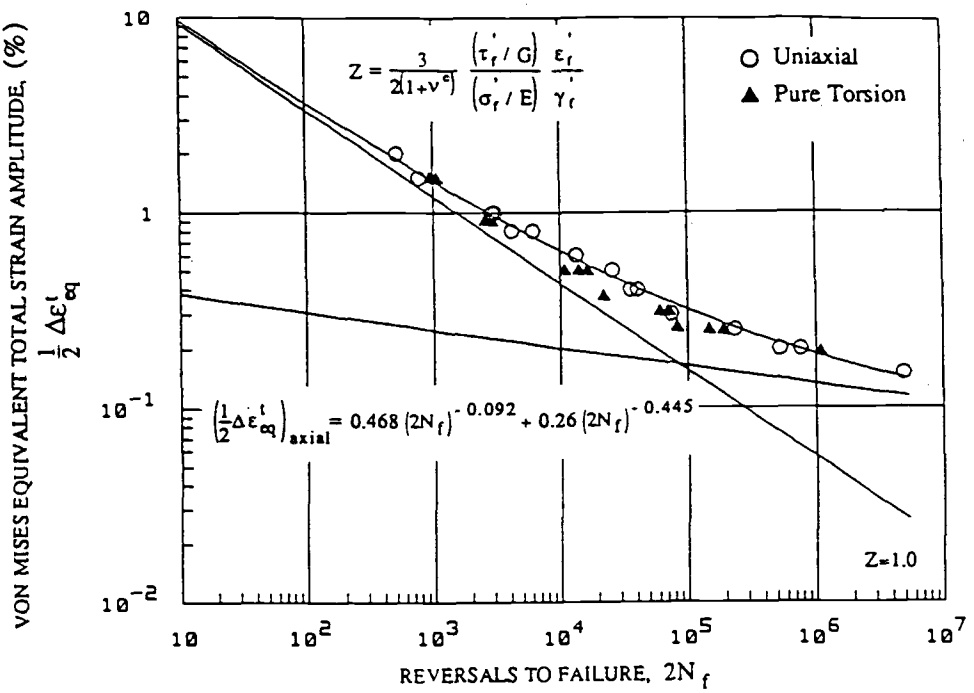

FIG. 12—*Analysis of pure torsion fatigue data using von Mises equivalent total strain on 1045 steel material tested at room temperature. Solid line represents torsional correlation using uniaxial fatigue properties* [22].

Hence, the von Mises equivalent strain criterion should correlate the biaxial fatigue data. The von Mises criterion has been shown to correlate the biaxial fatigue data for some materials, especially at room temperature.

Figure 12 shows a reasonable correlation of pure torsion fatigue data of AISI 1045 steel with those of uniaxial fatigue data at room temperature using von Mises equivalent strain criterion [*22*] in which the experimental value of *Z*-parameter was found to be unity. However, the majority of the experimental results indicate that the von Mises criterion cannot predict biaxial fatigue data from that of the uniaxial fatigue response, and that the torsional fatigue life is consistently higher than that of uniaxial fatigue life at the same von Mises equivalent strain. This indicates that the transition cycle in torsional fatigue is higher than the transition cycle in uniaxial fatigue, leading to a value greater than one for the *Z*-parameter.

The uniaxial and pure torsional fatigue data reported by Bonacuse and Kalluri [*25*] on Haynes 188 material (a cobalt-base alloy) conducted at 1400°F (760°C) are shown in Figs. 13 and 14, respectively. The Haynes 188 uniaxial and pure torsion fatigue data, based on the von Mises equivalent total strain, are shown in Fig. 15. Using the proposed *Z*-parameter concept for this material (the *Z*-parameter was found to be 1.23), the pure torsion and uniaxial fatigue data of Fig. 15 combined into a simple curve as shown in Fig. 16. Figure 17 shows a good prediction of pure torsion fatigue life from uniaxial fatigue properties using the von Mises equivalent plastic strain modified by TF and the equivalent elastic strain modified by the proposed *Z*-parameter. As seen in Fig. 17, excellent agreement is achieved using the proposed model.

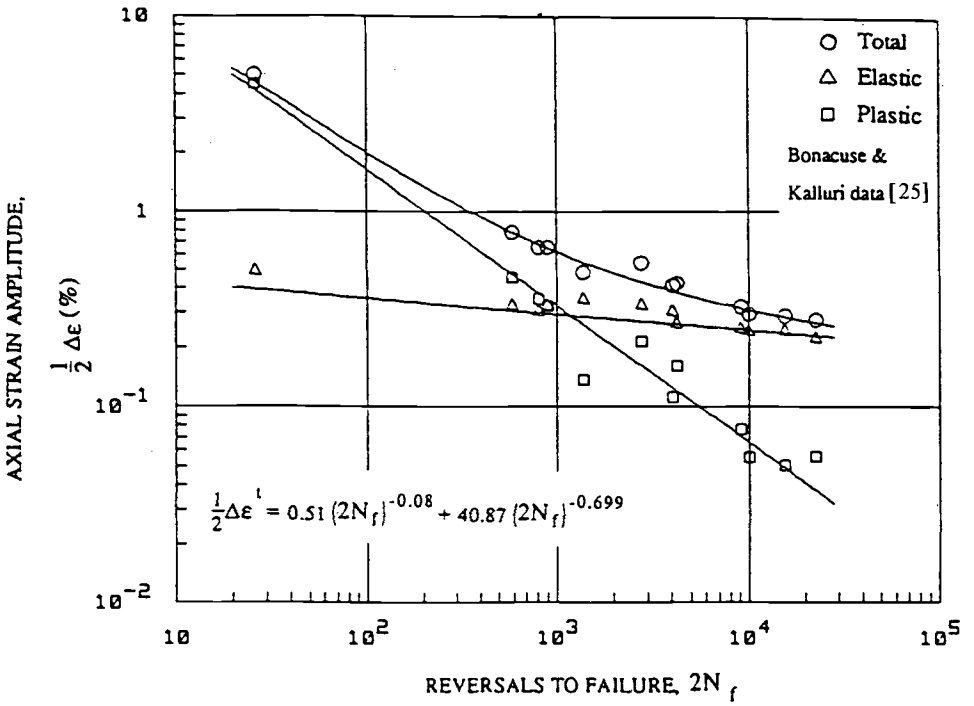

FIG. 13—*Axial strain amplitude versus number of cycle reversals to failure in uniaxial fatigue on Haynes 188 material (cobalt-base alloy) tested at 1400°F (760°C)* [25].

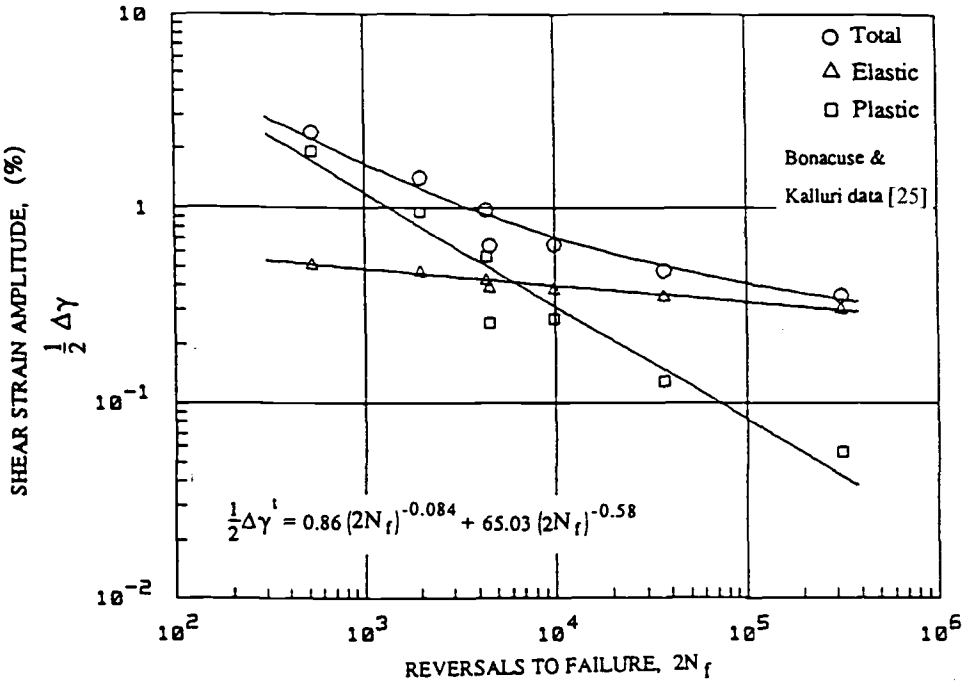

FIG. 14—*Shear strain amplitude versus number of cycle reversals to failure in pure torsion fatigue on Haynes 188 material (cobalt-base alloy) tested at 1400°F (760°C)* [25].

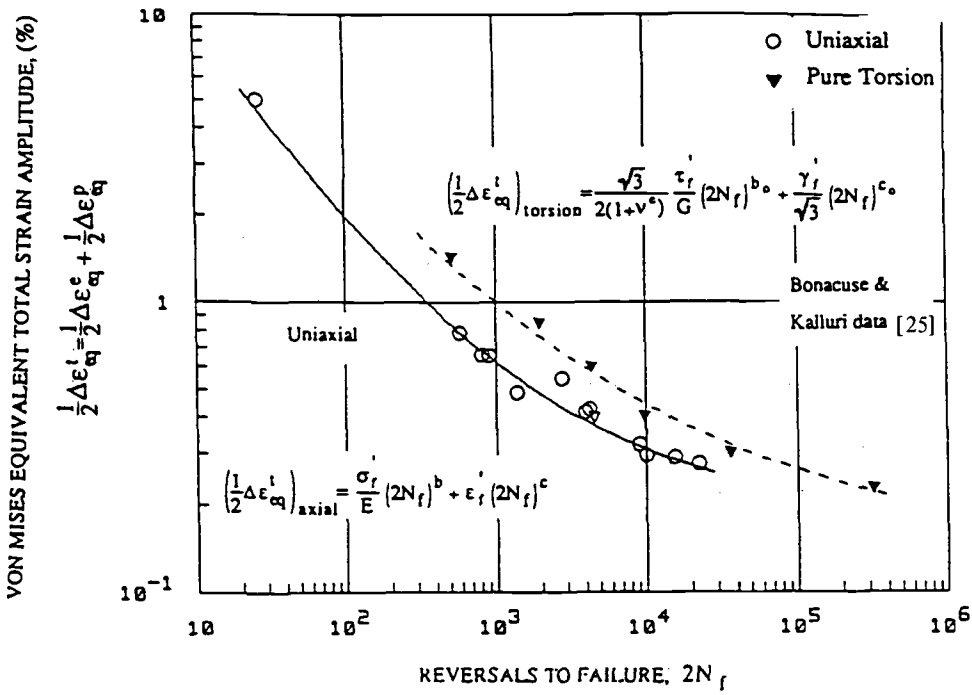

FIG. 15—*Analysis of pure torsion fatigue data using von Mises equivalent total strain amplitude on Haynes 188 material (cobalt-base alloy) tested at 1400°F (760°C). Solid line represents torsional correlation using uniaxial fatigue properties.*

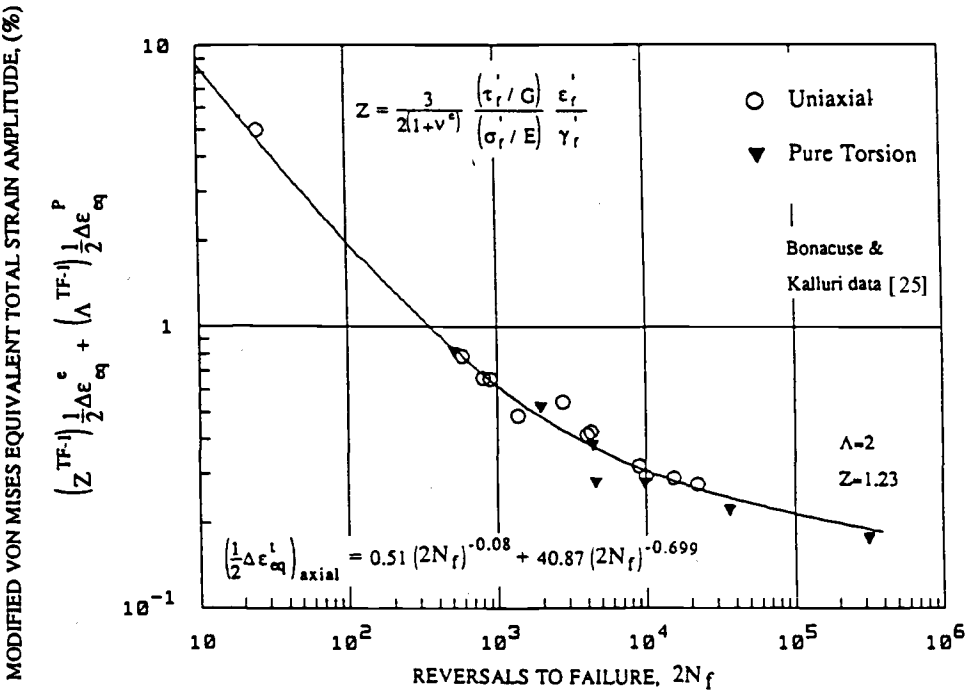

FIG. 16—*Analysis of uniaxial and pure torsion fatigue data using von Mises equivalent total strain amplitude modified by triaxiality factor, TF, and proposed Z-parameter. Solid line represents theoretical prediction from uniaxial fatigue properties.*

Summary and Conclusion

The triaxiality factor, TF, which accounts for the effect of stress-state on ductility has been used to correlate multiaxial fatigue data by modifying the von Mises equivalent strain range. A fatigue model that relates uniaxial, pure torsion, and combined axial-torsion (biaxial) fatigue data has been proposed. It is based on a transition point on the fatigue curve, which combines the fatigue ductility and strength coefficients of the material through the *Z*-parameter.

Acknowledgments

This research program was supported by a grant from the Pressure Vessel Research Council under the guidance of Material/Fabrication and Design divisions and by the National Science Foundation (Grant No. MSM-811407).

References

[*1*] Taira, S., Inoue, T., and Takahashi, M., "Low-Cycle Fatigue Under Multiaxial Stresses," *Proceedings,* 10th Japan Congress on Testing Materials-Metallic Materials, 1967, pp. 18–23.

[*2*] Shewchuk, J., Zamrik, S. Y., and Marin, J., "Low-Cycle Fatigue of 7075-T651 Aluminum Alloy in Biaxial Bending," *Experimental Mechanics,* Vol. 8, 1968, pp. 504–512.

[*3*] Ellison, E. G. and Andrews, J. M. H., "Biaxial Cyclic High-Strain Fatigue of Aluminum Alloy RR58," *Journal of Strain Analysis,* Vol. 8, No. 3, 1973, pp. 209–219.

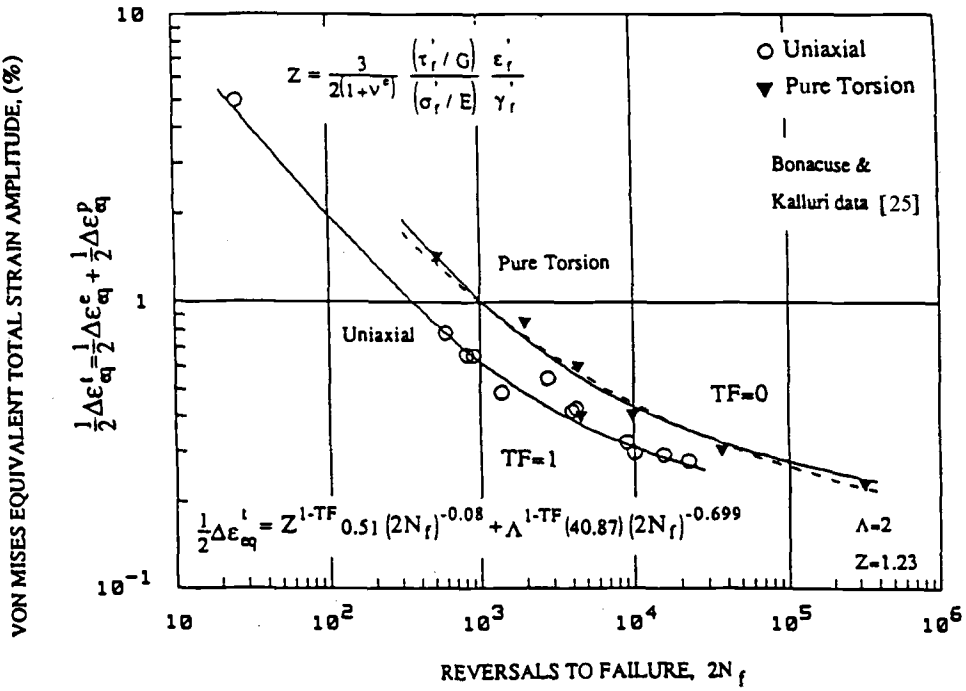

FIG. 17—*Analysis of pure torsion fatigue data using von Mises equivalent total strain amplitude modified by triaxiality factor, TF, and proposed Z-parameter on Haynes 188 material (cobalt-base alloy) tested at 1400°F (760°C). Solid line represents torsional correlation using uniaxial fatigue properties.*

[4] Meurer, H. P., Hanswillemenke, H., Breitling, H., and Dietz, W., "Biaxial Fatigue Tests on Thin Walled Tubes of NiCr23Col12Mo (Inconel 617) at 950°C," Paper 42, *Proceedings,* Third International Conference on Biaxial/Multiaxial Fatigue, Vol. 2, April 1989, Stuttgart, FRG.

[5] Parsons, M. W. and Pascoe, K. J., "Development of a Biaxial Fatigue Testing Rig," *Journal of Strain Analysis,* Vol. 10, 1975, pp. 1–9.

[6] Blass, J. J. and Zamrik, S. Y., "Multiaxial Low-Cycle Fatigue of Type 304 Stainless-Steel," Oak Ridge National Laboratory, ORNL/TM-5609, October 1976.

[7] Saken, M., Ohnami, M., and Sawada, M., "Fracture Modes and Low Cycle Biaxial Fatigue at Elevated Temperature," *Journal of Engineering Materials and Technology,* July 1987, Vol. 109, pp. 236–243.

[8] Kandil, F. A., Brown, M. W., and Miller, K. J., "In Mechanical Behavior and Nuclear Applications of Stainless-Steel at Elevated Temperatures," Book 280, The Metal Society, London, 1982, pp. 203–209.

[9] Shatil, G., Smith, D. J., and Ellison, E. G., "Low-Cycle Fatigue Testing of Structural Steel Under Biaxial Strain," Department of Mechanical Engineering, University of Bristol, Bristol BS81TR, 1989.

[10] Davis, E. A. and Connelly, F. M., "Stress Distribution and Plastic Deformation in Rotating Cylinders of Strain-Hardening Materials," *Journal of Applied Mechanics,* 1959, pp. 25–30.

[11] Manson, S. S. and Halford, R. R., "Multiaxial Low-Cycle Fatigue of Type 304 Stainless," *Journal of Engineering Materials and Technology,* 1977, pp. 283–285.

[12] Manjoine, M. J., "Damage and Failure at Elevated Temperature," *Journal of Pressure Vessel Technology,* Vol. 105, February 1983, pp. 58–62.

[13] Marloff, R. H. and Johnson, R. L., "The Influence of Multiaxial Stress on Low Cycle Fatigue of Cr-Mo-V Steel at 1000°F," *Welding Research Council Bulletin,* No. 264, December 1980.

[14] Marloff, R. H., Johnson, R. L., and Willson, W. K., "Biaxial Low-Cycle Fatigue of Cr-Mo-V Steel at 1000°F (538°C) by use of Triaxiality Factors," *Multiaxial Fatigue, ASTM STP 853,* K. J. Miller

and M. W. Brown, Eds., American Society for Testing and Materials, Philadelphia, 1985, pp. 637–650.

[15] Lohr, R. D. and Ellison, E. G., "A Simple Theory for Low Cycle Multiaxial Fatigue," *Fatigue of Engineering Materials and Structures,* Vol. 3, 1980, pp. 1–17.

[16] Liddle, M. and Miller, K. J., "Multiaxial High Strain Fatigue," *Proceedings,* Third International Conference on Fracture, Munich, 1973.

[17] Brown, M. W. and Miller, K. J., *Fatigue of Engineering Materials and Structure,* Vol. 1, 1979, pp. 217–229.

[18] Bonacuse, P. J. and Kalluri, S., "Results of Inphase Axial-Torsional Fatigue Experiments on 304 Stainless Steel," NASA TM 101464, March 1989.

[19] Bannantine, J. A. and Socie, D. F., "Observation of Cracking Behavior in Tension and Torsion Low Cycle Fatigue," *Low-Cycle Fatigue, ASTM STP 942,* American Society for Testing and Materials, Philadelphia, 1988.

[20] Socie, D. F., Kurath, P., and Koch, J., "A Multiaxial Fatigue Damage Parameter," *Biaxial and Multiaxial Fatigue,* EGF 3, M. W. Brown and K. J. Miller, Eds., Mechanical Engineering Publications, London, 1989, pp. 535–550.

[21] Smith, R. N., Watson, P., and Topper, T. H., "A Stress-Strain Function For Fatigue of Metals," *Journal of Materials,* Vol. 5, 1970, pp. 767–778.

[22] Leese, G. E. and Morrow, J., in *Multiaxial Fatigue, ASTM STP 853,* K. J. Miller and M. W. Brown, Eds., American Society for Testing and Materials, Philadelphia, 1985, pp. 482–496.

[23] Fash, J. W., Socie, D. F., and McDowell, D. L., "Fatigue Life Estimates for a Simple Notched Component Under Biaxial Loading," *Multiaxial Fatigue, ASTM STP 853,* K. J. Miller and M. W. Brown, Eds., American Society for Testing and Materials, Philadelphia, 1985, pp. 497–512.

[24] Wareing, J., "Fatigue Crack Growth in Type 316 Stainless Steel and a 20% Cr, 25% Ni/Nb Stainless Steel at Elevated Temperature," *Metallurgical Transactions A,* Vol. 6, 1975, p. 1367.

[25] Bonacuse, P. J. and Kalluri, S., "Elevated Temperature Torsional Fatigue Behavior of a Cobalt-Base Alloy," ASTM-NASA Workshop on Multiaxial Fatigue, San Francisco, CA, April 1990.

[26] Lefebvre, D. F., "Hydrostatic Pressure Effect on Like Prediction in Biaxial Low-Cycle Fatigue," *Biaxial and Multiaxial Fatigue, EGF3,* M. W. Brown and K. J. Miller, Eds., 1989, Mechanical Engineering Publications, London, pp. 511–533.

[27] Mowbray, D. F., "A Hydrostatic Stress-Sensitive Relationship for Fatigue Under Biaxial Stress Condition," *Journal of Testing and Evaluation,* Vol. 8, No. 1, January 1980, pp. 3–8.

Nan-Ming Yeh[1] *and Erhard Krempl*[2]

An Incremental Life Prediction Law for Multiaxial Creep-Fatigue Interaction and Thermomechanical Loading

REFERENCE: Yeh, N.-M. and Krempl, E., **"An Incremental Life Prediction Law for Multiaxial Creep-Fatigue Interaction and Thermomechanical Loading,"** *Advances in Multiaxial Fatigue, ASTM STP 1191*, D. L. McDowell and R. Ellis, Eds., American Society for Testing and Materials, Philadelphia, 1993, pp. 107–119.

ABSTRACT: An incremental multiaxial life prediction law (IMLP) is proposed which consists of the three-dimensional thermoviscoplasticity theory based on overstress (TVBO) combined with a multiaxial damage accumulation law (MDA) to compute the life-time or cycles-to-crack initiation. Crack growth is not considered in this paper but is needed to ascertain the useful life of a component. The method is intended for application to high-temperature low-cycle fatigue with and without hold times and for triangular and trapezoidal waveforms when creep-fatigue interaction takes place.

The deformation behavior is determined by solving the coupled differential equations of TVBO for the strain variation of interest, i.e., continuous cycling, hold times, or fast/slow or slow/fast loading. Only the cyclic neutral version of TVBO is used here, although cyclic hardening and recovery of state formulations are available.

The incremental damage accumulation law consists of a fatigue and a creep damage rate equation. When the sum of creep and fatigue damage reaches 1, crack initiation is said to occur. The damage accumulation equations assume that the combined actions of stress and inelastic strain rate contribute to damage and that damage evolution does not influence the constitutive equation. Fatigue damage always accumulates, but a negative creep damage rate is possible to allow for healing (creep damage is, however, always positive). In accordance with scarce experimental evidence, the maximum inelastic shear strain rate, a hydrostatic pressure-modified effective stress, as well as a parameter which depends on the multiaxiality of loading are used in each damage rate equation. The multiaxiality loading parameter depends on maximum inelastic shear strain rate for fatigue damage, while it is a function of maximum principal stress for creep damage.

All material constants for TVBO and MDA are determined from isothermal tests on Type 304 Stainless Steel (SS) at 538°C using data of Zamrik [*1*], Blass and Zamrik [*2*], and Blass [*3*]. The damage accumulation law correlates fatigue life under biaxial (tension-torsion) cycling with and without hold times. Only the results of one biaxial test series were available to compare the generally favorable predictions (correlations) with experiments.

KEY WORDS: thermoviscoplasticity, multiaxial creep-fatigue interaction, thermomechanical loading, 304 stainless steel, thermal fatigue

The design of machines and devices for application in severe loading conditions, such as variable temperature, multiaxial stress state, variable frequency, and hold times with creep and relaxation, is a problem of growing importance. The interrelationships between the thermal

Research associate[1] and professor of mechanics[2], respectively, Mechanics of Materials Laboratory, Rensselaer Polytechnic Institute, Troy, NY 12180-3590.

and the mechanical deformation, between creep and fatigue, and between the multiaxial stress state and the failure mode are very complicated and need to be modeled.

Creep-fatigue interaction is a problem occurring in high-temperature nuclear vessels, jet engines, and steam and gas turbines due to temperature changes arising from startups and shutdowns and has been widely studied. In simulated service testings, components are subjected to periodic sawtooth, trapezoidal, and other thermomechanical loadings to study the time-dependent low-cycle fatigue damage development. Significant time(rate)-dependent effects are found. The analysis of the low-cycle fatigue life of these structural components must not only account for the time (rate) dependency but also for multiaxiality of the stress state.

Most of the creep-fatigue interaction problems were investigated at isothermal, uniaxial conditions. The approaches range from algebraic to incremental formulations. The former must assume a typical cycle, whereas arbitrary loading histories can be considered using the incremental laws.

Coffin [*4*] introduced the frequency-modified Coffin-Manson equation with redefined frequency for hold-time fatigue tests to describe the low-cycle fatigue behavior under uniaxial trapezoidal waveform loadings. To account for slow-fast, fast-slow wave form effects Coffin [*5*] proposed the "frequency separating method," in which the tension-going frequency plays a major role in the fatigue life computation. Manson et al. [*6*] developed the "strain range partitioning" method to calculate the low-cycle fatigue life under uniaxial creep-fatigue interaction. This method is then extended to the analysis of multiaxial creep-fatigue interaction conditions [*1,7*].

Majumdar and Maiya [*8*] introduced an incremental life prediction law for uniaxial creep-fatigue interaction. Later Majumdar extended it to a multiaxial version and correlated the biaxial time-dependent fatigue life of 304 SS at 1000°F [*9*]. Krempl et al. [*10*] modified Majumdar and Maiya's [*8*] law. Essentially, plastic strain was replaced by stress. This new law was combined with the viscoplasticity theory based on overstress (VBO) [*11*] to correlate and predict the low-cycle fatigue lives under uniaxial creep-fatigue interaction conditions.

Usually isothermal life prediction laws are applied to thermal fatigue by considering only the highest temperature (usually the worst). Unfortunately, thermomechanical fatigue experiments [*12*] can exhibit a much lower fatigue life than those found at the highest temperature of the cycle under the same mechanical loading. Extension of life prediction to variable temperature conditions requires that material properties be introduced as a function of temperature and that the effects of thermal expansion be properly recognized. One such approach will be presented below.

Life prediction laws which lend themselves naturally to the evaluation of the life spent under variable loading are those formulated in incremental form [*8,10,13*]. By virtue of their incremental nature they can be integrated for any stress or strain path and give an indication of the life used up under such paths. In the case of periodic steady-state cycling, only one cycle needs to be considered as in the case of algebraic laws.

Due to the path dependence of the inelastic deformation of metals, material models for the prediction of deformation must also be formulated in an incremental fashion. Such an incremental formulation couples naturally with an incremental life prediction law. However, it is also possible to integrate the constitutive equation for a certain typical cycle, to plot the results in terms of stress versus strain, and to determine the quantities of interest for algebraic life prediction laws from the calculated hysteresis loops instead of from the experimental ones.

The purpose of this paper is to introduce an incremental multiaxial life prediction law (IMLP) for multiaxial creep-fatigue interaction under thermomechanical loading. IMLP consists of the three-dimensional thermoviscoplasticity theory based on overstress (TVBO) [*14*] and a multiaxial damage accumulation law (MDA). Time-dependent thermomechanical behavior and temperature-dependent material properties are modeled by TVBO, and the mul-

tiaxial creep-fatigue damage is determined by integrating two temperature-dependent damage rate equations using the inelastic strain rates and stress computed from TVBO. The calculated cycles to failure are compared with the observed values and the results are discussed.

Theory

Thermoviscoplasticity Theory Based on Overstress (TVBO)

The theory developed by Lee and Krempl [*14*] is for infinitesimal strain and orthotropy. It is of unified type and does not use a yield criterion and loading/unloading conditions. The elastic strain is formulated to be independent of thermomechanical path and the inelastic strain rate is a function of overstress, the difference between stress σ, and the equilibrium stress $\mathbf{g}$; it is a state variable of the theory.

The long-term asymptotic values of stress, equilibrium stress, and kinematic stress rates, which can be obtained for a constant mechanical strain rate and ultimately constant temperature, are assumed to be independent of thermal history as are the ultimate levels of the rate-dependent overstress and of the rate-independent contribution to the stress, see Yao and Krempl [*15*]. Therefore, the material functions and constants can in principle be obtained from isothermal tests within the temperature range of interest.

All material constants can be functions of temperature. This dependence is not explicitly displayed. The temperature dependence can be the usual Arrhenius relation or can deviate from that model.

For the representation of the equations, the usual vector notation for the stress tensor components σ and the small strain tensor components ε are used. Boldface lower and upper case letters denote 6×1 and 6×6 matrices, respectively.

Flow Laws—In the context of an infinitesimal theory, the total strain rate, $d\varepsilon/dt$, is considered to be the sum of elastic, $d\varepsilon^{el}/dt$, inelastic, $d\varepsilon^{in}/dt$, and thermal strain rates, $d\varepsilon^{th}/dt$,

$$\dot{\varepsilon} = \dot{\varepsilon}^{el} + \dot{\varepsilon}^{in} + \dot{\varepsilon}^{th} \tag{1}$$

A superposed dot represents the total time derivative, d/dt.

For each strain rate, a constitutive equation is postulated. The elastic strain is assumed to be independent of thermal history, therefore,

$$\dot{\varepsilon}^{el} = \frac{d}{dt}(\mathbf{C}^{-1}\sigma) = \mathbf{C}^{-1}\dot{\sigma} + \dot{\mathbf{C}}^{-1}\sigma \tag{2}$$

where $\mathbf{C}^{-1}$ is the compliance matrix. The additional term $\dot{\mathbf{C}}^{-1}\sigma$ contributes to the total strain rate for temperature-dependent elastic material properties. It insures that the elastic behavior is path-independent, see Lee and Krempl [*16*].

The inelastic strain rate is only a function of the overstress $\mathbf{x}$. It denotes the difference between the stress σ and the equilibrium stress $\mathbf{g}$, a vector state variable of the theory. Accordingly,

$$\dot{\varepsilon}^{in} = \mathbf{K}^{-1}\mathbf{x} \tag{3}$$

The viscosity matrix $\mathbf{K}^{-1}$ controls the rate dependence through the positive, decreasing viscosity function $k[\Gamma]$.

The thermal strain rate is given by

$$\dot{\varepsilon}^{th} = \alpha[T]\dot{T} \tag{4}$$

with $\alpha[T]$ the temperature-dependent coefficient of thermal expansion vector. T is the temperature difference from some datum temperature.

Growth Laws for the State Variables—In addition, growth laws for the two state variables of TVBO [*14*], the equilibrium stress **g**, and the kinematic stress **f**, are modified and are given as

$$\dot{\mathbf{g}} = q[\Gamma]\left(\dot{\sigma} + \frac{\mathbf{x}}{k[\Gamma]}\right) + \dot{T}\frac{\partial q[\Gamma]}{\partial T}\sigma - \left(\frac{q[\Gamma]E - E_t}{A}\right)\mathbf{z}\dot{\phi} \tag{5}$$

$$\mathbf{f} = \frac{E_t}{1 - \dfrac{E_t}{E}}\frac{\mathbf{x}}{Ek[\Gamma]} \tag{6}$$

respectively, with

$$\Gamma^2 = \mathbf{x}^t\mathbf{H}\mathbf{x},\ \dot{\phi}^2 = (\dot{\boldsymbol{\varepsilon}}^{in})^t\mathbf{Q}\dot{\boldsymbol{\varepsilon}}^{in},\ \mathbf{x} = \sigma - \mathbf{g}, \text{ and } \mathbf{z} = \mathbf{g} - \mathbf{f} \tag{7}$$

In the above Γ is the overstress invariant, and $\dot{\phi}$ is the rate of inelastic strain path length. The dimensionless modified shape functions q controls the shape of the stress-strain diagram. E_t is the tangent modulus at the maximum strain of interest and can be positive, zero, or negative. The vector **z** represents the difference between the equilibrium stress **g** and the kinematic stress **f**, and the value A is the difference between g_1 and f_1 in the asymtotic state. **H** and **Q** are dimensionless matrices representing orthotropy. For isotropy, their components are chosen to yield the von Mises effective stress and inelastic incompressibility, respectively. Asymptotic analyses for the uniaxial isothermal case in Refs *15* and *17* show that $\dot{\mathbf{f}}$ determines $\dot{\sigma}$ ultimately. The purpose of Eq 6 is to set this slope, which can be positive, zero, or negative. The representations of the material matrices for isotropy are given in the Appendix.

The theory given above represents cyclic neutral behavior. Rate sensitivity, relaxation, and creep are modeled. Since no recovery of state is included, the creep behavior is controlled by the sign of E_t. If $E_t > 0$ the equations can only represent primary creep. Primary and secondary creep may be modeled for $E_t = 0$; primary, secondary, and tertiary creep can be represented in principle if $E_t < 0$. Note also that E_t sets the slope of the stress-inelastic strain curve of the maximum inelastic strain of interest through Eq 6, see the discussion of VBO in Refs *11,15,17*.

When recovery of state is included in the model [*18–20*], the creep behavior is no longer completely controlled by the sign of E_t and secondary creep can be reproduced at stress levels which are in the linear region of the stress-strain diagram. Also, the isothermal formulation of VBO has been extended to cyclic hardening [*21–22*]. It is possible to include this property as well as recovery of state in the TVBO theory.

The Incremental, Multiaxial Damage Accumulation Law

The multiaxial damage accumulation law (MDA) is proposed based on the modification of the incremental life prediction law for uniaxial creep-fatigue interaction [*13*]. The model includes the effect of hydrostatic stress on creep and fatigue damage.

The importance of hydrostatic stress on the low-cycle fatigue life has been acknowledged [*23–24*]. Ductile materials can become brittle under hydrostatic tension, while brittle materials may become ductile under hydrostatic pressure. To model the hydrostatic effects the triaxiality factor $TF\,(= \sigma_{kk}/\sigma_{eff})$ is used in the model, where σ_{kk} is the first stress invariant and σ_{eff} is the von Mises effective stress. (Tensor notation is used in this part of the paper.)

The present law is intended for the prediction of crack initiation, which is assumed to occur

along the plane of maximum inelastic shear strain rate [25]. The creep damage is assumed to be cavity type, which initiates on grain boundaries normal to the maximum principal tensile stress direction [9,26]. The proposed incremental multiaxial damage accumulation law consists of a fatigue and a creep damage rate equation $\dot{D}_f$ and $\dot{D}_c$, respectively. Damage is only a counter and its evolution does not influence the constitutive equations. Fatigue and creep damage are set to be zero initially (for a virgin or fully annealed material), and crack initiation occurs if the sum of fatigue and creep damage reaches 1. The incremental law is then given as

$$\dot{D}_f = \frac{L_f^{\pm}}{T_f} \left| \frac{\dot{\varepsilon}_{in}^s}{\dot{\varepsilon}_f} \right|^{nf} \left| \frac{\sigma_{eff}}{\sigma_f} \right|^{mf} MF_f \tag{8}$$

$$\dot{D}_c = \frac{L_c^{\pm}}{T_c} \left| \frac{\dot{\varepsilon}_{in}^s}{\dot{\varepsilon}_c} \right|^{nc} \left| \frac{\sigma_{eff}}{\sigma_c} \right|^{mc} MF_c \tag{9}$$

where

$$MF_f = \{1 + a(1 - TF)\}^{mf} \tag{10}$$

$$MF_c = \{1 + b(1 - TF)\}^{mc} \tag{11}$$

Failure is said to occur when

$$D_f + D_c = 1 \tag{12}$$

$L_f^{\pm}$ is the fatigue loading function which models the effects of multiaxial loading and temperature T. It is assumed to be controlled by the ratio of $\dot{\varepsilon}_{in}^n$ and $\dot{\varepsilon}_{in}^s$, where $\dot{\varepsilon}_{in}^s$ is the value of the normalized maximum inelastic shear strain rate, and where $\dot{\varepsilon}_{in}^n$ is the value of normalized inelastic strain rate perpendicular to the plane on which $\dot{\varepsilon}_{in}^s$ acts [9,25]. The word "normalized" denotes that the multiaxial inelastic strain rates reduce to the uniaxial value for uniaxial loading. Accordingly,

$$\dot{\varepsilon}_{in}^s = \tfrac{2}{3}|\dot{\varepsilon}_{in}^1 - \dot{\varepsilon}_{in}^3| \tag{13}$$

$$\dot{\varepsilon}_{in}^n = 2(\dot{\varepsilon}_{in}^1 + \dot{\varepsilon}_{in}^3) \tag{14}$$

where $\dot{\varepsilon}_{in}^1$, $\dot{\varepsilon}_{in}^2$, and $\dot{\varepsilon}_{in}^3$ are the principal inelastic strain rates with $\dot{\varepsilon}_{in}^1 \geq \dot{\varepsilon}_{in}^2 \geq \dot{\varepsilon}_{in}^3$. For the case considered here (axial and torsional loadings), $\dot{\varepsilon}_{in}^n = \dot{\varepsilon}_{in}$ and $\dot{\varepsilon}_{in}^s = [(\dot{\varepsilon}_{in})^2 + \tfrac{1}{3}(\dot{\gamma}_{in})^2]^{1/2}$, where $\dot{\varepsilon}_{in}$ and $\dot{\gamma}_{in}$ are the inelastic axial strain rate and inelastic engineering shear strain rate, respectively. $L_c^{\pm}$ is the creep loading function which represents the effects of the multiaxial loading and temperature, it is a function of the ratio of maximum principal stress σ_1 and the von Mises effective stress σ_{eff} [9]. We define

$$L_f^{\pm} \equiv L_f^{\pm}[\omega, T] = \begin{cases} L_f^{+}[T], & \omega \geq 0 \\ L_f^{-}[T], & \omega < 0 \end{cases} \tag{15}$$

$$L_c^{\pm} \equiv L_c^{\pm}[\beta, T] = \begin{cases} L_c^{+}[T], & \beta > 0 \\ L_c^{-}[T], & \beta < 0 \end{cases} \tag{16}$$

where

$$\omega = \frac{\dot{\varepsilon}_{in}^n}{\dot{\varepsilon}_{in}^s}, \quad \beta = \frac{\sigma_1}{\sigma_{eff}}$$

$L_f^{\pm} > 0$ is postulated and the fatigue damage always accumulates, but a negative creep damage rate is allowed (creep damage is, however, always positive) through $L_c^{\pm}$. For instance, $L_c^{+} = 1$ and $L_c^{-} = -1$ are assumed for the uniaxial case in tension and compression, respectively [*13*]. MF_f and MF_c are two multiaxiality factors, which are used to model the hydrostatic effects on fatigue and creep damage, respectively. Constants T_f, T_c, $\dot{\varepsilon}_f$, and $\dot{\varepsilon}_c$ in Eqs 8–9 are introduced for dimensional considerations. They are set equal to 1 in the appropriate units. The other constants, n_f, m_f, σ_f, n_c, m_c, σ_c, a, and b, must be determined from appropriate axial, torsional, and biaxial tests with and without hold time.

Numerical Experiments

Evaluation of Constants

To model the multiaxial thermal time-dependent fatigue behavior, the material properties of TVBO and MDA must be known as a function of temperature. For a complete determination of the viscoplastic properties, strain rate change and relaxation tests are needed. Since such results are generally not available, the present analysis uses whatever data are available augmented by "educated guesses" of the behavior to arrive at the material constants. The temperature-dependent material properties of TVBO and MDA are found from isothermal conditions and are interpolated for variable temperature. For instance, a decrease in modulus and flow stress with increasing temperature has been assumed in Fig. 1 for an A1 alloy of Ref *28*.

TVBO together with Eqs 8–16 constitute the incremental multiaxial life prediction law and must now be applied. The boundary conditions and the material properties must be specified for calculation. The integration of the coupled set of differential equations is performed on a SUN 3 work station.

The steady-state hysteresis loops under tension, torsion, and proportional biaxial loading with and without hold time for 304 SS at 538°C [*1*] are used to approximately determine the material constants of TVBO at 538°C. The constants are listed in Table 1.

Using TVBO and MDA lifetime at 538°C can be calculated. Experimental failure points of uniaxial, torsional, and biaxial low-cycle fatigue tests with and without hold time for 304 SS at 538°C [*2,3*] are used to identify the material constants of MDA. Using uniaxial low-cycle fatigue tests with and without hold time, the constants n_f, σ_f, and m_f, and n_c, σ_c, and m_c are determined assuming

$$L_f^{\pm} = \begin{cases} L_f^{+} = 1, \dot{\varepsilon}_{in} \geq 0 \\ L_f^{-} = 0, \dot{\varepsilon}_{in} < 0 \end{cases} \tag{17}$$

$$L_c^{\pm} = \begin{cases} L_c^{+} = 1, \sigma \geq 0 \\ L_c^{-} = -1, \sigma < 0 \end{cases} \tag{18}$$

and $MF_f = MF_c = 1$.

TABLE 1—*Material properties of TVBO for AISI 304 SS.*

E (MPa) = 155 000 $\quad \nu = 0.29$
$q[\Gamma] = \Psi[\Gamma]/E$
Viscosity function: $k[\Gamma] = k_1\left(1 + \dfrac{\Gamma}{k_2}\right) - k_3$
k_1 = 314 200 (s), k_2 = 60 (MPa), k_3 = 28
Shape function: $\Psi[\Gamma] = c_1 + (c_2 - c_1)\exp(-c_3\Gamma)$
c_1 = 79500 (MPa), c_2 = 151 900 (MPa), c_3 = 0.18 (MPa^{-1})
E_t = 2460 (MPa), A = 236 (MPa), inelastic Poisson's ratio: $\eta = 0.5$

TABLE 2—*Material properties for damage accumulation law.*

Fatigue Damage	Creep Damage
$T_f = 1$ (s)	$T_c = 1$ (s)
$\dot{\epsilon}_f = 1$ (1/s)	$\dot{\epsilon}_c = 1$ (1/s)
$n_f = 0.83$	$n_c = 0.27$
$\sigma_f = 1000$ (MPa)	$\sigma_c = 1021.6$ (MPa)
$m_f = 1.835$	$m_c = 5.5$
$a = -0.3146$	$b = -0.1184$

For torsion $L_f^+ = L_f^-$ is postulated since the direction of shear should have no influence on crack initiation, and $L_c^- = 0$ because no healing was reported in Ref *9*. Then $MF_f = MF_c = 0.5$ is assumed for torsion which enables "a" and "b" to be calculated. $L_f^\pm$ and L_c^+ for torsion are then determined using the data for torsional tests with and without hold time.

For proportional biaxial loadings $L_c^- = 0$ is also assumed since no healing was found in Ref *9*. $L_f^\pm$ and L_c^+ can be evaluated from biaxial tests with and without hold time using the calculated values of MF_f and MF_c according to Eqs 10 and 11, respectively. Iteration between axial, torsional, and biaxial data using Eqs 8–12 yields refined values of the above constants. The material properties for MDA are shown in Table 2.

The dependence of the fatigue loading function $L_f^\pm$ on $|\omega|$ is shown in Fig. 1, where $|\omega|$ is determined at the maximum strain of the cycle. In Fig. 1, L_f^+ increases from 0.17 to 1 as $|\omega|$ increases from 0 (pure torsion) to 1 (uniaxial), while the opposite is true for L_f^-, which decreases from 0.17 to 0 while $|\omega|$ increases from 0 to 1. For biaxial loading $0 \leq |\omega| \leq 1$. The creep loading function L_c^+ versus β is shown in Fig. 2. β is determined at the maximum strain of interest. L_c^+ increases from 0.3 to 1 as β increases from 0.577 (pure torsion) to 1 (uniaxial). For biaxial cases β is between 0.577 and 1. L_c^- is assumed to be equal to -1 for the uniaxial compression to account for the healing effect observed in the experiments [*13,27*]. For the torsional case and biaxial cases ($\beta < 0$), L_c^- is postulated to be zero since no healing was reported in Ref *9*.

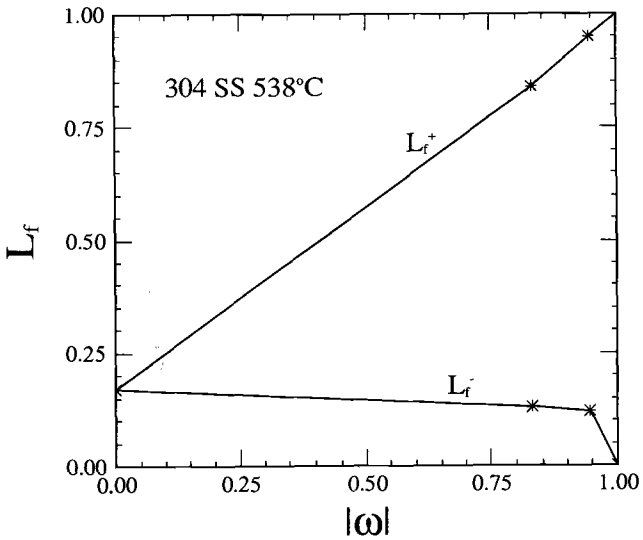

FIG. 1—*Fatigue loading functions versus* $|\omega|$ *for 304 SS at 538°C.*

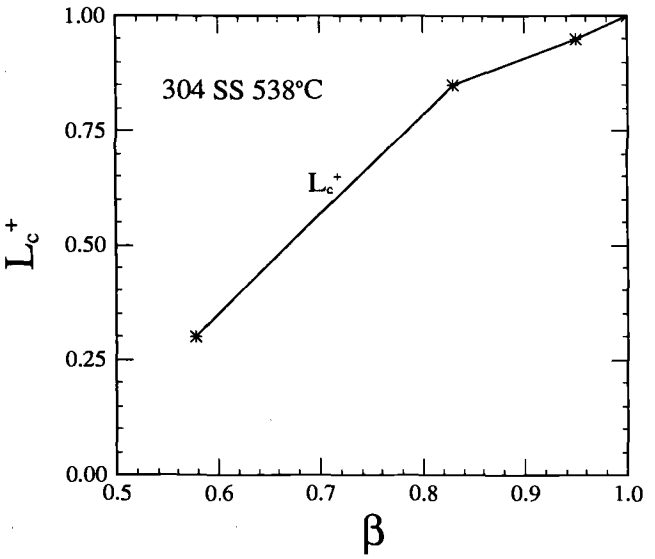

FIG. 2—*Creep loading function versus β for 304 SS at 538°C.*

Deformation Behavior

Deformation behavior computed using TVBO are shown in Figs. 3 and 4. In Fig. 3 two hysteresis loops for completely reversed strain-controlled loading at a strain amplitude of ±0.5% at steady state at 538°C are shown. Tensile and symmetric holds of 600 s are introduced. The inelastic strain range of the symmetric hold test is slightly larger than that of the tensile hold test. Steady-state hysteresis loops for slow-fast and fast-slow tests are shown in Fig.

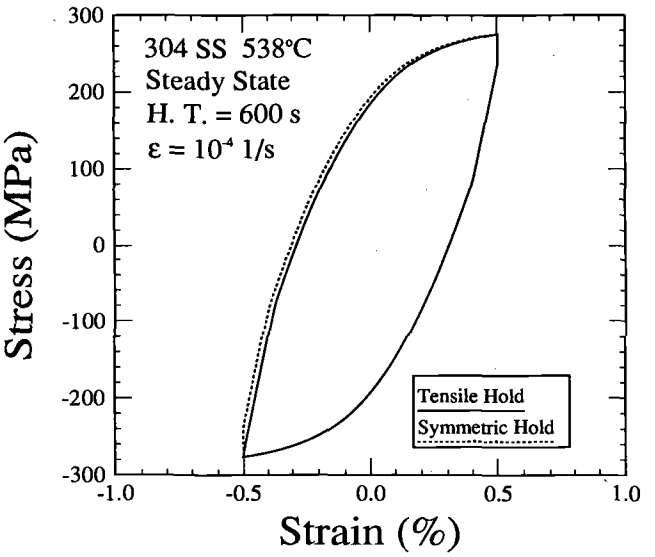

FIG. 3—*Strain-controlled steady-state hysteresis loops of 304 SS at 538°C under tensile hold and symmetric hold loadings.*

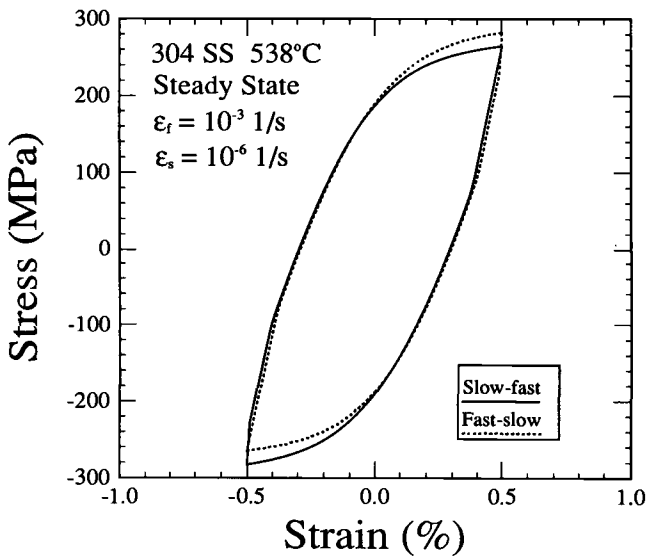

FIG. 4—*Strain-controlled steady-state hysteresis loops of 304 SS at 538°C under slow/fast and fast/slow loadings. Near-vertical drops are at the transitions from fast to slow loadings.*

4. A near vertical drop is observed in the transition of changing from the fast strain rate 10^{-3} 1/s to the slow strain rate 10^{-6} 1/s.

Life Prediction

The calculated and observed biaxial low-cycle fatigue lives together with two lines indicating a deviation of a factor of 2 in life are shown in Figs. 5 and 6 for the cases without and with hold time, respectively. Because of the scarcity of the experimental data, only the data points for strain ratio $R = 2$ ($R = \Delta\gamma/\Delta\epsilon$) are predictions in Fig. 5. The predicted lives in Fig. 5 are within the bounds and are acceptable. The results of the uniaxial, torsional, and biaxial hold-time tests are shown in Fig. 6. Although three points are outside of the bounds, the trend is correct and is thus acceptable.

Discussion

IMLP, which consists of the thermoviscoplasticity theory based on overstress (TVBO) and the multiaxial damage accumulation law (MDA), is applied to correlate and predict the low-cycle fatigue lives of 304 SS at 538°C under biaxial creep-fatigue interaction. The material constants of TVBO and MDA for 304 SS at 538°C are identified using the experimental data of Refs *1* and *2–3*, respectively. In TVBO theory used here, effects of recovery, aging, and cyclic hardening are neglected. There are some indications that recovery and aging are important at 538°C in 304 SS. A quantitative assessment of these effects, however, cannot be obtained from the available low-cycle fatigue data. They are consequently not modeled.

If IMLP is applied to thermal fatigue, both Eqs 1 and 5 have additional terms. These additional terms influence not only the elastic but also the inelastic behavior [*16*] and consequently affect the predicted low-cycle fatigue lives. The temperature-dependent material properties of TVBO and MDA can be determined from isothermal tests at different temperatures.

Although the calculated lives in Fig. 6 do show three points which are beyond the limits of

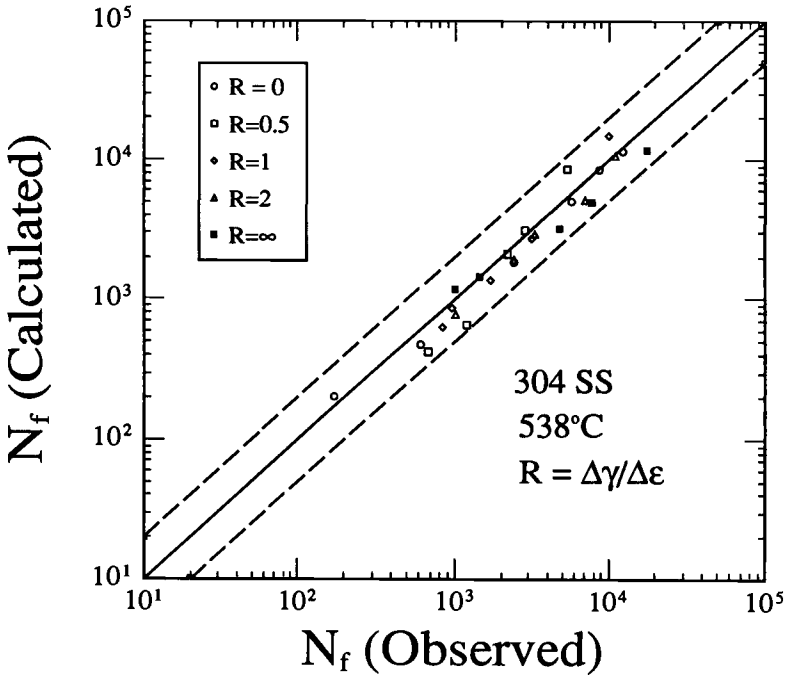

FIG. 5—*Observed fatigue lives versus calculated fatigue lives using the IMLP for different biaxial loadings. The data for* R = *2 are predictions.*

a factor of ±2 on life, the trends of the computed lives are in the proper direction. The three points are a uniaxial hold-time test, a biaxial $R = 1$ hold-time test, and a symmetric hold-time test in torsion. It can be seen from Table 2 in Ref *9* that the fatigue life of the uniaxial test with 0.5% strain range and 60 min tensile hold time (the first out-of-bound point) is unusually short. The biaxial test has the smallest effective strain range of all the tests, and the deformation behavior shows very little inelasticity. In this region small deviations of the predicted stress-strain behavior from the real one can play an important role in the life calculation. It should be further considered that a complete data set was not available for determination of the constants. Some properties had to be assumed. Deviations have to be expected. The final unusual point is for the torsional test with 0.55% effective strain range and 6 min symmetric hold time. The calculated value is much lower than the observed value. We have no explanation for this behavior.

Conclusions

The present paper intends to show the capabilities of modeling the time-dependent multiaxial thermal fatigue behavior using the thermoviscoplasticity theory based on overstress (TVBO) and the multiaxial damage accumulation law (MDA). The trends are encouraging. For the complete evaluation of the predictive capability, a consistent set of data is necessary. Some will be used to determine the needed material constants, others should be used to check on the predictive capability of the theory. Variable amplitude and thermal fatigue tests should be included in the latter set. Finally, MDA is not restricted to periodic loadings due to its incremental formulation; it can in principle be applied to arbitrary deformation histories which include proportional and nonproportional loadings.

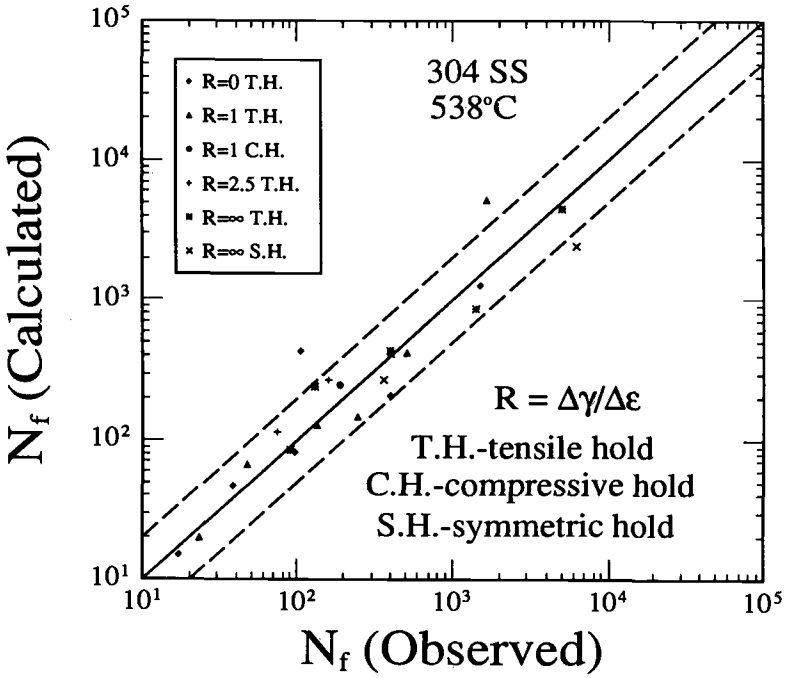

FIG. 6—*Observed fatigue lives versus calculated fatigue lives using the IMLP for different biaxial hold time loadings.*

Acknowledgment

This research was supported by DARPA/ONR Contract N00014-86-k0770 with Rensselaer Polytechnic Institute.

APPENDIX

Matrices for Isotropy

The nonzero components of the symmetric elastic modulus matrix $\mathbf{C}^{-1}$ and the symmetric viscosity matrix $\mathbf{K}^{-1}$ are represented by

$$\begin{aligned}(C^{-1})_{11} &= (C^{-1})_{22} = (C^{-1})_{33} = 1/E \\ (C^{-1})_{44} &= (C^{-1})_{55} = (C^{-1})_{66} = 1/G \\ (C^{-1})_{ij} &= -\nu/E,\ i, j = 1, 2, 3, \text{ and } i \neq j\end{aligned} \tag{A-1}$$

and

$$\begin{aligned}(K^{-1})_{11} &= (K^{-1})_{22} = (K^{-1})_{33} = 1/Ek[\Gamma] \\ (K^{-1})_{44} &= (K^{-1})_{55} = (K^{-1})_{66} = 3/Ek[\Gamma] \\ (K^{-1})_{ij} &= -\tfrac{1}{2}Ek[\Gamma],\ i, j = 1, 2, 3, \text{ and } i \neq j\end{aligned} \tag{A-2}$$

where inelastic incompressibility is assumed and $G = \dfrac{E}{2(1+\nu)}$.

The positive decreasing viscosity function $k[\Gamma]$, dimension of time, controls the rate dependence. **H** and **Q** are dimensionless matrices; the nonzero components are given by

$$H_{11} = H_{22} = H_{33} = 1, H_{44} = H_{55} = H_{66} = 3$$
$$H_{ij} = -0.5, i, j = 1, 2, 3, \text{ and } i \neq j, \tag{A-3}$$

and

$$Q_{11} = Q_{22} = Q_{33} = 1, Q_{44} = Q_{55} = Q_{66} = \tfrac{1}{3}$$
$$Q_{ij} = -0.5, i, j = 1, 2, 3, \text{ and } i \neq j, \tag{A-4}$$

respectively.

The coefficient of thermal expansion vector is α

$$\alpha^t = [\alpha\ \alpha\ \alpha\ 0\ 0\ 0] \tag{A-5}$$

All components are material properties which must be identified for a given material.

References

[1] Zamrik, S. Y., "The Application of 'Strain Range Partitioning Method' to Multiaxial Creep-Fatigue Interaction," Paper No. 16, AGARD Conference Proceedings No. 243, April 1978.

[2] Blass, J. J. and Zamrik, S. Y., "Multiaxial Low-Cycle Fatigue of Type 304 Stainless Steel," *Proceedings,* ASME-MPC Symposium on Creep-Fatigue Interaction, 1976, American Society of Mechanical Engineers, New York, pp. 129–159.

[3] Blass, J. J., Oak Ridge National Laboratory Reports ORNL/TM-6438, Oak Ridge, TN, 1979.

[4] Coffin, L. F., Jr., "Fatigue at High Temperature," *Fatigue at Elevated Temperatures, ASTM STP 520,* A. E. Carden, A. J. McEvily, and C. H. Wells, Eds., American Society for Testing and Materials, Philadelphia, 1973, pp. 5–34.

[5] Coffin, L. F., Jr., "The Concept of Frequency Separation in Life Prediction for Time-Dependent Fatigue," *Proceedings,* ASME-MPC3 Symposium on Creep-Fatigue Interaction, R. M. Curran, Ed., American Society of Mechanical Engineers, New York, NY, 1976, pp. 349–363.

[6] Manson, S. S., Halford, G. R., and Hirschberg, M. H., "Creep-Fatigue Analysis by Strain-Range Partitioning," *Proceedings,* First Symposium on Design for Elevated Temperature Environment, American Society of Mechanical Engineers, New York, NY, 1971, pp. 12–28.

[7] Manson, S. S. and Halford, G. R., "Multiaxial Creep-Fatigue Life Analysis using Strainrange Partitioning," *Proceedings,* ASME-MPC3 Symposium on Creep-Fatigue Interaction, R. M. Curran, Ed., American Society of Mechanical Engineers, New York, NY, 1976, pp. 299–322.

[8] Majumdar, S. and Maiya, P. S., "A Damage Equation for Creep-Fatigue Interaction," *Proceedings,* ASME-MPC3 Symposium on Creep-Fatigue Interaction, R. M. Curran, Ed., American Society of Mechanical Engineers, New York, NY, 1976, pp. 323–326.

[9] Majumdar, S., "Designing Against Low-Cycle Fatigue at Elevated Temperature," *Nuclear Engineering and Design,* Vol. 63, 1981, pp. 121–135.

[10] Krempl, E., Lu, H., Satoh, M. and Yao, D., "Viscoplasticity Based on Overstress Applied to Creep-Fatigue Interaction," *Low Cycle Fatigue, ASTM STP 942,* H. D. Solomon, G. R. Halford, L. R. Kaisand, and B. N. Leis, Eds., American Society for Testing and Materials, Philadelphia, 1987, pp. 123–139.

[11] Krempl, E., McMahon, J. J., and Yao, D., "Viscoplasticity Based on Overstress with Differential Growth Law for the Equilibrium Stress," *Mechanics of Materials,* Vol. 5, 1986, pp. 35–48.

[12] Bill, R. C., Verrilli, M. J., McGaw, M. A., and Halford, G. R., "A Preliminary Study of the Thermomechanical Fatigue of Polycrystalline Mar M-200," NASA TP-2280, AVSCOM TR 83-C-6, February 1984.

[13] Satoh, M. and Krempl, E., "An Incremental Life Prediction Law for Creep-Fatigue Interaction," *Material Behavior at Elevated Temperatures and Components Analysis,* ASME Pressure Vessel and Piping Division, New York, Vol. 60, Y. Yamada, R. L. Roche, and F. L. Cho, Eds., 1982, pp. 71–79.

[14] Lee, K. D. and Krempl, E., "An Orthotropic Theory of Viscoplasticity Based on Overstress for Thermomechanical Deformations," *International Journal of Solids and Structures,* Vol. 27, 1991, pp. 1445–1459.

[15] Yao, D. and Krempl, E., "Viscoplasticity Theory Based on Overstress. The Prediction of Monotonic and Cyclic Proportional and Nonproportional Loading Paths of an Aluminum Alloy," *International Journal of Plasticity,* Vol. 1, 1985, pp. 259–274.

[16] Lee, K. D. and Krempl, E., "Uniaxial Thermomechanical Loading. Numerical Experiments using the Thermal Viscoplasticity Theory Based on Overstress," *European Journal of Mechanics, A/Solids,* Vol. 10, 1991, pp. 175–194.

[17] Sutcu, M. and Krempl, E., "A Simplified Orthotropic Viscoplasticity Theory Based on Overstress," *International Journal of Plasticity,* Vol. 6, 1990, pp. 247–261.

[18] Choi, S. H. and Krempl, E., "The Orthotropic Viscoplasticity Theory Based on Overstress with Static Recovery Applied to The Modeling of Long Term High Temperature Creep Behavior of Cubic Single Crystals," Report MML 89-3, Rensselaer Polytechnic Institute, Troy, NY, December 1989.

[19] Majors, P. S. and Krempl, E., "A Recovery of State Formulation for the Viscoplasticity Theory Based on Overstress," *Proceedings,* Conference on High Temperature Constitutive Modeling: Theory and Application, A. D. Freed and K. P. Walker, Eds., American Society of Mechanical Engineers, New York, NY, 1991, pp. 235–250.

[20] Yeh, N. M. and Krempl, E., "A Thermoviscoplastic Analysis of Uniaxial Ratchetting Behavior of SiC/Ti Fibrous Metal Matrix Composites," *Proceedings,* Sixth Technical Conference of American Society for Composites, Technomic Publishing Co., Westport, CN, 1991, pp. 329–337.

[21] Krempl, E. and Yao, D., "The Viscoplasticity Theory Based on Overstress Applied to Ratchetting and Cyclic Hardening," *Low Cycle Fatigue and Elasto-Plastic Behavior of Materials,* K.-T. Rie, Ed., Elsevier Applied Science, New York, 1987, pp. 137–148.

[22] Krempl, E. and Choi, S. H., "Viscoplasticity Theory Based on Overstress: The Modeling of Ratchetting and Cyclic Hardening of AISI Type 304 Stainless Steel," *Nuclear Engineering and Design,* Vol. 133, 1992, pp. 401–410.

[23] Libertiny, G. Z., "Short-Life Fatigue under Combined Stresses," *Journal of Strain Analysis,* Vol. 2, 1967, pp. 91–97.

[24] Manson, S. S. and Halford, G. R., "Multiaxial Low-Cycle Fatigue of Type 304 Stainless Steel," *Journal of Engineering Materials and Technology,* Vol. 99, 1977, pp. 283–285.

[25] Brown, M. W. and Miller, K. J., "A Theory for Fatigue Failure under Multiaxial Stress-Strain Conditions," *Proceedings of the Institute of Mechanical Engineers,* Vol. 187, 1973, pp. 217–229.

[26] Hayhurst, D. R., "Creep Rupture under Multiaxial States of Stress," *Journal of Mechanics and Physics of Solids,* Vol. 20, 1972, pp. 381–390.

[27] Majumdar, S. and Maiya, P. S., "Waveshape Effects in Elevated Temperature Low-Cycle Fatigue of Type 304 Stainless Steel," *Inelastic Behavior of Pressure Vessel and Piping Components,* PVP-PB-028, American Society of Mechanical Engineers, New York, 1978, pp. 43–54.

[28] Krempl, E. and Yeh, N. M., "Residual Stresses in Fibrous Metal Matrix Composites. A Thermoviscoplastic Analysis," *Proceedings,* IUTAM Symposium on Inelastic Deformation of Composite Materials, G. J. Dvorak, Ed., Springer-Verlag, New York, 1990, pp. 411–443.

K. Dang-Van[1]

Macro-Micro Approach in High-Cycle Multiaxial Fatigue

REFERENCE: Dang-Van, K., **"Macro-Micro Approach in High-Cycle Multiaxial Fatigue,"** *Advances in Multiaxial Fatigue, ASTM STP 1191*, D. L. McDowell and R. Ellis, Eds., American Society for Testing and Materials, Philadelphia, 1993, pp. 120–130.

ABSTRACT: An original methodology for fatigue resistance of mechanical structure is presented. Our approach relies on a "macro-micro" analysis. Here micro stresses in misoriented elements are evaluated when the macroscopic loading path is known. Multiaxial fatigue criteria are then proposed. Some industrial applications are shown.

KEY WORDS: multiaxial fatigue criterion, high-cycle fatigue, fatigue limit, macro-micro approach, micro stress evaluation

Nomenclature

$A_{ijhk}(M,m)$	Elastic localization tensor
c	Kinematic hardening modulus
E_{ij}	Macroscopic strain tensor
k	Actual yield limit
k^{lim}	Elastic shakedown limit of k^* according to Papadopoulos theory
k^*	Radius of the stabilized hypersphere surrounding the loading path
$L(t)$	Loading path
m	Current point of $V(M)$
M	Point of the structure where the fatigue analysis is made
p	Microscopic hydrostatic tension
P	Macroscopic hydrostatic tension
s	Microscopic deviatoric stress tensor
S	Macroscopic deviatoric stress tensor
t	Time
$V(M)$	Characteristic macroscopic volume surrounding Point M
ϵ	Microscopic strain tensor
ϵ^e	Microscopic elastic strain tensor
ϵ^p	Microscopic plastic strain tensor
ϵ^p_{eq}	Microscopic equivalent plastic strain
μ	Shear modulus
ρ	Microscopic residual stress tensor
ρ^*	Stabilized microscopic residual stress tensor
σ	Microscopic stress tensor
Σ	Macroscopic stress tensor
τ	Shear stress

[1] Laboratoire de Mecanique des Solides, CNRS URA 317, Ecole Polytechnique, 91128 Palaiseau, France.

Introduction

During the last four decades, most research efforts have been devoted to low-cycle fatigue. Most industrial applications, however, involve high-cycle fatigue. Many multiaxial fatigue criteria exist. However, the design of structures which have to resist fatigue is still a problem; engineers have to perform difficult, expensive, and time-consuming experiments to find the fatigue limit of a mechanical component. Generally, this is done on the structure itself.

The origin of multiaxiality comes from different factors:

1. External loading.
2. Geometry of the structure: it is well-known that in the vicinity of notches, the stress state is multiaxial even if the loading is uniaxial.
3. Residual stresses which are multiaxial by nature.

For example, the stress cycles on the critical loading of a crankshaft are represented in Fig. 1. They are a combination of out-of-phase torsion and bending. Figure 2 shows the evolution over one revolution of the stress tensor Σ in the critical zone of an integrated ball bearing. From these individual examples, it can be seen that multiaxial loading paths are often encountered. The degrees of complexity of multiaxial loadings were discussed in Ref *1*. An original multiaxial fatigue limit criterion is reviewed in this paper based on a macro-micro approach whose latest developments are presented.

Presentation of the "Macro-Micro" Method in High-Cycle Fatigue

For constant stress or strain range, the concept of fatigue limit corresponds to a stress or strain "level" (amplitude and stress level) just enough to produce the initiation and the propagation of a crack. In this paper, we assume that a fatigue limit exists for complex loadings, too. For homogeneous materials, the initiation of fatigue cracks takes place in critical zones of stress concentration such as geometric discontinuities, fillets, notches. . . . There are still discussions on the concept of initiation itself, depending on the scale at which the phenomenon is observed; it is sometimes considered a micropropagation problem. Care should be exercised when using fracture mechanics at the grain scale because the local stress σ is different from the macroscopic applied stresses Σ. The first fatigue phenomena are microscopic and local and usually occur in grains which have undergone local plastic deformation in characteristic intracrystalline bands. The local (or microscopic) parameters (σ, ϵ) are different from the macroscopic parameters derived by classical engineering computations (Σ, E). The different steps of the calculations are described in Fig. 3. Step 2 corresponds to the macroscopic-to-microscopic passage. This problem is solved by distinguishing two scales:

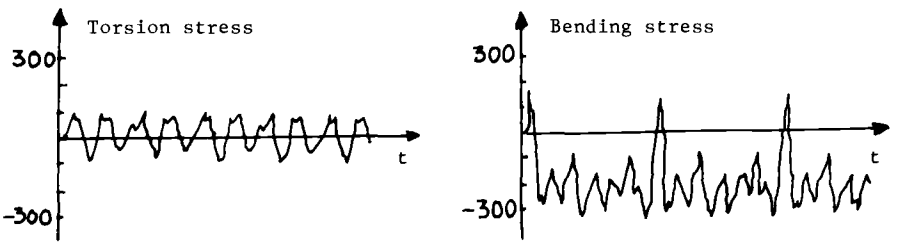

FIG. 1—*Stress cycles on the critical zone of a crankshaft.*

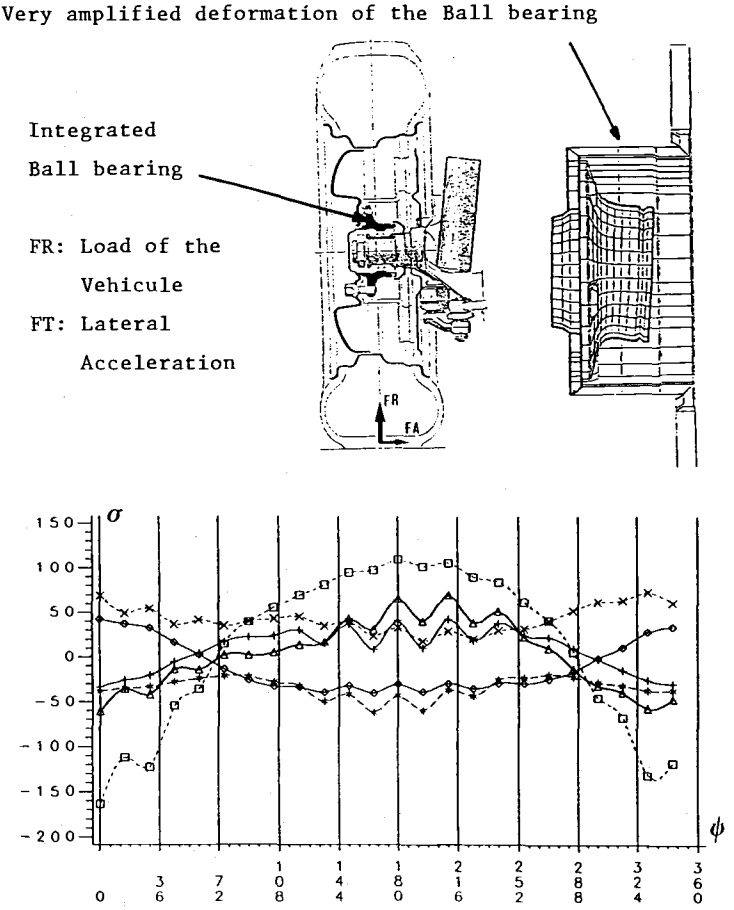

FIG. 2—*Evolution over one revolution of the wheel of the components of the stress tensor of a ball bearing.* ψ = *angle of rotation of the wheel.*

1. A macroscopic scale characterized by an elementary representative volume $V(M)$ surrounding the point M where the fatigue analysis is made and representing, for instance, an element of a finite element mesh or corresponding to the dimension of a strain gauge. This is the usual scale considered by engineers; mechanical macroscopic variables $\Sigma(M,t)$, $E(M,t)$ are assumed to be homogeneous in $V(M)$ at any time, t.
2. A microscopic scale of the order of the grain size (or some grain sizes) corresponding to a subdivision of $V(M)$; the microscopic quantities σ and ϵ are not homogeneous and differ from Σ and E; even if the mean value of σ equals Σ, the local stress σ can fluctuate.

More precisely, σ and Σ are related by the following exact relation

$$\sigma_{ij}(m,t) = A_{ijhk}(M,m)\Sigma_{hk}(M,t) + \rho_{ij}(m,t) \tag{1}$$

In the above equation $A_{ijhk}(M,m)$ is the elastic localization tensor and ρ is the local residual stress field. Let us note that A_{ijhk} could be correlated with the microstructure of the material.

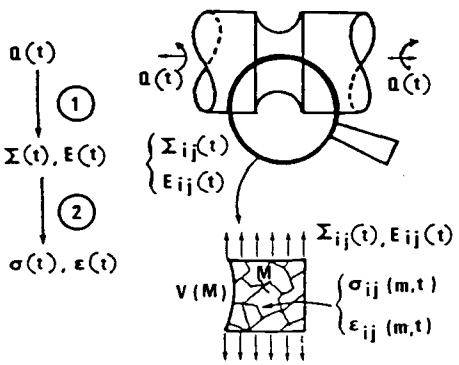

FIG. 3—*Different steps of the proposed fatigue calculations, macroscopic and microscopic scale.*

This point, however, is not addressed here. A_{ijhk} can be obtained in theory by solving six elastic boundary value problems on volume V [one for each (hk) component]. Near the fatigue limit, the applied stresses are rather low, and it is reasonable to suppose that σ tends toward a pseudo-shakedown state (pure shakedown corresponds to no damage). Then Melan's theorem states that beyond a certain time, t, a time-independent residual stress field $\rho^*_{ij}(m)$ exists such as

$$\sigma_{ij}(m,t) = A_{ijhk}(M,m)\Sigma_{hk}(M,t) + \rho^*_{ij}(m) \tag{2}$$

that never violates the local plastic criterion.

For example, in the case of an inclusion submitted to uniform plastic strain ϵ^p_{ij} and embedded in an elastic matrix, both having same elastic coefficients, one has

$$\sigma_{ij}(t) = \Sigma_{ij}(t) - 2\mu\epsilon^p_{ij}(t) \tag{3}$$

$$\rho_{ij}(t) = -2\mu\epsilon^p_{ij}(t) \tag{4}$$

These relations can be obtained if the total strain of the matrix and inclusion are supposed to be the same, i.e.

$$E = \epsilon^e + \epsilon^p \tag{5}$$

Then, multiplying both sides by the common elastic compliance one obtains Eq 3. (There is no volume change under plastic deformation $\epsilon^p_{ii} \neq 0$.)

The fatigue criterion is then expressed by means of the microscopic stress tensor σ, which is known at each time, t, if ρ is known. It is possible to describe quite precisely the loading path because the local microscopic stress tensor in the stabilized state is known at each time, t, of the cycle. From Eq 2, the computation of $\sigma_{ij}(t)$ is limited to the computation of ρ^*, which is independent of time when shakedown occurs.

Evaluation of the Microscopic Residual Stress

The principle of the method given in Ref *1* is recalled. This method is based on:

1. Generalized Melan's theorem as given by Mandel et al. [*2*] studying elastic shakedown of elastoplastic structures with combined kinematic and isotropic hardening.
2. A minimum assumption detailed below.

The elastic domain of the material is defined by

$$g(\sigma - c\epsilon^p) = k^2(\epsilon^p_{eq}) \tag{6}$$

where ϵ^p is the plastic strain tensor, and c is a positive constant characterizing linear kinematic hardening, and

$$\epsilon^p_{eq} = \sqrt{\tfrac{2}{3}(\epsilon^p_{ij} \cdot \epsilon^p_{ij})} \tag{7}$$

k is supposed to be a strictly increasing function of the considered plastic strain range. Then a necessary condition for elastic shakedown is that a certain time t_1, a certain fixed (i.e., independent of t) residual stress field $\rho^{*(x)}$ and plastic strain field $\epsilon^p(x)$ exist such that

$$\forall\ t > t_1,\ g[\sigma^{el}(x,t) + \rho^{*(x)} - c\epsilon^p(x)] < k^2(\epsilon^p_{eq}) \tag{8}$$

where σ^{el} is the stress obtained if pure elastic behavior is assumed.

In our case the representative volume $V(M)$ represents the elastoplastic structure, and σ^{el} corresponds to $A \cdot \Sigma$ of Eq 1,2 or to Σ if A could be taken equal to identity. (This simplification is possible when the matrix and the inclusion are of the same nature.)

For the sake of simplicity, the von Mises norm is chosen so that only the deviatoric part of stress intervenes. Splitting the stress tensor Σ (resp. σ) in deviatoric part dev $\Sigma = S$ (resp. s) and hydrostatic part $P =$ trace $\Sigma/3$ (resp. p)

$$\Sigma_{ij} = S_{ij} + P\,\delta_{ij} \tag{9}$$

Equation 8 is rewritten (A is supposed equal to identity)

$$\forall\ t > t_1,\ J_2[S(t) - z] < k^2 \text{ with } z = -\operatorname{dev}\rho + c\epsilon^p \tag{10}$$

z *is thus the center and* k *the radius of an hypersphere which sould contain all the loading path* L(t) *for any time* $t > t_1$. However, this condition is not enough to determine z, so that another hypothesis is needed. We make the assumption that *the* z *solution corresponds to the smallest hypersphere that contains all the loading path* L(t). Then for a given stress cycle $L(t)$ corresponds to a given z. This point is illustrated in Fig. 4; H_1 corresponds to a possible hypersphere and H_2 is the smallest one. Dev(ρ^*) can be taken approximately equal to z.

It is important to notice that the precise knowledge of the local elastoplastic constitutive equations, which are impossible to obtain, is not necessary. The proposed method gives an approximate way to characterize the local stress tensor in the pseudo-stabilized state.

The case of an inclusion embedded in an elastic matrix is important for a better understanding of the method because it is based on the following image: crack initiation near the fatigue limit happens in some critically oriented grains which have undergone plastic deformation. In that case, $z = -(2\mu + c)\epsilon^p \simeq -2\mu\epsilon^p$; shakedown hypothesis means that ϵ^p becomes independent of the time, t. In this example, the local residual stress is directly related to the local plastic strain ϵ^p, so that trace (ρ^*) = 0. Thus the macroscopic and the microscopic hydrostatic tension are equal ($P = p$). If the inclusion can be considered as spherical or ellipsoidal, it can be proved by Eshelby's method that the plastic strain is uniform in the inclusion. The local residual stress is then also uniform. Outside the inclusion, the stress pattern is more complex. As fatigue

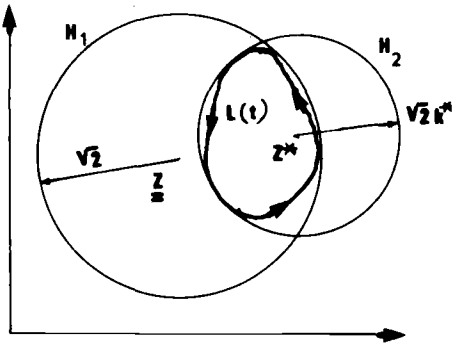

FIG. 4—*Evolution of the local residual stress: construction of the smallest hypersphere* H_2 *containing the loading path* L(*t*).

cracks appear very often at the surface, it is also interesting to examine surface inclusions. In this case, the residual stress inside an hemispherical inclusion is in general no more uniform even if plastic strain is supposed uniform [*3*]. However, this variation is not very important and one can neglect it at first approximation. In Fig. 5, the σ_{xx} stress pattern is represented in the case of an inclusion embedded in an infinite media (because of symmetry only half the figure is represented) and in the case of a hemispheric surface inclusion. The uniform plastic strain tensor of the inclusion corresponds to Type B after the terminology of M. Brown and K. Miller [*4*].

Let us return to the general problem of determination of local residual stress in the pseudo-stabilized state. Knowing the stress cycle $S_{hk}(t)$, $t \in [t,t + T]$, [(h,k) must be relative to the fixed axis relative to the material], one discretizes in N tensors S_i associated with N different times, t_i. Variations $(S_{i+1} - S_i)$ are considered as infinitesimally small. Then there are two ways to find ρ^*.

The first way is to use a mathematical method based on the theorem of Karatheodory as suggested by Papadopoulos [*5*]. The second way is based on the following "physical" algorithm [*1*] represented in Fig. 6. The initial elastic domain C_0 is featured by the circle of radius R_0 (R_0 corresponds to the initial value of k from Eq 6), the center of which coincides with M. The stress state can be represented by **MS**. As **MS** follows the loading path represented by Γ, let S_j be the first point outside C_0; plastic strain has to occur. As a result, the elastic domain is now C_j. The translation from O to O_j corresponds to kinematic hardening. The growth of the radius from R_0 to R_j is for isotropic hardening. As the load keeps varying, active parts of the loading path will keep the elastic domain changing in the way described above. Numerical simulations on examples show that after some cycles, a limit convex C_l with center O_l, radius R_l which encloses the whole curve Γ is found. $O_l M$ corresponds to the stabilized z, which corresponds approximately to the local residual stress tensor. Details of the algorithm to define the state $(i + 1)$ characterized by S_{i+1} and R_{i+1} from i characterized by S_i and R_i is given in Ref *1*. The precision of the method is improved as the radius R grows slower (weak isotropic hardening). Thus the isotropic hardening coefficient χ defined by

$$R_{i+1} = R_i + \chi \epsilon^p_{eq} \tag{11}$$

should be small. On the other hand, speed of convergence varies in the same way as χ. Therefore, a compromise between precision and duration of the calculation has to be found.

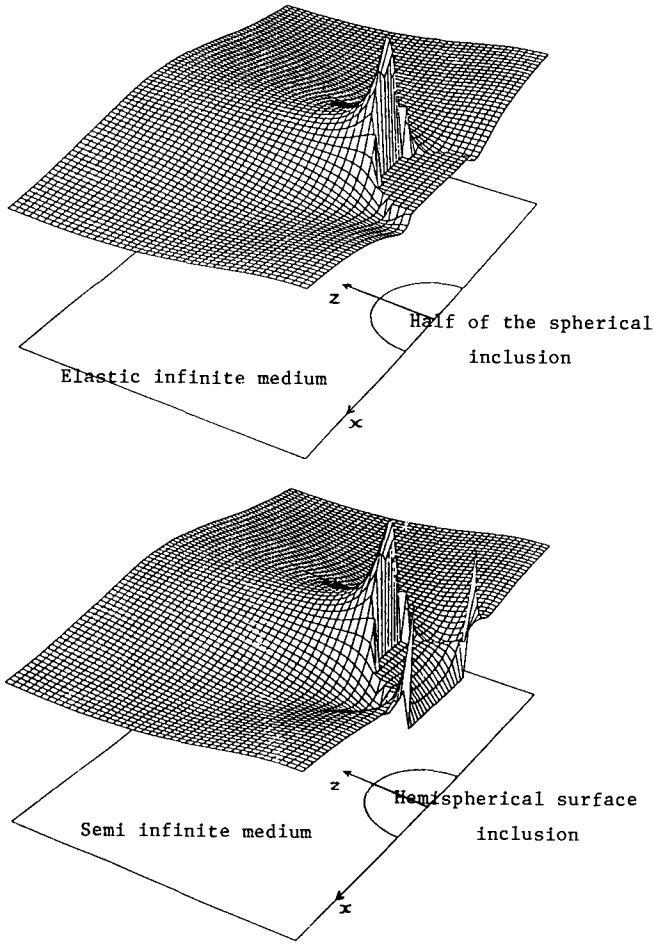

FIG. 5—*Qualitative stress pattern σ_{xx} in the neighborhood of a spherical inclusion in an infinite medium and of a hemispherical surface inclusion in a semi-infinite medium and submitted to uniform plastic of Type B.*

Fatigue Limit Criteria

As σ_{ij} is approximatively known at any time, t, it is natural to try (as in plasticity) to take the loading path into account. Thus a reasonable fatigue criterion could be stated as follows: crack initiation will occur in a critically oriented grain of volume $V(M)$ which has undergone plastic strains, if, for at least one time, t, of the stabilized cycle, one has

$$f[\sigma(m,t)] > O \text{ for } m \in V(M) \tag{12}$$

In such a criterion the current stress state is considered and damage happens at a precise instant of the loading path. As cracks usually occur in transgranular slip bands, the local shear acting on these planes is an important parameter. In the same way the hydrostatic tension accelerates damage formation (this parameter is preferred to normal stress because it is easier to use, being an invariant; furthermore, it can be interpreted as the mean value of normal

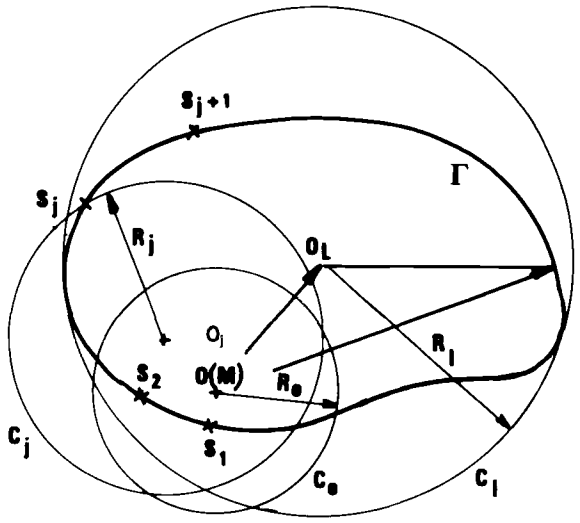

FIG. 6—*Illustration of the scheme to compute the stabilized residual stress and the local shear stress.*

stress). Taking these remarks into account, one can choose for $f(\sigma)$ a relation between the local shear stress τ and the local hydrostatic tension p. The simplest criterion is a linear relationship between these parameters

$$f(\sigma) = \tau + ap - b \tag{13}$$

The safety domain is delimited by straight lines. This domain can be determined by uniaxial experiments of tension and torsion on classical fatigue machines. For example, the endurance domain and two typical loading paths are represented in Fig. 7. In this figure, τ is the algebric shear acting on an oriented direction.

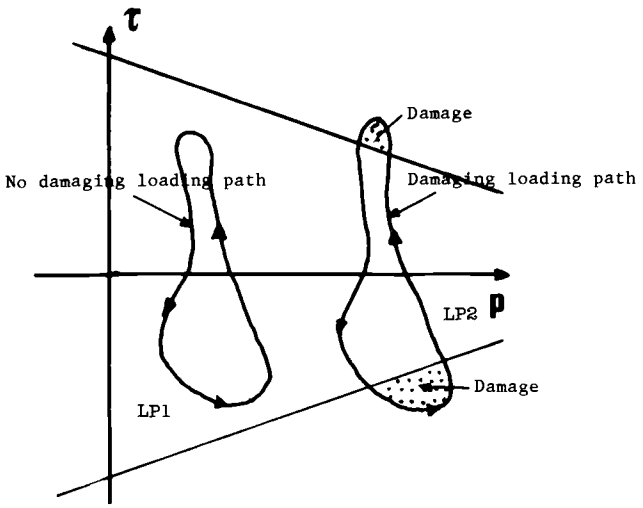

FIG. 7—*Endurance domain of two typical loading paths: LP1 = no damage; LP2 = damage.*

To check automatically the fatigue resistance of a structure can be rather difficult because at each point one has to consider the plan on which the loading path $(\tau, p)(t)$ is "maximum" relative to the criterion. From Ref *1*, this computation can be simplified as follows: $\tau(t)$ = Tresca $[\sigma(t)]$ is calculated over the cycle period. For this, it is important to note that

$$\text{Tresca } [\sigma(t)] = \text{Tresca } [s(t)] = \text{Max}_{IJ} \mid \sigma_I(t) - \sigma_J(t) \mid \tag{14}$$

where σ_I, σ_J are principal microscopic stresses.

Evaluate the quantity d, defined by

$$d = \max \left[\frac{\tau(t)}{b - ap(t)} \right] \tag{15}$$

The maximum is to be taken over the cycle $(0 < t < T)$. If $d > 1$, fatigue failure will occur. Working this way, all couples (τ, p) are situated in the positive part of τ (Fig. 8). All facets which could be involved by the crack initiation are automatically reviewed. Couples (τ, p) verifying

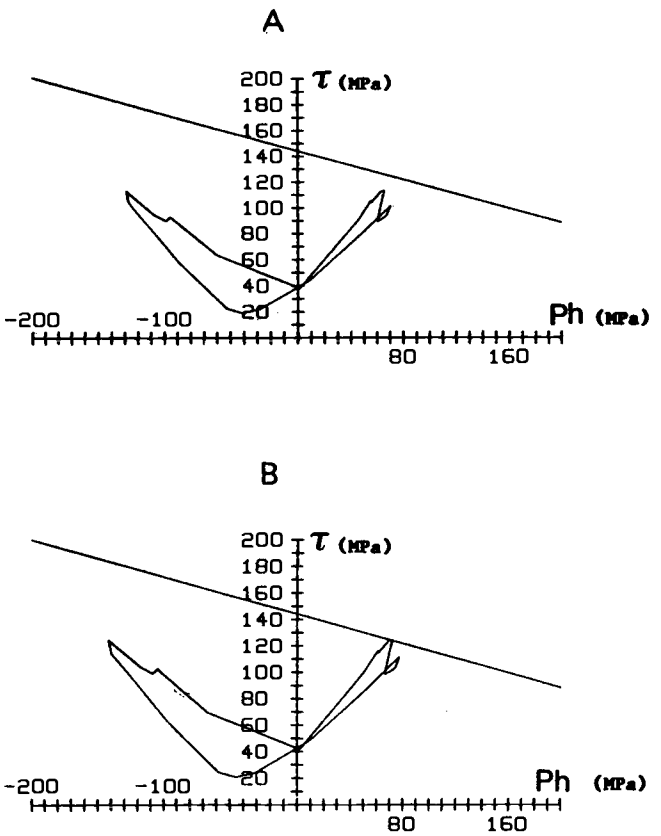

FIG. 8—*Application of the proposed method to predict the fatigue resistance of the ball bearing in Fig. 2:* (A) *no crack initiation predicted and found;* (B) *crack initiation observed.*

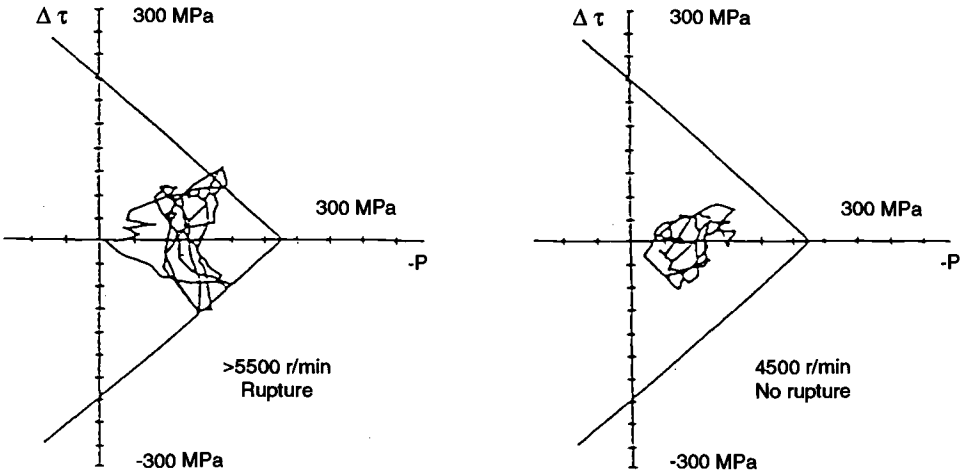

FIG. 9—*Prediction of fatigue behavior of a crankshaft.*

condition $d > 1$ are associated with defined facets and so the criterion also gives the direction of the crack initiation.

This method of fatigue computation is widely used in France to predict the fatigue behavior of mechanical structures. For instance, prediction on an integrated ball bearing is recalled in Fig. 8. Prediction on fatigue behavior of a crankshaft by a similar procedure is represented in Fig. 9.

Another alternative is to use the octahedral shear $J_2(\sigma(t))$ instead of $\tau(t)$. This method, however, does not give the critical facets.

Alternatively Papadopoulos recently proposed another method based on the macro-micro approach and an original interpretation of fatigue limit [*5*].

Following Papadopoulos, the fatigue resistance corresponds to stabilization of microscopic strain, i.e.:

1. Elastic shakedown of grains corresponds to endurance.
2. Plastic shakedown will induce damage and fracture because of subsequent cyclic softening.
3. The shakedown analysis as presented (in particular in Eq 10) is used to derive z^* and k^*.

Then Papadopoulos assumes that the grains will shakedown elastically if k^* is less than some limit value K^{lim}, which depends of the local hydrostatic tension. For instance

$$k^{\text{lim}} = \beta - \alpha \cdot p \tag{16}$$

The fatigue criterion will be

$$k^* + \alpha \cdot p < \beta \tag{17}$$

α and β are two constants which can be identified by two different tests.

By this method, it is not necessary to again describe the whole local loading path once k^* is determined. In many cases, the obtained predictions are very similar to the first methods.

Final Remarks

From a metallurgical point of view, cracks initiations have in general many possible origins depending on the nature of the material. For instance, in an homogeneous metal free of residual stresses, cracks initiation in many experiments is observed to occur in persistent slip bands near surface grains. In many other cases they occur near metallurgical singularities like hard inclusions. So it seems difficult to give simple fatigue criteria based on "plastic" analysis. However, in all cases, local plastic deformations are observed, so that the associated microscopic residual stress can modify in an important way the stress pattern in the critical representative volume V (see, for instance, Fig. 5). The proposed methods correspond to attempts to take into account a mean value of the microscopic residual stresses to gain a better description of the local stress state. Thus volume V corresponds more to a "mean" grain than to a precise misoriented grain.

As crystal plasticity is considered, the yield function should be based on resolved shear stress rather than on the von Mises function. However, in relation to the "mean" grain, it is natural to use a mean resolved shear stress, which is known to be equal to J_2.

References

[1] Dang-Van, K., Griveau, B., and Message, O., "On a New Multiaxial Fatigue Limit Criterion: Theory and Application," *Biaxial and Multiaxial Fatigue,* EGF Publication 3, M. W. Brown and K. Miller, Eds., pp. 479–496.

[2] Mandel, J., Zarka, J., and Halphen, B., "Adaptation d'une structure à écrouissage cinématique," *Mech. Res. Comm.,* Vol. 4, 1977, pp. 309–314.

[3] Deperrois, A. and Dang-Van, K., "Inclusions de Surface et Singularité Epine," *Comptes Rendus Academie des Sciences; Paris;* tome 311, Série II, 1990, pp. 1285–1290.

[4] Brown, M. W. and Miller, K. J., "A Theory for Fatigue Failure under Multiaxial Stress-Strain Conditions," *Proceedings of the Institution of Mechanical Engineers,* Vol. 187, 1973, pp. 65–73.

[5] Papadopoulos, Y., "Fatigue Polycyclique des Métaux, une Nouvelle Approche," Ph.D. thesis, Ecole Nationale des Ponts et Chaussèes, Paris, 1987.

Experimental Multiaxial Fatigue Studies

Sreeramesh Kalluri[1] *and Peter J. Bonacuse*[2]

In-Phase and Out-of-Phase Axial-Torsional Fatigue Behavior of Haynes 188 Superalloy at 760°C

REFERENCE: Kalluri, S. and Bonacuse, P. J., **"In-Phase and Out-of-Phase Axial-Torsional Fatigue Behavior of Haynes 188 Superalloy at 760°C,"** *Advances in Multiaxial Fatigue, ASTM STP 1191*, D. L. McDowell and R. Ellis, Eds., American Society for Testing and Materials, Philadelphia, 1993, pp. 133–150.

ABSTRACT: Isothermal, in-phase and out-of-phase axial-torsional fatigue experiments have been conducted at 760°C on uniform gage section, thin-walled tubular specimens of a wrought cobalt-base superalloy, Haynes 188. Test control and data acquisition were accomplished with a minicomputer. Fatigue lives of the in- and out-of-phase axial-torsional fatigue tests have been estimated with four different multiaxial fatigue life prediction models, a majority of which were developed primarily for predicting axial-torsional fatigue lives at room temperature. The models investigated were: (1) the von Mises equivalent strain range, (2) the modified multiaxiality factor approach, (3) the modified Smith-Watson-Topper parameter, and (4) the critical shear plane method of Fatemi, Socie, and Kurath. In general, life predictions by the von Mises equivalent strain range model were within a factor of 2 for a majority of the tests, and the predictions by the modified multiaxiality factor approach were within a factor of 2, while predictions of the modified Smith-Watson-Topper parameter and of the critical shear plane method of Fatemi, Socie, and Kurath were unconservative and conservative, respectively, by up to factors of 4. In some of the specimens tested under combined axial-torsional loading conditions, fatigue cracks initiated near extensometer indentations. Two design modifications have been proposed to the thin-walled tubular specimen to overcome this problem.

KEY WORDS: axial-torsional fatigue, elevated temperature, life prediction, multiaxiality, in-phase loading, out-of-phase loading, cobalt-base superalloy

Nomenclature

b, c	Exponents of axial elastic and plastic strain range-life relations
b_t, c_t	Exponents of torsional elastic and plastic strain range-life relations
k	Constant in Fatemi-Socie-Kurath parameter
n, n'	Monotonic and cyclic axial strain-hardening exponents
n_t, n_t'	Monotonic and cyclic torsional strain-hardening exponents
B, C	Coefficients of axial elastic and plastic strain range-life relations
B_t, C_t	Coefficients of torsional elastic and plastic strain range-life relations
E, G	Young's and shear moduli
K, K'	Monotonic and cyclic axial strength coefficients
K_t, K_t'	Monotonic and cyclic torsional strength coefficients

[1] Senior research engineer, Sverdrup Technology, Inc., NASA Lewis Research Center Group, 21000 Brookpark Rd., MS 49-7, Cleveland, OH 44135.

[2] Research engineer, U.S. Army Research Laboratory, Vehicle Propulsion Directorate, NASA Lewis Research Center, 21000 Brookpark Rd., MS 49-7, Cleveland, OH 44135.

MF, TF Multiaxiality and triaxiality factors
N_f Cycles to failure
$\%RA$ Percent reduction in area
Δ Denotes range of the variable
γ, ϵ Engineering shear and axial strain amplitudes
γ'_f, ϵ'_f Torsional and axial fatigue ductility coefficients, $C_t/2^{(1+c_t)}$ and $C/2^{(1+c)}$
γ_{max} Maximum engineering shear strain amplitude
γ_{xy}, γ_{yz}, γ_{zx} Orthogonal engineering shear strains
ϵ_1 First principal strain amplitude
ϵ_e, ϵ_p Axial elastic and plastic strain amplitudes
ϵ_{eq} von Mises equivalent strain amplitude
ϵ_{xx}, ϵ_{yy}, ϵ_{zz} Orthogonal normal strains
λ Proportionality constant, γ/ϵ
ν_e, ν_p Elastic and plastic Poisson's ratios
ν_{eff} Effective Poisson's ratio
σ, τ Axial and shear stress amplitudes
σ_0, τ_0 Mean axial and shear stresses
σ_1, σ_2, σ_3 Principal stresses
σ_1^{max} Maximum stress on the maximum principal strain plane
σ'_f, τ'_f Axial and torsional fatigue strength coefficients, $BE/2^{(1+b)}$ and $B_tG/2^{(1+b_t)}$
σ_n^{max} Maximum normal stress on the maximum shear strain plane
σ_y, τ_y Axial and shear yield strengths
σ_u Ultimate tensile strength
ϕ Phase angle between axial and engineering shear strain waveforms

Introduction

Fatigue lives under cyclic multiaxial loading conditions can differ significantly from those observed under "equivalent" cyclic uniaxial loading conditions. This can be attributed to the additional damage and deformation mechanisms that are activated under multiaxial loading conditions [*1–4*]. In order to develop and verify multiaxial fatigue life prediction models, it is imperative that fatigue tests be conducted under multiaxial loading conditions. Thin-walled tubular specimens are used to investigate the fatigue behavior of engineering alloys under combinations of: (1) axial and torsional; (2) axial and internal/external pressure; and (3) axial, torsional, and internal/external pressure loading conditions.

Numerous investigations have been conducted over the last two decades on thin-walled tubular specimens to characterize the fatigue behavior of several engineering alloys under combined axial and torsional loading conditions [*5–19*]. These investigations involved both in-phase, $\phi = 0°$ [*5–19*], and out-of-phase, $\phi \neq 0°$ [*5,7,8,11–17,19*], strain-controlled, axial-torsional fatigue tests and were performed with various values of λ [*5–7,10,13–17*]. The types of engineering alloys studied included an aluminum alloy [*5*], low alloy steels [*7,11,13–15*], stainless steels [*6,10–12,16,18,19*], and nickel-base superalloys [*8,9,11,13,14,17*]. A great many of these investigations were conducted at room temperature [*5–15,17–19*] with only a few studies conducted at elevated temperatures [*6,16*]. This can be primarily attributed to the added complexity of performing axial-torsional fatigue tests at elevated temperatures. However, the development of minicomputers during the last decade and the subsequent application of these minicomputers to fatigue test control and data acquisition have reduced the difficulties in conducting elevated temperature axial-torsional fatigue tests.

In this study, fatigue behavior of a wrought cobalt-base superalloy, Haynes 188, has been investigated at 760°C by subjecting thin-walled tubular specimens to combined cyclic axial

and torsional loads. Strain-controlled, in-phase as well as out-of-phase axial-torsional fatigue tests have been conducted, in air, with different proportionality constants. Fatigue lives of the elevated temperature in- and out-of-phase axial-torsional tests have been estimated with four different multiaxial fatigue life prediction models. A majority of these models were originally developed for room temperature applications. Constants for the multiaxial fatigue life prediction models were obtained from previously generated axial and torsional fatigue data of Haynes 188 [*20*]. Fatigue crack initiation occurred near the extensometer indentations in some of the specimens tested under combined axial and torsional loads. To alleviate this problem, it is proposed that either an hourglass or a straight section detail be machined within the uniform gage section of the thin-walled tubular specimen.

Material Description

The wrought cobalt-base superalloy, Haynes 188, was supplied by a commercial vendor in the form of hot-rolled, solution-annealed, round bars with a nominal diameter of 50.8 mm. The chemical composition of the superalloy in weight percent is as follows: <0.002 S; 0.002 B; 0.012 P; 0.1 C; 0.4 Si; 0.034 La; 0.75 Mn; 1.24 Fe; 13.95 W; 21.84 Cr; 22.43 Ni; and the balance is cobalt. The grain size of the supplied material ranges from 45 to 65 μm.

Experimental Details

Specimen

All the fatigue data and properties presented in this paper have been generated by using uniform gage section, thin-walled tubular specimens (Fig. 1) that were fabricated from a single heat of Haynes 188. The outer surface of each tubular specimen was polished such that the final polishing marks were parallel to the longitudinal axis of the specimen. The cylindrical bore of each specimen was finished with a honing operation to inhibit fatigue crack initiation from the inner surface. The prescribed surface roughness average values for the inner and outer surfaces of the tubular specimen were 0.2 and 0.4 μm, respectively.

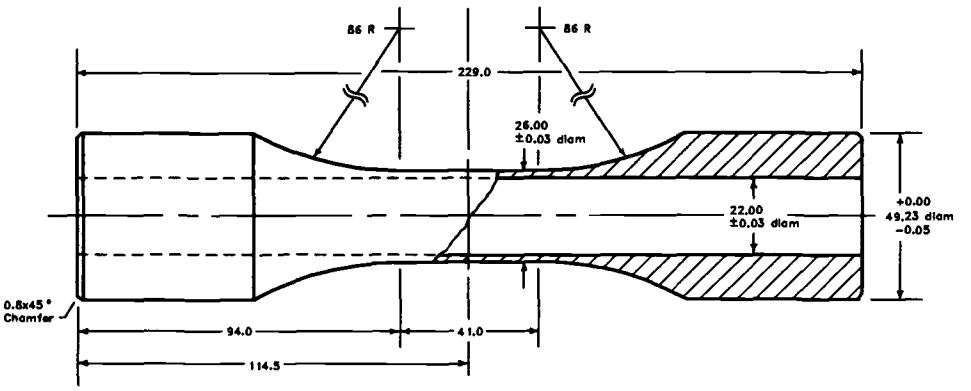

All dimensions are in millimeters.

FIG. 1—*Geometry of the thin-walled tubular fatigue specimen.*

Test System and Extensometer

All the fatigue tests were conducted on a servohydraulic axial-torsional test system. A commercial high-temperature extensometer was used to measure and control axial and engineering shear strains. Two indentations were pressed into the outer surface (within the uniform section) of the thin-walled tubular specimen with a fixture that allowed the indentation force to be precisely controlled. These indentations were 80 μm deep and 25 mm apart and were used to mount the quartz probes of the extensometer on the specimen. The indentations prevented slippage of the extensometer during a fatigue test. Additional details on the test system and extensometer are available in Refs *18* and *21*. The tubular specimens were inductively heated to the required test temperature. Chromel-alumel thermocouples, spot-welded just outside the gage section, were used to monitor and control the specimen temperature. Variation of temperature along the uniform section of the specimen was within 1% of the nominal test temperature. Additional details on the heating system and on the temperature profile determination are provided in Ref *20*.

Test Control and Data Acquisition

All in- and out-of-phase axial-torsional fatigue tests have been conducted at 760°C in air, under strain control, and at a frequency of 0.1 Hz. Fully reversed triangular waveforms with the required values of λ and ϕ were generated to control axial and engineering shear strains. Computer software developed specifically for axial-torsional fatigue testing and a 16-bit minicomputer were used for dual waveform generation and data acquisition [*21*]. Engineering shear strain was controlled at the mean radius of the thin-walled tubular specimen in all the fatigue tests. Because the outer diameter-to-thickness ratio for the tubular specimen is 13 (Fig. 1), uniform distribution of shear stress through the thickness of the tubular specimen has been assumed. In each fatigue test, cyclic stress-strain data were acquired at logarithmic intervals until failure of the specimen. Failure was defined as a 10% reduction in either the axial or the torsional peak load from the last recorded cycle.

Fatigue Database

Baseline Axial and Torsional Properties

Monotonic axial and torsional, axial fatigue ($\lambda = 0$), and torsional fatigue ($\lambda = \infty$) tests were conducted previously [*20*] on thin-walled tubular specimens of Haynes 188 (Fig. 1) at 760°C. In Ref *20* a Ramberg-Osgood type stress-strain relation was used to describe the monotonic and cyclic stress-strain curves under axial and torsional loading conditions. The relations for the monotonic axial and engineering shear stress-strain curves are as follows

$$\epsilon = \frac{\sigma}{E} + \left[\frac{\sigma}{K}\right]^{1/n} \quad \text{for monotonic axial test} \tag{1}$$

or

$$\gamma = \frac{\tau}{G} + \left[\frac{\tau}{K_t}\right]^{1/n_t} \quad \text{for monotonic torsional test}$$

The relations for cyclic axial and engineering shear stress-strain curves can be obtained by replacing n, n_t, K, and K_t in Eq 1 by n', n_t', K', and K_t', respectively. The fatigue life relations used in Ref *20* to describe the axial and torsional fatigue data are as follows

$$\Delta\epsilon = B(N_f)^b + C(N_f)^c \tag{2}$$

$$\Delta\gamma = B_t(N_f)^{b_t} + C_t(N_f)^{c_t} \tag{3}$$

Monotonic and cyclic, axial and engineering shear stress-strain properties, and axial and torsional fatigue properties for Haynes 188 at 760°C [*20*] are listed in Table 1.

Combined Axial-Torsional Fatigue Data

In this program, in- and out-of-phase axial-torsional fatigue tests have been conducted at 760°C on thin-walled tubular specimens of Haynes 188 (Table 2). In-phase fatigue tests (ϕ = 0°) were conducted with nominal λ values of 0.86, 1.73, and 3.46. Out-of-phase tests were conducted with λ = 1.73 and ϕ = 30°, 60°, and 90°. These test conditions were selected to investigate different proportionality constants and phase angles for Haynes 188. Two out-of-phase fatigue tests (λ = 1.73 and ϕ = 90°) have also been conducted with 0.1-Hz sinusoidal waveforms for axial and engineering shear strains to study the effect of waveform on fatigue life. The axial and shear stresses and axial and engineering shear strains reported in Table 2 were obtained from near half-life hysteresis loops for all the tests. There were two specimens, one in-phase test and one out-of-phase test, that did not fail, and these tests have been classified as runouts. In all the in- and out-of-phase axial-torsional specimens that developed fatigue cracks, the fatigue crack that caused failure occurred nearly perpendicular to the maximum normal strain direction.

For similar values of controlled axial and engineering shear strain ranges, the out-of-phase tests exhibited significantly more hardening than the in-phase tests. For example, in Table 2, two specimens (HY26 and HY65) have been tested under similar axial and engineering shear strain ranges. Specimen HY65 tested under an out-of-phase loading condition (ϕ = 90°)

TABLE 1—*Mechanical properties of Haynes 188 at 760°C.*

Mechanical Property	Axial Property[a]	Shear Property[a]
Monotonic stress-strain properties:		
Elastic modulus, E, G (GPa)	170.2	64.4
Elastic Poisson's ratio, ν_e	0.321	. . .
Plastic Poisson's ratio, ν_p	0.5	. . .
Yield strength, 0.2%, σ_y, τ_y (MPa)	268	163
Strength coefficient, K, K_t (MPa)	512	264
Strain hardening exponent, n, n_t	0.093	0.083
Percent reduction in area, %RA	55.1	. . .
Ultimate tensile strength, σ_u (MPa)	490	. . .
Cyclic stress-strain properties:		
Strength coefficient, K', K'_t (MPa)	891	589
Strain hardening exponent, n', n'_t	0.113	0.142
Fatigue properties:		
Elastic exponent, b, b_t	−0.082 3	−0.100
Plastic exponent, c, c_t	−0.730	−0.715
Elastic coefficient, B, B_t	0.009 13	0.0184
Plastic coefficient, C, C_t	0.590	2.17
Strength coefficient, σ'_f, τ'_f (MPa)	823	635
Ductility coefficient, ϵ'_f, γ'_f	0.489	1.78

[a] Data from Ref *20*.

TABLE 2—*In-phase and out-of-phase axial-torsional fatigue data of Haynes 188 at 760°C.*

Specimen Number	λ	ϕ	$\Delta\epsilon$	$\Delta\gamma$	$\Delta\sigma$, MPa	σ_0, MPa	$\Delta\tau$, MPa	τ_0, MPa	N_f
HY51	0.87	0°	0.00963	0.00833	789	−4	227	−1	739
HY30	0.86	0°	0.00653	0.00563	586	−3	357	−1	12 136
HY31	1.70	0°	0.01472	0.02504	802	−1	427	1	310
HY26	1.71	0°	0.00815	0.01393	668	−2	377	0	910
HY11	1.70	0°	0.00549	0.00934	629	0	358	−1	1 906
HY10	1.69	0°	0.00408	0.00689	566	4	331	−2	6 261[a]
HY9	1.67	0°	0.00306	0.00510	510	10	304	−5	18 517[a]
HY28	1.69	0°	0.00240	0.00406	432	38	261	−8	255 536[b]
HY35	3.48	0°	0.00657	0.02285	443	−5	477	0	671
HY37	3.47	0°	0.00325	0.01128	361	−3	419	0	2 929
HY50	1.79	30°	0.00390	0.00698	586	−16	357	8	12 136[a]
HY54	1.80	60°	0.00387	0.00698	624	2	375	1	11 564[a]
HY53	1.81	60°	0.00386	0.00698	631	−4	380	1	20 693[a]
HY60	1.69	90°	0.01089	0.01844	1013	−8	611	0	393[c]
HY65	1.73	90°	0.00806	0.01393	964	−9	574	1	944
HY66	1.73	90°	0.00808	0.01397	910	−10	544	0	1 088[a]
HY61	1.71	90°	0.00549	0.00937	782	−6	453	1	2 270
HY38	1.76	90°	0.00440	0.00776	726	−15	422	4	4 624[d]
HY68	1.75	90°	0.00448	0.00782	727	−1	427	0	9 264[a]
HY56	1.77	90°	0.00394	0.00697	666	−25	392	7	10 524[a,d]
HY46	1.75	90°	0.00393	0.00689	674	8	415	3	16 003[a]
HY64	1.74	90°	0.00295	0.00514	523	−75	338	23	250 000[b]

[a] Main crack that caused specimen failure was at an extensometer indentation.
[b] Specimen did not fail. Test was a runout.
[c] Specimen buckled slightly.
[d] Test was conducted with sinusoidal waveforms.

exhibited 44% more axial and 52% more torsional hardening than specimen HY26, which was tested under an in-phase loading condition ($\phi = 0°$).

For cyclic lives less than 6000, no significant difference was observed in the fatigue lives of in- and out-of-phase axial-torsional fatigue tests with similar values of the applied axial and engineering shear strains. However, for cyclic lives greater than 6000, the out-of-phase tests exhibited cyclic lives that were greater than the corresponding in-phase fatigue lives by factors of 1.5 to 3 or more (Table 2). The fatigue lives of specimens tested with the sinusoidal waveforms were slightly lower than those tested with triangular waveforms (compare HY38 with HY68 and HY56 with HY46 in Table 2). However, these fatigue lives were within a factor of 2 and the cyclic hardening under these two types of waveforms was almost identical.

Specimen failure in both the in- and out-of-phase axial-torsional fatigue tests (with the exception of one datum) was caused by a crack at an extensometer indentation whenever N_f exceeded 6000 cycles. In one out-of-phase test, HY66 in Table 2, specimen failure due to indentation cracking was observed at $N_f = 1088$. However, this specimen actually lasted slightly longer than another specimen, HY65 in Table 2, that did not crack at an indentation under the same loading condition. Failure of specimens due to a crack at the indentation was also observed in the case of axial ($\lambda = 0$) and torsional ($\lambda = \infty$) fatigue tests [*20*]. However, the number of such specimens was relatively small (compared with the number of specimens that failed due to a crack at an indentation among the in- and out-of-phase tests) and the data corresponding to those specimens were omitted in computing the axial and torsional fatigue properties listed in Table 1.

Life Prediction

Many life prediction models have been proposed to estimate fatigue life under combined cyclic axial-torsional loading conditions [*1,2,5,6,9,11,13,14,16,20,22,23*]. Some of these models include parameters based on the von Mises equivalent strain range [*2,22*], the von Mises equivalent strain range modified with a multiaxiality factor [*20,23*], the principal strains and/or stresses [*5,11*], and on a combination of maximum shear strain and the normal stress and/or normal strain acting on the maximum shear plane [*1,6,9,11,13,14,16*]. Most of these fatigue life prediction models were verified with room temperature axial-torsional data. In this study, four models have been chosen, one from each of the above categories, to evaluate their applicability to the high temperature in- and out-of-phase axial-torsional fatigue data of Haynes 188.

The models investigated are: (1) the von Mises equivalent strain range [*22*], (2) the modified multiaxiality factor approach [*20*], (3) the modified Smith-Watson-Topper parameter [*11*], and (4) the critical shear plane method of Fatemi, Socie, and Kurath [*13,14*]. The first three models require only axial fatigue data to predict fatigue lives under combined axial-torsional loads, whereas the fourth model requires both the axial and torsional fatigue data. The predictive capabilities of the same four models were previously investigated [*20*] with the elevated temperature torsional fatigue data of Haynes 188 at 760°C. It was found in Ref *20* that for estimating the torsional fatigue ($\lambda = \infty$) lives with the axial fatigue ($\lambda = 0$) properties of Haynes 188 at 760°C, the von Mises equivalent strain range model was conservative by up to a factor of 3, predictions by the modified multiaxiality factor approach were within a factor of 2, while the modified Smith-Watson-Topper parameter was unconservative by up to a factor of 6. The critical shear plane method of Fatemi, Socie, and Kurath correlated the axial ($\lambda = 0$) and torsional ($\lambda = \infty$) fatigue data to within a factor of 2.5.

In the following sections, brief descriptions of the models and their fatigue life predictive capabilities for the in- and out-of-phase axial-torsional fatigue tests of Haynes 188 are presented.

The von Mises Equivalent Strain Range Model

This model reduces a given cycle of multiaxial strains to a uniaxial equivalent strain range as shown in Eq 4 [*2,22*].

$$\Delta\epsilon_{eq} = \frac{\left[(\Delta\epsilon_{xx} - \Delta\epsilon_{yy})^2 + (\Delta\epsilon_{yy} - \Delta\epsilon_{zz})^2 + (\Delta\epsilon_{zz} - \Delta\epsilon_{xx})^2 + \frac{3}{2}(\Delta\gamma_{xy}^2 + \Delta\gamma_{yz}^2 + \Delta\gamma_{zx}^2)\right]^{1/2}}{\sqrt{2}\,(1 + \nu_{eff})} \tag{4}$$

Implementation of this model requires knowledge of all six components of strain throughout the cycle [*22*]. For the in- and out-of-phase tests, an extreme condition in the cycle, the time at which a maximum or a minimum of a strain component occurs is selected as the reference time for all the strain components. The range for each strain component (the difference between the strains at the reference time and the current time) is then computed at each point in time for that cycle. At each point in time the equivalent strain range is computed using Eq 4. The maximum equivalent strain range computed over a cycle is then used in the axial fatigue life relation (Eq 2) for life prediction.

The von Mises equivalent strain range for the in-phase tests has been computed with the maximum axial strain as the reference because in an in-phase test the axial and engineering shear strains reach their respective maxima simultaneously. However, in an out-of-phase test the axial and engineering shear strains reach their respective maxima at separate points in a cycle. Therefore, for each out-of-phase axial-torsional fatigue test, the equivalent strain range has been computed twice: once with the maximum axial strain as the reference, and a second time with the maximum engineering shear strain as the reference. The larger of the two values was used for fatigue life prediction. For a given cycle, ν_{eff} was computed with the following equation by using the near half-life axial hysteresis loop.

$$\nu_{eff} = \left[\frac{\Delta\epsilon_e\nu_e + \Delta\epsilon_p\nu_p}{\Delta\epsilon}\right] \tag{5}$$

where $\Delta\epsilon_e = \Delta\sigma/E$, and $\Delta\epsilon_p = \Delta\epsilon - \Delta\epsilon_e$.

Another way of calculating the equivalent strain range is to compute the equivalent strain at each point in a multiaxial loading cycle and then obtain the range from the computed values. However, determination of the sign (positive or negative) for the equivalent strain at each point in a general multiaxial loading cycle is a difficult task and can be erroneous if it is not properly linked to the dominant strain component. Note that the method described for computing the von Mises equivalent strain range with Eq 4 is the preferred method because it eliminates the ambiguity involved with the sign determination for the equivalent strain. In a general multiaxial loading cycle, if it is difficult to determine the extreme conditions in a cycle, the von Mises equivalent strain range can be computed with Eq 4 by taking each point in the cycle as a reference point. The largest value of the computed equivalent strain range can then be used for life prediction. For the triangular waveform in- and out-of-phase fatigue tests on Haynes 188 at 760°C, computation of the equivalent strain range by the maximum strain point reference method and the individual point reference method yielded identical results. In the case of sinusoidal waveform out-of-phase tests, the difference between the equivalent strain ranges computed by the maximum strain point reference method and the individual point reference method was less than 0.8%. Since the difference is small and the maximum strain point reference method is simpler to implement, it was used for computing the von Mises

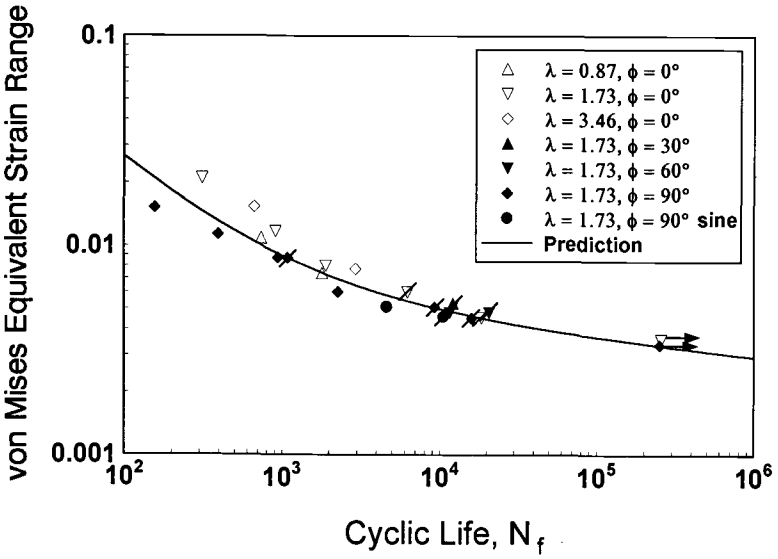

FIG. 2—*Life prediction by the von Mises equivalent strain range model.*

equivalent strain range for all the combined loading axial-torsional fatigue tests on Haynes 188.

The life prediction curve obtained by the von Mises equivalent strain range method and the in- and out-of-phase axial-torsional fatigue data are shown in Fig. 2. Data points corresponding to specimens that failed due to a crack at an extensometer indentation are marked with a slash (/). Constants for the life prediction curve were obtained from the axial fatigue properties of Haynes 188 at 760°C (Table 1). In general, fatigue lives of the in-phase tests were underpredicted and fatigue lives of the out-of-phase tests were overpredicted by this model. However, with the exception of a few data points, the predicted fatigue lives of both the in- and out-of-phase tests were within a factor of two of the observed fatigue lives (Fig. 3).

Modified Multiaxiality Factor Approach

Manson and Halford [*23*], in their discussion of the work by Blass and Zamrik [*6*], proposed a multiaxiality factor that was based on the triaxiality factor of Davis and Connelly [*24*] to account for the effect of stress state on the ductility of a material. The original proposal of Manson and Halford required that the von Mises equivalent inelastic strain range under multiaxial conditions be multiplied by the multiaxiality factor. Bonacuse and Kalluri [*20*] extended the approach to the total von Mises equivalent strain range as shown in the following equation.

$$\Delta\epsilon_{eq} = \left(\frac{B}{MF^{b/c}}\right)(N_f)^b + \left(\frac{C}{MF}\right)(N_f)^c \tag{6}$$

where

$$MF = \frac{1}{2 - TF};\ TF \leq 1$$
$$MF = TF;\ TF \geq 1 \tag{7}$$

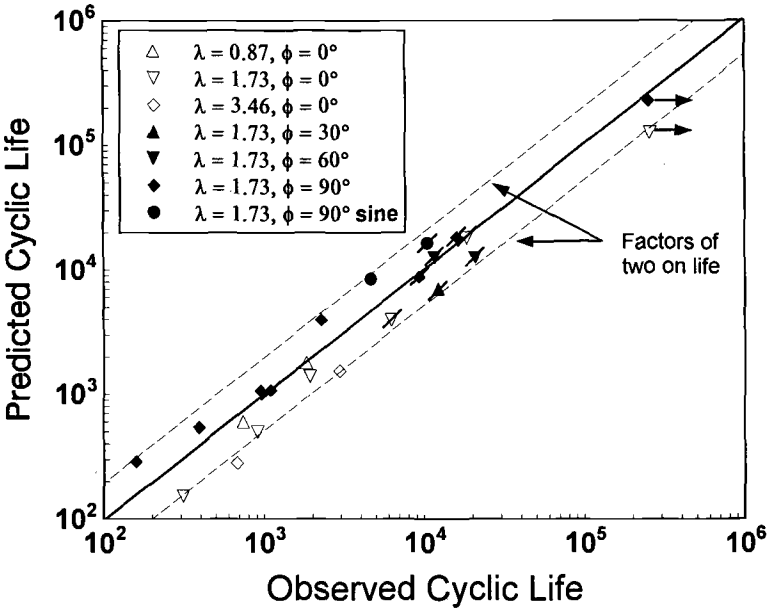

FIG. 3—*Comparison of the observed and predicted lives by the von Mises equivalent strain range model.*

and

$$TF = \frac{(\sigma_1 + \sigma_2 + \sigma_3)}{\left[\frac{\sqrt{(\sigma_1 - \sigma_2)^2 + (\sigma_2 - \sigma_3)^2 + (\sigma_3 - \sigma_1)^2}}{\sqrt{2}}\right]} \tag{7}$$

In the case of combined axial-torsional loading, MF assumes values between 0.5 (torsional loading; $TF = 0$) and 1.0 (axial loading; $TF = 1$). For the in- and out-of-phase axial-torsional fatigue tests, the total equivalent von Mises strain range has been computed as described previously, and the MF has been computed at the maximum axial strain and at the maximum engineering shear strain in the cycle. Note that for an in-phase test only one such computation is necessary. For an out-of-phase test the larger of the two computed values of the MF was used for life prediction (Eq 6). Note that each combined axial-torsional fatigue test, either in phase or out of phase, has a different value of MF (between 0.5 and 1.0) depending upon the control conditions (λ and ϕ). Thus, depending upon the value of MF, Eq 6 describes a separate life prediction curve for each combined axial-torsional fatigue test. Lower and upper bound life prediction curves for the combined axial-torsional fatigue tests were obtained with $MF = 1.0$ and $MF = 0.5$, respectively (Fig. 4). Constants for these curves were obtained from axial fatigue properties of Haynes 188 at 760°C (Table 1). Most of the in- and out-of-phase axial-torsional fatigue data were within the lower and upper bound curves predicted by this model (Fig. 4). Fatigue life predictions obtained by accounting for the MF of each combined axial-torsional fatigue test were within a factor of 2 of the observed lives (Fig. 5).

Comparison of Figs. 3 and 5 shows that life predictions by the modified multiaxiality factor approach are better than those by the von Mises equivalent strain range model for in-phase

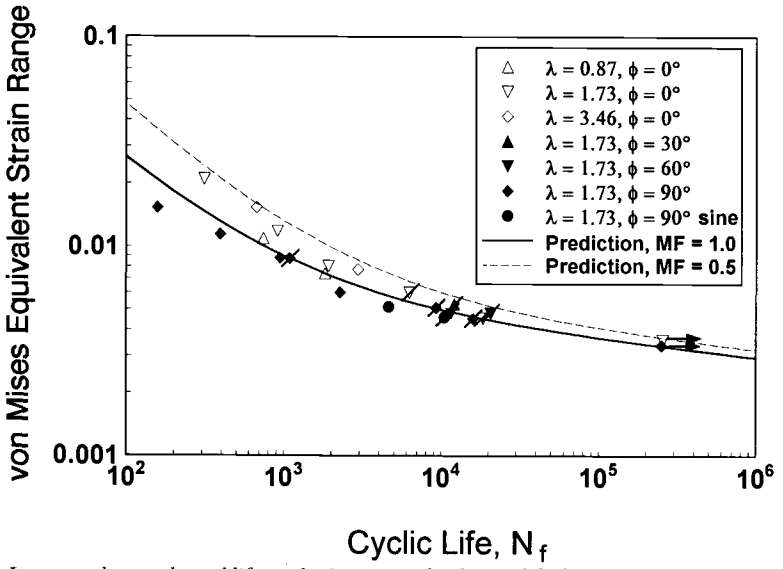

FIG. 4—*Lower and upper bound life prediction curves by the modified multiaxiality factor approach.*

tests ($\phi = 0°$) and for out-of-phase tests for which $\phi \neq 90°$. The life predictions by the modified multiaxiality factor approach do not show any improvement over the von Mises equivalent strain range model for out-of-phase tests with $\phi = 90°$ because MF is very nearly equal to one for these tests.

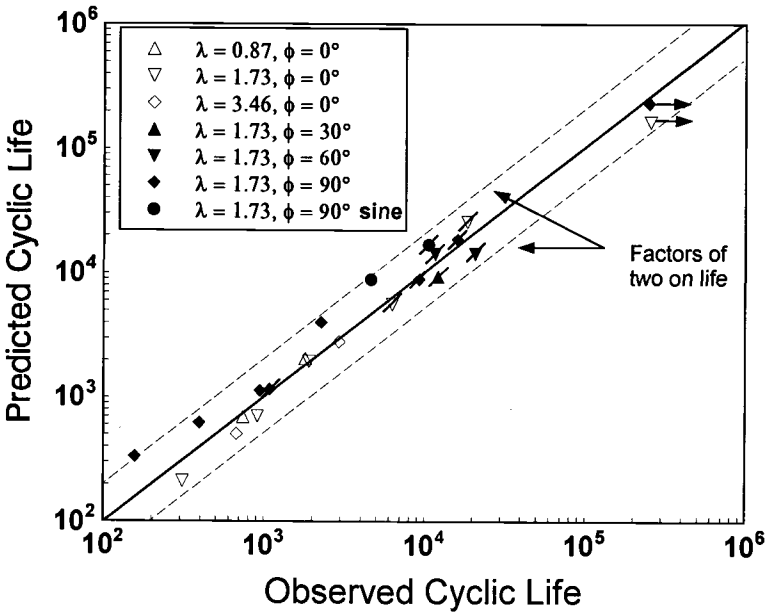

FIG. 5—*Comparison of the observed and predicted lives by the modified multiaxiality factor approach.*

Modified Smith-Watson-Topper Parameter

Smith, Watson, and Topper [*25*] proposed a stress-strain function to account for the effect of mean stress on the fatigue life of metals. Socie [*11*] argued that larger stresses (due to the extra hardening) in out-of-phase axial-torsional loading would have an effect on fatigue life that is similar to the effect of tensile mean stress on axial fatigue life and extended usage of the Smith-Watson-Topper parameter to axial-torsional fatigue life prediction.

$$\frac{\Delta\epsilon_1}{2}\,\sigma_1^{\max} = \sigma_f'\,\epsilon_f'(2N_f)^{b+c} + \frac{\sigma_f'^{\,2}}{E}(2N_f)^{2b} \tag{8}$$

The modified Smith-Watson-Topper parameter was successfully used to predict the room temperature fatigue life under in- and out-of-phase axial-torsional loading conditions for materials that crack in a tensile mode, i.e., cracks initiate and propagate perpendicular to the maximum principal strain direction [*11,12*].

In this model, the magnitude and the plane of the maximum principal strain amplitude are determined first for a given cycle of axial-torsional loading. The maximum principal strain amplitude is then multiplied by the maximum normal stress that occurs on that plane. The constants for life prediction (Eq 8) were obtained from the axial fatigue properties of Haynes 188 at 760°C (Table 1). For the in- and out-of-phase axial-torsional fatigue tests on Haynes 188, which exhibited a tensile mode of cracking, life predictions by this model were unconservative by up to a factor of four with the largest deviations occurring for the out-of-phase tests (Figs. 6 and 7). Other investigators have reported unconservative fatigue life predictions by the modified Smith-Watson-Topper parameter for materials that exhibit a shear mode of failure, i.e., initiation and propagation of cracks parallel to the maximum shear plane [*14*].

The Critical Shear Plane Method of Fatemi, Socie, and Kurath

The importance of the plane of maximum shear for crack initiation in multiaxial fatigue loading was recognized by Brown and Miller [*1*], Blass and Zamrik [*6*], and Kanazawa et al. [*7*]. Their work indicated that parameters based on the maximum shear strain and the normal strain acting on the plane of maximum shear strain should be considered for prediction of fatigue failure under multiaxial stress-strain conditions. Socie and his coworkers [*9,11*] proposed the addition of a normal stress term to the shear and normal strain terms. The critical shear plane method developed by Fatemi and Socie [*13*] and Fatemi and Kurath [*14*] considers the maximum shear strain and the normal stress on the plane of maximum shear strain:

$$\gamma_{\max}\left(1 + k\frac{\sigma_n^{\max}}{\sigma_y}\right) = (1+\nu_e)\frac{\sigma_f'}{E}(2N_f)^b + \frac{k}{2}(1+\nu_e)\frac{\sigma_f'^{\,2}}{E\sigma_y}(2N_f)^{2b} + (1+\nu_p)\epsilon_f'(2N_f)^c + \frac{k}{2}(1+\nu_p)\epsilon_f'\frac{\sigma_f'}{\sigma_y}(2N_f)^{b+c} \tag{9}$$

The Fatemi-Socie-Kurath model was successfully used to predict room temperature in- and out-of-phase axial-torsional fatigue lives for materials that exhibit a shear mode of failure [*13,14*]. Application of this model to the in- and out-of-phase, axial-torsional, Haynes 188 fatigue data has yielded very conservative life predictions (Fig. 8). The material property constant k (Eq 9) was determined in Ref *20* by using both the axial ($\lambda = 0$) and torsional ($\lambda = \infty$) fatigue data of Haynes 188 according to the procedure described by Fatemi and Kurath [*14*]. The value of k was equal to 1.0 for the fatigue life regime of interest in this study

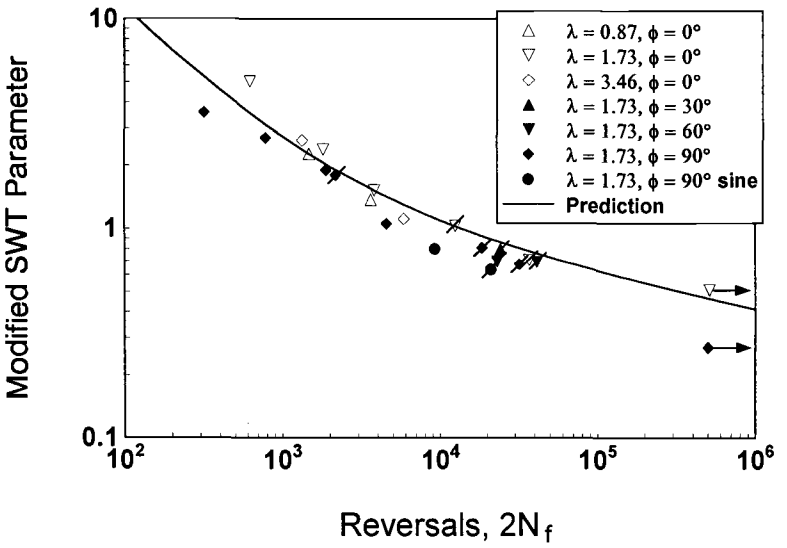

FIG. 6—*Life prediction by the modified Smith-Watson-Topper parameter.*

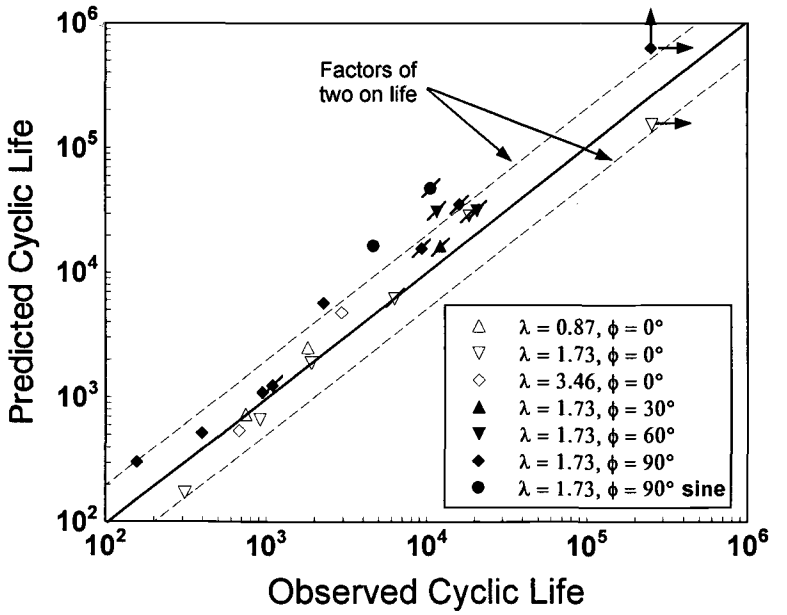

FIG. 7—*Comparison of the observed and predicted lives by the modified Smith-Watson-Topper parameter.*

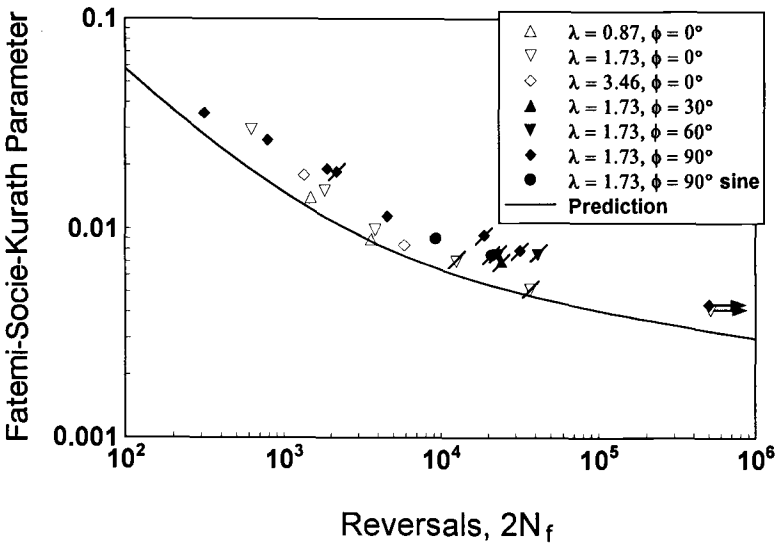

FIG. 8—*Life prediction by the Fatemi-Socie-Kurath model.*

[*20*]. Other constants for predicting the combined axial-torsional fatigue lives with Eq 9 were obtained from the axial fatigue properties of Haynes 188 at 760°C (Table 1). Life predictions by this method were conservative by up to a factor of four or more for the combined axial-torsional fatigue tests (Fig. 9).

Discussion

Cyclic Hardening

For Haynes 188 at 760°C, as mentioned earlier, the out-of-phase axial-torsional fatigue tests exhibited more cyclic axial and torsional hardening than the corresponding in-phase tests. Similar hardening behavior was observed in out-of-phase axial-torsional tests for a low alloy steel [*13*], stainless steels [*11,12,16,19*], and a nickel-base superalloy [*17*]. For Haynes 188 at 760°C, the axial stress-strain curves exhibited less hardening under in-phase loading ($\lambda = 1.73$ and $\phi = 0°$) and more hardening under out-of-phase loading ($\lambda = 1.73$ and $\phi = 90°$) compared to the cyclic stress-strain curve obtained from axial fatigue tests ($\lambda = 0$). Similar behavior was observed even for the cyclic engineering shear stress-strain curves under these combined axial-torsional loading conditions. For out-of-phase tests with $\lambda = 1.73$ and $\phi = 90°$, both the triangular and sinusoidal waveform tests exhibited similar hardening behavior which implies that the wave shape effects at the test frequency of 0.1 Hz are not very significant.

Indentation Cracking

In this study thin-walled tubular specimens that exhibited cyclic lives greater than 6000 cycles under combined axial-torsional loads typically failed due to a crack at an extensometer indentation (Table 2). No such cracking was observed in previously conducted room temperature studies on 304 and 316 stainless steels even though the cyclic lives were as high as 37 000 cycles [*18,19*]. This observation indicates that Haynes 188 at 760°C is a notch-sensitive material. Note from Table 2 that indentation cracking occurred in seven out of twelve out-of-phase

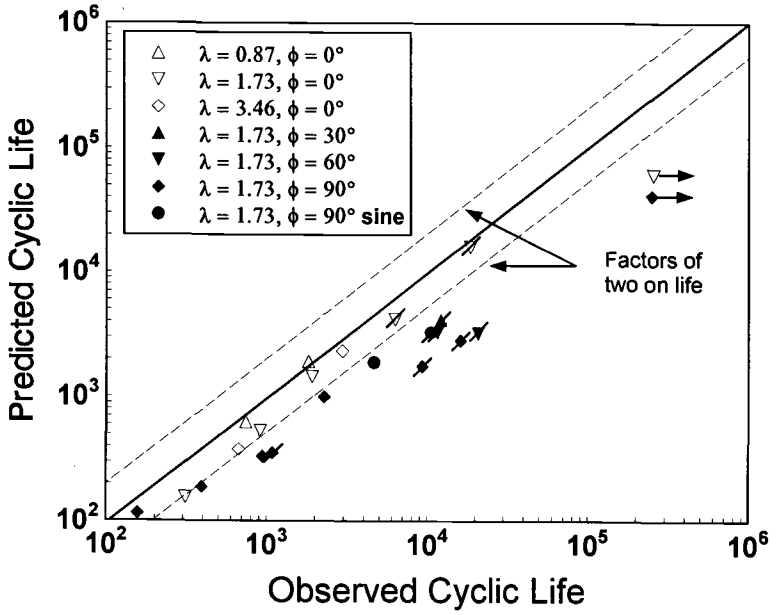

FIG. 9—*Comparison of the observed and predicted lives by the Fatemi-Socie-Kurath model.*

axial-torsional tests, whereas such a cracking occurred in only two out of the ten in-phase tests. Also, indentation cracking was noticed at a low cyclic life of 1088 in the out-of-phase tests, whereas it was not noticed in the in-phase tests until a cyclic life of 6261. The additional hardening occurring in the out-of-phase axial-torsional fatigue tests may have increased the notch sensitivity of the material, which may be the reason for the frequent and early occurrence of indentation cracking under out-of-phase loading conditions compared to the in-phase loading conditions.

As mentioned earlier, between the two out-of-phase axial-torsional tests that had similar loading conditions (HY65 and HY66 in Table 2), the specimen that exhibited cracking at the indentation (HY66 with N_f = 1088) actually lasted slightly longer than the one that did not crack at an indentation (HY65 with N_f = 944). Thus, the effect of indentation cracking on the observed fatigue lives may not be very large. In any case, the life predictions by the four models used in the study are valid because they were based on cyclic life data from those axial and torsional fatigue specimens which did not exhibit any indentation cracking [*20*]. In the absence of indentation cracking, if the fatigue lives of the specimens that exhibited indentation cracking were to increase, the life predictions by the von Mises equivalent strain range model and the modified multiaxiality factor approach would be conservative, the life predictions by the modified Smith-Watson-Topper parameter would be less unconservative, and the predictions by the Fatemi-Socie-Kurath model would be more conservative compared to the respective life predictions shown in Figs. 2 through 9 by these models.

Alternative Tubular Specimen Designs

Design of the thin-walled tubular specimen can be modified for notch-sensitive materials to prevent cracking at extensometer indentations. The modifications proposed involve machining of either a uniform cylindrical detail (Fig. 10) or an hourglass cylindrical detail (Fig. 11)

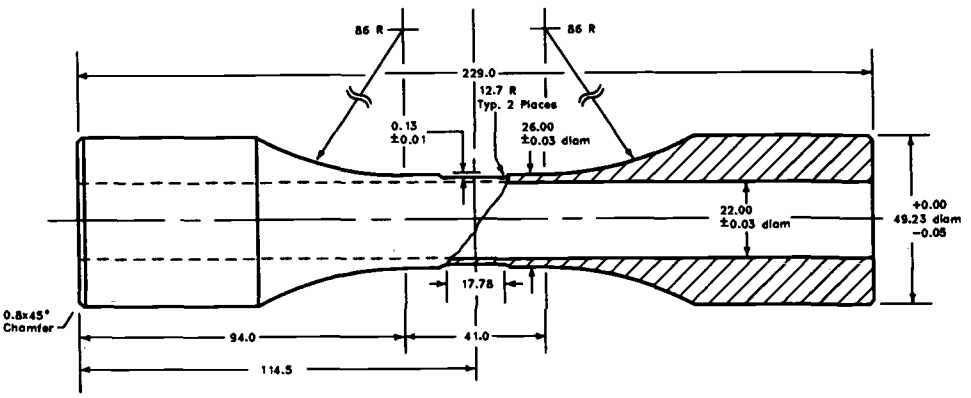

All dimensions are in millimeters.

FIG. 10—*Thin-walled tubular specimen with a uniform cylindrical detail in the gage section.*

within the gage section of the specimen. The indentations for mounting the extensometer would be pressed outside the cylindrical details in both of these designs. These designs greatly reduce the chances of cracking at the indentations because: (1) the highly stressed region is confined to the center of the tubular specimen and is removed from the indentations, and (2) the depth of indentations (80 μm) is smaller than the depth of the cylindrical details (130 $\pm$ 10 μm). However, these modified designs require additional computations, which are not required for the uniform gage section design (Fig. 1), to estimate the axial and engineering shear strains at the minimum section of the specimen. In addition to the extra machining that is required, either of the proposed cylindrical details may introduce a temperature gradient within the gage section. Specimen designs containing similar cylindrical details have been used for multiaxial fatigue testing. Some of these thin-walled tubular specimen designs were summarized by Lefebvre [*26*].

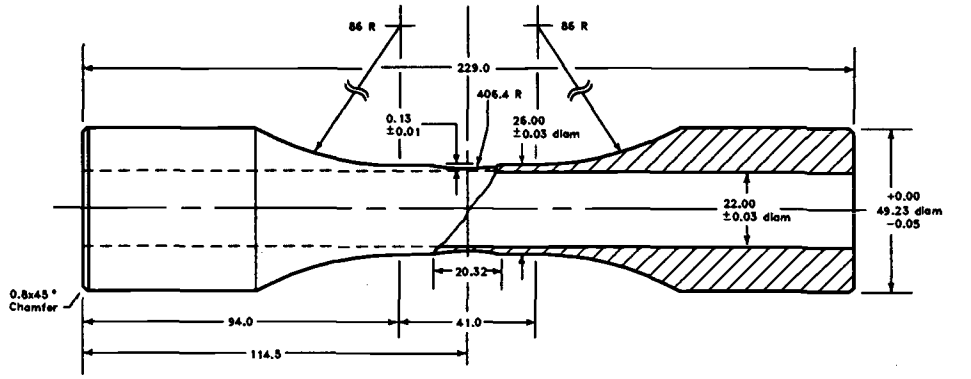

All dimensions are in millimeters.

FIG. 11—*Thin-walled tubular specimen with an hourglass cylindrical detail in the gage section.*

Conclusions

In-phase and out-of-phase axial-torsional fatigue tests have been conducted at 760°C on thin-walled tubular specimens fabricated from a wrought cobalt-base superalloy, Haynes 188. In-phase fatigue tests with nominal engineering shear to axial strain ratios of 0.87, 1.73, and 3.46 and out-of-phase fatigue tests with a nominal engineering shear to axial strain ratio of 1.73 and with phase angles of 30°, 60°, and 90° have been conducted. Fatigue lives of the elevated temperature in- and out-of-phase axial-torsional tests were estimated with four multiaxial life prediction models, and the predicted cyclic lives were compared with the observed cyclic lives. The following conclusions were drawn from this study.

1. More cyclic axial and torsional hardening occurred under out-of-phase axial-torsional loading conditions than under in-phase axial-torsional loading conditions for Haynes 188.
2. Some of the thin-walled tubular specimens of Haynes 188 tested under combined axial-torsional loads failed due to a crack at an extensometer indentation. The number of such specimens was greater in the out-of-phase tests than in the in-phase tests. This phenomenon, in general, was attributed to the notch sensitivity of Haynes 188 at 760°C. The additional hardening that occurred in the out-of-phase tests might have increased the degree of notch sensitivity of the material.
3. For cyclic lives less than 6000 (when compared on the basis of applied axial and engineering shear strain ranges), no significant difference was observed between the fatigue lives of in- and out-of-phase axial-torsional tests, while for cyclic lives greater than 6000 cycles, out-of-phase tests lasted factors of 1.5 to 3 or more longer than the in-phase tests.
4. Fatigue life predictions of the in-phase and out-of-phase axial-torsional tests were: (1) within a factor of 2 for a majority of tests for the von Mises equivalent strain range model, (2) within a factor of 2 for the modified multiaxiality factor approach, (3) unconservative by up to a factor of 4 for the modified Smith-Watson-Topper parameter, and (4) conservative by up to a factor of 4 for the Fatemi-Socie-Kurath model.
5. Two design modifications were proposed to prevent specimen failure due to a crack at an extensometer indentation. These modifications add either a uniform cylindrical detail or an hourglass cylindrical detail within the gage section of the thin-walled tubular specimen.

Acknowledgment

The diligent efforts of Chris Burke in performing the high temperature axial-torsional fatigue tests are gratefully acknowledged.

References

[1] Brown, M. W. and Miller, K. J., "A Theory for Fatigue Failure under Multiaxial Stress-Strain Conditions," *Proceedings, Institution of Mechanical Engineers,* Vol. 187, No. 65/73, 1973, pp. 745–755.
[2] Krempl, E. in *The Influence of State of Stress on Low-Cycle Fatigue of Structural Materials: A Literature Survey and Interpretive Report, ASTM STP 549,* American Society for Testing and Materials, Philadelphia, 1974, pp. 1–46.
[3] Garud, Y. S., "Multiaxial Fatigue: A Survey of the State of the Art," *Journal of Testing and Evaluation,* Vol. 9, No. 3, May 1981, pp. 165–178.
[4] Miller, K. J. and Brown, M. W., "Multiaxial Fatigue: A Brief Review," *Fracture 84,* Proceedings of the Sixth International Conference on Fracture held in New Delhi, India, Pergamon Press, New York, 1984, pp. 31–56.
[5] Zamrik, S. Y., "An Investigation of Strain Cycling Behavior of 7075-T6 Aluminum Under Combined State of Strain: The Effects of Out-of-Phase, Biaxial Strain Cycling on Low Cycle Fatigue," NASA CR-72843, National Aeronautics and Space Administration, Washington, DC, January 1972, pp. 1–32.

[6] Blass, J. J. and Zamrik, S. Y., "Multiaxial Low-Cycle Fatigue of Type 304 Stainless Steel," *ASME-MPC Symposium on Creep-Fatigue Interaction, MPC-3,* R. M. Curran, Ed., The American Society of Mechanical Engineers, New York, December 1976, pp. 129–159.

[7] Kanazawa, K., Miller, K. J., and Brown, M. W., "Low-Cycle Fatigue Under Out-of-Phase Loading Conditions," *Journal of Engineering Materials and Technology,* July 1977, pp. 222–228.

[8] Socie, D. F. and Shield, T. W., "Mean Stress Effects in Biaxial Fatigue of Inconel 718," *Journal of Engineering Materials and Technology,* Vol. 106, July 1984, pp. 227–232.

[9] Socie, D. F., Waill, L. A., and Dittmer, D. F., "Biaxial Fatigue of Inconel 718 Including Mean Stress Effects," *Multiaxial Fatigue, ASTM STP 853,* K. J. Miller and M. W. Brown, Eds., American Society for Testing and Materials, Philadelphia, 1985, pp. 463–481.

[10] Wu, H. C. and Yang, C. C., "On the Influence of Strain-Path in Multiaxial Fatigue Failure," *Journal of Engineering Materials and Technology,* Vol. 109, April 1987, pp. 107–113.

[11] Socie, D. F., "Multiaxial Fatigue Damage Models," *Journal of Engineering Materials and Technology,* Vol. 109, October 1987, pp. 293–298.

[12] Jones, D. J. and Kurath, P., "Cyclic Fatigue Damage Characteristics Observed for Simple Loadings Extended to Multiaxial Life Prediction," NASA CR-182126, National Aeronautics and Space Administration, Washington, DC, June 1988, pp. 1–93.

[13] Fatemi, A. and Socie, D. F., "A Critical Plane Approach to Multiaxial Fatigue Damage Including Out-of-Phase Loading," *Fatigue and Fracture of Engineering Materials and Structures,* Vol. 11, No. 3, 1988, pp. 149–165.

[14] Fatemi, A. and Kurath, P., "Multiaxial Fatigue Life Predictions Under the Influence of Mean-Stresses," *Journal of Engineering Materials and Technology,* Vol. 110, October 1988, pp. 380–388.

[15] Fatemi, A. and Stephens, R. I., "Biaxial Fatigue of 1045 Steel Under In-Phase and 90 Deg Out-of-Phase Loading Conditions," *Multiaxial Fatigue: Analysis and Experiments, AE-14,* G. E. Leese and D. Socie, Eds., Society of Automotive Engineers, Warrendale, PA, 1989, pp. 121–138.

[16] Nitta, A., Ogata, T., and Kuwabara, K., "Fracture Mechanisms and Life Assessment Under High-Strain Biaxial Cyclic Loading of Type 304 Stainless Steel," *Fatigue and Fracture of Engineering Materials and Structures,* Vol. 12, No. 2, 1989, pp. 77–92.

[17] Jayaraman, N. and Ditmars, M. M., "Torsional and Biaxial (Tension-Torsion) Fatigue Damage Mechanisms in Waspaloy at Room Temperature," *International Journal of Fatigue,* Vol. 11, No. 5, 1989, pp. 309–318.

[18] Bonacuse, P. J. and Kalluri, S., "Results of Inphase Axial-Torsional Fatigue Experiments on 304 Stainless Steel," NASA TM-101464, National Aeronautics and Space Administration, Washington, DC, March 1989, pp. 1–19.

[19] Bonacuse, P. J. and Kalluri, S., "Axial-Torsional Fatigue: A Study of Tubular Specimen Thickness Effects," to appear in *Journal of Testing and Evaluation,* Vol. 21, No. 3, May 1993.

[20] Bonacuse, P. J. and Kalluri, S., "Elevated Temperature Axial and Torsional Fatigue Behavior of Haynes 188," NASA TM 105396, National Aeronautics and Space Administration, Washington, DC, June 1992, pp. 1–22.

[21] Kalluri, S. and Bonacuse, P. J., "A Data Acquisition and Control Program for Axial-Torsional Fatigue Testing," *Application of Automation Technology to Fatigue and Fracture Testing, ASTM STP 1092,* A. A. Braun, N. E. Ashbaugh, and F. M. Smith, Eds., American Society for Testing and Materials, Philadelphia, 1990, pp. 269–287.

[22] "Case 1592-7," *Cases of ASME Boiler and Pressure Vessel Code,* American Society of Mechanical Engineers, New York, 1975, pp. 388–389.

[23] Manson, S. S. and Halford, G. R., Discussion to the paper "Multiaxial Low Cycle Fatigue of Type 304 Stainless Steel" by J. J. Blass and S. Y. Zamrik, *Journal of Engineering Materials and Technology,* Vol. 99, No. 3, July 1977, pp. 283–285.

[24] Davis, E. A. and Connelly, F. M., "Stress Distribution and Plastic Deformation in Rotating Cylinders of Strain-Hardening Material," *Journal of Applied Mechanics,* Transactions of the American Society of Mechanical Engineers, Vol. 81, 1959, pp. 25–30.

[25] Smith, K. N., Watson, P., and Topper, T. H., "A Stress-Strain Function for the Fatigue of Metals," *Journal of Materials, JMSLA,* Vol. 5, No. 4, December 1970, pp. 767–778.

[26] Lefebvre, D. F., Ameziane-Hassani, H., and Neale, K. W., "Accuracy of Multiaxial Fatigue Testing with Thin-Walled Tubular Specimens," *Factors That Affect Precision of Mechanical Tests, ASTM STP 1025,* R. Papirno and H. C. Weiss, Eds., American Society for Testing and Materials, Philadelphia, 1989, pp. 103–114.

Hong Lin[1] *and Hamid Nayeb-Hashemi*[1]

Effects of Material Anisotropy on Cyclic Deformation and Biaxial Fatigue Behavior of Al-6061-T6

REFERENCE: Lin, H. and Nayeb-Hashemi, H., **"Effects of Material Anisotropy on Cyclic Deformation and Biaxial Fatigue Behavior of Al-6061-T6,"** *Advances in Multiaxial Fatigue, ASTM STP 1191,* D. L. McDowell and R. Ellis, Eds., American Society for Testing and Materials, Philadelphia, 1993, pp. 151–182.

ABSTRACT: Anisotropic cyclic stress-strain curves (CSSCs) and fatigue lives were obtained from fully reversed fatigue tests in strain control on two orientations of an Al-6061-T6 plate (along the rolling direction and the transverse direction). The experiments were conducted at room temperature in air under three loading conditions: tension/compression, torsion, and combined tension/torsion in-phase. Based on the CSSCs data, the anisotropic constitutive relations of the material were obtained by using Hill's anisotropic plasticity theory. Yield loci and flow behavior were determined and compared to theoretical predictions. Two anisotropic effective stress-effective strain criteria were evaluated. During the fatigue tests, fatigue cracking behavior was observed. The damage mechanism of the material was shear dominated. Four multiaxial fatigue life prediction models representing three different concepts were used to correlate the anisotropic fatigue life data of the plate under the biaxial loadings. A new shear cracking model incorporated with material anisotropy coefficients is proposed and correlated with the fatigue life data very well.

KEY WORDS: cyclic stress-strain curves, anisotropic constitutive relations, biaxial fatigue cracking behavior, biaxial fatigue life prediction models, material anisotropy effects, Al-6061-T6

Nomenclature

M_{ij}	Anisotropic coefficients in the yield function by Shih and Lee
α_i, α_j	Constants in Shih's yield function describing Bauschinger's effect
k	The parameter in Shih's yield function describing the size of the yield surface
F, G, H, L, M, N	Anisotropic coefficients in Hill's yield function
τ_{max}, γ_{max}	Maximum shear stress and maximum shear strain amplitudes
ϵ_n, σ_n	Tensile strain and stress amplitudes normal to the plane of maximum shear
σ_{n0}	The mean normal stress amplitude on the plane of maximum shear
n	The material constant in the fatigue damage model by Fatemi and Socie
σ_n^{max}	The maximum normal stress on the plane of maximum shear
σ_y	Yield stress of a material under monotonic tension
σ_1	Maximum principal stress amplitude
ϵ_1	Maximum principal strain amplitude

[1] Graduate student and professor, respectively, Mechanical Engineering Department, Northeastern University, Boston, MA 02115.

E Young's modulus of a material
σ_u Ultimate tensile strength of a material
λ Ratio of applied strains: $\lambda = \gamma/\epsilon$
ϵ, γ Applied axial and shear strains
P, T Load and torque
δ, θ Elongation and twist angle
a Radius of the specimen
$\bar{\sigma}, \bar{\epsilon}$ Effective stress and effective strain
γ_e, ϵ_e Shear and axial strains, elastic parts
γ_p, ϵ_p Shear and axial strains, plastic parts
α A material constant depending on the Poisson's ratio of the material
S_i Generalized stress deviator
$N_{1.0\ mm}$ Number of cycles to failure using the 1.0 mm crack length failure criterion
N_{final} Number of cycles to the rupture of the specimen
$N_{10\%}$ Number of cycles to failure using the 10% load or torque drop criterion
A_i, B_i The material anisotropic coefficients in the new fatigue life prediction model: $A_i(\gamma_{max} + B_i\epsilon_n)$ by Lin and Hashemi

Introduction

Fatigue life predictions represent one aspect of the durability assessments of engineering structures. Two approaches have been used in fatigue analysis: local stress-strain and fracture mechanics. In the local stress-strain approach, stresses and strains in critical locations of the structures are assumed to control the fatigue life. Cracks are assumed to initiate and propagate in the structures in the same manner as they do in the smooth laboratory specimens. A number of multiaxial fatigue life prediction models have been proposed by applying the local stress-strain approach [*1–3*]. Three general concepts have been recognized, which are effective stress/strain, plastic work, and critical plane. Although extensive research has been conducted on multiaxial fatigue, no single model can correlate the test data of a variety of materials and loading conditions. This is due to the fact that fatigue cracking behavior depends on loading conditions, material microstructure, and strain amplitude.

Most engineering materials exhibit some degree of anisotropy in their mechanical behavior. Extremely anisotropic materials like composites and single crystals are becoming more prominent nowadays. It is important to include the material anisotropy effects in multiaxial fatigue life prediction models to improve the reliability in the design as well as in the safety evaluation. However, until now, the material anisotropy effect has not been accounted for in any multiaxial fatigue life prediction models, although its importance has been noticed [*3,4*]. To investigate the effect of material anisotropy on multiaxial fatigue life prediction, both the anisotropic constitutive relations of the subject material and its fatigue cracking behavior under multiaxial loading conditions should be studied. Anisotropic constitutive relations, which include a yield function, a flow relation, and a hardening rule, are the basis to calculate the correlating parameters in multiaxial fatigue life prediction models. Moreover, for anisotropic materials, the fatigue cracking behavior may depend on its orientations and loading histories. The life prediction model should be proposed according to the actual fatigue cracking behavior. The parameters in the model must be evaluated based on the anisotropic constitutive relations of the subject material.

In the present research, strain-controlled fatigue tests are conducted on two orientations of an orthotropic Al-6061-T6 plate under three loading conditions: tension/compression, torsion, and combined tension/torsion in-phase. The anisotropic constitutive relations of the plate are obtained based on its cyclic stress-strain curves (CSSCs). Fatigue cracking behavior

is studied during the fatigue tests. A new multiaxial fatigue life prediction model incorporated with material anisotropy effects is proposed and correlated with the fatigue test data.

Background

CSSCs and Anisotropic Constitutive Relations

The cyclic stress-strain curve concept was introduced in the 1960s to characterize the cyclic behavior of a material [*5,6*]. There are three experimental methods available to measure the CSSC of a material: constant strain amplitude (CSA), multiple step test (MST), and incremental step test (IST). The detailed description and comparison of these three methods can be found in Ref *7*. CSSCs depend on the microstructures of materials. Depending on the initial state of a material, the strain hardening of the material under cyclic loading may increase (cyclic hardening), decrease (cyclic softening), or remain the same (cyclic stability). In many cases, the three phenomena may occur and the sequence may vary. The effect of the microstructure of a material on its CSSC has been reviewed [*8,9*]. Any microstructural feature that causes inhomogeneous distribution of plastic strains will result in higher strain hardening and shorter fatigue life. CSSCs also depend on the loading conditions. Usually, the CSSC of a material is obtained from the laboratory uniaxial tests on smooth specimens. However, structures are often subjected to multiaxial loading conditions, and multiaxial stress states often exist at some critical locations of the structures such as notches, geometric discontinuities, etc. Therefore, correlation between uniaxial and multiaxial CSSC test data becomes important. Two effective stress-effective strain criteria have been used to correlate multiaxial test data: the Tresca type, $\tau_{max} - \gamma_{max}$, and the von Mises type, $\bar{\sigma} - \bar{\epsilon}$ [*10–12*].

In most studies of CSSCs of materials, the subject materials were assumed to be isotropic. Anisotropic effective stress-effective strain criteria for the correlation of anisotropic multiaxial CSSCs data are rarely investigated. To obtain the anisotropic constitutive relations of an anisotropic material which are needed to obtain the anisotropic effective stress-effective strain criteria, the sources of the anisotropy have to be identified and modeled. There are at least two sources of anisotropy in metals, and they may not be completely independent of each other. One is largely due to preferred orientation of grains and nonrandom distribution of second phase particles and/or inclusions. This source is termed *material anisotropy* in this study, which gives rise to the dependence of yield strength and strain-hardening property on material orientation. Another source is related to the development of back stress or internal residual stress caused by prior plastic deformation such as the Bauschinger effect. This is termed *plastic deformation anisotropy* and is a loading history dependent phenomenon, and the anisotropy is observed upon subsequent load reversal.

Research on anisotropic constitutive relations of metals has been extensive [*12–21*]. Two different approaches, i.e. the crystallographic approach [*16,17*] and the macroscopic continuum approach [*13,15,18–21*], have been applied to model the yield behavior of anisotropic metals. In the macroscopic continuum approach, no reference is made to the orientations of individual grains. The yield surface of the polycrystal under consideration is described by an assumed analytical yield function, the parameters of which are determined experimentally. The anisotropic behavior of the polycrystal is thus accounted for only through the characteristics of the assumed yield function, not by means of the crystallographic texture of the material. In 1948, Hill proposed a generalization of the von Mises yield function for the state of anisotropy possessing three orthogonal planes of symmetry. His yield function is expressed as [*13*]:

$$2f = F(\sigma_y - \sigma_z)^2 + G(\sigma_z - \sigma_x)^2 + H(\sigma_x - \sigma_y)^2 + 2L\tau_{yz}^2 + 2M\tau_{zx}^2 + 2N\tau_{xy}^2 \qquad (1)$$

where F, G, H, L, M, N are constants depending on the yield stresses in the three principal material anisotropic directions. Hill's yield function and an associated flow rule are the most widely used formulations for the constitutive relations of anisotropic materials [*12,20,21*].

Shih and Lee [*18*] proposed another anisotropic plasticity theory which extended Hill's theory. Their yield function was expressed as:

$$3f = M_{ij}(\sigma_i - \alpha_i)(\sigma_j - \alpha_j) - k^2 = 0 \tag{2}$$

where M_{ij} describes the variation of the yield stresses with material orientations, and α_i and α_j describe the strength difference between the tensile and compressive yield stresses. The size of the yield surface is given by the parameter k.

Multiaxial Fatigue Life Prediction Models

Successful multiaxial fatigue life prediction modeling requires understanding the fatigue cracking behavior of the subject material. Extensive research on smooth specimens under uniaxial fatigue condition has shown that fatigue crack nucleation usually occurs at stress concentrations on or immediately below the specimen surface. These stress concentrations may result from surface roughness, grain boundaries, or inclusions. Besides these sources of crack nucleation, cracks can be nucleated from persistent slip bands (PSBs) formed during fatigue loading [*22,23*]. For most materials, the formation of PSBs first occurs in those grains whose slip planes are most closely aligned with the plane of maximum shear. Crack nucleation depends on the shear stress acting on the slip planes rather than the normal stress. Forsyth defined crack nucleation and early growth on shear planes as Stage I growth (Mode II) and crack propagation on the planes normal to the maximum tensile stress as Stage II growth (Mode I) [*24*]. Materials which form slip bands under uniaxial loading also produce slip bands under torsion. As early as the 1920s, Gough [*25*] reported that shafts subjected to torsional fatigue could fail in two general modes. In one mode, cracks propagated in the axial or circumferential directions of the shaft, i.e. on the maximum shear planes. In the second mode, cracks propagated along a 45° direction to the axis of the shaft, i.e. on maximum tensile planes. Since then, increasing research has been conducted on torsional fatigue, and the two general failure modes are observed repeatedly [*26–30*]. Recently, Bannantine and Socie [*31*] studied the cracking behavior of several materials under tension/torsion biaxial fatigue conditions. The fatigue cracking behavior was found to depend on loading mode, strain amplitude, and material microstructure.

A large number of multiaxial fatigue life prediction models have been proposed. Three concepts have been generally recognized: effective stress/strain, plastic work/energy, and critical plane. The effective stress/strain concept was proposed at the early stage of multiaxial fatigue research and still remains popular [*32–35*]. According to this concept, the two- or three-dimensional stress/strain state is reduced to an effective scalar parameter, usually by using either the Tresca criterion or the von Mises criterion. An effective parameter-fatigue life relationship may then be obtained similar to the S-N correlation. The plastic work/energy concept was proposed in the 1960s [*36,37*]. The hysteresis energy was used to correlate fatigue life. Recently, Garud [*38*] and Ellyin et al. [*39–41*] continued to investigate in this direction.

The critical plane concept requires that the failure plane be identified and the load spectra with respect to that plane be analyzed. In his early research on high cycle fatigue, Findley used maximum shear stress modified with the normal stress acting on the plane of maximum shear to correlate fatigue life data [*42,43*]. McDiarmid also proposed a critical plane model for high cycle multiaxial fatigue in the early 1970s [*44,45*] based on the maximum shear stress and maximum normal stress on the plane of maximum shear. In low cycle fatigue research, strain

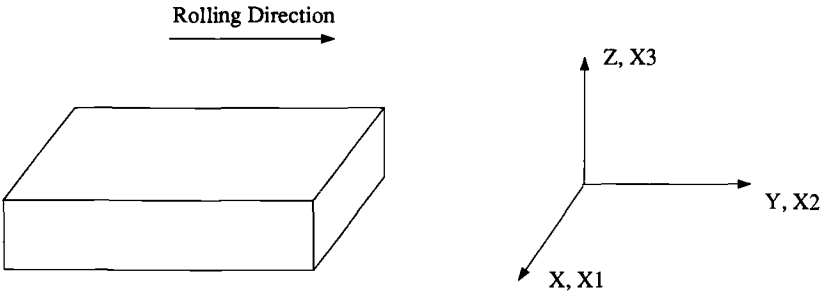

FIG. 1—*The Cartesian coordinates of the Al-6061-T6 plate, which coincide with the principal axes of the material anisotropy. X is in the TD direction, Y is in the RD direction, and Z is in the through-thickness direction.*

parameters instead of stress parameters are usually used in fatigue life prediction models. Brown and Miller proposed a general function $\Gamma(\gamma_{max}, \epsilon_n)$ for the correlation of shear damage fatigue data [*46*]. Socie et al. [*47*] proposed another shear cracking model, $\gamma_{max} + \epsilon_n + \sigma_{n0}/E$, which simplified the Γ function by Brown and Miller. In the model by Socie et al., a mean stress parameter, σ_{n0}, was introduced to account for the mean stress effect. Recently, Fatemi and Socie [*48*] proposed another shear cracking model, $\gamma_{max}(1 + n\sigma_n^{max}/\sigma_y)$, to correlate the shear cracking fatigue data for both in-phase and out-of-phase loadings. In this model, the additional hardening caused by out-of-phase loading was taken into account by σ_n^{max}. Moreover, a tensile cracking parameter, $\sigma_1\epsilon_1$,[2] was proposed by Smith et al. during uniaxial fatigue [*49*] and has been successfully used by Socie [*50*] for the correlation of multiaxial fatigue data of tensile cracking behavior.

Although a large number of multiaxial fatigue life prediction models have been proposed, all are obtained based on research treating the subject materials as isotropic. To the best of our knowledge, the effect of material anisotropy has not been accounted for in any model. The purpose of this research is to conduct biaxial fatigue tests on the orthotropic Al-6061-T6 plate and to propose a new biaxial fatigue life prediction model incorporating material anisotropy effects.

Experimental Procedure

Material

The material selected for this investigation is Al-6061-T6 plate cold rolled in one direction. The Al-6061 alloy is a lightweight, medium-strength, corrosion-resistant material for general structural usage. After the T6 temper treatment, it retains the material anisotropy, but the plastic deformation anisotropy due to prior plastic work is eliminated. The nominal chemical composition of the material is: Mg: 1.0%, Si: 0.6%, Cu: 0.25%, Cr: 0.25%, Fe: 0.7%, Mn: 0.15%, Zn: 0.25%, Ti: 0.15%, Al: balance. The nominal monotonic mechanical properties are: E = 69 000 MPa, σ_y = 276 MPa, σ_u = 310 MPa, and elongation in 50 mm = 12%. The plate has three orthogonal planes of symmetry, and the Cartesian coordinates axes are taken to coincide with the principal axes of anisotropy as shown in Fig. 1. The etched microstructure along both the rolling direction and the transverse direction of the plate is shown in Fig. 2. The material anisotropy of the plate is caused by the presence of elongated grains and the alignment of the precipitates along the rolling direction, as shown in Fig. 2.

[2] The original notation was $\sigma_1^{max}\frac{\Delta\epsilon_1}{2}$.

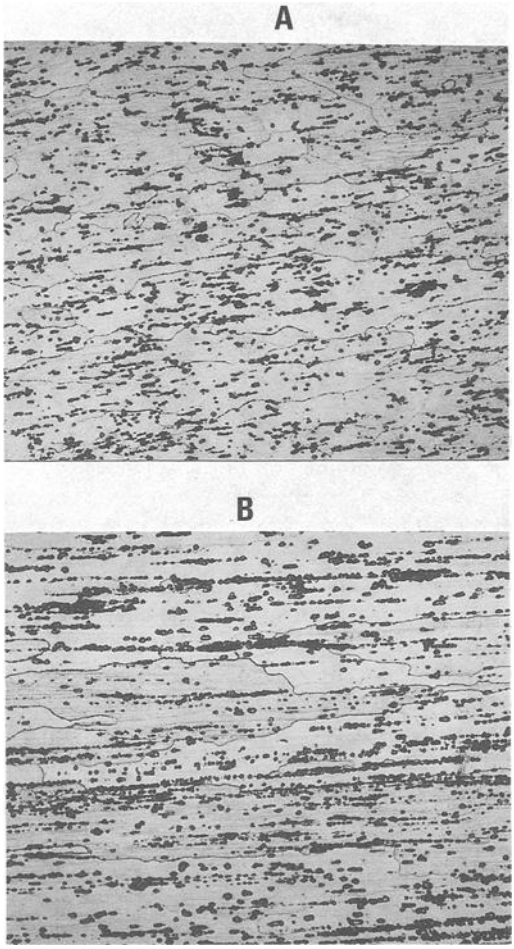

FIG. 2—*Photomicrographs showing the etched microstructure of the Al-6061-T6 plate:* (A) *in the XZ plane perpendicular to RD direction, and* (B) *in the YZ plane. The grains were elongated, and the precipitates were aligned along the RD.*

Specimen Configuration

Solid cylindrical specimens 9.5 mm in diameter were prepared from the plate along two orientations: (1) along the rolling direction (RD), and (2) along the transverse direction (TD) in the plate plane. The specimen configuration is shown in Fig. 3. The surface of the specimens was polished successively with finer grits to a mirror-like finish.

Testing System

Fully reversed fatigue tests were conducted on the two orientations of specimens in strain control at room temperature under three loading conditions: tension/compression ($\lambda = \gamma/\epsilon = 0$), torsion ($\lambda = \infty$), and combined tension/torsion in-phase ($\lambda = 0.8$, $\lambda = 2$). Tests were performed on a servo-hydraulic close-looped Instron 1322 biaxial testing system with strain

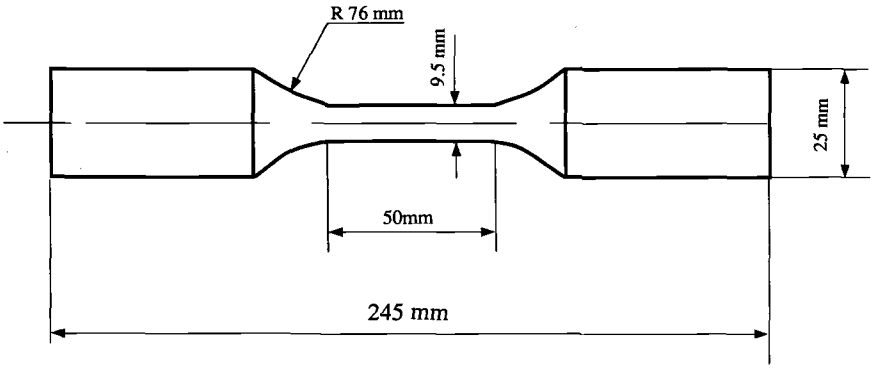

FIG. 3—*A schematic diagram of the specimen configuration.*

rates between 10^{-3} and 10^{-4} 1/s. Strains were measured by an Instron biaxial extensometer of 10 mm gage length. Load-elongation and torque-twist data were recorded by X-Y recorders.

Results

Monotonic Stress-Strain Curves

The monotonic stress-strain curves of RD and TD specimens under both tension and torsion are shown in Fig. 4, which are the averages of multiple-specimen tests. From the monotonic stress-strain curves, it is found that the material is elastically isotropic, but plastically anisotropic. The stress responses of the two orientation specimens in the plastic regime are different. The TD specimens show higher stress response than the RD specimens under monotonic tension. Under torsion, the RD specimens show higher stress response. The plastic deformation behavior of a material depends on its microstructure, which can be changed by heat treatment. For the Al-6061-T6 plate used in the present study, the grains have been elongated and the second phase particles have been aligned along the rolling direction, which causes the observed anisotropy in plastic regime.

Cyclic Stress-Strain Curves (CSSCs)

Cyclic stress-strain curves are obtained by using both CSA and MST methods. Results of the two methods are the same. Cyclic stresses on the specimen surface under proportional biaxial loading were calculated by using the following equations:

$$\tau = \frac{1}{2\pi a^3}\left(3T + \theta \left.\frac{\partial T}{\partial \theta}\right|_{\epsilon}\right) \tag{3}$$

$$\sigma = \frac{1}{2\pi a^2}\left(2P + \theta \left.\frac{\partial P}{\partial \theta}\right|_{\epsilon}\right) \tag{4}$$

These equations were derived in detail in [*51*], which was an extension of the derivation by Nadai [*52*]. All specimens showed small initial hardening at the beginning of loading. After several cycles, small softening occurred, then the hysteresis loops saturated. This cyclic behavior has been explained previously [*53*]. The initial hardening may be caused by the increase in dislocation density and their interactions. This process does not last long because of the interaction between dislocations and particles. When the interaction of dislocations and par-

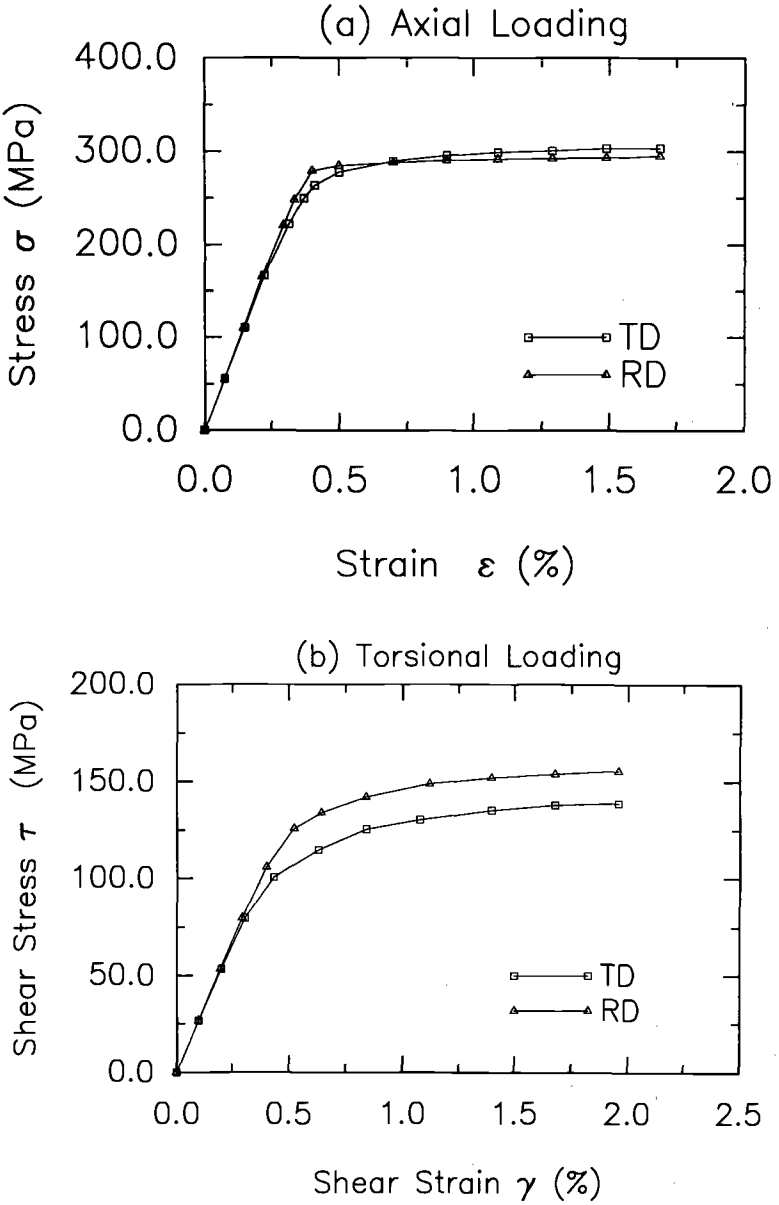

FIG. 4—*Typical monotonic stress-strain curves in the RD and TD directions showing elastic-isotropic, but plastic-anisotropic behavior:* (a) *under tensile loading, and* (b) *under torsional loading.*

ticles becomes dominant, subsequent softening begins. The anisotropic CSSCs of the two orientations of specimens are shown in Fig. 5, which is in agreement with the monotonic stress-strain responses shown in Fig. 4. Under tension/compression, TD specimens show higher cyclic stress responses; however, under torsion, RD specimens show higher cyclic stress responses.

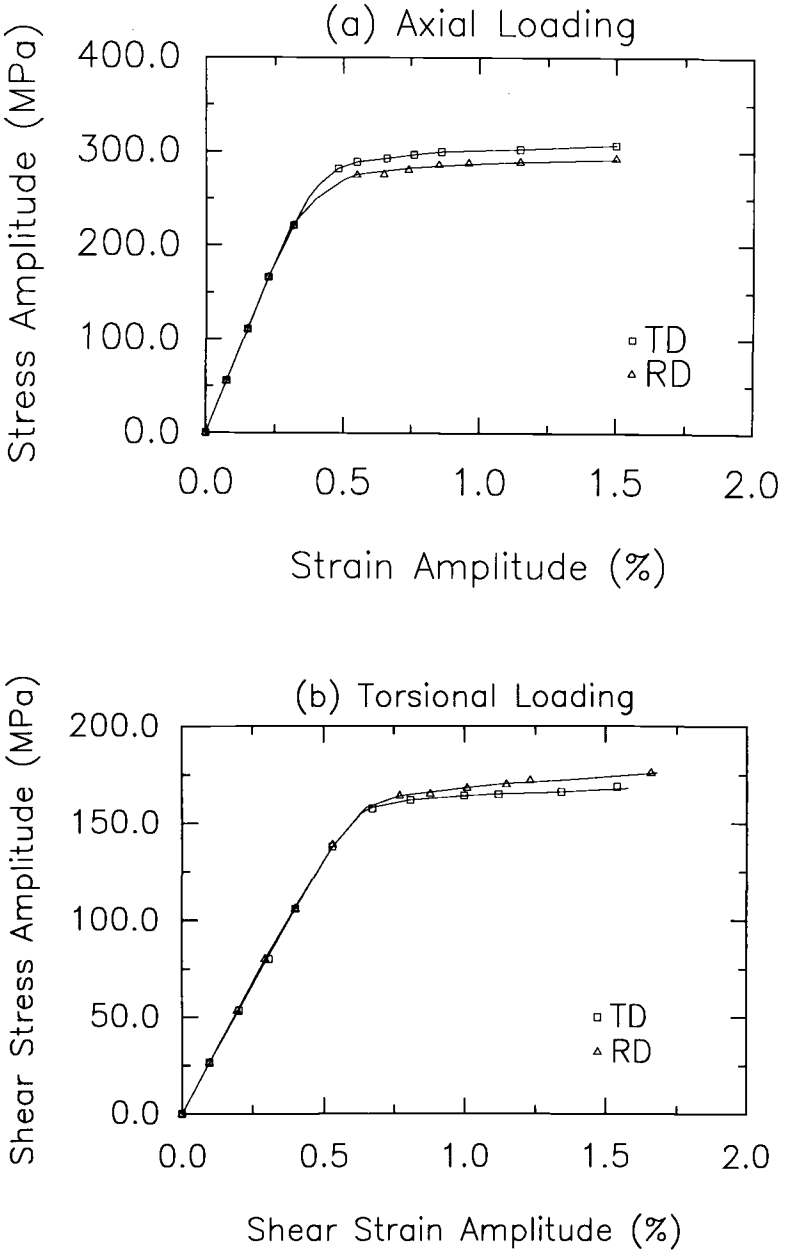

FIG. 5—*Cyclic stress-strain curves in the RD and TD directions:* (a) *under tension/compression, and* (b) *under cyclic torsion.*

Anisotropic Constitutive Relations

Shih and Lee [*18*] extended Hill's macroscopic continuum formulation of anisotropic constitutive relations of solids. Their formulation is used in this study and is expressed as:

Yield function:

$$3f = M_{ij}\sigma_i\sigma_j - k^2 = 0 \tag{5}$$

Effective stress:

$$\bar{\sigma}^2 = M_{ij}\sigma_i\sigma_j \tag{6}$$

Flow relation:

$$d\epsilon_i^p = \frac{3}{2}\frac{d\bar{\epsilon}^p}{\bar{\sigma}} S_i \tag{7}$$

Stress deviator:

$$S_i = \frac{2}{3} M_{ij}\sigma_j \tag{8}$$

The anisotropic coefficients, M_{ij}, represent the dependence of yielding stresses on the principal orthotropic directions of the material. Based on the cyclic stress-strain curves of the plate, M_{ij} was determined in detail in Ref *51*. The results are as follows:

$$M_{11} = 1, \quad M_{22} = 1.127, \quad M_{33} = 1.375$$

$$M_{12} = -0.376, \quad M_{13} = -0.624, \quad M_{23} = -0.751$$

$$M_{66} = 3.13, \quad M_{55} = 3.02, \quad k = 292 \text{ MPa}$$

compared with the isotropic case, where

$$M_{11} = M_{22} = M_{33} = 1$$

$$M_{12} = M_{13} = M_{23} = -0.5$$

$$M_{44} = M_{55} = M_{66} = 3$$

The plate does exhibit some degree of anisotropy. Yield surface depends on the definition of yielding. For small offset strain yielding definitions (50 $\mu\epsilon$), the Bauschinger effect is more prominent. In this study, a big offset strain of 0.2% is used as the definition of yielding, as we intend to model the material anisotropy rather than plastic deformation anisotropy. By using the 0.2% offset strain yield criterion, the test data show a negligible Bauschinger effect. As a result, the α_i and α_j terms in the original formulations by Shih and Lee are taken as zero as shown in Eqs 5 through 8.

The yield loci are then established for the two orientations under combined tension/torsion loading.

Yield loci:
TD:

$$\sigma^2 + 3.13\tau^2 = 292^2 \tag{9}$$

RD:

$$1.127\sigma^2 + 3.02\tau^2 = 292^2 \tag{10}$$

compared with the isotropic case:

$$\sigma^2 + 3\tau^2 = k^2 \tag{11}$$

The experimental data are plotted together with the above yield functions in Fig. 6. Using Levy and von Mises's assumption, $d\epsilon_i^p/S_i$ = constant, and using yield functions as the plastic potential functions, the flow relations can be obtained for the two orientations under biaxial loadings. In this formulation, the flow rules are obtained based on the isotropic hardening assumption, i.e. the initial yield surface can only expand. From the comparison between experimental data and theoretical prediction on the flow relations (see Fig. 7) and the effective stress-effective strain modeling (see Fig. 8*a*, $\bar{\sigma} - \bar{\epsilon}$), the isotropic hardening assumption seems appropriate. Hecker [*14*] and Stout et al. [*54*] also concluded that if yielding is defined by a big offset strain (0.2%), then the yield loci usually expand isotropically. Moreover, variation of the anisotropic parameters M_{ij} with strain levels and the inclusion of α_i and α_j terms into the yield functions can also be done to enable translation and distorsion of yield surfaces. The discussion of this topic is beyond the scope of this paper.

Test of normality rule for biaxial loading can be done by comparing the experimental data

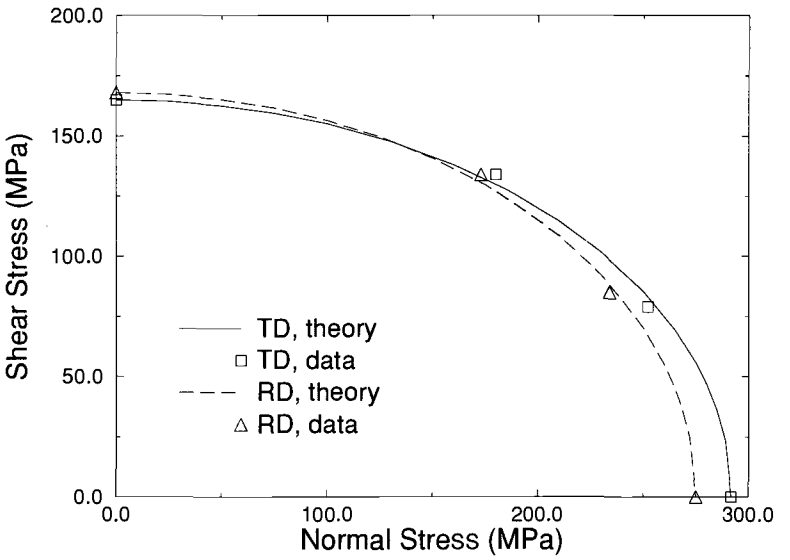

FIG. 6—*Yield loci in the RD and TD directions under cyclic tension/torsion loading using 0.2% off-set strain yield definition.*

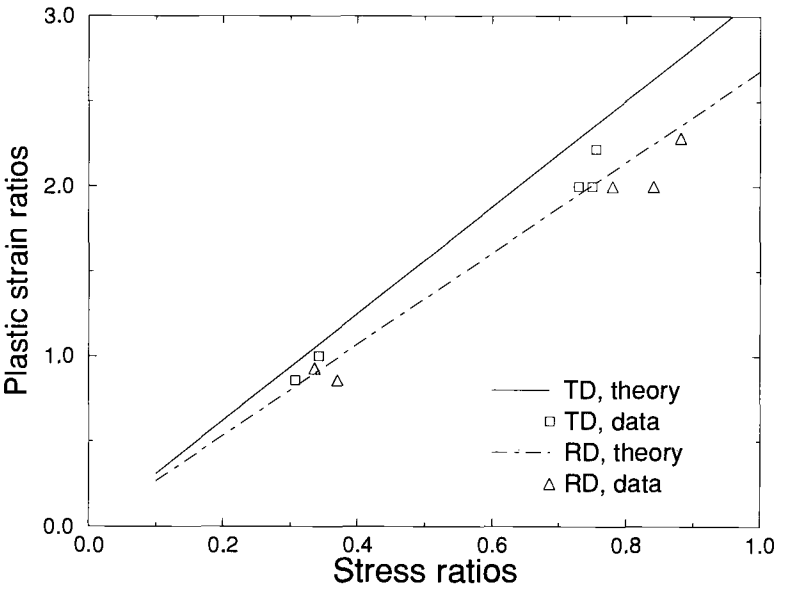

FIG. 7—*A plot of plastic strain ratio* $d\gamma_p/d\epsilon_p$ *versus stress ratio* τ/σ *under the biaxial loading in the RD and TD directions.*

to the prediction of the flow relation. The flow relations of the two orientations under the biaxial loading conditions can be expressed as:

TD:

$$\frac{d\gamma_p}{d\epsilon_p} = \frac{M_{66}}{M_{11}}\frac{\tau}{\sigma} = 3.13\frac{\tau}{\sigma} \tag{12}$$

RD:

$$\frac{d\gamma_p}{d\epsilon_p} = \frac{M_{55}}{M_{22}}\frac{\tau}{\sigma} = 2.68\frac{\tau}{\sigma} \tag{13}$$

compared with the isotropic case, where

$$\frac{d\gamma_p}{d\epsilon_p} = 3\frac{\tau}{\sigma} \tag{14}$$

The experimental data are plotted together with the above flow relations as shown in Fig. 7. The prediction of the anisotropic constitutive equation formulation and the experimental data is in reasonable agreement.

Effective Stress-Effective Strain Criteria

The concept of effective stress-effective strain is used to reduce multiaxial stress-strain responses to a universal stress-strain curve, generally the one measured in uniaxial tension. An

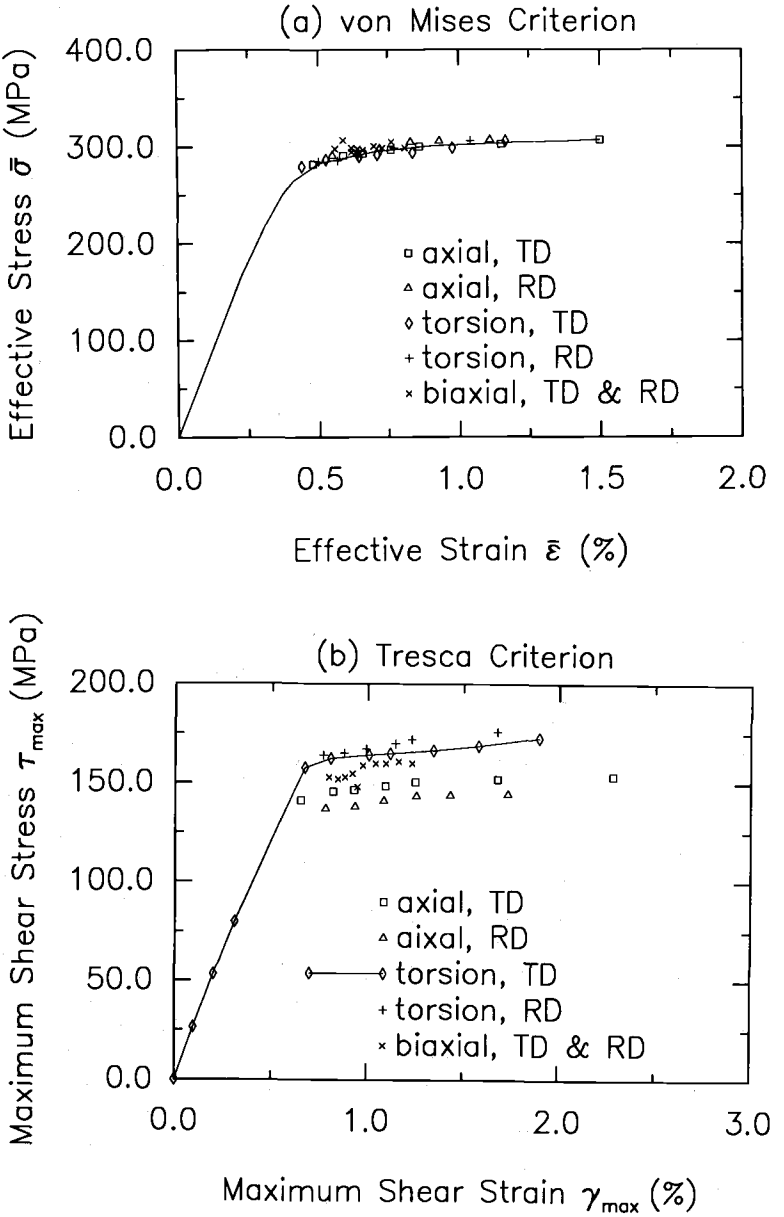

FIG. 8—*Correlation of two effective stress-effective strain criteria with the CSSCs test data in both RD and TD orientations under the three cyclic loading conditions: tension/compression, torsion, and combined tension/torsion in-phase* ($\lambda = 0.8$, $\lambda = 2$): (a) $\bar{\sigma} - \bar{\epsilon}$, (b) $\tau_{max} - \gamma_{max}$.

effective stress-effective strain criterion of the von Mises type, $\bar{\sigma} - \bar{\epsilon}$, could be obtained from the following anisotropic constitutive relations.

$$\bar{\sigma}^2 = M_{ij}\sigma_i\sigma_j \tag{15}$$

$$d\epsilon_i^p = \frac{3}{2}\frac{d\bar{\epsilon}^p}{\bar{\sigma}} S_i \tag{16}$$

$$\bar{\epsilon}_e = \sqrt{\epsilon_e^2 + \alpha\gamma_e^2} \tag{17}$$

$$\bar{\epsilon} = \bar{\epsilon}_e + \bar{\epsilon}_p \tag{18}$$

where α is a constant depending on Poisson's ratio of the material [*55*]. The correlation of the $\bar{\sigma} - \bar{\epsilon}$ criterion with the experimental data is shown in Fig. 8*a*. It is apparent that this criterion correlates the test data of the plate very well. Brown and Miller [*10*] used $\tau_{max} - \gamma_{max}$ as the effective stress-effective strain criterion for the test data of 1% Cr-Mo-V steel. This criterion can also be obtained from the anisotropic constitutive relations.

The correlation of the $\tau_{max} - \gamma_{max}$ criterion with the test data of the plate is shown in Fig. 8*b*, which is poor. Stout et al. [*12*] also evaluated anisotropic effective stress-effective strain criteria for Al-2024-T6. They found that a nonquadratic Hill's criterion gave the best correlation and that the Tresca-type $\tau_{max} - \gamma_{max}$ criterion did not correlate with the test data.

Fatigue Failure Criteria

In the local strain approach, the criterion of fatigue failure is not definite. Although the final rupture of the specimen is a natural choice, N_{final} (fatigue life at the final rupture) is rarely used as a failure criterion. Most researchers use some arbitrary load or torque drops (usually 10% load or torque drop) as their failure criteria, and some also tried to relate their load/torque drop criteria to physical damage behavior [*30,56–58*]. Other researchers used a crack length as the failure criterion [*47,59*]. In Ref *47*, a crack length of 1.0 mm was used as the failure criterion.

In the low cycle fatigue tests of a given material, the number of initiated cracks, their length, their depth, and the stage of initiation depend on the loading condition and specimen geometry. For the solid cylindrical specimens and the strain ranges applied in this study, under cyclic torsion, cracks initiated on the specimen surface very early. The rate of crack growth along the specimen axis was much faster than the rate of crack growth into the specimen thickness. At the 10% torque drop point, the length of the visible cracks could be several centimetres long. As a result, $N_{1.0\ mm}$ (fatigue life at a visible crack of 1.0 mm) was much less than $N_{10\%}$ (fatigue life at 10% load/torque drop). Moreover, in torsional fatigue tests, even $N_{10\%}$ can be significantly smaller than N_{final}. However, under tension/compression, cracks appeared on the specimen surface quite late, at about 70 to 90% of N_{final}. $N_{1.0\ mm}$, $N_{10\%}$, and N_{final} were almost the same in tension/compression fatigue tests. In other words, under torsion, $N_{1.0\ mm}$ does not reflect the actual failure of the specimen at all, but in tension/compression tests, it does. In addition, as crack initiation and the early crack growth depends on the loading condition and specimen geometry in low cycle fatigue tests, it is not always easy to measure the crack lengths and to record their initiation accurately.

The load/torque drop failure criterion relates the failure definition directly to the load/torque carrying capacity of the specimen, and it is very convenient to apply this criterion in fatigue test experiments, which are the two major advantages of this failure criterion. However, this failure criterion lacks a physical damage basis in terms of crack length. The ambiguity of

the failure criterion is an inherent feature of the local strain approach, which needs further research and collaboration among researchers. Similar to the well-accepted 0.2% offset strain yield definition, the 10% load or torque drop failure criterion can be a feasible criterion at present. As a result, the 10% load or torque drop is used as the fatigue failure criterion in this study.

Fatigue Cracking Behavior

Fatigue cracking behavior was observed during the biaxial fatigue tests of the two orientations of specimens. After the fatigue tests, specimens were inspected using the liquid penetrant method to manifest the cracks and their orientations. Photographs of the cracks on the specimen surface are shown in Figs. 9 through 11. The orientations of the planes of maximum shear under the three loading conditions, i.e. pure torsion, tension/compression, and combined tension/torsion, are also shown in Figs. 9 through 11. Under torsional loading, cracks initiated and propagated along the specimen axis, i.e. on the planes of maximum shear (PMS). Both RD and TD specimens displayed the same shear cracking behavior, as shown in Fig. 9. Cracks initiated early, at about 10 to 20% of $N_{10\%}$. Some cracks linked and became major

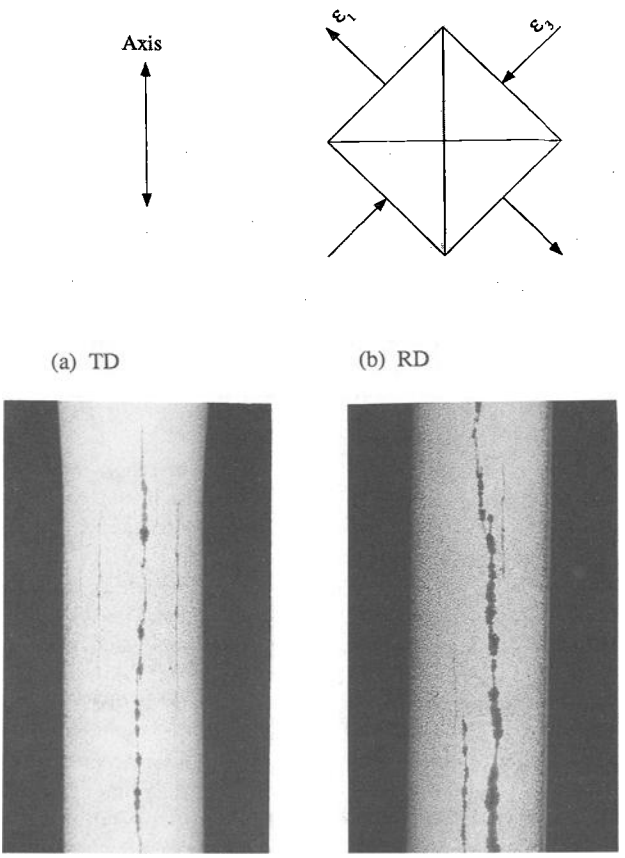

FIG. 9—*Photographs showing the cracks, their orientations, and the planes of maximum shear on the specimen surface under pure torsion:* (a) *a TD specimen, and* (b) *an RD specimen.*

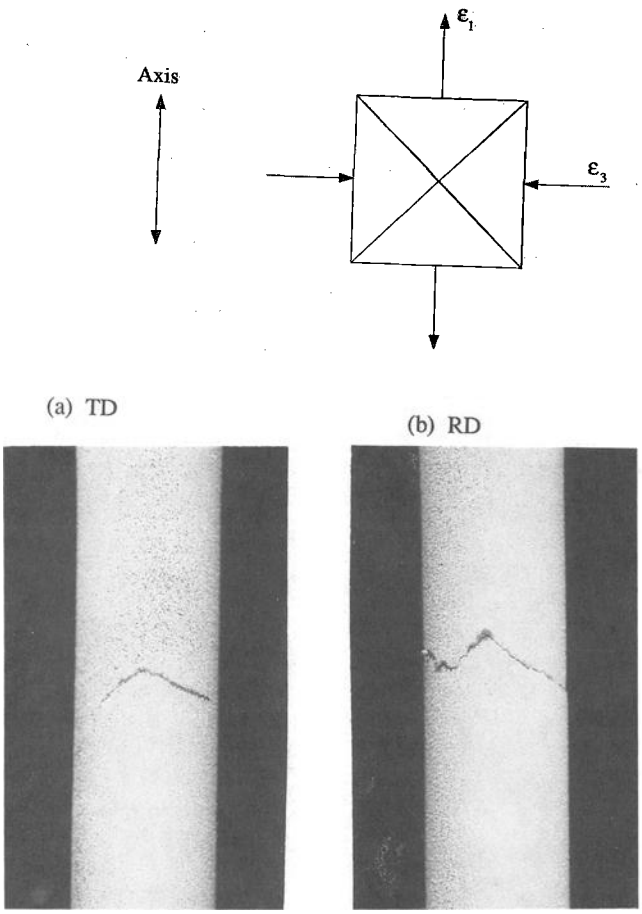

FIG. 10—*Photographs showing cracks, their orientations, and the planes of maximum shear on the specimen surface under tension/compression:* (a) *a TD specimen, and* (b) *an RD specimen.*

cracks at later stages of growth. The final length of the major cracks were as long as several centimetres. All cracks were along the specimen axis; no cracks initiated and propagated along the circumferential direction (another PMS). This phenomenon has been observed repeatedly during torsional fatigue tests [*26,30,60*].

Under tension/compression loading, the RD and TD specimens also displayed similar shear cracking behavior. Cracks initiated and remained on the planes 45° to the specimen axis (PMS) for the majority of the fatigue life (Fig. 10). Cracks initiated late, and only a couple of cracks were visible on the specimen surface at the 10% load drop point, which was true for all specimens tested under tension/compression. Under combined tension/torsion loading conditions, cracks also initiated early and remained on the maximum shear planes for both the RD and the TD specimens (Fig. 11). The number of visible cracks under biaxial loading seemed to be more than that under tension/compression loading, but less than that under torsional loading. The fatigue cracking behavior of this material appeared to be shear dominated. The material anisotropy seemed to have a negligible effect on the fatigue cracking behavior.

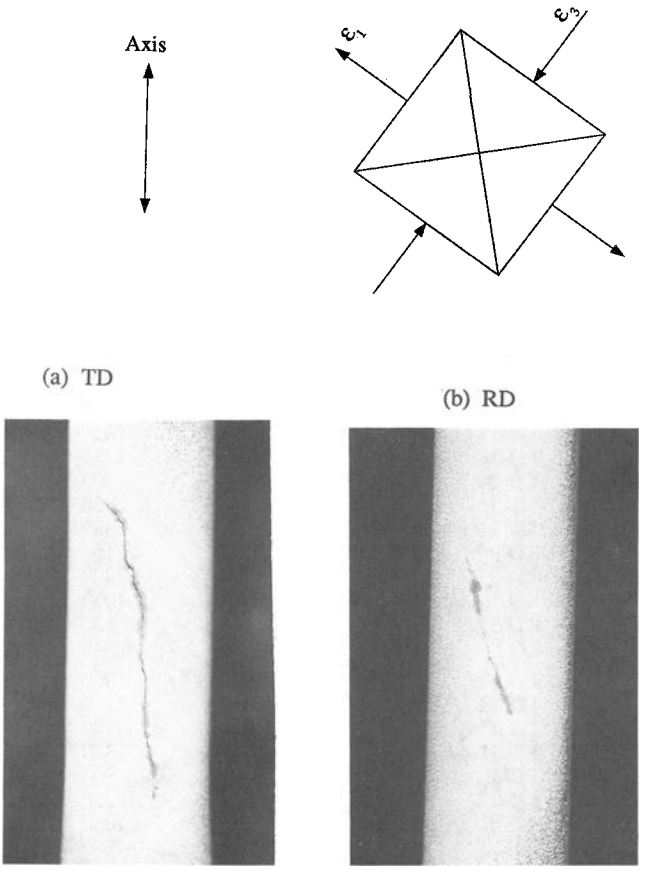

FIG. 11—*Photographs showing the cracks, their orientations, and the planes of maximum shear on the specimen surface under combined tension/torsion in-phase:* (a) *a TD specimen, and* (b) *an RD specimen.*

Fatigue Life Prediction Models

The biaxial fatigue test results of the TD and RD specimens are given in Table 1, which includes the specimen identification number, the applied strain amplitude, and the corresponding fatigue life.

The anisotropic fatigue life data of the RD and TD specimens under both tension/compression and pure torsion loading conditions are shown in Fig. 12, which are in agreement with the anisotropic cyclic stress-strain responses of the material. Under tension/compression, higher cyclic stress and shorter fatigue life data were obtained from the TD specimens. Under torsion, however, higher cyclic stress and shorter fatigue life data were found from the RD specimens (see Fig. 5 and Fig. 12). In order to correlate the fatigue life data of the RD and TD specimens under the three loading conditions, a multiaxial fatigue life prediction model is needed. The successful model should be proposed based on the actual physical cracking behavior observed during the fatigue tests and evaluated based on the anisotropic constitutive relations of the Al-6061-T6 plate.

TABLE 1—*The biaxial fatigue test results of the TD and RD specimens.*

Identification Number	$\Delta\epsilon/2$, %	$\Delta\gamma/2$, %	$N_{10\%}$	λ
TD-21		0.672	6100	∞
TD-12		0.81	3450	∞
TD-19		1.008	1850	∞
TD-18		1.12	1600	∞
TD-29		1.34	1330	∞
TD-8		1.58	570	∞
RD-35		0.77	2350	∞
RD-20		0.882	1725	∞
RD-16		0.994	1400	∞
RD-4		1.01	1130	∞
RD-34		1.148	880	∞
RD-5		1.232	600	∞
TD-13	0.48		2420	0
TD-35	0.59		1230	0
TD-24	0.66		800	0
TD-22	0.76		650	0
TD-17	0.86		380	0
RD-9	0.56		2150	0
RD-33	0.65		1400	0
RD-19	0.74		1050	0
RD-30	0.85		530	0
RD-6	0.96		340	0
TD-34	0.4	0.81	1060	2
TD-23	0.45	0.9	850	2
TD-27	0.5	1.01	720	2
TD-31	0.5	0.41	1310	0.8
TD-5	0.55	0.45	900	0.8
RD-27	0.38	0.76	1230	2
RD-21	0.43	0.86	1050	2
RD-26	0.475	0.95	800	2
RD-28	0.525	0.425	1960	0.8
RD-32	0.58	0.46	1140	0.8

For isotropic materials, the following multiaxial fatigue life prediction models have been proposed representing three different concepts: the shear cracking model by Socie et al. [*47*], $\gamma_{max} + \epsilon_n + \sigma_{n0}/E$, and the tensile cracking model (SWT) [*49*], $\sigma_1\epsilon_1$. In these two models, the critical plane concept and the observed actual cracking behavior were taken into consideration. The other two models are: the effective strain, $\bar{\epsilon}$, and the plastic work [*39*], $\bar{\epsilon}_p\bar{\sigma}$. Based on the anisotropic constitutive relations of the Al-6061-T6 plate (Eqs 5 through 8), these four models are evaluated and correlated with the fatigue life data of the RD and the TD specimens.

Figures 13 through 16 show the correlation of the four models with the fatigue test data of the TD and RD specimens. From Figs. 13 and 14, it is obvious that the tensile cracking model and the plastic work model cannot correlate the test data of either RD or TD specimens. From Fig. 15, it is found that the effective strain model, $\bar{\epsilon}$, offers good correlation for the data of RD specimens, but poor correlation for the data of TD specimens. The parameter appearing in Fig. 16, $\gamma_{max} + \epsilon_n$, is from the model $\gamma_{max} + \epsilon_n + \sigma_{n0}/E$ proposed by Socie et al. [*47,50*]. Since, in our fully reversed fatigue tests, the mean stress term, σ_{n0}, is zero, only $\gamma_{max} + \epsilon_n$ is shown in Fig. 16. Figure 16 shows that the shear cracking model, $\gamma_{max} + \epsilon_n$, gave better correlations for

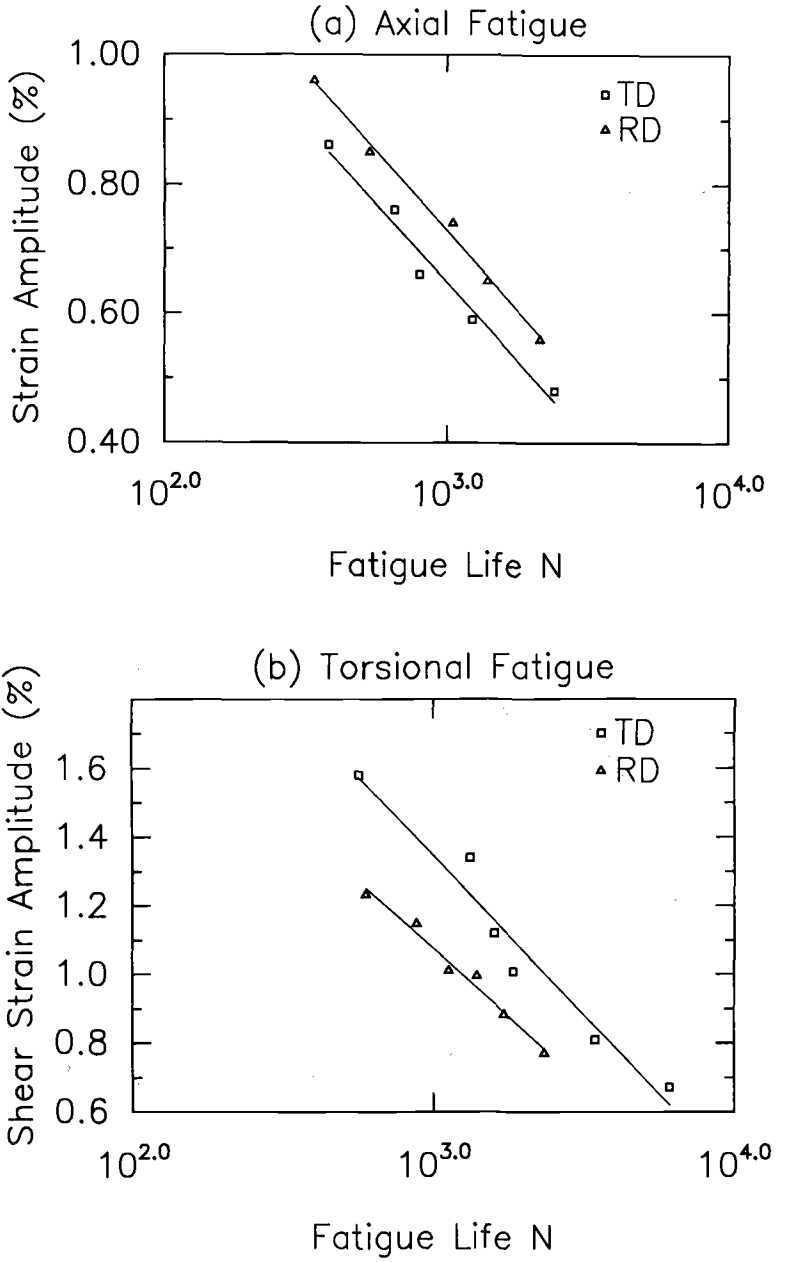

FIG. 12—*Comparisons between the fatigue lives of TD and RD orientations:* (a) *under tension/compression loading, and* (b) *under pure torsion.*

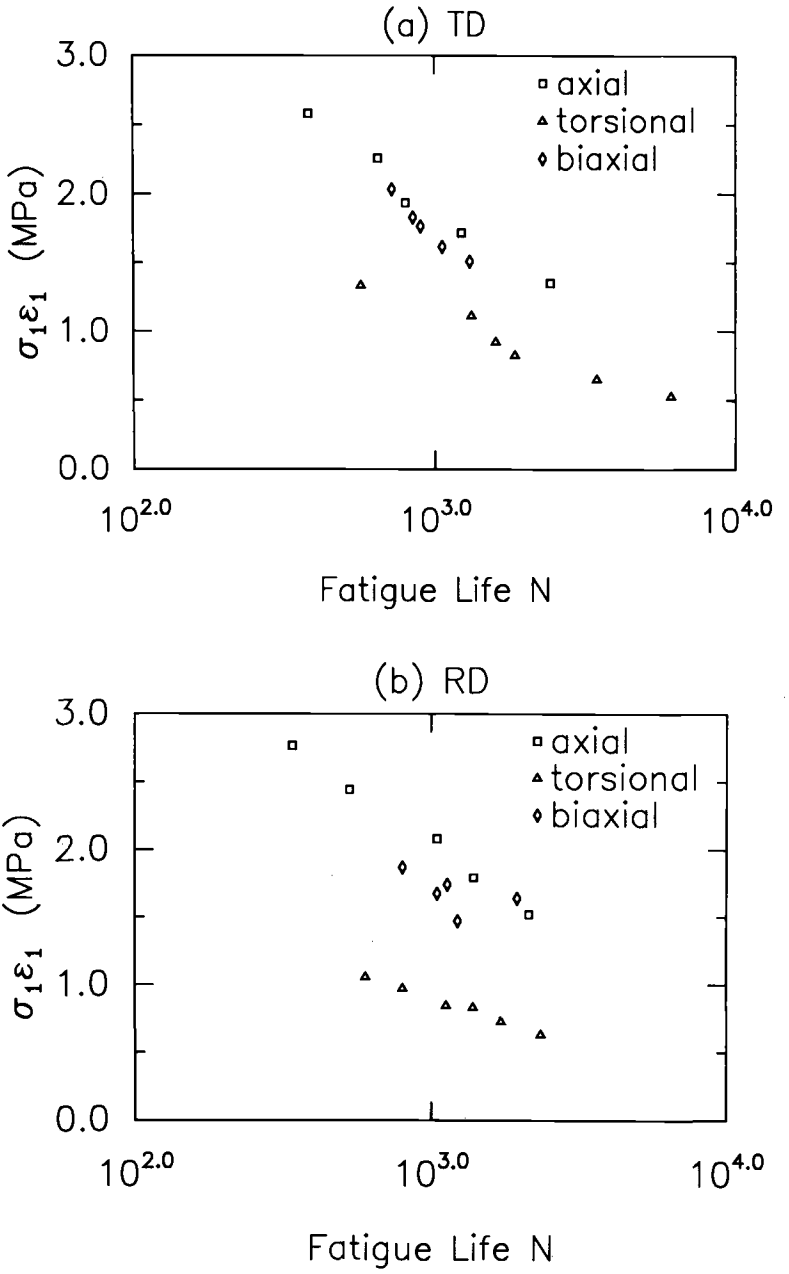

FIG. 13—*A plot of the tensile cracking parameter* $\sigma_1\epsilon_1$ *versus fatigue life* N *for both TD and RD orientations under the three loadings: tension/compression, torsion, and combined tension/torsion in-phase.*

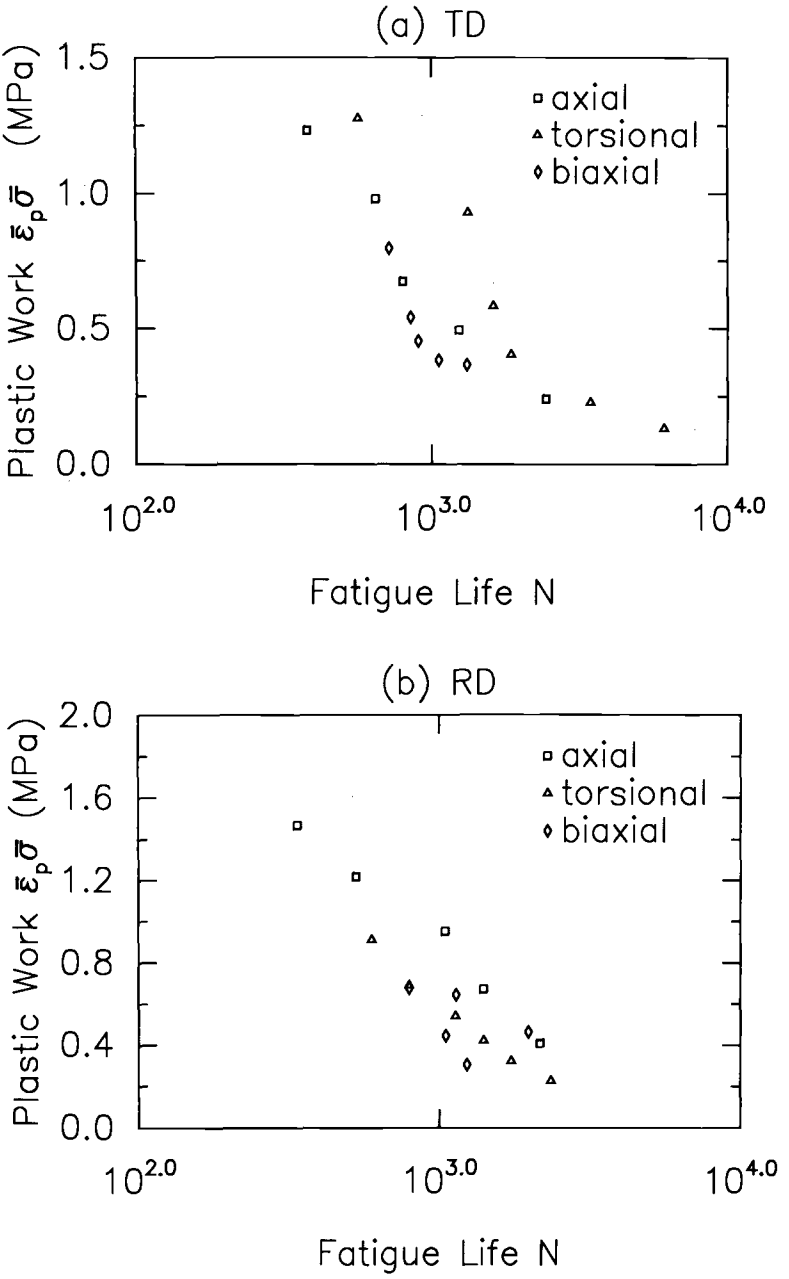

FIG. 14—*A plot of the plastic work parameter,* $\bar{\varepsilon}_p\bar{\sigma}$, *versus fatigue life,* N, *for both TD and RD orientations under the three loadings.*

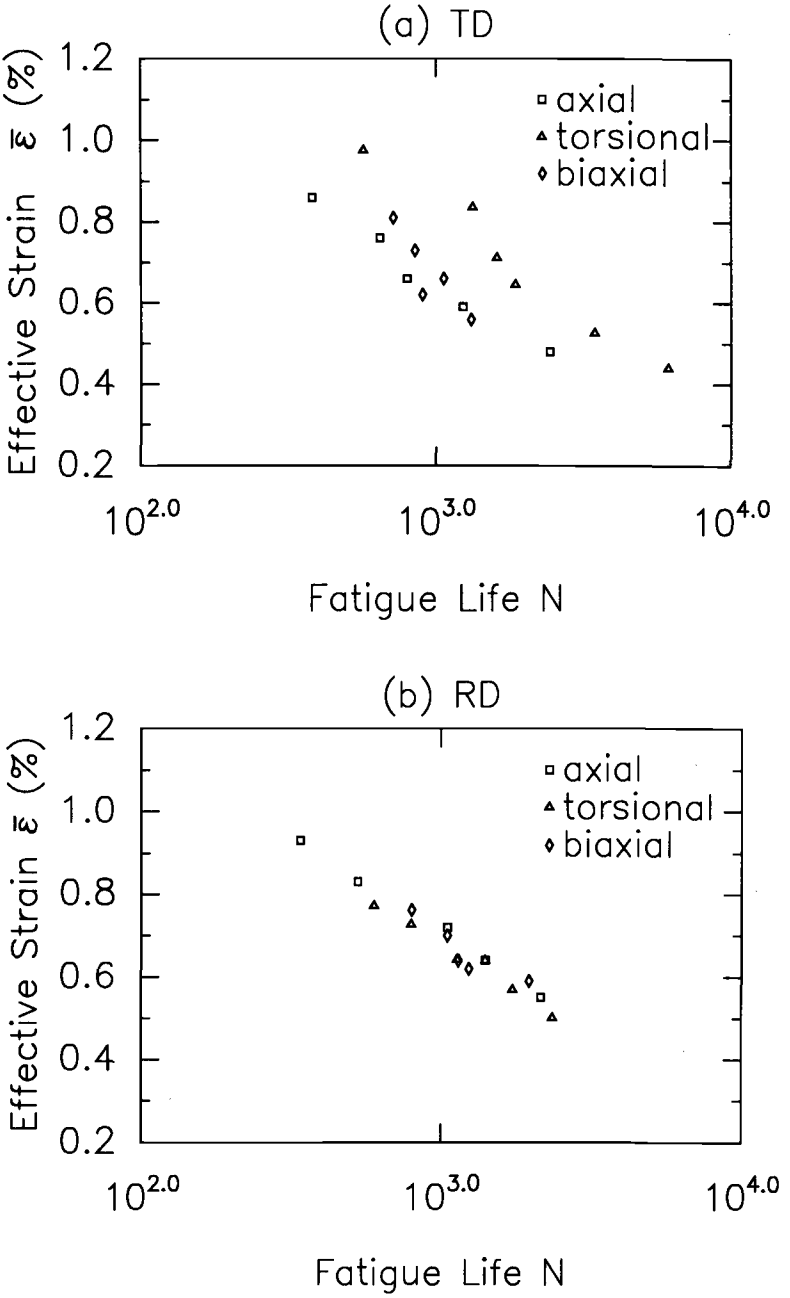

FIG. 15—*A plot of the effective strain parameter, $\bar{\varepsilon}$, versus fatigue life, N, for both TD and RD orientations under the three loadings.*

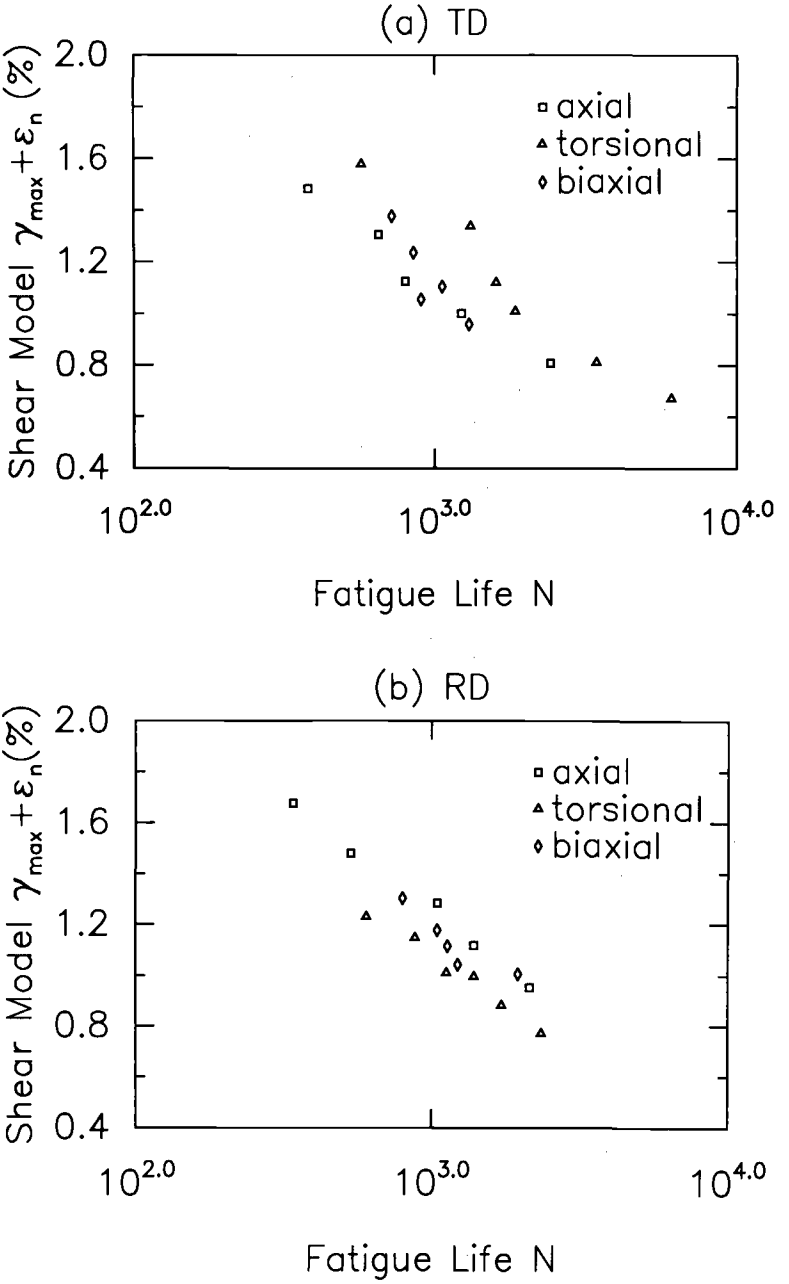

FIG. 16—*A plot of the shear cracking parameter* $\gamma_{max} + \epsilon_n$ *versus fatigue life,* N, *for both TD and RD orientations under the three loadings.*

both RD and TD specimens than the plastic work and tensile models, but the correlations are still not satisfactory.

The fatigue cracking behavior of both RD and TD specimens under the biaxial loading conditions has been observed to be shear cracking dominated. For the shear cracking damage mechanism, two parameters on the PMS are found to control fatigue life: γ_{max} and ϵ_n. Therefore, it is not surprising that the tensile cracking model did not correlate with the test data because it cannot reflect the actual shear cracking behavior observed during the tests. The effective strain and the plastic work models treat all planes similarly and average the stress/strain responses across multiple planes. As a result, the relationship between the correlating parameters and the fatigue life lacks physical interpretation with respect to multiaxial fatigue failures occurring usually on some definite planes.

Among the four models, the shear cracking model, $\gamma_{max} + \epsilon_n$, is supposed to show the best correlation as it represents the actual shear cracking behavior. But its correlation with the test data of both TD and RD specimens is not satisfactory (Fig. 16). This is due to the fact that this model was originally proposed for the fatigue damage evaluation of an isotropic material [*47*]. For anisotropic materials, the model has to be modified in order to take the material anisotropy effect into consideration.

A new multiaxial fatigue life prediction model is proposed here in order to predict the anisotropic multiaxial fatigue life of the Al-6061-T6 plate:

$$A_i(\gamma_{max} + B_i\epsilon_n) = f(N) \tag{19}$$

where γ_{max} and ϵ_n are the fatigue life controlling parameters on the plane of maximum shear, and A_i and B_i are material anisotropy coefficients whose values depend on the material orientation. The right-hand side is the torsional fatigue life baseline data. A_i is introduced to reduce the two torsional fatigue life baseline data obtained from TD and RD orientations into one. B_i is needed to correlate the data under tension/compression with those under pure torsion. According to the Cartesian coordinates shown in Fig. 1, for the transverse direction (TD), $i = 1$; for the rolling direction (RD), $i = 2$; and for the normal direction, $i = 3$.

From the pure axial and the pure torsional fatigue test data of the TD and RD specimens, the values of A_i and B_i were determined as follows:

TD:

$$A_1 = 0.8, \qquad B_1 = 2.0$$

RD:

$$A_2 = 1, \qquad B_2 = 0.2$$

Compared with the isotropic model, $\gamma_{max} + \epsilon_n$:

$$A_1 = A_2 = A_3 = 1, \qquad B_1 = B_2 = B_3 = 1$$

The values of B_i were obtained from the correlation between the data of pure axial fatigue tests and the data of pure torsional fatigue tests. In the modeling of the biaxial fatigue data of shear cracking behavior, the torsional fatigue life data are used as the baseline data. Although γ_{max} is the major controlling parameter for the shear damage, ϵ_n plays an important role. Under pure torsion, $\epsilon_n = 0$, mechanical interlocking occurs, and high friction forces are developed between crack surfaces which are irregularly shaped as the cracks propagate through the individual grains. However, under tension/compression loading, $\epsilon_n \neq 0$. ϵ_n and the resulting nor-

mal stress, σ_n, tend to open the crack surfaces and reduce the friction forces between them and finally increase the crack growth rate. Recognizing the significance of ϵ_n, Brown and Miller [*46*] proposed a general function for the fatigue data of shear cracking behavior: $\Gamma(\gamma_{max}, \epsilon_n)$. The simplest form of this Γ function is $\gamma_{max} + \epsilon_n$, which has been used by Socie et al. to model the test data of an isotropic material [*47*].

In our model $A_i(\gamma_{max} + B_i\epsilon_n)$, B_i represents the amount of contribution of ϵ_n to fatigue damage. For a material with a higher σ_y, ϵ_n will cause higher stress response, σ_n, and consequently more fatigue damage. As a result, a larger value of B_i should be obtained from the correlation of the experimental data. We see from the data of the Al-6061-T6 plate, along the TD orientation, that σ_y = 292 MPa and B_1 = 2.0. Along the RD orientation, σ_y = 275 MPa and B_2 = 0.2. The correlations of $\gamma_{max} + B_i\epsilon_n$ with the fatigue test data of both TD and RD specimens are shown in Fig. 17 and are very good.

The values of A_i were obtained by reducing the two torsional fatigue life data of the TD and RD orientations (see Fig. 12*b*) into one single baseline data. Without A_i, the torsional fatigue life data of the two orientations are still distributed along two separate lines (see Fig. 17), even though B_i has been introduced to model the multiaxial loadings. When finding A_i, we used the torsional fatigue life data of the RD orientation as the baseline data, which means A_2 = 1 for RD orientations. Then the torsional fatigue data of the TD specimens were correlated with those of the RD specimens, which resulted in A_1 = 0.8 for the TD orientation. A plot of this new model, $A_i(\gamma_{max} + B_i\epsilon_n)$, with the fatigue life data of both TD and RD orientations under the biaxial loading conditions is shown in Fig. 18 and is remarkably good.

A_i and B_i are the material anisotropy coefficients in the fatigue life prediction model, in a sense similar to that of M_{ij} in the yield function. The values of A_i and B_i depend on the material orientation, and they can be obtained by conducting pure axial and pure torsional fatigue tests along the principal anisotropic directions of an anisotropic material only. Physically, A_i and

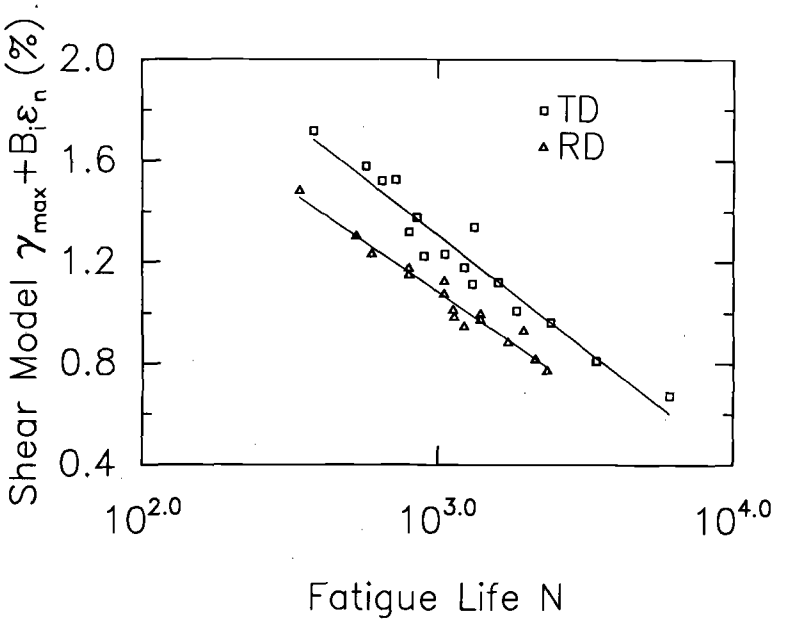

FIG. 17—*A plot of the shear cracking parameter with one material anisotropy factor* B_i: $\gamma_{max} + B_i\epsilon_n$ *versus fatigue life,* N, *for both TD and RD specimens under the three loadings. TD orientation:* B_1 = *2.0, RD orientation:* B_2 = *0.2.*

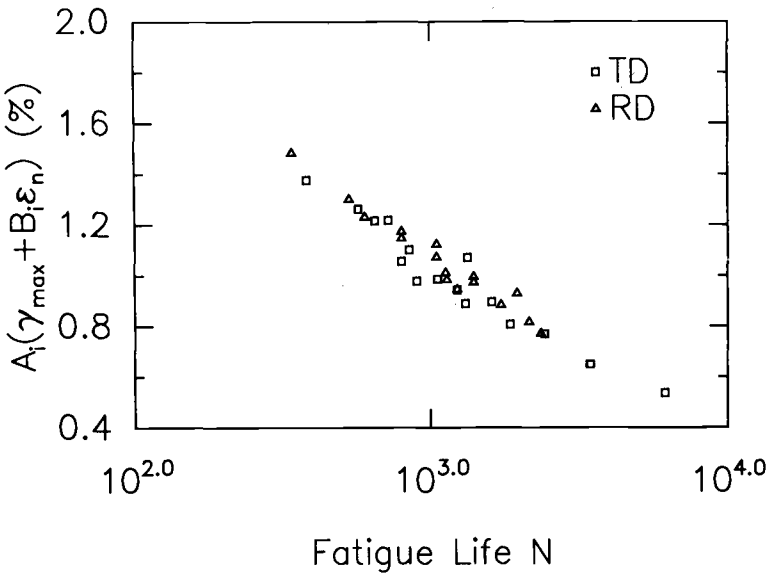

FIG. 18—*A plot of the new model,* $A_i(\gamma_{max} + B_i\epsilon_n)$*, versus fatigue life,* N*, of both TD and RD orientations under the biaxial loading conditions: for TD orientation:* $A_1 = 0.8$; $B_1 = 2.0$; *for RD orientation:* $A_2 = 1$; $B_2 = 0.2$.

B_i must depend on the microstructure of the plate, i.e. grain size, spacing among the second phase particles, etc. Further research is needed to relate these constants quantitatively to the microstructure of the material.

Discussion

As shown in Figs. 4 and 5, the stress responses in the plastic range of the two orientations are different under either axial loading or torsional loading. However, the differences are not significant. In order to verify that the differences are due to the material anisotropy rather than the experimental scatter, both monotonic and cyclic tests were conducted on multiple companion specimens. The same plastic anisotropy behavior was obtained from the multiple specimen tests, i.e. the TD specimens showed higher stress responses under axial loading, but the RD specimens showed higher stress responses under torsional loading. Figures 4 and 5 were the averages of the multi-specimen tests. Statistical analysis was also performed to evaluate the differences between the TD and RD stress responses and the experimental error involved in the stress measurement [*51*]. It was found that the expected uncertainties in the stress measurement were less than the differences between the TD and RD stress responses and that the TD and RD stress responses were statistically different. Finally, the observed anisotropy in stress responses was in good agreement with the observed anisotropy in fatigue lives, as shown in Figs. 5 and 12. Under axial loading, the TD specimens not only showed higher stress responses, but shorter fatigue lives as well. However, under torsional loading, the RD specimens showed higher stress responses and shorter fatigue lives. As a result, we believe that the differences between TD and RD stress responses are indeed due to the material anisotropy, even though this is not significant.

The constitutive relations of the material were obtained based on the cyclic stress-strain responses of TD and RD orientations and the measured plastic strain ratios, R and P. Detailed

discussion on this topic can be found in Ref *51*. The values of the M_{ij} matrix reflect the magnitude of the material anisotropy. Since $M_{11} \neq M_{22} \neq M_{33}$, the Al-6061-T6 plate is definitely an orthotropic material, which is expected from the one direction cold rolling process. Therefore, in order to model its fatigue damage, it is necessary to obtain its anisotropic constitutive relations rather than simply assuming it is isotropic.

For the solid cylindrical specimen used in this work, under torsional or axial-torsional loading conditions, there is a shear stress gradient across its cross section, while in a thin-wall tube specimen, the most commonly used specimen configuration in multiaxial fatigue experiments, the shear stress, is approximately uniform across the thickness. In the present study, all the shear stresses and shear strains are for the specimen surface rather than the average across the cross section. Therefore, the shear stress–shear strain responses obtained in this work do represent the true material responses, and they should be the same as those obtained from the thin-wall tube specimens. Similarly, since crack initiation usually occurs on the specimen surface for both solid and thin-wall tube specimens, crack initiation and the orientations of the cracks on the specimen surface depend on the stress-strain state on the specimen surface only. However, the specimen geometry difference will affect the fatigue life. In a solid specimen, the rate of the Mode III crack growth from the surface into the elastic core must be slower than that in a thin-wall tube specimen with the same applied shear strain because the stress gradient exists in the solid specimen. As a result, the solid specimen will have a longer torsional fatigue life than a thin-wall tube specimen with the same applied shear strain. Moreover, this specimen geometry's effect on fatigue life depends strongly on the definition of fatigue failure. If fatigue failure is defined as the final rupture, this geometry effect can be very large. We used the 10% torque drop as the failure criterion in our torsional fatigue tests. Cracks were relatively shallow in our torsional fatigue tests, so the geometry effect is also relatively small for our results.

Our extensometer gage length is 10 mm, and our specimen gage length is 50 mm. Generally, fatigue life may depend on the extensometer gage length if the two gage lengths are different and the failure criterion is defined by load/torque drop. In this work, the 10% load/torque drop was used as the fatigue failure criterion, and the fatigue tests were stopped before the final rupture of the specimens. In the pure axial fatigue tests, all the visible cracks were inside the extensometer gage length. In the pure torsional and axial-torsional biaxial fatigue tests, the density of cracks were approximately uniform through the entire specimen gage length, and almost every specimen developed a few major cracks which nucleated inside the extensometer gage length initially but grew outside later. Since we stopped the fatigue tests before the final rupture of the specimens and no failure cracks were outside the extensometer gage length, we believe that the extensometer gage length has a negligible effect on our fatigue life results.

The multiaxial fatigue life prediction of an anisotropic material is a new and difficult endeavor. In this work, we demonstrated that, in order to model the multiaxial fatigue damage of anisotropic materials, the following methodology should be followed. First, the anisotropic constitutive relations of the material should be obtained. Secondly, the fatigue cracking behavior of the material under the multiaxial loading conditions should be investigated. Finally, a multiaxial fatigue damage model must be proposed based on the observed cracking behavior and evaluated from the anisotropic constitutive relations. This methodology was successful for the modeling of the orthotropic Al-6061-T6 plate, and it should be applicable for the modeling of other materials with more significant anisotropy.

In the anisotropic constitutive relations and the multiaxial fatigue damage model of an anisotropic material, many material anisotropic coefficients may appear, such as the M_{ij} in the yield function and A_i, B_i in the fatigue damage model in this work. These material coefficients are the basic information needed to model an anisotropic material, and they usually represent the dependence of some specific mechanical properties on the material orientations. For iso-

tropic materials, these material coefficients have fixed values, but for anisotropic materials they have to be determined by testing the material along its principal anisotropic directions under pure uniaxial loading conditions. Eventually, these material coefficients will be incorporated into a model for the prediction of material responses under multiaxial loading conditions [*13*,*18*,*51*,*61*]. One should not think of these material coefficients as curve-fitting constants. In curve fitting, all of the available experimental data from different material orientations under every loading path must be analyzed to find the curve-fitting constants. But to obtain the material coefficients, only the experimental data of principal anisotropic directions under pure uniaxial loading conditions (pure axial, pure torsional, etc.) are needed. Once they are found, the resulting model incorporated with them can be used to predict the material responses in the principal orthotropic directions as well as other directions under more complicated multiaxial loading paths. In this work, for example, M_{ij} was obtained from pure axial and pure torsional tests along TD and RD orientations, but the yield function and the flow relations can predict the yielding and plastic flow of the material under multiaxial loading conditions. Similarly, in our fatigue damage model, A_i and B_i were found from pure axial and pure torsional fatigue test data, but the model can predict the fatigue life of the material under biaxial loading conditions. The present theoretical and experimental investigation was limited to the principal orthotropic directions TD and RD under fully reversed proportional axial-torsional loading conditions; however, further investigation is being performed on other material orientations and more loading paths [*51*].

Conclusions

Low cycle fatigue tests were conducted on TD and RD specimens made from an orthotropic Al-6061-T6 plate under three loading conditions: tension/compression, torsion, and combined tension/torsion in-phase. The following conclusions were obtained:

1. The CSSCs and fatigue lives along the RD and TD directions of the anisotropic Al-6061-T6 plate were obtained under biaxial loading conditions. Under torsion, higher cyclic stress responses and shorter fatigue lives were obtained for the RD specimens. Under tension/compression, however, the TD specimens gave higher cyclic stress responses and shorter fatigue lives.
2. The anisotropic constitutive relations of the Al-6061-T6 plate were obtained using Hill's anisotropic plasticity theory. Based on the evaluation of yield loci and flow relations, the constitutive relations agreed with the test data reasonably well.
3. The von Mises-type effective stress-effective strain criterion obtained from the anisotropic constitutive relation correlated with the CSSCs test data very well, but the Tresca-type $\tau_{max} - \gamma_{max}$ criterion did not correlate with the CSSCs test data.
4. The fatigue cracking behavior of the TD and RD specimens was observed during the fatigue tests. Cracks were initiated and propagated on the maximum shear planes for both the TD and RD orientations under biaxial loading conditions. The fatigue damage of the material appeared to be shear dominated. The material anisotropy seemed to have no effect on fatigue cracking behavior, although it did have effects on fatigue life.
5. Four multiaxial fatigue life prediction models of three different concepts were evaluated employing the anisotropic constitutive relations. These models were used to correlate the fatigue life data. The tensile cracking model, the plastic work model, and the effective strain model gave poor correlations. The shear cracking behavior of the material could not be reflected by these three models. A new shear cracking model incorporating material anisotropy effects was proposed, $A_i(\gamma_{max} + B_i\epsilon_n)$, and it correlated with the fatigue life data of TD and RD orientations under biaxial loadings very well. The dependence of the anisotropic coefficients

A_i and B_i on the material orientation was shown, and suggestions were made concerning their physical significance. Further research is needed to relate them to the microstructure of the material.

References

[1] Garud, Y. S., "Multiaxial Fatigue: A Survey of the State of the Art," *Journal of Testing and Evaluation,* Vol. 9, 1981, pp. 165–178.

[2] Brown, M. W. and Miller, K. J., "Two Decades of Progress in the Assessment of Multiaxial Low-Cycle Fatigue Life," *Low-Cycle Fatigue and Life Prediction, ASTM STP 770,* American Society for Testing and Materials, Philadelphia, 1982, pp. 482–499.

[3] Leese, G. E., "Engineering Significance of Recent Multiaxial Research, *Low Cycle Fatigue, ASTM STP 942,* American Society for Testing and Materials, Philadelphia, 1988, pp. 861–873.

[4] Fernando, U. S., Miller, K. J., and Brown, M. W., "Computer Aided Multiaxial Fatigue Testing," *Fatigue and Fracture of Engineering Materials and Structures,* Vol. 13, 1990, pp. 387–398.

[5] Morrow, J., in *Cyclic Plastic Strain Energy and Fatigue of Metals, ASTM STP 378,* American Society for Testing and Materials, Philadelphia, 1965, pp. 45–87.

[6] Landgraf, R. M., Morrow, J., and Endo, T., "Determination of the Cyclic Stress-Strain Curve," *Journal of Material,* 1969, Vol. 4, pp. 176–188.

[7] Pickard, A. C. and Knott, J. F., "Effect of Testing Method on Cyclic Hardening Behavior in Face-Centered Cubic Alloys," *Low Cycle Fatigue, ASTM STP 942,* American Society for Testing and Materials, Philadelphia, 1988, pp. 58–76.

[8] Laird, C., in *Work Hardening in Tension and Fatigue,* A. W. Thompson, Ed., Metallurgical Society of AIME, New York, 1977, p. 150.

[9] Stark, E. A. and Lutjering, G., "Cyclic Plastic Deformation and Microstructure," *Fatigue and Microstructure,* ASM seminars, St. Louis, 1978, American Society for Metals, Metals Park, OH, pp. 205–243.

[10] Brown, M. W. and Miller, K. J., "Biaxial Cyclic Deformation Behavior of Steels," *Fatigue of Engineering Materials and Structures,* 1979, Vol. 1, pp. 93–106.

[11] Fatemi, A. and Stephens, R. I., "Cyclic Deformation of 1045 Steel under In-Phase and 90° Out-of-Phase Axial-Torsional Loading Conditions," *Multiaxial Fatigue: Analysis and Experiments,* SAE AE-14, Society of Automotive Engineers, Warrendale, PA, 1990, pp. 139–147.

[12] Stout, M. G., Hecker, S. S., and Bourcier, R., "An Evaluation of Anisotropic Effective Stress-Strain Criteria for the Yield and Flow of 2024 Aluminum Tubes," *Journal of Engineering Materials and Technology, Transactions,* American Society of Mechanical Engineers, New York, Vol. 105, 1983, pp. 242–249.

[13] Hill, R., "A Theory of the Yield and Plastic Flow of Anisotropic Metals," *Proceedings of the Royal Society of London,* Vol. A193, 1948, pp. 281–297.

[14] Hecker, S. S., "Experimental Studies of Yield Phenomena in Biaxially Loaded Metals," *Constitutive Equations in Viscoplasticity: Computational and Engineering Aspects,* American Society of Mechanical Engineers, New York, 1976, pp. 1–33.

[15] Edelman, R. and Drucker, D. C., "Some Extensions of Elementary Plasticity," *Journal of the Franklin Institute,* Vol. 251, No. 6, 1951, p. 581.

[16] Bishop, J. F. W. and Hill, R., "A Theory of the Plastic Distorsion of a Polycrystalline Aggregate Under Combined Stress," *Philosophical Magazine,* Vol. 142, 1951, pp. 414–427.

[17] Hutchinson, J. W., "Elastic-Plastic Behavior of Polycrystalline Metals and Composites," *Proceedings of the Royal Society of London,* Vol. A319, 1970, pp. 247–272.

[18] Shih, C. F. and Lee, D., "Further Developments in Anisotropic Plasticity," *Journal of Engineering Material and Technology, Transactions,* American Society of Mechanical Engineers, New York, Vol. 100, 1978, pp. 294–302.

[19] Ikegami, K., "Experimental Plasticity on the Anisotropy of Metals," *Mechanical Behavior of Solids,* Proceedings of Euromech 115, Villiard-de-Lans, France, 1979, J. P. Boehler, Ed., Nijhoff/Editions du CNRS, The Hague/Paris, pp. 201–241.

[20] Frederking, R. M. W. and Sidebottom, D. M., "An Experimental Evaluation of Plasticity Theories for Anisotropic Metals," *Journal of Applied Mechanics, Transactions,* American Society of Mechanical Engineers, New York, 1971, pp. 15–22.

[21] Harvey, S. J., "The Use of Anisotropic Yield Surfaces in Cyclic Plasticity," *Multiaxial Fatigue, ASTM STP 853,* American Society for Testing and Materials, Philadelphia, 1985, pp. 49–53.

[22] Forsyth, P. J. E., "Slip Band Damage and Extrusion," *Proceedings of the Royal Society of London,* Vol. A242, 1957, pp. 198–202.

[23] Frost, N. E., Marsh, K. I., and Pook, L. P., *Metal Fatigue,* Oxford University Press, London, 1974.
[24] Forsyth, J. E., *The Physical Basis of Metal Fatigue,* American Elsevier Publishing Co., Inc., New York, 1969.
[25] Gough, H. J. *The Fatigue of Metals,* Van Nostrand, New York, 1926.
[26] Miller, K. J. and Chandler, D. C., "High Strain Torsion Fatigue of Solid and Tubular Specimens," *Proceedings, Institution of Mechanical Engineers,* Vol. 184, No. 25, 1969–70, pp. 433–448.
[27] Hurd, N. J. and Irving P. E., "Factors Influencing Propagation of Mode III Fatigue Cracks under Torsional Loading," *Design of Fatigue and Fracture Resistant Structures, ASTM STP 761,* American Society for Testing and Materials, Philadelphia, 1982, pp. 212–233.
[28] Hashemi, H. N., McClintock, F. A., and Ritchie, R. O., "Micromechanical Modeling of Mode III Fatigue Crack Growth in Rotor Steels," *International Journal of Fracture,* Vol. 23, 1983, pp. 163–185.
[29] Tschegg, E. K., "Mode III and Mode I Fatigue Crack Propagation Behavior under Torsional Loading," *Journal of Material Science,* Vol. 18, 1983, pp. 1604–1614.
[30] Hurd, N. J. and Irving, P. E., "Smooth Specimen Fatigue Life and Microcrack Growth Mode in Torsion," *Multiaxial Fatigue, ASTM STP 853,* American Society for Testing and Materials, Philadelphia, 1985, pp. 267–284.
[31] Bannantine, J. A. and Socie, D. F., "Observation of Cracking Behavior in Tension and Torsion," *Low Cycle Fatigue, ASTM STP 942,* American Society for Testing and Materials, Philadelphia, 1988, pp. 899–921.
[32] Taira, S., Inoue, T., and Yoshida, T., "Low Cycle Fatigue Under Multiaxial Stresses," (in the case of combined cyclic tension-compression and cyclic torsion at room temperature), *Proceedings,* The Twelth Japanese Congress on Materials Research, 1969, pp. 50–55.
[33] Gough, H. J. and Pollard, H. V., "The Strength of Metals under Combined Alternating Stresses," *Proceedings, Institute of Mechanical Engineers,* Vol. 131, 1935, pp. 3–54.
[34] Sines, G., "Fatigue Criterion under Combined Stresses or Strains," *Journal of Engineering and Materials Technology, Transactions,* American Society of Mechanical Engineers, New York, Vol. 103, 1981, pp. 82–90.
[35] Dowling, N. E., "Torsional Fatigue Life of Power Plant Equipments Rotating Shafts," DOE/RA/29353-1, 1982, Westinghouse R&D Center.
[36] Feltner, C. E. and Morrow, J., "Microplastic Strain Hysteresis Energy as a Criterion for Fatigue Fracture," *Journal of Basic Engineering, Transactions,* American Society of Mechanical Engineers, New York, Vol. 83, 1961, pp. 15–22.
[37] Halford, G. R., "The Energy Required for Fatigue," *Journal of Materials,* Vol. 1, 1966, pp. 3–18.
[38] Garud, Y. S., "A New Approach to the Evaluation of Fatigue under Multiaxial Loadings," *Journal of Engineering Materials Technology, Transactions,* American Society of Mechanical Engineers, New York, Vol. 103, 1981, pp. 118–125.
[39] Lefebre, D., Neale, K. W., and Ellyin, F., "A Criterion for Low Cycle Fatigue Failure under Biaxial State of Stress," *Journal of Engineering Materials and Technology, Transactions,* American Society of Mechanical Engineers, New York, Vol. 103, 1981, pp. 1–6.
[40] Ellyin, F. and Golos, K., "Multiaxial Fatigue Damage Criterion," *Journal of Engineering Materials and Technology, Transactions,* American Society of Mechanical Engineers, New York, Vol. 110, 1988, pp. 63–68.
[41] Ellyin, F., Golos, K., and Xia, Z., "In-Phase and Out-of-Phase Multiaxial Fatigue," *Journal of Engineering Materials and Technology, Transactions,* American Society of Mechanical Engineers, New York, Vol. 113, 1991, pp. 112–118.
[42] Findley, W. N., "Combined Stress Fatigue Strength of 765-T61 Aluminum Alloy with Superimposed Mean Stresses and Corrections for Yielding," Technical Notes 2924, NACA, 1953.
[43] Findley, W. N., "Fatigue of Metals Under Combined Stresses," *Transactions of the American Society of Mechanical Engineers,* Vol. 79, 1957, pp. 1337–1348.
[44] McDiarmid, D. L., "Failure Criteria and Cumulative Damage in Fatigue under Multiaxial Stress Conditions," Ph.D. thesis, City University, London, 1972.
[45] McDiarmid, D. L., "A General Criterion of Fatigue Failure under Multiaxial Stress," *Proceedings,* International Conference of Pressure Vessel Technology, American Society of Mechanical Engineers, New York, 1973, pp. 851–862.
[46] Brown, M. W. and Miller, K. J., "A Theory for Fatigue Failure under Multiaxial Stress-Strain Condition," *Proceedings, Institute of Mechanical Engineers,* Vol. 187, 1973, pp. 745–755.
[47] Socie, D. F., Wail, L. E., and Dittmer, D. F., "Biaxial Fatigue of Inconel 718 Including Mean Stress Effect," *Multiaxial Fatigue, ASTM STP 853,* American Society for Testing and Materials, Philadelphia, 1985, pp. 463–478.

[48] Fatemi A. and Socie, D. F., "A Critical Plane Approach to Multiaxial Fatigue Damage Including Out-of-Phase Loading," *Fatigue and Fracture of Engineering Material Structures,* Vol. 11, 1988, pp. 145–165.
[49] Smith, R. N., Watson, P., and Topper, T. H., "A Stress-Strain Function for the Fatigue of Metals," *Journal of Materials,* Vol. 5, 1970, pp. 767–778.
[50] Socie, D. F., "Multiaxial Fatigue Damage Models," *Journal of Engineering Materials and Technology, Transactions,* American Society of Mechanical Engineers, New York, Vol. 109, 1987, pp. 293–298.
[51] Lin, H., "Multiaxial Plasticity and Fatigue Life Predictions of Anisotropic Al-6061-T6," Ph.D. thesis, Mechanical Engineering Department, Northeastern University, Boston, MA.
[52] Nadai, A., *Theory of Flow and Fracture of Solids,* 2nd ed., McGraw-Hill, New York, 1950.
[53] Chung, Y. S. and Abel, A., "Low Cycle Fatigue of Some Aluminum Alloys," *Low Cycle Fatigue, ASTM STP 942,* American Society for Testing and Materials, Philadelphia, 1988, pp. 94–106.
[54] Stout, M. G., Martin, P. L., Helling, D. E., and Canova, G. R., "Multiaxial Yield Behavior of 1100 Aluminum Following Various Magnitudes of Prestrain," *International Journal of Plasticity,* Vol. 1, 1985, pp. 163–174.
[55] Bannantine, J. A., Comer, J. J., and Handrock, J. L., *Fundamentals of Metal Fatigue Analysis,* Prentice-Hall, Englewood Cliffs, NJ, 1990, p. 246.
[56] Fash, J. W., Socie, D. F., and McDowell, D. L., "Fatigue Life Estimates for a Simple Notched Component under Biaxial Loading," *Multiaxial Fatigue, ASTM STP 853,* American Society for Testing and Materials, Philadelphia, 1985, pp. 497–513.
[57] Lee, S.-B., "A Criterion for Fully Reversed Out-of-Phase Torsion and Bending," *Multiaxial Fatigue, ASTM STP 853,* American Society for Testing and Materials, Philadelphia, 1985, pp. 553–568.
[58] Fatemi, A. and Kurath, P., "Multiaxial Fatigue Life Predictions under the Influence of Mean-Stresses," *Journal of Engineering Materials and Technology, Transactions,* American Society of Mechanical Engineers, New York, Vol. 110, 1988, pp. 380–388.
[59] Leese, G. E. and Morrow, J., "Low Cycle Fatigue Properties of a 1045 Steel in Torsion," *Multiaxial Fatigue, ASTM STP 853,* American Society for Testing and Materials, Philadelphia, 1985, pp. 482–495.
[60] Hashemi, H. N., "Failure Modes of Specimens Containing Surface Flaws under Cyclic Torsion," *Experimental Mechanics,* March 1987, pp. 51–56.
[61] Krempl, E., "The Influence of State of Stress on Low-Cycle Fatigue of Structural Materials: A Literature Survey and Interpretive Report," in *ASTM STP 549,* American Society for Testing and Materials, Philadelphia, 1974.

DISCUSSION

R. J. DiMelfi[1] *(written discussion)*—You evaluated a set of correlation parameters associated with one specific rolling process and consequent grain morphology. It would be interesting to see how these parameters depend on grain aspect ratio, for example. Do you have any idea or model for how this dependence would appear?

H. Lin and H. N. Hashemi (authors' closure)—We have not obtained any quantitative model relating the anisotropic coefficients M_{ij}, A_i, and B_i to the microstructure of the one-direction cold-rolled Al-6061-T6. Further research is needed to relate these coefficients to the material microstructure, such as grain aspect ratio and/or precipitates' spacing. The well-known Hall-Petch relationship [*1*] might be helpful when attempting to relate them. The correlation between material microstructure and the macroscopic properties of the material, i.e. yield stress, endurance limit, or fracture toughness, has been a subject of considerable interest and importance for many years. The effect of microstructure factors such as grain size, precipitates, inclusions, etc. on cyclic deformation and fatigue behavior has been investigated and

[1] Argonne National Laboratory, RE-207, Argonne, IL 60439.

reviewed [*1–4*], but the subject is not yet fully understood and only a few simple explanations are presented.

References

[*1*] Armstrong, R. M., "The Yield and Flow Stress Dependence on Polycrystal Grain Size," *Yield, Flow and Fracture of Polycrystals,* T. N. Baker, Ed., Applied Science Publishers, London, 1983, pp. 1–31.

[*2*] Taira, S., Tanaka, K., and Hoshina, M., "Grain Size Effect on Crack Nucleation and Growth in Long-Life Fatigue of Low-Carbon Steel," *Fatigue Mechanisms, ASTM STP 675,* American Society for Testing and Materials, Philadelphia, 1978, pp. 135–173.

[*3*] Stark, E. A. and Lutjering, G., "Cyclic Plastic Deformation and Microstructure," Fatigue and Microstructure, American Society for Metals, Metals Park, OH, 1978, pp. 205–243.

[*4*] Francois, D., "The Influence of the Microstructure on Fatigue," *Advances in Fatigue Science and Technology,* NATO ASI Series, Kluwer Academic Publishers, Dordrecht, The Netherlands, 1988, pp. 23–76.

Jerôme Weiss[1] *and André Pineau*[1]

Continuous and Sequential Multiaxial Low-Cycle Fatigue Damage in 316 Stainless Steel

REFERENCE: Weiss: J. and Pineau, A., **"Continuous and Sequential Multiaxial Low-Cycle Fatigue Damage in 316 Stainless Steel,"** *Advances in Multiaxial Fatigue, ASTM STP 1191,* D. L. McDowell and R. Ellis, Eds., American Society for Testing and Materials, Philadelphia, 1993, pp. 183–203.

ABSTRACT: Tension and torsion low-cycle fatigue tests were carried out on thin tubular specimens of 316 stainless steel, tested at both room temperature and 600°C. Two types of experiments were performed: (1) conventional continuous isothermal tests, and (2) isothermal sequential tests with different sequences of tension/compression and torsional loading. Most of these tests were carried out under air environment at the equivalent total strain amplitude of $\Delta\varepsilon_t/2 = \pm 0.80\%$ in tension or $\Delta\gamma_t/2 = \pm 0.80\sqrt{3}\%$ in torsion. Optical and scanning electron microscopy were used to analyze the failure modes, the orientation of microcracks and macrocracks which lead to failure, and crack density.

Continuous tests show two main results: (1) it is confirmed that, for the same equivalent von Misès strain, the fatigue lives in torsion are larger than those observed in tension; (2) detailed examinations of the microcracks' orientation showed that Stage I initiation followed by Stage II growth occurs only at room temperature or at elevated temperature under vacuum. At 600°C, however, Stage I crack initiation is bypassed due to the formation of external hematite (Fe_2O_3) and internal (Fe-Cr rich) oxides.

These results are used to explain qualitatively the significant deviations observed in the sequential tests from the Miner linear cumulative damage rule. A quantitative model based on a Monte Carlo simulation is developed to account for the results of sequential tests in which crack initiation and crack growth were coplanar. This model includes three fatigue damage laws: (1) a nucleation rate equation; (2) a push/pull or torsion crack growth law; and, (3) a criterion for crack coalescence. It is shown that this model is able to reproduce with good accuracy the results of sequential push/pull → torsion tests carried out at 600°C.

KEY WORDS: multiaxial fatigue, sequential tests, damage measurements, oxidation, Monte Carlo-type simulation

Nomenclature

$A, B, C, B_1, B_2, \alpha, \beta, \alpha', \omega_1, \omega_2$	Constants
a	Half crack length on surface
c	Crack depth
c_0	Initial crack length
c_F	Crack length at failure
D	Damage parameter ($D = N/N_F$ = number of applied cycles for a given loading mode/number of cycles to failure for the same loading)
N	Number of cycles
N_F	Number of cycles to failure

[1] Centre des Materiaux, Ecole des Mines, BP 87, 91003 Evry-Cedex (France).

N_i Number of cycles necessary to initiate the first microcrack
R_I, R_{II} Length of the influence zone for coalescence in Mode I and Mode II, respectively
γ Shear strain
ε Tensile strain
η Linear density of microcracks
θ Angle of the influence zone for coalescence
λ' Strain ratio ($\lambda' = \Delta\gamma_t/\Delta\varepsilon_t$)
σ Tensile stress
σ_R Tensile strength to failure
τ Shear stress
τ_R Shear strength to failure ($\tau_R = \sigma_R/\sqrt{3}$)
χ Surface density of microcracks

Subscripts

t total
p plastic

Introduction

Many components and structures are subjected to complex loading conditions which lead eventually to fatigue crack initiation and crack propagation. For a long time most of the studies dealing with fatigue damage have been limited to uniaxial, mainly tensile situations. Moreover, most of the multiaxial fatigue studies have been carried out in the regime corresponding to the fatigue limit. In the past two decades, the regime associated with low-cycle fatigue (LCF) has received increased attention. It is usually observed that at room temperature in the absence of any pronounced environmental effects for the same applied von Misès equivalent plastic strain amplitude, the fatigue life under torsion loading is larger than that determined under push/pull conditions (see, for example, Ref *1*). It is also usually observed that the most damaging loading is that corresponding to 90° out-of-phase multiaxial low-cycle fatigue. Typically in austenitic stainless steel it has been shown that the fatigue life may be reduced by a factor as large as 10 (see, for example, Ref *2*). A limited number of studies have been devoted to the multiaxial LCF behavior of materials tested at elevated temperature, this in spite of the fact that it is well accepted that oxidation can significantly modify the fatigue damage micromechanisms (see, for example, Ref *3*).

A wide variety of correlations between the mechanical loading parameters and the fatigue life have been proposed (see, for instance, recent studies on austenitic stainless steels [*4*,*5*]). For many investigators, however, it is now clear that the most promising way of tackling the problem of life prediction is to take into account the directional aspect of fatigue damage instead of fitting endurance curves with any kind of an equivalent loading parameter. One of the best methods to study the directional aspect of fatigue damage is to carry out sequential LCF experiments. For instance, push/pull loading followed, during the second part of the sequence, by torsional loading (or the opposite) can be extremely detrimental to fatigue life and can thus lead to a cumulative damage much different from that expected by considering each loading type separately (see, for example, Ref *6*). An understanding of this type of behavior lies in the knowledge of the orientation and shape aspects of cracks which differ from one stress state to another. Qualitatively it is easily understood that shear cracks nucleated during the torsion loading can easily propagate by Mode I growth during the push/pull loading when applied as the second part of the sequence. At elevated temperature, however, the situation

may be quite different because of the presence of an oxide film at the free surface of the specimen. This temperature influence is one of the reasons why, in the present work, an attempt is made to investigate in detail the directional aspect of fatigue damage in a widely used material, i.e., 316 L stainless steel, at both room temperature and 600°C.

The aims of the present work are: (1) to study the effects of sequential multiaxial LCF loading on damage behavior; (2) to study the influence of multiaxial loading on the fatigue damage mechanisms, in particular in relation to the effect of stress-assisted oxidation; (3) to develop a model based on a Monte Carlo–type simulation to account for the effect of sequential LCF loading by using the results of quantitative metallography concerning crack density, length, and orientation.

Material and Experimental Procedures

The material investigated is a 316 stainless steel with a low carbon content and a controlled content of nitrogen. The chemical composition is given in Table 1. This heat is very similar to another 316 stainless steel which was thoroughly investigated in a previous study [*7*]. An annealing treatment was applied at 1100°C for 90 min, followed by water quenching. This produced an average grain size of 50 μm. Tubular specimens with an outer diameter of 19.5 mm and a wall thickness of 1.5 mm were mechanically polished using 3-μm diamond paste. Details of specimen preparation are found in Refs *8* and *9*.

Fatigue tests were carried out using a servohydraulic tension-torsion machine under strain-control conditions with a sinusoïdal fully reversed waveform at a frequency of 0.05 Hz. Axial and shear strain amplitudes were measured with a biaxial mechanical extensometer. A radiation furnace was used for the tests carried out at 600°C. The longitudinal temperature gradient along the gage length of the specimens was maintained at less than 2°C. Data acquisition was performed on X-Y recorders and by microcomputer. Further data processing permits the calculation of the von Misès equivalent stress and strain amplitudes. The method used to calculate these amplitudes for out-of-phase loading is described elsewhere [*8,9*].

Both continuous and sequential fatigue tests were performed. Sequential tests included two independent successive phases with different types of loading. During the first phase a variable percentage of the fatigue life is applied with a given loading mode (for example, push/pull), followed by another type of loading (for example, fully reversed torsion) applied to failure.

Both optical and scanning electron microscopy (SEM) observations were made on the free surface of the specimens on longitudinal sections and on fracture surfaces. Microprobe analysis was also used to determine the composition of the oxides formed at the free surface of the specimens tested at elevated temperature.

Results of Mechanical Tests

Figures 1 and 2 show that, at both room temperature and 600°C, the fatigue life of specimens tested under fully reversed torsion is much larger than that of specimens tested under push/pull conditions. These results confirm those which were obtained previously on the same material at room temperature [*10,11*]. Figure 1 also includes the results of two additional tests which were carried out in order to determine the effect of oxidation. In the first test, the spec-

TABLE 1—*Chemical composition of the investigated steel (wt%).*

C	S	P	Si	Mn	Ni	Cr	Mo	N	B	Co	Cu	Al
0.021	0.007	0.033	0.41	1.74	12.27	17.18	2.40	0.080	0.0032	0.21	0.15	0.040

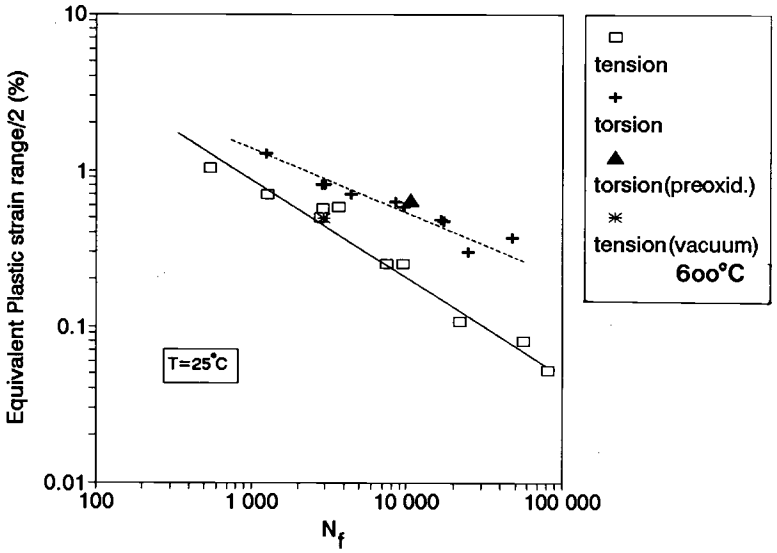

FIG. 1—*Tension-compression and torsional fatigue life at room temperature. The results of further tests are indicated: (1) torsional life of a preoxidized specimen and (2) push/pull life of a specimen tested at 600°C under vacuum.*

imen was preoxidized at 600°C without any applied strain for 4 h before being tested under fully reversed torsion at room temperature. It is observed that this high-temperature exposure produced no significant effect on the fatigue life, thus suggesting that air environment and mechanical deformation have to be applied simultaneously in order to generate a detrimental environmental effect. In the second test, the material was tested at 600°C under push/pull load-

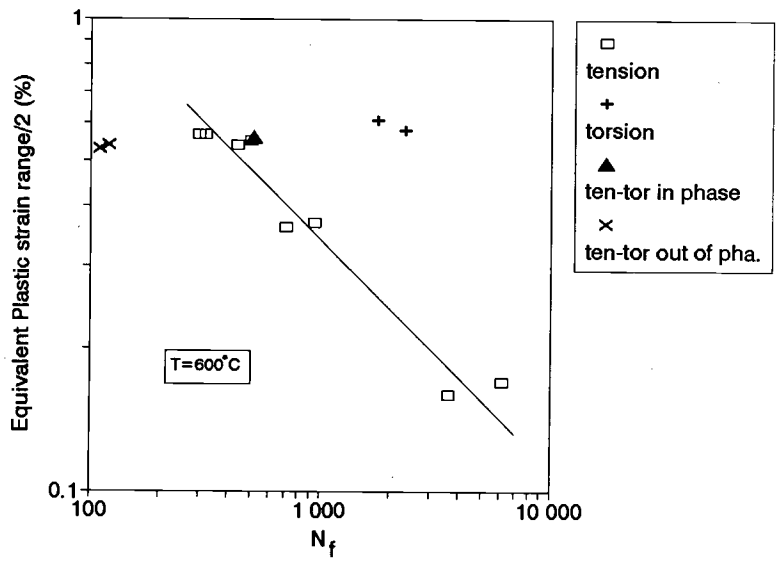

FIG. 2—*Fatigue life at 600°C under air environment. Comparison between various types of loading: tension-compression, torsion, in-phase tension-torsion* ($\Delta\gamma_t/\Delta\varepsilon_t = \sqrt{3}$) *and 90° out-of phase tension-torsion* ($\Delta\gamma_t/\Delta\varepsilon_t = \sqrt{3}$).

ing ($\Delta\varepsilon_p/2 = \pm 0.55\%$) and vacuum ($5 \cdot 10^{-6}$ torr) [*12*]. Under these conditions, the fatigue life is found to be the same as that determined at room temperature. This clearly indicates that the reduction in fatigue life observed when the test temperature is increased from room temperature to 600°C is essentially due to an environmental effect, as already reported in a previous study [*12*].

Figure 2 shows the results of multiaxial tests carried out at 600°C under both in-phase and 90° out-of-phase loading and with $\lambda' = \Delta\gamma_p/\Delta\varepsilon_p = \sqrt{3}$. It is observed that in-phase tension-torsion loading has no significant difference to the uniaxial fatigue life. This observation is similar to that found at room temperature on a ferritic steel [*9*] and a 13% Cr steel [*13*]. On the other hand, as observed by other investigators (see, for example, Ref *2*), the fatigue life is greatly decreased when 90° out-of-phase tension-torsion loading is applied.

The results of sequential LCF tests carried out at room temperature and at 600°C are given in Figs. 3 and 4, respectively. In these tests the total strain amplitude, $\Delta\varepsilon_t/2$ was $\pm 0.80\%$ ($\Delta\gamma_t/2 = \pm 1.38\%$), which corresponds to a plastic strain amplitude, $\Delta\varepsilon_p/2$ of $\pm 0.55\%$ ($\Delta\gamma_p/2 = \pm 1.02\%$). Large deviations from the Miner linear cumulative damage rule are observed in Figs. 3 and 4. At room temperature, the remaining push/pull fatigue life is significantly reduced by initial torsional fatigue. This result is similar to that observed by other investigators (see, for example, Ref *6*). On the other hand, prior cycling under push/pull conditions has much less effect on the remaining torsional life, a behavior similar to that observed by other investigators (see, for instance, Refs, *6*, *13*, and *14*). Figure 4 shows that at 600°C an opposite behavior is observed since $D_1 + D_2$ is much lower for push/pull → torsion sequence loading than for torsion → push/pull. In particular, it is worth noting that the torsional remaining life is almost negligible when the damage introduced during the first sequence loading reaches a value close to 0.50. Here it should be mentioned that the damage parameters, D_1 and D_2, were calculated by using the results shown in Figs. 1 and 2 as base lives in terms of plastic strain amplitudes. These base lives were taken as follows. At room temperature, $N_F = 3250$ for $\Delta\varepsilon_p/2 = \pm 0.58\%$, and $N_F = 9600$ for $\Delta\gamma_p/2 = \pm 1.10\%$. At 600°C, $N_F = 300$ for $\Delta\varepsilon_p/2 = \pm 0.56\%$, and $N_F = 2000$ for $\Delta\gamma_p/2 = \pm 1.02\%$.

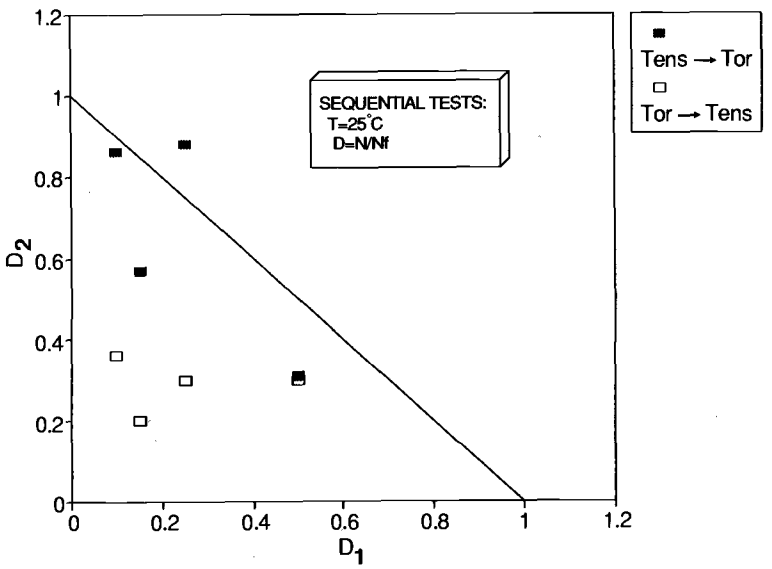

FIG. 3—*Cumulative fatigue damage at 25°C for tension → torsion and torsion → tension sequential loadings.*

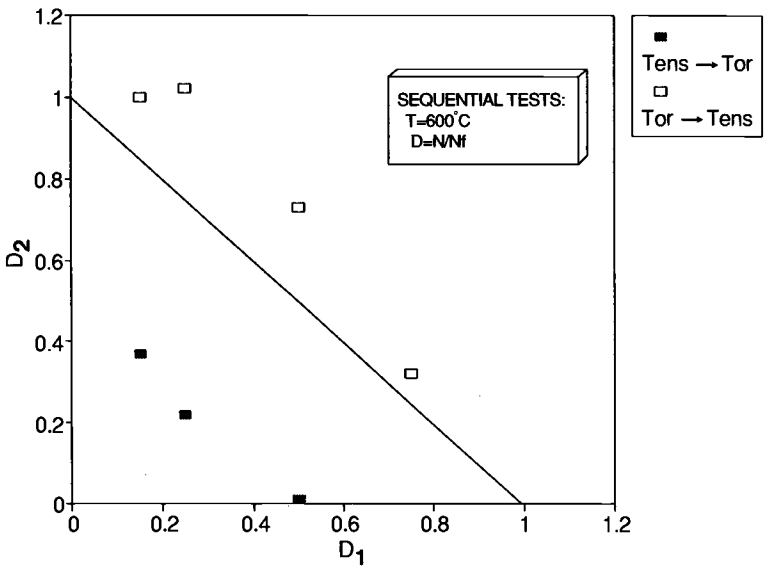

FIG. 4—*Cumulative fatigue damage at 600°C for tension → torsion and torsion → push/pull sequential loadings.*

It is well known that, in stainless steel tested in particular at room temperature, prior strain cycling under given conditions can have a significant effect on the stress response measured during the second cycling sequence when the material is tested under different conditions (see, for example, Ref *10*). It was also observed that small-strain-history effects exist, especially during the first few cycles of the second cyclic loading. A detailed description of these effects is beyond the scope of the present paper. In all tests, the stabilized cyclic stress-strain curves associated with the second cycling were not noticeably affected by prior cyclic deformation, such that damage calculations in terms of stress instead of plastic strain lead to conclusions similar to those shown in Figs. 3 and 4.

Microstructural Observations

Fatigue damage is associated with a population of transgranular microcracks nucleated at the free surface of the specimens. These microcracks coalesce and propagate as a main crack. Detailed observations were made to characterize the orientation of these microcracks and their density in order to model the results of mechanical tests.

Microcrack Orientation at Crack Initiation

In order to determine the statistical distribution of microcrack orientation, observations were made both on the free surface (inner and outer diameter of tubular specimens) and on a longitudinal section of continuously cycled specimens, as indicated in Fig. 5. The results of these observations made on microcracks which have a length on the order of one grain size ($\simeq$50 μm) are given using the representation shown in Figs. 6, 7, and 8, where the ratio of the number of microcracks measured in various directions is drawn. This is useful to define the relative orientation of the fatigue microcracks observed on both surfaces.

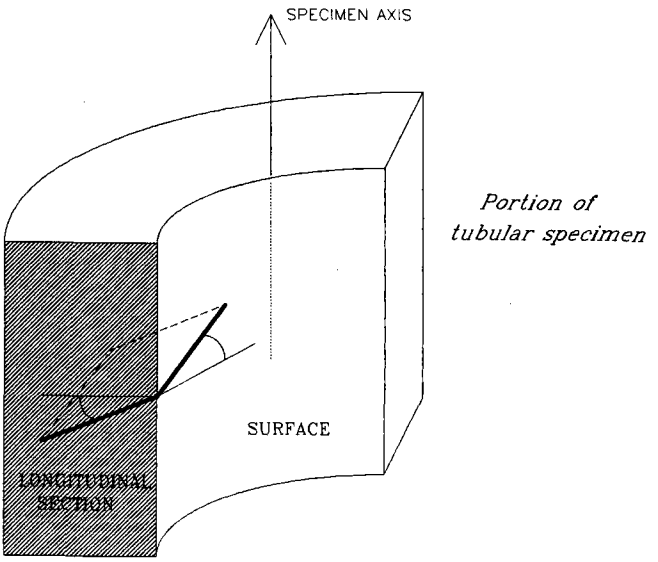

FIG. 5—*Sketch showing the orientations of fatigue microcracks measured on a specimen free surface and on a longitudinal section.*

At room temperature, microcracks initiate on maximum shear planes (Figs. 6*a* and 8*a*) which correspond to Stage I crack initiation, while, at elevated temperature under air environment, the situation is completely different since microcracks nucleate under opening mode (Figs. 6*b* and 8*b*). Furthermore, Fig. 7 shows that, at 600°C under vacuum, crack initiation under push/pull conditions occurs under shear mode loading since both Types A and B orientations (using the terminology introduced by Brown and Miller [*15*]) are observed. Thus, at elevated temperature, Stage I crack initiation is bypassed due to environmental effects.

In the absence of any deformation, at elevated temperature under an oxidizing environment like air, a very thin protective [chromite (Cr_2O_3)] oxide layer is formed at the free surface of austenitic stainless steels. The growth of this protective layer is described by a parabolic kinetics law [*16,17*]. The presence of this Cr_2O_3 oxide film seems to have no effect on crack initiation when the material is tested at room temperature. Figure 1 shows the result of a test carried out on a preoxidized specimen. A number of observations were made on the free surface of LCF specimens tested at elevated temperature which show that, under cyclic deformation, the situation is altered significantly. It was observed that the nature of the oxides was different and that the kinetics of oxidation were also markedly modified by cyclic deformation. The present study concentrates only on the types of oxides which were observed as films with a thickness typically as large as 20 to 30 μm.

Two types of oxide, different from Cr_2O_3, were identified on the LCF specimens: (1) an external layer of Fe_2O_3 oxide (hematite) (Figs. 9 and 10); (2) internal oxidation leading to the formation of complex Fe-Cr oxides (Fig. 10). Atomic compositions of both types of oxide determined by microprobe analysis are given in Table 2. It is worth noting that nickel does not appear to be oxidized. Preferential internal and external oxidation often takes place close to microcracks, as shown in Fig. 9, but not exclusively. In a number of circumstances oxide flakes are observed independent of the formation of microcracks. Actually, internal and external oxidation processes seem to occur before microcrack formation and not the reverse. The importance of cyclic plasticity on oxide formation is clearly illustrated in Fig. 10, where preferential

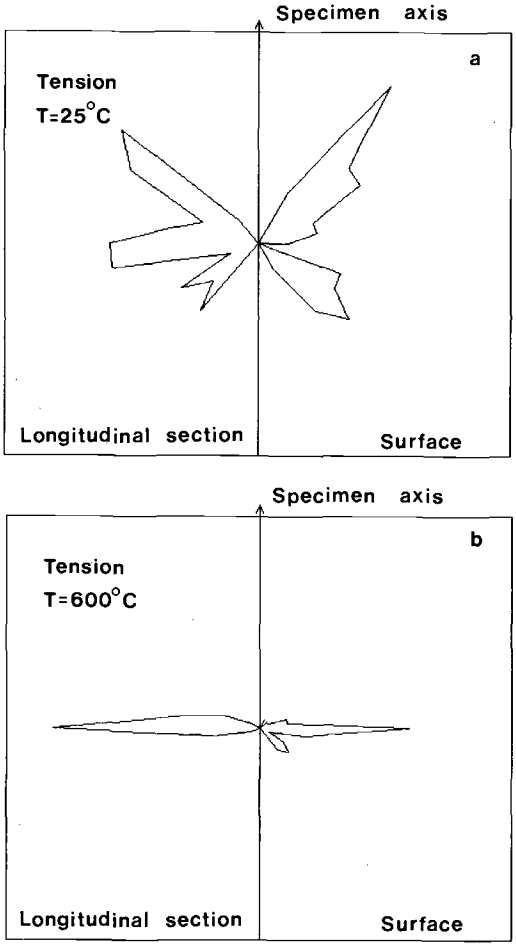

FIG. 6—*Orientations of microcracks determined on specimen free surfaces and on longitudinal sections for push/pull tests* ($\Delta\varepsilon_p/2 = 0.55\%$) *at room temperature* (a) *and at 600°C* (b).

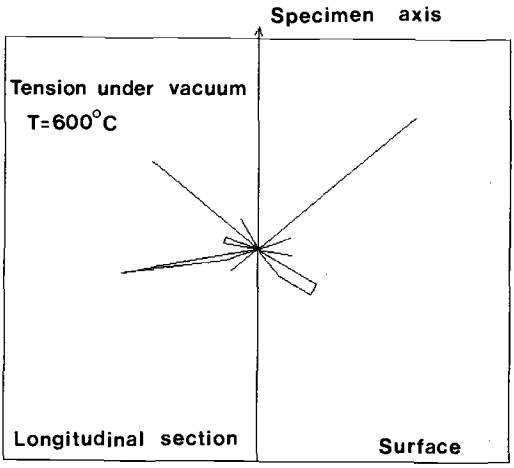

FIG. 7—*Orientations of microcracks measured on an LCF specimen tested under tension-compression* ($\Delta\varepsilon_p/2 = 0.50\%$) *at 600°C under vacuum.*

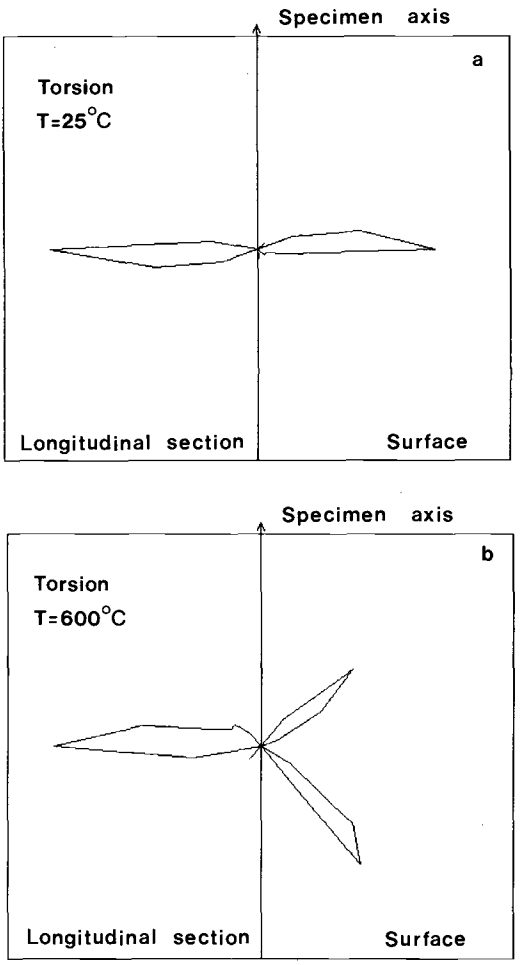

FIG. 8—*Microcracks orientations observed on torsional LCF specimens* ($\Delta\gamma_p/2$ = *1.05%) tested at room temperature* (a), *or at 600°C* (b).

growth of the internal Fe-Cr oxide is observed to take place along intense slip bands acting as diffusion short circuits for iron and chromium [*18*].

The relatively thick ($\simeq 30\ \mu$m) external layer of Fe-Cr oxide is brittle, as indicated by Schütze [*19,20*]. It can therefore break under opening mode, as shown in Fig. 9 for a torsional test, leading to the formation of a microcrack which eventually propagates into the metal. This interpretation is in good agreement with the results of microcrack orientations reported in Figs. 6*b* and 8*b*.

Preferential Crack Orientation during Crack Propagation

The initiation stage of fatigue damage, associated with the nucleation of microcracks, is not drastically dependent on loading type because it is essentially controlled by shear modes. It is, however, strongly dependent on temperature through environmental effects as described in

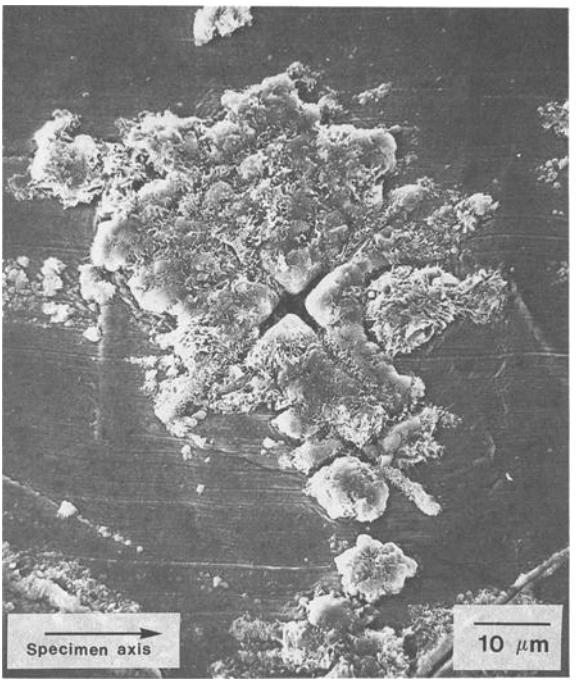

FIG. 9—*SEM observation showing oxide formation at the free surface of a torsional LCF specimen* ($\Delta\gamma_p/2$ = *1.05%) tested at 600°C. Crack initiation along the directions corresponds to maximum principal tensile stress.*

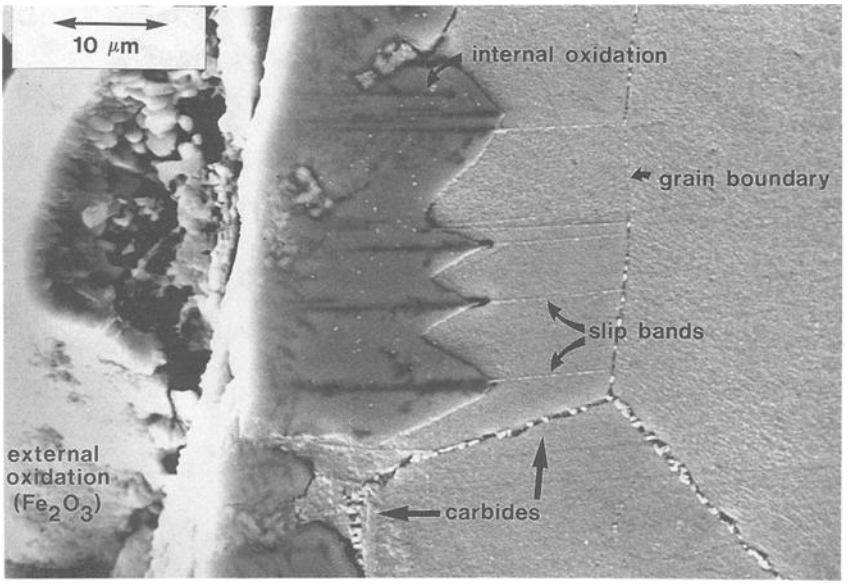

FIG. 10—*SEM observation of a longitudinal section of a torsional LCF specimen* ($\Delta\gamma_t/2 = \pm 1.38\%$) *tested at 600°C showing preferential internal oxidation along intense slip bands.*

TABLE 2—*Oxide chemical analysis determined by microprobe analysis (atomic %).*

	O	Fe	Cr	Ni	Mn	Mo
External oxidation	58.9	40.0	0.6	0.4	0.1	...
Internal oxidation	53.5	13.0	29.0	3.1	...	1.4

the previous section. The situation is opposite for the stage of fatigue damage corresponding to macrocrack propagation. It is now well established that for proportional loadings the preferential orientation of macroscopic cracks depends only on the strain ratio $\lambda' = \Delta\gamma_p/\Delta\varepsilon_p$. Macroscopic cracks propagate along maximum shear planes only for large values of the λ' ratio. Otherwise they propagate essentially under opening Mode I (see, for example, Ref *21*). Hence, in a number of circumstances microcracks have to bifurcate between their initiation and their subsequent growth. This is the situation observed for continuous push/pull fatigue at room temperature and continuous torsional LCF at 600°C. At the present time, there is no theory that models in a comprehensive manner all the details related to the crack bifurcation phenomenon. However, these remarks on the existence of easy crack propagation planes can be used, in addition to our observations on microcrack orientation, to explain qualitatively the results of sequential multiaxial LCF tests reported in Figs. 3 and 4.

At room temperature, it is not surprising to observe that prior torsional LCF produces a large detrimental effect on the subsequent push/pull fatigue life (Fig. 3) since shear microcracks due to torsional loading (Fig. 8*a*) are located in the plane corresponding to easy propagation for tensile cracks. Similarly, at elevated temperature, microcracks initiated during push/pull fatigue are located along preferential propagation planes for shear cracks (Fig. 6*b*). This explains qualitatively the fact that, in both cases, $D_1 + D_2$ is lower than 1. On the other hand, at elevated temperature, Mode I torsional microcracks observed in Fig. 8*b* have to bifurcate or a new population of Mode I microcracks has to be initiated corresponding to tensile loading when the torsion → push/pull sequence is applied. This explains also, at least qualitatively, the fact that after this type of sequence (or after the push/pull → torsion sequence at room temperature) $D_1 + D_2$ is larger than 1.

A Quantitative Model for Sequential Multiaxial LCF Life

The model which will be described in detail in this section is based on a simulation of crack initiation, subsequent crack growth, and crack coalescence. It applies only to situations in which no crack bifurcation between initiation and macroscopic propagation is observed, that is, the push/pull → torsion sequence at elevated temperature and the torsion → push/pull sequence at room temperature. This limitation, as explained earlier, is related to the difficulties encountered when crack extension is no longer coplanar. The laws for crack initiation and for crack growth are derived from the results of metallographical observations which are presented first before describing the numerical simulation used in the model.

Crack Initiation Laws

These laws were derived from the measurement of the linear density, η, of secondary cracks observed on polished longitudinal sections of specimens. This linear density is converted into a surface density, χ, by using simple stereological relations. Additional details are given in the Appendix. The surface density, χ, of microcracks which are larger than 50 μm is written as

$$\chi(N) = \chi_0 x(N - N_i) \tag{1}$$

where N is the number of applied cycles and N_i is the number of cycles necessary to initiate the first 50-μm crack. At 600°C, it was assumed that $N_i = 0$, which is probably a conservative assumption but which may not be too far from reality because of the strong environmental effect discussed earlier. At room temperature, a relationship obtained previously for 316 stainless steel and based on an experimental correlation between N_i and the number of cycles to failure, N_F, was used [*11*]. In Eq 1, the factor χ_0 was found to be an increasing function of plastic strain amplitude, $\Delta\varepsilon_p/2$, for push/pull tests and was expressed as

$$\chi_0 = B(\Delta\varepsilon_p/2)^4 \tag{2}$$

where B is a constant equal to $8 \cdot 10^{-7}$ (units: $\Delta\varepsilon_p$ in %, χ_0 in μm^{-2}). This expression applies to tests carried out at 600°C. For shear mode loading at room temperature, it was found that

$$\chi_0 = \text{constant} = 8 \cdot 10^{-9} \tag{3}$$

independent of the applied plastic shear strain amplitude, $\Delta\gamma_p/2$, at least in the relatively small range of $\Delta\gamma_p/2$ values which was investigated ($0.80\% < \Delta\gamma_p/2 < 1.40\%$). Further work is necessary to investigate the effect of plastic shear strain amplitude on the nucleation rate of shear microcracks.

Crack Growth Laws

Two methods described elsewhere [*7*] were used to derive crack propagation laws. The first one, which applies essentially to push/pull LCF tests, relies upon measurements of striation spacings on the fracture surfaces as a function of the depth of the main crack, c. In this method it is assumed that the striation spacing is equal to the macroscopic crack growth rate, dc/dN. Tests at various plastic strain amplitudes, $\Delta\varepsilon_p/2$, led to the following expression

$$dc/dN = A(\Delta\varepsilon_p/2)^\alpha c^\beta \tag{4}$$

where $\alpha = 1.5$, $\beta = 1.45$, $A = 6.8 \cdot 10^{-4}$ at 25°C, and $A = 3.1 \cdot 10^{-3}$ at 600°C (units: c and dc/dN in μm, $\Delta\varepsilon_p$ in %).

The second method was applied to torsional tests since no striations were observed for shear loading. This method is based, as described in the Appendix, on measurements of crack depth histograms on longitudinal sections. The observation of secondary cracks showed that the crack front can be considered to adopt a semi-elliptical shape with an aspect ratio q = small axis length/large axis length = c/a equal to 1 for push/pull conditions and equal to 0.5 for shear mode loading. These determinations of crack depth were used for the assessment of the in-depth crack growth rate, dc/dN, under pure torsion, which was expressed as

$$dc/dN = C(\Delta\gamma_p/2)^{\alpha'} c^{\beta'} \tag{5}$$

where $\alpha' = 3.7$, $\beta' = 2.6$, and $C = 5.8 \cdot 10^{-8}$ at room temperature, with the same units as those used in Eq 4 (Fig. 11).

A Two-Dimensional Simulation of Sequential Multiaxial LCF Damage

A simplified 2D Monte Carlo–type simulation was developed to model sequential LCF tests in which no crack bifurcation effect was observed between both phases of the sequence, that

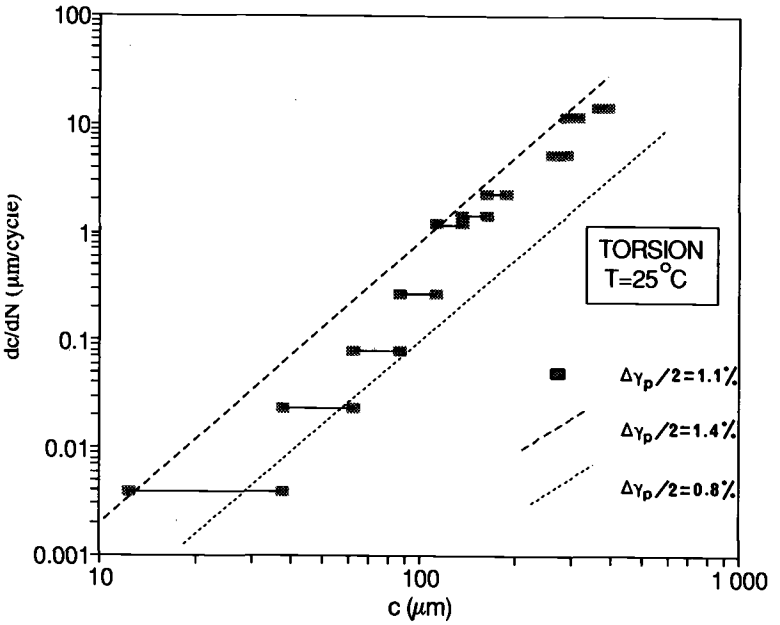

FIG. 11—*Results of crack growth rate measurements under shear mode loading at room temperature using histograms of secondary cracks lengths.*

is, those which produced a cumulative damage lower than 1. A 2D representation was adopted for the sake of simplicity. In this model, the "matrix" is represented by a set of grains with a mean size of 50 μm. The grain size can easily be changed. Simulations were made with matrixes of 1250 grains and 16 · 10^3 grains. This method can therefore be used to investigate size effects on fatigue life. In the present paper, only preliminary results are presented. A larger account of the results are given elsewhere [*22*].

In this simulation, microcracks of 50-μm length are nucleated randomly with a nucleation rate given by Eq 1, then propagate according to Eq 4 for tensile loading or Eq 5 for shear loading, and eventually coalesce to form a macroscopic crack leading to final fracture. Note that our simulation is different from the calculations presented by Hoshide and Socie [*23*]. These authors used a dislocation model to compute the nucleation of cracks within individual grains. Moreover, in their model, both Mode I and mixed mode growth were simulated using the concept of an equivalent strain-intensity factor. In our simulation, the only stage of fatigue damage which is unknown is that corresponding to crack coalescence, since crack nucleation and crack growth are simulated using experimental laws. In our model, an "influence zone" was associated with each crack tip to simulate crack coalescence. This zone was modeled as a triangular sector of angle θ (30°), with the apex located at the crack tip and with a height R measured in the direction parallel to the crack plane. Coalescence is assumed to take place when the influence zones corresponding to two neighboring cracks are intersecting. It was assumed that the length of the influence zone, R, was proportional to the length of each individual crack, a, and to the square of the applied stress. This type of expression was adopted because it corresponds to the Dugdale-Barenblatt plastic zone size. Thus, under Mode I loading, the influence zone, R_I, was written as

$$R_I = \omega_1 a(\sigma/\sigma_R)^2 \tag{6}$$

where σ is the applied tensile stress, σ_R is the strength to failure (σ_R = 1500 MPa), and ω_1 is a constant which was taken as equal to 0.42. This value was adopted to fit, with reasonable accuracy, the results of continuous push/pull tests at 600°C. Similarly, the influence zone for shear mode loading, R_{II}, was expressed as

$$R_{II} = \omega_2 a(\tau/\tau_R)^2 \tag{7}$$

where τ_R is the shear strength to failure ($\tau_R = 1500/\sqrt{3} = 870$ MPa). It was observed that, in order to represent with good accuracy the results of torsional LCF tests at room temperature, the value of ω_2 should be taken much larger than ω_1 and equal to $\sim 14\omega_1 = 5.88$. This strongly suggests that crack coalescence occurs much more easily under shear mode loading than under tensile loading. An example of the dramatic effect of crack coalescence under shear mode loading is given in Fig. 12. This micrograph shows the damage at failure observed on the surface of an LCF specimen tested at 600°C under sequential push/pull ($\Delta\varepsilon_p/2 = \pm 0.55\%$) → torsion ($\Delta\gamma_p/2 = \pm 0.95\%$) loading. The specimen which was initially subjected to $N_1 = 150$ cycles of tensile LCF ($D_1 = 0.50$) was able to tolerate only $N_2 = 25$ cycles under torsional loading, leading to an extremely low value for the second damage, D_2 of the order of 1%. Analytical and numerical calculations similar to those published recently for monotonic loading would

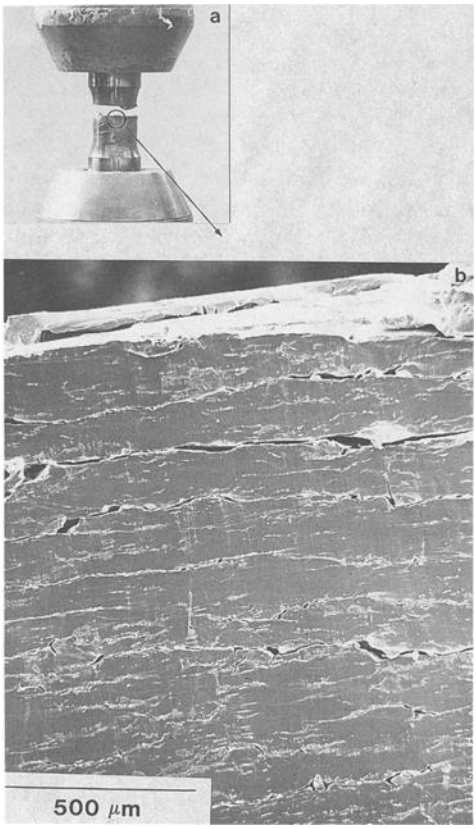

FIG. 12—*Sequential push/pull → torsion test carried out at 600°C:* (a) *macroscopic aspect of the main shear crack;* (b) *Details observed on the specimen surface.*

be useful to understand this localization of plastic deformation in shear due to the presence of microcracks [*24*].

Examples of the results obtained from this 2D simulation are given in Fig. 13 where the effect of the number of microcracks initiated by push/pull loading applied at elevated temperature on the propagation and the subsequent coalescence of shear cracks is clearly observed. The application of this simulation to continuous push/pull tests at 600°C and continuous torsion tests at 25°C is shown in Fig. 14 where good agreement between the experimental and the simulated fatigue life is observed. This agreement is partly due to the choice of the parameters ω_1 and ω_2, which can be considered as adjustable parameters at this stage. The application of the model to sequential LCF tests is more convincing. This is illustrated in Fig. 15 for the push/pull ($\Delta\varepsilon_p/2 = 0.55\%$) → torsion ($\Delta\gamma_p/2 = 0.95\%$) sequence, which was shown to produce a large deviation from the Miner linear cumulative damage rule (Fig. 4). Figure 15 shows that our simulation also reproduces reasonably well the observed behavior. A similar conclusion was reached for the torsion → push/pull sequence loading applied at room temperature [*22,25*]. More details are given elsewhere, where the scatter in the results of numerical simulations and the size effect associated with the number of simulated grains is analyzed [*25*].

Conclusions

1. For the same equivalent von Misès strain, the life under continuous cyclic torsion is larger than that of the push/pull loading at both room temperature and 600°C. At elevated temperature, the in-phase tension-torsion life is similar to the push/pull life, whereas 90° out-of-phase tension-torsion loading with $\lambda' = \Delta\gamma_t/\Delta\varepsilon_t = \sqrt{3}$ produces a significant reduction in fatigue life.

2. At room temperature, sequential torsion → tension-compression tests lead to fatigue lives much lower than those calculated using the simple Miner linear cumulative damage rule, while sequential tension-compression → torsion tests are much less damaging. At 600°C, the opposite is observed.

3. At elevated temperature, oxide formation at the free surface of specimens is considerably altered by cyclic deformation. An external layer of Fe_2O_3 oxide is formed. An internal layer of Fe-Cr rich oxide is observed to grow preferentially along intense slip bands acting as diffusional short circuits.

4. Observations of the orientation of the microcracks initiated from the free surface of the specimens show that Stage I crack initiation is bypassed by stress-assisted oxidation.

5. The results of sequential LCF tests are explained qualitatively by considering the orientations of the planes associated with crack initiation and crack growth. Sequential tests produce fatigue lives much lower than those calculated using the Miner linear cumulative damage rule when the extension of the fatigue cracks is coplanar from crack initiation to crack growth. Otherwise, fatigue lives larger than those expected from the same rule are observed when crack bifurcation takes place from crack initiation to macroscopic crack propagation.

6. A two-dimensional quantitative model based on a Monte Carlo–type simulation reproduces with good accuracy the results of tests in which no crack bifurcation is taking place between crack initiation and crack growth. In this model, a nucleation law and a crack growth law established from the results of quantitative metallography are introduced. Crack coalescence is simulated with a technique based on the concept of plastic zones associated with the tips of each microcrack. The results of these simulations suggest that crack coalescence occurs much more easily under shear than under tension.

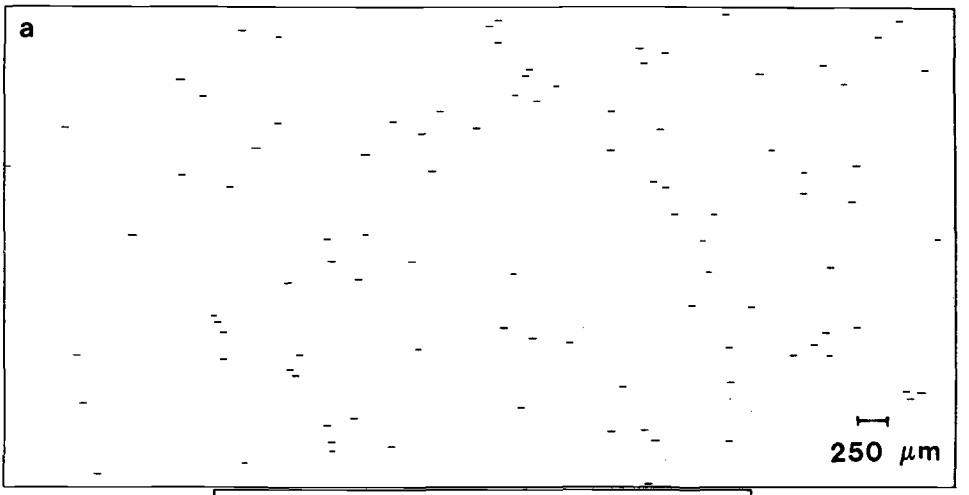

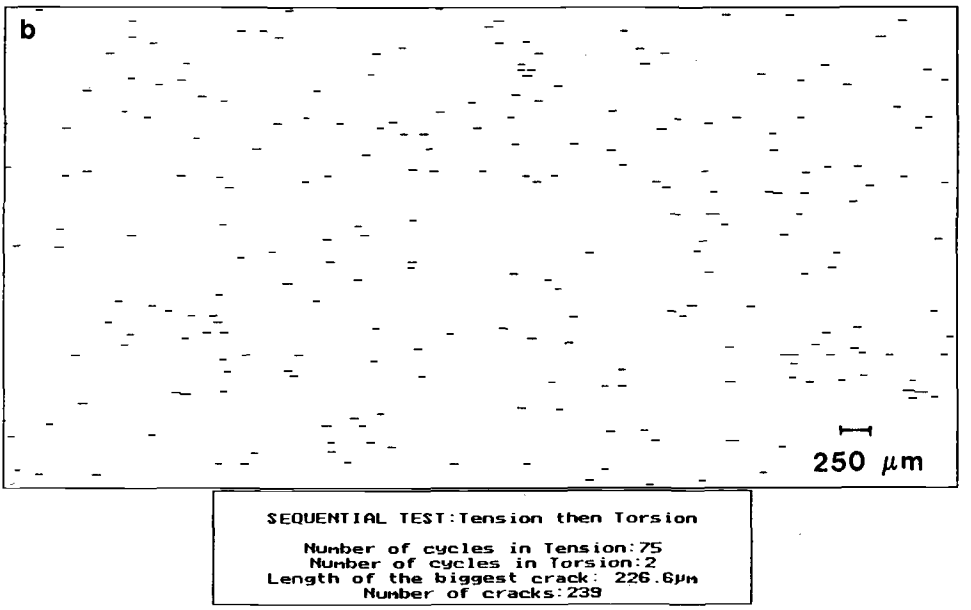

FIG. 13—*Monte Carlo–type simulation of a sequential push/pull ($\Delta\varepsilon_t/2 = \pm 0.80\%$) → torsion ($\Delta\gamma_t/2 = \pm 1.38\%$) LCF test. The specimen axis is vertical. The number of cracks and length of the longest crack after various cycling sequences are indicated.*

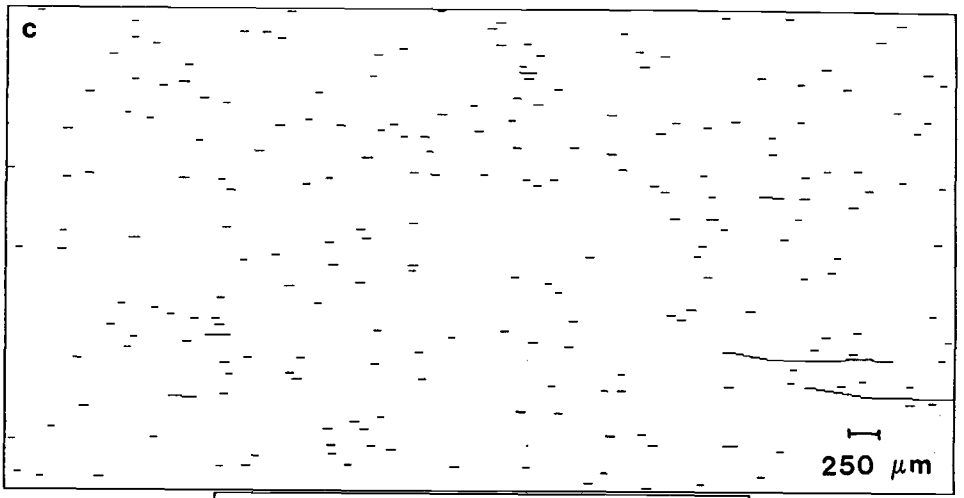

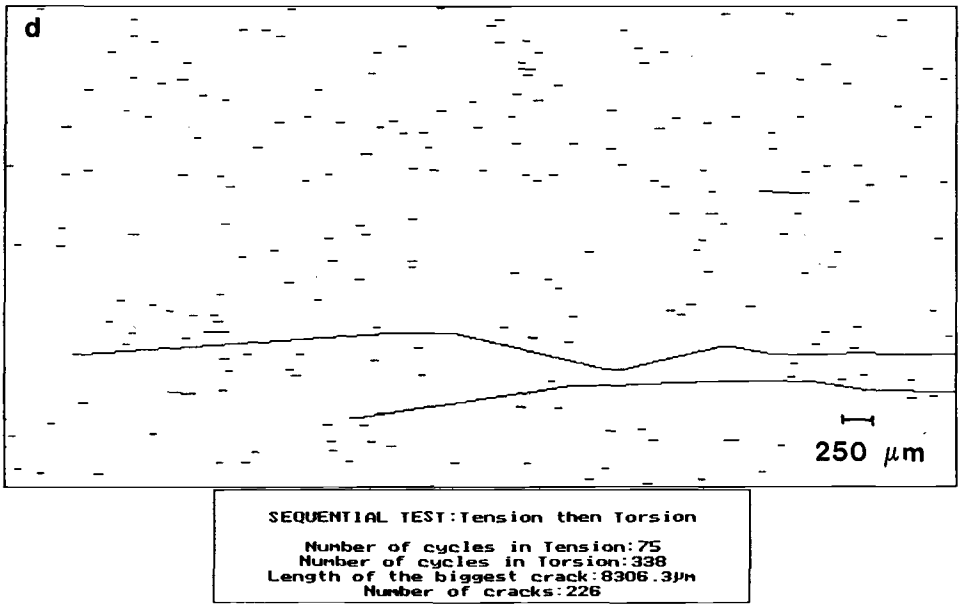

FIG. 13—*Continued.*

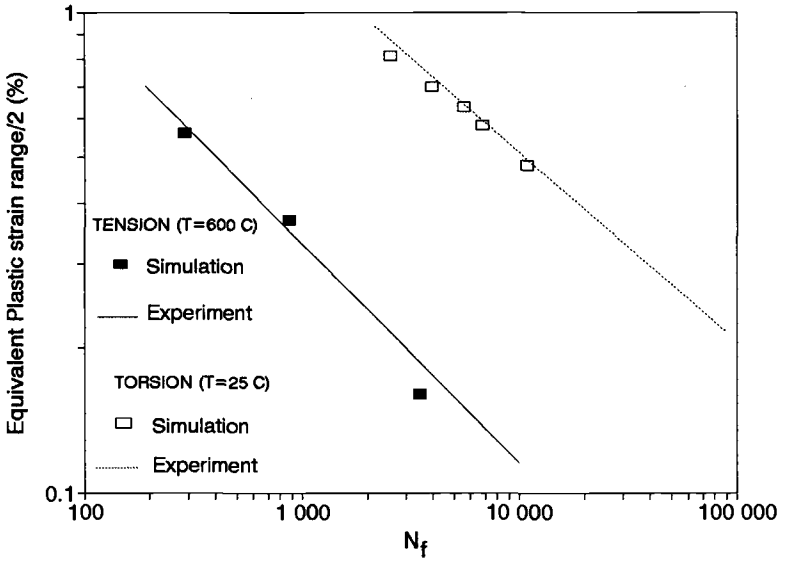

FIG. 14—*Comparison of measured and simulated fatigue lives at 600°C under tension-compression loading and at room temperature under torsional loading.*

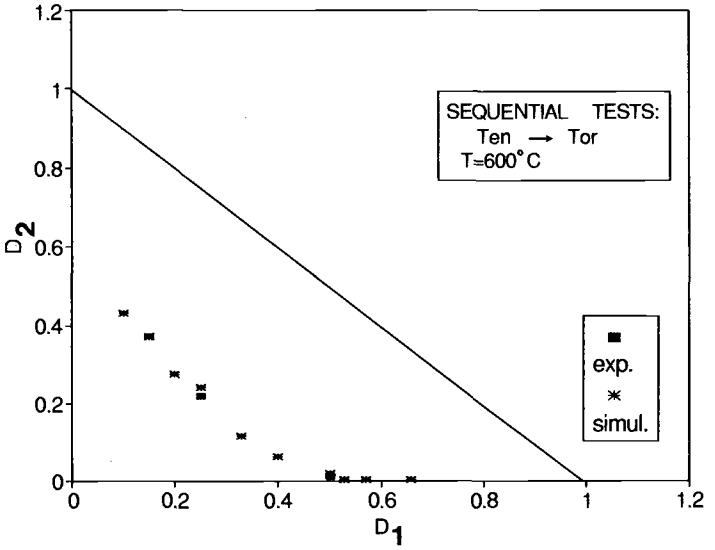

FIG. 15—*Comparison of measured and simulated fatigue lives for sequential push/pull → torsion LCF at 600°C.*

Acknowledgments

Financial support from the "Service Central de la Sûreté des Installations Nucléaires" (SCSIN) is acknowledged.

APPENDIX

Determination of Crack Densities Law and Crack Growth Laws From the Analysis of Histograms of Crack Depth on Longitudinal Sections

In LCF specimens tested at elevated temperature, direct measurement of the surface density of microcracks from surface observations is not easy because of the presence of an oxide layer on the free surface. On the other hand, secondary microcracks can be observed on a longitudinal polished section. The size distribution of these cracks can be characterized by histograms representing the linear density, η, as a function of crack size, as explained in a previous study [7]. The linear density is defined as the number of cracks per unit length on a longitudinal section along the specimen axis. These histograms can be used to determine the fatigue crack growth rate.

The depth of each microcrack is measured at high magnification ($\sim \times 400$). The results are reported using class interval Δ ($\Delta = 50\ \mu$m). Linear densities, η_i, are calculated for each class. The crack fronts are assumed to have a semi-elliptical shape with an aspect ratio $q = c/a$, where a is the semi-length of the long axis of the ellipse at the external surface. The surface density, χ, is then determined from linear density using a simple stereological relation [26], i.e.

$$\chi = \eta/a \tag{A1}$$

Thus for the class corresponding to the interval, i, the surface density is given by

$$\chi_i = q\eta_i/c_i \tag{A2}$$

It can be assumed that the total surface crack density, χ, increases linearly with the number of fatigue cycles, i.e.

$$\chi(N) = \chi_0 x(N - N_i) \tag{A3}$$

where N_i is the number of cycles necessary to initiate the first microcrack which has a length of 50 μm. This assumption was verified in a previous work devoted also to 316 stainless steel [27]. In the present study, the validity of this assumption was verified by: (1) measurements of crack densities on a number of interrupted tests, and (2) the existence of a good correlation between crack growth rates derived from the analysis of crack length histograms and crack propagation rates inferred from striation spacing measurements carried out on tension-compression LCF specimens. It can easily be shown that the crack growth rate, dc/dN, can be expressed as [25]

$$dc/dN = \chi_0\Delta/\chi_i \tag{A4}$$

Equation A4 was used to determine crack growth laws for both push/pull and torsional fatigue. Examples of results for shear mode loading are given in Fig. 11, where the intervals corresponding to this method are shown for a test carried out at $\Delta\gamma_p/2 = \pm 1.10\%$, while only the mean values for two other tests ($\Delta\gamma_p/2 = 0.80$ and 1.40%) are indicated. These results show that, for a given plastic strain amplitude, the crack growth rate can be expressed as a power function of crack depth, i.e.

$$dc/dN = B_1 c^{\beta} = B_2 \chi_0 c^{\beta} \tag{A5}$$

The constant χ_0 is calculated by integrating Eq A4, which leads to

$$\chi_0 = \left[\frac{c_F^{1-\beta} - c_0^{1-\beta}}{1 - \beta} \right] \cdot \frac{1}{(N_F - N_i)B_2} \tag{A6}$$

where $c_F (= 5\ \text{mm})$ is the final crack length at failure, and c_0 ($= 25\ \mu\text{m}$) is the initial crack length. In Eq A6, N_i was taken as equal to zero for tests carried out at 600°C because it is felt that crack initiation occurs easily under these conditions due to strong environmental effects. At room temperature, N_i was determined from the results of a previous study devoted to 316 stainless steel [*11,27*].

References

[*1*] Brown, M. W. and K. J. Miller, "Initiation and Growth of Cracks in Biaxial Fatigue," *Fatigue of Engineering Materials and Structures,* Vol. 1, 1979, pp. 231–246.

[*2*] Socie, D. F., "Multiaxial Fatigue Damage Models," *Journal of Engineering Materials and Technology,* Vol. 109, 1987, pp. 293–298.

[*3*] Coffin, L. F., "Fatigue at High Temperature," *Fracture 1977,* Vol. 1, ICF 4, Waterloo, Canada, 19–24 June 1977, D. M. R. Taplin, Ed., pp. 263–292.

[*4*] Bertini, L., "Life Predictions by Three Creep-fatigue Interaction Models: Influence of Multiaxiality and Time-variable Loadings," *Materials at High Temperatures,* Vol. 9, No. 1, 1991, pp. 23–29.

[*5*] Bertini, L. and Vitale, E., "Biaxial and Uniaxial Fatigue Life Prediction for Austenitic Stainless Steel Specimens and Components," *Fatigue under Biaxial and Multiaxial Loading,* ESIS 10, K. Kussmaul, D. McDiarmid, and D. Socie, Eds., 1991, Mechanical Engineering Publications, London, pp. 393–411.

[*6*] Miller, K. J., "Metal Fatigue-Past, Current and Future," *Proceedings of the Institution of Mechanical Engineers,* Vol. 205, 1991, pp. 1–14.

[*7*] Levaillant, C., Grattier, J., Mottet, M., and Pineau, A., "Creep and Creep-fatigue Intergranular Damage in Austenitic Stainless Steels: Discussion of the Creep-Dominated Regime," *Low Cycle Fatigue, ASTM STP 942,* H. D. Solomon, G. R. Halford, L. R. Kaisand, B. N. Leis, Eds., American Society for Testing and Materials, Philadelphia, 1988, pp. 414–437.

[*8*] Doquet, V., "Comportement et endommagement de deux aciers à structure CC et CFC en fatigue oligocyclique, sous chargement multiaxial non proportionnel," thesis, Ecole des Mines de Paris, 1989.

[*9*] Doquet, V. and Pineau, A., "Multiaxial Low Cycle Fatigue Behaviour of a Mild Steel," *Fatigue under Biaxial and Multiaxial Loading,* ESIS 10, K. Kussmaul, D. McDiarmid and D. Socie, Eds., 1991, Mechanical Engineering Publications, London, pp. 81–101.

[*10*] Cailletaud, G., Doquet, V., and Pineau, A., "Multiaxial Behaviour of an Austenitic Stainless Steel: Microstructural Observations and Microstructural Modelling," *Fatigue under Biaxial and Multiaxial Loading,* ESIS 10, K. Kussmaul, D. McDiarmid and D. Socie, Eds., 1991, Mechanical Engineering Publications, London, pp. 131–149.

[*11*] Jacquelin, B., Hourlier, F., and Pineau, A., "Crack Initiation under Low-cycle Multiaxial Fatigue," *Multiaxial Fatigue, ASTM STP 853,* K. J. Miller and M. W. Brown, Eds., American Society for Testing and Materials, Philadelphia, 1985, pp. 285–313.

[*12*] Levaillant, C., Rezgui, B., and Pineau, A., "Effects of Environment and Hold Times on High Temperature Low Cycle Fatigue Behaviour of 316 L Stainless Steel," ICM3 Conference, Vol. 2, Cambridge, England, August 1979, pp. 163–172.

[*13*] Robillard, M. and Cailletaud, G., "Directionally Defined Damage in Multiaxial Low-cycle Fatigue: Experimental Evidence and Tentative Modelling," *Fatigue under Biaxial and Multiaxial Loading,* ESIS 10, K. Kussmaul, D. McDiarmid, and D. Socie, Eds., 1991, Mechanical Engineering Publications, London, pp. 103–130.

[*14*] Harada, S. and Endo, T., "On the Validity of Miner's Rule under Sequential Loading of Rotating Bending and Cyclic Torsion," *Fatigue under Biaxial and Multiaxial Loading,* ESIS 10, K. Kussmaul, D. McDiarmid, and D. Socie, Eds., 1991, Mechanical Engineering Publications, London, pp. 161–178.

[*15*] Brown, M. W. and Miller, K. J., "A Theory for Fatigue Failure under Multiaxial Stress-strain Conditions," *Proceedings of the Institution of Mechanical Engineers,* Vol. 187, 1973, pp. 745–755.

[16] Wood, G. C., "High Temperature Oxidation of Alloys," *Oxidation of Metals,* Vol. 2, No. 1, 1970, pp. 11–55.
[17] Stott, F. H., and Wei, F. I., "High Temperature Oxidation of Commercial Austenitic Stainless Steels," *Materials Science and Technology,* Vol. 5, 1989, pp. 1140–1147.
[18] Kant, I. and Gust, W., "Fundamentals of Grain and Interphase Boundary Diffusion," Ziegler Press, Stuttgart, 1988.
[19] Schütze, M., "Deformation and Cracking Behaviour of Protective Oxides Scales on Heat-resistant Steels under Tensile Strain," *Oxidation of Metals,* Vol. 24, No. 3/4, 1985, pp. 199–232.
[20] Schütze, M., "Plasticity of Protective Oxide Scales," *Materials Science and Technology,* Vol. 6, 1990, pp. 32–38.
[21] M. Sakane, M. Ohnami, and M. Sawada, "Fracture Modes and Low-Cycle Biaxial Fatigue Life at Elevated Temperature," *Journal of Engineering Materials and Technology,* Vol. 109, 1987, pp. 236–243.
[22] Weiss, J. and Pineau, A., "Microstructurally-based Simulation of Multiaxial Low-Cycle Fatigue Damage of 316L Stainless Steel in Terms of the Behaviour of a Crack Population," *Proceedings,* Low Cycle Fatigue and Elasto-Plastic Behaviour of Materials, Berlin, 7–11 Sept. 1992, Elsevier Applied Science, 1992, pp. 82–87.
[23] Hoshide, T. and Socie, D. F., "Crack Nucleation and Growth Modeling in Biaxial Fatigue," *Engineering Fracture Mechanics,* Vol. 29, 1988, pp. 287–299.
[24] Anderson, P. M., Fleck, N. A., and Johnson, K. L., "Localization of Plastic Deformation in Shear Due to Microcracks," *Journal of the Mechanics and Physics of Solids,* Vol. 38, No. 5, 1990, pp. 681–699.
[25] Weiss, J. and Pineau, A., "Endommagement multiaxial en viscoplasticité cyclique à haute température de l'acier Z02 CND 17–13," Rapport MM/JW-AP 06/91, Centre des Matériaux, Ecole des Mines, Paris, June 1991.
[26] Underwood, E. E., "Quantitative Stereology," Addison Wesley Publishing Company, 1970.
[27] Levaillant, C., "Approche métallographique de l'endommagement d'aciers inoxydables austénitiques sollicités en fatigue plastique ou en fluage: description et interprétation physique des interactions fatigue-fluage-oxydation," Thèse Ecole des Mines, Paris, June 1984.

DISCUSSION

R. J. DiMelfi[1] *(written discussion)*—As we know, in 316 stainless steel, when high-temperature cycling involves tensile hold periods or a slow-fast sawtooth loading, fatigue cracks can nucleate and grow intergranularly. In your Monte Carlo–type simulations of multiple crack development and coalescence, would it be possible to modify your crack nucleation and growth laws to address the transition to intergranular fracture under these loading conditions? For example, could you include a physically based weighting factor from energy considerations that reflects the relative ease of intergranular versus transgranular crack propagation as loading conditions change or grain boundaries become more environmentally sensitive?

J. Weiss and A. Pineau (author's closure)—Yes, in our simulations, in principle it is possible to modify crack nucleation and growth laws to take into account the transition to intergranular fracture. In particular for crack growth we have proposed a law which takes into account the accelerating effect of intergranular damage on fatigue crack propagation [*1*]. Further work is presently being carried out to include this effect.

Reference

[1] Levaillant, C., Grattier, J., Mottot, M., and Pineau, A., "Creep and Creep-Fatigue Intergranular Damage in Austenitic Stainless Steels: Discussion of the Creep-Dominated Regime," *Low Cycle Fatigue, ASTM STP 942,* 1988, pp. 414–437.

[1] Argonne National Laboratory, RE-207, Argonne, IL 60439.

Sam Y. Zamrik[1] *and Daniel C. Davis*[1]

A Simple Test Method and Apparatus for Biaxial Fatigue and Crack Growth Studies

REFERENCE: Zamrik, S. Y. and Davis, D. C., **"A Simple Test Method and Apparatus for Biaxial Fatigue and Crack Growth Studies,"** *Advances in Multiaxial Fatigue, ASTM STP 1191,* D. L. McDowell and R. Ellis, Eds., American Society for Testing and Materials, Philadelphia, 1993, pp. 204–219.

ABSTRACT: A simple method and unique test apparatus are presented for conducting fatigue and fatigue crack growth studies using plate-type specimens under biaxial bending. The test method and apparatus design make use of the concept of anticlastic bending of a plate with a rhombic configuration. The simplicity and uniqueness of the test apparatus are that with one constant load amplitude, a wide variety of stress or strain biaxial ratios can be attained by varying only the lengths of the rhombic plate diagonals. The test apparatus and rhombic plate specimens have been used for low cycle fatigue, cumulative fatigue damage, and mixed-mode fatigue crack growth studies of engineering materials under biaxial bending. Some results from these previous research studies will be discussed in this present paper to illustrate the utility of the test method and apparatus.

KEY WORDS: biaxiality, multiaxiality, low-cycle fatigue (LCF), rhombic plate, anticlastic bending, fatigue crack growth

Nomenclature

a, b	Minimum and maximum rhombic plate half diagonals, respectively
D	Plate stiffness
E	Modulus of elasticity
F	Applied lateral load at rhombic plate corners
h	Plate thickness
L	Length along section JK of the specimen (Fig. 2)
M_L	Moment per unit length along length L
M_{yy}, M_1	Maximum bending moment
M_{xx}, M_2	Minimum bending moment
P	Total applied single load
P_{max}	Maximum applied load amplitude
P_Y	Yield load
$w(x, y)$	Middle surface thin rectangular plate deflection
x, y	In-plane coordinates
β	Crack orientation to maximum principal stress direction
ε_1	Maximum in-plane principal strain
ε_2	Minimum in-plane principal strain
ν	Poisson's ratio
ϕ	Biaxial ratio

[1] Professor and associate professor, respectively, The Pennsylvania State University, Department of Engineering Science and Mechanics, University Park, PA 16802.

σ_1 Maximum in-plane principal stress (stress normal to crack tip)
σ_2 Minimum in-plane principal stress (stress parallel to crack tip)
σ_y Material yield strength
Θ_0 Crack fracture angle

Introduction

A simple method and unique test apparatus for conducting fatigue studies using plate-type specimens under biaxial bending have been developed. The test method, specimen design, and fatigue loading apparatus make use of the concept of anticlastic bending of a rhombic plate whereby the state of stress and strain biaxiality at the plate surface is dependent only on the surface curvatures. In anticlastic bending of a plate with a rhombic configuration, one surface curvature is in tension while the other surface curvature are in compression [*1*]. The simplicity and uniqueness of this test method and test apparatus is that with only a single constant load amplitude, a great number of stress or strain biaxial ratios can be attained by simply changing the diagonal dimensions of the rhombic plate specimen. Although the test apparatus and rhombic plate specimen were developed in the 1960s, detailed descriptions of either have never been published in the literature. Because of recent interest on the part of researchers in industry and academia in multiaxial fatigue, the authors decided to publish a description of this simple test method and apparatus for conducting biaxial fatigue and crack growth studies under anticlastic bending.

The impetus to develop test methods and apparatuses for multiaxial fatigue studies originated in the pressure vessel industry where fatigue design life data of pressure vessel steels were in great need. In application, these steels are subject to biaxial stress states that result mainly from thermal cycling and mechanical bending loads. Typically, in vessel and piping walls the states of stress are biaxial tension and/or biaxial compression. Some of the earliest experimental efforts to develop specimens and fixtures for simulating biaxial fatigue loadings were in the 1950s. Stout et al. [*2–4*] developed a wide cantilever beam reverse bending specimen in which different states of stress or strain biaxiality could be attained by varying the width-to-thickness ratios. A biaxial stress ratio ($1{:}\phi = \sigma_2/\sigma_1$) of 2:1 (for ideal plastic material) could be attained by designing the specimen with a width-to-thickness ratio of 5. This stress ratio is encountered in pressure vessel and piping walls. However, the 2:1 stress state was limited to the central region of the width of the cantilever beam specimen. Fatigue life data under this biaxial stress state were expressed in terms of cycles to fracture. Sachs et al. [*5*] and Weiss et al. [*6*] modified this technique to produce a wider range of stress ratios from 1:0 to 2:1. These stress ratios correspondingly produced in-plane principal strain biaxial ratios ($1{:}\phi = \epsilon_2/\epsilon_1$) from $2{:}-1$ to 1:0. Blaser et al. [*7*] and Bowman and Dolan [*8–10*] developed test rigs to fatigue rectangular plate and circular plate-type specimens. Different biaxial stress states could be produced at the plate surface by varying ratios of the lateral dimensions to the plate thickness. In these test rigs the cyclic loading was generated by applying a pulsating pressure on one lateral side of the simply supported plate specimens. Ives [*11*] modified this method to obtain completely reversed bending by subjecting simply supported circular plate specimens to pressure alternating on one of the two lateral surfaces. Shewchuk et al. [*12*] modified this method by developing oval plate-type specimens which could attain stress ratios from 1:1 to 2:1, with the corresponding surface strain ratios ranging from 1:1 to 1:0. Pascoe et al. [*13,14*] conducted low cycle fatigue tests using cruciform specimens of steel materials at room temperature. The tests were conducted at principal strain ratios $\phi = -1, -\frac{1}{2}, 0, \frac{1}{2}, +1$. The test data were plotted in terms of maximum principal strain range versus cycles to failure on logarithmic coordinates. For a given strain range the equal biaxial loading resulted in the shortest fatigue life. Within recent years most biaxial fatigue studies have been conducted using thin-walled cylindrical (or

tubular) specimens: The different cyclic loading conditions used in these studies included completely reversed torsion, combined axial-torsion, combined torsion-bending, and either of the latter two combined loading cases with either internal or external cyclic pressure loadings. Some of these studies, conducted at both room and elevated temperature environments, can be found in a number of recent publications [*15–18*]. For combined axial-torsion (biaxial) fatigue testing using thin-walled cylindrical specimens, as an example, stress ratios from 1:−1 to 1:0 and the corresponding principal strain ratios from 1:−1 to 2:−1 can be attained [*19*].

Most of the previously described methods for biaxial fatigue testing produce positive stress ratios, whereas, at discontinuities such as welds at nozzle-pressure vessel shell junctures and at turbines blade root junctures, negative stress ratios are encountered principally due to bending loads. To produce these types of biaxial stress states in bending, Zamrik and Goto [*20,21*] developed the anticlastic bending testing apparatus and rhombic plate specimen in the mid-1960s. They used the apparatus and specimens for biaxial low cycle fatigue studies of an aluminum plate material. Since that time, Zamrik and colleagues [*22–26*] have used the testing apparatus and rhombic plate specimen for the conduct of a number of studies on biaxial fatigue and mixed-mode fatigue crack growth of engineering materials. For example, Zamrik and Tang [*22*] used the anticlastic bending testing apparatus and rhombic plate specimen to study cumulative damage theories under multiaxial fatigue. Also, the test apparatus and rhombic plate specimen have been used for biaxial fatigue crack initiation and propagation studies of engineering materials under bending [*23–26*]. What follows in this paper is a discussion of the advantages and disadvantages of the anticlastic bending method in comparison with some other methods for biaxial fatigue testing. A description of the rhombic plate specimen and anticlastic bending fatigue test apparatus designs are given. This paper will also discuss results from some of these previous publications [*21–26*] as examples of applications of the anticlastic bending test apparatus and rhombic plate specimen in biaxial fatigue research. In Appendix A, equations are developed which relate the single constant applied load amplitude (P) to the stress biaxial ratio.

Features of Anticlastic Bending Applied to the Rhombic Plate Specimen Design

A schematic of the rhombic plate specimen and loading configuration for anticlastic bending is shown in Fig. 1. Two bending moments (M_{xx}, M_{yy}) are produced. One moment M_{xx} is positive and the other moment M_y is negative. As a result, one surface curvature will be in tension while the other surface curvature will be in compression, as shown in Fig. 2. Since the stresses are proportional to the radii of surface curvatures, a great number of stress and strain biaxial ratios can be produced by simply changing the length of the diagonals ($2a$, $2b$) of the specimen while maintaining a single constant loading amplitude (F) applied at the corners. The principal stress ratios that can theoretically be attained with the rhombic plate specimen design are between 1:−1 and 1:0 or 2:1. The choice of the ratio 1:0 or 2:1 depends on the ratio of the most narrow diagonal of the specimen to the specimen thickness (h). The stress ratios 1:0 and 2:1 may be difficult to attain merely using the rhombic plate specimen. A more likely biaxial fatigue specimen for attaining these stress ratios (1:0 and 2:1) would be a cantilever beam type specimen as discussed previously [*2–6*]. Also, the corresponding principal strain ratios that can theoretically be attained using the rhombic plate specimen are between 1:−1 to 2:−1 or 1:0. The stress ratios from 1:−1 to 1:0 and the corresponding strain ratios 1:−1 to 2:−1 also agree exactly with the stress and strain ratios that can be attained from combined axial-torsion fatigue testing using thin-walled cylindrical specimens. Figures 3*a* and 3*b* show, respectively, the regions of stress and strain ratios that can be attained for biaxial fatigue loadings when using a wide cantilever beam, circular and oval plate-type, or a rhombic plate-type specimen.

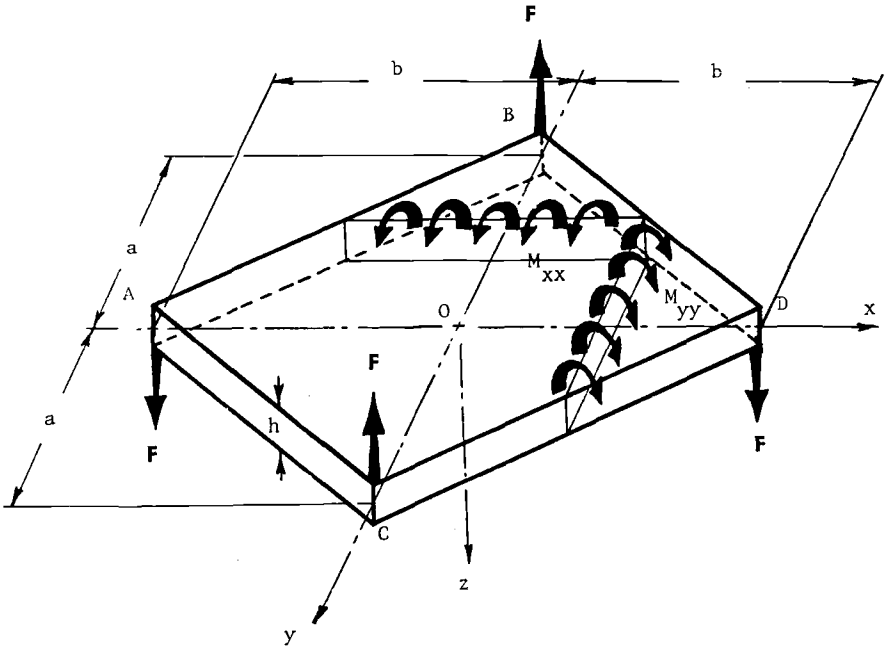

FIG. 1—*Schematic of rhombic plate specimen loading system under anticlastic bending.*

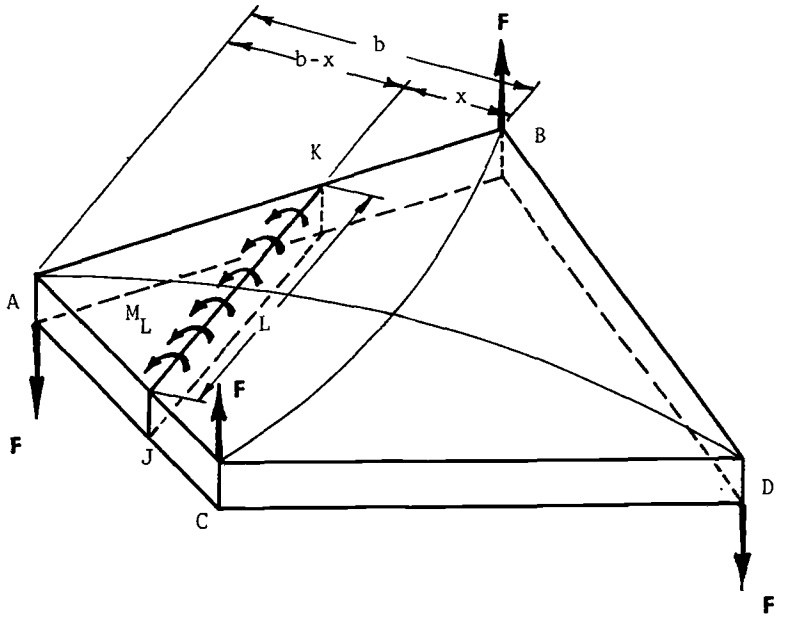

FIG. 2—*Schematic of rhombic plate surface curvature under anticlastic bending.*

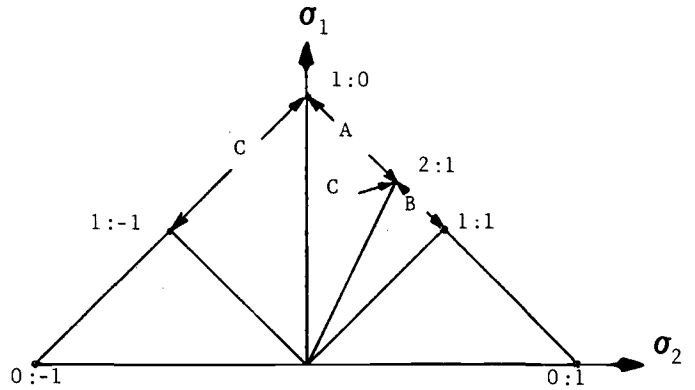

FIG. 3*a*—*Stress ratios attained by:* (A) *wide cantilever bending beam specimen,* (B) *pressured oval plate specimen,* (C) *rhombic plate specimen.*

A unique feature of the anticlastic bending method when applied to the rhombic plate design is the uniform stress and strain distribution over a wide area of the specimen surface. This is because the rhombic plate can be assumed to be constituted of beams of uniform strength along its two diagonals by a simple beam theory approximation [*27*]. Whereas, for both the wide-cantilever beam and the pressured-plate specimens, only a limited area in the central portion of either specimen is subject to the maximum stress or strain state. As a comparison to the pressured-plate techniques, the anticlastic bending of a rhombic plate method is more convenient for detecting and observing the initiation and growth of cracks on the surface of the specimen. The fact that the stress-strain distribution over the rhombic plate surface is uniform under cyclic loading also provides an advantage in easily obtaining the magnitude of the stresses and strains at the specimen surfaces. Even though there is a continuous change in the stress-strain relation for the material as the number of cycles increases, the varying stress-strain relation is the same over the entire surface of the rhombic plate. Therefore, the strain-deflection relation at the beginning of the test remains unchanged throughout the test as far as the assumption of linear distribution of strain in the direction of the thickness holds. Hence,

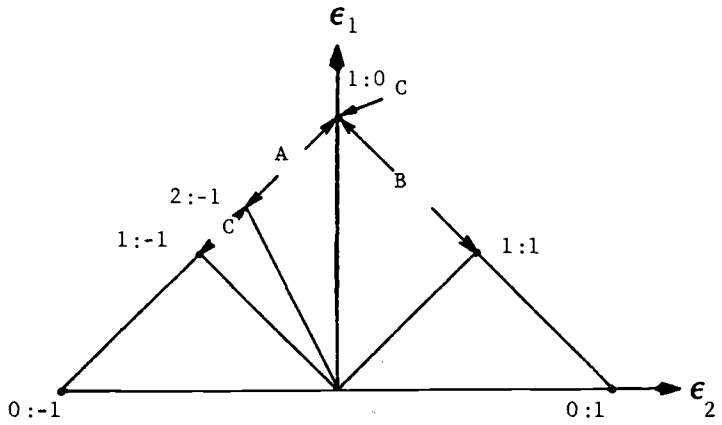

FIG. 3*b*—*Strain ratios attained by:* (A) *wide cantilever bending beam specimen,* (B) *pressured oval plate specimen,* (C) *rhombic plate specimen.*

once the strain-deflection relation is initially calibrated, before testing begins, the only required measurement needed during the testing is the deflection of the plate.

From the viewpoint of economy and ease in conducting biaxial fatigue testing, reverse bending of plate specimen has a great advantage over other methods such as completely reverse torsion, combined axial-torsion loading of cylindrical specimens, and internal-external pressurization of tubular (cylindrical) specimens. In reverse bending fatigue testing there is far less concern in maintaining good alignment of the test machine as required in combined axial-torsion fatigue testing. Biaxial fatigue testing methods using tubular specimens are prone to buckling problems due to large plastic deformation involved in a unit strain cycle. Testing tubular specimens under internal-external pressure cycling has led to problems of highly stressed spots outside the specimen gage section. Both of these problems could cause a premature failure of the specimen. However, from an academic point of view, there are several advantages for using combined axial-torsion (biaxial) fatigue testing with thin-walled tubular specimens over reverse bending fatigue testing methods. The thin-walled cyclindrical specimens practically eliminate the influence of through-thickness stress-strain gradients. Also, the stress-strain responses in low cycle fatigue tests can be measured directly from the hysteresis loop; whereas in plate bending there are some ambiguities in the computation of the plastic strain range from the total strain range and load measured in low cycle fatigue testing. The difficulty lies in determining the stress range under plastic deformation. Also, there is a disadvantage associated with the through-thickness stress or strain gradients in reverse bending. However, if the criterion for fatigue failure is crack initiation or growth of a surface crack to a certain length, then this disadvantage can be tolerated to some extent because the primary interest becomes the influence of the biaxial stress state on crack initiation or growth rather than to determine the absolute values of low cycle fatigue life under various states of biaxial stresses.

Rhombic Plate Specimen and Test Equipment Designs for Biaxial Fatigue Testing Under Anticlastic Bending

Specimen Design

Drawings of a 3 by 3 and 2 by 3 rhombic plate specimens are shown in Figs. 4*a* and *b*. For the half diagonal dimensions shown, the specimens will have biaxial stress ratios of $\phi = -1$ and -0.45, respectively. In Appendix A, Eq A8 defines $\phi = -[a^2/b^2]$, where a is the rhombic plate's minimum diagonal length and b is the maximum half diagonal length. The rhombic plate specimens are designed with widened corners. A hole is drilled through each of the corners such that rollers can be fixed over the corners and held in place by pins (Fig. 5). Ideally, a point load would be applied at the specimen corners, as shown in Fig. 1; however, the stress concentrations due to the point loading could cause premature failure. Applying the loads to the specimen through low contact friction rollers will distribute the load more uniformly over the specimen surface and also reduces mean stress and in-plane normal stress effects. The surfaces and edges of the specimen should be polished to eliminate any defects that could cause premature failure. To better ensure a thin plate behavior, specimen thickness should be less than 10% of the minimum diagonal length.

Test Equipment and System

The test equipment and system consists of the anticlastic bending fatigue loading apparatus and the fatigue testing system.

Fatigue Loading Apparatus—Basically, the test apparatus consists of four holders, four shelters, and the upper and lower connectors to the die sets. The apparatus with the specimen

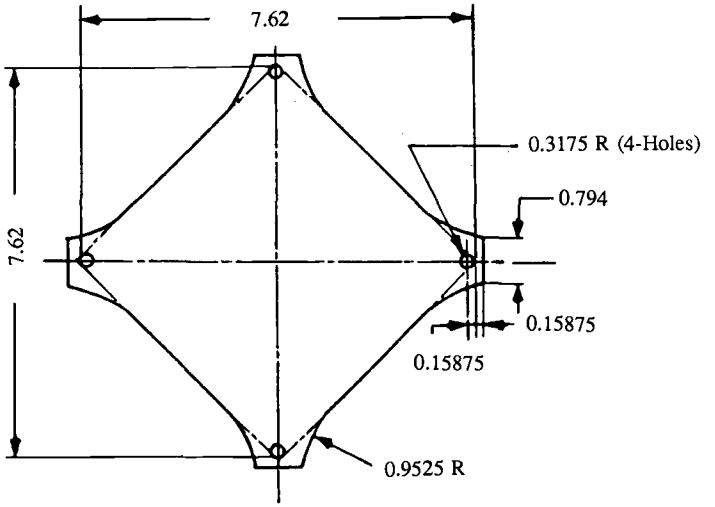

FIG. 4*a*—*3 by 3 rhombic plate specimen (all dimensions in cm).*

installed is shown schematically in Fig. 6, and all the major components are identified. The apparatus is basically designed to simply support the rhombic specimen at its corners by the use of four holders and to apply the cyclic bending loads. Two of the holders in the apparatus are attached to the stationary die set through the lower connectors. Two opposite corners of the rhombic plate specimen with the attached rollers are inserted in these two holders. The other two holders are connected to the moving part of the die set, and the other two opposite corners of the specimen with attached rollers are in these holders. During fatigue testing these latter two holders, along with the two inserted opposite corners of the specimen, are cycled by the moving die set, which is connected to the fatigue machine load train. The two opposite corners of the rhombic plate specimen connected to the lower holders remain stationary during fatigue testing. The specimen with rollers (Fig. 5) is held in place and aligned within the holders by four shelters. By loading the rhombic plate specimen as described above, anticlastic bending can be produced as shown schematically in Fig. 2. Hence, the two cyclic bending

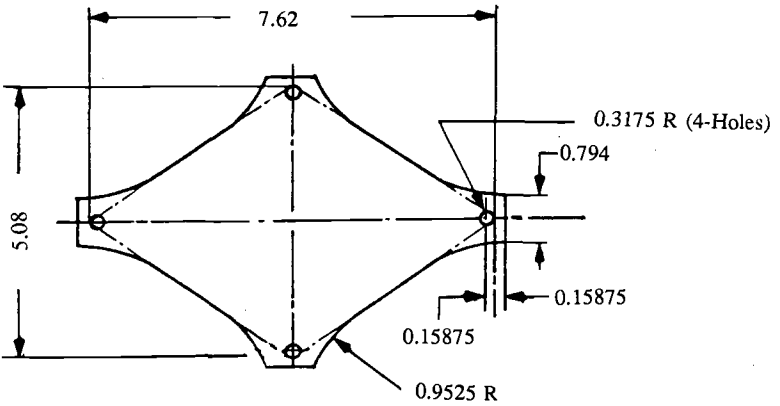

FIG. 4*b*—*2 by 3 rhombic plate specimen (all dimensions in cm).*

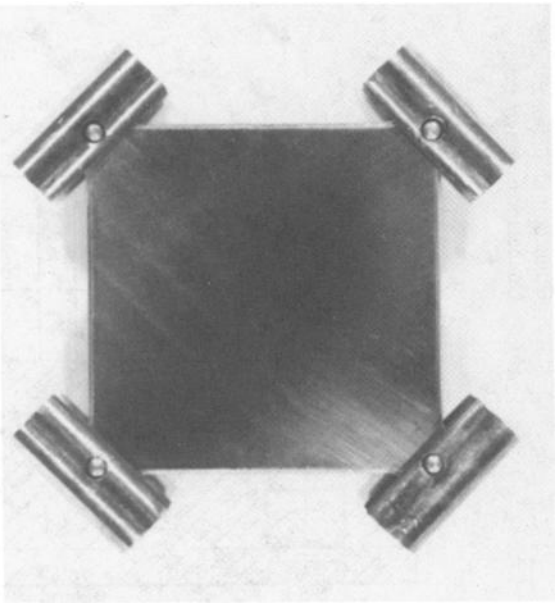

FIG. 5—*Rhombic plate specimen with roller supports.*

moments, M_{xx} and M_{yy}, generated in the rhombic specimen loading system can be in general of equal or different magnitudes, but will be opposite in signs. A photograph of the loading apparatus with installed specimen is shown in Fig. 7. The dial gage shown is attached to measure the relative displacement between the moving and stationary die sets. The dial gage readings can also be used to easily monitor the applied load on a specific specimen type during fatigue testing if pretest load-displacement calibrations were made.

The present fatigue loading apparatus is designed to hold a rhombic plate specimen with a shorter diagonal at a minimum of 2.0 in. (5.08 cm) and a longer diagonal at a maximum of 4.0 in. (10.16 cm). The test apparatus has a maximum deflection amplitude of ± 1.0 in. (± 2.54 cm).

Fatigue Testing System—The fatigue loading apparatus with the rhombic plate specimen is designed to be installed in the load assembly of a standard closed-loop servohydraulic fatigue testing machine for uniaxial loading. The test machine should have a capacity of at least 10 kips (44 kN). The apparatus (Fig. 8) is shown in a fatigue testing system in the Fatigue and Fracture Laboratory at The Pennsylvania State University. The consoles are equipped with modules containing electronics to control, monitor, and provide readouts of the magnitude and waveform of the loading functions applied to the specimen.

Some Examples of Biaxial Fatigue Studies Using the Anticlastic Bending Method

What follows are results from several previous studies on low cycle fatigue and fatigue crack growth using the anticlastic bending fatigue loading apparatus and rhombic plate specimens. The objective in presenting these studies in the present paper is to illustrate the utility of the test method and apparatuses. The test method and apparatus have principally been used by Zamrik and colleagues at The Pennsylvania State University. In the future, as the test method and apparatus gain wider usage, improved methodologies will certainly be developed for studying fatigue and crack growth mechanisms in materials.

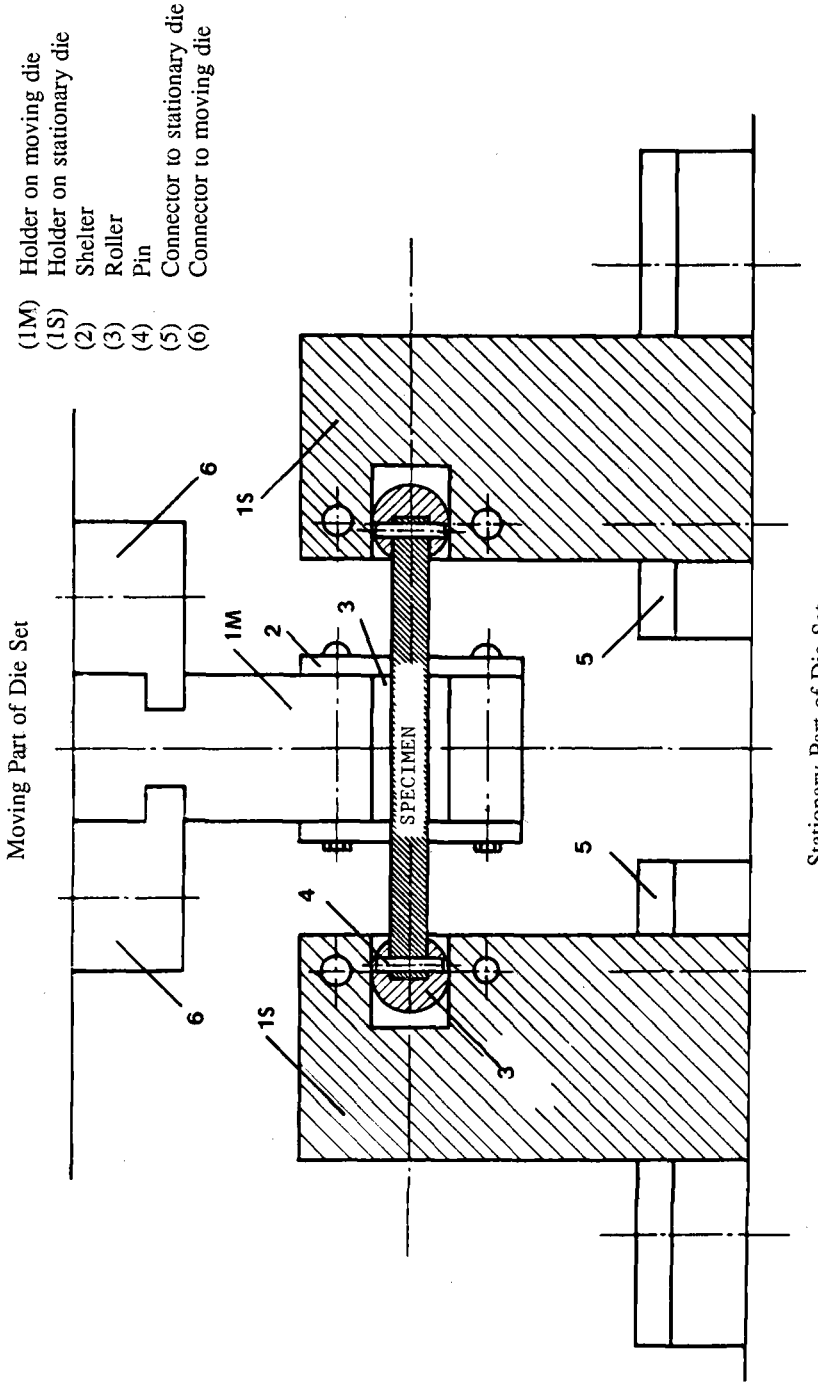

FIG. 6—*Schematic of anticlastic bending loading apparatus identifying all major components.*

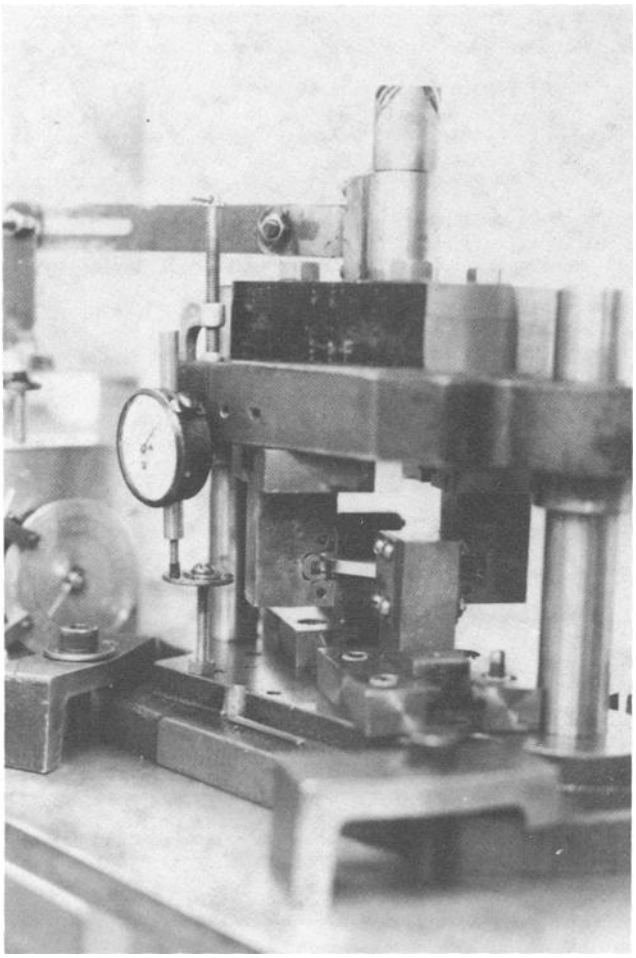

FIG. 7—*Photograph of anticlastic bending loading apparatus with specimen installed.*

In the initial work, Zamrik and Goto [*20,21*] conducted a series of biaxial fatigue tests using the rhombic plate specimen and fatigue loading apparatus at strain biaxial ratios $\phi = -1$, -0.9, -0.8, and -0.5. The material was a 7075-T56 aluminum plate. Fatigue life from the test results were plotted in terms of maximum strain range, the maximum shear strain range, and the octahedral shear strain range. The evaluation showed that the octahedral shear strain theory is a good failure theory for multiaxial strain low-cycle fatigue at room temperature. Using the octahedral shear strain range theory, Zamrik and Goto compared biaxial fatigue data from tests conducted using the anticlastic bending test apparatus and rhombic plate specimens to fatigue data on a similar aluminum alloy by Sacks and Weiss [*5,6,28*], who used cantilever beam specimens. They found that the Sacks and Weiss biaxial fatigue data correlated well with their data, resulting in a curve that fit a Coffin-Manson type relation for the low cycle regime.

Zamrik and colleagues [*24–26*] have also employed the anticlastic bending method for conducting biaxial fatigue crack growth studies using an aluminum alloy and a stainless steel. The rhombic plate specimens were dimensioned for several biaxial ratios ($\phi = -1, -0.7, -0.45$).

FIG. 8—*Photograph of anticlastic bending loading apparatus in a fatigue testing machine.*

In these studies a starter crack with these approximate dimensions, length ($2c_0$) = 0.1 in. (0.254 cm), depth (a_0) = 0.025 in. (0.6 cm), and width = 0.006 in. (0.015 cm), was machined into the surface of one side of the rhombic plate specimens by an electrical discharge machining (EDM) method. In the Zamrik and Shabara study [*24*], using 6061-T651 aluminum and 304 stainless steel, it was found that the state of stress biaxiality affects not only the rate of crack growth but also the mode of crack propagation. Under biaxial fatigue crack propagation, it is presently accepted that if the stress component parallel to the crack direction is tensile, little effect is observed on crack growth; however, if the parallel stress component is compressive, the crack propagation rate is enhanced [*29–31*]. Theoretical work by Shah and Kobayashi [*31*] and Miller and Kfouri [*32*] indicated that the stress intensity factor and the crack tip displacement is greatest for $\phi = -1$. The Zamrik and Shabara study on both the aluminum and stainless steel materials found that at the same stress intensity factor the crack growth rate in specimens with $\phi = -1$ was greater than those at ratios $\phi = -0.70$ and -0.45. Zamrik and Shabara also observed the mode of crack propagation. At biaxial stress ratios of $\phi = -0.45$ and -0.7, crack propagation was by an open mode in the original direction of the EDM slot

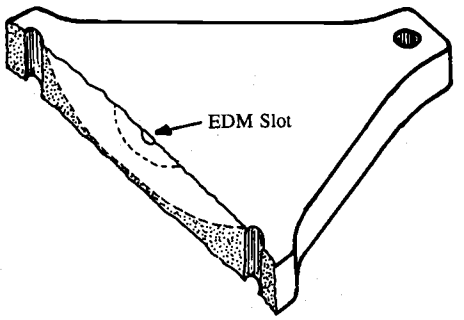

FIG. 9*a*—*Crack opening fracture mode of rhombic plate under anticlastic bending.*

orientation as shown in Fig. 9*a*. Only at a stress biaxial ratio $\phi = -1$ did the crack abandon its propagation path from the initial EDM slot direction and assume a new propagation mode in shear along the surface at a path 45° to the original slot direction (Fig. 9*b*). This phenomenon of transition from opening to shear mode under biaxial bending at a stress biaxial ratio $\phi = -1$ is uniquely observed under anticlastic bending.

More recently Zamrik et al. [*26*] investigated the effects of initial surface flaw (EDM slot) orientation (β) and the state of stress biaxiality on crack fracture angle (Θ_0) using a 6061-T651 aluminum material. Rhombic plate specimens, as illustrated by Fig. 10, dimensioned for two stress biaxial ratios ($\phi = -0.45$ and -1) were used. For the first case ($\phi = -0.45$), an EDM slot was machined on one surface of a rhombic plate specimen each at an initial orientation angle $\beta = 30$, 45, or 60° to the maximum principal direction. For the second case ($\phi = -1$), an EDM slot was machined into one surface of a rhombic plate specimen each at an initial orientation angle $\beta = 0$, 45, 60, 75, or 90°. The loading cycle was from zero to $P_{max} = 850$ lb (3.8 kN). This value of P_{max} chosen would yield a stress intensity factor at the crack tip greater than the threshold value, while at the same time, the yield stress of the 6061-T651 aluminum material would not be exceeded. A model was proposed by Zamrik et al. [*24*] for predicting Θ_0 (average value of Θ_{0A} and Θ_{0B}) versus β, and it was compared with a published approach by Woo and Ling [*33*]. As shown in Fig. 11, the proposed model [*24*] is in close agreement with

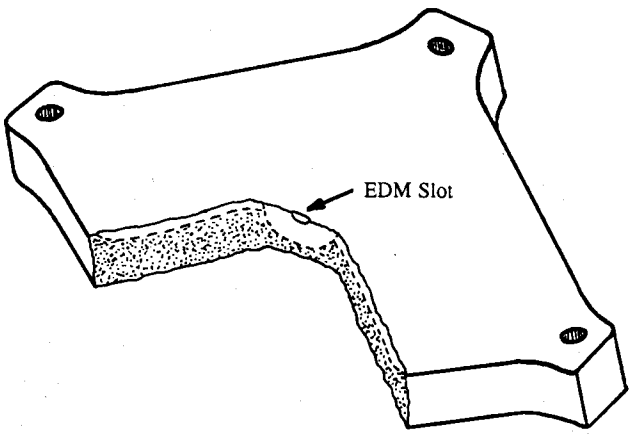

FIG. 9*b*—*Shear fracture mode of rhombic plate specimen at $\phi = -1$ under anticlastic bending.*

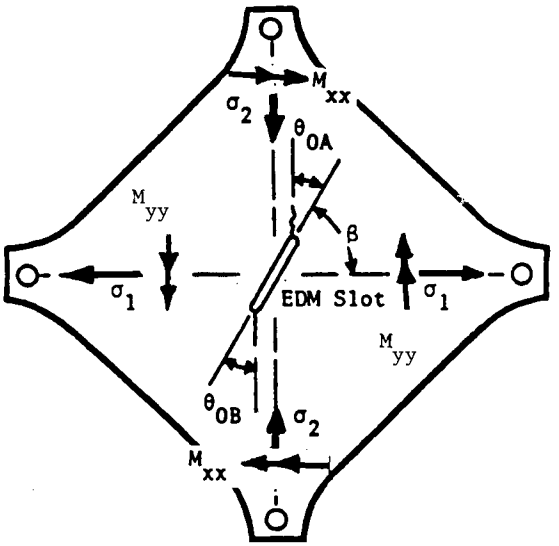

FIG. 10—*Schematic for rhombic plate specimen with EDM slot precrack.*

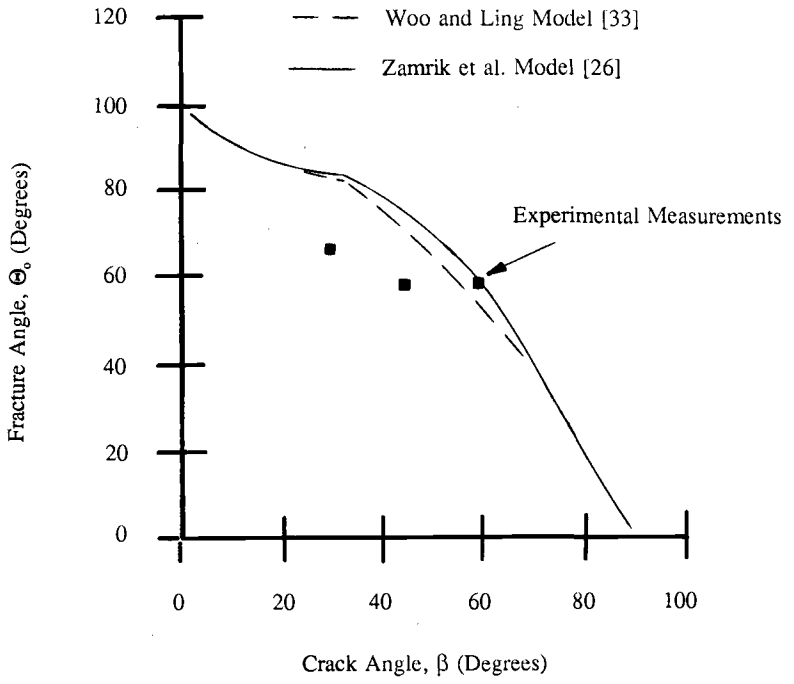

FIG. 11—*Fracture angle (Θ_0) versus initial crack orientation (β) under biaxial fatigue.*

the Woo and Ling [*33*] model. However, there are discrepancies between both theoretical models and the experimental measurements obtained from the anticlastic bending fatigue crack growth tests. The discrepancies can be attributed to the fact that the theoretical models consider only two dimensional stress problems achieved by using thin sheet specimens, whereas the rhombic plate specimens used in this investigation were relatively thick with respect to the limits of these theoretical models.

Summary and Conclusions

In this paper the design and application of a unique test apparatus were presented for conducting biaxial low cycle fatigue studies under a method of anticlastic bending using a plate specimen with a rhombic configuration. The design of the fatigue loading apparatus is unique in that with a constant load amplitude a great number of stress or strain biaxial ratios can be generated by changing only the diagonals of the rhombic plate specimen. Another unique feature of the fatigue loading apparatus and rhombic plate specimen design is that there is a uniform distribution of the biaxial stress-strain state over a wide surface area of the rhombic plate specimen. Hence, mixed-mode fatigue crack initiation and growth studies under biaxial bending can be ideally conducted. Several mixed-mode fatigue crack growth and low cycle fatigue studies for engineering materials have been conducted over the years using the rhombic plate specimen and the anticlastic bending fatigue loading apparatus.

Acknowledgments

The authors wish to acknowledge those who have participated in research activities using the anticlastic bending fatigue loading apparatus and rhombic plate specimens, to include: D. Allison, F. M. Baghat, T. Goto, A. Seibi, M. A. Shabara, and P. Y. Tang.

APPENDIX A

Relationships Between the Applied Load (P), Stress Biaxial Ratio, and Yield Strength

To derive the relation between the applied load (P) and the stress biaxial ratio (ϕ), reference will be made to Fig. 2. For a rhombic plate ($b > a$), the bending moment per unit length along section JK of length L taken a distance x from the diagonal BC is

$$M_L = F(b - x)/L \tag{A1}$$

where F is the load applied at each corner. By using similar triangles

$$L = 2(b - x)[a/b] \tag{A2}$$

Substituting Eq A2 into Eq A1 yields

$$M_L = (F/2)[b/a] \tag{A3}$$

The applied load (P) is equal to $2F$, and therefore

$$M_L = (P/4)[b/a] \tag{A4}$$

Since Eq A4 is independent of the distance x, M_L will be the same along the diagonal AD and $M_L = M_{yy} = M_1$. The maximum in-plane principal stress is then

$$\sigma_1 = 6M_1/h^2 \tag{A5}$$

combining Eqs A4 and A5 yields

$$\sigma_1 = (3P/2h^2)[b/a] \tag{A6}$$

Similar derivations can obtain expressions for $M_{xx} = M_2$ and minimum in-plane principal stress (σ_2), where

$$\sigma_2 = -(3P/2h^2)[a/b] \tag{A7}$$

Hence, the stress biaxial ratio (ϕ) can be defined in terms of the plate diagonals as

$$\phi = -[a^2/b^2] \tag{A8}$$

and then specimens of different stress biaxial ratios can be tested without changing the loading amplitude (P). Finally, by applying Eqs A6 and A7 to the von Mises yield criterion for the plane stress condition, for example, the yield load (P_Y) can be determined as

$$P_Y = [2h^2a\sigma_y]/[3b(1 - \phi + \phi^2)^{1/2}] \tag{A9}$$

where σ_y is the material's yield strength. Then for $P = P_{max} < P_Y$, fatigue testing would be in the high cycle regime, and for $P = P_{max} > P_Y$ fatigue testing would be in the low cycle regime.

References

[1] Timoshenko, S., *Theory of Plates and Shells,* McGraw-Hill, Inc., New York, 1959.

[2] Gross, J. H., Tsang, S., and Stout, R. D., "Factors Affecting Resistance of Pressure Vessel Steels to Repeated Overloading," *The Welding Journal,* Vol. 32, Research Supplement, 1953, pp. 23-S–30-S.

[3] Gross, J. H. and Stout, R. D., "Plastic Fatigue Properties of High Strength Pressure Vessel Steels," *The Welding Journal,* Vol. 34, Research Supplement, 1955, pp. 161-S–166-S.

[4] Tor, S. S., Ruzek, J. M., and Stout, R. H., "Repeated Load Tests on Welded and Prestrained Steels," *The Welding Journal,* Vol. 31, No. 5, Research Supplement, 1952, pp. 238-S–246-S.

[5] Sachs, G., Gerberich, W. W., Weiss, V., and Latorre, J. V., "Low-Cycle Fatigue of Pressure Vessel Materials," *ASME Proceedings,* Vol. 60, 1961, pp. 512–529.

[6] Weiss, V., Sessler, J. and Packman, P., "Effect of Several Parameters on Low-Cycle Fatigue Behavior," *Acta Metallurgica,* Vol. 11, No. 7, 1963, pp. 809–816.

[7] Blaser, R. U., Tucker, Jr., J. T., and Kooistra, L. F., "Biaxial Fatigue Tests on Flat-Plate Specimens," *The Welding Journal,* Vol. 31, No. 3, Research Supplement, 1952, pp. 161-S–168-S.

[8] Bowman, C. E. and Dolan, T. J., "Biaxial Fatigue Properties of Pressure Vessel Steels," *The Welding Journal,* Vol. 32, No. 11, Research Supplement, 1953, pp. 529-S–537-S.

[9] Bowman, C. E. and Dolan, T. J., "Studies of Biaxial Properties of Pressure Vessel Steels," *The Welding Journal,* Vol. 34, No. 1, Research Supplement, 1965, pp. 102-S–109-S.

[10] Bowman, C. E. and Dolan, T. J., "Resistance of Low-Alloy Steel Plates to Biaxial Fatigue," *The Welding Journal,* Vol. 35, No. 2, Research Supplement, 1956, pp. 102-S–109-S.

[11] Ives, K. D., "Equibiaxial Low-Cycle Fatigue Properties of Typical Pressure-Vessel Steels," Report No. 7548, The Babcock and Wilcox Company Research Center, Alliance, OH, April 1964.

[12] Shewchuk, J., Zamrik, S. Y., and Marin, J., "Low-Cycle Fatigue of 7075-T651 Aluminum Alloy in Biaxial Bending," *Experimental Mechanics,* Vol. 8, 1968, pp. 504–512.

[13] Pascoe, K. J. and de Villiers, J. W. R., "Low-Cycle Fatigue of Steels Under Biaxial Straining," *Journal of Strain Analysis,* Vol. 2, 1967, pp. 117–126.

[14] Parsons, M. W. and Pascoe, K. J., "Development of a Biaxial Fatigue Testing Rig," *Journal of Strain Analysis,* Vol. 10, 1975, p. 102.

[15] *Multiaxial Fatigue, ASTM STP 853,* K. J. Miller and M. W. Brown, Eds., American Society for Testing and Materials, Philadelphia, 1985.
[16] *Low Cycle Fatigue, ASTM STP 942,* H. D. Solomon, G. R. Halford, L. R. Kaisand, and B. N. Leis, Eds., American Society for Testing and Materials, Philadelphia, 1988.
[17] *Advances in Lifetime Predictive Techniques, ASTM STP 1122,* M. R. Mitchell and R. W. Landgraf, Eds., American Society for Testing and Materials, Philadelphia, 1991.
[18] ASTM Symposium on Multiaxial Fatigue, 14–15 October 1992, San Diego, CA.
[19] Marin, J., *Mechanical Behavior of Engineering Materials,* Prentice Hall, Inc., Englewood Cliffs, NJ, 1962.
[20] Gotto, T., "A Study of Low-Cycle Fatigue Under Multiaxial Strain Cycling," M. S. thesis, The Pennsylvania State University, University Park, PA, 1966.
[21] Zamrik, S. Y. and Goto, T., "The Use of Octahedral Shear Strain in Biaxial Low-Cycle Fatigue," *In Materials Technology an Inter-American Approach,* ASME, New York, 1968, pp. 551–562.12.
[22] Zamrik, S. Y. and Tang, P. Y., "Aspects of Cumulative Fatigue Damage under Multiaxial Strain Cycling," *Mechanical Behavior of Materials,* Vol. II, Society of Material Sciences, Japan, 1972, pp. 381–390.
[23] Zamrik, S. Y. and Baghat, F. M., "A J-Integral Analysis to Fracture Toughness of Plates Containing Surface Cracks," *Transactions of ASME, Journal of Pressure Vessel Technology,* Vol. 97, Series J, No. 4, Nov. 1975, pp. 284–290.
[24] Zamrik, S. Y. and Shabara, M. A., "The Application of Fracture Mechanics Analysis to Crack Growth in a Biaxial Stress Field," *Proceedings,* IV Inter-American Conference on Materials Technology, Venezuela, 1975, pp. 472–477.
[25] Zamrik, S. Y. and Allison, D., "The Effect of Surface Flaw Orientation on Fatigue Crack Growth due to Biaxial Bending," ASME Proceeding on Failure Prevention and Reliability, Vol. 9, ASME, New York, September 1987, pp. 81–86.
[26] Zamrik, S. Y., Seibi, A., and Davis, D. C., "Fatigue Crack Initiation from an Induced Angled Surface Crack under Biaxial Anticlastic Bending," *Fatigue Under Biaxial and Multiaxial Loadings,* K. Kussmaul, D. McDiarmid, and D. Socie, Eds., Mechanical Engineering Publications, London, 1991, pp. 223–238.
[27] Timoshenko, S., *Strength of Materials,* Part 1, D. Van Nostrand Co., Inc. New York, 1956.
[28] Liu, S., Lynch, J. J., Ripling, E. J., and Sachs, G., "Low Cycle Fatigue of Aluminum Alloy 245-T in Direct Stress," *Metals Technology,* February 1948, pp. 96–98.
[29] Kibler, J. J. and Roberts, R., "The Effects of Biaxial Stresses on Fatigue and Fracture," *Transactions of the ASME Journal of Engineering for Industry,* November 1970, pp. 727–734.
[30] Hilton, P. D., "Plastic Intensity Factors for Cracked Plates Subject to Biaxial Loading," *International Journal of Fracture,* Vol. 9, No. 2, June 1973, pp. 149–156.
[31] Shah, R. C. and Kobayashi, A. S., "Stress Intensity Factor for an Elliptical Crack Approaching the Surface of a Plate in Bending," *Stress Analysis and Growth of Cracks, ASTM STP 513,* American Society for Testing and Materials, 1972, Philadelphia, pp. 22–36.
[32] Miller, K. J. and Kfouri, A. P., "Elastic-Plastic Finite Element Analysis of Crack Tip Fields Under Biaxial Loading Conditions," *International Journal of Fracture,* Vol. 10, No. 3, September 1974, pp. 393–404.
[33] Woo, C. W. and Ling, L. H., "On Angled Crack Initiation Under Biaxial Loading," *Journal Strain Analysis,* Vol. 19, 1984, pp. 51–59.

Multiaxial Stress-Strain Behavior

Charles E. Bakis,[1] *Michael G. Castelli,*[2] *and J. Rodney Ellis*[3]

Thermomechanical Loading in Pure Torsion: Test Control and Deformation Behavior

REFERENCE: Bakis, C. E., Castelli, M. G., and Ellis, J. R., **"Thermomechanical Loading in Pure Torsion: Test Control and Deformation Behavior,"** *Advances in Multiaxial Fatigue, ASTM STP 1191,* D. L. McDowell and R. Ellis, Eds., American Society for Testing and Materials, Philadelphia, 1993, pp. 223–243.

ABSTRACT: An investigation of thermomechanical testing and deformation behavior of tubular specimens under torsional loading is described. Experimental issues concerning test accuracy and control specific to thermomechanical loadings under a torsional regime are discussed. A series of shear strain-controlled tests involving the nickel-base superalloy Hastelloy X were performed with various temperature excursions and compared to similar thermomechanical uniaxial tests. The concept and use of second invariants of the deviatoric stress and strain tensors as a means of comparing uniaxial and torsional deformations is presented and critiqued for its applicability to the present data. The hardening behavior of the torsional specimens is also briefly presented and discussed in light of previous thermomechanical tests conducted under uniaxial conditions.

KEY WORDS: thermomechanical testing, deformation, torsion, Hastelloy X, deviatoric invariants, elevated temperature

In most high-temperature engineering applications, components are subjected to complex combinations of thermal and mechanical loadings during service. Such thermomechanical loadings have long been identified as limiting factors in the design of structural components. In addition, certain structural alloys display unique deformation behaviors under specific thermomechanical paths, behaviors which are not experienced under more commonly investigated isothermal conditions [*1–3*]. This potential for life-limiting behavior and unique deformation response under thermomechanical loading is clearly sufficient to warrant careful consideration and investigation.

Despite the demonstrated need for closely controlled thermomechanical deformation (TMD) experiments, such experiments are seldom performed due to numerous experimental complexities introduced (e.g., phasing between the mechanical component of loading and temperature, dynamic temperature gradients, and cyclic temperature control). Many of these issues are further complicated in axial strain-controlled tests in which thermal strains have a first order effect on the test control variable, the specimen's total strain [*1,4–6*]. If a specific mechanical strain range is desired, an accurate account of and compensation for the thermal strain component must be maintained throughout the test. Even with digital test control, this remains a complex task.

[1] Department of Engineering Science and Mechanics, The Pennsylvania State University, 227 Hammond Bldg., University Park, PA 16802.

[2] Sverdrup Technology Inc., Lewis Research Center Group, 2001 Aerospace Parkway, Brook Park, OH 44141.

[3] NASA Lewis Research Center, 21000 Brookpart Rd., Mail Stop 49-7, Cleveland, OH 44135.

One approach to minimize or potentially eliminate the coupling between mechanical and thermal strains is to perform thermomechanical strain-controlled tests under torsion. Under such conditions, the strain in the loading direction (pure shear) is theoretically not affected by temperature excursions. Thus, there is no need to account for thermal strain effects and, as a result, test control is greatly simplified [*7,8*]. Moreover, a torsion test enables the measurement of the entire mechanical strain tensor with a single measurement, whereas two or three measurements are required to measure the full mechanical strain tensor in a uniaxial test. Typically, however, only the strain in the loading direction is measured in a uniaxial test. The transverse strains are dependent upon the temperature and relative amounts of elastic and plastic deformation and are therefore difficult to predict.

The objectives of this investigation were, first, to develop testing capabilities and investigate testing issues concerning closely controlled TMD experiments in torsion, and second, to make comparisons between uniaxial and torsional TMD based on equivalent effective stresses and strains. The second objective was accomplished by conducting torsional and uniaxial TMD experiments with equivalent effective strain limits based on the second invariant of the deviatoric strain tensor. The effective strain limits were calculated from the first cycle of the uniaxial TMD response and subsequently used to dictate the imposed strain values for the analogous test in torsion. By forcing the second invariant of the deviatoric strain tensors to be identical during the first cycle of deformation, appropriate data comparisons could be made in a second deviatoric stress-strain space. Such comparisons were designed to address the validity of the sole use of this scalar quantity for the purposes of comparing and predicting TMD behavior.

Experimental Details

Specimens

The material used for this study was Hastelloy X[4], a nickel-base solid-solution-strengthened alloy commonly used in high-temperature power generation applications. The torsional and uniaxial specimens were fabricated from separate heats of material. All of the material used in this investigation was produced in accordance with Aerospace Material Specification 5754H and was solution heat treated. The chemical compositions of each heat are shown in Table 1.

The specimen geometries are shown in Fig. 1. Smooth shank ends were used to allow gripping with hydraulically actuated collet grips. Earlier investigations with both geometries [*4,9*] have shown the specimens to be well suited for axial and torsional deformation studies on monolithic materials.

Torsional Test Apparatus

All experiments were conducted in an air environment. Heating was provided by an audio frequency induction heater outfitted with the coil fixture partially shown in Fig. 2 and described completely in Ref *10*. This fixture supports three coil segments which are independently adjustable in the transverse and axial directions. The three coil segments were wired in series, thereby enabling the use of a single, closed-loop temperature controller. Since no forced cooling was employed, conduction through the water-cooled grips served as the major mechanism for specimen cooling. An enclosure was used around the test frame to minimize the effects of air currents.

A triangular waveform was used for both shear strain and temperature control. This allowed

[4] Hastelloy X is a trademark of Haynes International, Inc., Kokomo, IN.

TABLE 1—*Chemical composition of the material heats of Hastelloy X.*

	Torsion Heat	Uniaxial Heat
Element	Composition, wt. %	
C	n 0.084	0.069
Mn	0.55	0.58
Si	0.64	0.48
S	0.001	0.001
P	0.021	0.022
Cr	20.83	21.11
W	0.37	0.40
Ni	Balance	Balance
Mo	8.74	8.46
Co	1.65	1.72
Cu	...	0.09
Al	...	0.06
Ti	...	<0.02
Fe	18.42	18.88
B	0.0036	0.0040

a constant shear strain rate to be maintained throughout the cycle. Cycle periods were dictated by the ability to cycle the specimen's temperature and maintain close control over the desired waveform. This resulted in a 4-min cycle period. The uniaxial TMD tests used for comparison in this study were conducted with an 8-min cycle period due to limitations related to accurate thermal strain compensation [*1,4*]. Such limitations did not arise in the torsional TMD experiments as no thermal strain compensation was required. Previous work on Hastelloy X indicated that a factor of two difference in strain rates should have a negligible effect on the material's deformation response in the temperatures of interest [*1,11*]. Therefore, in an effort to expedite testing, the torsional cycle times were maintained at 4 min. Load in the axial direction was maintained at zero in load control. Shear stress in the gage length was assumed nearly constant through the wall thickness and, as such, was based upon the mean radius (r) in the following manner

$$\tau = \frac{2Tr}{\pi(r_o^4 - r_i^4)} \tag{1}$$

where T is the torque, r_o is the outer radius, and r_i is the inner radius. This approximation is considered reasonable since the mean radius is six times the wall thickness.

The temperature and shear strain waveforms were time phased with a value of either 0 degrees (in phase) or 180 degrees (out of phase). Therefore, given that all the tests were initiated at the mean temperature of the temperature range, the in-phase (IP) and out-of-phase (OP) torsional tests corresponded to the cases of initial temperature increase and decrease, respectively. For example, an IP test with a temperature range of 400 to 600°C would initiate at 500°C and begin loading with temperature increasing towards 600°C. Note that the mechanical effects of positive or negative strain are identical in pure shear-type loading and the sign is strictly an issue of convention. Thus, the difference between IP and OP deformation in this study rests exclusively on the condition of initially loading towards the hot (IP) or cold (OP) extreme of the temperature range. This is not the case for the uniaxial TMD experiments

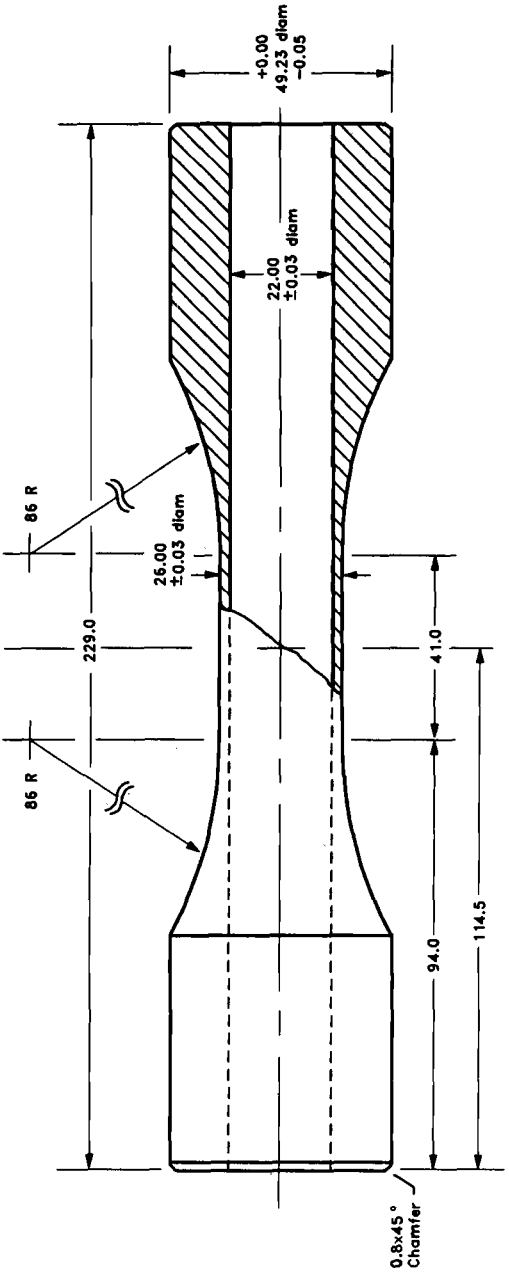
+0.00
49.23 diam
−0.05
22.00
±0.03 diam
86 R
26.00
±0.03 diam
229.0
41.0
86 R
94.0
114.5
0.8x45°
Chamfer

(a)

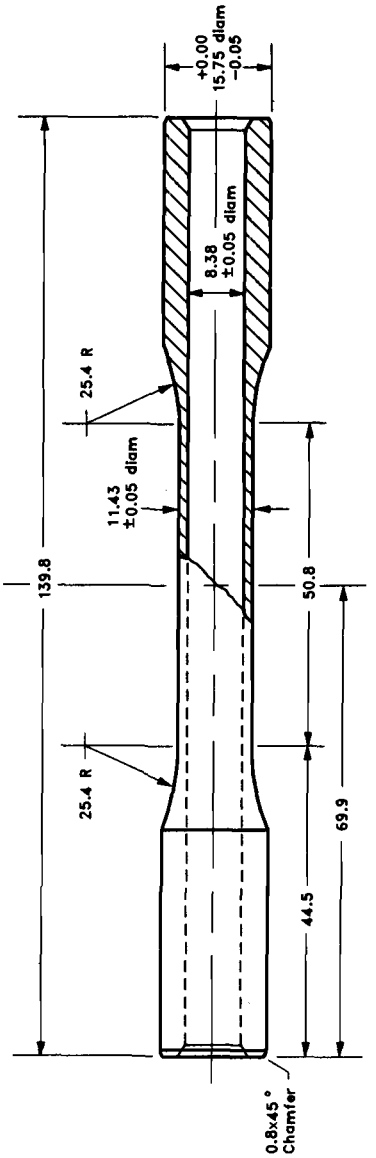

FIG. 1—*Specimen geometries:* (a) *torsion;* (b) *uniaxial.*

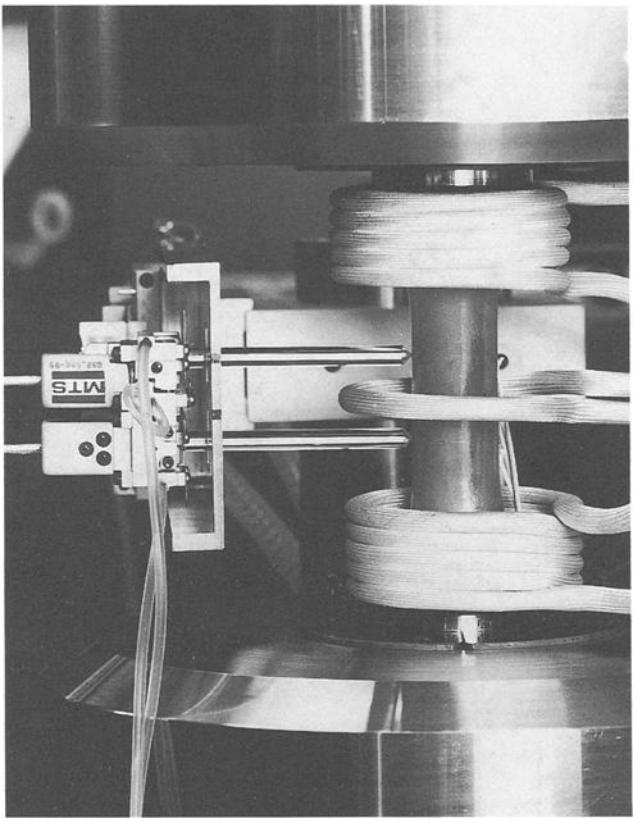

FIG. 2—*Torsional test apparatus showing instrumented specimen in place.*

where IP or OP implies that the maximum temperature coincides with the maximum tensile or compressive mechanical strain, respectively [*4*].

A minicomputer was used to command the temperature and shear strain control signals. Temperature, torque, axial strain, and shear strain were digitally recorded at a rate of one sample point per second (with each sample point representing the average of 100 measurements over the previous second). Axial and shear strains were measured with a water-cooled extensometer utilizing quartz probes with a gage length of 25 mm. The probes were spring loaded against indents of 250 μm nominal depth indented on the outside diameter of the specimen (Figs. 2 and 3). The extensometer provided an output which was proportional to the lateral displacement, s, of the lower probe relative to the upper probe. It was assumed that $s = r\phi$, where r is the mean radius and ϕ is the angle of twist in the gage length. The shear strain, γ, was then calculated as follows

$$\gamma = \frac{s}{l_0} \tag{2}$$

where l_0 is the nominal gage length of the extensometer (25 mm). Additional details of the axial/torsional testing facility, including additional figures, are given in Refs *12* and *13*.

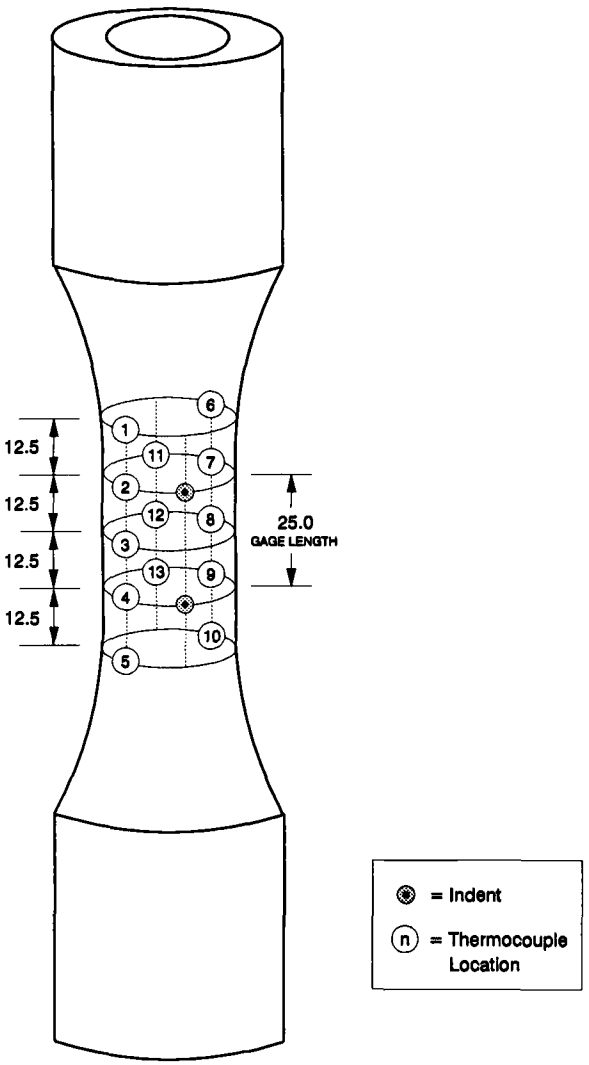

FIG. 3—*Extensometer indents and thermocouple locations on a torsional specimen (dimensions in mm).*

Dynamic Temperature Distribution

An early goal of the investigation was to obtain a uniform dynamic temperature response over the specimen's gage length during the 200°C temperature excursions. The temperature distribution was monitored by spot welding 13 K-type thermocouples at 12.5-mm intervals along the central portion of the specimen as shown in Fig. 3. Nine of the thirteen thermocouples were located within the specimen's gage section (the central 25-mm parallel section), and the remaining four were located in the constant radius transition region. Dynamic temperature extremes in the gage length were generally within $\pm 1\%$ of the target absolute temperatures. Figure 4 shows the triangular temperature profiles measured by the six gage-section ther-

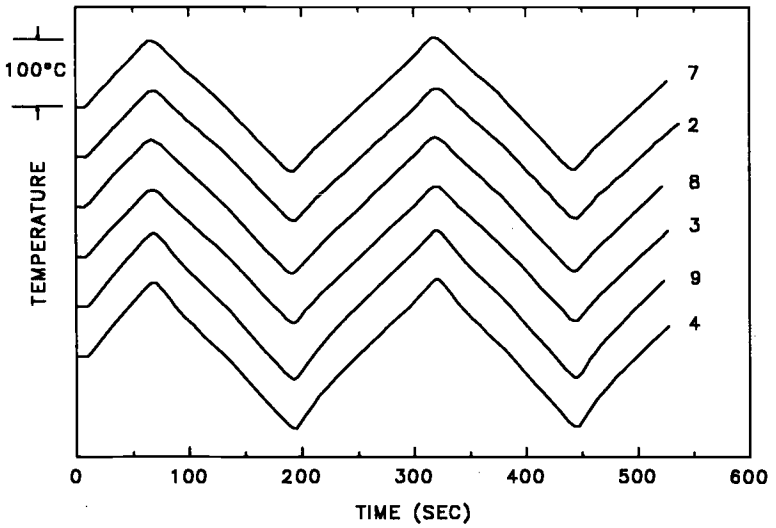

FIG. 4—*Triangular temperature waveforms measured by gage-section thermocouples during the first two thermal cycles.*

mocouples during the first two cycles. All thermocouples were initially at the same temperature and are separated here for convenience of presentation. Thermocouples 2 and 7 were near the top extensometer probe, 3 and 8 were at the middle, and 4 and 9 were near the bottom extensometer probe. Cycle times less than 4 min resulted in excessive deviations from the intended time-temperature profiles near the peaks and valleys because of limitations on the thermal response time of the system. In general, the linearity of the temperature waveforms improved at upper positions on the specimen (i.e., Thermocouples 2 and 7) due to quicker thermal responses. As a result of this condition, temperature control was improved by locating the controlling thermocouple at an upper-gage-section location. Additional details of the method of obtaining accurate, well-controlled temperature distributions and phasing for tubular specimens are given in Ref *4*.

Sources of Apparent Shear Strain Measurements

In this study, apparent or artificial shear strain measurements are defined as shear strains detected or indicated by the extensometer that have no real counterpart in the specimen. Two potential sources of apparent shear strain were identified. The first is promoted by mechanical crosstalk existing in the extensometer, and the second is a result of an axial misalignment of the extensometer indentations.

Many axial-torsion extensometers indicate a small apparent strain along one axis as a result of straining along the other axis. This mechanical coupling effect is commonly referred to as mechanical crosstalk. The shear strain output registered during a purely axial deformation is the component of particular interest for the present investigation. This component of apparent shear strain was a consequence of the axial strains resulting from thermal expansion during temperature cycling. The axial strains (thermal strains) during the 200°C temperature excursions ranged from 0.004 to 0.006 m/m peak to peak, depending on the average coefficient of thermal expansion in a particular temperature regime. On a calibration fixture supplied by the

manufacturer of the extensometer, axial strains of this magnitude resulted in apparent shear strains of about 10 μm/m. Relative to the shear strains of 0.005 m/m envisioned for a typical torsional TMD test, the mechanical crosstalk on the shear strain measurement due to axial thermal strains was deemed negligible (see additional analysis and discussion of this topic in Ref *14*).

Apparent shear strains due to the axial misalignment of the extensometer indentations can result from both an initial offset (due to indentation placement) and mechanical twist of the specimen. With changing temperature, the specimen will undergo expansion (or contraction) in the longitudinal, radial, and circumferential directions. If the indents are not in exact alignment along the longitudinal axis (as would normally be the case during any non-zero shear strain applied during a torsion test) the circumferential change will result in a relative indent displacement and, thus, an apparent shear strain.

Investigations of the effects of indentation misalignment were carried out for cyclic temperature variations of $\pm$ 100°C at various applied torques. However, given the resulting magnitudes of the apparent shear strains relative to the mechanical shear strains, this source of error was determined to be secondary. A more detailed discussion of the apparent strain effects of indentation misalignment is given in Ref *14*.

Torsional Test Parameters and Data Interpretation

Second Deviatoric Invariants

One common method of relating the deformation behavior of materials subjected to multiaxial loads is based on the second invariants of the deviatoric strain and stress tensors, J_2' and J_2, respectively [*15*]

$$J_2' = \tfrac{1}{6}[(\epsilon_x - \epsilon_y)^2 + (\epsilon_x - \epsilon_z)^2 + (\epsilon_y - \epsilon_z)^2] + \tfrac{1}{4}(\gamma_{xy}^2 + \gamma_{xz}^2 + \gamma_{yz}^2) \tag{3}$$

$$J_2 = \tfrac{1}{6}[(\sigma_x - \sigma_y)^2 + (\sigma_x - \sigma_z)^2 + (\sigma_y - \sigma_z)^2] + \tau_{xy}^2 + \tau_{xz}^2 + \tau_{yz}^2 \tag{4}$$

Use of the deviatoric component as a basis for yield (von Mises criterion) and inelastic behavior is very common, as the hydrostatic part of the stress is assumed to be unimportant for the onset of inelastic behavior of isotropic, polycrystalline metals. Assuming that the deformation behavior is similar in tension and compression (for mathematical convenience), use of the third invariant of the deviatoric stress tensor (J_3) is eliminated. Consequently, many yield and general viscoplastic constitutive theories are based exclusively on the J_2 and J_2' components of the stress and strain tensors, respectively.

One of the objectives of this study is to investigate the appropriateness of these assumptions under thermomechanical loading conditions. Through the use of existing uniaxial TMD data, parameters can be selected for the torsional TMD test which allow direct comparisons in a J_2' -J_2 stress-strain space. For example, conducting strain-controlled biaxial and uniaxial tests at the same J_2' limits and J_2' rate should result in similar trends in J_2 if the material has a viscoplastic flow surface well characterized by these parameters.

Unified viscoplastic constitutive theories developed to describe a material's viscoplastic behavior often involve complex mathematical frameworks. The functional forms of such theories frequently incorporate multiple internal state variables (tensors and scalars) evolving as functions of internal state, stress, and temperature. As a result, a predicted deformation response corresponding to a specific loading condition is not straightforward or obvious. Given a viscoplastic constitutive theory where the stress is introduced through an effective

value of only the J_2 component, it is obvious that by enforcing identical J_2 values for two different stress states (axial or torsional), the resulting J_2' values would be identical. However, it is not obvious that by enforcing identical J_2' values for two different strain states, the resulting J_2 values would be identical. Therefore, a representative J_2-based viscoplastic theory proposed by Robinson [*16,17*] was used to examine this condition and result. We note here that in this viscoplastic formulation the flow and evolutionary laws are taken as functions of the effective (external stress minus internal stress) J_2 components.

Two loading paths were used to examine the equivalence of the total J_2 paths theoretically predicted by equating the limits and rates of J_2', namely, uniaxial and torsional states. When the deformations (for any characterized material) were calculated and graphed in J_2'-J_2 space, the dual loops representing one fully reversed load cycle fell exactly on top of one another (Fig. 5). As the magnitudes of the invariants are irrelevant to the objective of the example, the invariants were normalized to their respective maximum values. Since both invariants are quadratic functions, they are always positive. Consequently, there are two J_2'-J_2 loops for every one stress-strain loop—one for the first strain-half of the cycle ($\gamma > 0$), and one for the second strain-half of the cycle ($\gamma < 0$). The results of this example demonstrate that indeed the J_2 paths predicted are equivalent for the two J_2' strain states imposed. It is reasonable to conclude that other J_2-based theories will predict identical responses in terms of J_2 when equivalent limits and rates of J_2' in uniaxial and torsional states are applied.

Based on the outcome of the above exercise, it was decided to conduct the torsional experiments at the limits of J_2' dictated by the existing uniaxial TMD database for Hastelloy X [*1*]. Here the goal was to determine whether or not the resulting deformations in the two types of tests could be correlated in a J_2'-J_2 space. The uniaxial TMD tests were conducted with fully reversed constant mechanical strain amplitudes. The expression for J_2' under a uniaxial state of stress is given by

$$J_2' = \frac{\epsilon^2}{3}(1 + \nu^{\text{eff}})^2 \tag{5}$$

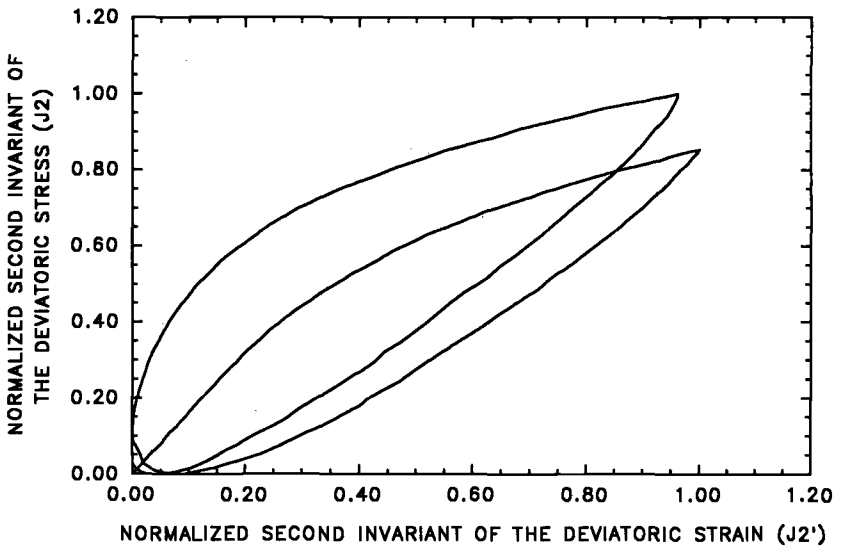

FIG. 5—*Predicted viscoplastic deformation in J_2'-J_2 space of a hypothetical material which obeys J_2-based constitutive laws during either shear or uniaxial loading at common limits and rate of J_2'.*

where ϵ is the corresponding axial strain component and ν^{eff} is the effective Poisson's ratio. Full strain tensor measurements for uniaxial TMD tests were not available; therefore, the rule of mixtures expression for ν^{eff} was used to estimate the missing transverse strains required to calculate J_2'

$$\nu^{eff} = \frac{\nu^{el}\epsilon^{el} + \nu^{pl}\epsilon^{pl}}{\epsilon^{el} + \epsilon^{pl}} \tag{6}$$

In Eq 6, superscripts "el" and "pl" refer to elastic and plastic components, respectively. The temperature dependent values used for ν^{el} were taken from Ref *18*. These values were generated from the same heat of material used for the torsional specimens in this study. The assumed value for ν^{pl} was ½. In calculating the J_2' values for any given uniaxial TMD cycle, two values for ν^{eff} were used: one for $\epsilon > 0$ and a second for $\epsilon < 0$. These two values of ν^{eff} were calculated based on the temperatures and $\epsilon^{el}/\epsilon^{pl}$ ratios existing at the maximum and minimum strain limits of the cycle, respectively. This method closely approximated a point-by-point calculation of ν^{eff}. Note that as the material experiences a change in the $\epsilon^{el}/\epsilon^{pl}$ ratio (i.e., the uniaxial cyclic stress increases or decreases) under fully reversed constant mechanical strains, ν^{eff} will change and, hence, the J_2' limits for each cycle will change during a constant uniaxial strain test.

The value of J_2' in a torsion test is given by the expression

$$J_2' = \frac{\gamma^2}{4} \tag{7}$$

Clearly, there is no dependence on any unmeasured strains in the above expression. Hence, there is a simple, proportional relationship between J_2' and the applied shear strain, γ. Furthermore, unlike the uniaxial case, a constant shear strain amplitude test implies a constant J_2' amplitude test.

It was not desirable (or trivial) to conduct the torsional TMD experiments with variable J_2' limits to mimic the uniaxial J_2' limits throughout the course of the test. Therefore, the torsional TMD J_2' limits were chosen to match those found in the first cycle of the uniaxial TMD data. Because the J_2' limits are matched only during the first deformation cycle, the forthcoming comparisons of J_2 and J_2' in torsional and uniaxial TMD tests are restricted to include only the first cycle.

A question remains concerning the equivalence of J_2' rates in the uniaxial and torsional tests due to the variation in the Poisson's ratio in the uniaxial tests over the course of the cycle. That is, does the triangular axial mechanical strain waveform used in the uniaxial test correspond to a triangular shear strain waveform in the torsion test if we are trying to maintain identical J_2' values throughout the cycle? The question can be addressed by taking uniaxial stress-strain data for a given cycle and computing the corresponding equivalent shear strains on a point-by-point basis. The result of such a calculation is shown in Fig. 6. Superposed on the discrete values of equivalent shear strain is a triangular waveform representing the actual control variable during a torsional test. It is clear that the equivalent shear strains fall quite closely to the triangular waveform. This indicates that the triangular shear strain waveform will closely approximate the variation of J_2' resulting from the triangular uniaxial strain waveform.

In summary, it has been shown that if we can measure or calculate limits of J_2' for a particular cycle from a strain amplitude-controlled uniaxial TMD test, we can easily duplicate these values of J_2' in a strain-controlled torsion test, such that the applied J_2' waveforms, rates, and limits are nearly identical for that cycle in both tests.

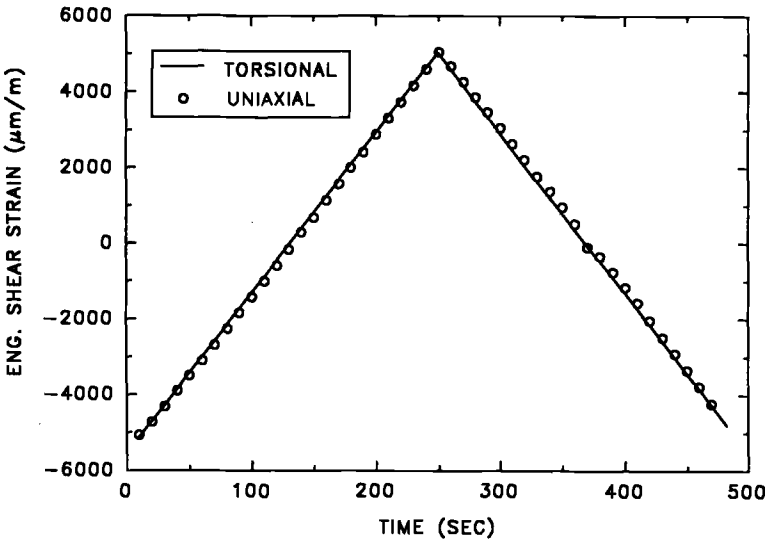

FIG. 6—*Variation of equivalent shear strain from a uniaxial test and actual shear strain from a torsional test.*

Test Matrix

The test matrix showing the limits and sequences of temperature and strain for torsional and uniaxial specimens is given in Table 2. Because the shear strain limits of the torsional experiments were chosen to match the J_2' limits experienced on the first cycle of the strain-controlled uniaxial TMD tests, the shear strain limits in Table 2 are not necessarily fully reversed. The uniaxial mechanical strain limits were fully reversed.

The temperature ranges for the torsional test matrix were selected based on previous experience with uniaxial TMD of Hastelloy X [*1*], which revealed that the 400 to 600°C temperature regime results in increased hardening because it maximizes the combined strain aging effects of carbide precipitation and solute drag. The 600 to 800°C temperature range also provokes significant hardening at 600°C, but strong thermal recovery mechanisms at 800°C lessen the hardening at the cold extreme of the cycle (relative to that at either extreme of the 400 to 600°C temperature regime) and induce softening at the hot extreme of the cycle. Hastelloy X

TABLE 2—*Test matrix.*

Torsional Specimen	Temperature[1]/ Strain Sequence	Temperature Range, °C	Engineering Shear Strain Limits, Max/ Min (m/m)	Corresponding Uniaxial Specimen[2]
ATHX10	H, C/+, −	400–600	0.005 20/−0.005 17	UHX458
ATHX11	C, H/+, −	400–600	0.005 16/−0.005 20	UHX448
ATHX6	H, C/+, −	600–800	0.005 37/−0.005 38	UHX467
ATHX15	C, H/+, −	600–800	0.005 19/−0.005 12	UHX484
ATHX9	H, C/+, −	800–1000	0.005 34/−0.005 23	UHX459
ATHX12	C, H/+, −	800–1000	0.005 17/−0.005 30	UHX491

[1] H and C correspond to hot and cold temperature limits.
[2] All uniaxial specimens were cyclically loaded at ±0.0030 m/m mechanical strain.

saturated immediately in the 800 to 1000°C temperature regime in the previous uniaxial experiments and therefore exhibited no softening or hardening.

Results and Discussion

Initial cyclic stress-strain loops (up to the third strain reversal) for the in-phase and out-of-phase torsional tests are shown in Fig. 7. By the third strain reversal, the 400 to 600°C loop is nearly symmetric about zero stress, while the deformation responses at higher temperatures

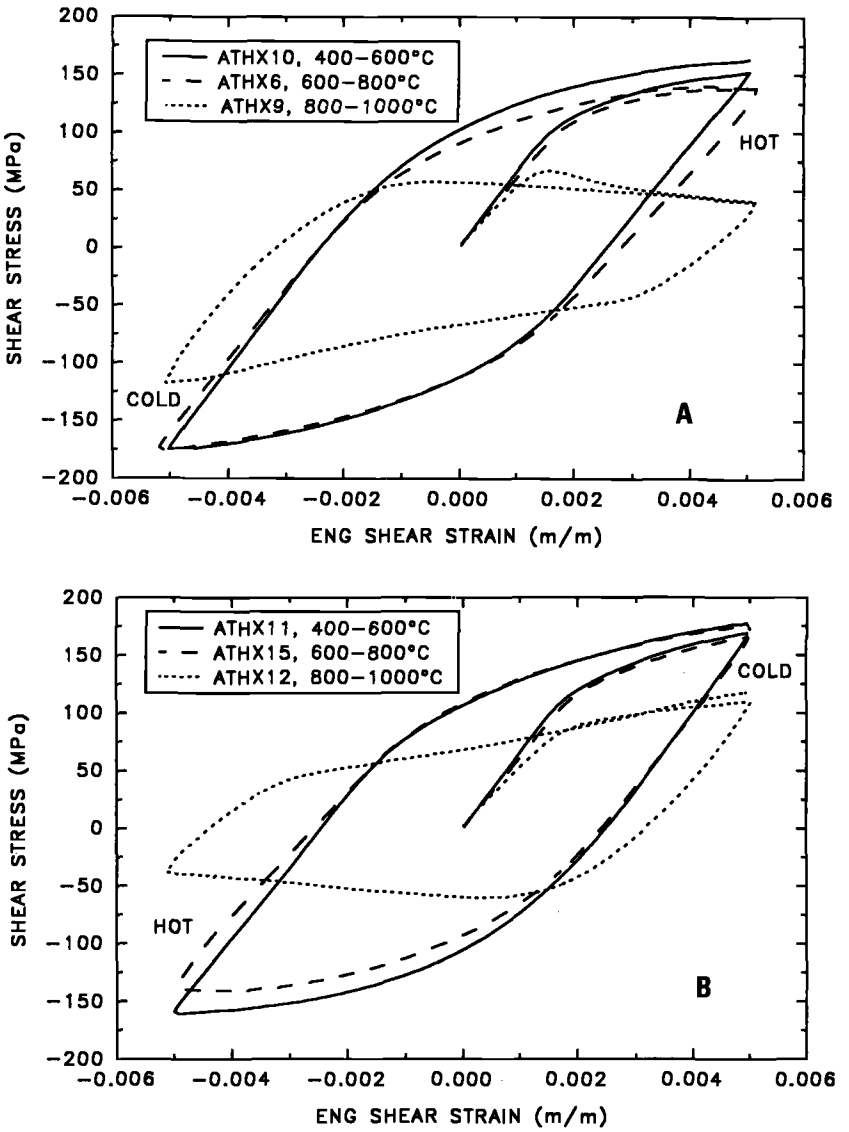

FIG. 7—*Initial stress-strain loops for torsional tests:* (A) *in-phase;* (B) *out-of-phase.*

exhibit notable mean stresses. Note the significant loss of load-carrying capability (stress relaxation) of the 800 to 1000°C TMD specimens, particularly at the 1000°C limit. Also evident is the decreasing slope of the unloading path with increased temperatures. Technically, one cannot infer a shear modulus from such slopes due to the time-dependent deformation and changing temperature during the loading cycle. However, for a fixed thermomechanical loading regime, cycle-dependent changes in the slope of the unloading path would qualitatively indicate a metallurgical change and/or damage development in the material being tested. This occurrence will be pointed out subsequently.

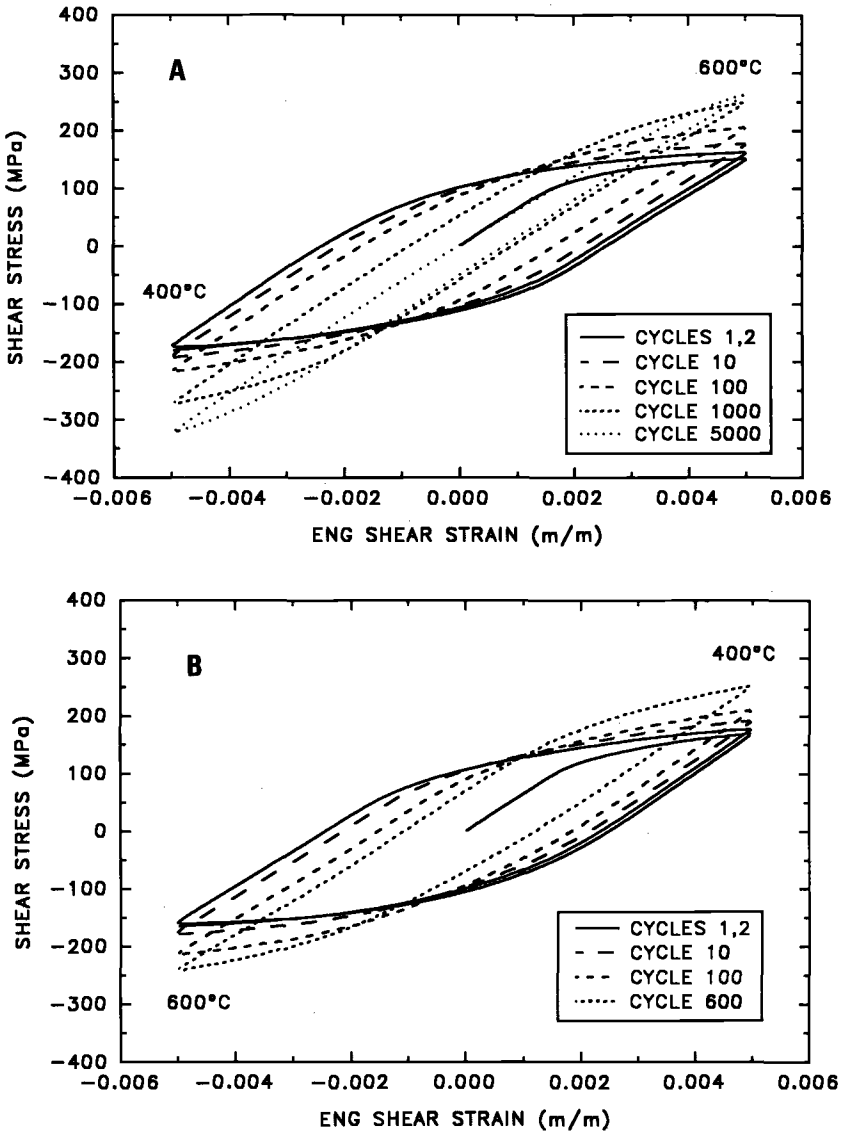

FIG. 8—*Stress-strain loops during torsional TMD tests in the 400 to 600°C temperature range:* (A) *in-phase;* (B) *out-of-phase.*

Substantial cyclic stress hardening is evident in the stress-strain loops shown in Fig. 8 for the 400 to 600°C IP and OP tests, particularly at the 400°C temperature limit as evidenced best by the longer duration in-phase test. Specimens tested in the 600 to 800°C range revealed substantial hardening at the 600°C limit and softening at the 800°C limit (Fig. 9). An interesting feature in the IP and OP 600 to 800°C tests that was not observed in the uniaxial tests is the decreasing slope of the unloading path from the 800°C limit with respect to cycles. The slope of the unloading path in the cooler half of the cycle remained essentially constant, however. An additional 600 to 800°C test not included in this paper displayed similar behavior, sup-

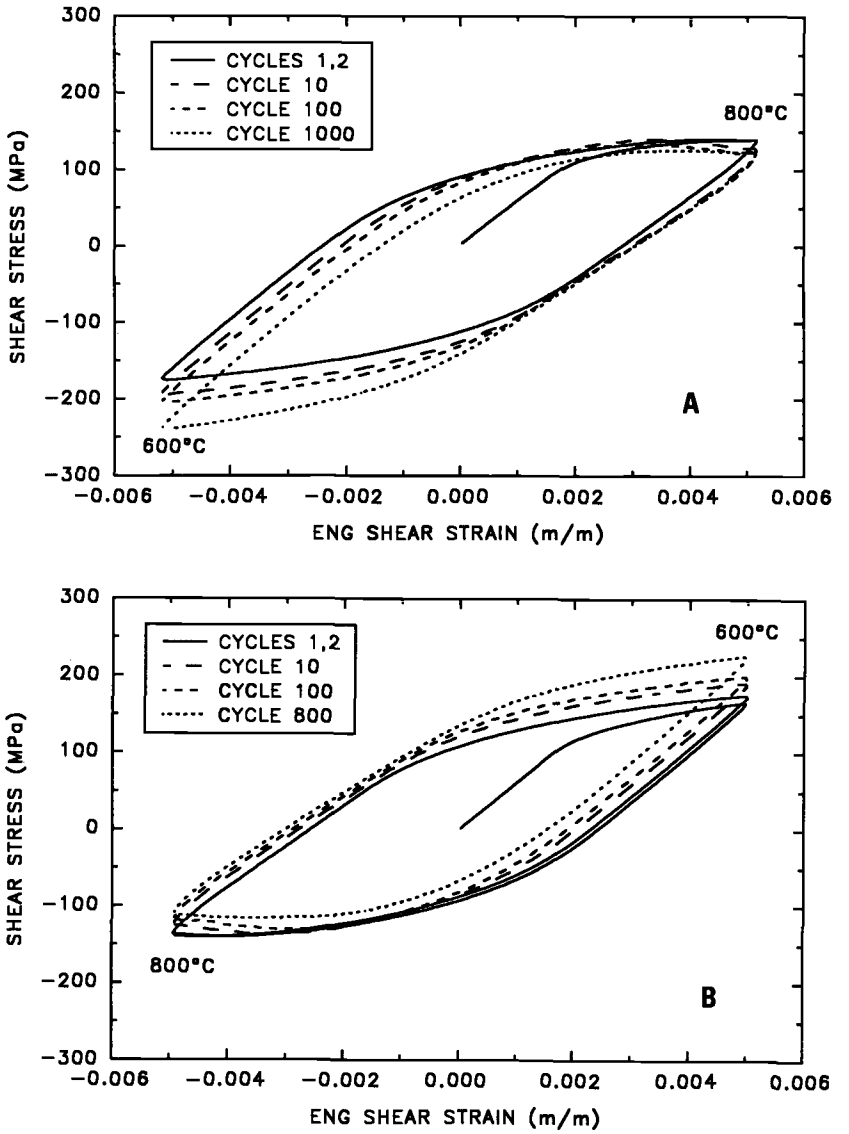

FIG. 9—*Stress-strain loops during torsional TMD tests in the 600 to 800°C temperature range:* (A) *in-phase;* (B) *out-of-phase.*

porting the repeatability of this result. A detailed microstructural investigation would be needed in order to determine whether or not physical changes in the alloy promoted this phenomenon. No sequential stress-strain loops for the 800 to 1000°C tests are included herein because the material was essentially cyclically neutral throughout both the IP and OP tests.

As evidence of the repeatability of the hardening trends, duplicate 400 to 600°C IP tests are shown in Fig. 10 (ATHX1 was prematurely terminated due to a heater malfunction and therefore excluded from the test matrix). The shear stress values have been normalized with respect to their first cycle values. Normalized shear stresses in this comparison were measured at the point of shear strain reversal. The agreement between the two data sets is exceptionally good. Also clearly evident by the hardening trends is the initially higher rate of hardening at the 600°C temperature limit up to about 100 cycles, followed by an accelerated hardening rate (on a log scale) at the 400°C temperature limit beginning at about 500 cycles. This behavior is similar to that observed during the uniaxial TMD testing of Hastelloy X in this temperature range where a greater degree of hardening was found to result from the combined effects of solute drag and precipitation hardening [*1,11*].

An interesting axial-torsional interactive effect observed in the torsional tests is axial strain ratchetting. This phenomenon is often referred to as the Poynting-Swift effect [*19–21*]. The maximum and minimum axial strains of select cycles are shown in Fig. 11 for two extreme examples. The first example is a 800 to 1000°C IP test in which 0.0018 m/m axial strain accumulated within 40 cycles; the second is a 600 to 800°C IP test in which −0.0018 m/m axial strain accumulated after 2700 cycles. In all tests but one, axial strain ratchetted in the positive direction. A comprehensive investigation of the room-temperature axial ratchetting phenomenon by Wack [*22*] with several metallic materials in torsion led to the following conclusions: the sign of the axial ratchet is theoretically positive; and the amount of ratchet per cycle seems material dependent, is highly influenced by axial forces, and is sensitive to the loading history. Since the present experiments were conducted at elevated temperatures at which viscous effects are significant, the relative influence of the factors cited by Wack may differ. For example, the average rates of axial ratchetting in the 800 to 1000°C tests were up to two orders of

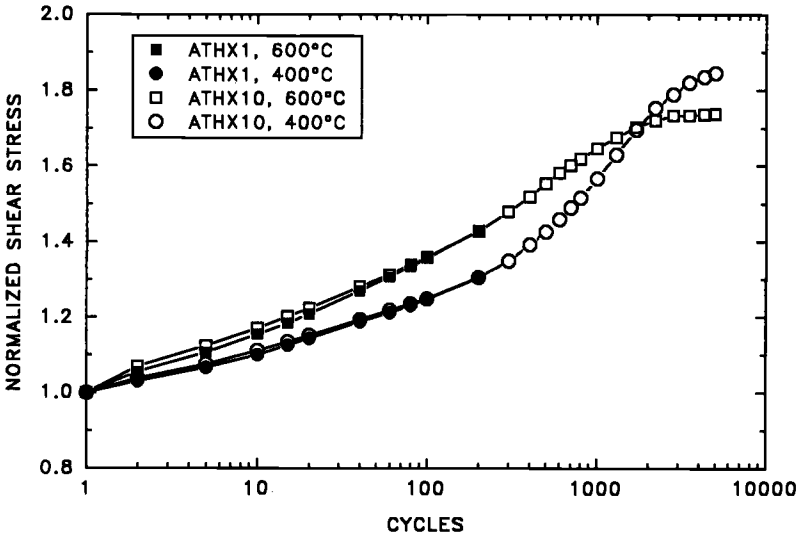

FIG. 10—*Comparison of hardening in two in-phase torsional TMD tests with the 400 to 600°C temperature range.*

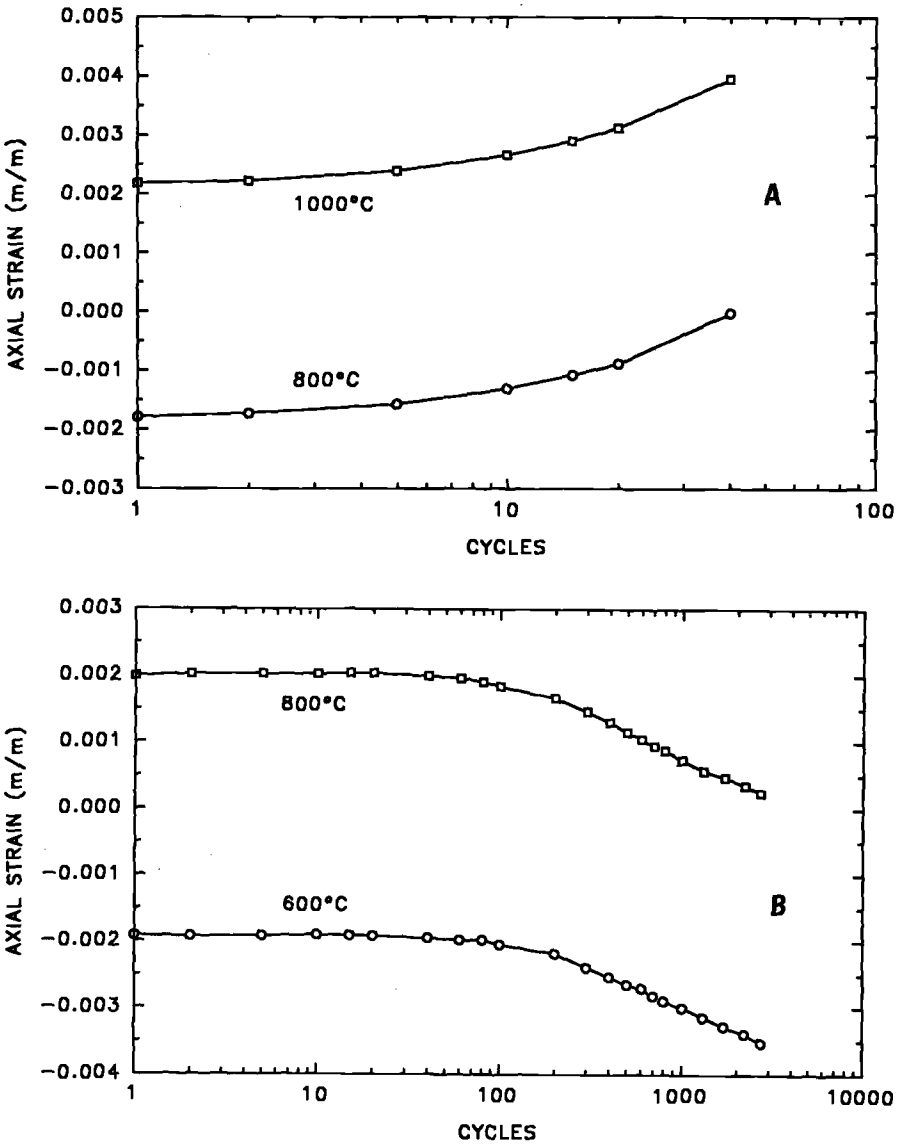

FIG. 11—*Examples of axial strain ratchetting in torsional TMD tests:* (A) *800 to 1000°C, in-phase;* (B) *600 to 800°C, in-phase.*

magnitude greater than those seen in the lower temperature regimes. As the ratchetting required at least several cycles (in the extreme case) before it accumulated to a measurable quantity, it was felt to have no influence on the first-cycle deformation and corresponding values of J_2'.

Comparisons of first-cycle thermomechanical deformations in the J_2'-J_2 space are given for the three temperature ranges in Figs. 12–15. In these figures, coincidental zero values of both J_2' and J_2 exist only at the start of the test. Overall, the correlations of the uniaxial and torsional

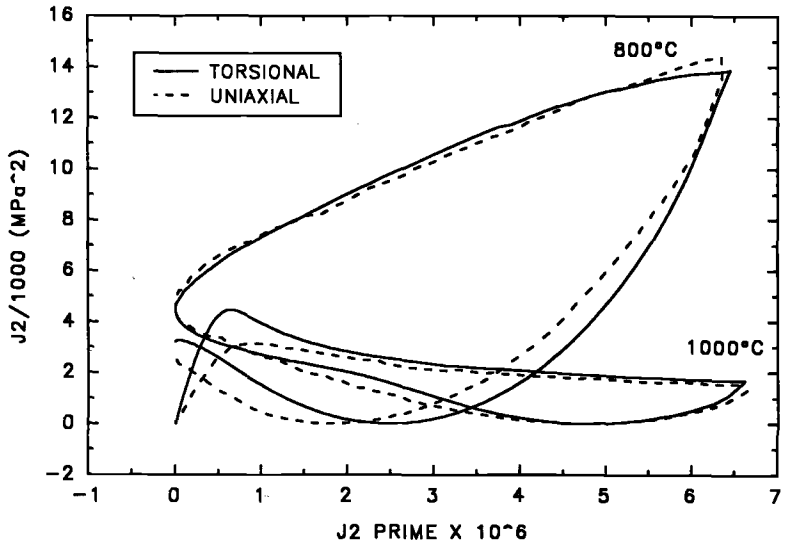

FIG. 12—*First cycle J_2'-J_2 loops for torsional and uniaxial tests in 800 to 1000°C temperature range: hot/cold temperature sequence.*

data were excellent in the 800 to 1000°C temperature range (Fig. 12). The only portion of this loop where the data did not agree exceptionally well is the initial loading. This may be a result of the slight error introduced in the uniaxial J_2' calculations based on the assumptions of using ν^{eff}. The 600 to 800°C data also resulted in fairly good agreement (Fig. 13). This result clearly suggests that the multiaxial TMD behavior of Hastelloy X is well characterized by the scalar parameter J_2 at these temperatures.

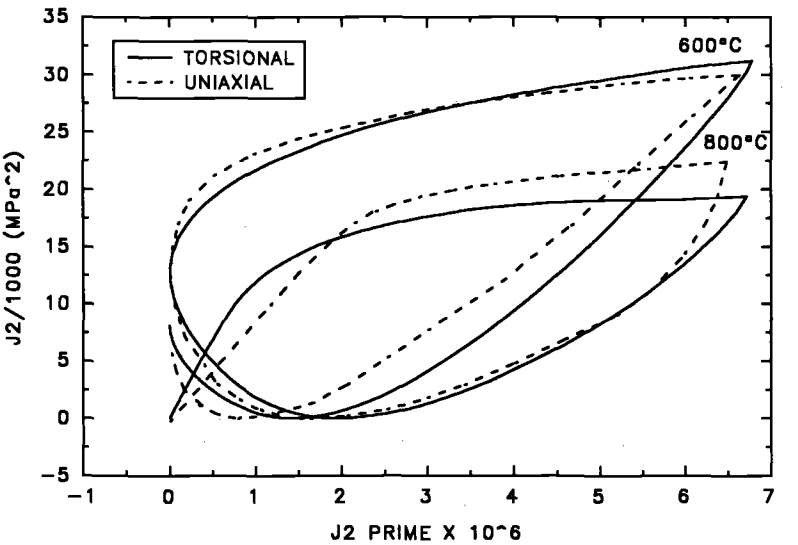

FIG. 13—*First cycle J_2'-J_2 loops for torsional and uniaxial tests in 600 to 800°C temperature range: hot/cold temperature sequence.*

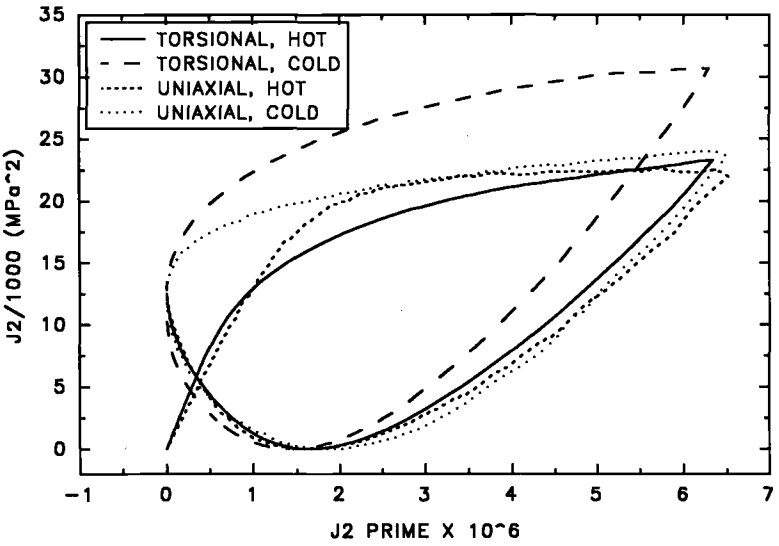

FIG. 14—*First cycle* J_2'-J_2 *loops for torsional and uniaxial tests in 400 to 600°C temperature range: hot/cold temperature sequence.*

In contrast to the higher-temperature correlations, the 400 to 600°C IP and OP correlations (Figs. 14 and 15, respectively) were not good, particularly during the second strain half of the cycle. Note that the Bauschinger effect was much more pronounced in the IP and OP uniaxial loading cases. Unfortunately, because of the thermomechanical nature of the cycle (i.e., the continually changing elastic modulus) it is difficult to isolate or quantify this effect.

Recall that the 400 to 600°C temperature range is where the most hardening occurs due to

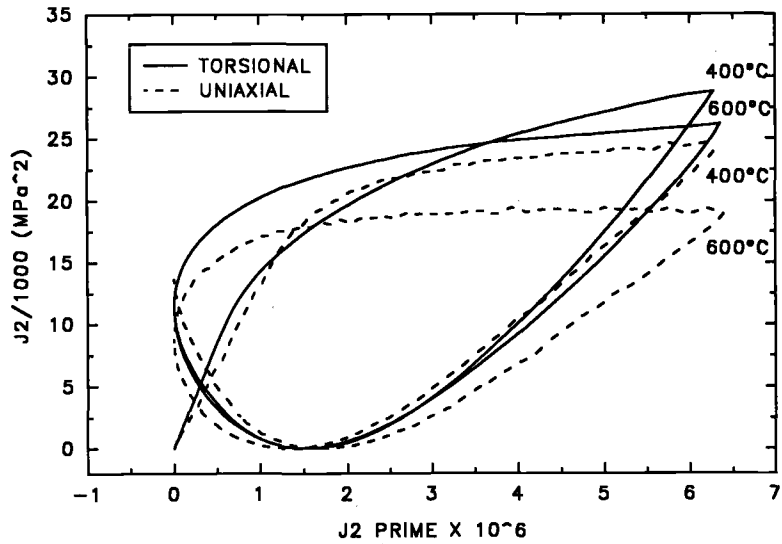

FIG. 15—*First cycle* J_2'-J_2 *loops for torsional and uniaxial tests in 400 to 600°C temperature range: cold/hot temperature sequence.*

the interaction of carbide precipitation and solute drag [*1,11*]. Considering that the hardening is greatest in this temperature range, the results suggest that the hardening mechanisms active in torsional TMD are significantly different from those in uniaxial TMD. Deformation behaviors may be slightly influenced by the heat of material from which the specimens were fabricated, but this is not a likely explanation for the significant differences seen here. In the 400 to 600°C temperature range, a J_2-based description of the viscoplastic deformation does not appear capable of collapsing the axial and torsional TMD. In similar fashion, other investigators have also seen increased isothermal hardening (with a cobalt-base superalloy) in torsional deformation versus axial deformation when the tests are compared with von Mises-type stresses and strains [*23*].

Conclusions

Techniques developed under uniaxial conditions to control mechanical strain/temperature phasing were effectively transferred to torsional TMD conditions. The TMD tests were conducted in strain control without compensation for thermal strains. This is the primary advantage of torsional, strain-controlled TMD testing over uniaxial, strain-controlled TMD testing where thermal strain compensation introduces control complexities. However, with the extensometry employed in this study, secondary sources of error may arise under TMD conditions relating to apparent shear strain measurements promoted by indent misalignment and extensional strain ratchetting. A simple analysis revealed that the magnitudes of these errors are negligible.

Based on the limited amount of data generated, the following conclusions can be made concerning the hardening of Hastelloy X during TMD in torsion: (a) the 400 to 600°C tests resulted in the most hardening, particularly at the 400°C temperature limit; (b) the 600 to 800°C tests resulted in hardening at the 600°C temperature limit and softening at the 800°C limit; and (c) the 800 to 1000°C tests resulted in a saturated material response at both temperature limits. All temperature ranges investigated resulted in non-zero mean shear stresses.

First-cycle thermomechanical torsional and uniaxial deformations were compared. The experiments were based on forcing identical values for the second invariant of deviatoric strain tensor (J_2') and comparing the resulting values for the second invariant of the deviatoric stress tensor (J_2). The following results were obtained: (a) excellent correlation was exhibited in the 800 to 1000°C TMD tests; (b) fairly good correlation was obtained in the 600 to 800°C TMD tests; and (c) fair to poor correlations were experienced in the 400 to 600°C TMD tests. The results suggest that the deformation of Hastelloy X is well described by a classical J_2-based viscoplastic theory in the upper temperature ranges where reduced kinematic hardening takes place and recovery effects are dominant. In those temperature ranges involving substantial kinematic hardening (e.g., 400 to 600°C), the hardening mechanisms active in uniaxial and torsional loadings appear significantly different: the Bauschinger effect in the 400 to 600°C uniaxial TMD was consistently stronger. In these cases, the deformation loops did not agree in the J_2'-J_2 state space.

Acknowledgments

The first author would like to thank the NASA/ASEE fellowship program for providing the funding that made possible his summer residence at NASA LeRC, where this work was carried out. The authors also wish to acknowledge S. Arnold, P. Bonacuse, A. Freed, and S. Kalluri for their insightful discussions on the experimental and analytical aspects of this work. Also, technical assistance in the laboratory from C. Burke, R. Corner, D. Pech, R. Shinn, and S. Smith is greatly appreciated.

References

[1] Castelli, M. G., Miner, R. V., and Robinson, D. N., "Thermomechanical Deformation Behavior of a Dynamic Strain Aging Alloy, Hastelloy X," *Thermo-Mechanical Fatigue Behavior of Materials, STP 1186,* in press, H. Sehitoglu, Ed., American Society for Testing and Materials, Philadelphia, 1993, pp. 000–000.

[2] Murakami, S., Kawai, M., and Ohmi, Y., "Effects of Amplitude-History and Temperature-History on Multiaxial Cyclic Behavior of Type 316 Stainless Steel," *Journal of Engineering Materials and Technology, Transactions of ASME,* Vol. 111, 1989, pp. 278–285.

[3] Bhattachar, V. and Stouffer, D. C., "A Constitutive Model for the Thermomechanical Fatigue Response of René 80," Sixth TMF Workshop, 5–6 June 1991, NASA LeRC, Cleveland, OH.

[4] Castelli, M. G. and Ellis, J. R., "Improved Techniques for Thermomechanical Testing in Support of Deformation Modeling," *Thermo-Mechanical Fatigue Behavior of Materials,* in press, H. Sehitoglu, Ed., American Society for Testing and Materials, Philadelphia, 1993, pp.

[5] Hopkins, S. W., "Low-Cycle Thermal Mechanical Fatigue Testing," *Thermal Fatigue of Materials and Components, STP 612,* D. A. Spera and D. F. Mowbray, Eds., American Society for Testing and Materials, Philadelphia, 1976, pp. 157–169.

[6] Jones, W. B., Schmale, D. T., and Bourcier, R. J., "A Test System for Computer-Controlled Thermomechanical Fatigue Testing," SAND-88-2183C, Sandia National Laboratories, Albuquerque, NM, 1988.

[7] Ellis, J. R. and Robinson, R. N., "Some Advances in Experimentation Supporting Development of Viscoplastic Constitutive Models," NASA CR-174855, LeRC, Cleveland, OH, April 1985.

[8] Jordan, E. H., "Biaxial Thermo-Mechanical Fatigue," *Proceedings,* 4th Annual Hostile Environments and High Temperature Measurements Conference, 24–25 March 1987, Windsor Locks, CT, Society for Experimental Mechanics, Bethel, CT, pp. 1–6.

[9] Bonacuse, P. J. and Kalluri, S., "Axial-Torsional Fatigue: A Study of Tubular Specimen Thickness Effects," NASA TM-103637, LeRC, Cleveland, OH, December 1990.

[10] Ellis, J. R. and Bartolotta, P. A., "Adjustable Induction Heating Coil," NASA Tech Brief, Vol. 14, No. 11, November 1990, p. 50.

[11] Miner, R. V. and Castelli, M. G., "Hardening Mechanisms in a Dynamic Strain Aging Alloy, Hastelloy X, During Isothermal and Thermomechanical Cyclic Deformation," *Metallurgical Transactions,* Vol. 23A, Feb. 1992, pp. 551–562.

[12] Bartolotta, P. A. and McGaw, M. A., "A High Temperature Fatigue and Structures Testing Facility," NASA TM-100151, LeRC, Cleveland, OH, August 1987.

[13] Bonacuse, P. J. and Kalluri, S., "Results of Inphase Axial-Torsional Fatigue Experiments on 304 Stainless Steel," NASA TM-101464, LeRC, Cleveland, OH, March 1989.

[14] Castelli, M. G., Bakis, C. E., and Ellis, J. R., "Experimental Investigation of Cyclic Thermomechanical Deformation in Torsion," NASA TM-105938, LeRC, Cleveland, OH, November, 1992.

[15] Mendelson, A., *Plasticity: Theory and Application,* Krieger, Malabar, FL, 1983.

[16] Robinson, D. N., "A Unified Creep-Plasticity Model for Structural Metals at High Temperature," ORNL/TM-5969, Engineering Technology Division, ORNL, Oak Ridge, TN, October 1978.

[17] Robinson, D. N. and Swindeman, R. W., "Unified Creep-Plasticity Constitutive Equations for Structural Alloys at Elevated Temperatures," ORNL/TM-8444, Engineering Technology Division, ORNL, Oak Ridge, TN, October 1982.

[18] Kalluri, S. and Bonacuse, P. J., "A Data Acquisition and Control Program for Axial-Torsional Fatigue Testing," *Applications of Automation Technology to Fatigue and Fracture Testing, STP 1092,* A. A. Braun, N. E. Ashbaugh, and F. M. Smith, Eds., American Society for Testing and Materials, Philadelphia, 1990, pp. 269–287.

[19] Poynting, J. H., *Proceedings of the Royal Society, Series A,* Vol. 82, 1909, pp. 546–559.

[20] Poynting, J. H., *Proceedings of the Royal Society, Series A,* Vol. 86, 1912, pp. 543–561.

[21] Swift, H. W., *Engineering,* Vol. 163, 1947, pp. 253–257.

[22] Wack, B., "The Torsion of a Tube (or a Rod): General Cylindrical Kinematics and Some Axial Deformation and Ratchet Measurements," *Acta Mechanica,* Vol. 80, 1989, pp. 39–59.

[23] Bonacuse, P. J. and Kalluri, S., "Elevated Temperature Axial and Torsional Fatigue Behavior of Haynes 188," NASA TM-105396, LeRC, Cleveland, OH, June 1992.

Dominique Nouailhas,[1] *Didier Pacou,*[1] *Georges Cailletaud,*[2] *Fabienne Hanriot,*[2] *and Luc Rémy*[2]

Experimental Study of the Anisotropic Behavior of the CMSX2 Single-Crystal Superalloy Under Tension-Torsion Loadings

REFERENCE: Nouailhas, D., Pacou, D., Cailletaud, G., Hanriot, F., and Rémy, L., **"Experimental Study of the Anisotropic Behavior of the CMSX2 Single-Crystal Superalloy Under Tension-Torsion Loadings,"** *Advances in Multiaxial Fatigue, ASTM STP 1191,* D. L. McDowell and R. Ellis, Eds., American Society for Testing and Materials, Philadelphia, 1993, pp. 244–258.

ABSTRACT: A thin tube made in single crystal is submitted to tension-torsion loading. The axis of the tube coincides with the ⟨001⟩ material axis. Local strain measurements made by means of strain gages experimentally demonstrate that the deformation is mainly localized in the ⟨110⟩ type zones. This is confirmed by microstructural observations of replicas. An experimental loading surface in these soft zones is derived. An analysis of the experimental data is successfully made through the Schmid law, involving both cube and octahedral slip.

KEY WORDS: multiaxial loading, superalloy single crystal, loading surface, slip traces, Schmid law

The use of single-crystal superalloys for new generations of turbine blades needs the development of constitutive equations that are able to properly predict the cyclic behavior of these anisotropic materials. To this end, several experimental studies were conducted on various single-crystal superalloys, but mainly under uniaxial loadings following different crystallographic orientations, typically: ⟨001⟩, ⟨111⟩, ⟨011⟩, and ⟨123⟩.

Another way to investigate the anisotropy is to perform tension-torsion tests on thin-walled tube specimens grown in the ⟨001⟩ direction. In that case, the sample is no longer a "material element," and the analysis of the experiment requires a precise determination of local quantities. The present paper deals with the experimental study of this "structure," which is detailed in the following sections. The first results, obtained at 950°C, have led to the definition of a set of new tests at room temperature in order to have access to local strain measurements by the use of strain gages. Due to the cubic symmetry, two areas corresponding to ⟨100⟩ and ⟨110⟩ require special attention. Various loading paths are explored such as tension, torsion, and in-phase tension-torsion. The yield domain is also explored in the axial stress-shear stress plane for these two orientations. Experimental results are interpreted on the basis of Schmid law predictions. The last section discusses activated slip systems. The analysis of the slip traces is made by a replica technique. Both octahedral and cube slips are present for torsion. Only octahedral slip is activated in tension. The relative amount of slip is studied for tension-torsion cases. The ⟨110⟩ regions are more deformed than the ⟨100⟩ ones. The last result concerns the rotation of the normal during plastic flow. It is shown that for tension-torsion loading with

[1] Research engineer and technician, respectively, ONERA, BP 72, 92322 Châtillon Cedex, France.
[2] Maître de Recherche, research engineer, directeur de Recherche, respectively, CNRS, Centre des Matériaux, Ecole des Mines de Paris BP 87, 91003 Evry Cedex, France.

dominant torsion the initial yield direction is in pure shear. The flow in the tension direction occurs only for increasing load. The stress at which the axial plastic strain flow starts depends on the slip system interactions. This type of test allowed us to get information on the interaction matrix for micromechanical models.

Testing Machine, Material, and Specimen

The installation is a tension-torsion fatigue machine consisting of two hydraulic jacks with hydrostatic levels. The force and torque measurements are made by a load cell. A PID (proportional, integral, differential) regulation loop slaves each actuator to the programmed force, torque, angle, displacement, and deformation components. Under a maximum frequency of 25 Hz, the capacities of the machine are: force = $\pm 63\,000$ N, torque = ± 500 N·m, displacement = ± 20 mm, and angle = $\pm 60°$.

The system is connected to a computer so that it can be controlled in real time while the tension and torsion data are being acquired. Various loading paths can be imposed, and a specific program for the detection of yield surfaces has been written.

For the tests at high temperature, the specimen is heated by a medium-frequency induction system carrying an inductor specially designed for it. This inductor heats the specimen isothermally, producing a very good temperature distribution [*1*] (± 3°C along the gage length). The temperature is regulated in time by a PID measurement made with an infrared sight.

At high temperature, the strains are obtained from displacement measurements by using an equivalent length depending on the specimen geometry [*2,3*]. At room temperature, strain gage measurements are used.

The shear stress τ is evaluated on the outside surface of the specimen by using a viscoplasticity correction [*4*] so that finally the chosen value lies between the elastic and perfectly plastic calculations.

The material is the CMSX2 single-crystal nickel base alloy. Tubes are manufactured by SNECMA by the directional solidification process, and the ⟨001⟩ orientation of each tube is taken with respect to the dendritic growth direction. The composition range in weight percent is given in Table 1. Appropriated thermal treatment TR1 is applied (Table 1) in order to get a homogeneous distribution of cuboidal γ' precipitates of a size of about 0.5 μm. The high-volume fraction of γ' ($\approx 65\%$) gives the alloy its excellent creep resistance. An R2 treatment is applied (Table 1) after final precision rectification and polishing of the specimens.

Due to the impossibility of manufacturing a tubular single-crystal longer than 14 cm, the ends of the thin-walled tube specimen are made in Hastelloy X and brazed on the useful single-crystal part. The inside and outside diameters are 14 and 16 mm, respectively, and the gage

TABLE 1—*CMSX2 composition and thermal treatments, %.*

Ni	C	Cr	W	TA	Co	Al	
Base	0.001	7.77	8.06	6.00	4.64	5.5	
Ti	Mo	Fe	Mn	Si	Hf	S	P
1.00	0.61	0.02	0.001	0.005	0.01	0.0001	0.001

Heat Treatments

T = 1315°C/3 h/vacuum
R1 = 1100°C/10 h/argon
R2 = 870°C/16 h/argon

length is 24 mm. For the tests at room temperature, the crystallographic orientations ⟨100⟩ and ⟨110⟩ are checked by the Laü X-ray back reflection method, and two rosette microstrain gages are stuck on these precise orientations as illustrated in Fig. 1.

Assuming that the only mechanism responsible for the plastic deformation is the crystallographic slip, all the test results will be interpreted using Schmid's law. The potential slip systems are given in Fig. 2 for torsion loadings. In tension, only octahedral slip can occur since the specimen is oriented in ⟨001⟩ direction, and eight systems contribute to the plastic deformation with the same Schmid factor of $1/\sqrt{6}$. In torsion, two cases have to be considered, assuming either cube (Fig. 2*a*) or octahedral slip (Fig. 2*b*) and for both situations: ⟨100⟩ and ⟨110⟩. In either case, the yield stresses in shear predicted by Schmid law are lower for ⟨110⟩ than for ⟨100⟩ and are in the ratio of $\sqrt{2}$ ($\tau_{100} = \sqrt{2}\,\tau_{110}$).

An illustration of the resulting behavior under tension-shear loading is given in Fig. 3. The diagram represents the theoretical surfaces obtained from the Schmid criterion in the axial stress (σ_{33})-shear stress (σ_{23}) plane; for the first two cases (Figs. 3*a* and 3*b*), the coordinate system corresponds to the crystallographic directions ⟨100⟩, ⟨010⟩, ⟨001⟩; and for the other ones (Figs. 3*c* and 3*d*), the coordinate system corresponds to the directions ⟨110⟩, ⟨$\bar{1}$10⟩, ⟨001⟩. Only octahedral slip is introduced for Fig. 3*a* and Fig. 3*c*; both cube and octahedral slip are involved for Fig. 3*b* and Fig. 3*d*. The diagram is made with a reference stress in tension equal to 1000 MPa (i.e., a critical resolved shear on octahedral planes of 408 MPa). The critical resolved shear stress is also chosen equal to 408 MPa for the cube slip systems. Such an exercise shows that the results obtained are far from a quadratic criterion like von Mises [*5*] or Hill [*6*]. In Figs. 3*a* and 3*c*, due to the lack of available slip systems, the material is quite rigid in shear; it can be noted, for instance, that the yield in pure shear should only be reached for a 1000-MPa stress in the region around ⟨100⟩, and that this yield remains high in the region around ⟨110⟩ ($1000/\sqrt{2}$ MPa). The changes in shape relating to the occurrence of cube slip

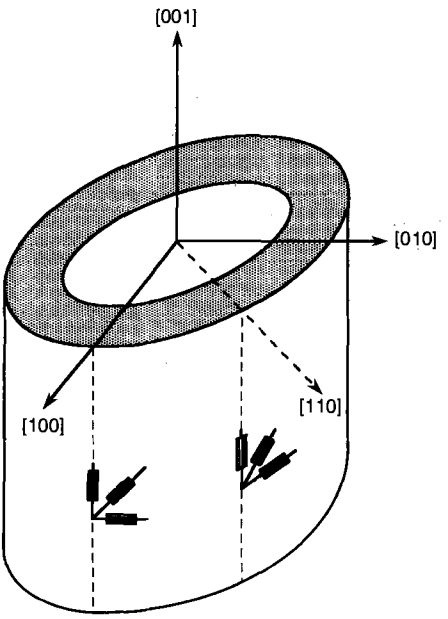

FIG. 1—*Schematic location of the strain gages on the thin tube specimen.*

can be checked in Figs. 3*b* and 3*d*, where the polygons previously obtained are truncated by the new slip activation. The resulting values in shear are then $1000/\sqrt{3}$ MPa in the region around ⟨100⟩, and $1000/\sqrt{6}$ MPa in the region around ⟨110⟩. It can be concluded that the presence of cube slip strongly decreases the yield limit in shear, and that, for any kind of slip, the ⟨110⟩ regions are softer than the ⟨100⟩ ones.

Tension-Torsion Test at 950°C

Several tension-torsion tests were conducted, which are detailed elsewhere [*7,8*]. The main features observed at this temperature are the following:

1. The hardening is mainly kinematic.
2. The mechanical behavior is highly strain-rate dependent.
3. No extra hardening occurs during 90° out-of-phase tension-torsion loading.
4. The subsequent torsion is not affected by the initial tension-compression loading and vice versa, which indicates there is no interaction between octahedral systems (activated in tension) and cube systems (activated in torsion).
5. Deformations are heterogeneous in torsion.

We limit ourselves here to the presentation of one test to illustrate this last point, which is the purpose of the present paper. The specimen is loaded in cyclic torsion with increasing levels. The angle is imposed under a sinusoidal wave form signal corresponding to a strain rate of about 10^{-3} s^{-1}. The only measurement in the test is the "mean value" of the plastic shear strain by using the equivalent length in torsion. At this temperature, the isotropic hardening is negligible, and only two or three cycles are needed to reach the mechanical steady state. Figure 4 shows the slip traces observed on the outside surface of the specimen at the end of the test. Horizontal and vertical traces, characteristic of cube slip, are not evenly distributed along the circumference. They are localized on four zones only, each 90°, and are then the indication of a strong heterogeneity of the deformation in torsion. A Laüe control has localized these traces in the neighborhood of type ⟨110⟩ areas, which are then the more deformed zones, which is in good agreement with the remarks made in the previous section.

This heterogeneity is also confirmed by a finite element computation of the specimen. In the F.E. code ZEBULON [*9*] developed at School of Mines of Paris and used for this application, the plastic strains are calculated through a crystallographic model based on slip theory [*10*], in which octahedral and cube slip systems are taken into account. The material constants were identified from uniaxial data on ⟨001⟩ and ⟨111⟩ oriented specimens at 950°C [*11*]. The applied load is an angular displacement of 2.26° on one end of the specimen, the other end being enchased. The loading rate is directly taken from the experimental recording. Figure 5 presents the mesh of the specimen (1024 twenty-node elements, 21 984 degrees of freedom). A detail of the central part is shown in Fig. 5*B* with the accumulated plastic strain contours, which are maximum in ⟨110⟩ areas and minimum in the ⟨100⟩ zones. The value of the shear strain in the ⟨110⟩ region is twice the value of the shear strain in the ⟨100⟩ region. In the model, the cube systems are activated. As there are no local strain measurements, the comparison was restricted to the torque-angle curves; a good agreement was found between experimental data and the simulation [*12*].

Tension-Torsion Tests at Room Temperature

This set of results, experiments, and calculations has led to the determination of a new experimental program at room temperature, which is detailed in the present section. Three

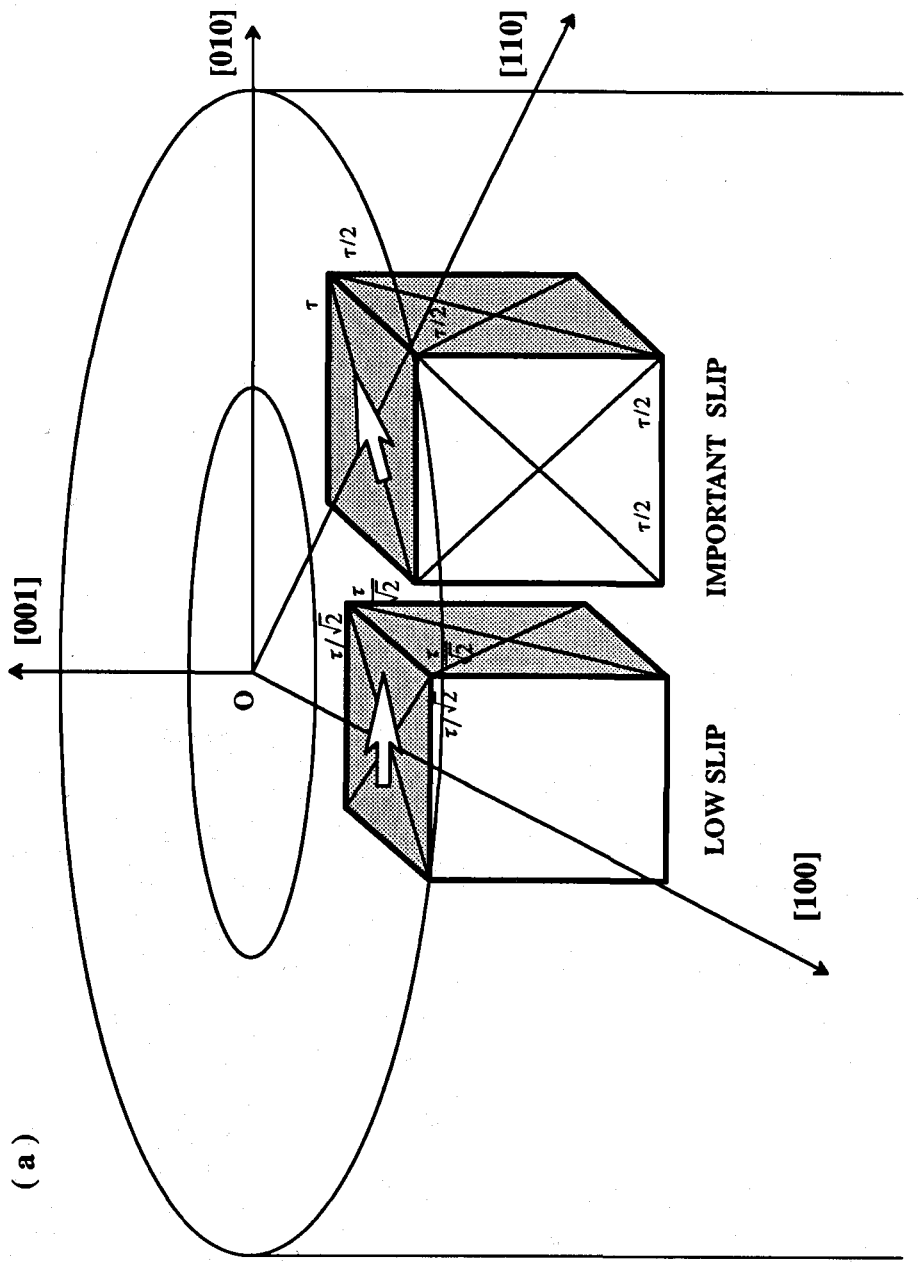
[010]
[110]
[001]
[100]
O
τ
τ/2
τ/2
τ/2
τ/2
τ/√2
τ/√2
τ/√2
τ/√2
IMPORTANT SLIP
LOW SLIP
(a)

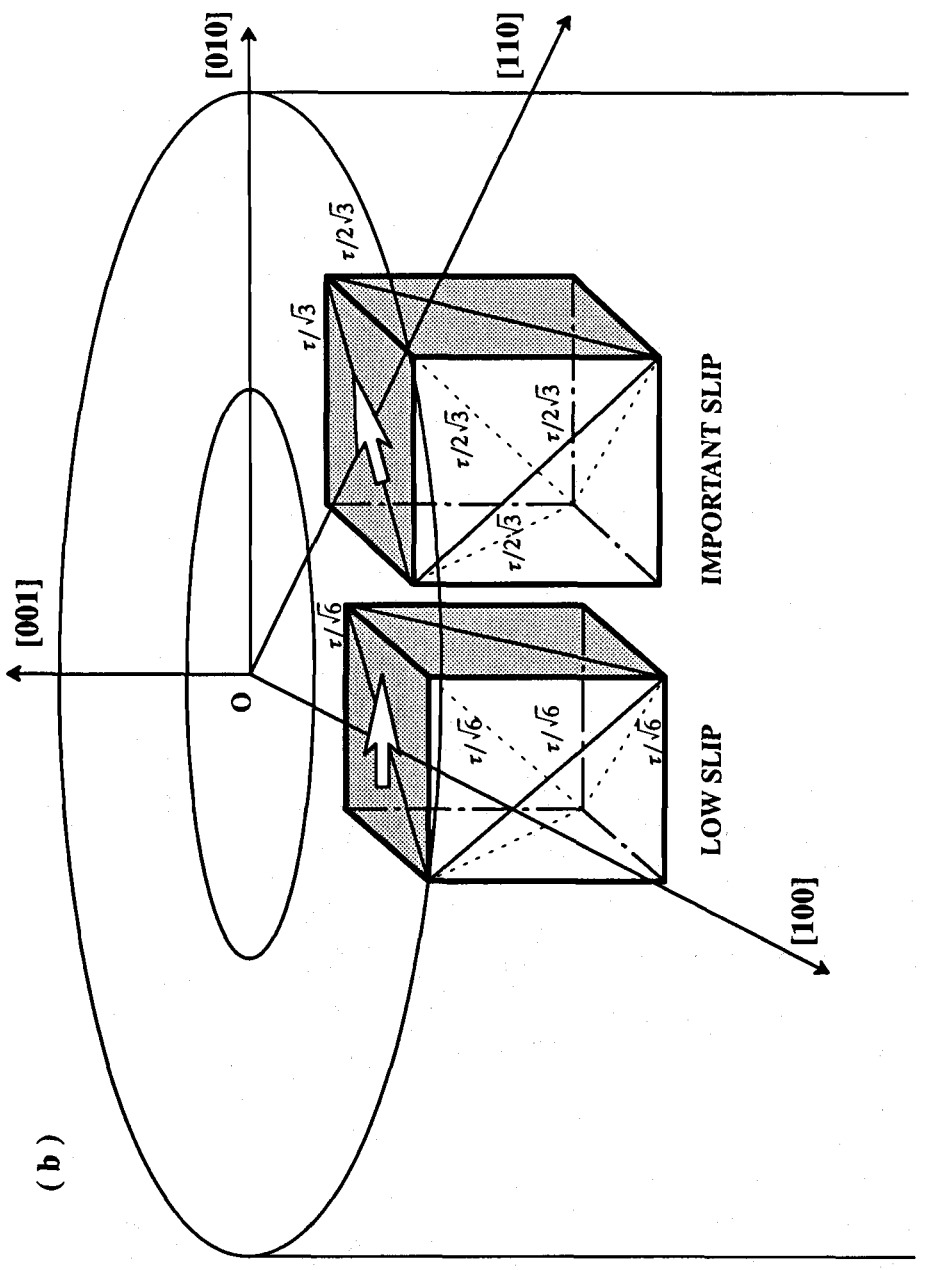

FIG. 2—*Potential slip systems in torsion:* (a) *cube systems;* (b) *octahedral systems.*

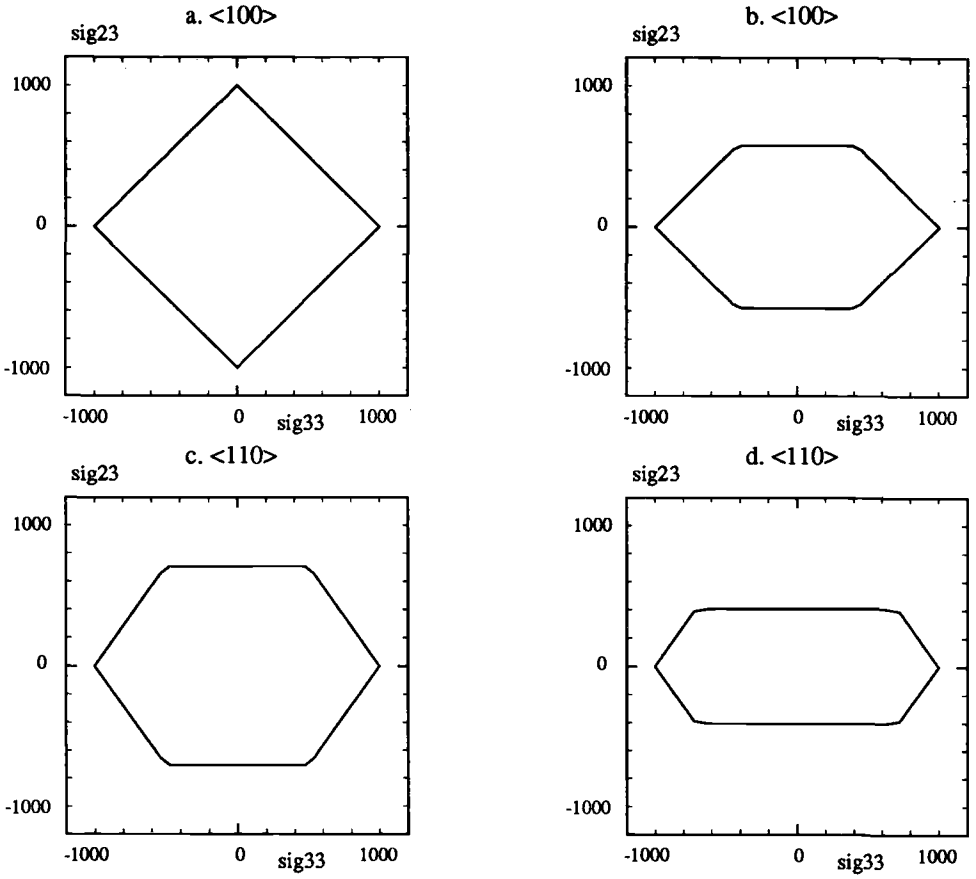

FIG. 3—*Theoretical yield surfaces predicted by Schmid law (stresses in MPa):* (a) *Octahedral slip only, coordinate system* ⟨*100*⟩, ⟨*010*⟩, ⟨*001*⟩; (b) *Octahedral and cube slip, coordinate system* ⟨*100*⟩, ⟨*010*⟩, ⟨*001*⟩; (c) *Octahedral slip only, coordinate system* ⟨*100*⟩, ⟨$\bar{1}$*10*⟩, ⟨*001*⟩; (d) *Octahedral and cube slip, coordinate system* ⟨*100*⟩, ⟨$\bar{1}$*10*⟩, ⟨*001*⟩.

tests are performed under angle and displacement control, with a low plastic straining in order to save the specimen for a subsequent microstructural observation. Additional tests under torque and force control are specially designed to deliver the shape of the yield domain in the shear stress–axial stress plane. For all the tests, the secondary orientations are checked, and strain gages are located in the ⟨100⟩ and the ⟨110⟩ regions. They allow us to get local measurements of the strain and to quantitatively confirm the observations made at high temperature.

The specific tests for yield surface exploration are actually running on virgin and strain-hardened states. We limit the presentation to one of the first results, which corresponds to the initial domain in ⟨110⟩ area. The surface is determined by following radial stress paths away from the origin. The loading path always returns to the origin, and the opposite direction is then explored. Twelve search lines are followed. A small von Mises equivalent offset of yielding corresponding to 10^{-4} mm/mm has been selected. Preliminary tests on the offset influence have shown that there is no difference in the resulting stress diagram with a smaller offset ($5 \cdot 10^{-5}$ mm/mm).

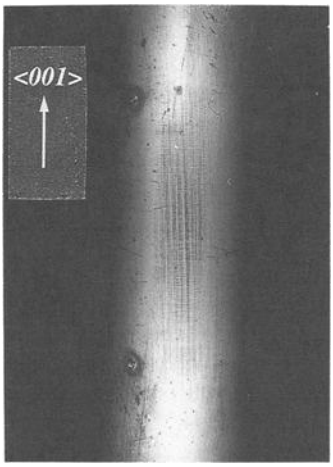

FIG. 4—*Slip traces observed on the specimen after a torsion test.*

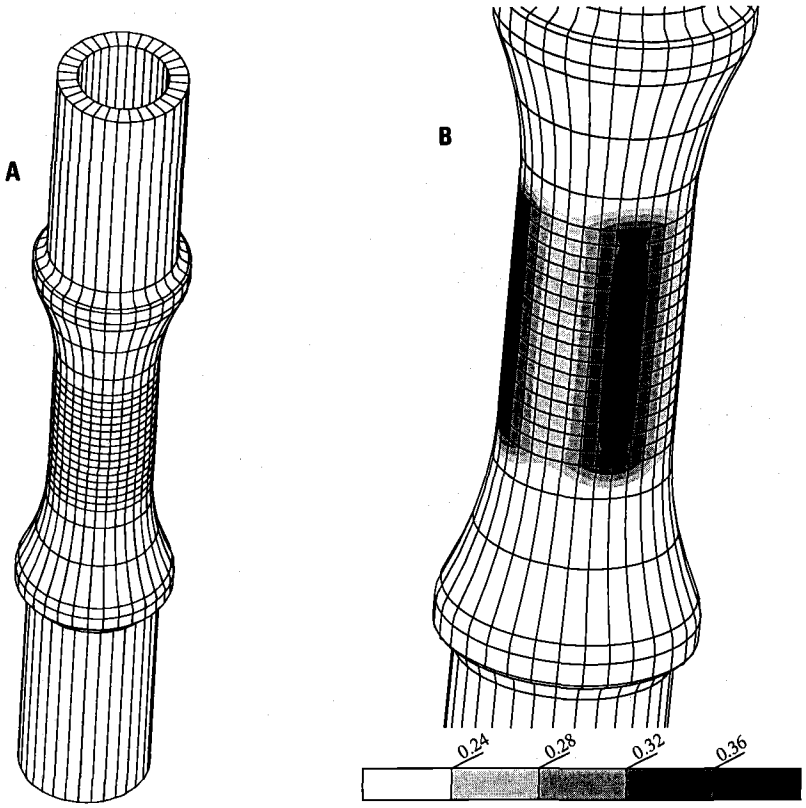

FIG. 5—*Finite element analysis of the torsion specimen (specimen axis: ⟨001⟩):* (A) *mesh;* (B) *plastic shear strain contours predicted by a micromechanical model (%).*

In the tension-torsion test, we have analyzed the stress response, and a microstructural study has also been made to determine the slip traces. The imposed loading paths, under angle and displacement control, are the following:

Sp1. Monotonic reference tensile curve.
Sp2. Symmetrical cyclic torsion (five cycles).
Sp3. In-phase repeated tension-torsion (Sequences 1, 2, and 3) followed by single torsion (Sequence 4). The corresponding loading in the axial stress (σ_{33})–shear stress (σ_{23}) plane is given in Fig. 6.

All the tests are performed at the same rate of $10^{-3}\,s^{-1}$. The heterogeneity of shear strains is confirmed experimentally by the strain-gage measurements. Figure 7 shows the recorded torque–shear strain curves in the ⟨110⟩ and in the ⟨100⟩ regions. At the first cycle, the plastic strain is much greater in ⟨110⟩ than in ⟨100⟩ (more than a factor of 10). After five cycles, the plastic strain amplitude is reduced due to the presence of a significant isotropic hardening, and the behavior tends to become elastic in ⟨100⟩ region. However, if the yield shear stress for ⟨110⟩ is lower than for ⟨100⟩, the ratio is greater than predicted by Schmid law. One could suspect the effect of a stress redistribution in the specimen due to the nonhomogeneous plastic strain flow. No precise answer to this question can be found without a finite element analysis at room temperature.

Table 2 summarizes the main results in terms of stresses for the three tests Sp1 (tension), Sp2 (torsion), and Sp3 (in-phase tension-torsion). For this last test, several values are reported: (1) the yield stress in torsion—in this case, the behavior is still elastic in tension and the con-

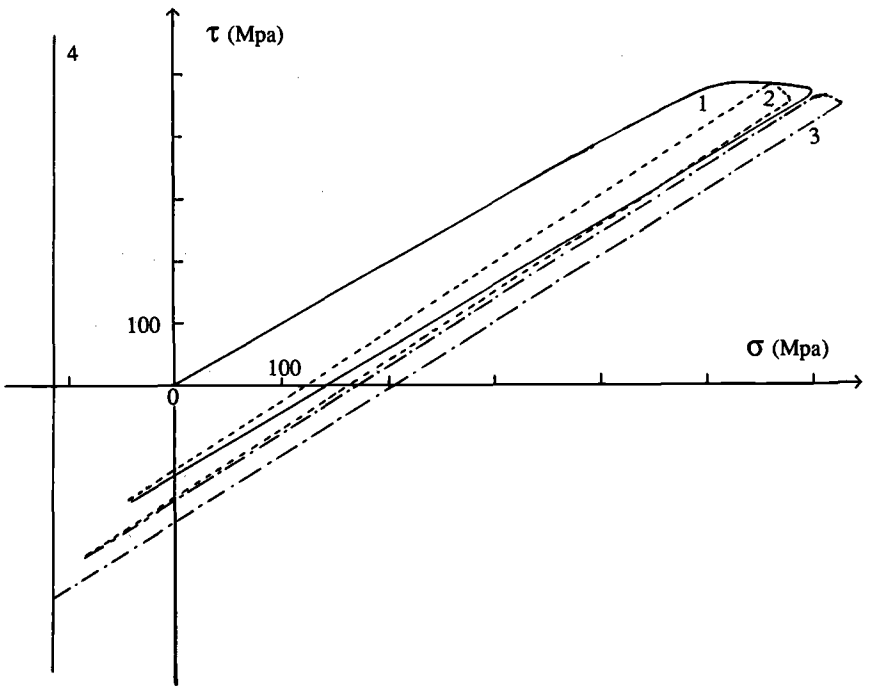

FIG. 6—*Loading path in the stress plane in the in-phase tension-torsion test.*

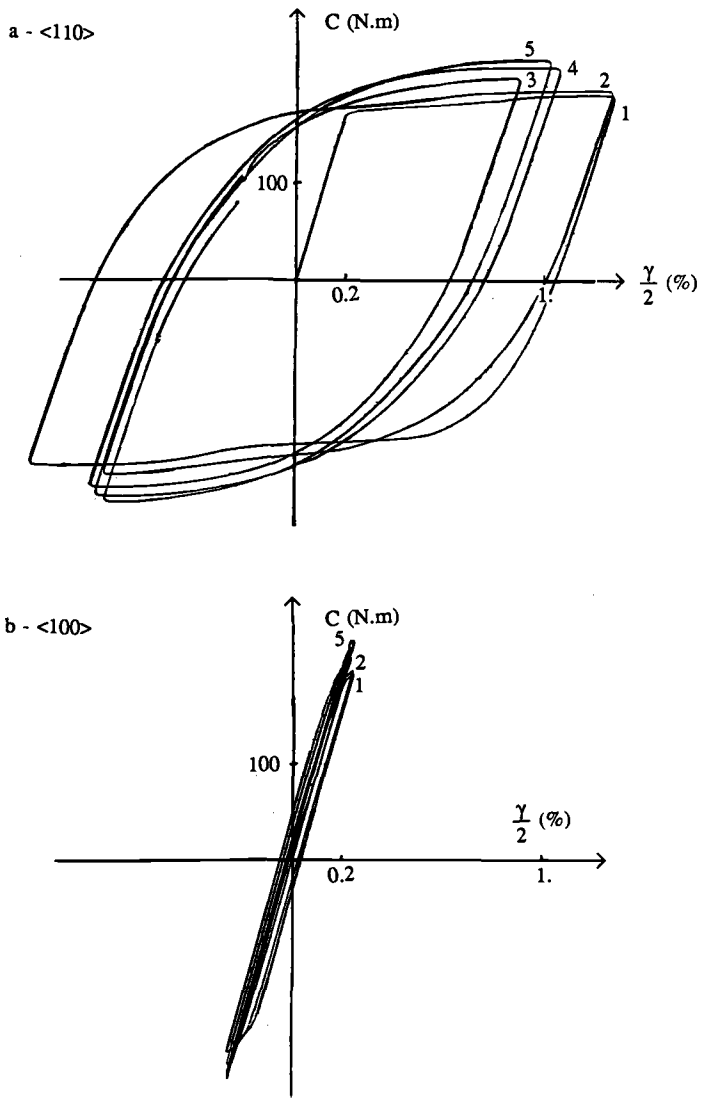

FIG. 7—*Shear curves recorded in a torsion test (torque versus shear strain):* (a) ⟨*110*⟩ *area;* (b) ⟨*100*⟩ *area.*

current value of σ is listed; (2) the yield stress in tension (after hardening in torsion), together with the concurrent value of τ; (3) the saturated value in torsion for this first cycle; (4) the yield stress and saturated stress for the subsequent pure torsion. Except for the case of the tension loading, for which all the points of the surface are equivalent from a crystallographic point of view, the yield first occurs in the ⟨110⟩ regions. Nevertheless, the difference between the two regions (soft zones ⟨110⟩ and hard zones ⟨100⟩) does not correspond with the expected factor from Schmid theory. Instead of $\sqrt{2}$, we respectively obtain for the ratio $\tau_{\langle 100\rangle}/\tau_{\langle 110\rangle}$: 1.08 in pure torsion, 1.06 on the shear component of the in-phase test, and 1.08 on the axial component of the in-phase test. There is not a clear explanation of this fact up to now; again, it

TABLE 2—*The various experimental stress states (MPa).*

Orientation	⟨100⟩	⟨110⟩
Tension	σ_{yield} = 800 to 950	
Cyclic torsion	τ_{yield} = 522	τ_{yield} = 485
In-phase tension torsion (Cycle 1)	τ_{yield} = 391 (σ = 410) σ_{yield} = 512 (τ = 485) $\tau_{sat.}$ = 482	τ_{yield} = 370 (σ = 375) σ_{yield} = 476 (τ = 460) $\tau_{sat.}$ = 486
Subsequent torsion (σ = −112)	τ_{yield} = 525 $\tau_{sat.}$ = 560	τ_{yield} = 525 $\tau_{sat.}$ = 560

could be related to stress redistribution in the specimen. At least it can be shown that the results of the first three tests are consistent with the data coming from the surface evaluation. This is illustrated for the ⟨110⟩ region in Fig. 8. The chosen reference stress in tension is 920 MPa; the points corresponding to the pure torsion test and to the in-phase test are plotted in the diagram, together with the measured yield surface. As the measurement of the yield surface has been generally made twice, two points are present on most of the search lines. The shape is in good agreement with the theoretical observations; for instance, it can be seen that the yield level in shear is not seriously affected by the superposition of a tension component. This is due to the fact that the critical mechanism in this case is cube slip, which is confirmed by the value of the yield (with octahedral slip only, the yield value in shear should be equal to $920/\sqrt{2}$ MPa, i.e., 650 MPa). Two yield surfaces have been plotted on the diagram. The continuous line cor-

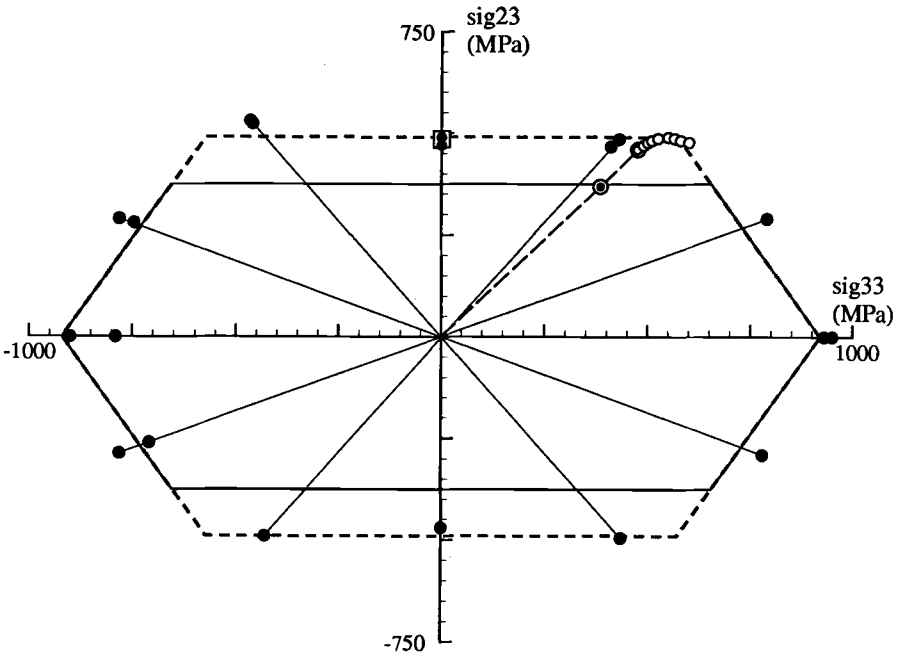

FIG. 8—*Initial yield surface in the ⟨110⟩ region.*

responds to the assumption that the cube slip has the same critical resolved shear stress as that of the octahedral slip ($920/\sqrt{6}$ MPa, i.e., 375 MPa); this appears to be generally not verified excepted for the incipient flow for shear in the in-phase test. The dotted line is obtained by supposing that the critical resolved shear stress on cube systems is equal to 490 MPa. The assumption that cube slip is more difficult than octahedral slip is likely at room temperature. As a matter of fact, it seems that this last value is an upper limit obtained with hardening. Due to their particular deformation mechanisms, single crystals have a different behavior during the first loading and subsequent ones, so that the evaluation of the yield surface probably does not represent a true initial yield in each direction. That explains why the yield surface obtained is consistent with the asymptotic value in pure shear for Test Sp2 and for Test Sp3. In the last case, one can verify that during the imposed angle-displacement loading, the representative point is attracted to the corner in the stress plane.

An essential feature of the behavior confirmed with the experimental research of the yield surface is that the plastic flow is in pure shear for radial tension-torsion loading with a small amount of tension. This confirms the existence of a horizontal zone in the yield criterion. The plastic flow in tension is found only with high values of the axial stress component. From a theoretical point of view, the corner corresponds to a loading path defined by an angle of 40.5° with the horizontal axis in the (σ_{33})-(σ_{23}) plane if we consider 490 MPa as the critical value for the cube-resolved shear stress. Additional search lines, which are not shown in Fig. 8 for the sake of clarity, have shown that no axial flow occurs with an angle of 55°, and a very low flow is observed for a value of 45°. The observed incipient tensile flow is consistent with the theoretical value.

Observation of the Slip Traces

The comparison of the traces on the specimens tested in pure torsion demonstrates that the localization of the shear bands in the ⟨110⟩ regions is more pronounced at high temperature (950°C) than at room temperature; in the first case (Fig. 4), the slip seems to be restricted to the ⟨110⟩ areas, and in the second case, very thin traces prependicular to the specimen axis can be seen all around the specimen. In both cases, the slip traces correspond to cube planes. The amount of shear strain corresponding to cube systems is not easy to evaluate due to the fact that the slip direction of the dominant system becomes parallel to the outside surface of the specimen in the critical ⟨110⟩ region. A detailed study of the traces on the specimen Sp2 has been made by means of replicas and interferometry. This technique has been recently used to characterize the slip bands on fatigue specimens [*13*]. Typical results are given in Fig. 9; Fig. 9*a* shows the horizontal slip lines taken with a scanning electron microscope at low magnification. The corresponding picture obtained by interferometry is shown in Fig. 9*b*; it confirms the presence of slip bands at the surface of the specimen, with very low steps (0.8 μm). The same microstructural study has been made on the Sp3 specimen. The microstructure is much more complex; due to the combined tension-torsion loading, both octahedral and cube slips are present. A general view of the slip bands is given in Fig. 10. The four octahedral planes were found to be active, together with the cube ones. The traces of the octahedral planes have a sinusoidal form, while the cube traces appear as fine horizontal lines. In fact, they were likely not active at the same time (octahedral planes during the tension-torsion loading, cube planes during the subsequent pure torsion loading). As we did not see any influence of the first loading on the torsion loading, it can be concluded that there is no significant hardening effect from the octahedral planes on the cube planes. This result is consistent with the observations at high temperature. A more detailed illustration of the surface is given in Fig. 11. The first view (Fig. 11*a*) shows that cube and octahedral systems are simultaneously present. Figures 11*b* and 11*c* correspond to an increasing magnification; they reveal the γ' structure and also the fact that

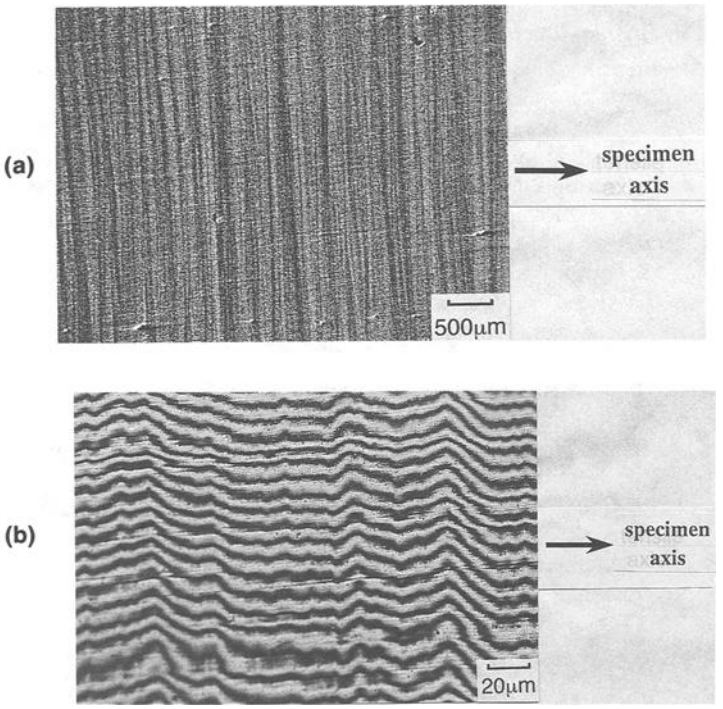

FIG. 9—*Shear bands in pure torsion in the ⟨110⟩ area (Test Sp2):* (a) *SEM view of the surface;* (b) *image obtained by interferometry (λ = 548 nm).*

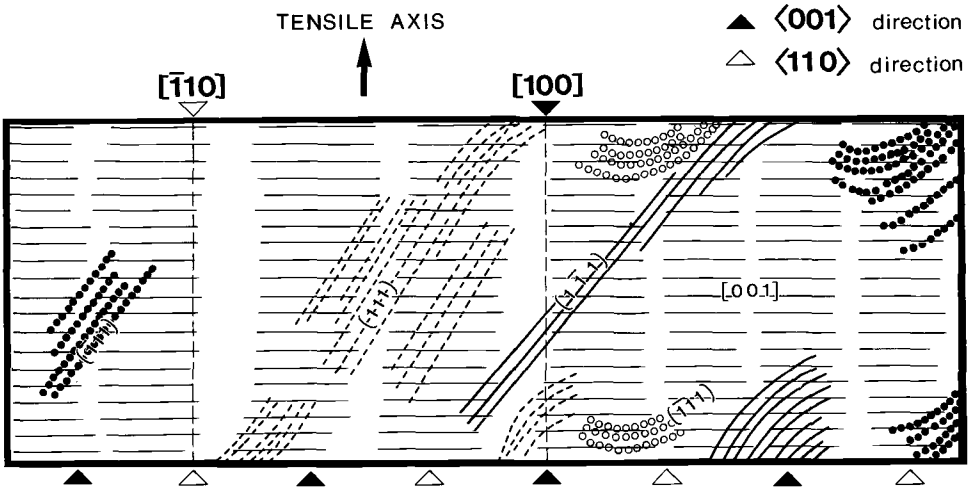

FIG. 10—*General view of the specimen for in-phase tension-torsion (Test Sp3); scheme of the slip bands on the surface replica (back scattered electron image).*

octahedral slip; _____ cube slip

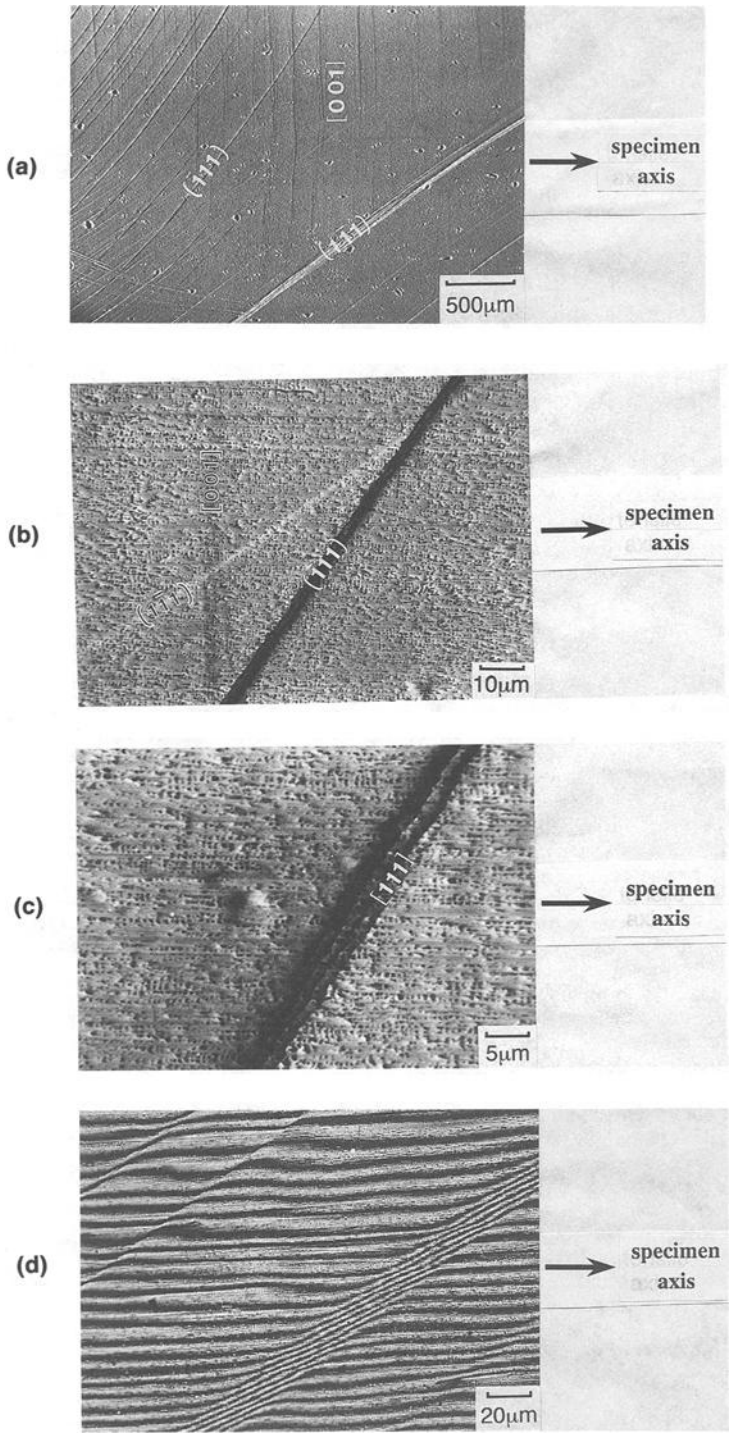

FIG. 11—*Shear bands for in-phase tension-torsion in the ⟨110⟩ area (Test Sp3):* (a,b,c) *SEM views of the surface;* (d) *Image obtained by interferometry (λ = 548 nm).*

several bands can be seen inside a large one. The interferometry (Fig. 11*d*) demonstrates that the step corresponding to the octahedral plane is much higher than the step of the cube one (2.5 μm).

Conclusions

The main experimental results of this study are the following:

1. Cube slip is predominant for pure torsion loading, at high temperature, and at room temperature.
2. A strong strain localization occurs at 950°C and at room temperature in the four ⟨110⟩ zones; in the first case, it was visible to the naked eye on the specimen, and the computed ratio (plastic shear strain for ⟨110⟩/plastic shear strain for ⟨100⟩) was around 2; in the second case, the measured ratio by means of strain gages was about 10.
3. The yield surfaces determination was made with strain gages on a single-crystal tube; the shape corresponds to the theoretical response evaluated from Schmid law for a given area of the specimen, but the relation between the yield stress values collected in two regions (⟨100⟩ and ⟨110⟩) should be further investigated, essentially by means of structural calculations.

References

[1] Policella, H. and Pacou, D., "High Temperature Tension-Torsion Testing Machine," *La Recherche Aérospatiale,* No. 5, 1988, pp. 39–49.
[2] Cailletaud, G., "Remarques sur l'Essai de Traction Compresion Torsion," ONERA Report, RT No. 42, 1982.
[3] Cailletaud, G., Kaczmarek, H., and Policella, H., "Some Elements on Multiaxial Behaviour of 316 L Stainless Steel at Room Temperature," *Mechanics of Materials,* Vol. 3, No. 4, 1984, pp. 333–347.
[4] Delobelle, P., Oytana, C., and Mermet, A., "Appareillage pour l'Etude des Propriétés Rhéologiques des Matériaux," *Revue de Physique Appliquée,* No. 14, 1979, p. 933.
[5] Mises, von R. v., "Mechanik der Plastischen Formänderung von Kristallen," *Zeitschrift für Angewandte Mathematik und Mechanik,* Vol. 8, 1928, p. 161.
[6] Hill, R., "A Theory of the Yielding and Plastic Flow of Anisotropic Metals," *Proceedings of the Royal Society of London, Series A,* Vol. 193, 1948, pp. 281–297.
[7] Policella, H., Paulmier, P., and Pacou, D., "Mechanical Behaviour of the Single-Crystal Alloy CMSX2 at High Temperature. Experimental Results," *La Recherche Aérospatiale,* No. 4, 1990, pp. 47–63.
[8] Nouailhas, D., "Anisotropic Constitutive Equations for Cyclic Viscoplasticity: Application to the Case of Materials with Cubic Symmetry," *La Recherche Aérospatiale,* No. 3, 1990, pp. 11–28.
[9] Méric, L. and Cailletaud, G., "Single Crystal Modeling for Structural Calculations: Part II: Finite Element Implementation," *Journal of Engineering Materials and Technology,* Vol. 113, 1991, pp. 171–182.
[10] Méric, L., Poubanne, P., and Cailletaud, G., "Single Crystal Modeling for Structural Calculations: Part I: Model Presentation," *Journal of Engineering Materials and Technology,* Vol. 113, 1991, pp. 162–170.
[11] Nouailhas, D. and Freed, A. D., "A Viscoplastic Theory for Anisotropic Materials," *Journal of Engineering Materials and Technology,* Vol. 114, 1992, pp. 97–104.
[12] Méric, L., "Une Modélisation Mécanique du Comportement des Monocristaux," doctoral thesis, Ecole Des Mines, Paris, 1991.
[13] Hanriot, F., Fleury, E., and Rémy, L., "Orientation Dependence of the Cyclic Stress-Strain Behaviour of Nickel-Base Superalloy Single Crystals," *Proceedings of High Temperature Materials for Power Engineering,* E. Bachelet et al., Eds., Kluwer Academic Publishers, Dordrecht, The Netherlands, 1990, pp. 997–1006.

Seok Hwan Choi[1] *and Erhard Krempl*[2]

Viscoplasticity Theory Based on Overstress: The Modeling of Biaxial Cyclic Hardening Using Irreversible Plastic Strain

REFERENCE: Choi, S. H. and Krempl, E., **"Viscoplasticity Theory Based on Overstress: The Modeling of Biaxial Cyclic Hardening Using Irreversible Plastic Strain,"** *Advances in Multiaxial Fatigue, ASTM STP 1191,* D. L. McDowell and R. Ellis, Eds., American Society for Testing and Materials, Philadelphia, 1993, pp. 259–272.

ABSTRACT: Cyclic hardening behavior of stainless steel under various loading paths is modeled by using the small-strain, isotropic theory of viscoplasticity based on overstress. The cyclic hardening is modeled by postulating a growth law of an internal variable which is equivalent to isotropic hardening of yield surface plasticity. The growth of the hardening variable is formulated in a discrete way by using changes in the direction vector of the inelastic strain rate and the concept of irreversible plastic strain. The irreversible plastic strain is given as a function of variables representing amplitude, nonproportionality, and the history of the loading path. This formulation does not use separate growth laws for proportional and nonproportional loading. They are handled by a difference of the direction vectors of inelastic strain rate before and after it changes its direction. The capability of the model is demonstrated by numerical experiments for various loading conditions.

KEY WORDS: viscoplasticity, numerical experiments, cyclic hardening, path dependence, irreversible plastic strain, cross hardening, extra hardening

It is well known that annealed Type 304 stainless steel exhibits significant hardening under cyclic loading with load or strain reversal. The hardening behavior can be characterized by amplitude dependence [*1–3*], path dependence [*4–9*], history dependence [*10,11*], and combinations of all three. During the last decade various theories [*2,10–22*], time-independent or time-dependent, have been developed to model the observed cyclic hardening behavior for proportional and nonproportional loading paths. Most of the models, however, have difficulties in representing all the observed complicated features, especially cross hardening and the mean strain effect. Also, some of the theories apply only to cyclic loading but not to any arbitrary loading path with continuously changing direction of the deformation.

Previously the cyclic hardening behavior had been modeled with the theory of viscoplasticity based on overstress (VBO) by Yao and Krempl [*23,24*], in which separate measures for proportional and nonproportional loading paths were used, and by Krempl and Choi [*25*], in which the strain memory surface [*10*] was combined with Yao's formulation. The formulations, however, were not successful in representing the cross-hardening effect and the mean

[1] Graduate student, Mechanics of Materials Laboratory, Rensselaer Polytechnic Institute, Troy, NY 12180, now manager, DAEWOO Group, CPO. Box 2810, Seoul, Korea.

[2] Professor of mechanics, Mechanics of Materials Laboratory, Rensselaer Polytechnic Institute, Troy, NY 12180.

strain effect for all values of mean strain. In this paper, an attempt is made to model the cyclic hardening behavior in a simple way for any arbitrary loading path by using changes of the unit vector representing the direction of the inelastic strain rate and the concept of irreversible plastic strain.

The growth of the isotropic hardening variable of VBO is triggered by the direction change of inelastic strain rate. It, therefore, grows in a discrete manner under uniaxial or proportional cyclic loading and grows continuously under a deformation in which the inelastic strain rate changes its direction continuously. The amount of the growth is determined by the irreversible plastic strain which has been accumulated since the last direction change of the inelastic strain rate to the current state at which the direction of the inelastic strain rate changes again. The irreversible plastic strain accumulates with the cyclic loading, and the hardening stops when the irreversible strain is saturated. The definition of the irreversible plastic strain used here is based on the concept given in Ref *26*. For uniaxial loading, the irreversible plastic strain is obtained by subtracting reversible plastic strain from the accumulated plastic strain when the loading direction is reversed. The reversible plastic strain is the strain component which does not contribute to work hardening, e.g. the plastic strain in a stable hysteresis loop. This concept is extended here to a three-dimensional case by using the direction change of the inelastic strain rate. The concept of cyclic nonhardening range developed by Ohno [*12,18,19*], which is a modification of strain memory surface introduced by Chaboche [*10*], becomes equivalent to the concept of reversible plastic strain, the difference between the plastic strain and the irreversible plastic strain, under the uniaxial or biaxial proportional cyclic loading.

This formulation is fundamentally able to represent all the complicated phenomena observed experimentally and is indeed simple in structure. For the demonstration of the model capability, numerical experiments are performed on various loading paths in the axial-shear strain space. Included are uniaxial cycling for fixed amplitude with or without mean strain, axial cycling with increasing or decreasing two-step amplitude, proportional cyclic loading, step loadings for various numbers of steps, square loading, 90° out-of-phase loading, and cyclic loading alternating between the axial and shear directions.

Viscoplasticity Theory Based on Overstress (VBO)

The viscoplasticity theory based on overstress is a "unified" theory which considers the plasticity and creep in a unified way and does not use yield or loading/unloading conditions. The uniaxial and three-dimensional versions of VBO are given in Refs *27* and *28* for isotropy and in Refs *29* through *31* for anisotropy. The total strain rate is postulated to be the sum of the elastic and inelastic parts. The inelastic strain rate is given as a function of overstress, the difference between the stress and the equilibrium stress, which is a state variable of the theory. It is assumed that at an asymptotic state or in the fully inelastic region, the total stress is composed of rate-dependent, rate-independent, and kinematic stress contributions.

The small-strain, standard isotropic theory of VBO which models cyclic neutral behavior [*27,28*] is presented here. A set of coupled nonlinear differential equations representing VBO for isotropy is given by

$$\dot{e}_{ij} = \dot{e}^{el}_{ij} + \dot{e}^{in}_{ij} = \frac{1+\nu}{E}\dot{s}_{ij} + \frac{3}{2}\frac{1}{Ek[\Gamma]}(s_{ij} - g^d_{ij}) \tag{1}$$

$$\dot{g}^d_{ij} = \psi[\Gamma]\left(\frac{1}{1+\nu}\dot{e}^{el}_{ij} + \frac{2}{3}\dot{e}^{in}_{ij}\right) - \frac{1}{A}(g^d_{ij} - f^d_{ij})(\psi - E_t)\dot{\phi} \tag{2}$$

$$\dot{f}_{ij}^{d} = \frac{2}{3}\frac{E_t}{1 - E_t/E}\dot{e}_{ij}^{in} \tag{3}$$

$$\dot{\varepsilon}_{kk} = \frac{1 - 2\nu}{E}\dot{\sigma}_{kk} \tag{4}$$

A superposed dot indicates a time derivative, square brackets [] enclosing a symbol denote "function of," and the superscript, d, denotes the deviator of the tensor. σ_{ij} and ε_{ij} designate the stress and strain tensors, respectively, with s_{ij} and e_{ij} as the corresponding deviators. E and ν are the elastic constants, E_t is the tangent modulus at asymptotic state, and inelastic incompressibility is assumed. The state variables, g_{ij} and f_{ij}, are the equilibrium stress and the kinematic stress tensors, respectively. k and ψ are called viscosity function and shape function, respectively, and they are positive, decreasing functions of an invariant Γ defined as

$$\Gamma = \left\{\frac{3}{2}(s_{ij} - g_{ij}^{d})(s_{ij} - g_{ij}^{d})\right\}^{1/2} \tag{5}$$

$\dot{\phi}$ is the effective inelastic strain rate given by

$$\dot{\phi} = \left(\frac{2}{3}\dot{e}_{ij}^{in}\dot{e}_{ij}^{in}\right)^{1/2} \tag{6}$$

The quantity, A, dimension stress, in Eq 2 is the rate-independent contribution to the stress in the asymptotic state (see Fig. 1 of Ref *28*) and can be expressed as

$$A = \{g - f\} \tag{7}$$

The braces $\{\ \}$ denote the value at asymptotic state.

The above formulation models cyclic neutral behavior. The hardening due to the cyclic loading has been modeled with isotropic hardening in the context of yield surface rate-independent plasticity [*16*]. Also it is shown [*4*] that the cyclic hardening of 304 stainless steel is predominantly rate-independent. As a consequence, the cyclic hardening within VBO is implemented through the growth of A, which is equivalent to isotropic hardening variable of other plasticity theories.

Cyclic Hardening Formulation

The growth of the quantity, A, is triggered by the direction change of the inelastic strain rate. The direction of the inelastic strain rate can be represented by a unit tensor, $\mathbf{n}$, defined as

$$n_{ij} = \frac{\dot{e}_{ij}^{in}}{\|\dot{e}_{ij}^{in}\|} \tag{8}$$

The tensor, n_{ij}, can be expressed in a vector form for biaxial loading in the axial and shear direction.

$$\mathbf{n} = n_1\mathbf{e}_1 + n_2\mathbf{e}_2 \tag{9}$$

where $\mathbf{e}_1$ and $\mathbf{e}_2$ are the unit vectors in the direction of axial strain and shear strain, respectively, in the $\varepsilon - \gamma/\sqrt{3}$ space, n_1 and n_2 are the components of $\mathbf{n}$ in the respective directions.

When the direction of the inelastic strain rate changes, the magnitude of a difference tensor of the unit tensors before and after the change can be computed as

$$\|\Delta \mathbf{n}\| = \|\mathbf{n}|_t - \mathbf{n}|_{t_0}\| \tag{10}$$

The symbol $\| \ \|$ denotes the magnitude of the tensor, t_0 is the time at which the last direction change of the tensor $\mathbf{n}$ occurred, and t is the current time at which the tensor $\mathbf{n}$ changes its direction again. A segment is designated to be the loading path from time t_0 to time t. $\|\Delta \mathbf{n}\| = 0$ when the inelastic strain rate does not change its direction, and $\|\Delta \mathbf{n}\| = 2$ for the completely reversed loading path. For any other case, $\|\Delta \mathbf{n}\|$ is between 0 and 2. For computational purposes a lower bound $\|\Delta \mathbf{n}\|_{th}$ of $\|\Delta \mathbf{n}\|$ has to be stipulated; values smaller than this threshold value do not create a segment.

In an initial trial, the growth of A is assumed to be function of the accumulated irreversible plastic strain for one segment, $\Delta\beta$, as

$$\Delta A = a_5 \operatorname{sign}(\Delta\beta)(\|\Delta\beta\|)^{a_6} \tag{11a}$$

with A computed as

$$A = \sum_{i=1}^{n} \Delta A_i + A_0 \tag{11b}$$

where A_0 is the initial value of A.

$\Delta\beta$ in Eq 11a is computed from

$$\Delta\beta = \Delta\phi - a_1(\Delta\phi)^{a_2}(\|\Delta \mathbf{n}\|)^{a_3}(\beta)^{a_4} \tag{12a}$$

where β is the total accumulated irreversible plastic strain from the virgin state of the material and computed as

$$\beta = \sum_{i=1}^{n} \Delta\beta_i + \beta_0 \tag{12b}$$

where β_0 is the initial value. $\Delta\phi$ is the accumulated inelastic strain for one segment and is computed as

$$\Delta\phi = \int_{t_0}^{t} \dot{\phi}\, d\tau \tag{13}$$

$\Delta\phi$, $\Delta\beta$, and ΔA are computed only when $\|\Delta \mathbf{n}\|$ is not zero. The formulations are expressed in discrete form in Eqs 10 through 13 and can be handled numerically by implementing a $\|\Delta \mathbf{n}\|_{th}$ below which no changes occur for loading paths with the continuously changing tensor $\mathbf{n}$.

The total irreversible plastic strain, β, accumulates and finally saturates in cyclic loading. Then $\Delta\beta$ stays at zero for the following segments and the hardening stops unless $\Delta\phi$ or $\|\Delta \mathbf{n}\|$ changes. When $\Delta\phi$ or $\|\Delta \mathbf{n}\|$ changes, $\Delta\beta$ becomes nonzero (see Eq 12a), and A changes again (it may decrease or increase). For given $\Delta\phi$ and $\|\Delta \mathbf{n}\|$, the saturated value of β can be calculated by setting $\Delta\beta = 0$ in Eq 12a as

$$\beta_s = \left\{ \frac{1}{a_1} (\Delta\phi)^{1-a_2} (\|\Delta \mathbf{n}\|)^{-a_3} \right\}^{1/a_4} \tag{14}$$

Subscript s denotes "saturation." The material hardens under a cyclic loading when β_0 is smaller than β_s and softens when β_0 is larger than β_s. It is, therefore, possible to say that β_0 is zero at the annealed state, and β_0 can be larger than β_s after cold work leading to cyclic softening.

A total of six constants, a_1 through a_6, are employed in the above equations. The constants need to satisfy the following conditions to have the desired features

$$0 < a_2 < 1 \tag{15a}$$

$$a_3 > 0 \tag{15b}$$

$$a_4 > 0 \tag{15c}$$

Equation 15a is required for nonlinear amplitude-dependence, Eq 15b for path-dependence (extra hardening for nonproportional loading), and Eq 15c for a proper saturation. The determination of the constants, a_1 through a_6, under the constrictions of Eqs 15a through 15c requires trial and error procedures to match real experimental data quantitatively. Since β_s can be calculated by Eq 14, it is recommended to work with β_s in determining the constants. It should be noticed that the total hardening amount of A is proportional to $(\beta - \beta_0)$ when $a_6 = 1.0$ (see Eq 11a).

Numerical Simulation

For the demonstration of the model capability, numerical experiments are performed for various cyclic loading paths on axial-shear strain space ($\varepsilon - \gamma/\sqrt{3}$ space). The loading paths adopted here are, for comparison, based on the work given in Ref *2*. The purpose of the numerical experiments is the demonstration of the advantages and disadvantages of this new model. It is not intended to match the data precisely, and only the trend will be compared.

The material constants employed here are listed in Table 1. The constants required by cyclic neutral, isotropic VBO for 304 stainless steel are from Ref *24*. The only difference is that the initial value, A_0, is set to 120 MPa instead of 115 MPa. With the given constants, the nonlinear, coupled ordinary differential equations of VBO with cyclic hardening are integrated numerically by using the IMSL routine DGEAR on a Sun 3/60 work station. Due to the discrete growth law of A, the subroutine DGEAR is modified for convergence check at each time step which is determined inside the DGEAR program.

In the simulations, the effective strain rate, $\dot{\varepsilon}_e$, and the effective strain amplitude, ε_e, as well as the effective stress amplitude, σ_e, are used to compare the data obtained for various loading conditions. They are defined as

$$\dot{\varepsilon}_e = \left(\frac{2}{3} \dot{e}_{ij} \dot{e}_{ij} \right)^{1/2} \tag{16a}$$

$$\varepsilon_e = \left(\frac{2}{3} e_{ij} e_{ij} \right)^{1/2} \tag{16b}$$

$$\sigma_e = \left(\frac{3}{2} s_{ij} s_{ij}\right)^{1/2} \tag{16c}$$

Uniaxial Behavior

Figure 1 shows the stress-strain curve with unloading and reloading under strain control. The dotted line is the stress-strain curve for monotonic tensile loading. A small hardening occurred during the unloading/reloading procedure since the direction of the inelastic strain rate changed twice in an opposite direction. The plastic flow is continued with the constant slope, E_t. In Fig. 2 the hysteresis loop for the step-up two-amplitude cyclic loading is depicted. The further hardening after a change in amplitude is demonstrated well. The step-down two-amplitude test is shown in Fig. 3. History-dependent softening after a change in amplitude is observed. The softening rate is relatively small, and the final stress value at the small amplitude is, for the given number of cycles, higher than the stress level obtained in Fig. 2. The stress level at the larger amplitude in Fig. 2 is almost the same as that in Fig. 3. It should be noted that, when $a_6 = 1.0$, the final stress level will be identical regardless of the prior history. The effect

TABLE 1—*Material constants.*

MATERIAL CONSTANTS

$E = 195\,000.0$ MPa
$E_t = 2000.0$ MPa
$A_0 = 120.0$ MPa
$\beta_0 = 0.0$

VISCOSITY FUNCTION

$$k[\Gamma] = K_1\left(1 + \frac{\Gamma}{K_2}\right)^{-K_3}$$

where

$K_1 = 314\,200.0$ s
$K_2 = 60.0$ MPa
$K_3 = 21.98$

SHAPE FUNCTION

$$\psi[\Gamma] = C_1 + (C_2 - C_1)\exp(-C_3\Gamma)$$

where

$C_1 = w_1 + w_2 A$
$w_1 = 74\,740.0$ MPa
$w_2 = 37.04$
$C_2 = 182\,500.0$ MPa
$C_3 = 0.0783$ MPa^{-1}

CONSTANTS FOR HARDENING

$a_1 = 0.20$	$a_2 = 0.48$
$a_3 = 0.67$	$a_4 = 0.57$
$a_5 = 2000.0$ MPa	$a_6 = 1.10$

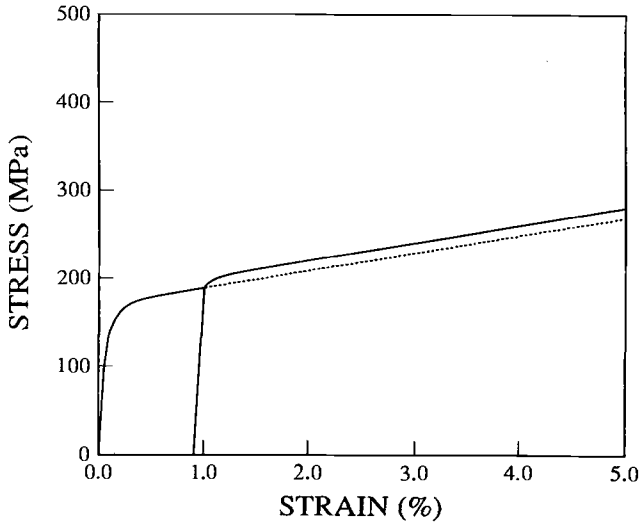

FIG. 1—*Stress-strain diagram with unloading and reloading at 1.0% strain for an effective strain tensile loading.*

of the mean strain is simulated in Fig. 4. The strain amplitude is the same as the small amplitude in Fig. 2. The hardening amount and the stress amplitude are not affected by the fairly large mean strain. This property is maintained at any mean strain value. However, no mean stress relaxation is modeled by the theory. The inclusion of a recovery form in the growth law for the kinematic stress could model mean stress relaxation. This is not done here.

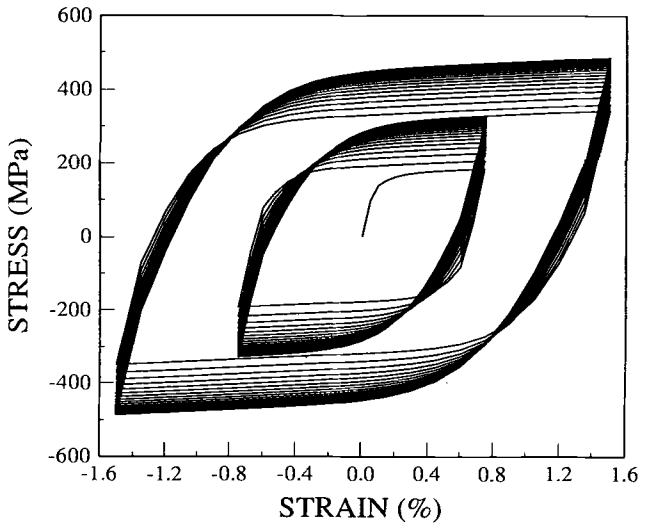

FIG. 2—*Completely reversed strain-controlled, two-amplitude step-up test. Effective strain ranges are 1.5 and 3.0%. Effective strain rate is* $3.0 \times 10^{-4}\ s^{-1}$.

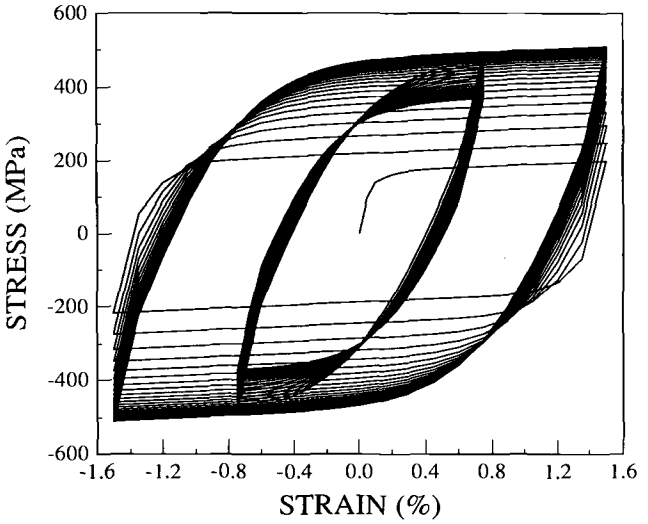

FIG. 3—*Completely reversed strain-controlled, two-amplitude step-down test. Effective strain ranges are 1.5 and 3.0%. Effective strain rate is* $3.0 \times 10^{-4}\ s^{-1}$.

Biaxial Cycling

Various loading paths including proportional loading and the 90° out-of-phase loading are simulated. Figure 5 shows the axial and shear stress trajectory for 90° out-of-phase loading along with the nearly stabilized stress ranges for axial, torsional, and proportional cycling. The extra hardening in out-of-phase loading is well demonstrated in the figure. In Fig. 6 the path-dependent hardening is presented for various loading paths. The square loading and the one-

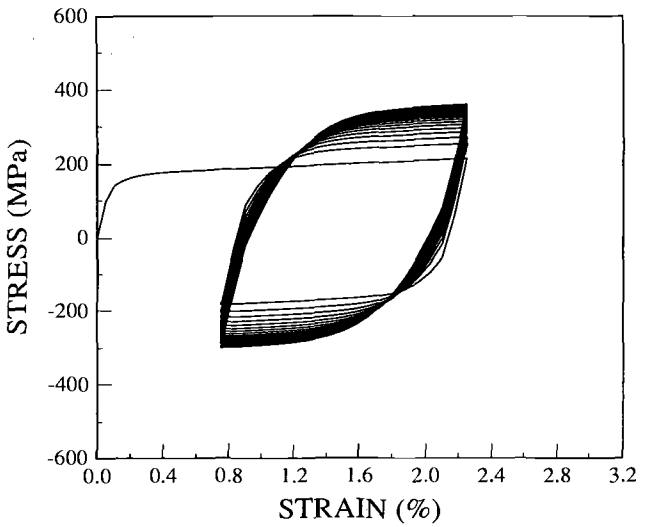

FIG. 4—*Completely reversed strain-controlled cyclic loading with mean strain of 1.5%. Effective strain range is 1.5%, and effective strain rate is* $3.0 \times 10^{-4}\ s^{-1}$.

or two-step loading produced more hardening than 90° out-of-phase loading, which is not in accordance with experiments reported [*2*]. The step loadings with 32 and 128 steps produced extremely small hardening, which is even lower than that obtained from the proportional loading.

For the illustration of the cross-hardening effect, the cyclic loading alternating between axial and shear directions reported in Ref *4* is simulated in Fig. 7. When the loading direction is changed to shear after a given number of cycles in the axial direction, an abrupt increase in stress level which is followed by gradual softening is well reproduced by the theory. However, the increase of the stress continues for several cycles after the direction change from axial to shear, whereas the stress increases only for the first cycle in experiments [*4*]. The reason is thought to be that the axial component of the inelastic strain rate is changing for a while due to the axial stress relaxation process. The changing of the axial inelastic strain rate causes the direction change of the tensor **n**. A similar behavior will be modeled from shear to axial loading.

Step Loading with Step Return Path

The step loadings simulated in Fig. 6 are for the straight (or proportional) return path. The difference between step return and the straight return is depicted in Fig. 8. Figure 9 shows the simulation results for 1-, 2-, and 32-step loadings with step return. The hardenings for 1- and 2-step loadings are almost same as those appearing in Fig. 6, but almost no hardening is produced for the 32-step loading. In this case $\Delta\phi$ is extremely small but the value of $\|\Delta\mathbf{n}\|$ is $\sqrt{2}$, which is a fairly large value. Then $\Delta\beta$ and β_s also become small (see Eqs 12a and 14), and consequently almost no hardening is modeled. The hardening observed for the step loadings with straight return in Fig. 6 is thought to be due to the straight (or proportional) return loading path. Since no experimental data for the step loading with step return path are available to the authors, it is not possible to make a comparison.

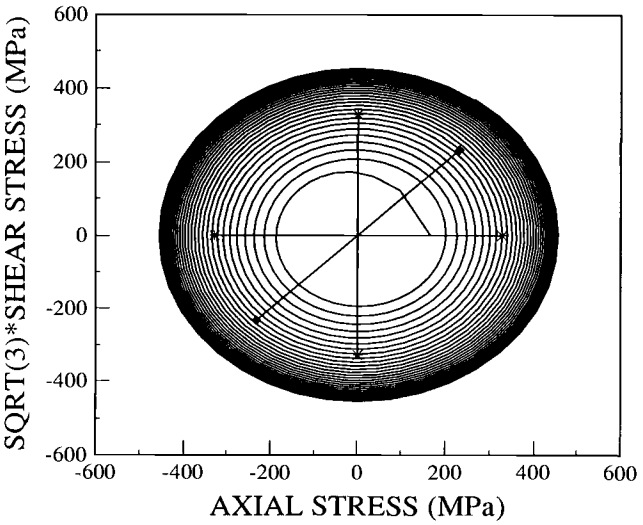

FIG. 5—*Strain-controlled 90° out-of-phase loading at an effective strain amplitude of* $\pm 0.75\%$ *and an effective strain rate of* $3.0 \times 10^{-4}\ s^{-1}$. *The graph of* $\sqrt{3}$* *shear stress versus axial stress is depicted. The diameters represent the stabilized stress ranges under axial (*) and torsional (*) cycling and under proportional cycling (♦).*

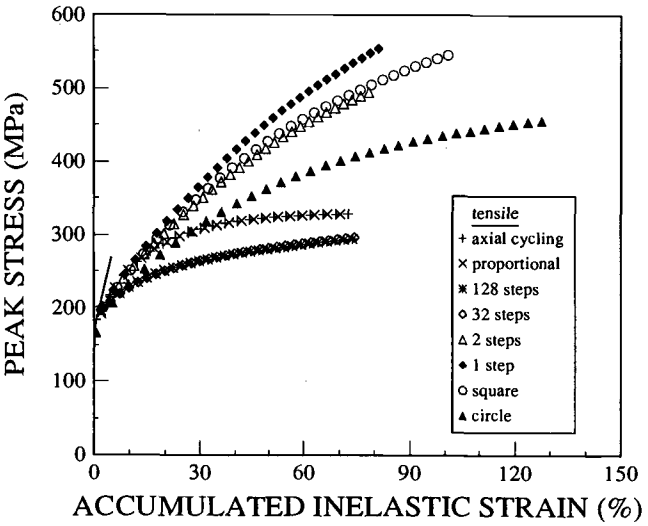

FIG. 6—*Effect of strain path on the cyclic hardening behavior. The effective strain range is 1.5% and the effective strain rate is* $3.0 \times 10^{-4}\ s^{-1}$.

Discussion

General

The previous cyclic hardening formulation using VBO given in Refs *25* and *32* modeled many hardening phenomena but cross hardening could not be modeled, and the modeling of the mean strain effect did depend on a parameter used for the strain memory surface. The formulation presented here is simple in structure and is fundamentally capable of representing all the observed cyclic hardening phenomena, including cross hardening. The amplitude-

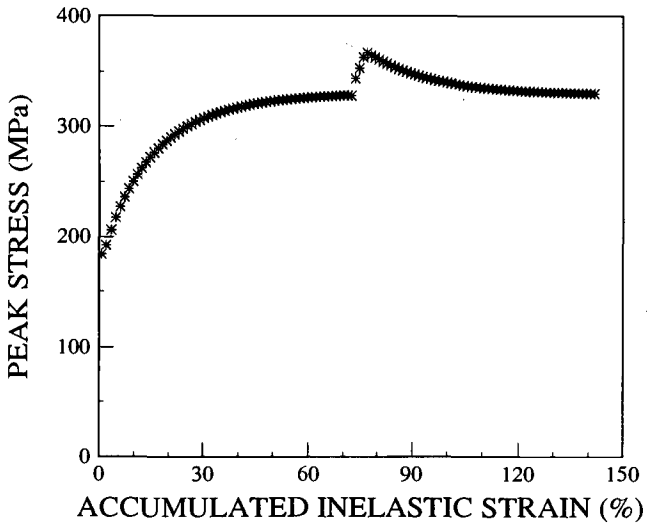

FIG. 7—*Cross-hardening effect. The loading condition is changed to shear after 30 cycles in axial direction. The effective strain amplitude is* $\pm 0.75\%$ *and the effective strain rate is* $3.0 \times 10^{-4}\ s^{-1}$.

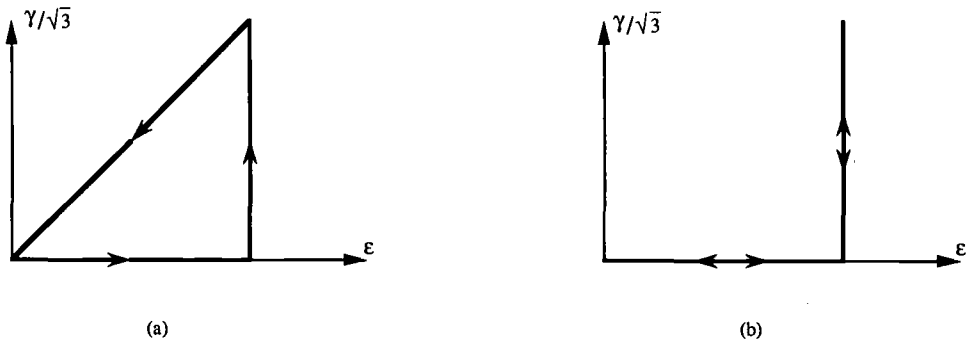

FIG. 8—(a) *Diagram of step loading with straight (proportional) return path;* (b) *diagram of step loading with step return path.*

dependent hardening is implemented through the dependence on $\Delta\beta$ and $\Delta\phi$, the path dependence through $\|\Delta\mathbf{n}\|$ and the history dependence through β. Also, the contributions of the three measures are coupled through the growth law (Eq 12a). Cross hardening observed by the cyclic loading alternating between axial and shear directions is modeled as shown in Fig. 7.

It is shown in Fig. 4 that the mean strain effect is modeled well except for the absence of mean stress relaxation. For the given number of cycles, the theory, however, produced more hardening under a square loading path than under 90° out-of-phase loading as shown in Fig. 6. It is observed that the inelastic strain rate is changing its direction at every instant not only for circular loading, but also for square loading. It is expected that the final hardening under 90° out-of-phase loading is still the highest because the saturated value of accumulated irreversible plastic strain, β_s, is larger for 90° out-of-phase loading than for square loading due to the difference of $\Delta\phi$ for the two cases (the same $\|\Delta\mathbf{n}\|$ is assumed).

The cyclic step loading produced very small hardening (the effective stress is even lower than for the proportional cyclic loading) when the number of steps is large (the step size becomes

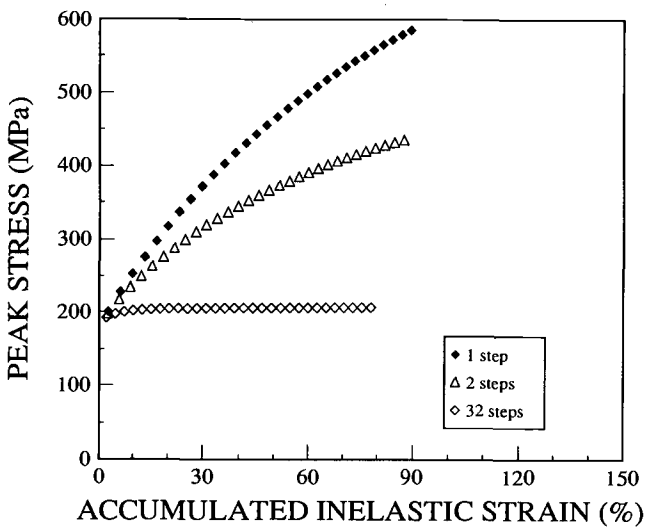

FIG. 9—*Hardening effect of step loading with step return path. The effective strain amplitude is* $\pm 0.75\%$ *and the effective strain rate is* $3.0 \times 10^{-4}\ s^{-1}$.

smaller as the number of steps increases). When the number of steps is small, the loading path becomes similar to the square loading and consequently produced extremely large hardening for the reason mentioned earlier. It is worthwhile to mention that the hardening under step loading with the step return path is different from that with the straight (proportional) return path. Step loading with the step return path produces almost no hardening when the number of steps is large.

The simple formulation presented here has shown encouraging modeling capabilities of observed cyclic hardening phenomena. Certain discrepancies are present which are discussed above. It is believed that the concept of irreversible plastic strain is valid, but that the specific implementation given in Eq 12a could be improved upon. It represents the simplest possibility, and more complicated expressions can be found which might improve the correlation between theory and experiment.

The cyclic hardening of 304 stainless steel is implemented through the isotropic hardening variable here. The possibility of modeling the nonproportional cyclic plasticity with a multiple kinematic hardening rule was discussed in Ref *33*. It is still not clear if the cyclic hardening of 304 stainless steel under nonproportional loading is due to isotropic hardening or kinematic hardening. Systematic experimental investigations on cyclic hardening behavior need to be done.

Comments on $\|\Delta\mathbf{n}\|$

It is necessary to discuss the numerical implementation of $\|\Delta\mathbf{n}\|$. The simulations above were done with the condition of $\|\Delta\mathbf{n}\| \geq 1.0 \times 10^{-5}$. When $\|\Delta\mathbf{n}\| < 1.0 \times 10^{-5}$, the program does not compute ΔA by presuming no direction change of the inelastic strain rate. Figure 10 shows the cross-hardening effect with the limit value of 1.0×10^{-10} for $\|\Delta\mathbf{n}\|$. As shown in the figure, the stress increase after the direction change from axial to shear is much larger than the increase appearing in Fig. 7. However, the limit value of 1.0×10^{-10} does not produce any

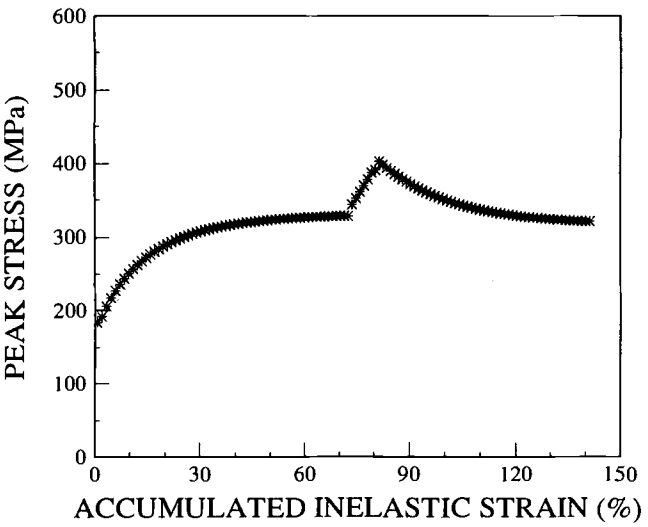

FIG. 10—*Cross-hardening effect with the limit value of* 1.0×10^{-10} *for* $\|\Delta\mathbf{n}\|$. *The effective strain amplitude is* $\pm 0.75\%$, *and the effective strain rate is* $3.0 \times 10^{-4}\ s^{-1}$.

remarkable difference for other loading conditions. Therefore it seems that the limit value of 1.0×10^{-5} for $\|\Delta \mathbf{n}\|$ in numerical implementation of the theory is acceptable for usual loading conditions.

Acknowledgment

The Department of Energy, under Grant DE-FG02-86ER13566, provided partial support of this research.

References

[1] Benallal, A., LeGallo, P., and Marquis, D., "An Experimental Investigation of Cyclic Hardening of 316 Stainless Steel and of 2024 Aluminum Alloy under Multiaxial Loadings," Paper L 10/3, *Proceedings,* Ninth International Conference on Structural Mechanics in Reactor Technology, North Holland, Amsterdam, 1987.

[2] Benallal, A., LeGallo, P., and Marquis, D., "Cyclic Hardening of Metals Under Complex Loadings," *Proceedings of MECAMAT,* International Seminar on the Inelastic Behavior of Solids: Models and Utilization, C. Oytana, Ed., Besançon, Mecamet, Centre de Villaroche, France, 1988, V/361–V/371.

[3] Krempl, E. and Lu, H., "The Path and Amplitude Dependence of Cyclic Hardening of Type 304 Stainless Steel at Room Temperature," *Biaxial and Multiaxial Fatigue, ECF Publication 3,* M. W. Brown and K. J. Miller, Eds., Mechanical Engineering Publications Ltd., London, 1989, pp. 89–106.

[4] Krempl, E. and Lu, H., "The Hardening and Rate-Dependent Behavior of Fully Annealed AISI Type 304 Stainless Steel under Biaxial In-Phase and Out-of-Phase Strain Cycling at Room Temperature," *ASME Journal of Engineering and Materials and Technology,* Vol. 106, 1984, pp. 376–382.

[5] McDowell, D. L., "On the Path Dependence of Transient Hardening and Softening to Stable States under Complex Biaxial Cyclic Loading," *Proceedings,* International Conference on Constitutive Laws for Engineering Materials: Theory and Application, Tucson, AZ, C. S. Desai and R. H. Gallagher, Eds., University of Arizona, Tuscon, AZ, January 1983, pp. 125–132.

[6] Cailletaud, G., Kaczmarek, H., and Policella, H., "Some Elements on Multiaxial Behavior of 316 L Stainless Steel at Room Temperature," *Mechanics of Materials,* Vol. 3, 1984, pp. 333–347.

[7] Ohashi, Y., Tanaka, E., and Ooka, M., "Plastic Deformation Behavior of Type 316 Stainless Steel Subject to Out-of-Phase Strain Cycles," *ASME Journal of Engineering Materials Technology,* Vol. 107, 1985, pp. 286–292.

[8] Tanaka, E., Murakami, S., and Ooka, M., "Effects of Plastic Strain Amplitude on Nonproportional Cyclic Plasticity," *Acta Mechanica,* Vol. 57, 1985, pp. 167–182.

[9] Ohashi, Y., Kawai, M., and Kaito, T., "Inelastic Behavior of Type 316 Stainless Steel Under Multiaxial Nonproportional Cyclic Stressings at Elevated Temperature," *ASME Journal of Engineering Materials Technology,* Vol. 107, 1985, pp. 101–109.

[10] Chaboche, J. L., Van, K. D., and Cordier, G., "Modelization of the Strain Memory Effect on the Cyclic Hardening of 316 Stainless Steel," Paper L 11/3, *Proceedings,* 5th International Conference on Structural Mechanics in Reactor Technology, Berlin, West Germany, North Holland, Amsterdam, 1979.

[11] Nouailhas, D., Cailletaud, G., and Policella, H., "On the Description of Cyclic Hardening and Initial Cold Working," *Engineering Fracture Mechanics,* Vol. 21, No. 4, 1985, pp. 887–895.

[12] Ohno, N., "A Constitutive Model of Cyclic Plasticity with a Nonhardening Strain Region," *ASME Journal of Applied Mechanics,* Vol. 49, 1982, pp. 721–727.

[13] Nouailhas, D., Policella, H., and Kaczmarek, H., "On the Description of Cyclic Hardening Under Complex Loading Histories," *Proceedings,* International Conference on Constitutive Laws for Engineering Materials: Theory and Application, Tucson, AZ, C. S. Desai and R. H. Gallagher, Eds., University of Arizona, Tucson, AZ, January 1983, pp. 45–49.

[14] Nouailhas, D., Chaboche, J. L., Savalle, S., and Cailletaud, G., "On the Constitutive Equations for Cyclic Plasticity Under Nonproportional Loading," *International Journal of Plasticity,* Vol. 1, 1985, pp. 317–330.

[15] Benallal, A. and Marquis, D., "Constitutive Equations for Nonproportional Cyclic Elasto-Viscoplasticity," *ASME Journal of Engineering Materials Technology,* Vol. 109, 1987, pp. 326–336.

[16] Benallal, A. and Marquis, D., "Constitutive Equations Describing Nonproportional Effects in Cyclic Plasticity," *Constitutive Laws for Engineering Materials: Theory and Applications,* C. S. Desai et al., Eds., Elsevier Science Publishing Co., Inc., Amsterdam, 1987, pp. 505–512.

[17] Dafalias, Y. F., "A Novel Bounding Surface Constitutive Law for the Monotonic and Cyclic Hardening Response of Metals," Paper L 3/4, *Transactions,* Sixth International Conference on Structural Mechanics in Reactor Technology, Paris, August 1981, North Holland, Amsterdam.

[18] Ohno, N. and Kachi, Y., "A Constitutive Model of Cyclic Plasticity for Nonlinear Hardening Materials," *ASME Journal of Applied Mechanics,* Vol. 53, 1986, pp. 395–403.

[19] Tanaka, E., Murakami, S., and Ooka, M., "A Constitutive Model of Cyclic Plasticity in Multiaxial Nonproportional Loading," Paper L 2/4, *Proceedings,* Eighth International Conference on Structural Mechanics in Reactor Technology, North Holland, Amsterdam, 1985.

[20] McDowell, D. L., "A Two-Surface Model for Transient Nonproportional Cyclic Plasticity: Part 1. Development of Appropriate Equations," *ASME Journal of Applied Mechanics,* Vol. 52, 1985, pp. 298–302.

[21] McDowell, D. L., "A Two-Surface Model for Transient Nonproportional Cyclic Plasticity: Part 2. Comparison of Theory with Experiments," *ASME Journal of Applied Mechanics,* Vol. 52, 1985, pp. 303–308.

[22] Doong, S. H. and Socie, D. F., "Constitutive Modeling of Metals Under Nonproportional Cyclic Loading," *Visco-Plastic Behavior of New Materials,* D. Hui and T. J. Kozik, Eds., Winter Annual Meeting of the ASME, San Francisco, CA, D. Hui and T. J. Kozik, Eds., ASME, NY, December 1989, pp. 43–52.

[23] Yao, D. and Krempl, E., "Cyclic Uniaxial and Biaxial Hardening of Type 304 Stainless Steel Modeled by the Viscoplasticity Theory Based on Overstress," *Proceedings,* Third Symposium on Nonlinear Constitutive Relations for High Temperature Application, University of Akron, Akron, OH, June 1986.

[24] Yao, D., "Theory of Viscoplasticity Based on Overstress with Applications," Ph.D. thesis, Rensselaer Polytechnic Institute, Troy, NY, 1987.

[25] Krempl, E. and Choi, S. H., "Viscoplasticity Based on Overstress: The Modeling of Ratcheting and Cyclic Hardening of AISI Type 304 Stainless Steel," *Nuclear Engineering and Design,* Vol. 133, 1992, pp. 401–410.

[26] Sleeswyk, A. W., James, M. R., Plantinga, D. H., and Maathuis, W. S. T., "Reversible Strain in Cyclic Plastic Deformation," *Acta Metallurgica,* Vol. 26, 1978, pp. 1265–1271.

[27] Krempl, E., McMahon, J. J., and Yao, D., "Viscoplasticity Based on Overstress with a Differential Growth Law for the Equilibrium Stress," *Mechanics of Materials,* Vol. 5, 1986, pp. 35–48.

[28] Yao, D. and Krempl, E., "Viscoplasticity Theory Based on Overstress. The Prediction of Monotonic and Cyclic Proportional and Nonproportional Loading Paths of an Aluminum Alloy," *International Journal of Plasticity,* Vol. 1, 1985, pp. 259–274.

[29] Sutcu, M. and Krempl, E., "A Simplified Orthotropic Viscoplasticity Theory Based on Overstress," *International Journal of Plasticity,* Vol. 6, 1990, pp. 247–261.

[30] Lee, K. D. and Krempl, E., "An Orthotropic Theory of Viscoplasticity Based on Overstress for Thermomechanical Deformations," *International Journal of Solids and Structures,* Vol. 27, 1991, pp. 1445–1459.

[31] Choi, S. H. and Krempl, E., "Viscoplasticity Theory Based on Overstress Applied to the Modeling of Cubic Single Crystals," *European Journal of Mechanics, A/Solids,* Vol. 8, No. 3, 1989, pp. 219–233.

[32] Choi, S. H., "Modeling of Time-Dependent Mechanical Deformation Behaviors of Metals and Alloys Using Viscoplasticity Theory Based on Overstress," Ph.D. thesis, Rensselaer Polytechnic Institute, Troy, NY, August 1990.

[33] Moosbrugger, J. C. and McDowell, D. L., "On a Class of Kinematic Hardening Rules for Nonproportional Cyclic Plasticity," *ASME Journal of Engineering Materials and Technology,* Vol. 111, 1989, pp. 87–98.

Steven M. Tipton[1] *and Julie A. Bannantine*[2]

Inelastic Stress-Strain Predictions for Multiaxial Fatigue Damage Evaluation

REFERENCE: Tipton, S. M. and Bannantine, J. A., **"Inelastic Stress-Strain Predictions for Multiaxial Fatigue Damage Evaluation,"** *Advances in Multiaxial Fatigue, ASTM STP 1191,* D. L. McDowell and R. Ellis, Eds., American Society for Testing and Materials, Philadelphia, 1993, pp. 273–297.

ABSTRACT: The inelastic stress-strain response of a material subjected to complex loading must be known or estimated in order to predict the fatigue life of a component using many current multiaxial fatigue damage models. This paper presents stress-strain predictions obtained using two incremental plasticity algorithms for several nonproportional loading paths.

The two algorithms both employ von Mises yield surfaces with kinematic hardening. However, one algorithm translates a single yield surface within a stationary limit surface using the hardening rules specified by Mróz and invokes a radial return for neutral loading. The other algorithm translates multiple yield surfaces (or a field of plastic moduli) according to a modified Mróz hardening rule proposed by Garud with no neutral loading provision. The algorithms are used to predict stress histories that are compared with measured responses from strain-controlled tests on normalized 1045 thin-walled tubes. A variety of nonproportional load paths were investigated. In general, relatively good agreement between predicted and measured stress-strain response for the two algorithms was observed for application to multiaxial fatigue evaluation. Strengths and weaknesses of each model are discussed.

KEY WORDS: nonproportional loading, multiaxial fatigue, kinematic hardening, two-surface, multisurface, von Mises yield surfaces, normality flow rule, cyclic plasticity, cyclic stress-strain stability, neutral loading

An increasing number of strain-based multiaxial fatigue damage parameters have been proposed over the last 20 years [*1–4*]. One popular approach combines stress and strain components to account for mean stress effects [*5*] under uniaxial loading. This approach has been extended conceptually to deal with multiaxial fatigue by considering the maximum principal stress/strain direction [*6,7*]. More recently, many parameters have been developed that utilize various combinations of stress and strain components (e.g., maximum shear strain amplitude and stress normal to the maximum shear plane) to correlate multiaxial fatigue life [*6–10*].

Recent advances in strain gage technology have contributed to the ability to conduct strain-based fatigue analyses. Miniature rosettes with gage lengths as small as 0.75 mm facilitate the measurement of localized states of multiaxial strain for many complex loading histories. Under repeatable cyclic load applications, strains in regions of interest (notches) often exhibit a transient response, but stabilize over a number of cycles. With the stabilized strain history in hand, an analyst is still left with the task of estimating the corresponding stress and unmeasured strain components before many multiaxial fatigue damage parameters can be implemented.

[1] Associate professor, The University of Tulsa, 600 S. College Ave., Tulsa, OK 74104.
[2] Staff engineer, IBM, 5600 Cottle Rd., San Jose, CA 95193.

For nonproportional load paths, an incremental plasticity analysis is required to make a valid estimation of a material's stress-strain response to a set of strain-controlled inputs. A number of incremental plasticity algorithms have been developed to deal with path-dependent constitutive material behavior [*10–17*]. More sophisticated models are under development that attempt to estimate detailed nonproportional responses, including transient hardening. However, these models require significant testing to characterize input parameters and are not appropriate for general, engineering use at the current time. Furthermore, for multiaxial fatigue life prediction, very accurate predictions in the transient portion of the deformation history are not as critical as the characterization of the cyclically stable response. Therefore, in this paper, two relatively simple models are described that utilize somewhat standard numerical components. Both models are capable of dealing with complex nonproportional loading, but neither provide a mechanism for dealing with transient behavior or initial material anisotropy. The algorithms are presented in terms of their similarities and differences. Their predictions are compared to the measured stress response of normalized 1045 steel thin-walled tubes under axial-torsional strain-controlled loading, generated by Subramanian [*18*].

Incremental Plasticity Algorithms

Incremental plasticity algorithms receive as input applied incremental strain and/or stress components and compute the corresponding remaining incremental components of the stress and strain tensors. All incremental plasticity models consist of the following major components:

1. Yield criterion.
2. Flow rule.
3. Hardening rule.

Both algorithms examined in this paper utilize the same yield criterion and flow rule, but employ different kinematic hardening rules. The two models will be referred to as "Model A" and "Model B" throughout the rest of this paper. Model A uses a Mróz hardening rule [*13*], and Model B uses a modified Mróz hardening rule proposed by Garud [*10,19*]. The two algorithms differ further in that Model A is a two-surface model with a von Mises kinematic yield surface and a fixed von Mises limit surface, similar to that proposed in Refs *14–17,* while Model B utilizes a field of von Mises yield surfaces (or plastic moduli, as proposed by Mróz [*13*]). Each component is described briefly below, followed by a description of how both models deal with transverse normal stress and strain components.

Yield Criterion

The yield criterion defines the conditions at which plastic flow occurs. The models under investigation in this paper utilize the von Mises yield criteria. This can be described in terms of principal stress components by

$$f = \tfrac{1}{2}[(\sigma_1 - \sigma_2)^2 + (\sigma_2 - \sigma_3)^2 + (\sigma_3 - \sigma_1)^2] - S_y^2 = 0 \tag{1}$$

where σ_i ($i = 1, 2, 3$) are the principal stresses, and S_y is the yield strength (or flow stress) defined by axial testing. Both models are capable of more general multiaxial loading, but in this paper, all analyses are conducted in axial-torsional stress space. On axes defined by σ ver-

sus τ, Eq 1 defines an ellipse and can be characterized as a circle on axes of σ versus $\sqrt{3}\tau$. In this case, the yield surface may be expressed as

$$f = [\sigma^2 + 3\tau^2] - S_y^2 = 0 \tag{1a}$$

Flow Rule

The normality flow rule, also called the Prandtl-Reuss relation [*20,21*], is utilized in both algorithms. The flow rule relates the plastic strain increment to (1) the existing state of stress, and (2) the applied stress increment. This approach can be stated most concisely by

$$\Delta\bar{\epsilon}^p = \lambda\bar{n} \tag{2}$$

or that plastic strain increment ($\Delta\bar{\epsilon}^p$) is colinear with the exterior normal ($\bar{n}$) to the yield surface at the current stress state. Drucker [*22*] also developed and validated this relation with thermodynamic definitions of work hardening. For the remainder of this paper, a Δ is used to denote an incremental quantity, and an overbar is used to denote a four-dimensional vector representing an abbreviated form of stress and strain tensors. In this study, stress and strain vectors may be expressed by their four nonzero components, and the total strain, $\bar{\epsilon}$, may be separated into elastic and plastic components as given by

$$\bar{\sigma} = \begin{bmatrix} \sigma_x \\ \sigma_y \\ \sigma_z \\ \tau_{xy} \end{bmatrix} \text{ and } \bar{\epsilon} = \begin{bmatrix} \epsilon_x \\ \epsilon_y \\ \epsilon_z \\ \gamma_{xy} \end{bmatrix} \text{ where } \bar{\epsilon} = \bar{\epsilon}^e + \bar{\epsilon}^p; \quad \bar{\epsilon}^e = \begin{bmatrix} \epsilon_x^e \\ \epsilon_y^e \\ \epsilon_z^e \\ \gamma_{xy}^e \end{bmatrix}; \quad \bar{\epsilon}^p = \begin{bmatrix} \epsilon_x^p \\ \epsilon_y^p \\ \epsilon_z^p \\ \gamma_{xy}^p \end{bmatrix} \tag{3}$$

With this convention, stress and plastic strain may be thought of as parallel (in this case, four-dimensional) spaces, with the plastic strain increment always colinear with the yield surface normal at the current stress state. The yield surface normal may be expressed as

$$\bar{n} = \frac{\dfrac{\alpha f}{\alpha\bar{\sigma}}}{\left[\dfrac{\alpha f}{\alpha\bar{\sigma}} \cdot \dfrac{\alpha f}{\alpha\bar{\sigma}}\right]^{1/2}} \tag{4}$$

The constant of proportionality, λ, in Eq 2 is defined by considering the plastic strain increment to be directly proportional to the projection of the stress increment onto the yield surface normal, as follows

$$\Delta\bar{\epsilon}^p = \frac{(\Delta\bar{\sigma} \cdot \bar{n})\bar{n}}{C} \tag{5}$$

where C is the generalized plastic modulus. Equation 5 can also be expressed as

$$C = \frac{\Delta\bar{\sigma} \cdot \Delta\bar{\epsilon}^p}{\Delta\bar{\epsilon}^p \cdot \Delta\bar{\epsilon}^p} \tag{6}$$

For uniaxial loading this reduces to

$$C = \frac{2}{3}\frac{\Delta\sigma_x}{\Delta\epsilon_x^p} \quad \text{or} \quad C = \frac{2}{3}E_p \tag{7}$$

where E_p is the slope or the uniaxial stress-plastic strain curve (or the plastic modulus). Both models utilize the uniaxial cyclic stress-strain curve. Model A uses an expression for C which is a function of the distance from the current stress point on the yield surface to the point on the limit surface with the same outward normal. The expression for C is developed in terms of the cyclic strength coefficient, K', and the cyclic strain hardening exponent, n', obtained from uniaxial stress-strain data (for details, refer to Eq 3.46 in Ref *23*). Model B uses a piecewise linear approximation of the cyclic stress-strain relation, as depicted in Fig. 1. When the state of stress has impinged upon a particular yield surface, f_i, and subsequent loading moves the surface, this surface is considered *active,* and the *active* plastic modulus is given by

$$C_i = \frac{2}{3}\frac{(R_{i+1} - R_i)}{(\epsilon_{i+1} - \epsilon_i) - \left(\dfrac{R_{i+1} - R_i}{E}\right)} \tag{8}$$

where R_i and ϵ_i are the segment endpoints (as shown in Fig. 1), and E is the elastic modulus.

Hardening Rule

Both of the hardening rules discussed in this paper are *kinematic* rules. This means the yield surfaces translate in stress space, without changing size or shape. The *hardening rule* dictates how the translation occurs. In Model A, the Mróz rule is applied to a single yield surface that translates relative to a stationary limit surface, as shown in Fig. 2. Stress increments that attempt to move outside the limit surface are returned radially to the surface. Model B used the Garud hardening rule to specify the motion of active yield surfaces within the field of plastic moduli.

Figure 3 illustrates how the Mróz and Garud rules differ in prescribing yield surface translation. In this figure, f_i represents the yield surface, f_Y, and f_{i+1} represents f_L for the two-surface model. The current state of stress, $\bar{\sigma}$, is on the active yield surface, f_i, whose center is located at $\bar{\alpha}_i$. A stress increment, $\Delta\bar{\sigma}$, is attempting to proceed outside the yield surface. The Mróz rule states that the yield surface center, $\bar{\alpha}_i$, is to move along the direction that joins exterior normal on the active yield surface, $\bar{n}_{\text{mroz}}$, at the current state of stress, $\bar{\sigma}$, with the geometrically similar point on the next yield surface, f_{i+1}. This movement is defined by $\Delta\bar{\alpha}_{i,\text{morz}}$ in Fig. 3. However, the Garud rule utilizes the exterior normal on the *next* yield surface, $\bar{n}_{\text{garud}}$, defined by the direction of the stress increment, $\Delta\bar{\sigma}$. The Garud rule then states that the yield surface motion should occur along a line joining the geometrically similar points on both surfaces, defined by identical exterior normals, $\bar{n}_{\text{garud}}$. For both rules, the magnitude of the motion is defined by ensuring that the updated state of stress, $\bar{\sigma} + \Delta\bar{\sigma}$, will lie exactly on the yield surface in its new position. It is this consistency requirement that partially motivated the development of the Garud rule. Although, theoretically, the Mróz kinematic hardening rule does not result in an intersection of yield surfaces [*24*] during implementation with a small but finite stress increment, a crossover or intersection may occur. Garud noticed that for nonproportional loading ($\Delta\sigma$ is not colinear with $\bar{n}_{\text{mroz}}$), as yield surfaces approach, the Mróz rule can cause them to come into contact at a point on f_{i+1} with dissimilar exterior normals, such that the yield surfaces overlap. The Garud approach eliminates this discrepancy.

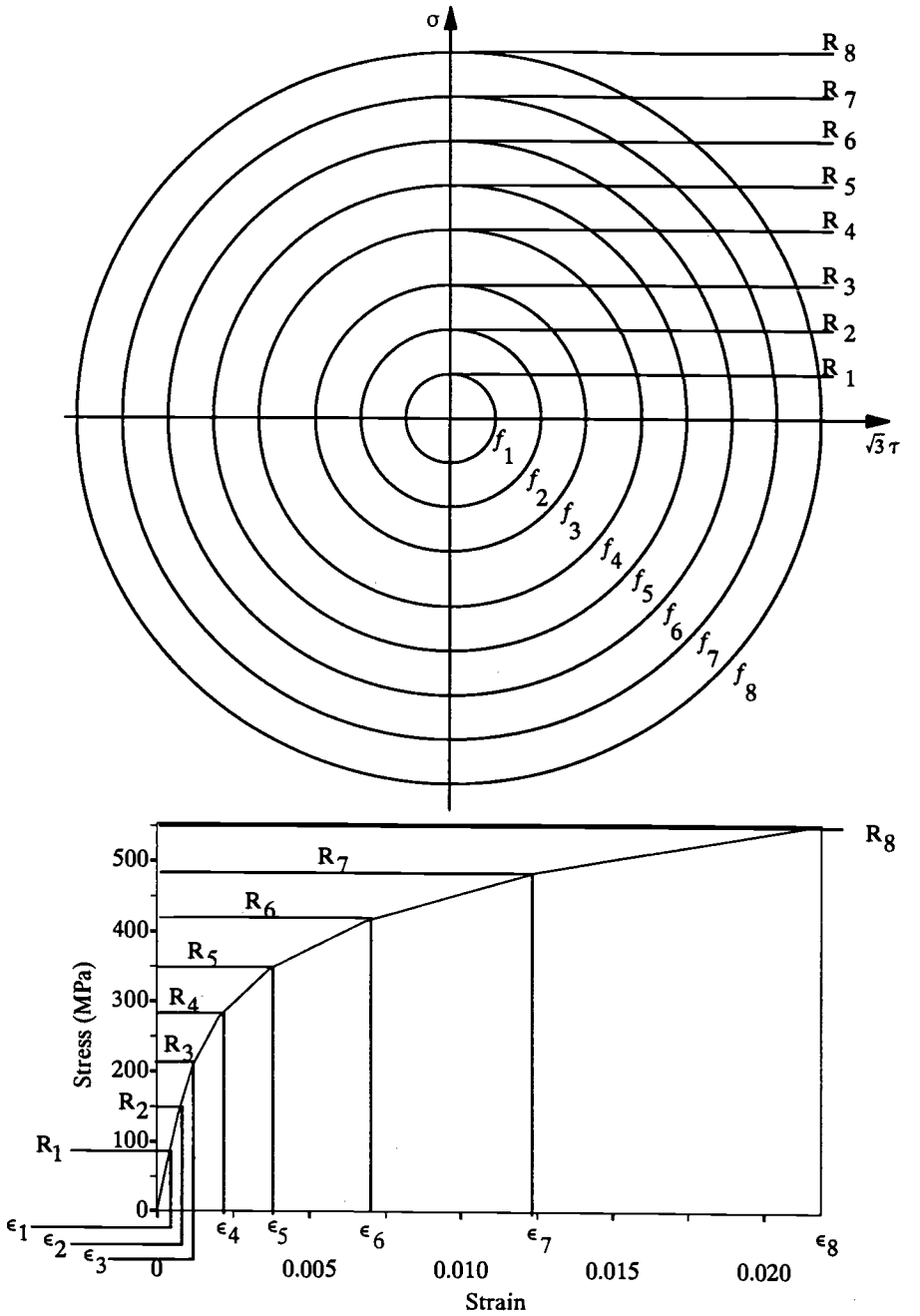

FIG. 1—*Field of plastic moduli and discretized cyclic stress-strain curve for normalized 1045 steel.*

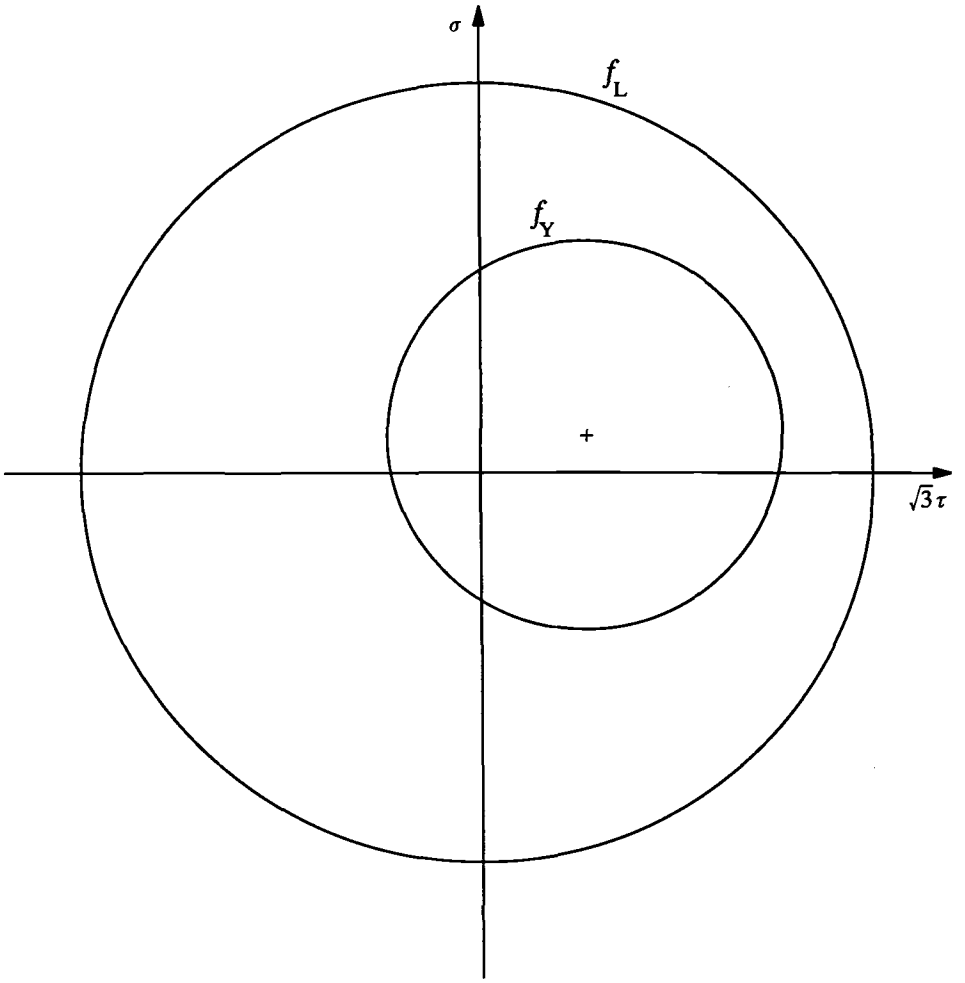

FIG. 2—*Two-surface Mróz model, consisting of a mobile yield surface and a stationary limit surface.*

Transverse Stress and Strain Components

It was stated earlier that, in this paper, stress and strain are being considered as four-dimensional vectors (Eq 8). However, in terms of input and output, both of the algorithms under investigation essentially operate as follows

$$\text{input: } \Delta\epsilon_x,\ \Delta\sigma_y,\ \Delta\sigma_z,\ \Delta\gamma_{xy}$$
$$\text{output: } \Delta\sigma_x,\ \Delta\epsilon_y,\ \Delta\epsilon_z,\ \Delta\tau_{xy}$$

The transverse stress increments, $\Delta\sigma_y$ and $\Delta\sigma_z$ (and the transverse stresses themselves), remain zero in this investigation. This is accomplished in each algorithm by imposing the requirement that

$$\Delta\epsilon_y^e = \Delta\epsilon_z^e = -\nu\Delta\epsilon_x^e \quad \text{or} \quad (\Delta\epsilon_y - \Delta\epsilon_y^p) = (\Delta\epsilon_z - \Delta\epsilon_z^p) = -\nu(\Delta\epsilon_x - \Delta\epsilon_x^p) \tag{9}$$

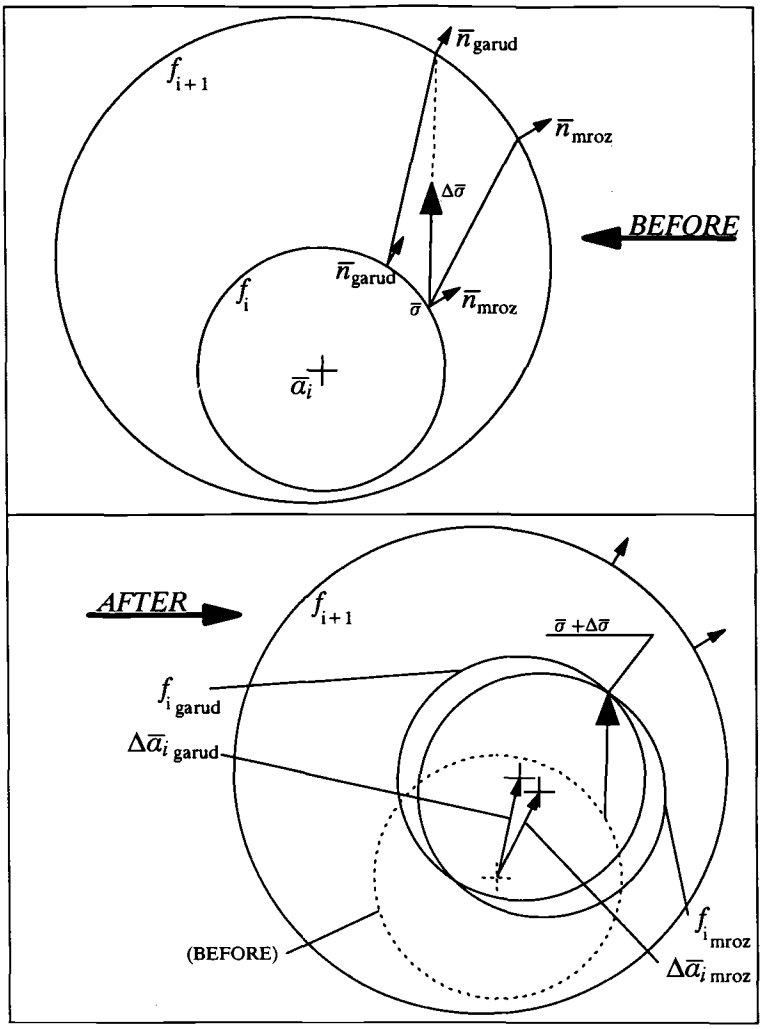

FIG. 3—*Illustration of how the Mróz and Garud hardening rules specify the translation of yield surface,* f_i, *based on the stress increment,* $\Delta\bar{\sigma}$, *and the current state of stress,* $\bar{\sigma}$.

where ν = Poisson's ratio, thus requiring only axial and torsional strain increments as input. The transverse strain is computed to ensure that transverse stress remains zero. It should be noted that transient behavior and initial material anisotropy are not considered by either approach. Further details may be found in Refs *23* and *25*.

Specimens, Material, and Input Load Histories

Subramanian [*18*] tested thin-walled tubes of normalized 1045 steel (machined from hot rolled bar stock) on a tension-torsion servohydraulic load frame with a processor/interface. Tests were run in strain control with an internal extensometer described in Ref *26* used to monitor axial and torsional strains. Specimen gage sections had an internal diameter of 25.4 mm and a wall thickness of 2.54 mm and were polished to a 0.5 μm surface finish.

The normalized 1045 steel was also utilized in the SAE Fatigue Design and Evaluation Committee Notched Shaft Round-Robin Program. Detailed data about the material's metallurgical and mechanical properties may be found in Ref *27*. The cyclic stress-strain curve for the material is shown in a piecewise linear form in Fig. 1. This curve was generated from an elastic modulus of 207 GPa, a cyclic strength coefficient, K', of 1258 MPa, and a cyclic strain hardening exponent, n', of 0.208. The eight linear segments illustrated in Fig. 1 were used to define the generalized plastic moduli (Eq 8) in Model B.

Five nonproportional load histories, generated by Subramanian [*18*], were investigated. Only nonproportional cases were examined in this paper since the two models under investigation yield identical results for proportional multiaxial stress states. The five cases are depicted in Figs. 4*a* through 4*c* and designated by

1. The 0.0015 triangle path.
2. The 0.0027 triangle path.
3. The 0.0015 right angle path.
4. The 0.0027 triangle path.
5. The 0.0015 circle path.

In general, the tests were run at equivalent von Mises equivalent strain amplitudes. The maximum shear strain was a factor of $\sqrt{3}$ times the maximum axial strain. The 0.0015 paths actually used an axial strain amplitude of 0.001 54, and the 0.0027 paths used axial strain amplitudes of 0.002 68. These paths are particularly challenging to incremental plasticity codes since each represents (to varying degrees) neutral loading, or stress paths approximately tangent to the yield surface. The stress-strain response for each tube is reported in this paper at the stable half-life.

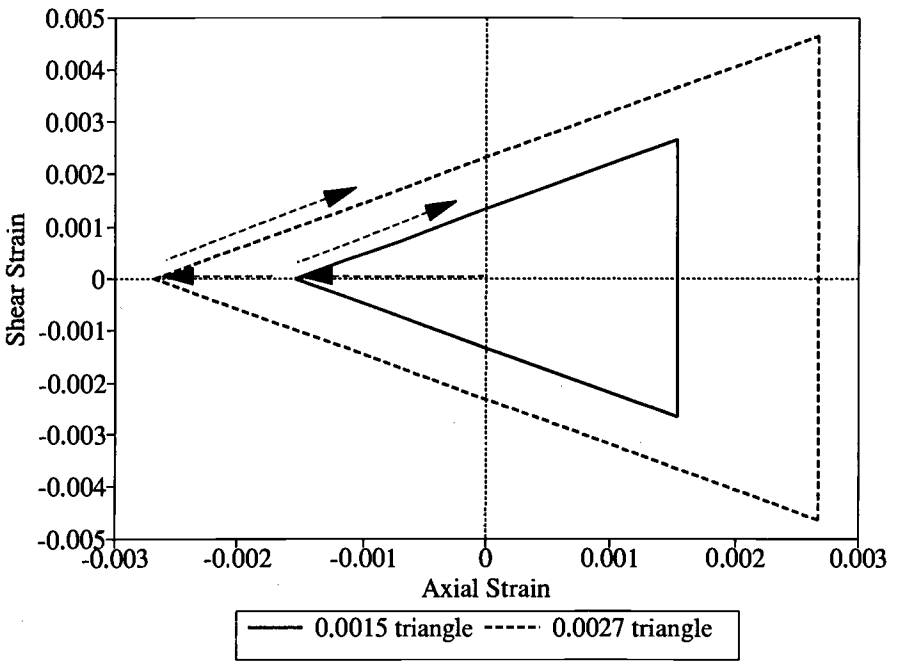

FIG. 4*a*—*Input strain histories for the triangle paths.*

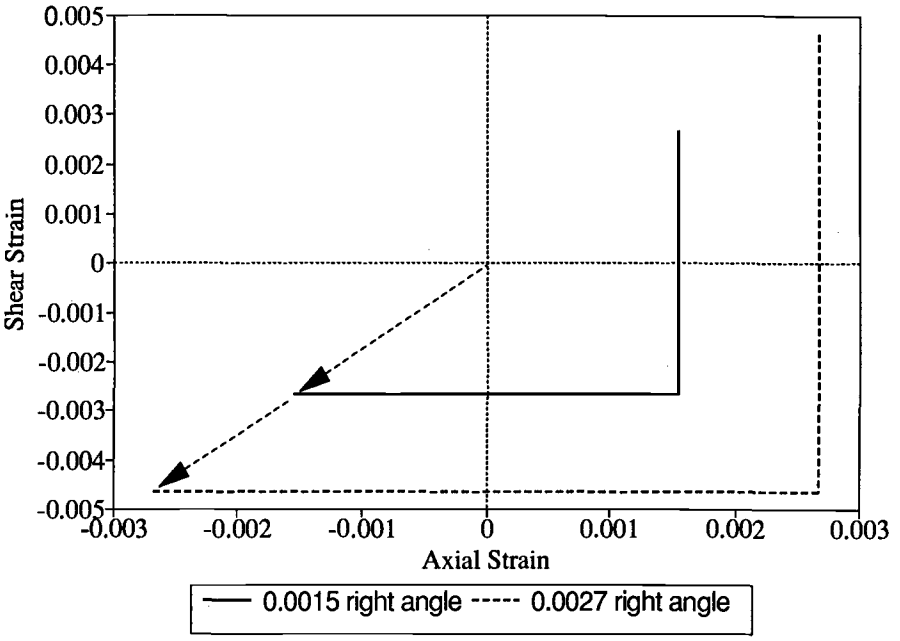

FIG. 4*b*—*Input strain histories for the right angle paths.*

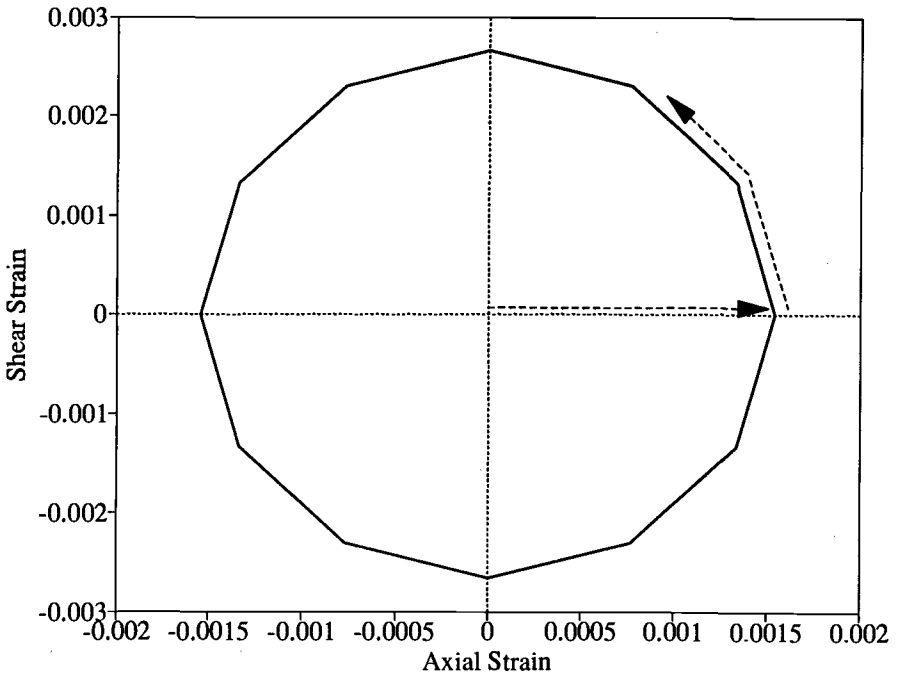

FIG. 4*c*—*Input strain history for the circle path.*

Stress-Strain Predictions and Experimental Results

The predictions from both algorithms and the measured thin-walled tube response are presented in Figs. 5 through 9 for the five loading cases, respectively. Each of these figures shows three plots: (a) the shear stress versus axial stress, (b) the axial stress versus axial strain, and (c) the shear stress versus shear strain. It is clear from these figures that Model A agrees more closely with the experimental results than does Model B. This is discussed in the next section along with a summarized comparison of the two models and details about their implementation.

Discussion

As is apparent in Figs. 5 through 9, Model A more closely predicts the material response than does Model B in terms of estimated peaks and valley values important to a fatigue analysis. Model A considerably out-performed Model B for the right angle paths. To explain the relative behavior of the two models, several apparent points are considered: (1) the inconsistency in the implementation of the Mróz hardening rule that is eliminated by the Garud modification, (2) the necessity for small increment size by both models, (3) the elastic neutral loading clause used in Model A and not in Model B, and (4) the fact that the Mróz rule specifies the direction of yield surface translation based only on the current state of stress while the Garud rule also utilizes the direction of the applied stress increment. Table 1 summarizes the two models and further guides this discussion.

The first point pertains to the primary motivation behind the modification of the Mróz hardening rule proposed by Garud. Since the target point on the next yield surface has a different outward normal than the current stress point (for a nonproportional load path), then a stress increment that causes two surfaces to converge will cause them to do so at geometrically

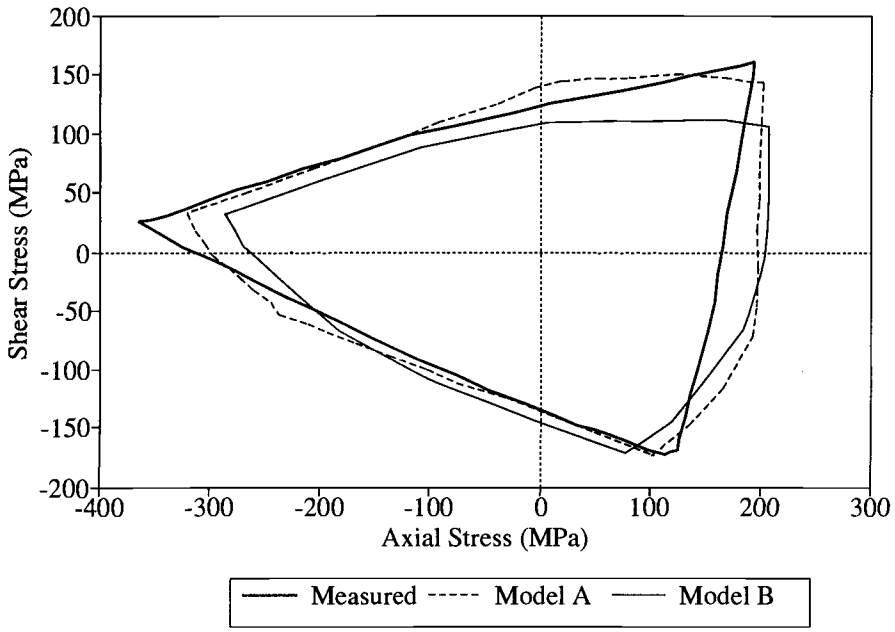

FIG. 5*a*—*Shear stress versus axial stress for the 0.0015 triangle path.*

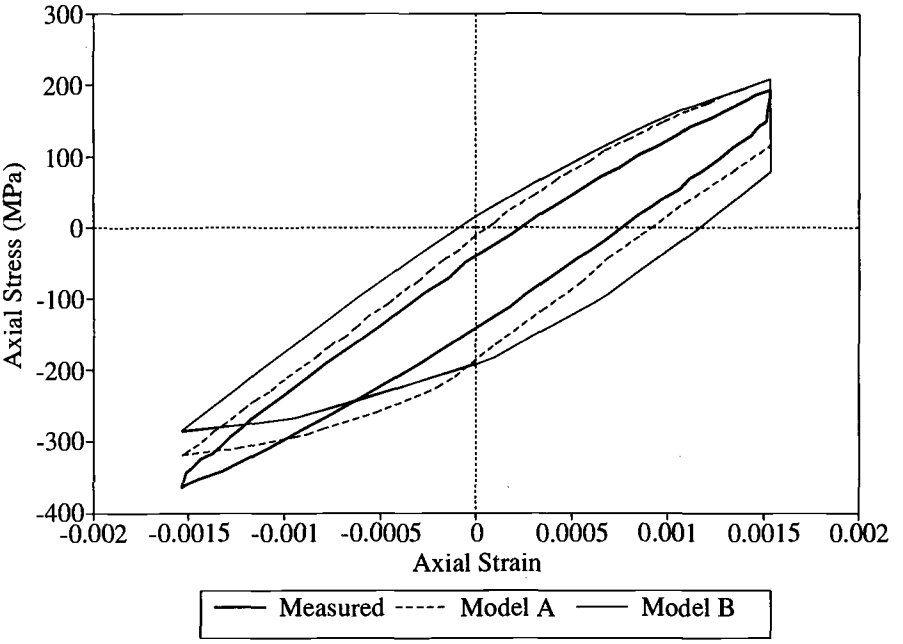

FIG. 5*b*—*Axial stress versus axial strain for the 0.0015 triangle path.*

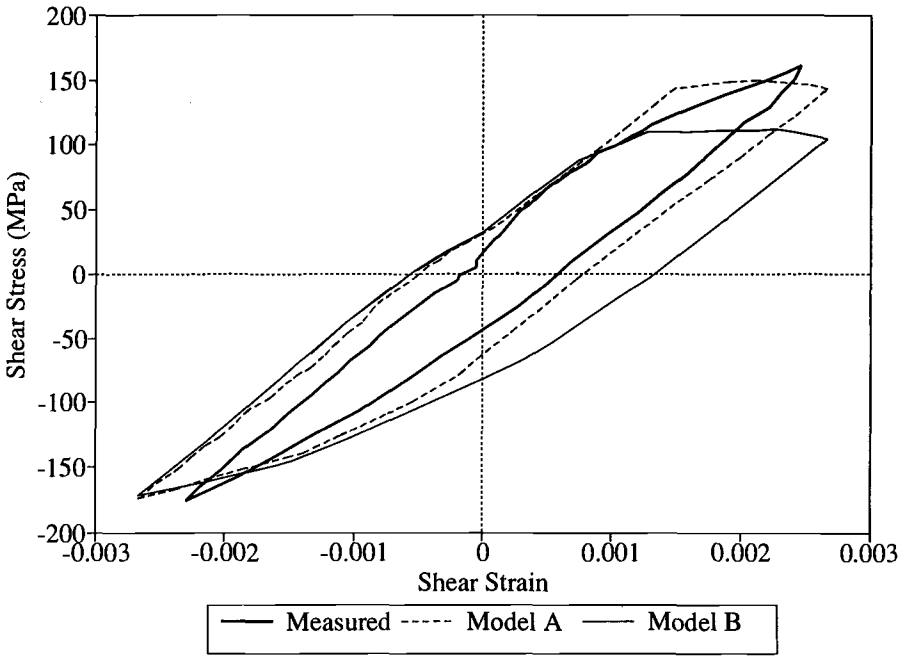

FIG. 5*c*—*Shear stress versus shear strain for the 0.0015 triangle path.*

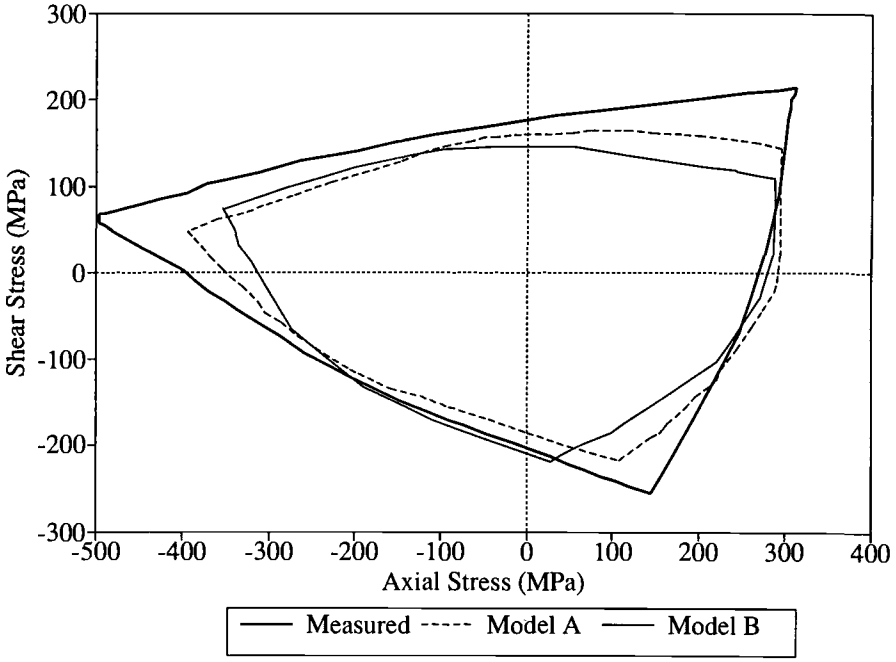

FIG. 6*a*—*Shear stress versus axial stress for the 0.0027 triangle path.*

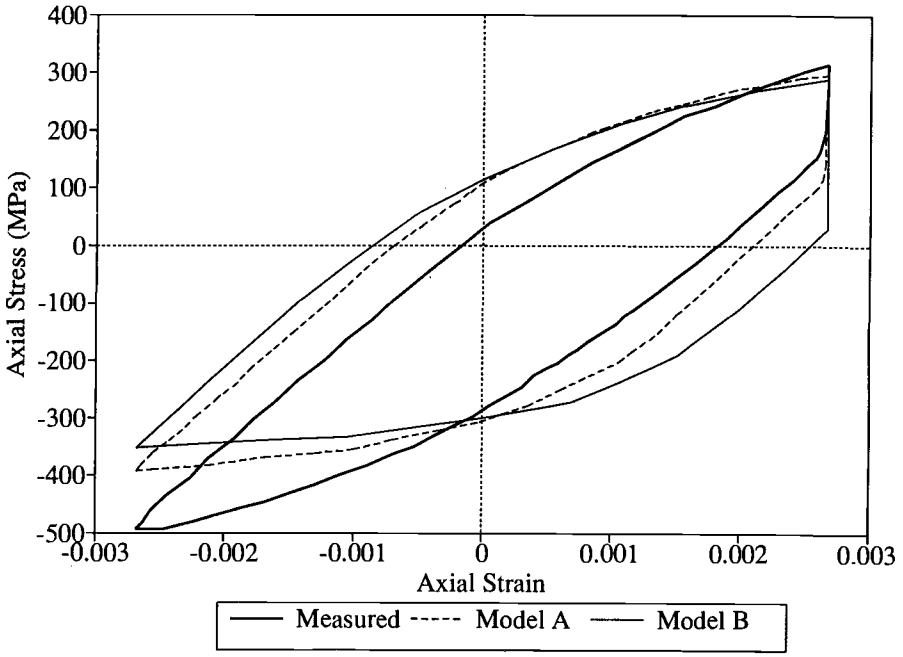

FIG. 6*b*—*Axial stress versus axial strain for the 0.0027 triangle path.*

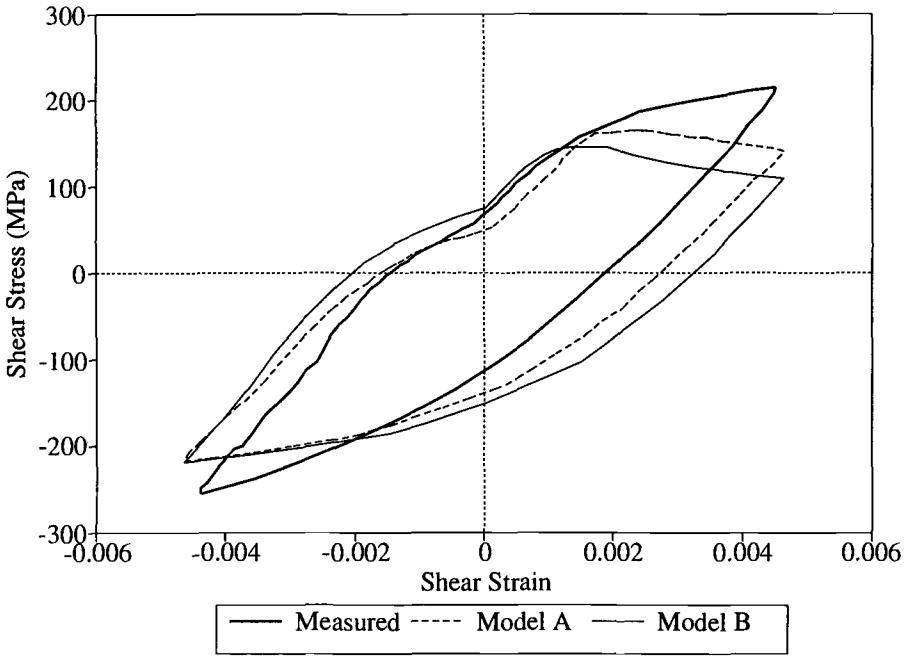

FIG. 6*c*—*Shear stress versus shear strain for the 0.0027 triangle path.*

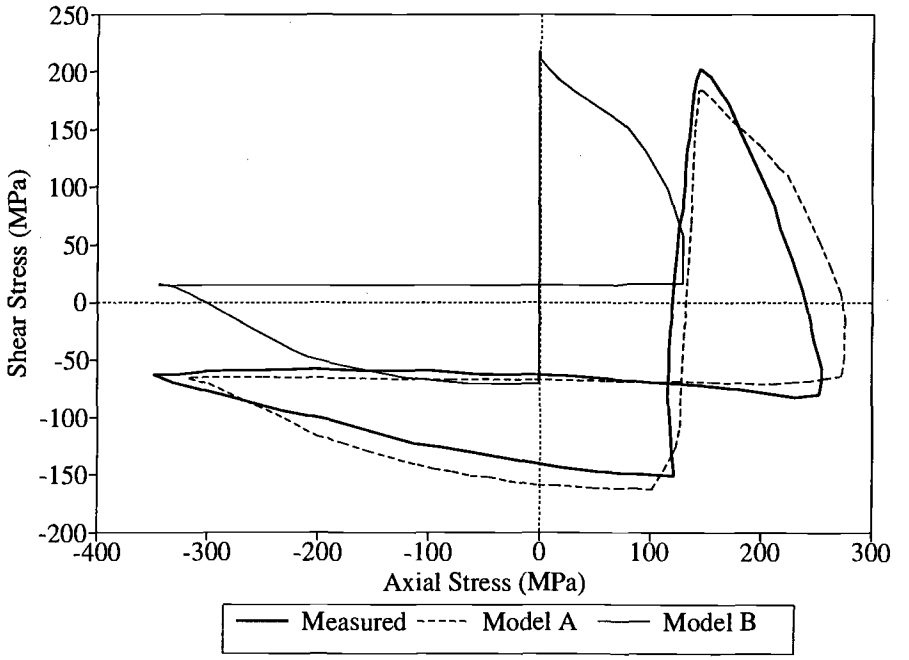

FIG. 7*a*—*Shear stress versus axial stress for the 0.0015 right angle path.*

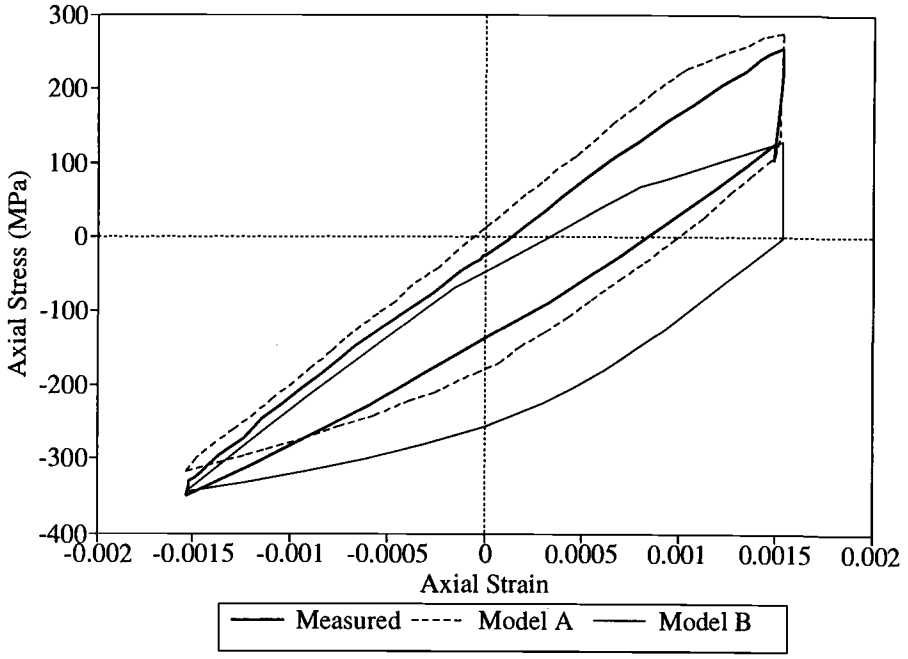

FIG. 7*b*—*Axial stress versus axial strain for the 0.0015 right angle path.*

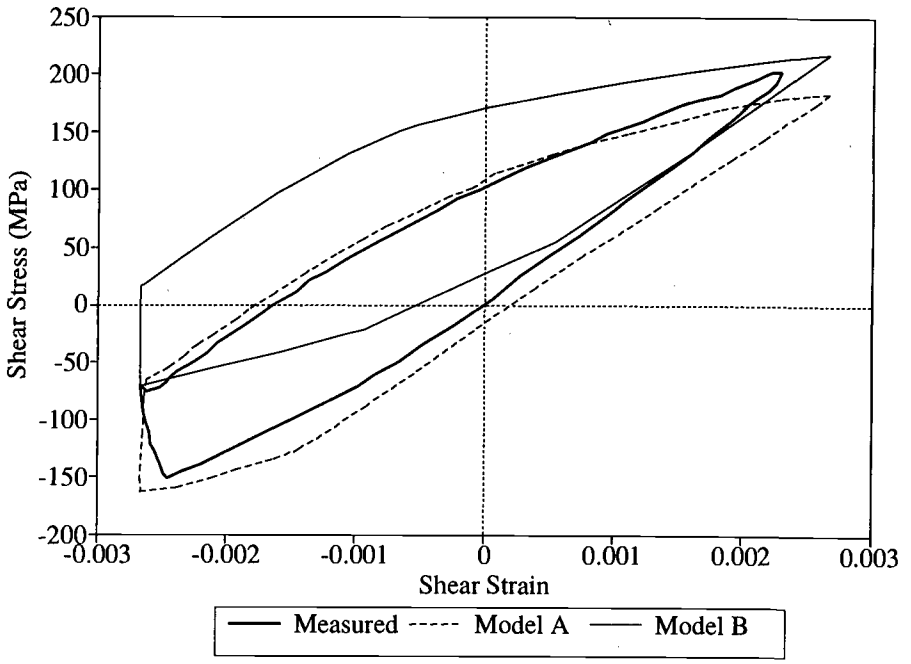

FIG. 7*c*—*Shear stress versus shear strain for the 0.0015 right angle path.*

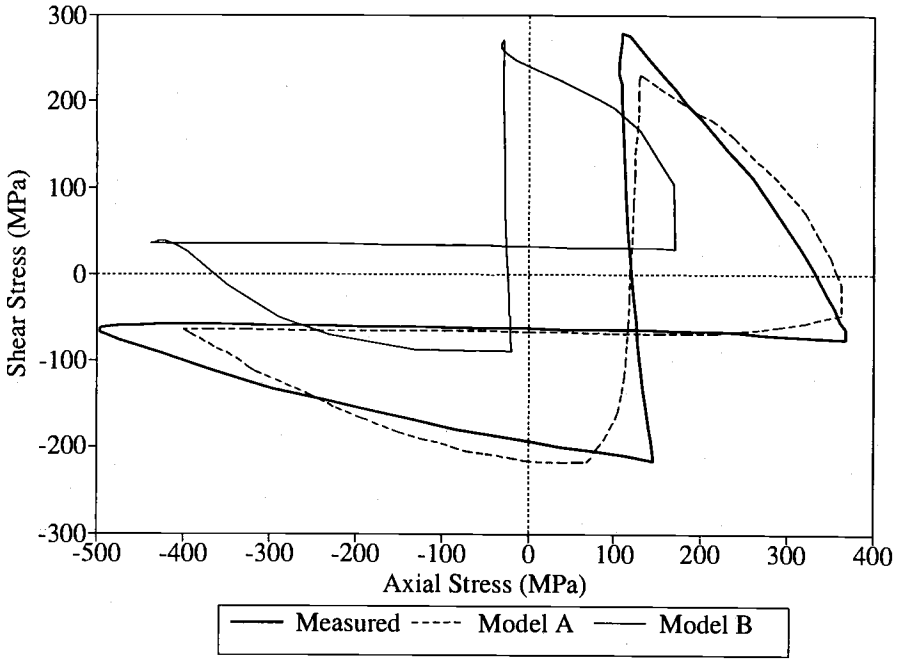

FIG. 8*a*—*Shear stress versus axial stress for the 0.0027 right angle path.*

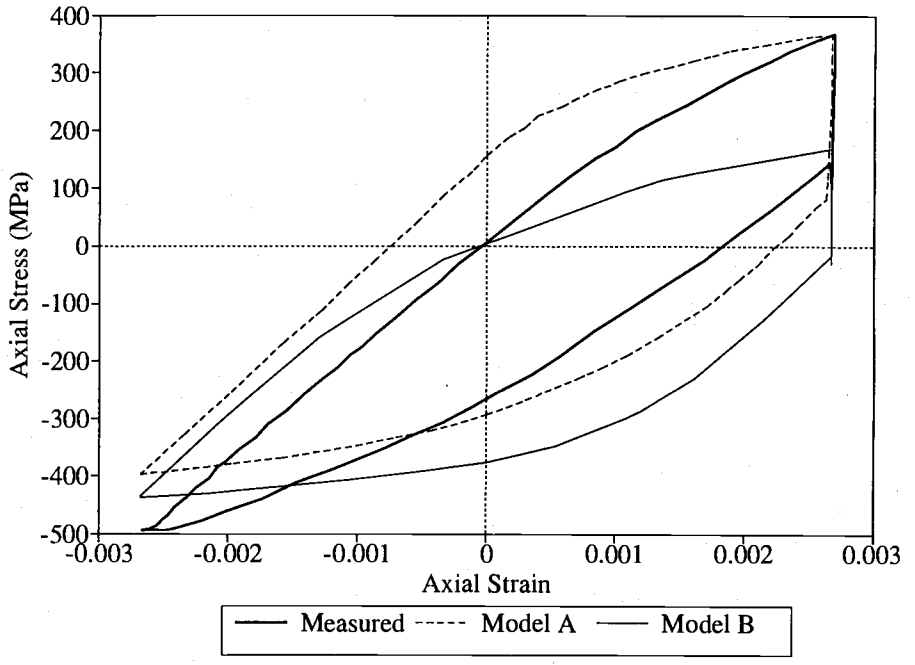

FIG. 8*b*—*Axial stress versus axial strain for the 0.0027 right angle path.*

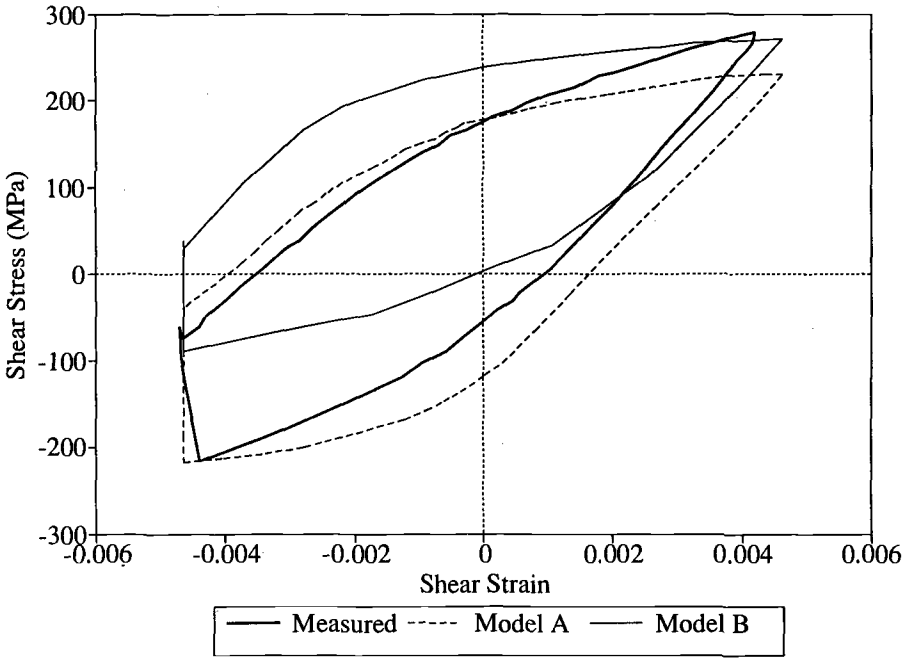

FIG. 8*c*—*Shear stress versus shear strain for the 0.0027 right angle path.*

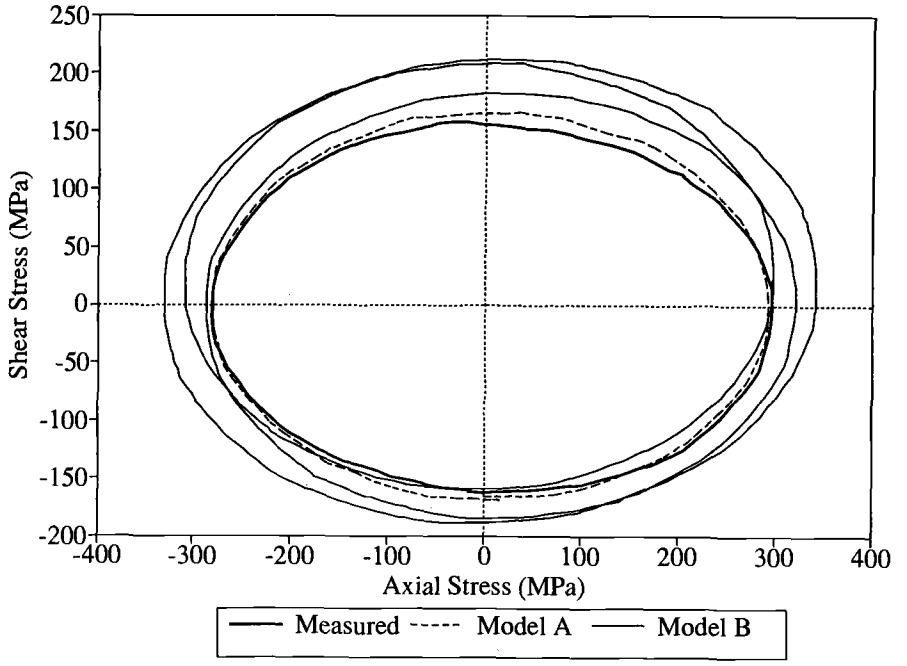

FIG. 9*a*—*Shear stress versus axial stress for the 0.0015 circle path. The Model B response was "quasi-stable," requiring three cycles to stabilize.*

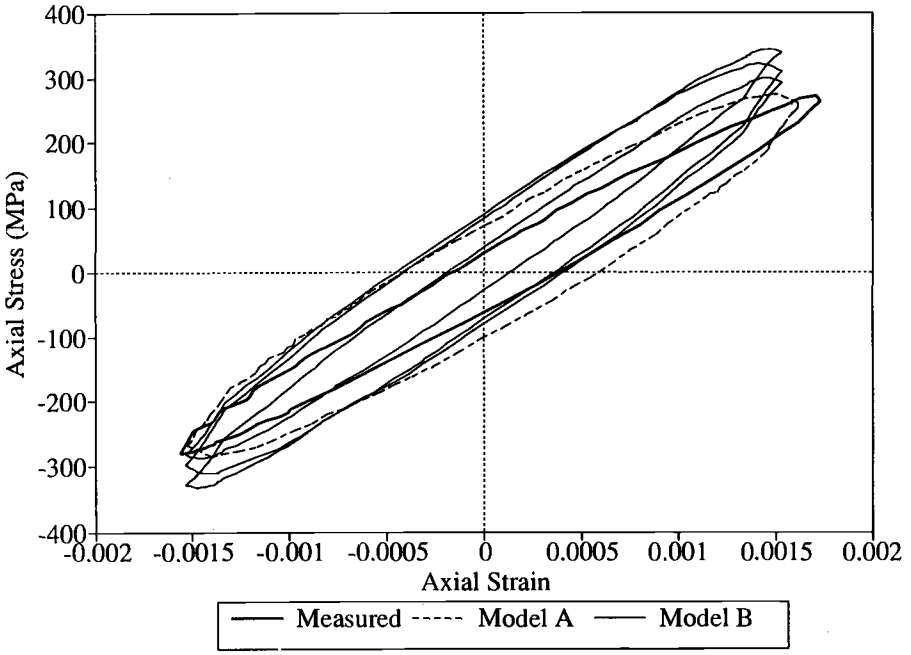

FIG. 9*b*—*Axial stress versus axial strain for the 0.0015 circle path. The Model B response was "quasi-stable," requiring three cycles to stabilize.*

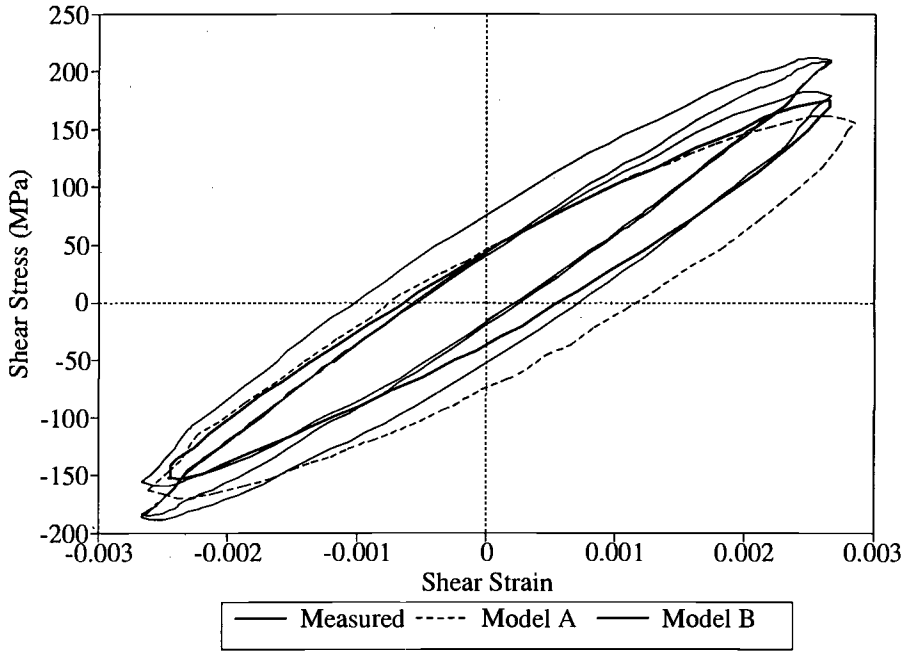

FIG. 9*c*—*Shear stress versus shear strain for the 0.0015 circle path. The Model B response was "quasi-stable," requiring three cycles to stabilize.*

TABLE 1—*Summary of two incremental plasticity models.*

	Model A	Model B
Yield criterion	von Mises	von Mises
Flow rule	Normality	Normality
Hardening rule	Two-surface (Mróz)	Multisurface (Garud)
Neutral loading clause	Elastic with radial return	No provision utilized
Increment size control	Automatic discretionary increment sizing	Manually controlled

dissimilar points, resulting in yield surface overlap. In theory this inconsistency does not exist since theoretical stress increments are infinitesimal. However, in the actual implementation of the Mróz translation of a kinematic yield surface using finite stress increments, special provisions are necessary to avoid the overlap problem. In Model A, the problem is avoided by using a refined step size and by simply forcing the contact point on the outer yield surface to define the location of the updated yield surface center, should the limit surface be exceeded. It has been recognized [*28*] that, once a stress reaches the next yield surface, f_{i+1}, in a field of plastic moduli, it is not necessary to establish the position of f_i until elastic unloading occurs ($\Delta\bar{\sigma} \cdot \bar{n} < 0$). For most stress-strain paths of engineering importance (including the histories examined in this paper), the limit surface is never encountered. Its purpose is to keep the stress values at reasonable upper limit values as defined by cyclic stress-strain data. In addition, in Model A the limit surface (outer surface) defines the plastic modulus, C, in the flow rule and the direction of yield surface translation in the hardening rule.

The second point must be examined carefully. The use of the Garud rule can apparently avoid implementation difficulties associated with large, nearly neutral stress increments (nearly tangent to the yield surface). The rule ensures that surfaces will contact correctly. However, what could be perceived as an implementation "advantage" can result in input increments that are not small enough to produce a numerically stable response. In fact, the predictions from Model B presented in Figs. 5 through 9 were made by breaking each linear segment of the input strain paths into ten divisions and successively inputting those increments. Larger increments were tried initially, but the use of ten increments satisfied numerical convergence. This means that, although Model B was physically capable of operating with larger increments, caution was required in the specifying the size of input strain increments, as with any incremental plasticity algorithm. Smaller divisions resulted in a stable response, but this solution represents indiscriminate discretization, which can produce unreasonably large output files for long stress histories and is unnecessary for simpler loading cases. In general, the algorithm could not be applied without a convergence study.

As mentioned previously, the Mróz rule (and any other hardening rule) must be carefully applied when load paths are neutral or near neutral. For these cases, the stress increment is tangent to the yield surface. This is described mathematically by

$$\Delta\bar{\sigma} \cdot \bar{n} = 0 \tag{10}$$

Model A utilizes a unique discretionary routine that automatically decreases the size of the input increment in proportion to: (1) the cosine of the angle between the stress increment and the yield surface normal

$$\cos(\theta) = \frac{(\Delta\bar{\sigma} \cdot \bar{n})}{\sqrt{\Delta\bar{\sigma} \cdot \Delta\bar{\sigma}}}, \tag{11}$$

and (2) the distance that the stress increment extends outside the yield surface. This routine, described in detail in Ref *23,* avoids the use of excessive input increments for small, proportional strain changes yet automatically provides increment size refinement for nonproportional loading or oversized strain increments. The model recognizes when Eq 10 is true (or very nearly true) and invokes a clause that updates stress and strain increments elastically and executes a radial return to the yield surface. Explicitly, the neutral loading clause was invoked when

$$|\Delta\bar{\sigma} \cdot \bar{n}| \leq \epsilon \tag{12}$$

where $\epsilon = 0.033\ R_y$, and R_y is the yield surface radius. This criterion was rather arbitrarily selected on the basis of experience and should be studied in future investigations.

The neutral loading clause in Model A, with the fourth point listed above, can explain some of the significant differences in the predictions made by the two algorithms. The need for special considerations with regards to neutral loading has been noted in the literature [*29*]. It appears that the neutral loading clause may be necessary to ensure that a *reasonable* stable response is attained. Referring to Figs. 9*a* through 9*c*, the response predicted by Model B may be considered only *quasi-stable* for the circle path. In Fig. 9*a*, the oval experimental response and Model A prediction are matched qualitatively by the Model B prediction for individual cycles, but the repeated, stable response predicted by Model B only becomes apparent over *three full cycles of loading.* This numerical consequence is not considered reasonable and could possibly have been avoided through the use of a neutral loading clause in the algorithm to prevent unwarranted yield surface shifting. Another factor that would have affected the results is the number of yield surfaces utilized. The quantitative effect of this parameter on multisurface plasticity models has not been investigated.

The fourth point listed above further explains the different behavior exhibited by the two algorithms. In Model B, the normal vector defined by the Garud rule for neutral loading cases can be substantially different from the Mróz normal vector. Referring to Fig. 10 (BEFORE), a yield surface is shown translated along the axial stress axis. At this point, the same exterior normal is defined by each model. In Fig. 10 (AFTER) the yield surfaces are schematically shown translated as prescribed by the two hardening rules. Notice that the two yield surface normals that define plastic straining for the next stress increment are considerably different. This could explain why the nearly neutral 0.0015 circular path causes Model B to exhibit more hardening than Model A. For the other paths (the triangle and right angle paths), where neutral loading occurs at varying degrees along the cycle, Model B predicts *less* hardening to occur. A considerable shift that occurs in the position of the stabilized response is predicted between the two approaches for the triangle input paths. However, it should be kept in mind that there are a number of differences between Models A and B, and the degree to which each influences the predicted response cannot be conclusively determined in this study.

Another factor that was observed to influence the stabilized response paths predicted by both models is the direction taken to initially reach the controlled strain input path. Note in Figs. 4*a* through 4*c* that the directions utilized in this study are given by dashed arrows. Taking a different direction can considerably shift the position of the predicted response. This is not surprising in light of the path-dependent nature of cyclic plasticity, but is not expounded upon further here, since experimental data is not available for comparison.

A final point should be noted pertaining to the ability of two-surface and multisurface models to predict "material memory." An advantage of a multisurface, kinematic model is its ability to "remember" a yield stress after a previous load increment caused strain hardening, as depicted in Fig. 11*a*. The technique used by the two-surface model to estimate a plastic mod-

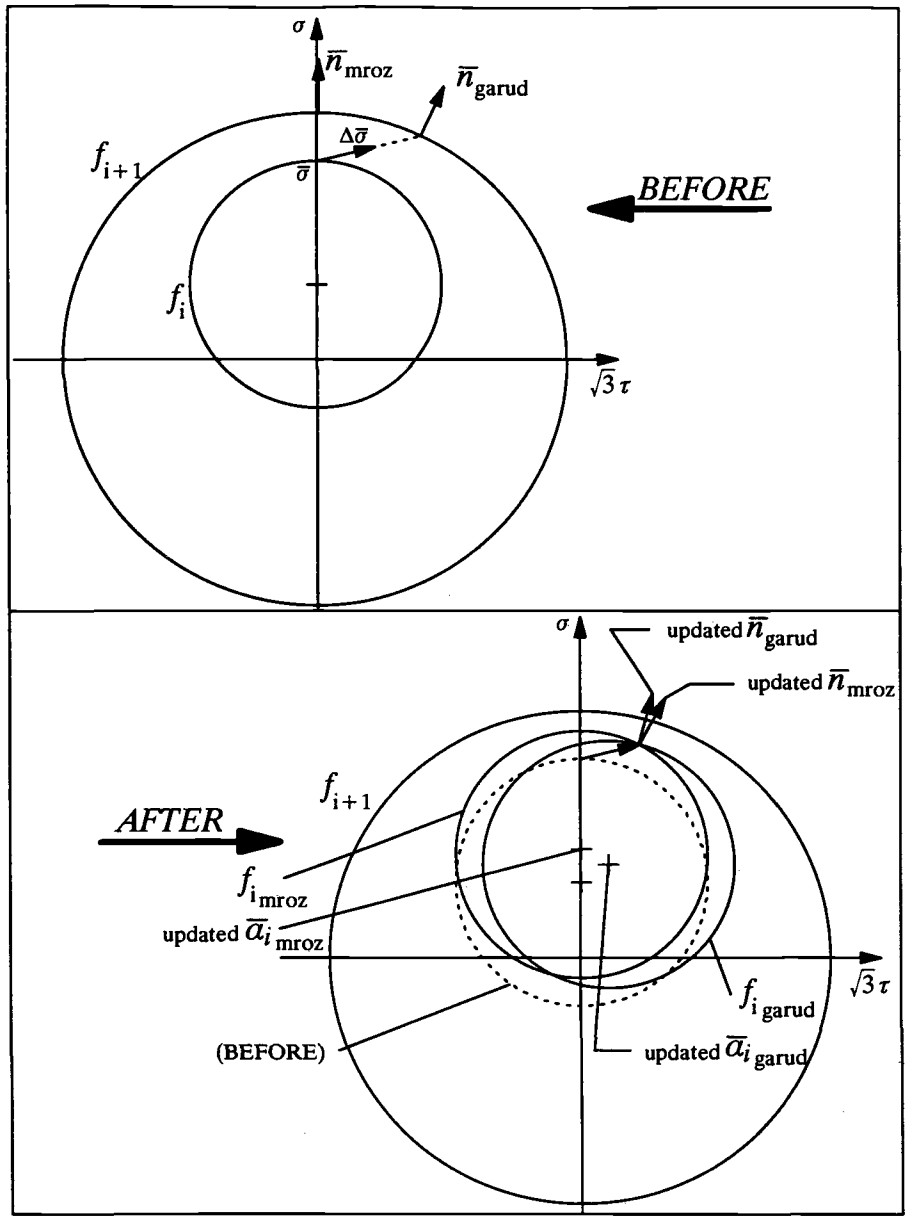

FIG. 10—*Demonstration of the difference in outward normals resulting from the Mróz and Garud hardening rules.*

ulus causes an underestimation of the reloading yield stress, as shown in Fig. 11*b*. Since the plastic modulus is taken to be a function of the distance from the current stress state to the limit surface, the fixed limit surface causes the underestimation to occur. However, for the strain paths investigated, this did not appear to adversely affect the peak and valley estimates from the two-surface model, as good correlation was observed with experimental data.

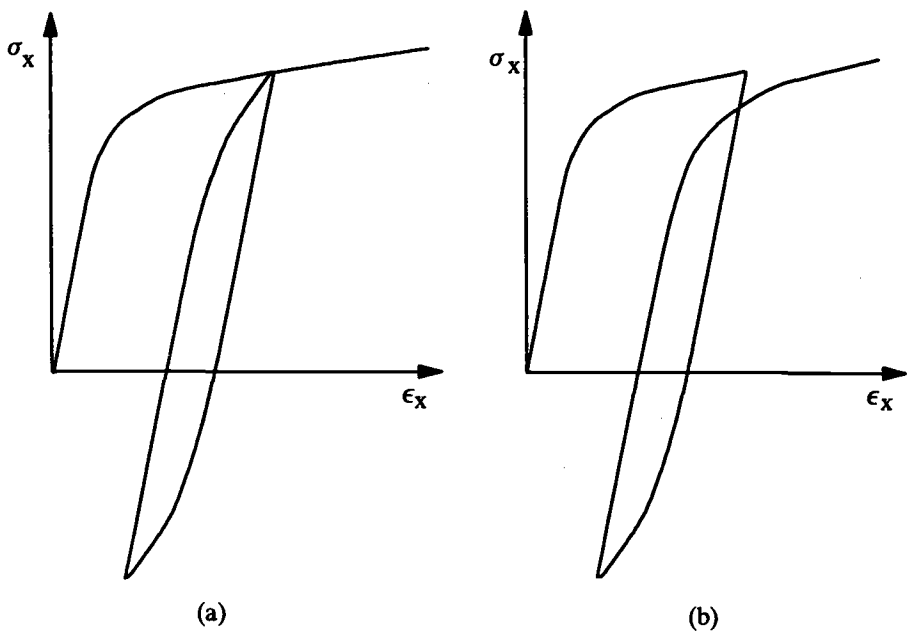

FIG. 11—*The material memory capability of* (a) *a multisurface, kinematic model and* (b) *the two-surface model.*

The effect of the "material memory" problem could be more influential for other input load histories.

The two models examined in this study represent solid foundations from which to launch more detailed investigations. A number of unresolved issues pertaining to the implementation of incremental plasticity theory have been identified. Future investigations should include more systematic studies on the effects of strain increment size and the number of multiple yield surfaces, the specification of yield surface translation, and the effect of a neutral loading clause.

Conclusions

1. Nonproportional stress responses predicted by Model A (a two-surface, kinematic algorithm utilizing a Mróz hardening rule and an elastic radial return clause for near neutral loading) more accurately agree with experimental results than do the predictions made by Model B (a multisurface, kinematic algorithm, utilizing the Garud hardening rule).

2. The degree to which the predicted responses of the two models differ cannot be attributed to any single difference between the two algorithms.

3. The importance of an adequately refined incremental step size was highlighted with regards to the detrimental effect of neutral loading on the implementation and stability of incremental plasticity algorithms.

4. The two-surface model avoids practical implementation problems regarding the necessity of small incremental inputs (and correspondingly large amounts of output information) through the use of a discretionary routine that automatically reduces input strain increment sizes when necessary.

5. A "neutral loading clause" (such as elastic stress-strain increment updating with radial

return) is recommended to avoid superfluous numerical behavior induced by undue yield surface shifting during near-neutral loading.

6. For the loading paths investigated, the "material memory" shortcoming of the two-surface model did not appear to diminish the ability of the model to estimate peak and valley quantities important to multiaxial fatigue damage analysis. Future investigations should include variable amplitude load histories.

7. This investigation has emphasized the need to conduct systematic studies to discern the effects of strain increment size, number of multiple yield surfaces, the specification of yield surface translation, and the effect and form of a neutral loading clause in evaluating generally applicable incremental plasticity algorithms.

References

[1] Brown, M. W. and Miller, K. J., "A Theory for Fatigue Failure under Multiaxial Stress-Strain Conditions," *Proceedings of the Institution of Mechanical Engineers,* Vol. 187, 1973, pp. 745–755.

[2] Lohr, R. D. and Ellison, E. G., "A Simple Theory for Low Cycle Multiaxial Fatigue," *Fatigue and Fracture of Engineering Materials and Structures,* Vol. 3, January 1980, pp. 1–17.

[3] Fuchs, H. O. and Stephens, R. I., *Metal Fatigue in Engineering,* John Wiley and Sons, New York, 1980, pp. 180–181.

[4] Zamrik, S. Y., "An Investigation of Strain Cycling Behavior of 7075-T6 Aluminum under Combined State of Strain," NASA CR-72843, Pennsylvania State University, University Park, PA, 1972.

[5] Smith, K. N., Watson, P., and Topper, T. H., "A Stress-Strain Function for the Fatigue of Metals," *Journal of Materials,* Vol. 5, No. 4, December 1970, pp. 767–778.

[6] Socie, D. F., "Multiaxial Fatigue Damage Models," *Journal of Engineering Materials and Technology,* American Society of Mechanical Engineers, Vol. 109, October 1987, pp. 293–298.

[7] Bannantine, J. A. and Socie, D. F., "Observations of Cracking Behavior in Tension and Torsion Low Cycle Fatigue," *Low Cycle Fatigue, ASTM STP 942,* Solomon, Halford, Kaisand, and Leis, Eds., American Society for Testing and Materials, Philadelphia, 1988, pp. 899–921.

[8] Fatemi, A. and Socie, D. F., "A Critical Plane Approach to Multiaxial Fatigue Damage Including Out-of-Phase Loading," *Fatigue and Fracture of Engineering Materials and Structures,* Vol. 11, No. 3, 1988, pp. 149–165.

[9] Jones, D. J. and Kurath, P., "Cyclic Fatigue Damage Characteristics Observed for Simple Loadings Extended to Multiaxial Life Prediction," NASA CR-182126, Lewis Research Center, June 1988.

[10] Garud, Y. S., "A New Approach to the Evaluation of Fatigue Under Multiaxial Loadings," *Transactions of the ASME, Journal of Engineering Materials and Technology,* Vol. 103, April 1981, pp. 118–125.

[11] Doong, S. H., "A Plasticity Theory of Metals Based on the Dislocation Substructure," Materials Engineering Report No. 148, University of Illinois at Urbana-Champaign, UILU-ENG89-3602, 1988.

[12] Drucker, D. C. and Palgen, L., "On Stress-Strain Relations Suitable for Cyclic and Other Loading," *Journal of Applied Mechanics,* Vol. 48, September 1981, pp. 479–485.

[13] Mróz, Z., "On the Description of Anisotropic Workhardening," *Journal of Mechanics Physics Solids,* Vol. 15, 1967, pp. 163–175.

[14] Dafalias, Y. F. and Popov, E. P., "A Model of Nonlinearly Hardening Materials for Complex Loading," *Acta Mechanica,* Vol. 21, 1975, pp. 173–192.

[15] Krieg, R. D., "A Practical Two-Surface Model for Transient Nonproportional Cyclic Plasticity," *Journal of Applied Mechanics,* September 1975, pp. 641–646.

[16] Lamba, H. S., "Nonproportional Cyclic Plasticity," Ph.D. dissertation, TAM Report No. 413, University of Illinois at Urbana-Champaign, 1976.

[17] McDowell, D. L., "A Two-Surface Model for Transient Nonproportional Cyclic Plasticity, Parts 1 and 2," *Journal of Applied Mechanics,* Vol. 52, June 1985, pp. 298–308.

[18] Subramanian, S., "Strain Path Dependence of Multiaxial Fatigue," M.S. thesis, Mechanical Engineering Department, University of Toledo, Toledo, OH, August 1989.

[19] Garud, Y. S., "Multiaxial Fatigue of Metals," Ph.D. dissertation, Stanford University, Mechanical Engineering Department, Stanford, CA, 1981.

[20] Prandtl, L., "Spannungsverteilung in Plastischen Doerpern," *Proceedings,* First International Congress on Applied Mechanics, Delft, Technische Boekhandel en Druckerij, J. Waltmann, Jr., 1925, pp. 43–54.

[21] Reuss, A., "Berueckichtigung Der Elastischen Formaenderungen in der Plastizitaetstheorie," *Zeitschrift für angewandte Mathematik and Mechanik,* Vol. 10, 1930, pp. 266–274.
[22] Drucker, D. C., "A More Fundamental Approach to Plastic Stress-Strain Relations," *Proceedings,* First U.S. National Congress of Applied Mechanics, American Society of Mechanical Engineers, New York, 1951, pp. 487–491.
[23] Bannantine, J. A., "A Variable Amplitude Multiaxial Fatigue Life Prediction Method," Ph.D. dissertation, Mechanical Engineering Department, The University of Illinois, Champaign, IL, 1989. (Also, Materials Engineering—Mechanical Behavior Report No. 151, UILU-ENG 89-3605, October 1989.)
[24] McDowell, D. L., "Evaluation of Intersection Conditions for Two-Surface Plasticity Theory," *International Journal of Plasticity,* Vol. 5, 1989, pp. 29–50.
[25] Tipton, S. M., "Fatigue Behavior in the Presence of a Notch," Ph.D. dissertation, Mechanical Engineering Department, Stanford University, Stanford, CA, 1985.
[26] Socie, D. F., Waill, L. A., and Dittmer, D. F., "Biaxial Fatigue of Inconel 718 Including Mean Stress Effects," *Multiaxial Fatigue, ASTM STP 853,* K. Miller and M. W. Brown, Eds., American Society for Testing and Materials, Philadelphia, 1985, pp. 463–481.
[27] Kurath, P., Downing, S. D., and Galliart, D. R., "Summary of Non-Hardened Notched Shaft Round Robin Program," *Multiaxial Fatigue, AE-14,* Society of Automotive Engineers, Warrendale, PA, 1989, pp. 13–31.
[28] Chu, C. C., "The Analysis of Multiaxial Cyclic Problems with an Anisotropic Hardening Model," *International Journal of Solid Structures,* Vol. 23, No. 5, 1987, pp. 569–579.
[29] Rees, "An Examination of the Neutral Loading Condition in Plasticity Theory," *Journal of Strain Analysis,* Vol. 23, No. 2, 1988, pp. 47–60.

DISCUSSION

Y. S. Garud[1] *(written discussion)*—The author(s) presented cyclic stress-strain response for a steel under five special strain paths in combined tension-torsion. The material response predictions were generated by two algorithms constructed and used independently by the two authors. The term *algorithm* refers to the computer code for numerical implementation of the plasticity theory; as such, it includes all assumptions of the theory, not just the hardening rule assumption, and also all the numerical approximations and logic needed for the computer code. Therefore, I will refer to these two algorithms by the letters A and B. Algorithm A uses a *multi-linear* (segmented) generalization of the uniaxial cyclic stress-strain curve while Algorithm B uses a *continuous* function for the generalization. Also, A incorporates Garud's hardening rule while B is based on the hardening rule of Mróz.

First, I would like to emphasize three aspects of Garud's hardening rule which appeared to be not well conveyed, if not misinterpreted: (1) the rule was developed to avoid the mathematical inconsistency in other rules (as explained previously[2]) *and not to enable large load step sizes in the solution procedure;* nor was it ever suggested by this discusser that the rule's ability to generally handle, in many cases, large steps be viewed as an advantage, let alone be implemented (and depended upon) in an algorithm. *Incremental* plasticity calculations must be treated in small enough steps to be generated internally within the code (based on the relative sizes of the yield surfaces and on the amount of deviation from the radial stress path); (2) it is not a requirement of the hardening rule that the equivalent stress-strain generalization (of the input uniaxial curve) be discretized in more than two linear segments; and (3) the hardening rule, which has nothing to do with the neutral loading, should not be applied to stress increments identified as causing no plastic strain.

[1] S. Levy Inc., 3425 S. Bascom Avenue, Campbell, CA 95008-7006.
[2] Garud, Y. S., "Prediction of Stress-Strain Response under General Multiaxial Loading," *Mechanical Testing for Deformation Model Development, ASTM STP 765,* R. W. Rohde and J. C. Swearengen, Eds., American Society for Testing and Materials, Philadelphia, 1982, pp. 223–238.

Second, very little is known (or shown) about the numerical approximations and the logic(s) followed independently in the two algorithms. However, it appears that Algorithm A did not address the condition of neutral loading (the usual way to handle this is to treat it elastically with radial return method *and* using small step size) and attempted to use large step size in the incremental solution. On the other hand, it is important to note that Algorithm B has a built-in (mathematical) requirement that the load increment *must* be sufficiently small (to avoid the case when updated stress cannot lie on the shifted yield surface, *no matter how much the shift is*).

Third, from the comparisons shown between the experimental stress-strain loops and the model predictions (based on the kinematic hardening) it seems that the difference may be attributable, at least in part, to the apparent increase in the elastic range (or additional hardening) not accounted for in the purely kinematic assumption. Also, the predictions are made for a material point response under uniform stress condition and material isotropy. Actual test data are obtained under some structural constraints and nonuniform stresses whose influence is not necessarily easy or obvious to discard.

For the above reasons, it is very difficult to judge and categorize the differences in predicted responses and the experimental observations on the basis of the hardening rules alone.

The maximum equivalent strain was limited to 0.15% in three of the five strain paths examined in this paper. What was the uniaxial cyclic stress-strain material data *below* 0.15% strain which they used to determine the model parameters needed for predicting the material response?

To appreciate the generality of their conclusions would the author(s) provide their views on how typical they consider the strain histories examined in this paper to be representative of engineering applications?

The only figure shown to illustrate (for the uniaxial loading case) the "material memory" shortcoming of the two-surface model also suggests that, if one were to impose cyclic strain with some fixed mean value, the final (stable) peak tensile stress and the resulting mean stress will actually be less than that predicted by the multi-surface model.

The conclusions and general applicability of this work must be examined carefully with the above considerations.

In the two-surface model (of Algorithm B) the definition of neutral loading changes when the yield surface and the limit surface (assumed to be fixed) are in contact (i.e., on the limit surface, plastic flow occurs only under tangential stress increment while, at the same time, the same stress increment on the yield surface would otherwise be treated as neutral). It is only an interesting observation upon which the author(s) may want to comment if it poses any conceptual and/or computational difficulties.

Finally, I would like to offer a possible physical explanation of why one should expect some instability in the solution of the nonlinear plasticity problem, independent of the hardening rule or the numerical difficulties. Suppose an initial loading in tension is applied to make the material yield; then the real material (as well as plasticity models) is known to show or exhibit a *fast* rate of stress relaxation when the loading is changed from tension to torsion (or from torsion to tension) *even when the strain in the initial direction of tension (or torsion) is held constant.* This relaxation is aided if, in addition to the change of load direction, there is applied strain reduction in the initial direction *At the same time* the material exhibits strain hardening when in the plastic state. Thus, there are two opposing tendencies which come into effect and, depending on the rate characteristics of the two, the actual behavior will show typical regions of transient, stable, quasi-stable, or unstable response—I think.

J. M. Tipton and J. A. Bannantine (authors' closure)—In order to avoid confusion, it should be clearly emphasized here that the Model A presented in the paper (which employs two-surface Mróz kinematic hardening) corresponds to Algorithm B in the above discussion. Simi-

larly, Model B in the paper (which employs multi-surface Garud kinematic hardening) corresponds to Algorithm A in the discussion above.

The numerical inconsistencies associated with the implementation of the Mróz hardening rule (and how they are avoided by the Garud modification) are discussed in detail in the paper. The authors agree that no one has ever advocated the ability of the Garud rule to generally handle larger numerical stress increments as "an advantage," but it can in fact do so. For nonproportional stress paths, there is always an incentive to utilize the smallest possible increment size to adhere to plasticity theory as closely as possible and avoid numerical difficulties associated with yield surface overlap. However, from a practical standpoint, smaller increment sizes increase run times and the quantity of output information, providing incentive to avoid the use on unnecessarily small step sizes. Balancing these two forces is critical to the implementation of incremental plasticity theory, and few studies exist in the open literature as to the optimization of increment size. The paper intended to make the point that, although the Garud rule can handle larger increment sizes, caution must be exercised. In general the discretionary routine used in Model A of this paper and described in Ref *23* could be considered a mechanism to avoid the standard, time-consuming convergence study needed to insure a valid solution. Further work on the discretionary routine is warranted to optimize its use for general applications.

When load increments are "neutral" or "near neutral," the Mróz rule is most susceptible to the numerical inconsistencies the Garud rule avoids. Since increment sizes are always finite, the "numerical robustness" of an algorithm employing the Mróz rule can be severely compromised without extremely small step sizes and/or a neutral loading provision (e.g., radial return with elastic update). However, the tendency for neutral loading increments to cause numerical difficulties to the Garud hardening rule is much less. Therefore, the paper intends to make the point that guidance is needed to prescribe a reasonable neutral loading clause and the conditions that invoke its use. Very few attempts have been made to address this problem.

The details of each code are fully available in Refs *23* and *25* of the paper. Model B did not address neutral loading, as just described.

The models were evaluated using stabilized experimental stress-strain data. No attempt is made to account for the extra hardening induced by cross-slip during nonproportional loading or material anisotropy in either model. Also, the authors are not aware of any studies on the influence of constraint imposed by specimen geometry (especially for thin-walled tubes) although that effect is believed to be negligible at the strain levels investigated.

It has been noted in the paper that several differences exist between Models A and B, and a more detailed study is needed to quantify the influence of components embedded in each.

The material properties at the strain levels investigated are described by uniaxial, cyclic stress-strain data, collected over the range of interest.

The authors do not believe that the engineering generality (or lack of it) of the strain paths has a significant influence on the conclusions drawn in the paper. The paths are intentionally severe in terms of nonproportionality and neutral loading, but no less severe than those endured by many engineering components.

The point of Fig. 11 was to emphasize points exactly like the one made in the discussion. Future work on two-surface models should address the "material memory" behavior. The conclusions are intended to highlight several unanswered questions pertaining to the implementation of incremental plasticity theory.

As pointed out in the paper, the limit surface is not encountered by the strain paths examined. Increments that attempt to extend beyond the limit surface are radially returned, and the yield surface is moved to satisfy consistency at the updated stress point. The authors do not believe that this poses any conceptual or numerical difficulties.

Yogendra S. Garud[1]

Cycle-Dependent Ratcheting Under Multiaxial Loads Including the Bauschinger Effect and Nonlinear Strain Hardening

REFERENCE: Garud, Y. S., **"Cycle-Dependent Ratcheting Under Multiaxial Loads Including the Bauschinger Effect and Nonlinear Strain Hardening,"** *Advances in Multiaxial Fatigue, ASTM STP 1191,* D. L. McDowell and R. Ellis, Eds., American Society for Testing and Materials, Philadelphia, 1993, pp. 298–309.

ABSTRACT: This paper presents a study of the phenomenon of cycle-dependent strain accumulation (ratcheting), especially under multiaxial steady and cyclic loads. The practical significance of ratcheting has become more apparent in recent years in dealing with the design/analysis of pressure-retaining components and structures which may be subjected to certain (reversed) thermal or seismic (dynamic) cyclic loads. A review of experimental observations on the fatigue and ratcheting response of such components suggests that the likely mode of failure (under the noted load combinations) is different from the plastic collapse (as assumed for design basis); this provides an opportunity to reduce the over-conservative safety margin requirements. Based on a brief survey of prior material test data and theoretical evaluations of the ratcheting under multiaxial stress conditions, it is concluded that a proper accounting of the material strain hardening and yield behavior (the Bauschinger effect) under multiaxial stresses is needed and can serve a useful purpose.

The nonlinear strain hardening and the Bauschinger effect are taken into account in this work by using the full implementation of incremental plasticity based on the generalized kinematic-type hardening proposed previously by the author. It is shown that, under certain combined stress conditions, the incremental plasticity predicts continued strain accumulation in each (half) cycle even for a kinematic-type hardening assumption. A number of characteristic observations on ratcheting under multiaxial loads are also predicted.

The case of triaxial steady stress with imposed cyclic strain is analyzed in detail; this is similar to typical loads on a pipe section. For such a case the theory predicts conditions of (local) wall thinning and circumferential growth (in the pipe section) that is limited mainly by the structural considerations. For Type 304 stainless steel and A333 Grade 6 carbon steel a graphical representation is developed showing allowable load combinations for various rates of strain accumulation. A simple relation is proposed between the (steady) primary stress and the (cyclic) secondary stress for a specified total ratchet strain as a criterion which is discussed with reference to the ASME Code. The extent of over-conservatism associated with the neglect of material strain hardening and with the (change in) mode of failure can be better judged by means of the results presented here. The paper is concluded with a discussion of related issues and the future direction.

KEY WORDS: cyclic strain accumulation, nonlinear strain hardening, rachet assessment diagrams, multiaxial stresses, carbon steel, stainless steel, ASME Code

Although the phenomenon of cycle-dependent (as opposed to *time* dependent) strain accumulation, especially under multiaxial combinations of steady and cyclic loads, has been known and well documented for many decades, its practical significance has become more apparent in recent years in at least three areas: (1) identification and evaluation of the *mode*

[1] Consultant, S. Levy Incorporated, 3425 S. Bascom Ave., Campbell, CA 95008.

of failure in pressure retaining components, particularly under infrequent *reversed* dynamic loads (such as due to a seismic event); (2) possible impact on *fatigue life* of the component undergoing strain accumulation; and (3) related safety margins and design/analysis within *Code procedures* [*1*].

For instance, the experimental work on pipes and piping components [*2–6*] demonstrates that the expected (typical) mode of failure is that of continued strain accumulation (ratcheting) or fatigue with ratcheting (as opposed to the plastic collapse). There are indications [*3,4*] that the fatigue life (or fatigue usage) may be adversely affected under some ratcheting conditions. Both these can have significant Code implications [*7,8*] since some of the basic premises are challenged; for example, in the treatment of seismic-type loads, opportunities exist to reduce the over-conservatism imposed by the (Code) assumption of a limit load (plastic collapse) type of failure.

Clearly, there exists the need to develop and improve upon methods of design/analysis to deal with the complex problems of combined static and cyclic multiaxial loads, including shakedown and strain accumulation phenomena. This need is further emphasized by a survey of prior experimental and theoretical works summarized in the next section; the survey also suggests the significance of, and the need to account for, the material strain hardening and yield behavior *(Bauschinger effect)* under multiaxial stresses in the evaluation of these phenomena.

This paper deals with a new theoretical evaluation of cycle-dependent ratcheting which explicitly accounts for the strain-hardening and the multiaxial Bauschinger effect through the use of a complete set of material constitutive relations in the form of an incremental plasticity with a generalized kinematic hardening. It is shown that, under combined states of stress, the incremental plasticity predicts *continued* strain accumulation in each (half) cycle even for a kinematic-type strain-hardening material. The case of triaxial *steady* stress with imposed *cyclic* strain is analyzed in detail; this is similar to typical loads on a pipe section. For such a case the theory predicts (local) wall thinning and circumferential growth (in the pipe section) which is limited mainly by *structural* considerations.

From results of the analysis (for Type 304 stainless steel and A333 Grade 6 carbon steel) a graphical representation, called the *ratchet assessment diagram (RAD)*, is developed showing load combinations for various rates of strain accumulation (on a *per cycle* basis). A simple relation is proposed (between stress allowables) for a specified total ratchet strain as a criterion, which is discussed in relation to the ASME Code considerations. Results under other combined multiaxial primary (steady) and secondary (cyclic) loads are also presented and discussed in relation to experimental observations.

Survey of Cycle-Dependent Ratcheting

Some of the recent work on cycle-dependent ratcheting (under multiaxial stresses) is briefly summarized here to illustrate significant observations; an exhaustive and critical review is beyond the scope of this paper. In an earlier work [*9*] it has been reported that *relatively* uniform *cumulative axial extensional deformation, up to about 20%, can be obtained before local instabilities disrupt the* uniform *strain accumulation* in the case of a hollow tube subjected to steady axial load with superimposed cyclic torsion. Yamanouchi et al. [*10*] have reported significant (progressive) diametral change of thin tube specimens (of Type 316 stainless steel) under steady pressure when cyclic axial strain is superimposed. Clément et al. [*11*] have recently reported that steady compressive—as opposed to tensile—axial loading when applied with cyclic torsion (on thin tubes of austenitic Type 316L steel and of annealed copper) resulted in nearly *uniform* progressive *shortening* of tubular specimens (before reaching instability in the buckling mode). Lebey and Roche [*12*] observed axial elongation of thin tubes (of

Type 304L stainless steel) under steady axial stress when cyclic torsion was applied. Likewise, a recent experimental work by Asada [*3*] on carbon steel tubes shows considerable (progressive) diametral growth from ratcheting under cyclic axial or torsional strain with a steady internal pressure. Also, Williams [*13*] reported *tenfold* strain accumulation in the circumferential direction (as compared to the axial strain accumulation) in pressurized specimens (of A333 carbon steel and A358 austenitic steel) when cyclic bending was superimposed.

Similar observations have been reported by others [*2,4,14,15*]. Important common factors suggested by these results are: (1) strains continue to accumulate on per cycle basis, (2) the accumulation can be limited (but not necessarily eliminated) by material hardening and mostly by structural constraints, and (3) significant changes in the yield response under multiaxial (nonradial) changes in the stress state following some prior yielding under a different stress state (i.e., the Bauschinger effect under multiaxial stresses).

Much of the early theoretical work is known to be restricted to idealized *nonworkhardening* [*9,16*] (or simple isotropic hardening) material behavior and simplified loads (e.g., uniaxial simplification or two-bar simulations for thermal cycling with steady multiaxial stress conditions) [*9,17*]. These simplifications introduce gross deviations in predicted ratcheting behavior compared to the observations; indeed, many investigators [*9,11,12,14,15*] have noted the failure of classical isotropic or kinematic hardening assumptions in reproducing the above significant observations under multiaxial stresses. In the following sections it is shown that a generalized kinematic hardening-based incremental plasticity approach can reproduce these observations and can make use of the inherent strain-hardening characteristics.

Plasticity Theory and Its Implementation

The type of structural and material deformation phenomena addressed under this investigation is assumed to be such that only *time-independent* response will be of dominant concern (notwithstanding the fact that it takes a finite time to apply any loading and to observe the response). That is, *time-dependent* phenomena, such as creep and stress relaxation, are excluded from consideration because either their contribution (to the total deformation) is relatively small or their impact can be assessed independently. Therefore, a suitable formulation of time-independent plasticity is selected.

The main focus of this work was to be able to investigate *any type of multiaxiality and any combination of static plus cyclic multiaxial components* of loading; as such, a full implementation of the plasticity theory was needed—however, details of all the *transient* (cycle-to-cycle changing) material properties need not be *explicitly* accounted for. Also, as noted above, it was considered important that the *strain-hardening* characteristics and the *Bauschinger effect* be accounted for (under the complex loads of interest). These two taken together significantly influence the material hardening (or softening) response under general multiaxial loading, including, especially, the change in yield characteristics in the direction of a shear component, for instance, as a result of prior yielding in the direction of a normal component (of the stress tensor).

The above requirements were sufficiently met by the formulation proposed earlier by the author [*18*] and shown to be promising for complex multiaxial loads [*18–20*]. These earlier applications dealt with the fully reversed type of loading, although, in principle, the (plasticity) formulation is also applicable in the presence of nonzero mean loads as well. Therefore, the same theory is used in this work.

Very briefly, the formulation utilizes the framework of classical (incremental) plasticity theory with three main components:

1. *An initial yield condition (as a multiaxial generalization of the elastic limit) that determines whether or not plastic strains will be induced during an increment of loading (start-*

ing from a stress-free state). The material is assumed to follow the elastic stress-strain relations prior to exceeding this condition. Here, von Mises yield criterion is used.

2. *A flow rule that relates the increment of plastic strain to the increment of stress.* For metals, the most commonly used rule is the *normality condition* (or the *associative flow rule*) according to which the (tensor) components of plastic strain *increment* are proportional to the corresponding (tensor) components of the *unit normal* to the yield surface at the current state of stress. The constant of proportionality is, in general, a nonnegative function of the stress, stress-increment, *and* the loading history. The normality condition is used in this work with the proportionality constant being defined by the concept of *field of plastic moduli* [*21*], which is essentially a multilinear generalization of the uniaxial stress-strain curve.
3. *A hardening rule that specifies changes in the yield condition and in the field of plastic moduli as a result of the prior plastic deformation.* Many such rules have been proposed over the years, and this area of research can at best be characterized as *very dynamic;* selection and justification of a particular rule is beyond the scope and need of this paper. On the basis of familiarity and useful predictive capabilities of earlier work [*18*, *20*], the hardening rule as described in these papers is adopted here. It differs from the previous commonly known rules (e.g., Prager-Ziegler and Mróz) mainly in that the direction of (kinematic) translation of a yield surface is made to depend on the direction (in the pseudo-space of stress tensor) of the stress increment itself, in addition to being dependent on the current state of stress and the loading history. Its implementation is such that the *consistency condition* is correctly satisfied for proportional as well as any *nonproportional* stressing [*20*, *22*].

In this work it is assumed that only the generalized (multilinear) *kinematic* hardening is operative. Also, the usual assumptions of incompressibility of plastic flow and the initial isotropy of material properties are maintained. The basic governing relations of incremental plasticity, including the generalized kinematic hardening rule, were documented in prior publications [*18–20*].

Based on the above formulation, a computer code named IPCRES (for Incremental Plasticity Calculations and Ratcheting Evaluation System) was developed [*23*]. It performs the needed computations by following a specified loading (of steady stresses plus cyclic strains) in small increments simulating the *material point* response. The code development and its implementation were carried out using an IBM-PC compatible microcomputer.

Material Properties Data

The above plasticity formulation requires two elastic constants (Young's modulus and Poisson's ratio) and a number of pairs of stress-strain values (e.g., from uniaxial cyclic strain tests) so as to fit a multilinear curve defining the (field of) plastic moduli. In this work two materials were investigated: Type 304 stainless steel and A333 Grade 6 carbon steel. For each material two idealizations were employed for the stress-strain curve (as input to the IPCRES code): (1) a multilinear fit to the *actual* uniaxial cyclic stress-strain tests data [*13*], and (2) a trilinear fit based on the Code minimum values of yield and ultimate strengths [*1*]. These idealizations are shown in Fig. 1. This selection (of the basic input parameters) allows us to compare or assess, in a limited way, the dependence of ratcheting on: (1) material properties, as examined here for the two materials, and (2) the flow stress curve variability, for a given material, within the range of a typical material curve and the curve based on the Code minimum properties. Note that the S_m value is same (137.9 MPa or 20 ksi) for both materials, where S_m is the Code *design stress intensity value* [*1*], a convenient reference value.

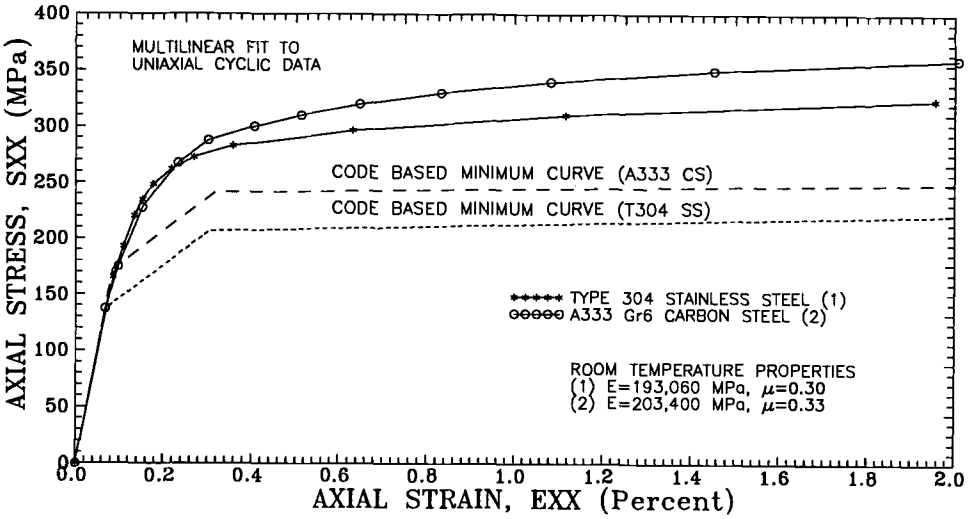

FIG. 1—*Multilinear approximations to uniaxial cyclic stress-strain data and to the Code-based minimum properties for a stainless steel and a carbon steel.*

Results and Discussion

The primary objective of this paper is to present the results of theoretical analysis (for ratcheting under multiaxial primary plus secondary type loads), which takes into account the material strain hardening and the Bauschinger effects, and to discuss these in relation to simplified Code evaluations; also, it is of interest to compare these results with those of the earlier analysis based on the deformation theory of plasticity, which does not account for these effects. These results and discussion are presented at the end of this section after comparing the IPCRES predictions of ratcheting response with the experimental observations under complex multiaxial loading conditions.

Steady Axial Load Plus Cyclic Torsion

Continued cyclic axial strain accumulation has been observed [*9,11,12*] on metal tubes subjected to steady axial load with cyclic torsional strain. This case of combined loading is very complex to analyze because the principal stress directions are not fixed. IPCRES predictions for the ten-cycle ratcheted strains for three values of steady axial stress are shown in Fig. 2 using the input uniaxial stress-strain characterization for Type 304 stainless steel as given in Fig. 1 (for the actual material curve). In this case, the secondary stress amplitude is equal to the modulus of elasticity in shear, G, times the (tensorial) torsional strain amplitude. These predictions are compared with the experimental data of Lebey and Roche [*12*] on thin tubes of Type 304L stainless steel; note that the uniaxial stress-strain properties for their specific material were not available to the author. However, the 0.2% offset yield strength for their material was given as 244 MPa (versus 282 MPa for the material used here in obtaining the predictions); therefore, only the steady axial stress values were normalized by the respective yield strengths in comparing the IPCRES predictions with the experimental curves also shown in Fig. 2 for the three steady axial stress ratios.

This comparison shows good qualitative agreement between the predictions and experimental observations. Although the difference can be attributed in part to likely differences in

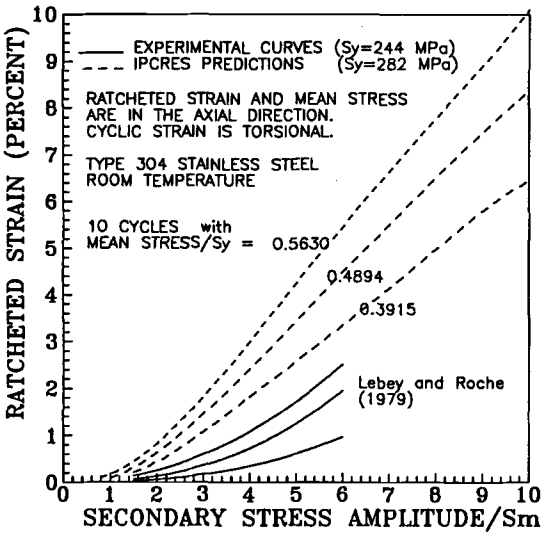

FIG. 2—*IPCRES predictions for material ratcheting response under steady axial stress plus cyclic torsional strains and comparison with experimental observations on tube specimens.*

the elastic and strain hardening properties of the actual test material and that used in the analysis, the overprediction of ratcheted strain is to be expected on at least two accounts: (1) the analysis is done for totally uniform states of stress and strain while the test specimen is subject to stress gradients, despite a uniform gage section, structural constraints, and nonuniform strains; and (2) the test material is likely to show continued isotropic hardening not fully accounted in the analysis.

Steady Internal Pressure Plus Cyclic Torsion

Figure 3 illustrates IPCRES results for the case of steady internal pressure stress and cyclic torsional strain; the continued growth in the hoop direction is seen to far exceed that in the axial direction as has been observed [*3*]. For a tube specimen of carbon steel (0.2% offset yield of 334 MPa) subjected to internal pressure (giving the primary hoop stress to yield stress ratio of 0.3265) and the (engineering) shear strain amplitude of 1.1%, the ratcheted hoop strain of about 1.5% was observed in the first ten cycles [*3*]. The corresponding IPCRES prediction (using the carbon steel input properties shown in Fig. 1, again, since the material specific property data for the test material were not available) shows the accumulated strain to be 5%. The above comments regarding the overprediction apply here, too. Indeed, the same report [*3*] shows that the actual shear stress amplitude goes from about 152 MPa in the first cycle to 192 MPa in the tenth cycle (to 238 MPa at the end of test), suggesting the continued isotropic hardening; the IPCRES calculation yields the fixed amplitude of 146 MPa.

Steady Internal Pressure Plus Cyclic Axial Strain

Continued cyclic hoop strain accumulation has also been observed in the case of tubes subjected to steady internal pressure and cyclic axial strains for Type 316 stainless steel [*10*] and for a carbon steel [*3*] at room temperature. Similar to the above analysis of other load com-

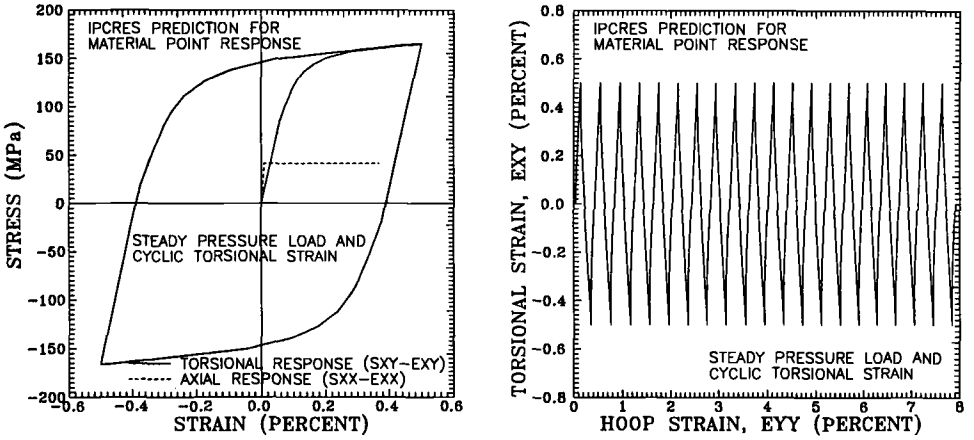

FIG. 3—*Stress-strain-ratcheting response predicted by IPCRES for the case of steady internal pressure (hoop stress = 0.6* S_m*) with superimposed cyclic torsion (± 1% engineering shear strain).*

binations, the IPCRES predictions for the material point response for this case of combined loading are also in qualitative agreement with these data.

Two other related points of interest are: (1) for equivalent loading, the axial strain cycling produced more ratcheting, 0.547%, than the torsional cycling, 0.389% (during 20th cycle). This is qualitatively in agreement with the earlier reported experimental observation [*14*] for which the authors have already offered the suggestion that *in some situations the sustained stresses may share common slip planes with the cyclic stresses and in others they may not;* (2) when only hoop stress is used, the IPCRES predictions of strain accumulation were *less* than if *all* stress components were present in the case of superimposed axial cycling; however, the opposite was found with torsional cycling (at least for Fig. 3 specifics).

From the above analysis of experimental data under multiaxial ratcheting it may be concluded that, in agreement with reported observations and unlike the earlier implementations of kinematic hardening [*14,21*], the IPCRES results suggest the continued accumulation of strain, at least for a uniform stress condition (as evaluated here for a material point response excluding any structural constraint or stress gradient effects). Although the agreement is qualitative, thus leaving room for further analysis and possible improvements for better accuracy, the predicted strains are consistently overestimated, thus providing some safety margin useful for simplified design analysis and Code calculations for combined multiaxial loads.

Ratchet Assessment Diagrams (RAD)

The case of steady triaxial stress state (simulating an internally pressurized straight pipe section) with superimposed cyclic axial strains (simulating the elastically calculated large *secondary* loads) is examined in detail. Here, the *primary* stress refers to the steady stress in the hoop direction; the secondary stress is equal to the (axial) strain amplitude multiplied by the modulus of elasticity. For each of the four material idealizations (Fig. 1), about 400 combinations of the primary and the secondary stresses were used to predict the material response (using IPCRES); each load case was run for 20 cycles of triangular-shaped strain wave. Results of these simulations were analyzed and are presented in the form of *ratchet assessment diagram* or RAD (analogous to the *Bree* diagram) as shown in Figs. 4 and 5; in these diagrams the (percent) strain value (as a contour label) corresponds to the total (hoop) strain at the end of tenth

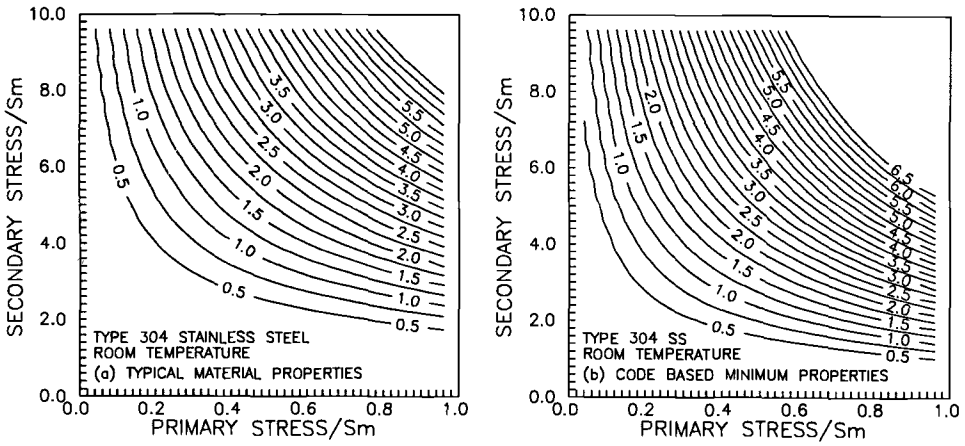

FIG. 4—*IPCRES results for the ratchet assessment diagrams showing lines of constant accumulated percent strain (ten cycles) for Type 304 stainless steel with typical and Code-based minimum properties.*

cycle. The iso-strain lines show the corresponding allowable combinations of the primary and secondary stress levels. As might be expected, due to the lower yield (flow) stress, the allowables based on the Code minimum properties are less than those for the typical material. The predicted *material* response for more than ten cycles is such that the rate of strain accumulation (on a *per cycle* basis) is constant; therefore, the same diagrams also represent very nearly the corresponding rates of strain accumulation.

Code Considerations

A few comments are offered in the following, with only a limited discussion, to interpret the above results from the viewpoint of Code considerations. Notwithstanding the assumption of time-independent behavior, the above results are likely to be conservative since, as noted ear-

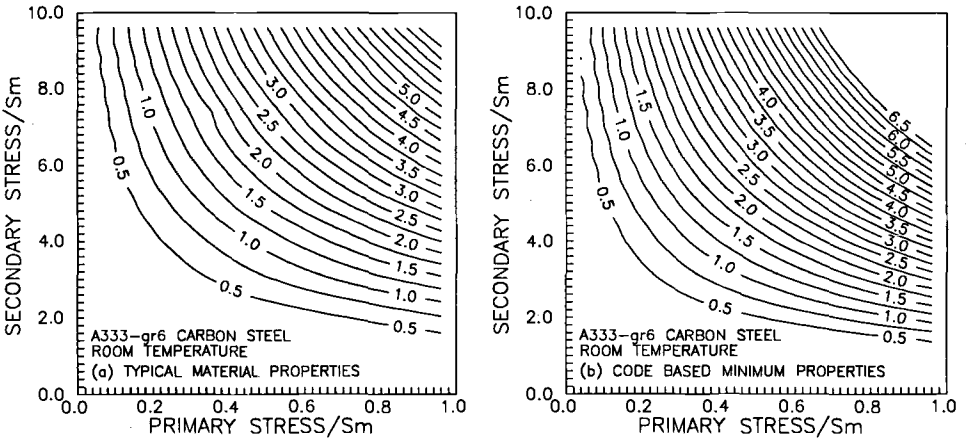

FIG. 5—*IPCRES results for the ratchet assessment diagrams showing lines of constant accumulated percent strain (ten cycles) for A333 Grade 6 carbon steel with typical and Code-based minimum properties.*

lier: (1) the possible (additional or transient) *isotropic hardening*, excluded from the formulation, is most likely to reduce the material strain accumulation; and (2) *structural* aspects of real applications (involving stress gradients and constraint conditions) are also likely to resist the uniform strain accumulation.

In general, for large allowable cumulative strains (above 2%), much larger values of *secondary* stress (Q) can be traded with smaller values of the *primary* stress (P) without exceeding the allowable total strain in a specified number of cycles. Thus, a simple (linear) criterion for limiting the total ratcheted strain can be expressed as follows

$$P + F \cdot Q \leq M \cdot S_m$$

where $F(\leq 1)$ and $M(> 1)$ are constant multiples, and $P < S_m$.

For example, from the ratchet diagram for Type 304 steel based on the Code minimum properties, for limiting total strain to 5% (maximum) in ten (or more) cycles the following three *linear*[2] relations between P and Q are suggested by the IPCRES results

$$P + (\tfrac{1}{3}) \cdot Q = 1.5 \times S_m \tag{1}$$

$$P + (\tfrac{1}{4}) \cdot Q = 2.0 \times S_m \tag{2}$$

$$P + Q = 5.0 \times S_m \tag{3}$$

(To use the first two relations one has to identify P and Q as separate quantities.) That is, if strain accumulation is the critical mode of failure, then the corresponding allowable stresses are larger than those for the plastic collapse ($P + Q \leq 3S_m$).

Comparison with Other Analysis

Edmunds and Beer [*16*] explored some theoretical aspects of *incremental collapse* in pressure vessels with simplifying assumptions of the *deformation theory* of plasticity, elastic-perfectly plastic material, and zero axial and radial steady stresses. Interestingly, for the case of internal pressure and axial cyclic straining, their results are qualitatively not too different from this study; however, there are differences of details. Both the studies suggest *continued* strain accumulation, even in presence of the generalized kinematic hardening as modeled in IPCRES, whenever the *elastic limit* is exceeded during any part of the multiaxial cyclic loading.

Figure 6 illustrates some points of comparison for the case of primary (hoop) stress equal to S_m and ten cycles. Figure 6*a* shows that the Edmunds and Beer analysis is sensitive to the choice of elastic stress value needed for their ratcheting evaluation, and that an arbitrary choice (here, flow stress equals average of the yield and ultimate strengths) can underpredict the strain accumulation (compared to IPCRES). At the very low stress levels, even the choice of 0.2% yield stress can underpredict the strains. Figure 6*b* compares the predictions of allowable stress combinations for 5% strain accumulation in ten cycles. Since IPCRES takes into account the (nonlinear) material strain hardening, the IPCRES allowables are higher than the corresponding Edmunds-Beer prediction based on σ_y = *elastic limit* (not shown) or on the 0.2% yield stress (as shown in Fig. 6*b*).

[2] Perhaps a nonlinear relation involving the product of primary and secondary stress components may be more satisfactory and can be easily deduced from these plots.

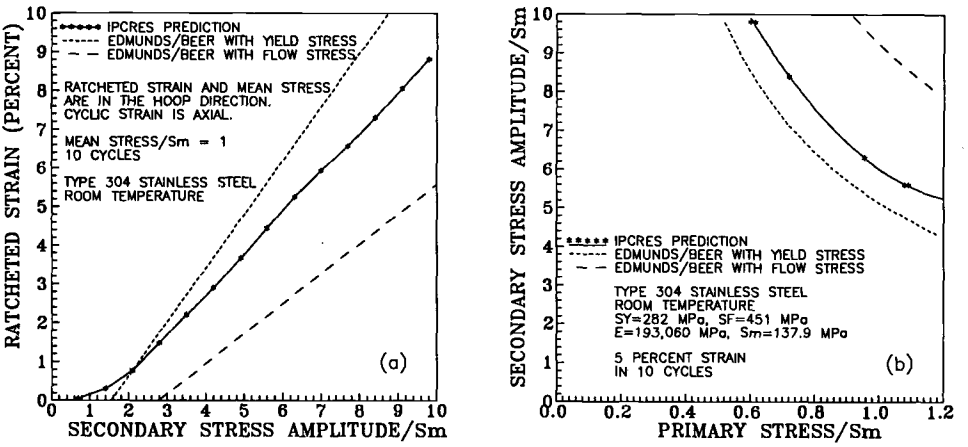

FIG. 6—*Comparison of IPCRES results with the analysis of Edmunds and Beer:* (a) *ratcheted strain at the end of tenth cycle as a function of the secondary stress amplitude (for steady hoop stress equal to* S_m*), and* (b) *allowable stress combinations for 5% strain accumulation in ten cycles.*

Conclusions and Future Work

Results of a theoretical exploration of cycle-dependent material ratcheting response under multiaxial steady and cyclic loads (similar to those anticipated in pressure retaining components) were presented. The theory used was an implementation of the incremental plasticity based on the author's model limited to the kinematic-type hardening [*18–20*]. This allowed for the inclusion of strain hardening and Bauschinger effects and the complete set of multiaxial state of stress in estimating the ratcheting.

The relatively large and uniform strain accumulation in the circumferential direction, as observed by many, for a tube (or a thin pipe) under internal pressure and cyclic axial or torsional strain, was predicted by the model. Also, progressive elongation (or shortening) in the axial direction, as observed for a tube under steady axial tension (or compression) and cyclic torsion, was predicted. For a few cases examined, the IPCRES results appear to confirm the effect of *directionality* of steady stresses relative to the direction of cyclic straining (for equivalent load intensities) in determining the strain accumulation.

Compared to the simplified analysis based on perfectly plastic response, it is shown that the use of strain-hardening characteristics reduces the over-conservatism related to strain accumulation criteria. The IPCRES results were presented in the form of ratchet assessment diagrams for two typical steels and were also expressed in terms of simple linear relations for allowable stresses which may prove to be useful estimates; in particular, since only a *homogeneous state of stress* was considered in these results, the *structural* considerations of stress gradients and constraints are likely to provide enough additional margins. For better utilization of the formulation and more accurate comparison with component/specimen tests data, it is preferable that the theory be incorporated in the framework of a finite element code. Preliminary work in this direction [*23*] has shown some encouraging results.

The main focus of this work was to investigate the *time independent* material response to *multiaxial* load combinations likely to cause *cycle dependent* strain accumulation; as such, several time-dependent (visco-plasticity) phenomena were not included: stress relaxation [*24*], creep [*25*], and strain-aging [*26*]. Significance of these phenomena, as observed for certain experimental loads and material conditions, needs further critical examination, especially

in relation to the *type, intensities, and rates* of loads and materials employed in service applications. The dynamic/seismic loads with a short duration of application may not allow enough time for significant impact. For other applications, the *lower bound* response predictions based on the use of Code minimum stress-strain data may be considered to reflect some margin against additional strain accumulation from such phenomena; however, this aspect needs further evaluation.

Acknowledgments

This work was sponsored by the Electric Power Research Institute (EPRI) of Palo Alto, California. The author wishes to thank S. W. Tagart, Jr. of EPRI for many useful interactions and active support of this work.

References

[1] ASME, *Boiler and Pressure Vessel Code, Section 3, Division 1,* American Society of Mechanical Engineers, New York, 1980.

[2] Kitamura, K. et al., "Study of Damage of Pressurized Pipes due to Vibration with Progressive Deformation," *IHI Engineering Review,* Vol. 14, No. 1, January 1981, pp. 9–16.

[3] Asada, Y., "Failure Criterion on Low-Cycle Fatigue with Excessive Progressive Deformation," Department of Mechanical Engineering, The University of Tokyo, Tokyo, Japan, 1989.

[4] Hara, F. and Shibata, H., "Ratcheting Fatigue in Full-Scale Piping Elements," *Transactions of the 6th SMiRT,* Paper No. K15/3, Paris, France, 17–21 Aug. 1981, North Holland Publishing Co., Amsterdam.

[5] Beaney, E. M., "Failure of Pipework Subjected to Seismic Loading," CEGB Report, Central Electricity Generating Board, BNL, Berkley, United Kingdom, 1989.

[6] English, W., Rangnath, S., et al., "Piping and Fitting Dynamic Reliability Program," EPRI Contract No. 1543-15, General Electric Co., San Jose, CA, 1986–1989.

[7] Guzy, D., "Piping Design Criteria and Research: Current NRC Activities and Dynamic Design," *Nuclear Engineering and Design,* Vol. 107, 1988, pp. 161–167.

[8] Tagart, S. W., Jr. and Ranganath, S., "Proposed Dynamic Stress Criteria for Piping," PVP-Vol. 237-1, ASME PVP92 Conference, New Orleans, June 1992; ASME, New York.

[9] Burgreen, D., "Review of Thermal Ratcheting," *Fatigue at Elevated Temperatures, ASTM STP 520,* American Society for Testing and Materials, Philadelphia, PA, 1973, pp. 535–551.

[10] Yamanouchi, H., Kino, H., and Nakano, S., "Ratchetting of Thin Tube Under Cyclic Axial Strain and Internal Pressure," *Proceedings,* Second International Conference on Mechanical Behavior of Materials, The American Society of Metals, Metals Park, OH, 1976, pp. 53–57.

[11] Clément, G., Acker, D., and Lebey, J., "A Practical Rule for Progressive Buckling," *Nuclear Engineering and Design,* Vol. 111, No. 2, 1989, pp. 209–216.

[12] Lebey, J. and Roche, R., "Tests on Mechanical Behavior of 304L Stainless Steel Under Constant Stress Associated with Cyclic Strain," *Fatigue of Engineering Materials and Structures,* Vol. 1, 1979, pp. 307–318.

[13] Williams, R. A., "TASK 4: Specimen Fatigue-Ratchetting Tests," draft for the final report under EPRI Contract RP 1543-15, transmittal from S. W. Tagart, Jr. of EPRI, August 1988.

[14] Hancell, P. J. and Harvey, S. J., "The Use of Kinematic Hardening Models in Multi-axial Cyclic Plasticity," *Fatigue of Engineering Materials and Structures,* Vol. 1, 1979, pp. 271–279.

[15] Harvey, S. J. et al., "Anisotropic Yield Surfaces in Cyclic Plasticity," *Fatigue of Engineering Materials and Structures,* Vol. 6, No. 1, 1983, pp. 89–99.

[16] Edmunds, H. G. and Beer, F. J., "Notes on Incremental Collapse in Pressure Vessels," *Journal of Mechanical Engineering Science,* Vol. 3, No. 3, 1961, pp. 187–199.

[17] Miller, D. R., "Thermal-Stress Ratchet Mechanism in Pressure Vessels," *Journal of Basic Engineering, Transactions of the ASME,* Vol. 81, June 1959, pp. 190–196.

[18] Garud, Y. S., "A New Approach to the Evaluation of Fatigue Under Multi-axial Loadings," *Methods for Predicting Material Life in Fatigue,* American Society of Mechanical Engineers, New York, 1979, pp. 247–263.

[19] Garud, Y. S., "A New Approach to the Evaluation of Fatigue Under Multiaxial Loadings," *Journal*

of Engineering Materials and Technology, Transactions of the ASME, Vol. 103, No. 4, 1981, pp. 118–125.

[*20*] Garud, Y. S., "Prediction of Stress-Strain Response under General Multiaxial Loading," *Mechanical Testing for Deformation Model Development, ASTM STP 765,* American Society for Testing and Materials, Philadelphia, 1982, pp. 223–238.

[*21*] Mróz, Z., "An Attempt to Describe the Behavior of Metals Under Cyclic Loads Using a More General Workhardening Model," *Acta Mechanica,* Vol. 7, No. 2–3, 1969, pp. 199–212.

[*22*] Nowack, H. et al., "Some Contributions to the Further Development of Low Cycle Fatigue Life Analysis Concepts for Notched Components under Variable Amplitude Loading," *Low-Cycle Fatigue, ASTM STP 942,* American Society for Testing and Materials, Philadelphia, PA, 1988, pp. 987–1006.

[*23*] Garud, Y. S., letter reports on EPRI Project No. RP2689-4 to S. W. Tagart, Jr., 25 Feb. 1989, 3 Nov. 1989, 12 Jan. 1990, 5 Feb. 1990, and 18 Dec. 1990.

[*24*] Pellissier-Tanon, A., et al., "Evaluation of the Resistance of Type 316 Stainless Steel Against Progressive Deformation," *Low-Cycle Fatigue and Life Prediction, ASTM STP 770,* American Society for Testing and Materials, Philadelphia, PA, 1982, pp. 69–80.

[*25*] Chaboche, J. L. and Nouailhas, D., "A Unified Constitutive Model for Cyclic Viscoplasticity and Its Applications to Various Stainless Steels," *Journal of Engineering Materials and Technology, Transactions of the ASME,* American Society of Mechanical Engineers, New York, Vol. 111, No. 4, 1989, pp. 424–430.

[*26*] Ruggles, M. B. and Krempl, E., "The Influence of Test Temperature on the Ratchetting Behavior of Type 304 Stainless Steel," *Journal of Engineering Materials and Technology, Transactions of the ASME,* Vol. 111, No. 4, 1989, pp. 378–383.

Multiaxial Micro/Macro Crack Growth Studies

Takashi Ogata,[1] *Akito Nitta,*[1] *and Joseph J. Blass*[2]

Propagation Behavior of Small Cracks in 304 Stainless Steel Under Biaxial Low-Cycle Fatigue at Elevated Temperature

REFERENCE: Ogata, T., Nitta, A., and Blass, J. J., **"Propagation Behavior of Small Cracks in 304 Stainless Steel Under Biaxial Low-Cycle Fatigue at Elevated Temperature,"** *Advances in Multiaxial Fatigue, ASTM STP 1191,* D. L. McDowell and R. Ellis, Eds., American Society for Testing and Materials, Philadelphia, 1993, pp. 313–325.

ABSTRACT: To investigate the initiation and propagation behavior of small cracks and the relationship between crack propagation and fatigue life, strain-controlled in-phase and 90° out-of-phase axial-torsional fatigue tests were conducted at 550°C, using tubular specimens of 304 stainless steel with and without surface notches. Each test was interrupted at frequent intervals to make a film replica of the outer surface of the specimen for examination with an optical microscope. Most of the fatigue life was spent in the propagation of small cracks less than 2 mm long. Regardless of loading conditions, the crack propagation rate correlated well with the equivalent shear strain range defined as a function of shear strain range and normal strain range on the plane of maximum shear strain range. The biaxial low-cycle fatigue life could be estimated from the relationship between the crack propagation rate and the equivalent shear strain range.

KEY WORDS: 304 stainless steel, biaxial low-cycle fatigue, high temperature, crack initiation, crack propagation, fatigue life prediction

Structural components are usually subjected in service to multiaxial low-cycle fatigue in regions of stress concentration. Particularly in high-temperature power-plant components, where mechanical and thermal stresses are superimposed, loading conditions are often nonproportional. Although life predictions of components under multiaxial stress conditions are necessary for design or remaining-life assessments, an appropriate fatigue-life assessment method has not been established because limited amounts of data have been obtained due to the complexity of the test techniques and equipment.

To investigate low-cycle fatigue mechanisms and life characteristics of 304 stainless steel, widely used as a structural material, under biaxial loading conditions, axial-torsional fatigue tests of tubular specimens have been conducted under proportional and nonproportional loading conditions at high temperatures [*1–3*]. From observations of macrocrack-growth directions and failure surfaces, failure modes were found to be distinctly separated into either Mode I or Mode II cracking under proportional loading, whereas mixed-mode cracking was observed under nonproportional loading. As a result, by taking the failure mechanism into account, a new biaxial fatigue criterion was proposed based on modification of the Γ-plane of Brown and Miller [*4*]. In addition, surface-crack observations during a limited number of fatigue tests indicated that the initiation of small cracks had taken place at an early stage in the fatigue life [*2*].

[1] Central Research Institute of Electric Power Industry, Tokyo, Japan.
[2] Oak Ridge National Laboratory, Oak Ridge, TN 37831-8051.

Since it has also been reported that most of the low-cycle fatigue life was spent in the propagation of small cracks under uniaxial fatigue conditions [*5*], microcrack propagation under biaxial low-cycle fatigue should be studied to understand the crack-propagation behavior and to assess the applicability of the biaxial fatigue-life criterion. Most of the crack-propagation studies under biaxial stress fields have been conducted using cruciform specimens with through-wall center notches to investigate the effect of stress biaxiality on macrocrack propagation under Mode I loading conditions [*6–8*]. The propagation behavior of small surface cracks has been investigated by Socie et al. using alloy 718 and 1045 steel at room temperature [*9*]. However, fatigue-crack initiation and propagation behaviors under proportional and nonproportional loading conditions at high temperatures have not been investigated before.

In this study, crack initiation and propagation were observed during biaxial low-cycle fatigue tests at high temperature by interrupting each test at frequent intervals and making a film replica of the specimen surface for examination with an optical microscope. The propagation behavior of small cracks and the relationship between the crack-propagation law and the fatigue-life criterion were investigated.

Experimental Procedure

As in previous biaxial low-cycle fatigue tests [*1–3*], the material used in this study was 304 stainless steel, solution treated for 10 min at 1050°C and water quenched. The chemical composition (wt%) was 0.05 C, 0.041 N, 0.47 Si, 0.83 Mn, 0.03 P, 0.009 S, 9.11 Ni, and 18.63 Cr. The test specimen was a thin-walled cylinder with inside and outside diameters of 10 and 13 mm, respectively, as shown in Fig. 1. The inner surface was lapped and the outer surface was sanded with successively finer grades of emery paper, ending with 1000 grit, then polished lightly with alumina powder. Both smooth specimens and surface-notched specimens were used. Each of the latter had a hole with a diameter of 0.1 mm and a depth of 0.1 mm at midlength on the outer surface produced by electro-discharge machining after polishing.

The tests were conducted in air using a servohydraulic axial-torsional fatigue machine with high-frequency induction heating. The temperature distribution over the gage length of 12.5 mm was controlled to within ± 3°C of the test temperature. The axial and torsional strains were simultaneously and independently measured by a high-temperature biaxial strain transducer as reported previously [*2*].

All tests were conducted under strain control with sinusoidal strain waveforms at 550°C. Values of the strain ratio, φ, defined as the ratio of the torsional strain range, $\Delta\gamma_{\theta z}$, to the axial strain range, $\Delta\epsilon_z$, were 0, 1.7, 3.7, and ∞ for in-phase tests, and 1.7 for 90° out-of-phase tests. For each strain ratio, tests were performed at several values of maximum principal strain range, $\Delta\epsilon_1$, at a maximum principal strain rate of 10^{-3}/s. Initiation and propagation of small cracks were observed by interrupting each test at predetermined numbers of cycles. After the specimen had cooled, the outer surface of the gage length was lightly polished with diamond paste to remove the oxide layer. A 0.038-mm-thick triacetate cellulose film was soaked in methyl acetate for 3 to 4 s and applied to the entire gage length for 180 s to replicate the surface. The film replica was transferred to a glass slide for subsequent examination with an optical microscope.

Results and Discussion

Observation of Surface Cracks

During in-phase tests of smooth specimens, small cracks about 50 to 100 μm long were observed to initiate mainly on grain boundaries approximately aligned with a direction of maximum shear strain range, $\Delta\gamma_{max}$, for all values of the strain ratio, φ. After initiation, the

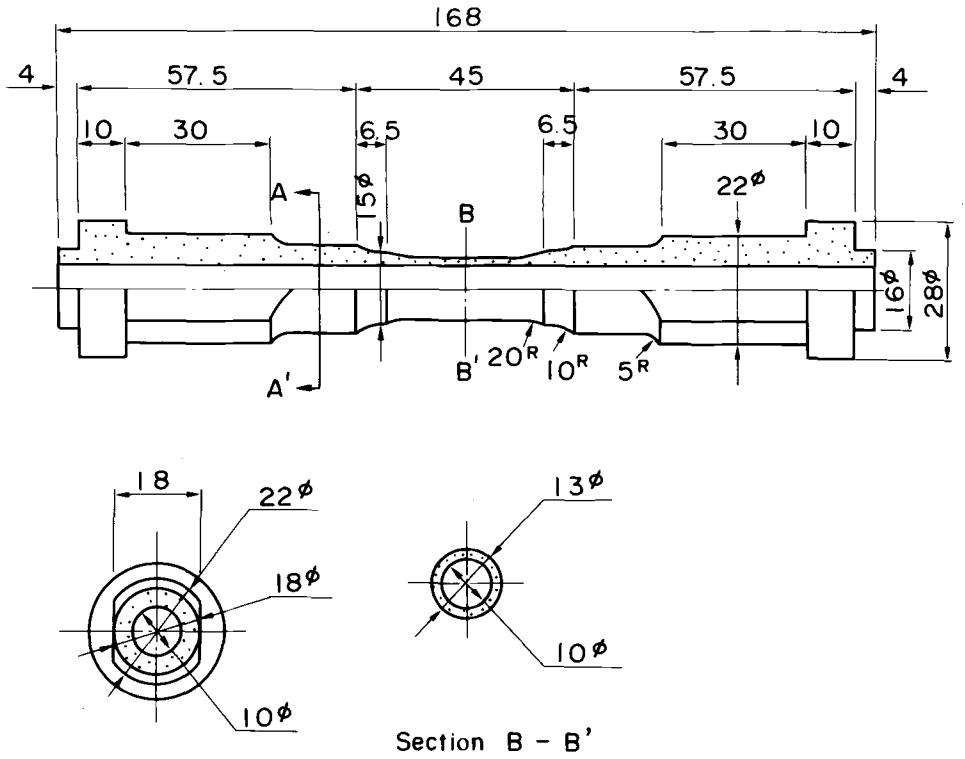

FIG. 1—*Specimen geometry.*

growth of small cracks alternated between the direction normal to $\Delta\epsilon_1$ and the $\Delta\gamma_{max}$ direction for $\varphi = 0$, while microcracks grew in the $\Delta\gamma_{max}$ direction for $\varphi = 1.7$, 3.7, and ∞. Although cracks propagated in the $\Delta\gamma_{max}$ direction to lengths of 5 mm or more for $\varphi = 3.7$ and ∞, the direction of growth changed to the direction normal to $\Delta\epsilon_1$ at a length of 2 mm for $\varphi = 0$ and 1.7.

During in-phase tests of surface-notched specimens, small cracks initiated at the notch in the direction normal to $\Delta\epsilon_1$ for all strain ratios and grew in the same direction as the cracks longer than 0.2 mm in smooth specimens. Linkage of small cracks was generally not observed in smooth and surface-notched specimens for $\Delta\epsilon_1 \leq 1.0\%$, while linkage of small cracks occurred in some specimens for $\Delta\epsilon_1 > 1.0\%$.

Typical results of crack observations during in-phase tests of smooth and surface-notched specimens for given values of φ and $\Delta\epsilon_1$ are shown in Fig. 2. Although there is a difference in crack-initiation direction between smooth and surface-notched specimens, main cracks propagated in the $\Delta\gamma_{max}$ direction in both types of specimens for all values of φ. During 90° out-of-phase tests of smooth and surface-notched specimens with $\varphi = 1.7$, microcracks initiated and grew in the circumferential direction, i.e., on the $\Delta\gamma_{max}$ plane with the larger value of normal strain range. The growth directions of the main macrocracks observed in this study are consistent with those observed in biaxial fatigue tests at 550°C reported previously [*2*].

Crack Propagation Behavior

Figure 3 shows the relationship between the crack length, $2l$, and the cycle ratio, defined as the ratio of the cycle number N, corresponding to a crack length of $2l$, to the cycle number

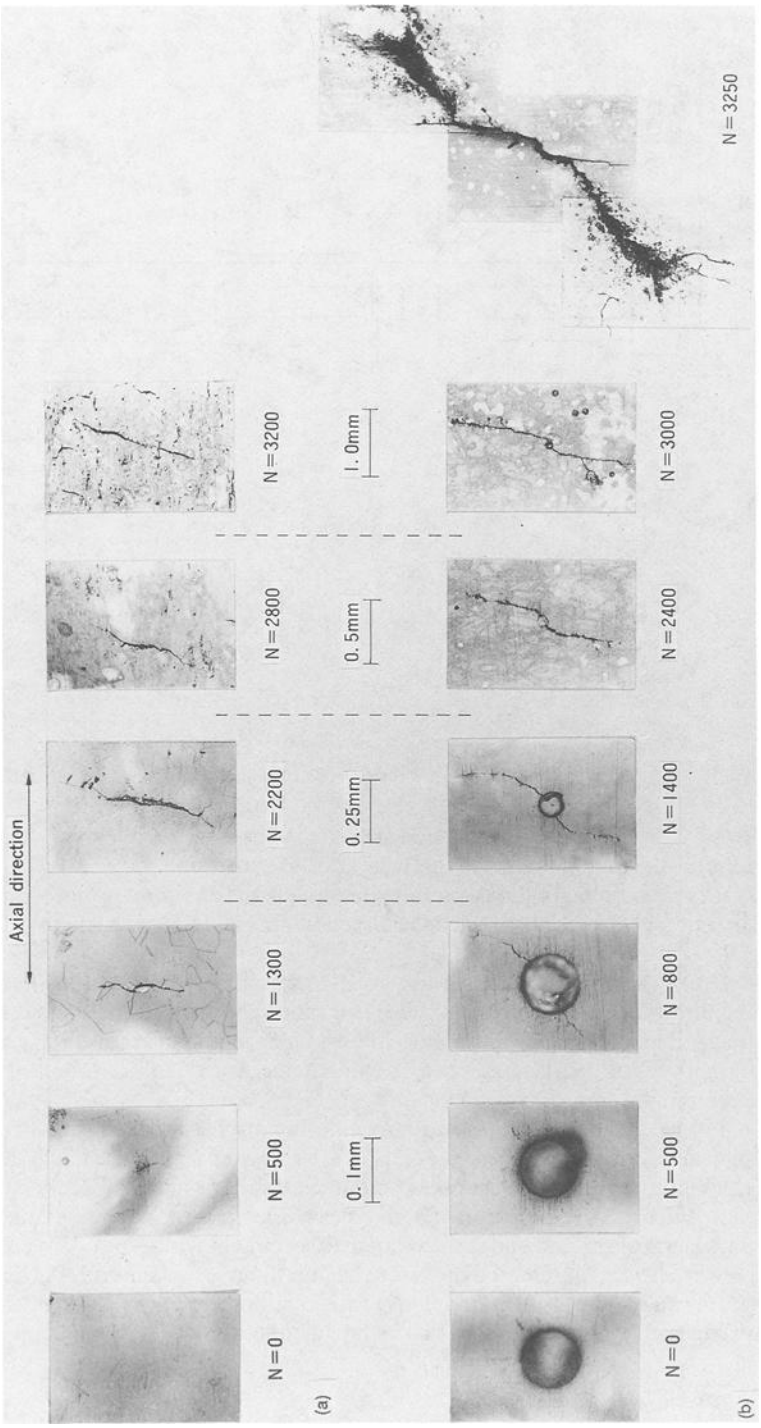
Axial direction
N=0
N=500
N=1300
N=2200
N=2800
N=3200
0.1mm
0.25mm
0.5mm
1.0mm
(a)
N=0
N=500
N=800
N=1400
N=2400
N=3000
N=3250
(b)

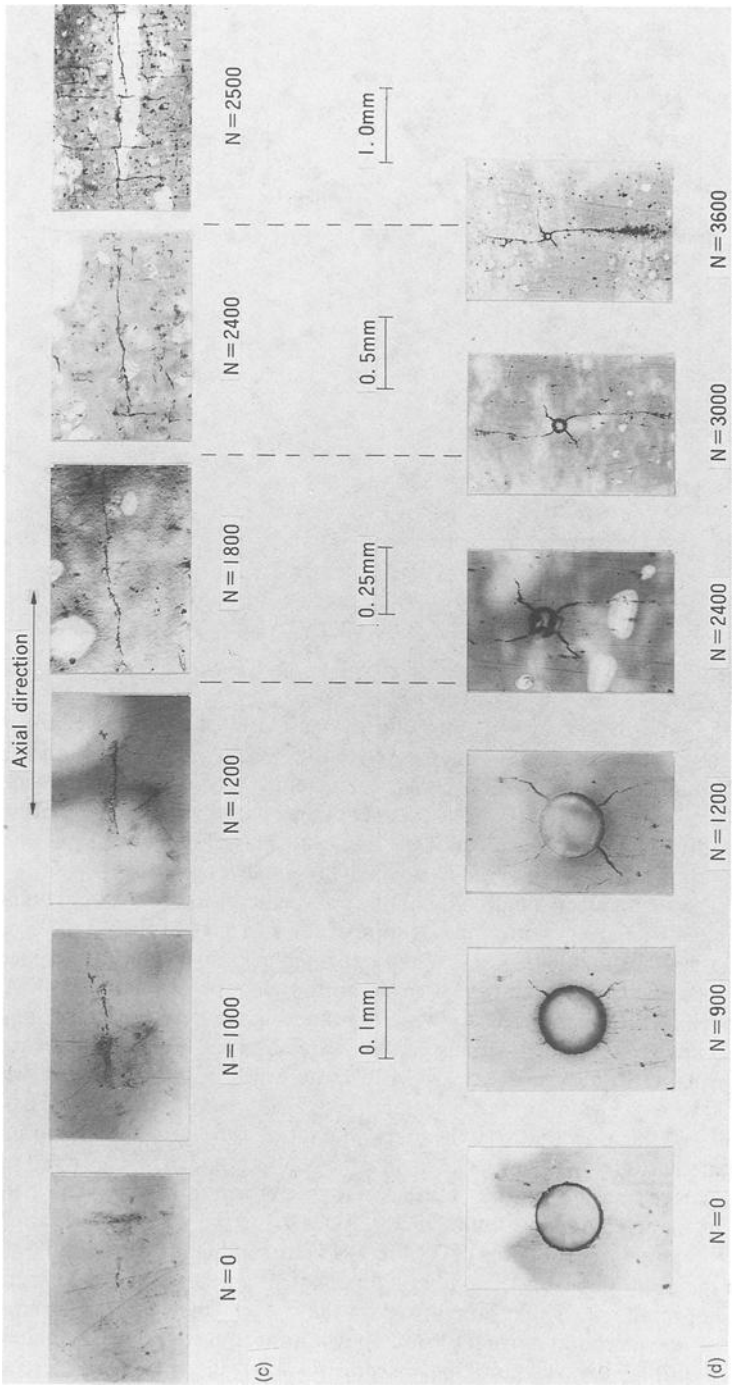

FIG. 2—*Crack initiation and propagation for smooth and surface-notched specimens:* (a) *smooth,* φ = *1.7 and* $\Delta\varepsilon_t$ = *1.0%;* (b) *notched,* φ = *1.7 and* $\Delta\varepsilon_t$ = *0.7%;* (c) *smooth,* $\varphi = \infty$ *and* $\Delta\varepsilon_t$ = *1.2%; and* (d) *notched,* $\varphi = \infty$ *and* $\Delta\varepsilon_t$ = *1.0%.*

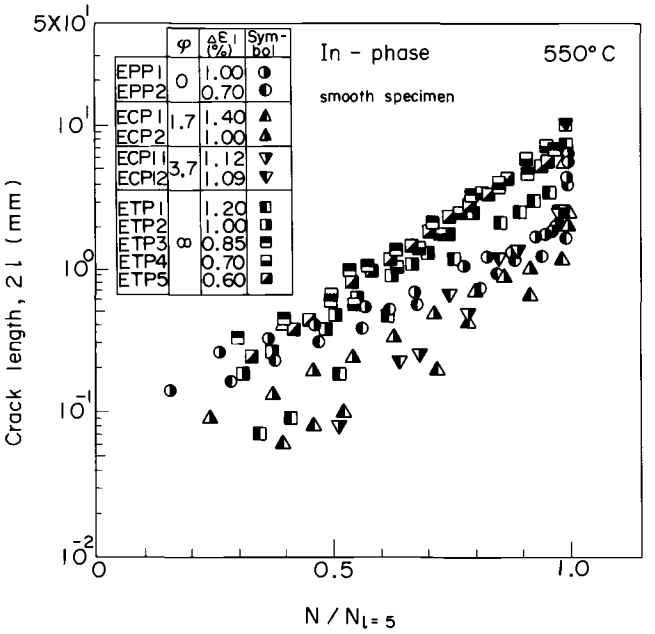

FIG. 3—*Crack length versus cycle ratio for in-phase tests of smooth specimens.*

$N_{l=5}$, corresponding to a crack length $2l$ = 10 mm, for in-phase tests of smooth specimens. Although some variation depending upon φ was observed in the $2l$ versus $N/N_{l=5}$ relationship, small cracks about 0.1-mm long initiated as early as $N/N_{l=5}$ of about 0.2, and most of the cycles required for cracks to grow to a length of 10 mm were spent in propagation of small cracks up to about 2 mm in length. In other words, most of the low-cycle biaxial fatigue life was consumed by microcrack propagation, as observed in uniaxial low-cycle fatigue tests [*5*].

It is evident from Fig. 3 that a crack length of about 2 mm was reached at $N/N_{l=5}$ of about 0.7 for $\varphi = \infty$, and $\Delta\epsilon_1 \leq 1.0\%$. The period of propagation of cracks from 2 to 10 mm in length was longer for $\varphi = \infty$ than for other values of φ. To investigate the reason for this difference, failure surfaces of all specimens were examined with a scanning electron microscope (SEM). Typical failure surfaces for $\varphi = 0$ and ∞ are shown at low and high magnification in Fig. 4. For $\varphi = 0$, marks indicative of rubbing or sliding contact were observed where the crack initially grew on the $\Delta\gamma_{max}$ plane. Striations were clearly visible where the crack subsequently grew in the direction normal to $\Delta\epsilon_1$. The failure surfaces for $\varphi = 1.7$ were similar to those for $\varphi = 0$. For both $\varphi = 0$ and 1.7, the aspect ratio of the crack, the ratio of the depth to the surface half length, was estimated as 0.8 to 1.0 at crack lengths of 1 to 10 mm. For $\varphi = 3.7$ and ∞, rubbing marks were observed on the entire fracture surface, as shown in Fig. 4*b*, where the crack grew on the $\Delta\gamma_{max}$ plane, and the aspect ratio was about 0.2 to 0.3 at a length of about 10 mm. Socie et al. [*9*] reported aspect ratios of 0.14 in 1045 steel and 0.3 to 0.6 in alloy 718 with crack growth on the $\Delta\gamma_{max}$ plane under axial and torsional fatigue at room temperature. Thus the aspect ratios of main cracks that propagated on the $\Delta\gamma_{max}$ plane were smaller than those that propagated in the direction normal to $\Delta\epsilon_1$. They appear to have propagated along the surface, rather than through the wall, until they became relatively large. Hence the period of propagation of cracks from 2 to 10 mm in length was longer for $\varphi = \infty$ than for $\varphi = 0$ and

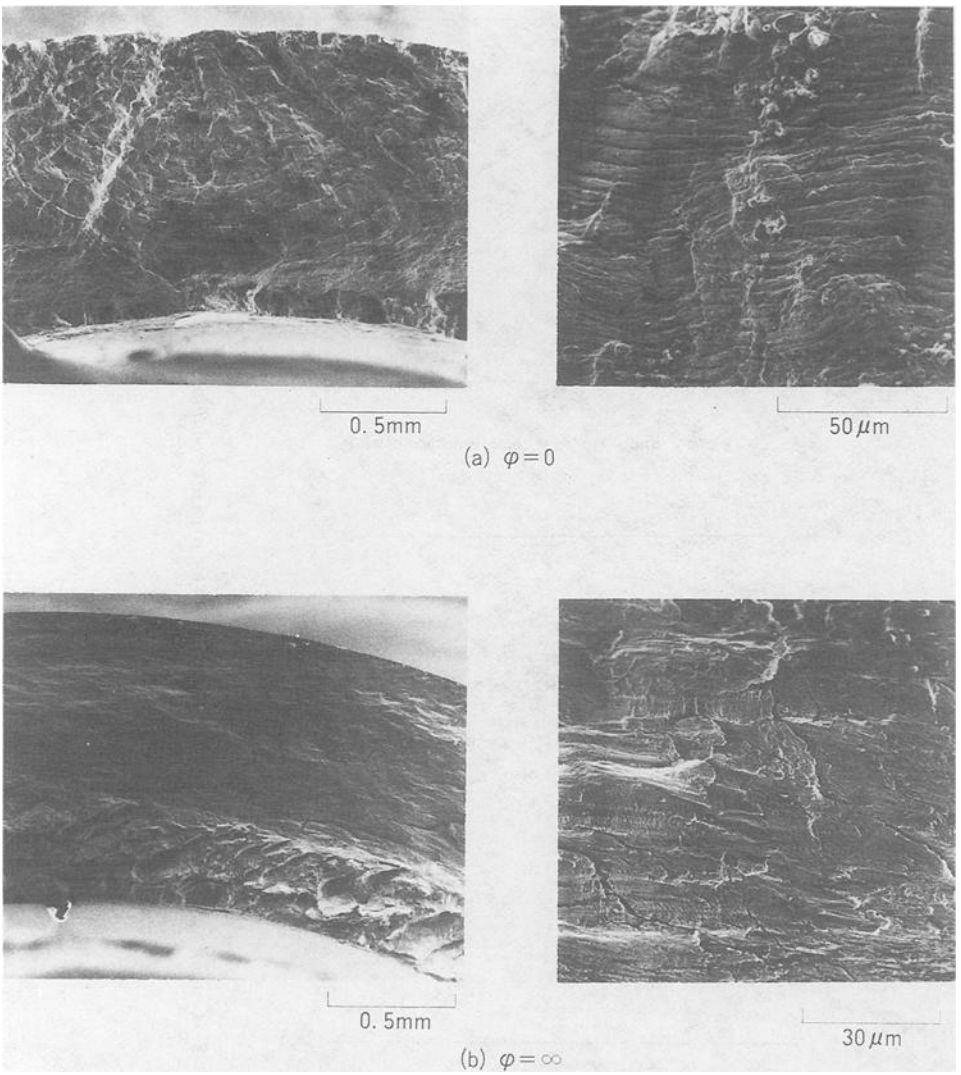

FIG. 4—*Typical SEM failure surfaces for given values of* φ.

1.7, as indicated in Fig. 3. However for $\varphi = 3.7$, this tendency is not evident in Fig. 3 because values of $\Delta\epsilon_1$ were greater than 1.0% and linkage of small cracks occurred.

Crack propagation rate at a given crack length was determined from the tangent to the curve of crack length versus number of cycles. Figure 5 shows the relationship between the crack propagation rate, dl/dN, and the crack half length, l, obtained from in-phase tests with $\varphi = 1.7$ and ∞, and from 90° out-of-phase tests with $\varphi = 1.7$. The crack propagation rate is proportional to crack half length for values of crack half length less than about 1 mm, i.e.

$$dl/dN \propto l \tag{1}$$

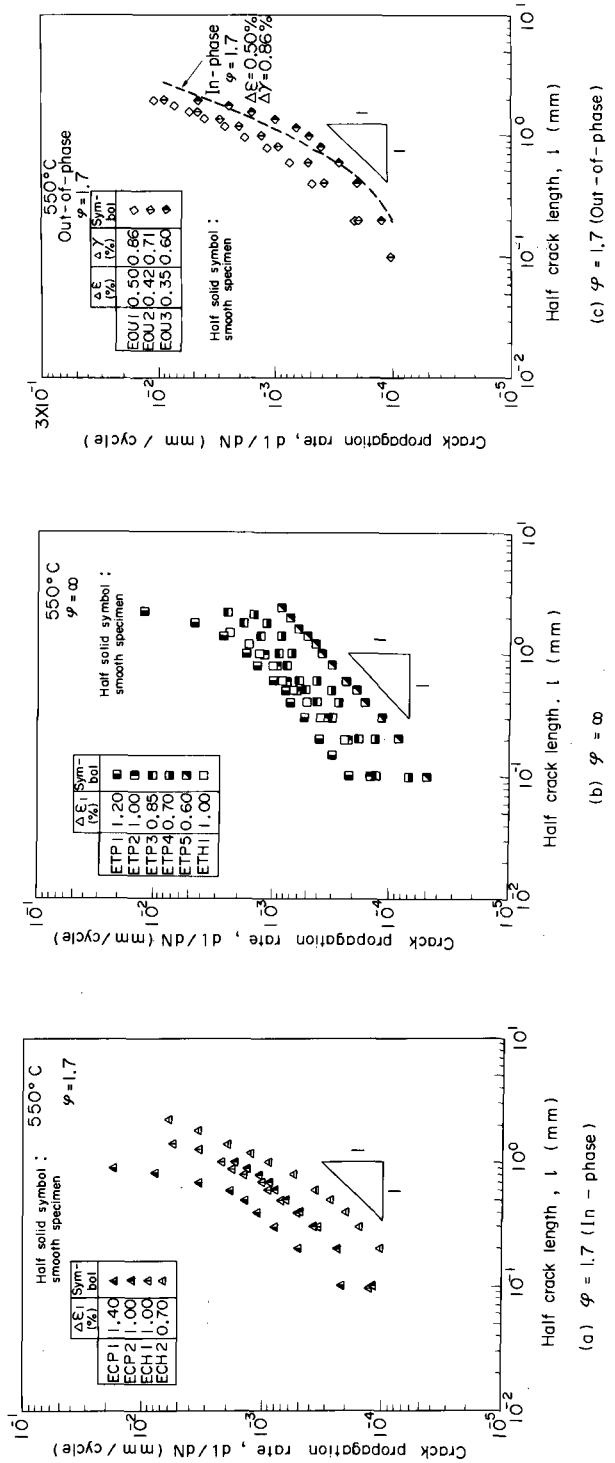

(a) φ = 1.7 (In - phase) (b) φ = ∞ (c) φ = 1.7 (Out - of - phase)

FIG. 5—*Crack propagation rate versus crack half length for given test conditions.*

This relationship holds for relatively larger crack lengths with $\varphi = \infty$. This seems to be associated with smaller aspect ratios for $\varphi = \infty$ as mentioned above.

Nishitani et al. reported that crack-propagation behavior could be studied effectively using test specimens with a small hole or surface notch [*10*]. Likewise in this biaxial fatigue study, crack-propagation behavior in surface-notched specimens was very similar to that in smooth specimens for crack half-lengths larger than 0.1 mm. Henceforth crack-propagation behavior will be discussed without distinction between smooth and surface-notched specimens.

In view of the influence of the maximum shear strain range, $\Delta\gamma_{max}$, on crack-propagation behavior, as discussed above, the relationship for crack propagation rate should include $\Delta\gamma_{max}$ as a control parameter. A possible form is

$$dl/dN = D(\Delta\gamma_{max}/2)^m l \tag{2}$$

where D and m are material constants, depending upon the strain conditions. The constants can be estimated from the relationship between dl/dN and $\Delta\gamma_{max}/2$ for a given value of l. Although it is difficult to obtain precise values due to limited data, m is approximately 2.0, as shown in Fig. 6.

For the in-phase tests in Fig. 6, at a given value of $\Delta\gamma_{max}/2$, the crack propagation rate increases as the strain ratio decreases or as the normal strain range, $\Delta\epsilon_n$, on the $\Delta\gamma_{max}$ plane increases. Furthermore, the crack propagation rate is significantly greater for the 90° out-of-phase tests with $\varphi = 1.7$, in which the ratio of $\Delta\epsilon_n$ to $\Delta\gamma_{max}$ is much larger than for in-phase tests.

In Fig. 7, crack propagation rate is plotted versus $(\Delta\gamma_{max}/2)^m l$ for $m = 2$. Although the crack propagation rate data for each strain ratio are well correlated by $(\Delta\gamma_{max}/2)^2 l$, a unique correlation applicable for all values of strain ratio has not been achieved.

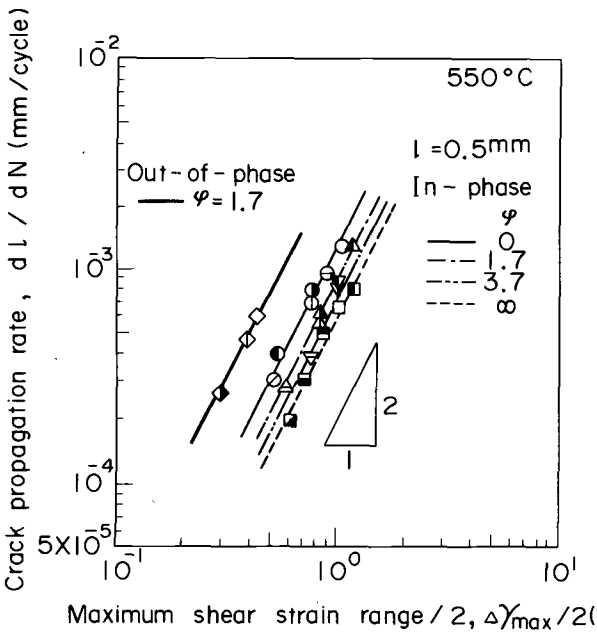

FIG. 6—*Crack propagation rate versus* $\Delta\gamma_{max}/2$ *for* $l = 0.5$ *mm and given test conditions. Symbols are consistent with those of Fig. 7.*

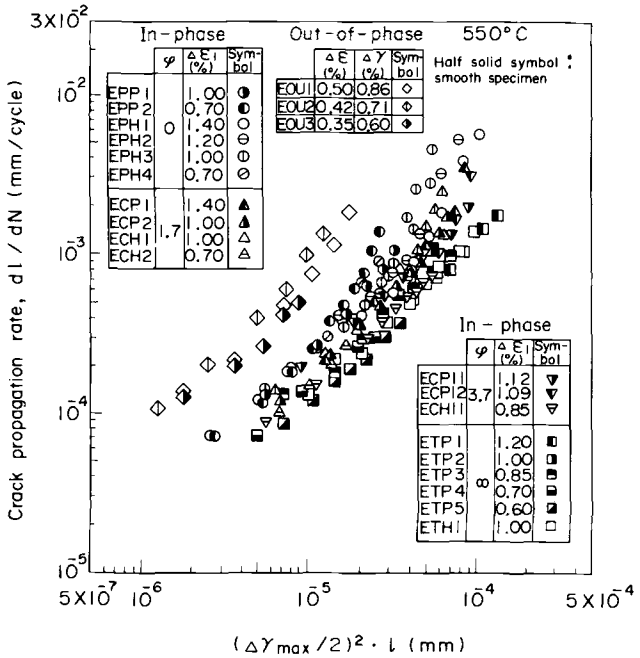

FIG. 7—*Crack propagation rate versus* $(\Delta\gamma_{max}/2)^2 l$ *for given test conditions.*

Equivalent Shear Strain Range Criterion

The influence of $\Delta\epsilon_n$ on crack propagation rate, as shown in Fig. 6, should obviously be taken into account. Both $\Delta\gamma_{max}$ and $\Delta\epsilon_n$ were already found to be controlling factors on biaxial fatigue life, based on analysis of strain-range versus life results and fractographic observations [*1,2*]. An equivalent shear strain range, $\overline{\Delta\gamma}$, defined as a function of $\Delta\gamma_{max}$ and $\Delta\epsilon_n$, was proposed as a fatigue-life criterion. This definition of $\overline{\Delta\gamma}$ was established by constructing contours of constant fatigue life, N_f, on the modified Γ-plane. Biaxial fatigue lives under proportional and non-proportional loading were well correlated with this $\overline{\Delta\gamma}$. To establish a similar definition of $\overline{\Delta\gamma}$ based on crack propagation rate, contours of constant dl/dN at a given crack half length were constructed on the modified Γ-plane.

These iso-dl/dN contours, obtained from the dl/dN versus $\Delta\gamma_{max}/2$ relationship at $l = 0.5$ mm, are shown in Fig. 8. Similarly shaped iso-dl/dN contours can be obtained for $0.05 \leq l \leq 1.0$ mm, within the range of linear proportionality between dl/dN and l. For in-phase tests, each of the iso-dl/dN contours is represented by a segment of an ellipse similar to the iso-N_f contours obtained in previous studies [*1–3*]. For out-of-phase tests, although only $\varphi = 1.7$ and a phase angle of 90° were included in this study, the iso-dl/dN contours are represented by straight lines, since straight lines were obtained previously as iso-N_f contours for out-of-phase tests with several values of strain ratio and phase angle [*1–3*]. The special case of $\varphi = \infty$, for which $\Delta\epsilon_n = 0$, is considered common to both in-phase and out-of-phase strain conditions. The definition of $\overline{\Delta\gamma}$ for each condition is given by the following equations based on the iso-dl/dN contours

$$\overline{\Delta\gamma} = [(\Delta\gamma_{max}/2)^2 + 10.5\Delta\epsilon_n^2]^{1/2} \text{ (In-phase)} \tag{3a}$$

$$\overline{\Delta\gamma} = (\Delta\gamma_{max}/2) + 1.2\Delta\epsilon_n \text{ (Out-of-phase)} \tag{3b}$$

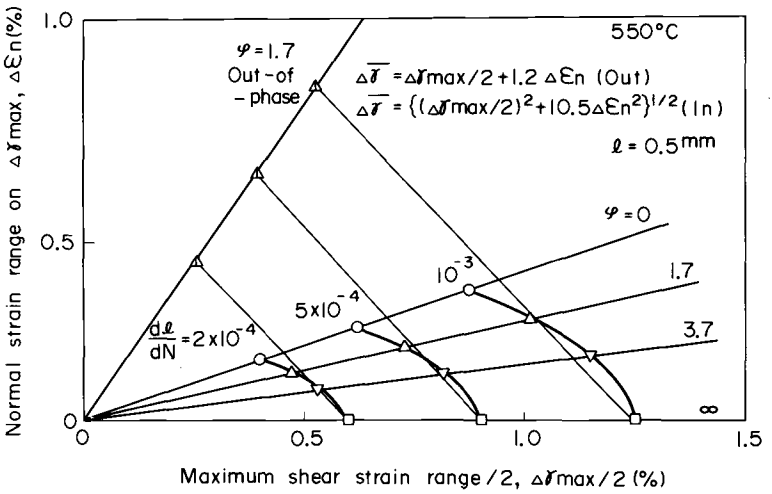

FIG. 8—*Iso*-dl/dN *contours on the modified* Γ*-plane for* l = *0.5 mm and given test conditions.*

The values of the material constants in these equations, given the limitation and scatter of the data, are nearly the same as the values in the fatigue-life criterion. This implies that the influence of φ or $\Delta\epsilon_n$ on the propagation of small cracks is also reflected in the fatigue life.

The relationship between dl/dN and $\overline{\Delta\gamma}^2 l$ is illustrated by the data for in-phase tests plotted in Fig. 9. All data, including those for 90° out-of-phase tests not plotted in Fig. 9, are contained within a narrow band because Eq 3 accounts for the influence of $\Delta\epsilon_n$ on propagation of small cracks. Since the data band is approximately linear with a slope of unity, the crack propagation rate can be represented by following equation

$$dl/dN = C\overline{\Delta\gamma}^2 l \tag{4}$$

where C is a material constant. Integration of Eq 4 results in the following equation for fatigue life

$$N_f = N_i + [\log_e (l_f/l_i)]/(C\overline{\Delta\gamma}^2) \tag{5}$$

where N_i is the number of cycles required to initiate a crack of half length l_i, and l_f is the final half length. With the assumptions $N_i = 0.2N_f$, $l_i = 0.1$ mm and $l_f = 2.0$ mm, based on the data in Fig. 3, and with values for C from Eq 4, corresponding to the upper and lower limits of the data band in Fig. 9, Eq 5 was used to estimate limits on fatigue life. The predictions are plotted as $\overline{\Delta\gamma}$ versus N_f in Fig. 10 for comparison with biaxial low-cycle fatigue data obtained previously [*3*]. Although there is a noticeable difference in slope, agreement between the prediction band and the data band in Fig. 10 is considered good, given the simplified forms of Eq 4 and the expression assumed for N_i, which implies that crack initiation and propagation have the same dependence on strain range.

The above results demonstrate that $\overline{\Delta\gamma}$ is an effective parameter for describing both crack propagation and fatigue life under biaxial loading. Once a formulation of $\overline{\Delta\gamma}$ such as Eq 3 has been established based on iso-dl/dN or iso-N_f contours and limited biaxial data, crack propagation rates and fatigue lives under biaxial loading can be estimated based on more abundant uniaxial data.

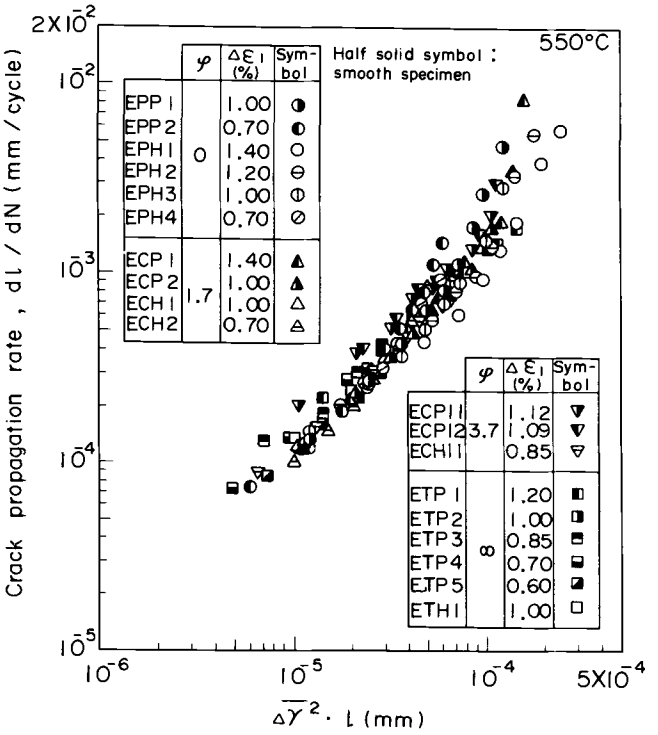

FIG. 9—*Crack propagation rate versus* $\overline{\Delta\gamma}^2 l$ *for given test conditions.*

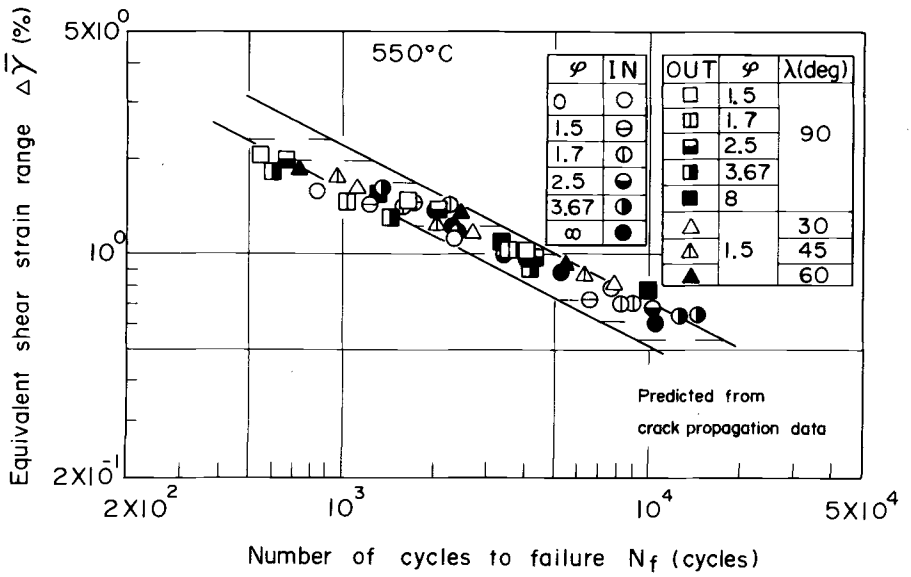

FIG. 10—*Equivalent shear strain range versus fatigue life. Symbols correspond to results of biaxial fatigue tests and lines to limits predicted from crack propagation data.*

Summary and Conclusions

Tests of 304 stainless steel were conducted at 550°C under biaxial low-cycle fatigue conditions, including proportional and nonproportional loading. Each test was interrupted at frequent intervals for observations of crack initiation and propagation to investigate the relationship between crack propagation and fatigue life. The results are summarized, and conclusions are drawn in the following:

1. Small cracks (about 50 to 100 μm in length) initiated mainly on grain boundaries approximately aligned with a plane of maximum shear strain range for all values of the strain ratio, φ. Crack growth alternated between the direction normal to the maximum principal strain range and the direction of the maximum shear strain range for $\varphi = 0$. Cracks grew on the plane of maximum shear strain range for $\varphi = 1.7$, 3.7, and ∞. These observations indicate that the maximum shear strain range strongly influences crack propagation in biaxial low-cycle fatigue.

2. Most of the fatigue life was spent in propagation of small cracks less than 2 mm in length, where the crack propagation rate was linearly proportional to the crack length. For $\varphi = \infty$, the linear relationship between the crack propagation rate and the crack length held at crack lengths greater than for $\varphi = 0$ and 1.7 because cracks grew as stable surface cracks with small aspect ratios.

3. In addition to the maximum shear strain range, the normal strain range on the plane of maximum shear strain range influenced the crack propagation rate in biaxial fatigue. That is, for a given maximum shear strain range, the crack propagation rate increased as the normal strain range on the plane of maximum shear strain range increased. The crack propagation rate was significantly greater for 90° out-of-phase strains because the ratio of normal strain range to shear strain range on the plane of maximum shear strain range was much larger.

4. Regardless of strain conditions, crack propagation rates were correlated well by the equivalent shear strain range, defined as a function of the shear strain range and the normal strain range on the plane of maximum shear strain range. Biaxial low-cycle fatigue life could be estimated from the relationship between the crack propagation rate and the equivalent shear strain range. Thus the equivalent shear strain range is considered useful for describing both crack propagation and fatigue life under biaxial loading.

References

[1] Kuwabara, K., Nitta, A., and Ogata, T., *Proceedings,* International Conference on Mechanical Behavior of Materials (ICM5), Vol. 2, Pergamon Press, Elmsford, NY, 1987, pp. 1173–1180.

[2] Nitta, A., Ogata, T., and Kuwabara, K., *Fatigue and Fracture of Engineering Materials and Structures,* Vol. 12, No. 2, 1989, pp. 77–92.

[3] Ogata, T., Nitta, A., and Kuwabara, K., *Fatigue under Biaxial and Multiaxial Loading,* ESIS10, Mechanical Engineering Publications, London, 1991, pp. 377–392.

[4] Brown, M. W. and Miller, K. J., *Proceedings, Institution of Mechanical Engineers,* Vol. 187, 1973, pp. 745–755.

[5] Nishitani, H. and Goto, M., *The Behavior of Short Fatigue Cracks,* EGF1, K. J. Miller and E. R. de los Rios, Eds., Mechanical Engineering Publications, London, 1986, pp. 461–478.

[6] Hoshide, T., Tanaka, K., and Yamada, A., *Fatigue of Engineering Materials and Structures,* Vol. 4, 1981, pp. 355–366.

[7] Brown, M. W. and Miller, K. J., in *Multiaxial Fatigue, ASTM STP 853,* American Society for Testing and Materials, Philadelphia, 1985, pp. 135–152.

[8] Kitagawa, H., Yuuki, R., Tohgo, K., and Tanabe, M., in *Multiaxial Fatigue, ASTM STP 853,* American Society for Testing and Materials, Philadelphia, 1985, pp. 164–183.

[9] Socie, D. F., Han, C. T., and Worthem, D. W., *Fatigue and Fracture of Engineering Materials and Structures,* Vol. 10, No. 1, 1987, pp. 1–12.

[10] Nishitani, H. and Kawagoishi, H., *Transactions, Japan Society of Mechanical Engineers,* Tokyo, Vol. 49, 1983, pp. 431–440.

Jean Yves Bérard,[1] *David L. McDowell,*[2] *and Stephen D. Antolovich*[3]

Damage Observation of a Low-Carbon Steel Under Tension-Torsion Low-Cycle Fatigue

REFERENCE: Bérard, J. Y., McDowell, D. L., and Antolovich, S. D., **"Damage Observation of a Low-Carbon Steel Under Tension-Torsion Low-Cycle Fatigue,"** *Advances in Multiaxial Fatigue, ASTM STP 1191,* D. L. McDowell and R. Ellis, Eds., American Society for Testing and Materials, Philadelphia, 1993, pp. 326–344.

ABSTRACT: Low-cycle fatigue tension-torsion tests were performed on a low-carbon steel. The formation of microcracks as a function of orientation and state of stress was studied. Quantitative measurements of microcrack density and length showed that microcracking occurred in the maximum shear direction for various stress states. Transgranular microcracks were mostly observed. An increasing amount of intergranular microcracks was observed for out-of-phase tension-torsion loading. A shear-based microcrack propagation approach incorporating a normal stress effect was shown to provide a better correlation of the damage distribution of a pure torsion test.

KEY WORDS: multiaxial fatigue, damage, damage anisotropy, crack initiation, metal fatigue

The nucleation and growth of fatigue cracks in structural components is of enormous importance. Much of the life of structural components is spent in developing microcracks of engineering size. Therefore, damage development during multiaxial fatigue is of most practical interest. An understanding of the physical processes associated with multiaxial fatigue is necessary to correctly model and perform fatigue life predictions. Damage can be defined as the nucleation and early propagation of microcracks. Using multiaxial fatigue experiments, principal strain and stress directions can be easily changed so that the directional aspect of fatigue damage can be studied. The objective of this paper is to study the relationship between the physical damage and the state of stress. The directional aspect of fatigue damage is presented and analyzed for a low-carbon steel used in the automotive industry.

Experimental Procedure

Material and Heat Treatment

The material used in this study was a hot-worked low-carbon steel supplied by USINOR-SACILOR (France). The material was forged into a bar with a cross section of 55 by 55 mm for the biaxial (tubular) specimens and into a bar of 25 by 25 mm for the uniaxial specimens. After forging, a heat treatment was performed to homogenize the structure. Heat treatments and the chemical composition are given in Table 1.

[1] Research engineer, IRSID Unieux, B.P. 50, 42702 FIRMINY Cedex, France.
[2] Professor, Georgia Institute of Technology, the George W. Woodruff School of Mechanical Engineering, Atlanta, GA 30332.
[3] Professor, Georgia Institute of Technology, School of Materials Engineering, Atlanta, GA 30332.

TABLE 1—*Chemical composition (wt%) and heat treatments.*[a]

Designation: French standards (NF): ES finish X.
U.S. standards: A620 finish Class 1.

C	Mn		Al	Ni	Cr
0.036%	0.198%	0.046%	0.024%	0.023%	· · ·
Cu	P		Si	S	N
0.017%	0.011%	0.008%	0.009%	0.003%	· · ·

[a] *Heat Treatment after Forging:*

Uniaxial Specimens	*Biaxial Specimens*
925°C for 30 min air cooling	925°C for 1 h 30 min air cooling
720°C for 2 h air cooling	720°C for 3 h air cooling

Specimens

Following heat treatment, uniaxial and biaxial specimens were machined to the dimensions shown in Figs. 1 and 2. The reference axis attached to the specimen as well as the convention used for designating the orientation of planes in the specimen wall are presented in Fig. 3. Biaxial specimens were electropolished to facilitate observations of surface cracking.

Test Procedure

The tests were performed in the Mechanical Properties Research Laboratory (MPRL) at the Georgia Institute of Technology using a closed-loop tension-torsion servohydraulic machine. The tests were carried out at room temperature under axial strain and shear strain control. For the pure torsion test, the axial load was controlled to zero, which ensured no axial constraint. The strain was controlled and measured with a calibrated biaxial extensometer. All the tests were carried out under computer control that generated the strain path and acquired data.

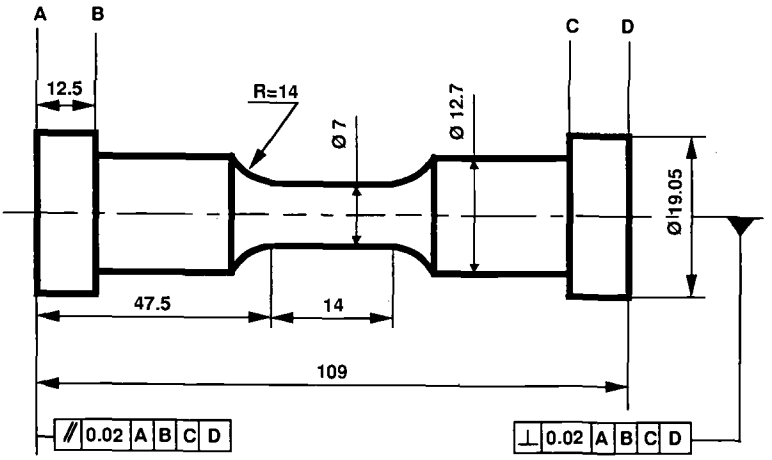

FIG. 1—*Uniaxial fatigue specimen (all dimensions in mm).*

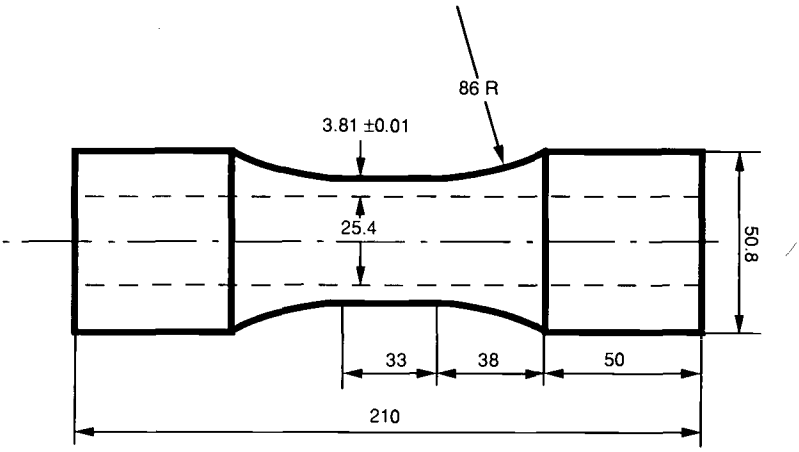

FIG. 2—*Biaxial fatigue tubular specimen (all dimensions in mm).*

During the tests, the effective von Mises strain rate was maintained at $10^{-3}\,s^{-1}$ by dividing each cycle into a number of linear segments. The actual strain path was piecewise linear. Since the material exhibited a sharp yield point, the strain range was slowly increased in the vicinity of the yield point to avoid the formation of Lüders bands within the specimen and to ensure homogeneous plastic deformation across the gage length.

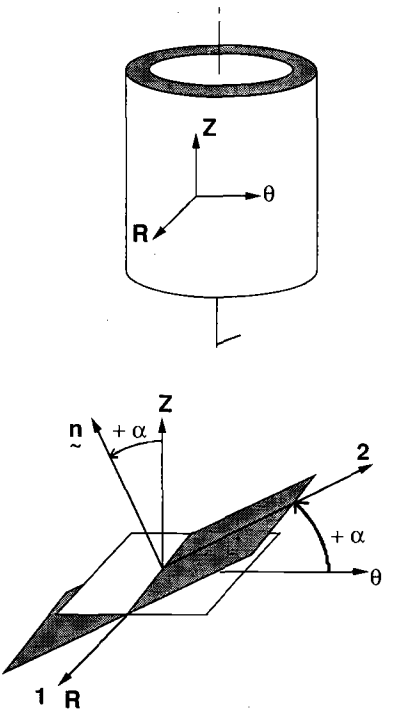

FIG. 3—*Reference axis and plane rotation convention.*

Metallurgical Evaluation Techniques

Cellulose acetate tape replicas of the gage sections were made during testing at periodic intervals. These were observed with an optical microscope equipped with a 35-mm camera to document microcrack initiation and growth and other surface-related phenomena. Repliças were examined after the tests to track crack nucleation and growth. Large areas away from the main crack were photographed at a magnification of ×260 to document damage development. From these photographs, montages of the surface were assembled. Using a computerized digitizing tablet, individual microcrack length and orientation measurements were performed. Care was taken to differentiate between transgranular and intergranular microcracks.

Results

Microstructure

Both longitudinal and transverse directions were observed and are shown in Fig. 4. No significant size or morphology differences were found optically. The structure was ferritic with some pearlite at the grain boundaries. The amount of pearlite, determined by quantitative metallography, was 3%. The average grain size was 20 μm as determined by the linear intercept method. The presence of spherical impurities was noted, but no hard inclusions were present. The hardness was measured as 75 HB.

Mechanical Tests

The test matrix and test results are given in Table 2.

Uniaxial Cyclic Stress-Strain Behavior—The uniaxial monotonic and cyclic behavior of the material was previously reported in Ref *1* and is summarized in Table 3. The following relation, shown in Fig. 5, described the cyclic behavior

$$\frac{\Delta\sigma}{2} = 1753\left(\frac{\Delta\varepsilon^p}{2}\right)^{0.34} \tag{1}$$

where $\Delta\sigma/2$ is the axial cyclic stress amplitude in MPa and $\Delta\varepsilon^p/2$ is the axial plastic strain amplitude.

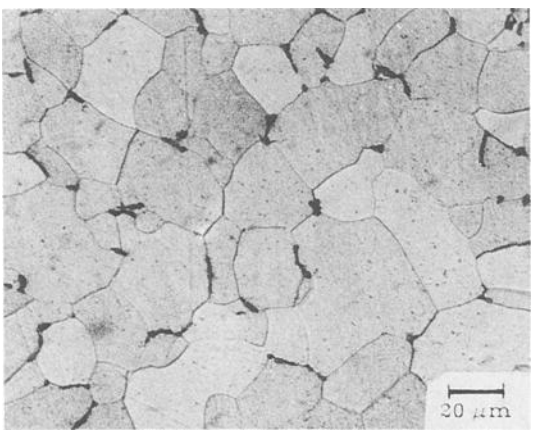

FIG. 4—*Material microstructure (nital etchant) ferritic matrix with pearlite at grain boundaries.*

TABLE 2—*Test results for XES steel.* N_i *is the number of cycles needed for a 1-mm surface crack.*

ID	Path Type	$\Delta\varepsilon/2$, %	$\Delta\sigma/2$, MPa	$\Delta\gamma/2$, %	$\Delta\tau/2$, MPa	Strain Ratio, $\lambda = \Delta\gamma/\Delta\varepsilon$	N_i
A	Tension	0.5	240	...	...	0	4 650
1	90° out-of-phase	0.25	253	0.43	130	1.7	4 400
2	Torsion	...	...	1.0	154	∞	1 500
3	Torsion	...	...	0.4	120	∞	34 000
4	Torsion	...	...	0.7	134	∞	5 500
6	Torsion	...	...	1.5	165	∞	900
7	Proportional	0.35	179	0.61	94	1.7	6 000

Torsional Cyclic Stress-Strain Behavior—The torsional cyclic behavior was studied with a series of pure torsion tests. The torsional tests results are given in Table 3. The stresses reported are the stresses at half the fatigue life. Mean shear stress and mean shear strain were used because they represented an average behavior across the wall thickness. The shear stress versus the plastic shear strain was plotted in Fig. 5. A power law relation was determined as

$$\frac{\Delta\tau}{2} = 444\left(\frac{\Delta\gamma^p}{2}\right)^{0.22} \tag{2}$$

where $\Delta\tau/2$ is the mean cyclic shear stress amplitude in MPa and $\Delta\gamma^p/2$ is the mean cyclic plastic shear strain amplitude.

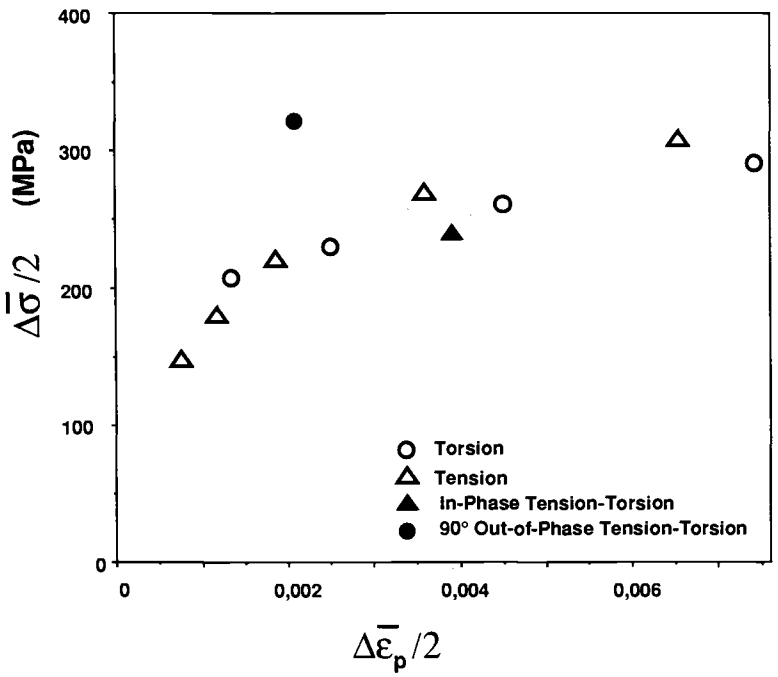

FIG. 5—*Multiaxial cyclic stress-strain behavior. Data are presented in terms of von Mises equivalent quantities.*

TABLE 3—*Baseline material properties, XES steel.*

	MONOTONIC TENSILE PROPERTIES	
E	Elastic modulus	205 000 MPa
$\sigma_{y\ 0.2\%}$	0.2% offset yield strength	219 MPa
σ_u	Ultimate strength	317 MPa
σ_f	True fracture strength	447 MPa
% RA	% reduction in area	85
K	Strength coefficient	580 MPa
n	Strain-hardening exponent	0.25
HB	Brinell hardness number	75 HB
	AXIAL CYCLIC PROPERTIES	
E	Elastic modulus	205 000 MPa
σ'_f	Fatigue strength coefficient	1086 MPa
b	Fatigue strength exponent	−0.15
ε'_f	Fatigue ductility coefficient	0.18
c	Fatigue ductility exponent	−0.44
K'	Cyclic strength coefficient	1753 MPa
n'	Cyclic strain hardening exponent	0.34
	TORSIONAL CYCLIC PROPERTIES	
G	Elastic shear modulus	78 000 MPa
K'_0	Cyclic strength coefficient	444 MPa
n'_0	Cyclic strain hardening exponent	0.22

Von Mises equivalent stress and plastic strain, normalized with respect to uniaxial values, were used to compare the axial and torsional cyclic behavior. The use of the von Mises equivalence gave a fair correlation between the axial and the torsional data.

Multiaxial Cyclic Stress-Strain Behavior—Under in-phase tension-torsion loading, the stress amplitude was of the same order as that of the equivalent uniaxial case as shown in Fig. 5. Nonproportional tension-torsion loading affected the cyclic stress response of the material. An extra 30% cyclic hardening was observed compared to the uniaxial reference curve. This extra hardening may be explained by the increase in the number of active slip systems, which thereby increase the slip system interactions. It is not as pronounced as has been observed for some low-stacking fault materials where the extra hardening under nonproportional loading can be as high as 100% of the uniaxial reference curve [*2–3*].

Uniaxial Fatigue Behavior—The uniaxial tension-compression fatigue response of the material was studied in Ref *1*. A strain-life relation of the form

$$\frac{\Delta\varepsilon_t}{2} = \frac{1086}{E}(2N_i)^{-0.16} + 0.185(2N_i)^{-0.44} \tag{3}$$

where $\Delta\varepsilon_t/2$ is the total strain amplitude, N_i is the number of cycles for crack initiation, E is the Young's modulus, provided a good fit of the experimental data. Initiation is defined as the number of cycles needed for the fatal crack to reach 1 mm.

Torsional Fatigue Behavior—To correlate pure torsion fatigue tests, shear stress and strain values at the outer fiber were used since crack initiation occurred there. For shear strain, a linear correction was used to transform mean radius shear strain into outside radius shear strain. The shear stress on the outer fiber was then computed as

$$\frac{\Delta\tau}{2} = 490\left(\frac{\Delta\gamma_t}{2}\right)^{0.25} \tag{4}$$

where $\Delta\tau/2$ is the shear stress amplitude in MPa, $\Delta\gamma_t/2$ is the total shear strain amplitude. This relation was obtained with the cyclic data on the mean radius. The number of cycles for crack initiation for different tests are summarized in Table 3. The von Mises equivalent plastic strain amplitude and equivalent stress amplitude is defined as

$$\frac{\Delta\bar{\varepsilon}^p}{2} = \sqrt{\left(\frac{\Delta\varepsilon^p}{2}\right)^2 + \frac{1}{3}\left(\frac{\Delta\gamma^p}{2}\right)^2} \tag{5}$$

$$\frac{\Delta\bar{\sigma}}{2} = \sqrt{\left(\frac{\Delta\sigma}{2}\right)^2 + 3\left(\frac{\Delta\tau}{2}\right)^2} \tag{6}$$

The von Mises equivalent plastic strain amplitude versus the number of reversals for crack initiation is shown in Fig. 6. There is no significant difference between tension and torsion results with the initiation criterion used (1-mm surface crack). This result agrees with the results from Socie et al. on Inconel 718 [*4*]. Of course, the authors recognize that this result is somewhat different from what is generally reported in the literature [*5*] where the results are analyzed in terms of a torque drop. For Test 2 ($\Delta\gamma/2$ = 1%), a 10% torque drop was reached at Cycle 2700. In this case, almost half of the life was spent in the propagation of microcracks. No sufficient data are available yet to assess if this result is amplitude and stress state independent. Obviously, this approach (1-mm surface crack) can be seen as conservative when one is

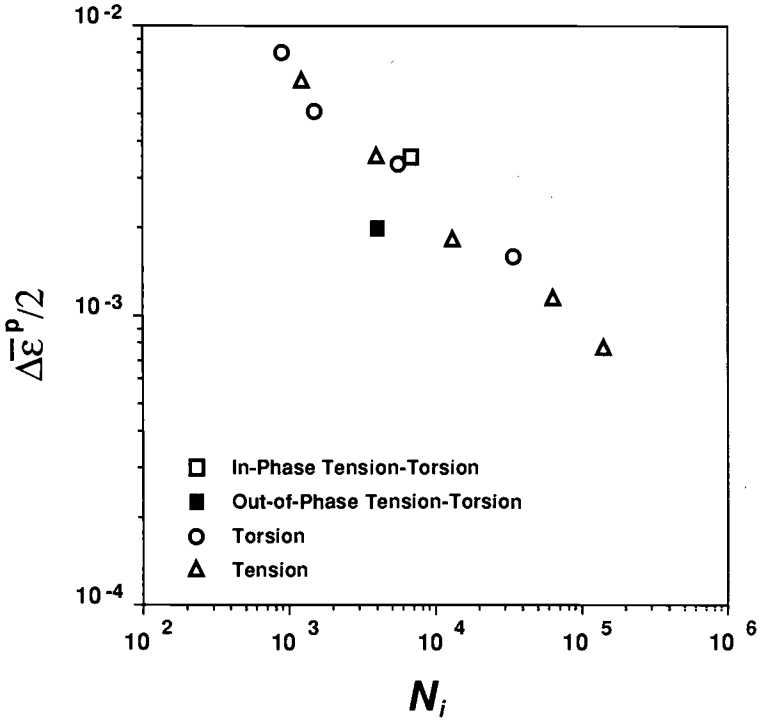

FIG. 6—*Coffin-Manson relation for tension, torsion, and tension-torsion data. The plastic strain amplitude is presented in terms of the von Mises equivalent value.*

trying to predict a component life from laboratory specimen test results. Another problem related to failure definition using the torque drop criterion is the possible specimen size dependence. Two specimens of different diameters having the same surface crack would show a different change in torque. A torsion fatigue specimen can be seen as a component in itself.

For this material, the equivalent von Mises approach seemed to provide sufficient correlation of both tension and torsion loading if the life to a given crack length (e.g., 1 mm) is used. During the torsion tests, no torque decrease was observed before the cracks were about 10 mm in length along the surface. The use of a change in torque peak value, therefore, does not seem to be a useful technique to detect crack initiation as pointed out by Ref *5*.

The definition of crack initiation is a critical issue for multiaxial fatigue correlation. Many researchers have used a change in compliance to define the point of crack initiation. This technique, although sensitive for uniaxial tension loading, lacks sensitivity for torsional loading. When different loading cases and different states of stress are compared, *the same surface crack length and the same crack aspect ratio should be used.* This approach was demonstrated by Beer [*6*] on Inconel 718. Crack depth and length for a series of mixed mode axial-torsional experiments were studied. It was found that up to 1 mm, all cracks had about the same aspect ratio.

Multiaxial Fatigue Behavior—For in-phase tension-torsion loading, lives were very similar to uniaxial tests (Fig. 6). The equivalent von Mises plastic strain amplitude was used for comparison. The strain-life relation provided a good life prediction. For out-of-phase tension-torsion loading, the life was shorter (by a factor of 3) than for uniaxial loading (Fig. 6), based on the same equivalent plastic strain amplitude. The cyclic stress amplitude was higher than for a comparable uniaxial test based on the equivalent plastic strain amplitude. For this type of test, a strain-based fatigue parameter shows some limitation, since the stress amplitude dependence is not taken into account. There was also increased slip activity with nonproportional loading; the density of slip traces on the specimen surface increased with nonproportional loading. Under strain-controlled conditions, the cyclic stress amplitude reflects the deformation substructure that develops. An important question to be answered is whether the difference in life can be explained based only on higher cyclic stress amplitude. From the data generated by Socie and coworkers on Inconel 718 and 1045 steel and analyzed by Bérard in Ref *7*, models which explicitly incorporate the cyclic stress amplitude accurately predict the lives. Although the predictions were correct, this did not necessarily mean that the analysis or underlying philosophy was correct. Microstructural observations should be performed to provide the physical basis [*8*]. If the dislocation structures are the same in nature, then classical analysis techniques incorporating the cyclic stress amplitude dependence should apply.

Observations

Damage Development—Microcracks propagated in the shear mode for all the loading cases (i.e., Mode II). This was observed by Fash [*9*] and Hua [*10*] on 1045 Steel. Figure 7 shows the damaged surface of one tested specimen under proportional loading conditions. Microcracks are preferentially oriented along the maximum shear strain range directions ($\sim 70°$ and $\sim -20°$). The main cracks were observed in one of the maximum plastic shear strain directions ($\sim 70°$ relative to the specimen axis; close to the specimen axis). These two planes experienced the same plastic shear strain amplitude and normal stress amplitude. If there was a normal stress effect on initiation, cracks would initiate on planes which experience higher normal stress amplitude. From the photomicrograph, this is not what was observed and was confirmed by quantitative measurements discussed below. The initiation process is apparently only shear governed for this material.

Figure 8 shows the damaged surface of a specimen tested under pure torsion loading ($\Delta\gamma/2$

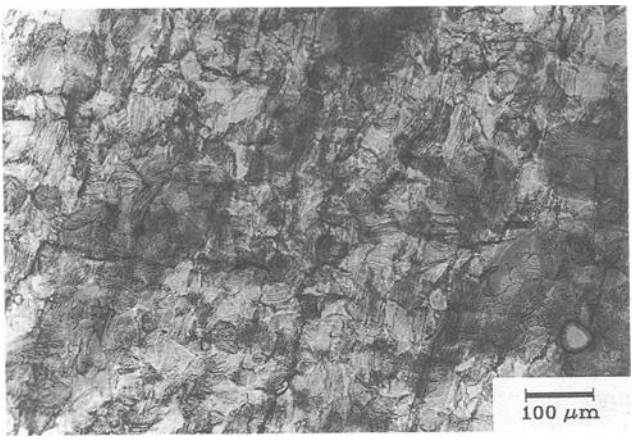

FIG. 7—*Photograph from replica of the damaged surface of Specimen 7 (in-phase tension-torsion). Specimen axis is vertical.* $\Delta\epsilon/2 = 0.35\% - \Delta\gamma/2 = 0.61\% - N_i = 6000$ *cycles.*

= 1%). Microcracks were present on both maximum plastic shear strain directions (0 and 90°C). Since there was no normal stress, one would expect to see as many dominant cracks in one direction as in the other. There were always more cracks in the 90° direction (along the specimen axis). The crack which caused fracture was always oriented along the specimen axis. In that respect, the proportional loading test presented before appears very much like a torsion test. No explanation has yet been given as to why long macroscopic torsion cracks are always observed along the specimen axis. De Los Rios et al. [*11*] tested 316 stainless steel at high temperature and reported damage accumulation. Microcracks were observed to have formed on planes perpendicular to the maximum principal stress. Crack initiation was caused by the maximum tensile stress for 316 stainless steel. Very interestingly, the microcracks under torsion loading which first propagated normal to the principal stress direction (45° relative to the specimen axis) eventually linked to form macrocracks oriented parallel to the specimen axis.

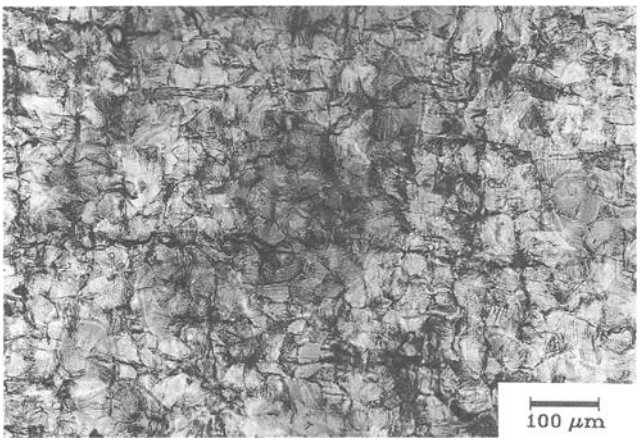

FIG. 8—*Photograph from replica of the damaged surface of Specimen 2 (pure torsion). Specimen axis is vertical.* $\Delta\gamma/2 = 1\% - N_i = 1500$ *cycles.*

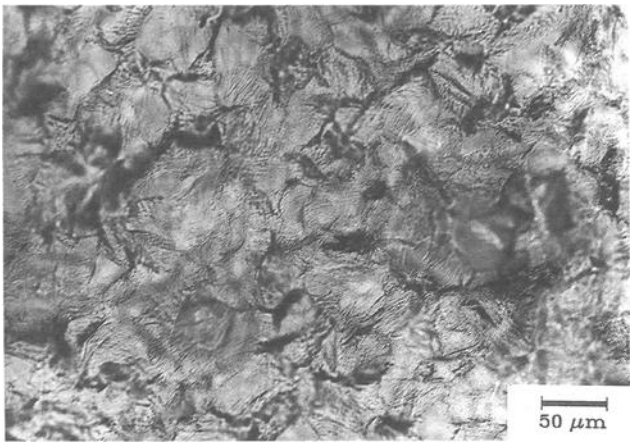

FIG. 9—*Photograph from replica of the damaged surface of Specimen 1 (90° out-of-phase tension-torsion). Specimen axis is vertical.* $\Delta\varepsilon/2 = 0.25\% - \Delta\gamma/2 = 0.43\% - N_i = 4400$ *cycles.*

A similar result was observed by Jacquelin et al. [*12*] for 316L stainless steel at room temperature where the fatigue cracks under torsion loading were oriented along the specimen axis.

The damaged surface from a nonproportional loading test is shown in Fig. 9. There was no evidence of preferred cracking orientation. Here the range of shear strain is more uniformly distributed among planes in all possible in-plane orientations. In this case, there was a significant increase in the number of intergranular microcracks which were seldom observed for proportional loading.

Crack Orientation Distribution—Fatigue damage can be characterized by the observation of microcracks. It is often observed that fatigue damage is anisotropic, so that crack orientation is an important parameter. A texture measurement was performed. A (110) pole figure was determined which did not show any preferred orientation. The material was initially isotropic so that the fatigue anisotropy was only mechanically induced. Two different types of measurements were made. In the first, microcrack density was measured as a function of the crack orientation. This measure should be closely related to the fatigue crack nucleation process since every individual crack was counted, regardless of its length. For the second, cumulative crack length was computed as a function of the crack orientation from the previous measurement. This measure should be more related to both the nucleation and the propagation phases. Both measurements are necessary to fully characterize the nucleation and microcrack propagation phases of the fatigue process. When conducting these measurements, it is essential to differentiate transgranular from intergranular cracking. Completely different mechanisms are involved for these cracking modes, and they would be expected to have different dependencies on the mechanical loading parameters. In this study, the major focus was on transgranular cracking. This was the dominant cracking mechanism for the temperature and strain amplitudes studied, except for 90° out-of-phase tension-torsion tests where both types were equally present.

1. Torsion Tests

The density of transgranular microcracks versus orientation is presented in Fig. 10 for a torsion test ($\Delta\gamma/2 = 1\%$). The peak values corresponded to the maximum plastic shear strain orientations at the surface (0 and 90°). The crack nucleation process is related to the cyclic

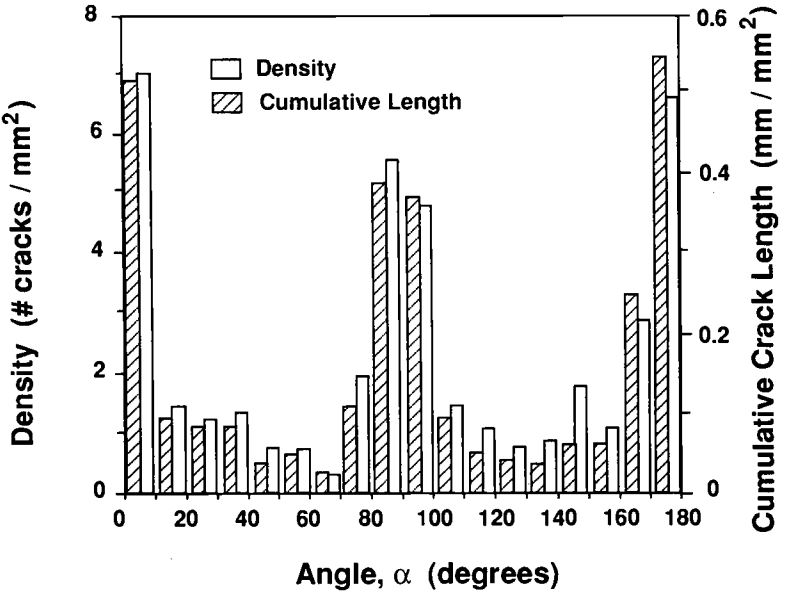

FIG. 10—*Transgranular microcrack density versus orientation and cumulative microcrack length versus orientation for a torsion test ($\Delta\gamma/2$ = 1%). Replica was taken at Cycle 1500.*

plastic shear strain because of the slip process associated with the formation and development of persistent slip bands. The cumulative crack length versus orientation is given in Fig. 10 for the same torsion test ($\Delta\gamma/2$ = 1%). The peak values corresponded to the maximum plastic shear directions (0 and 90°). Both distributions showed a $\cos^n \alpha$ type of nature. The value of the exponent n was computed by a log-log linear regression. For the density distribution as well as for the cumulative crack length distribution, the value of n was between 4 and 5.

The density of intergranular microcracks for this torsion test was much less than transgranular microcracks. There was no particular orientation with a higher density. Intergranular cracking is a complex process. There is no simple correlation between the cracking orientations and the mechanical loading parameters. This result agrees with what is generally observed for this type of material, which fails predominantly by transgranular cracking. The intergranular microcracks density increased with increased strain amplitude. For pure torsion loading, the cracking behavior was similar to the behavior under tension loading.

2. In-Phase Tension-Torsion Test

The density of transgranular microcracks versus orientation and the transgranular cumulative crack length versus orientation are shown in Fig. 11 for an in-phase tension-torsion test ($\Delta\varepsilon/2$ = 0.35% − $\Delta\gamma/2$ = 0.61%). The peak values were observed in the direction of maximum plastic shear strain range (73 and 163°). The two sets of planes corresponding to these two peaks experienced the same shear strain amplitude and normal stress amplitude. Planes with higher normal stress amplitudes did not show more cracking. This observation implies that the normal stress influence on cracking behavior was minimal. This material seems to be governed by pure shear for the strain biaxiality ratio studied. The density distribution of intergranular microcracks was relatively uniform and much less than the transgranular one.

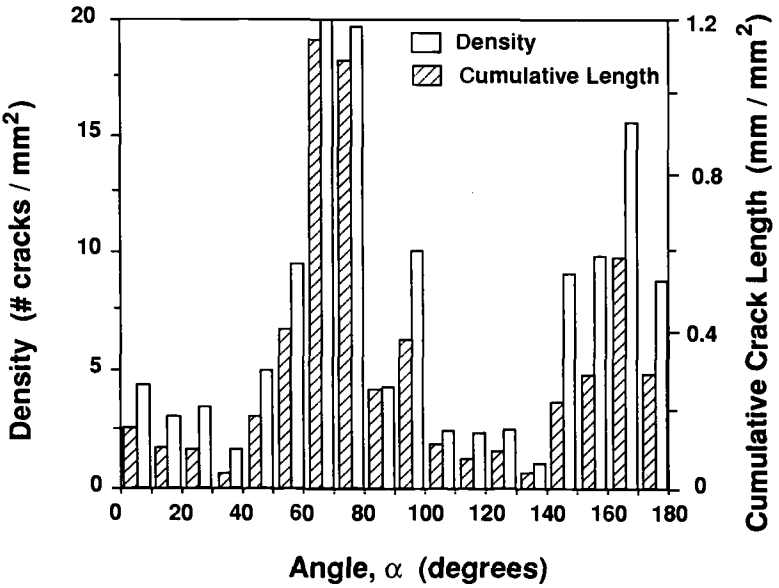

FIG. 11—*Transgranular crack density versus orientation and cumulative crack length versus orientation (in-phase tension-torsion test—*$\Delta\varepsilon/2 = 0.35\% - \Delta\gamma/2 = 0.61\%$*). Replica was taken at Cycle 6000.*

3. Out-of-Phase Tension-Torsion Test

The density of transgranular microcracks versus orientation and the cumulative crack length versus orientation are shown in Fig. 12. There was a well-defined peak around the 0° orientation. The phase difference between tension and torsion distributed the maximum shear strain on planes among all directions. On a plastic shear strain basis, all orientations should be equivalent. The 0° orientation experiences the highest normal stress range. Under out-of-phase loading, the normal stress effect may become more important.

There were practically no directions without cracking. A similar result was obtained by Kanazawa et al. [*13*] on a Cr Mo steel. A significant increase in intergranular microcracks was observed as shown in Fig. 13. There were almost as many intergranular microcracks as transgranular microcracks. Under nonproportional loading, the cyclic stress amplitude was higher. On a cyclic stress amplitude basis, this situation should be equivalent to a uniaxial test with a much higher strain amplitude. For high amplitude uniaxial tests, intergranular microcracking was observed [*1*]. The presence of intergranular cracking should be dependent on cyclic stress amplitude. If one considers the cumulative crack length versus orientation, there were slightly higher values for 0 and 180° than for 90°. There may be an influence of the normal stress across the plane of maximum shear strain amplitude. If this difference existed, it was only a second order effect.

Discussion

Various studies have focused on the fatigue life under different stress states. Some of the more recent studies have clearly demonstrated that the definition of failure strongly affects the correlation of any fatigue theory [*14*]. It has also been demonstrated that the range of stress states which can be achieved in axial-torsional loading is not sufficient, in general, to judge a

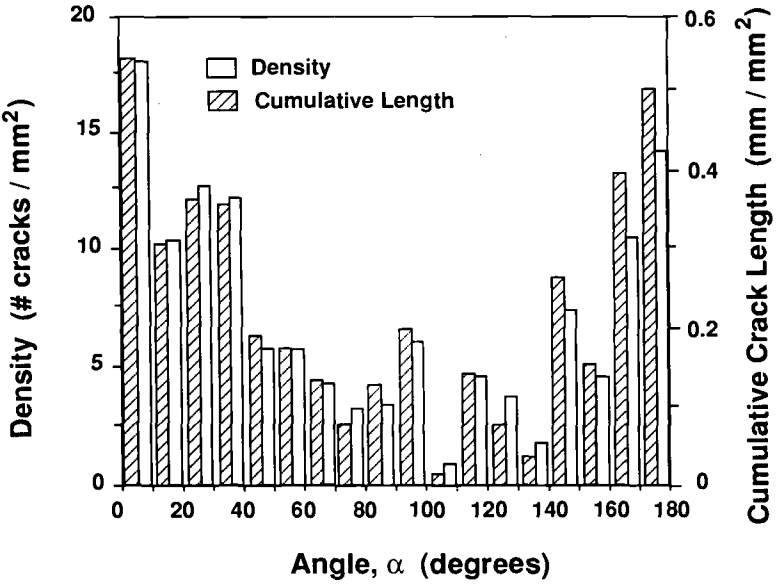

FIG. 12—*Transgranular microcrack density versus orientation and cumulative microcrack length versus orientation (90° out-of-phase tension-torsion test). $\Delta\varepsilon/2 = 0.25\% - \Delta\gamma/2 = 0.43\%$. Replica was taken at Cycle 4400.*

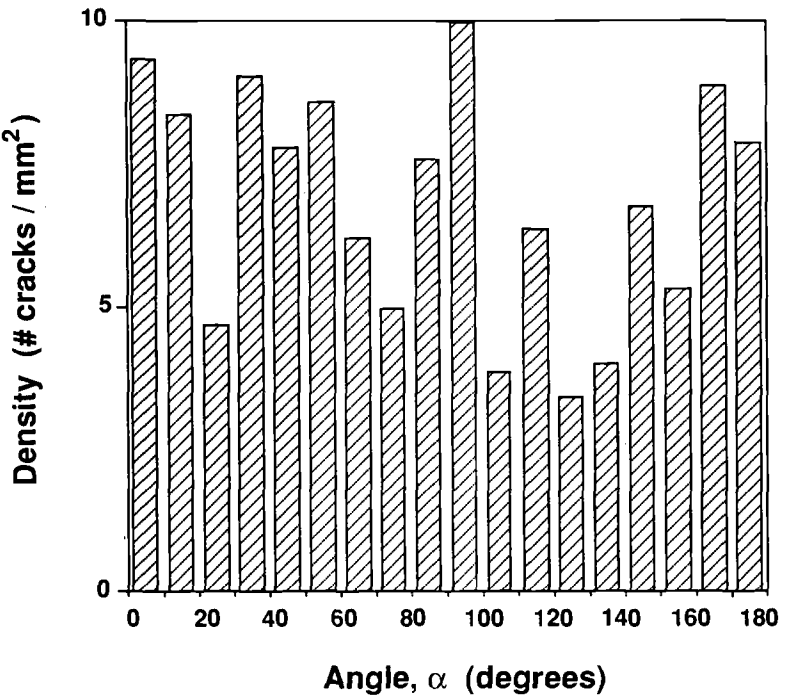

FIG. 13—*Intergranular microcrack density versus orientation (90° out-of-phase tension-torsion test). $\Delta\varepsilon/2 = 0.25\% - \Delta\gamma/2 = 0.43\%$. Replica was taken at Cycle 4400.*

fatigue failure theory [*15–18*]. In spite of this lack of generality afforded by axial-torsional tests, the information regarding crack density and cumulative crack length reported in the previous sections is useful in more fundamentally understanding the nature of fatigue damage evolution. Bérard [*7*] has shown that microcrack propagation in the material of this study can be correlated with the relation

$$\frac{da}{dN} = C(\Delta\bar{\sigma}\Delta\bar{\varepsilon}^p a)^{1.1} \tag{7}$$

for cracks on the order of the grain size up to a few mm in length, where C is a constant. Moreover, Eq 7 was shown to be superior to a purely strain-based crack growth law. Correlation was achieved for torsion, in-phase tension-torsion, and out-of-phase tension-torsion of thin-walled tubular specimens. Referring to Figs. 10 and 11 for the pure torsion and in-phase tests, it is clear that the transgranular fatigue microcracks lie principally along maximum shear strain planes for torsional and in-phase tension-torsion loadings. However, there is also a significant density of transgranular fatigue cracks along planes intermediate to the two maximum shear planes. The first important conclusion from such observations is that fatigue damage has a directional character. For this material, the orientation of maximum fatigue microcracks on the order of 1 mm clearly follows the maximum shear strain planes for in-phase loading and torsion. This feature has been observed for other ductile alloys as well [*5,19*]. However, the damage in orientations intermediate to the maximum shear planes is considerably less. Thus, the interpretation that Eq 7 is equivalent to a plastic work or hysteresis energy approach is misleading; it holds for microcrack growth on maximum shear planes for in-phase loading, which never changes character. However, if the loading changes its biaxial character, then a new directional damage evolution will result, interacting with the existing state of damage. This has been pointed out by Bannantine and Socie [*20*], Doquet and Pineau [*21*], etc. Clearly, fatigue damage is anisotropic, and the driving force for fatigue damage evolution should reflect anisotropy, in general, after accumulation of damage. Isotropic driving forces for fatigue damage, such as hysteresis energy, are inadequate descriptors of the fatigue damage distribution. The fatigue damage evolution rate may be represented adequately by an isotropic tensor function $\mathbf{F}$ [*22*], i.e.,

$$\mathbf{F} = \mathbf{F}(\Delta\sigma_{mn}, \Delta\varepsilon_{kl}, a_0 n_i, a_1 \mathbf{n}_i\mathbf{n}_j, \cdots) \tag{8}$$

where the $\mathbf{n}_i$ are the unit normal vectors to the maximum shear planes (planes of maximum damage), for example. Function $\mathbf{F}$ may depend on the invariants and joint invariants of its arguments. The a_0, a_1, etc. represent damage intensity. Essentially, critical plane fatigue theories address the identification of the appropriate set $\mathbf{n}_i$, representing the anisotropy of fatigue damage evolution [*18–19*]. It should be emphasized that the assignment of the function $\mathbf{F}$ in Eq 8 as an isotropic tensor function should not be confused with material isotropy; this provision ensures material frame indifference of damage evolution, a requirement of continuum mechanics, while permitting arbitrary anisotropy of the fatigue damage field. Indeed, fracture mechanics is based on the concept of critical planes and crack growth is idealized accordingly. As shown by McDowell and Bérard [*18*], the hysteresis energy or plastic work approach is furthermore a very special case even for proportional loading, since uniaxial and torsional experiments do not generally exhibit the same plastic work per cycle for the same life with the same physical failure definition, notwithstanding the anisotropy of fatigue damage.

The fatigue damage measured intermediate to the maximum shear planes for torsional loading (Fig. 10) provides a means of examining damage anisotropy. Since these plots represent

transgranular fatigue damage, the microcrack propagation approach in Eq 7 is especially relevant. From Eq 7, we may write

$$\frac{da}{dN} = 1.92 \times 10^{-4}(\Delta\tau\Delta\gamma^p)^{1.1}a^{1.1} \tag{9}$$

for the pure torsional fatigue, where C is a specific value based on experimentally observed propagation of the failure crack in a torsion test. Assuming that microcracks on other than maximum shear planes are also subjected to predominantly Mode II, Stage I growth, we may write

$$\frac{da(\alpha)}{dN} = 1.92 \times 10^{-4}(\Delta\tau\Delta\gamma^p \cos^2 2\alpha)^{1.1}a^{1.1} \tag{10}$$

for an arbitrary plane at angle α shown in Fig. 3 under pure torsional fatigue. Assuming an initial crack size a_0 for all α, we may integrate Eq 10 to get

$$a(\alpha) = \{-1.92 \times 10^{-5}(\Delta\tau\Delta\gamma^p \cos^2 2\alpha)^{1.1}N_i + a_0^{-0.1}\}^{-10} \tag{11}$$

where N_i is the number of cycles considered.

Alternatively, we may employ the ΔJ-based microcrack propagation model of McDowell and Bérard [*18*], which reduces to Eq 7 in either pure tension or pure torsion. The ratio of normal stress range to shear stress range on each plane under consideration is used to modify the cyclic crack opening behavior. On the maximum shear planes, for axial-torsional loading [*7,18*]

$$\frac{da}{dN} = C_p\left(\beta_p\left(\frac{\Delta\sigma_n/2}{\Delta\tau_n/2}\right)^{J_p+1} + 1\right)^m \left(\frac{\Delta\tau_n}{2}\frac{\Delta\gamma^p}{2}\right)^m a^m \tag{12}$$

Transforming to intermediate planes at an angle α for pure torsional fatigue, we may write

$$\frac{da(\alpha)}{dN} = 1.92 \times 10^{-4}[\tfrac{1}{3}\tan^2 2\alpha + 1]^{1.1}(\Delta\tau\Delta\gamma^p \cos^2 2\alpha)^{1.1}a^{1.1} \tag{13}$$

where $\beta_p = \frac{1}{3}$ and $J_p = 1$ are assumed. The value $\beta_p = \frac{1}{3}$ corresponds to a von Mises normalization of tension and torsion as observed for this material (i.e., $\Delta\bar{\sigma}\Delta\bar{\varepsilon}^p$ is constant for a given life); the J_p value of unity is also representative of other ductile materials studied [*7,18*]. The distribution of crack length which arises from Eq 13 for pure torsional fatigue is given by

$$a(\alpha) = \{-1.92 \times 10^{-5}[\tfrac{1}{3}\tan^2 2\alpha + 1]^{1.1}(\Delta\tau\Delta\gamma^p \cos^2 2\alpha)^{1.1}N_i + a_0^{-0.1}\}^{-10} \tag{14}$$

The angular distribution in Eqs 11 and 14 are very similar. However, the growth law (Eq 12) contains a normal stress effect which contributes to a higher microcrack propagation rate for planes intermediate to the maximum shear planes. For the shear strain amplitude of 1% shown in Fig. 10, using Eq 2 and the torsional fatigue data in Table 3, Eqs 11 and 14 are plotted in Fig. 14. Initial crack length $a_0 = 25$ μm was selected corresponding to a value close to the grain size as shown in Fig. 4. Also appearing in Fig. 14 is the average transgranular crack length angular distribution away from the site of the failure crack after 1500 cycles, the life at which

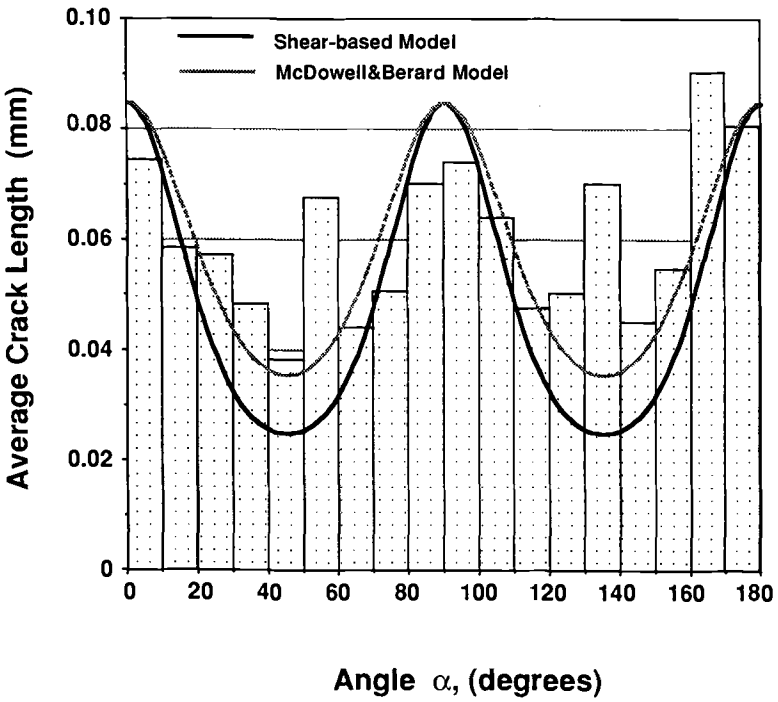

FIG. 14—*Average transgranular microcrack length versus orientation for a torsion test with theoretical predictions.* $\Delta\gamma/2 = 1\%$. *Replica was taken at Cycle 1500.*

a 1-mm crack was first observed. This N_i value was also used in Eqs 11 and 14 to produce Fig. 14. All microcracks in the montage of replicate photographs used to determine the experimental crack distribution in Fig. 14 were less than 400 μm, with approximately 10 to 30 cracks in each 10° orientation. Hence, the distribution is regarded as a statistically significant representation of the average crack length as a function of orientation. This average crack length distribution, obtained by dividing cumulative crack length by crack density for each 10° range, is considered as the logical baseline comparison for the nominal crack length distribution predicted by Eqs 11 and 14, even though the crack growth law constants in Eqs 9 and 13 were determined from tracking replicas of the 1-mm failure crack only. The actual failure crack away from the region considered had a larger initial crack length than the 25-μm value assumed in these calculations, as borne out by replica observation; the initial crack length for the failure crack is estimated from Ref *7* to be 220 μm. Several points can be made with regard to Fig. 14:

1. The microcrack propagation approach is able to capture the essence of the angular distribution of average crack length.
2. The formulation with additional normal stress dependence in Eq 12 appears to provide a better prediction for intermediate angles.
3. Both formulations somewhat underpredict microcrack growth in the maximum principal stress range orientations (α = 45°, 135°).

A very important consequence of this study is that microcrack propagation concepts can evidently be used to correlate damage evolution not only on maximum shear planes as in Ref 7, but also on intermediate planes with higher Mode I/Mode II mixity. In this sense, such an approach is a "critical plane" approach if a plane or set of planes can be identified as having either the highest cyclic driving force or the largest initial defect or perhaps both. Other critical plane theories, with the exception of fracture mechanics for macrocracks, tend to incorporate knowledge of only the driving force into the definition of critical planes. In the microcrack propagation approach, at least three factors can contribute to this definition:

1. Cyclic driving force.
2. Material resistance (e.g., Cp and m functions of α).
3. Initial defect size.

These three factors are directionally dependent. For an initially isotropic material with a uniform angular distribution of initial defects, the cyclic driving force alone may govern the critical plane definition. Otherwise, all the possibilities defy treatment by a model which contains only the driving force and, perhaps, variation of material resistance. An important implication of the foregoing is that cumulative damage for a sequence of multiaxial loading (e.g., torsion followed by tension) cannot be treated in general fashion using parametric cycle fraction concepts [*23–26*] unless these concepts are linked to microcrack distribution. Microcrack propagation approaches offer a means of doing this; in fact, they form the basis for a logical treatment of anisotropic fatigue damage mechanics analogous to that of creep damage mechanics [*27–29*]. The angular crack distribution that arises from one kind of cyclic loading condition may be employed as the initial defect distribution for subsequent loading of a different multiaxial character. The foregoing discussion has related primarily to proportional loading. A more complex issue that deserves further consideration is that of the microcrack distribution during highly nonproportional cyclic loading. It was shown earlier that the distribution of intergranular microcracks was fairly uniform for 90° out-of-phase loading, possibly due to exposure of more grain boundary precipitates (or phases) to high tensile stress. From the plot in Fig. 12, it appears that the distribution is biased towards the 0° (hoop) orientation of the tube, the orientation with the highest normal stress amplitude. All orientations in this case have essentially the same shear stress and strain ranges.

Conclusion

Physical damage was observed for different states of stress under tension-torsion loading. It consisted of an array of microcracks showing preferential orientations with respect to the loading directions. Microcracks initiated and propagated along directions of maximum shear strain. The material can be considered as a shear damaging material. Quantitative measurements of microcrack density and average length were performed. Transgranular microcracking was dominant for all states of stress except nonproportional tension-torsion loading where there was a significant number of intergranular microcracks. Fatigue damage approaches which do not consider the anisotropy of the fatigue damage evolution cannot describe the experimental observations. A shear-based microcrack propagation approach is discussed which can correlate the damage in critical orientations (maximum shear planes) for each loading condition considered. However, as shown here, it captures the trend but not the details of fatigue microcracking in other orientations. Neglect of the role of normal stress on these intermediate planes is a possible reason for this deficiency. The need for a fully anisotropic fatigue damage evolution model based on microcrack propagation is highlighted by the results.

References

[1] Bérard, J. Y., "Low Cycle Fatigue Behavior of a Low Carbon Steel," masters thesis, Georgia Institute of Technology, Atlanta, March 1989.

[2] McDowell, D. L., "A Two Surface Model for Transient Nonproportional Cyclic Plasticity," *Journal of Applied Mechanics,* June 1985, Vol. 52, pp. 298–315.

[3] Benallal, A. and Marquis, D., "Constitutive Equations for Nonproportional Cyclic Elasto-Viscoplasticity," *Journal of Engineering Materials and Technology, ASME,* Vol. 109, 1987, pp. 326–336.

[4] Socie, D. F., Waill, L. A., and Dittmer, D. F., "Biaxial Fatigue of Inconel 718 Including Mean Stress Effects," *Multiaxial Fatigue, ASTM STP 853,* K. J. Miller and M. W. Brown, Eds., American Society for Testing and Materials, Philadelphia, 1985, pp. 463–481.

[5] Fatemi, A. and Socie, D., "A Critical Plane Approach to Multiaxial Fatigue Damage Including Out of Phase Loading," *Fatigue Fracture of Engineering Materials and Structures,* 1988, Vol. 11, No. 3, pp. 149–165.

[6] Beer, T., "Crack Shapes During Biaxial Fatigue," *Report No. 106,* College of Engineering, University of Illinois at Urbana-Champaign, May 1984, UILU-ENG 84-3606.

[7] Bérard, J. Y., "A Micromechanical Approach to Biaxial Low Cycle Fatigue," Ph.D. thesis, Georgia Institute of Technology, Atlanta, June 1990.

[8] Saxena, A. and Antolovich, S. D., "Low Cycle Fatigue Crack Propagation and Substructures in a Series of Polycrystalline Cu Al Alloys," *Metallurgical Transactions A,* Vol. 6A, 1975, pp. 1809–1814.

[9] Fash, J., "An Evaluation of Damage Development During Multiaxial Fatigue of Smooth and Notched Specimens," *Report No. 123,* College of Engineering, University of Illinois at Urbana-Champaign, August 1985, UILU-ENG 85-3607.

[10] Hua, C. T., "Fatigue Damage and Small Crack Growth During Biaxial Loading," *Report No. 109,* College of Engineering, University of Illinois at Urbana-Champaign, July 1984, UILU-ENG 84-3009.

[11] De Los Rios, E. R., Kandil, F. A., Miller, K. J., and Brown, M. W., "A Metallographic Study of Multiaxial Creep-Fatigue Behavior in 316 Stainless Steel," *Multiaxial Fatigue, ASTM STP 853,* K. J. Miller and M. W. Brown, Eds., American Society for Testing and Materials, Philadelphia, 1985, pp. 669–687.

[12] Jacquelin, B., Hourlier, F. and Pineau, A., "Crack Initiation Under Low-Cycle Multiaxial Fatigue," *Multiaxial Fatigue, ASTM STP 853,* K. J. Miller and M. W. Brown, Eds., American Society for Testing and Materials, Philadelphia, 1985, pp. 285–313.

[13] Kanazawa K., Brown, M. and Miller, K. J., "Low Cycle Fatigue Under Out of Phase Loading Conditions," *Journal of Engineering Materials and Technology, ASME,* 1977, pp. 222–228.

[14] Bannantine, J. and Socie, D., "Observations of Cracking Behavior in Tension and Torsion Low Cycle Fatigue," *Low Cycle Fatigue, ASTM STP 942,* H. Solomon, G. Halford, L. Kaisand, and B. Leis, Eds., American Society for Testing and Materials, Philadelphia, 1988, pp. 899–921.

[15] Brown, M. W. and Miller, K. J., "Two Decades of Progress in the Assessment of Multiaxial Low Cycle Fatigue," *Low Cycle Fatigue and Life Prediction, ASTM STP 770,* C. Amzallag, B. Leis, and P. Rabbe, Eds., American Society for Testing and Materials, Philadelphia, 1982, pp. 482–499.

[16] Miller, K. J., "Metal Fatigue—Past, Current and Future," *Proceedings of the Institution of Mechanical Engineers, London,* 27th John Player Lecture, 1991.

[17] Lohr, R. and Ellison, E., "A Simple Theory for Low Cycle Multiaxial Fatigue," *Fatigue of Engineering Materials and Structures,* Vol. 3, 1980, pp. 1–17.

[18] McDowell, D. L. and Bérard, J. Y., "A ΔJ Based Approach to Biaxial Low Cycle Fatigue of Shear Damaged Materials," *Fatigue under Biaxial and Multiaxial Fatigue,* ESIS 10, Kussmaul, McDiarmid, and Socie, Eds., Mechanical Engineering Publications Ltd, London, 1991, pp. 413–432.

[19] Socie, D., "Multiaxial Fatigue Damage Models," *ASME Journal of Engineering Materials Technology,* Vol. 109, 1987, pp. 293–298.

[20] Bannantine, J. and Socie, D., "A Variable Amplitude Multiaxial Fatigue Life Prediction Method," *Fatigue under Biaxial and Multiaxial Fatigue,* ESIS 10, Kussmaul, McDiarmid and Socie, Eds., Mechanical Engineering Publications, Ltd, London, 1991, pp. 35–51.

[21] Doquet V. and Pineau, A., "Multiaxial Low Cycle Fatigue Behavior of a Mild Steel," *Fatigue under Biaxial and Multiaxial Fatigue,* ESIS 10, Kussmaul, McDiarmid, and Socie, Eds., Mechanical Engineering Publications, Ltd, London, 1991, pp. 81–101.

[22] Wang, C. C., "A New Representation Theorem for Isotropic Functions," Parts 1&2 *Archives of Rational Mechanics Analysis,* Vol. 36, 1970, p. 166.

[23] Lemaitre, J. and Plumtree, A., "Application of Damage Concepts to Predict Creep-Fatigue Failures," *ASME Journal of Engineering Materials and Technology,* Vol. 101, 1979, pp. 284–292.
[24] Bui-Quoc, T. and Biron, A., "A Phenomenological Approach for the Analysis of Combined Fatigue and Creep," *Nuclear Engineering and Design,* Vol. 71, 1982, pp. 89–102.
[25] Bui-Quoc, T., "Recent Developments of Damage Concepts Applied to Creep-Fatigue Combinations," Post-Conference Seminar on Inelastic Analysis and Life Prediction in High Temperature Environment, SMIRT-6, 1981, Paris.
[26] Manson, S. S., Halford, G. R., and Hirschberg, M. H., "Creep-Fatigue Analysis by Strain Range Partitioning," NASA TM X-67838, 1971.
[27] Kachanov, L., *Fundamentals of Fracture Mechanics,* Nauka, Moscow, 1974.
[28] Rabotnov, Y. N., *Creep Problems in Structural Members,* North Holland, Amsterdam, 1969.
[29] Chaboche, J. L., "Continuum Damage Mechanics: Present State and Future Trends," ONERA T.P. No. 1986-53, Séminaire Int. sur l'Approche Locale de la Rupture, Moret sur Loing, 3–5 Juin 1986.

Richard E. Link[1]

Mixed Mode Fatigue Crack Growth Behavior in a High-Strength Steel

REFERENCE: Link, R. E., **"Mixed Mode Fatigue Crack Growth Behavior in a High-Strength Steel,"** *Advances in Multiaxial Fatigue, ASTM STP 1191,* D. L. McDowell and R. Ellis, Eds., American Society for Testing and Materials, Philadelphia, 1993, pp. 345–358.

ABSTRACT: Most of the currently available methods for predicting fatigue crack growth in structures do not consider effects due to mixed-mode loading. This is partly due to the limited information available concerning the fatigue crack growth under mixed mode loading. Previous investigations of mixed mode effects on fatigue crack growth have shown that under combined opening and in-plane shear loading, the cracks turn abruptly so that the in-plane shear mode is eliminated [*1–3*]. Very little data are generated before the crack curvature eliminates the mixed mode loading. The changing orientation of the crack during the test makes analysis of the problem difficult and may cloud the intrinsic fatigue crack growth rate behavior under mixed mode loading. Situations can exist in engineering structures in which cracks may grow in a self-similar manner even under the influence of mixed mode loading. Examples of such situations are radial cracks in bearing races [*4*] and transverse cracks in rotating shafts under shear and bending loads. The cracks may not change orientation because the in-plane shear component is fully reversed. It is necessary to understand the effects of mixed mode loading on fatigue crack growth in order to properly predict the behavior of these components.

This paper presents the results of an investigation to measure the fatigue crack growth rate of a high-strength steel under various ratios of mixed mode loading while maintaining self-similar crack growth. A primary objective of this investigation was to generate data for relatively large amounts of crack growth under a wide range of mixed mode ratios. Several models for predicting the mixed mode fatigue crack growth rate from opening mode data are evaluated based on the data generated in this investigation.

KEY WORDS: fatigue crack growth, mixed mode fatigue, predictive models

The majority of research on the topic of fatigue crack growth has been concerned with opening mode loading of a crack. Relatively little work has been conducted in the area of combined or mixed mode loading. One of the earliest investigations into mixed mode fatigue crack growth was conducted by Iida and Kobayashi [*1*]. They tested center-cracked panels of aluminum with the crack oriented at various angles with respect to the tensile axis of the specimen to generate mixed mode loading. The amount of data generated was limited, but they reported increases in crack growth rate by a factor of two over that measured for Mode I loading at the same ΔK_I level. Tanaka [*5*] employed a similar specimen to investigate the threshold condition under mixed mode loading. He developed several models for calculating an equivalent stress intensity factor range, ΔK_{eq}, to correlate opening and mixed mode fatigue crack growth rate data. The equivalent stress intensities were based on fatigue crack growth models proposed by Weertman [*6*] and Lardner [*7*]. The Weertman model assumes that the crack advances when the sum of the absolute value of displacement at the crack tip reaches a critical value,

[1] Senior mechanical engineer, Fatigue and Fracture Branch, David Taylor Research Center, Annapolis, MD 21402.

and the Lardner model assumes that the growth rate is equal to the amount of reverse displacement at the crack tip. The crack tip displacements were calculated from the Bilby, Cottrell, and Swinden model for plastic yielding ahead of a crack. Tanaka generalized the models to the case of mixed mode loading and cast the fatigue crack growth law in the form

$$da/dN = C(\Delta K_{eq})^m \tag{1}$$

The equivalent stress intensity for the Weertman model was given as

$$\Delta K_{eq} = (\Delta K_I^4 + 8\Delta K_{II}^4)^{1/4} \tag{2}$$

and for the Lardner model

$$\Delta K_{eq} = (\Delta K_I^2 + 2\Delta K_{II}^2)^{1/2} \tag{3}$$

An approach utilizing the strain energy density factor range was proposed by Sih and Barthelemy [*8*] and later modified by Lam [*9*]. This theory was used to predict the results reported by Pustejovsky [*10*] for fatigue crack growth in titanium from an inclined center crack. The crack growth law is expressed as

$$\Delta a/\Delta N = C(\Delta S_{p,eff})^n \tag{4}$$

where $\Delta S_{p,eff}$ is

$$\Delta S_{p,eff} = 2/\pi[a_{11}(\theta)\Delta K_{I,eff}^2 + a_{12}(\theta)\Delta K_{I,eff}\Delta K_{II,eff} + a_{22}(\theta)\Delta K_{II,eff}^2 + a_{33}(\theta)\Delta K_{III,eff}^2] \tag{5}$$

and the coefficients, $a_{ij}(\theta)$, are functions of the elastic constants and the crack growth direction relative to the original crack plane, θ, and ΔK_{eff} is the stress intensity range corrected for crack closure [*8*]. The crack is assumed to grow in the direction of the minimum strain energy density, S_{min}.

More recently, Li [*11*] has described a general parameter, the vector crack tip displacement, $\overline{\mathbf{CTD}}$, to describe mixed mode fatigue crack growth. The vector $\overline{\mathbf{CTD}}$ is the vector sum of crack tip displacements associated with the opening and sliding modes of loading ($\overline{\mathbf{CTOD}}$ and $\overline{\mathbf{CTSD}}_e$, respectively). The direction of the component vectors is in the direction of crack growth that each mode of loading produces (45° to the maximum shear stress). The fatigue crack growth law is

$$da/dN = c(\Delta\mathbf{CTD})^m \tag{6}$$

where

$$\Delta\mathbf{CTD} = 4/(\pi\sigma_s E)[(\Delta K_I^2 + 3\Delta K_{II}^2)(\Delta K_I^2 + 2\Delta K_{II}^2 + 2\Delta K_I\Delta K_{II})^{1/2} \tag{7}$$

A common observation made in all of the previous investigations was that the crack would kink immediately upon initiation and tend to grow in a direction that minimized or eliminated the K_{II} component. Consequently, the majority of the mixed mode data in the literature has only a very small K_{II} component associated with it. Only Tanaka reported data for self-similar crack growth along the direction of the inclined crack. It was noted that self-similar growth was only seen when ΔK_{eff} was greater than 1.6 times the threshold stress intensity measured under mixed mode loading [*5*]. Furthermore, because the cracks kinked, the analyses

had to incorporate either an approximation or calculation of the stress intensity factor for a kinked crack, possibly clouding the intrinsic mixed mode crack growth behavior. More recently, Bold, Brown, and Allen [*12*] were able to achieve self-similar crack growth by sequentially loading a crack in pure Mode I followed by pure Mode II to simulate the loading history of shallow surface cracks subjected to rolling contact fatigue. They reported an increase in crack growth rate up to an order of magnitude over pure Mode I loading. Otsuka et al. have conducted several investigations of fatigue crack growth under Mode II loading and mixed mode loading. They reported that the conditions for generating self-similar crack growth under mixed mode loading are very material sensitive [*13,14*].

The objective of this investigation was to measure the fatigue crack growth rate for several mixed mode ratios while avoiding the added complexity of a kinked crack. By decoupling the problem into separate issues of mixed mode growth rate and crack kinking, it may be possible to develop a more complete understanding of the general mixed mode problem.

Details of Testing

Material Investigated

The material used in this study was a quenched and normalized Ni-Cr-Mo steel produced to MIL-S-23284, Class 2 [*15*] from a 406-mm-diameter forging. The chemical composition and material properties (designated GOH) are listed in Table 1 together with the specification requirements. The microstructure consisted of ferrite and spheroidized carbides and was uniformly fine-grained. The fatigue cracks were oriented in the L-R orientation.

Specimen Details

The specimen utilized in this investigation was a compact shear specimen developed by Richard and used in earlier studies of brittle fracture and fatigue crack growth under mixed Modes I and II loading [*16,17*]. The specimen and loading grip dimensions are detailed in Fig. 1. The Modes I and II stress intensity factors, K_I and K_{II}, were determined by Richard using finite element analysis and the results were reported in the form of graphs in Ref *16*. By fitting

TABLE 1—*Chemical composition and mechanical properties of Class 2 steel used in this investigation and specification requirements. (Elements values in weight percent.)*

	Actual Analysis	MIL-S-23284, Class 2
Carbon	0.22	0.26 max
Manganese	0.35	0.15–0.45
Phosphorous	0.002	0.020 max
Sulfur	0.005	0.020 max
Silicon	0.23	0.35 max
Nickel	2.91	2.75–3.50
Chromium	0.38	0.50 max
Molybdenum	0.56	0.25–0.60
Vanadium	0.05	0.05 max
0.01% yield strength, MPa	517	379 min
0.2% yield strength, MPa	490	...
Ultimate tensile strength, MPa	621	552–689
Elongation in 51 mm, %	28	22 min
Reduction of area, %	69	45 min

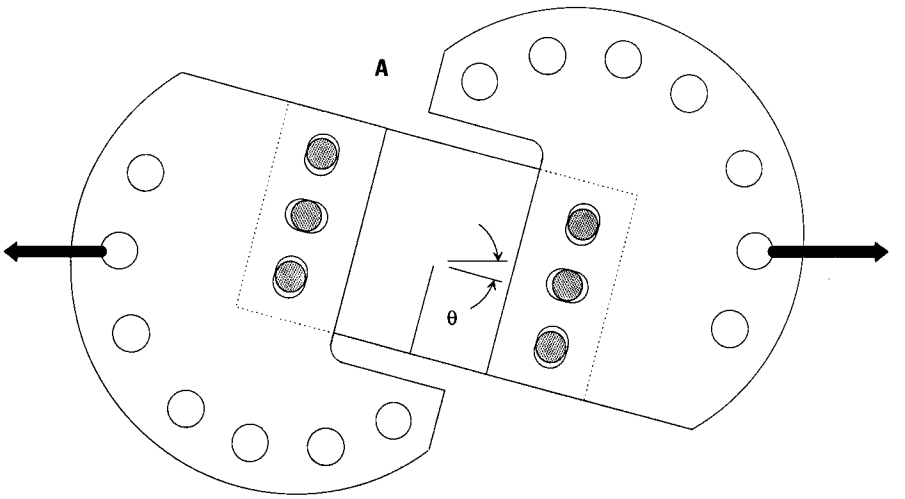

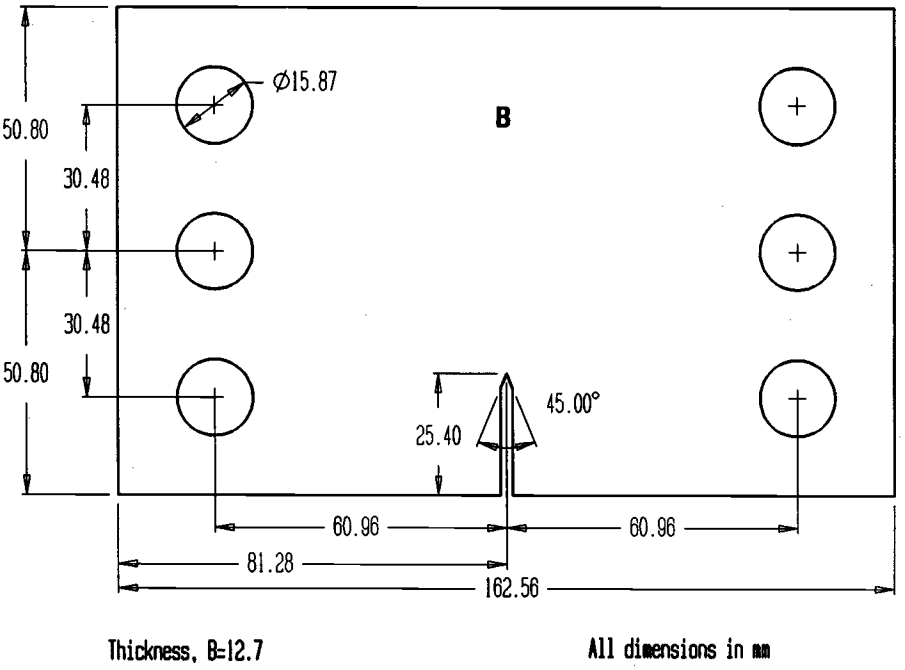

FIG. 1—(A) *Schematic drawing of the Richard mixed modes specimen and fixture used for mixed mode fatigue tests;* (B) *specimen, and* (C) *grip details.*

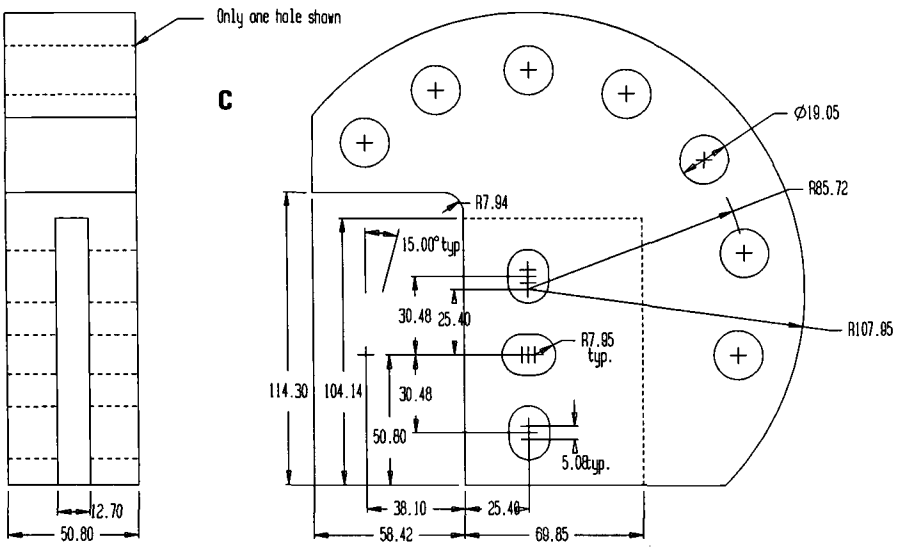

FIG. 1—*Continued.*

polynomial expressions to the graphical results of Richard, the stress intensity factors can be expressed as

$$K_{\mathrm{I}} = P(\pi a)^{1/2} F_{\mathrm{I}}/(WB_{\mathrm{eff}}) \tag{8}$$

$$K_{\mathrm{II}} = P(\pi a)^{1/2} F_{\mathrm{II}}/(WB_{\mathrm{eff}}) \tag{9}$$

where

$$F_{\mathrm{I}}(a/W, \theta) = [-5.05 + 85.60(a/W) - 442.79(a/W)^2 + 1122.8(a/W)^3 - 1358.4(a/W)^4 + 651.37(a/W)^5] \cos\theta,$$

$$F_{\mathrm{II}}(a/W, \theta) = [0.369 + 2.0663(a/W)] \sin\theta,$$

a = crack length,
W = specimen width,
$B_{\mathrm{eff}} = (BB_N)^{1/2}$,
B = specimen gross thickness,
B_N = specimen net thickness, and
θ = angle between crack plane and loading axis.

As the crack length increases, the ratio of $K_{\mathrm{II}}/K_{\mathrm{I}}$ varies as shown in Fig. 2 for several discrete values of θ. In general, the $K_{\mathrm{II}}/K_{\mathrm{I}}$ ratio decreases by a factor of 2 from the initial value at $a/W = 0.4$ to 0.7.

The tests were conducted in a computer-controlled, servo-hydraulic testing machine. The computer continuously monitored and periodically recorded load, crack length, number of cycles, and closure levels online. Crack length was monitored using reversed polarity d-c potential drop with a reference specimen connected in series. The current was maintained at 20 A. The use of reversed current and a reference specimen made it possible to compensate for voltage changes due to temperature fluctuations and thermal EMFs [*18*]. A photograph of the specimen, grips, and reference specimen is shown in Fig. 3.

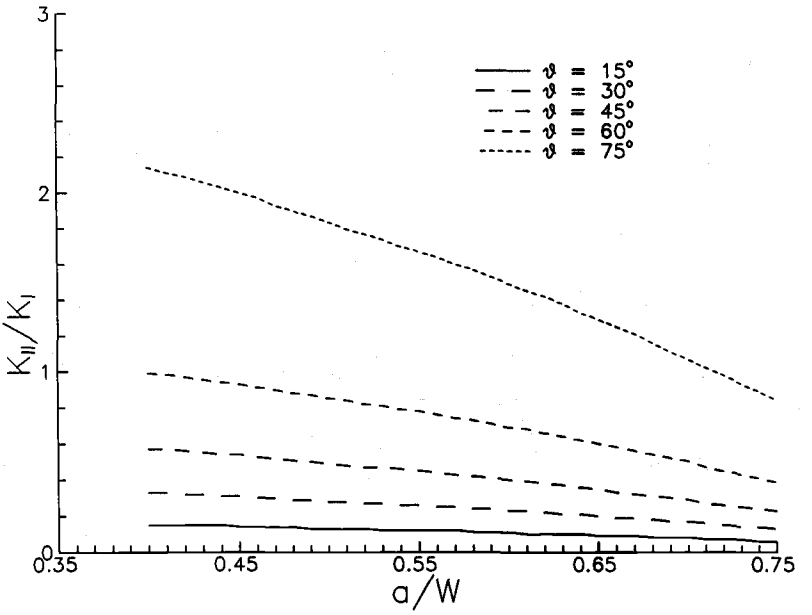

FIG. 2—$\Delta K_I/\Delta K_{II}$ *as a function of crack length for several values of the loading angle,* θ.

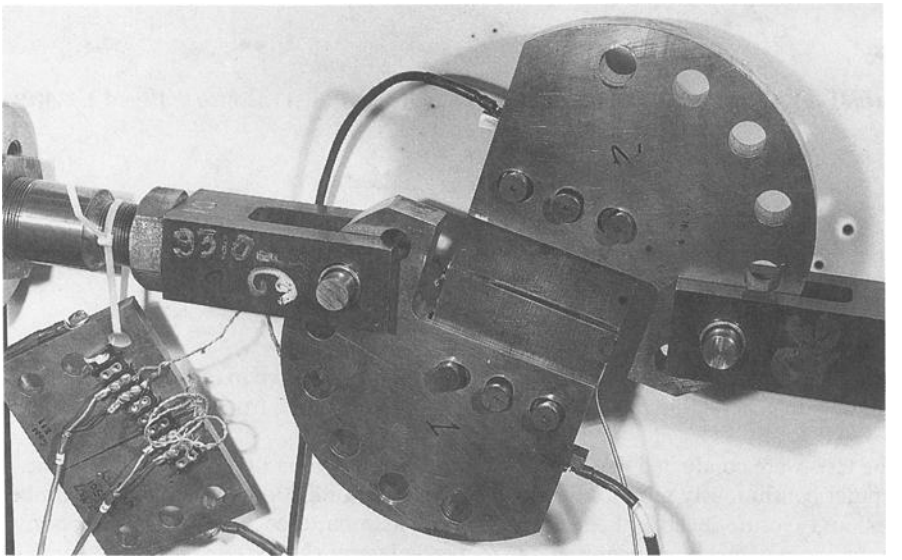

FIG. 3—*Photograph of the specimen in the grips. The reference specimen is visible in the lower left portion of the photograph.*

Mode I fatigue cracks were initiated by cyclic loading at an angle $\theta = 0$. The Mode I cracks were grown for a short distance at a constant ΔK_I, and then ΔK was gradually decreased to maintain C within the range $-0.08\ \text{mm}^{-1} \leq C \leq -0.04\ \text{mm}^{-1}$, where $C = (1/K)(dK/da)$, in accordance with the requirements of ASTM Test Method for Measurements of Fatigue Crack Growth Rates (E 647). During the decreasing ΔK portion, fatigue crack growth rate data under the pure Mode I condition were recorded. Following precracking, the grips were reoriented in the testing machine at an angle, θ, and mixed mode testing commenced with constant amplitude loading, stress ratio of 0.1 using a sinusoidal waveform at a frequency of 5 Hz.

In order to promote self-similar crack growth, side grooves were machined into the specimens. Initially, each side groove was 5% of the specimen thickness. These generally proved to be ineffective in maintaining control of the crack plane, as shown in Fig. 4. The side grooves only restrained the crack path at the specimen surface and only for a very short distance. Very deep side grooves of 30% of the specimen thickness (total reduction of 60%) were used to see if it would be at all possible to restrict the crack path to the specimen centerline. The deeper side grooves were partially successful in controlling the crack path. At the start of mixed mode loading, the crack would try to deviate from the intended plane. In most cases, the crack would abruptly reorient itself and start growing out of the side groove. This tendency was strongest at the mid-thickness point. After a small amount of crack growth, the crack would arrest, probably as a result of the reduced driving force due to the greater thickness as the crack grew out of the side groove. This behavior was observed for a number of tests, with K_{II}/K_I ratios varying from 0.5 to 2. Results from these tests were discarded. However, for three tests, the crack stayed nominally along the intended plane for a considerable distance. This behavior was only observed at relatively fast growth rates ($> 10^{-7}$ m/cycle). At longer crack lengths the 30% side groove was no longer capable of controlling the crack path and the crack would grow out of the side groove. A typical fracture surface from a mixed mode specimen with 30% side grooves is shown in Fig. 5. The $\Delta K_{II}/\Delta K_I$ ratio in this test varied from 1 to 2.

For one of the mixed mode tests, a single element strain gage was located on the back face of the specimen and used to detect crack closure and calculate an effective stress intensity. The automated technique discussed by Donald [*19*] was employed, except that the strain gage signal was utilized instead of a clip gage. The opening loads were on the order of 20% of the maximum load. The closure was primarily due to the irregular fracture surface resulting from the

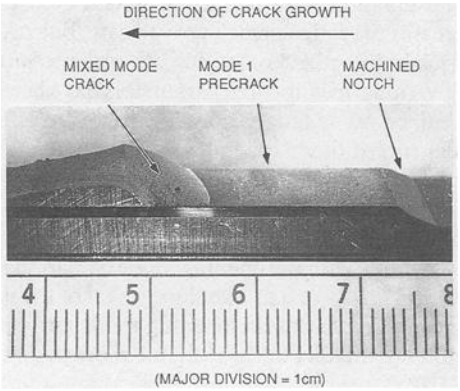

FIG. 4—*Photograph of the fracture surface of a specimen with 5% side grooves showing the crack deviating from the side groove.*

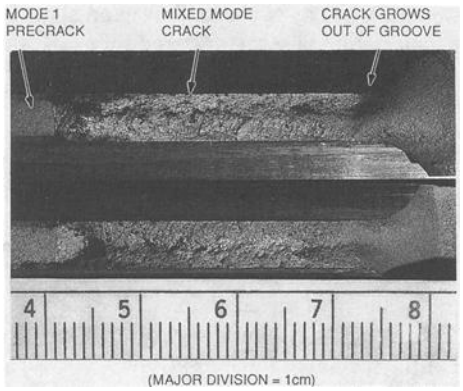

FIG. 5—*Fracture surface from specimen which exhibited self-similar mixed mode fatigue crack growth.*

nonplanar crack growth. There was evidence of fretting damage at many locations on the fracture surface as indicated by the dark areas in Fig. 5. It may well be possible that the closure levels for the Modes I and II components are different, but no independent measurements of individual closure levels was attempted. For purposes of calculation, it was assumed that the closure measured using the back face strain gage had an equal effect on reducing both the Mode I and Mode II stress intensities.

Results

The results for three tests with K_{II}/K_I ratios between 0.3 and 2 are presented in Fig. 6. The crack growth rate is plotted as a function of the opening mode stress intensity, ΔK_I. Also shown in the figure for reference is the fatigue crack growth rate measured under pure opening mode using a center-cracked specimen for the slow growth rates, and a Richard specimen with $\theta = 0°$ was used for the higher growth rates. Closure-corrected data are plotted with open symbols. Data from the mixed mode tests were restricted to portions of the test where the crack growth was nominally "steady-state." At the beginning of mixed mode loading when the crack tried to grow out of the side groove, the data showed excessive scatter (several orders of magnitude) and was not included in the evaluation of the predictive models. It would appear that the introduction of shear loads increases the fatigue crack growth rate, but ΔK_I alone underestimates the driving force on the crack in the mixed mode case. In order to more accurately represent the crack growth behavior, various driving force parameters have been utilized.

The various models for mixed mode fatigue crack growth were assessed by comparing the growth rate measured under mixed mode loading with the opening mode data, plotted as a function of the various "effective" driving force parameters. The crack growth rate is plotted as a function of an effective stress intensity factor developed by Tanaka, Eq 1, assuming that crack growth occurs according to the Weertman model, in Fig. 7. The model adjusts the mixed mode data so that it is nearly in line with the opening mode data for $\Delta K_{II}/\Delta K_I > 1$, but underestimates the growth rate for $\Delta K_{II}/\Delta K_I < 0.5$. The slopes of all of the mixed mode growth rate curves are consistently higher than that of the opening mode curve. The Lardner model of crack growth, Eq 2, tends to underpredict the growth rate more than the Weertman model, as shown in Fig. 8.

The results from using the strain energy density criterion, Eq 4, are plotted in Fig. 9, and the data are plotted as a function of the CTD criterion proposed by Li [*10*], Eq 5, in Fig. 10. Again,

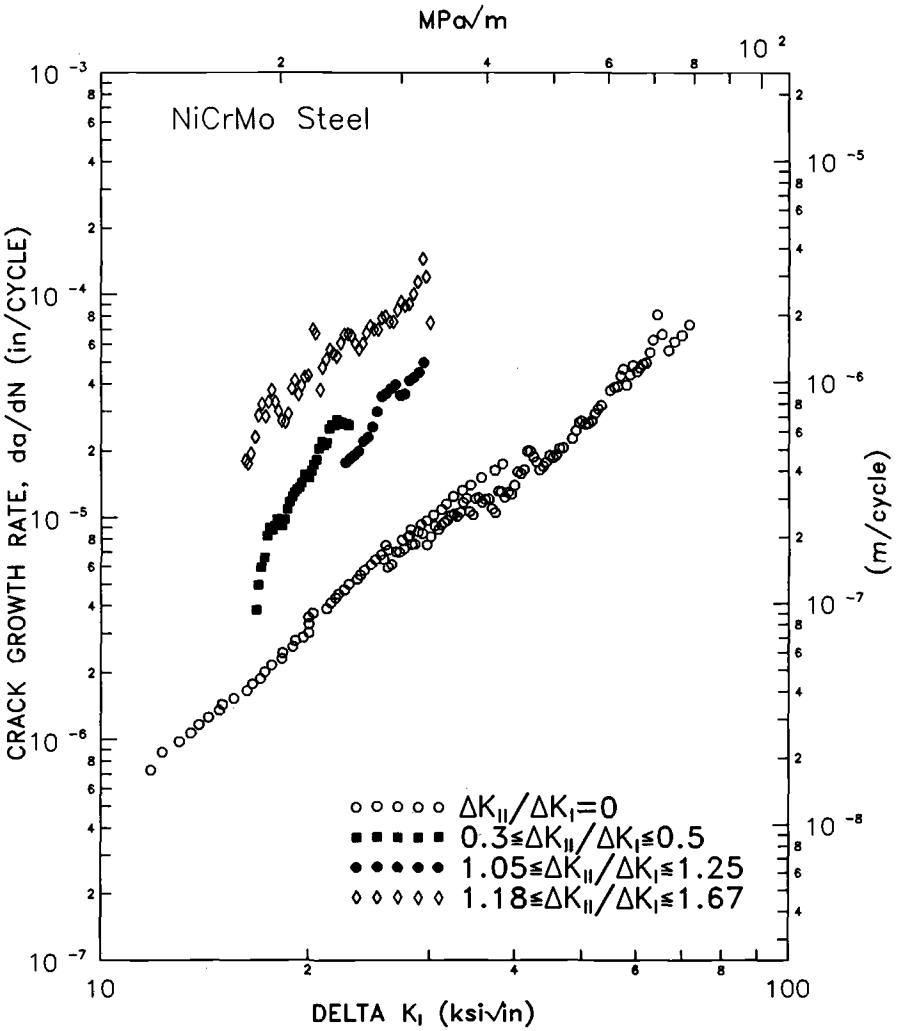

FIG. 6—*Fatigue crack growth rate as a function of opening mode stress intensity for several ratios of mixed mode loading. (Open symbols denote closure-corrected data.)*

there is a distinct difference in the slopes of the mixed mode results relative to the opening mode results.

Discussion

It proved difficult to conduct replicate tests that would add confidence to the experimental results. Several attempts were made to reproduce the data for the case of $\Delta K_{II}/\Delta K_I = 0.3$ to 0.5, but the crack always left the side groove immediately. From the limited data available from this investigation, it is difficult to make definitive statements about the applicability of the existing theories.

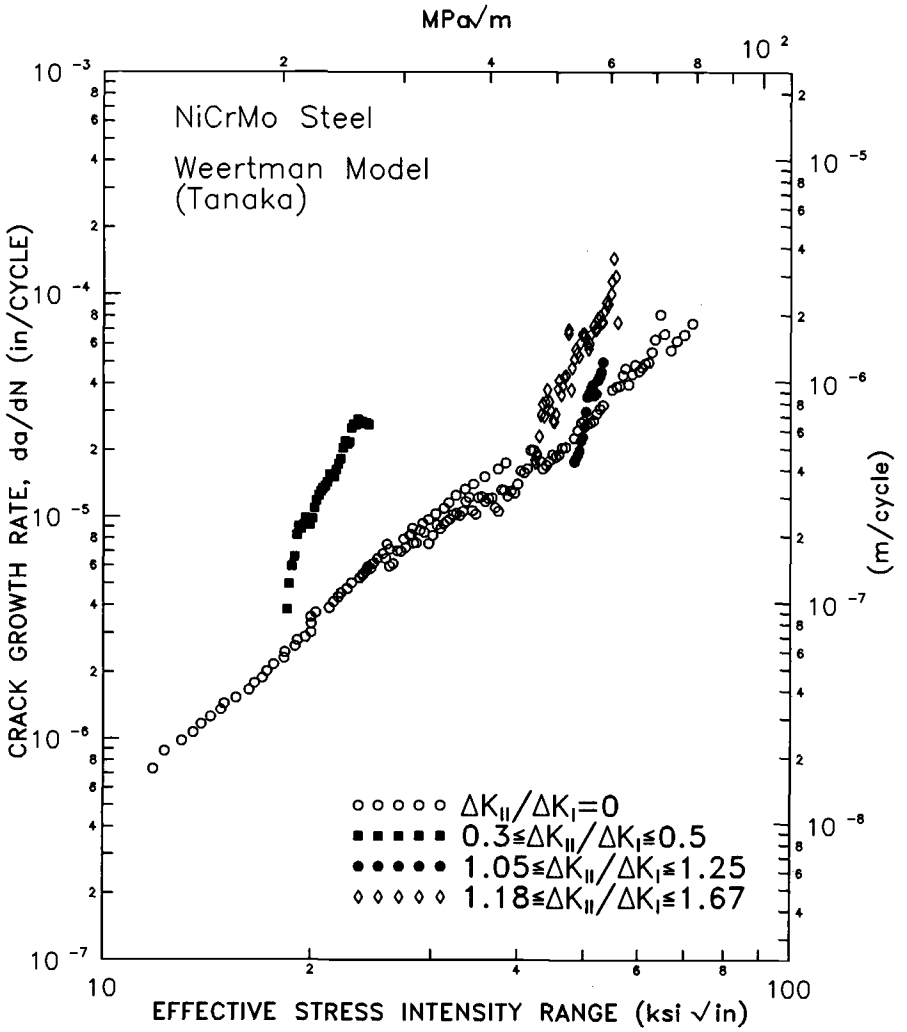

FIG. 7—*Fatigue crack growth rate as a function of* ΔK_{eff} *developed by Tanaka using the Weertman model of fatigue crack growth. (Open symbols denote closure-corrected data.)*

An implicit assumption in all of the theories is that the micromechanism of fatigue crack growth is the same under mixed mode loading as it is under opening mode loading. This is a necessary assumption if opening mode data is used to predict mixed mode behavior. Referring to Figs. 7 to 10, the mixed mode growth rate data has a higher slope regardless of the model used. It is quite possible that the steeper slope of the mixed mode data is indicative of a different or additional mechanism leading to an increased growth rate.

It was assumed that the presence of side grooves could be accounted for by using an effective thickness, B_{eff}. There may be higher order effects associated with the presence of deep side grooves that were not considered. A 3-D finite element analysis would probably be required to address this issue. It was observed that the side grooves led to reversed tunneling at the higher growth rates (Fig. 11). This behavior was also observed by Otsuka et al. [*14*] on smooth-sided specimens under cyclic Mode II loading, although to a much smaller degree. It was also

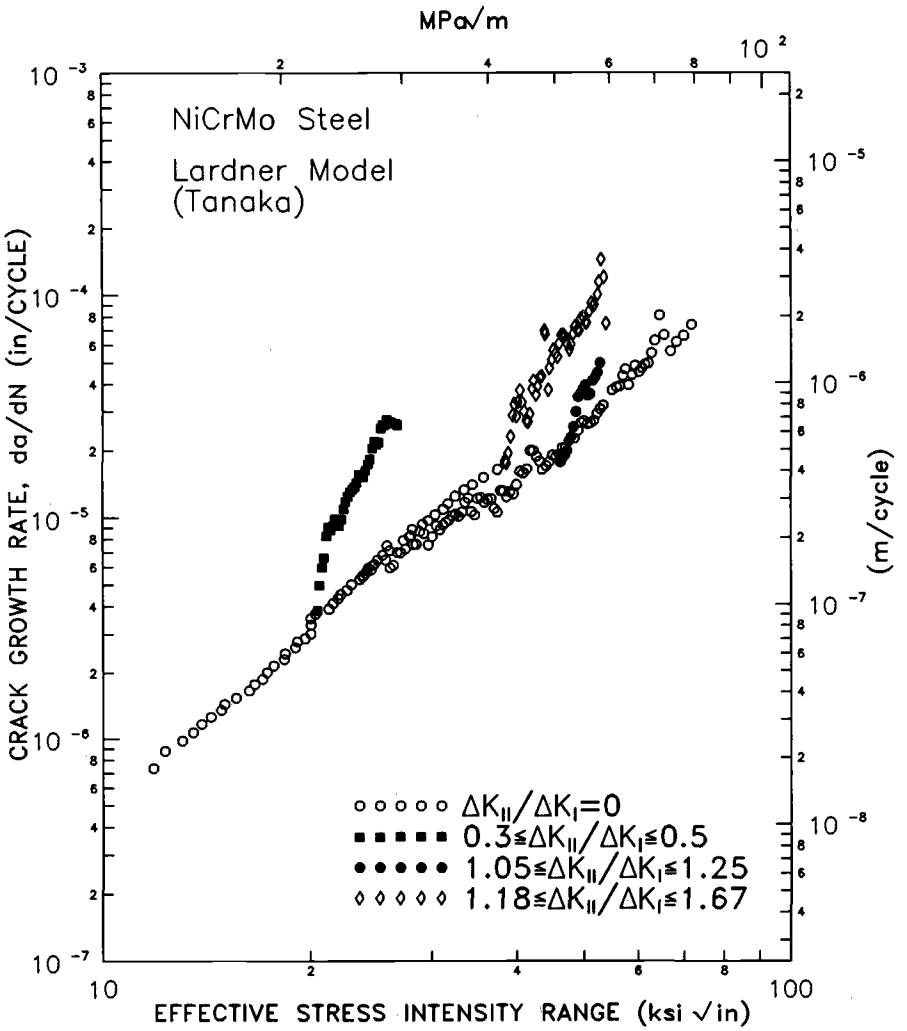

FIG. 8—*Fatigue crack growth rate as a function of* ΔK_{eff} *developed by Tanaka using the Lardner model of fatigue crack growth. (Open symbols denote closure-corrected data.)*

assumed that the closure levels determined using a back face strain gage were equal for both the Mode I and Mode II components. It is quite possible that the Mode II opening loads were higher than the Mode I opening loads because the rough fracture surfaces may interlock, thus preventing relative sliding between the two surfaces. If the Mode II opening loads were indeed higher than assumed, then the calculated effective driving force would be lower, further reducing the correlation between the opening and mixed mode data.

It has been shown previously that fatigue crack growth rate is a function of the size cyclic plastic zone at the crack tip [*20*] and that mixed mode fatigue crack growth rate thresholds are lower than opening mode thresholds because of enhanced plasticity at the crack tip under mixed mode loading [*21*]. In order to correlate the mixed mode and opening mode data, it may be necessary to perform elastic-plastic finite element analyses of mixed mode crack tip fields to determine the size and shape of the cyclic plastic zones.

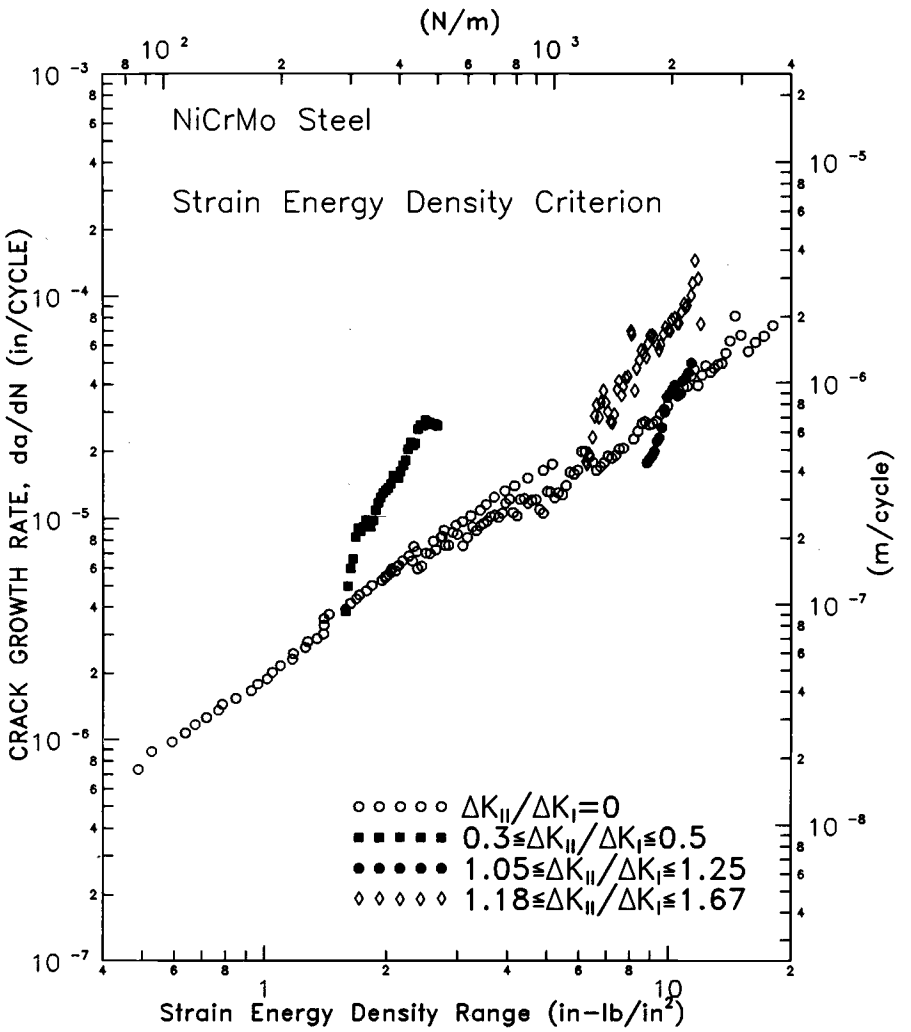

FIG. 9—*Fatigue crack growth rate as a function of the cyclic strain energy density factor, ΔS. (Open symbols denote closure-corrected data.)*

Summary

Fatigue crack growth rate tests were conducted on a Ni-Cr-Mo steel under mixed mode loading. Deeply side-grooved specimens were used in order to restrict the crack path in an attempt to force self-similar crack growth. The objective was to eliminate the added complexity of crack kinking from the mixed mode problem. This objective was only realized in a limited number of tests and was not generally reproducible. Rather than attempt to draw hard conclusions from the limited test results, the following observations were made regarding self-similar mixed mode fatigue crack growth in this steel:

1. The cracks generally tried to grow out of the side groove in an attempt to maximize the opening component and minimize the shear mode. The side grooves were only partly successful in restricting the crack path. In those cases where the crack stayed in the side groove, it

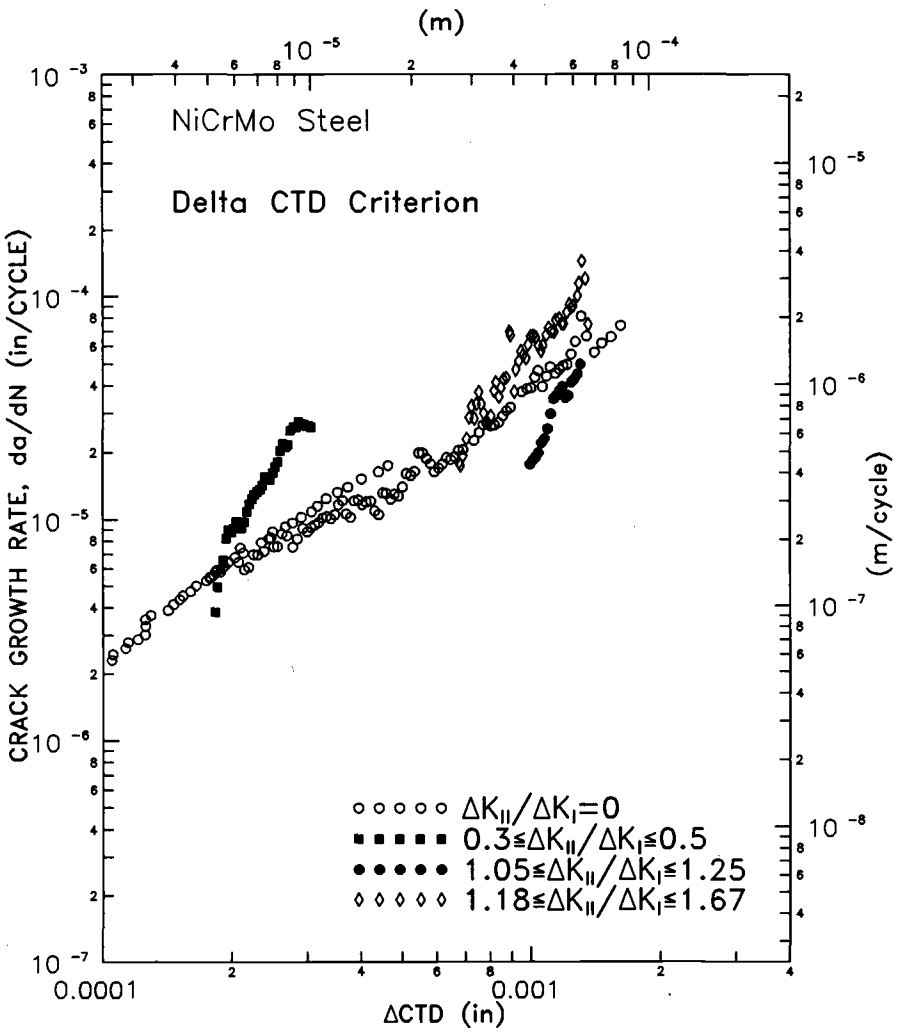

FIG. 10—*Fatigue crack growth rate as a function of vector crack tip displacement,* **ΔCTD.** *(Open symbols denote closure-corrected data.)*

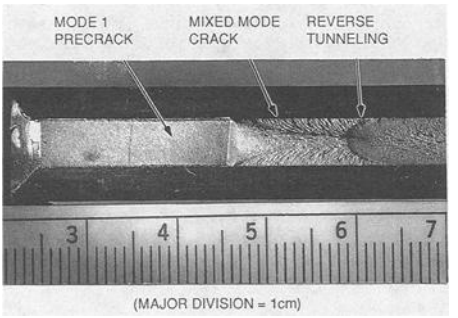

FIG. 11—*Reversed tunneling of fatigue crack.*

was possible to collect data for much greater amounts of crack growth than had been previously reported in the literature. It was difficult to reproduce data at any given mixed mode ratio because in replicate tests, the crack would sometimes grow out of the side groove.

2. Various theories to predict the mixed mode fatigue crack growth rate from opening mode data were applied to the experimental data. None of the theories were able to predict the mixed mode behavior from opening mode data. In all cases, the mixed mode data had a consistently higher slope than the pure opening mode data.

References

[1] Iida, S. and Kobayashi, A. S., "Crack Propagation Rate in 7075-T6 Plates Under Cyclic Tensile and Transverse Shear Loadings," *Transactions of the ASME,* December 1969, pp. 764–769.

[2] Roberts, R. and Kibler, J. J., "Mode II Fatigue Crack Propagation," *Journal of Basic Engineering, Transactions of ASME,* December 1971, pp. 671–680.

[3] Buzzard, R. J., Gross, B., and Srawley, J. E., "Mode II Fatigue Crack Growth Specimen Development," *Fracture Mechanics: Seventeenth Symposium, ASTM STP 905,* J. H. Underwood et al., Eds., American Society for Testing and Materials, Philadelphia, 1986, pp. 329–346.

[4] Hahn, G. T., Bhargava, V., Yoshimura H., and Rubin, C., "Analysis of Rolling Contact Fatigue and Fracture," *Advances in Fracture Research, ICF 6,* Vol. 1, New Delhi, 1984, pp. 295–316.

[5] Tanaka, K., "Fatigue Crack Propagation From a Crack Inclined to the Cyclic Tensile Axis," *Engineering Fracture Mechanics,* 1974, Vol. 6, pp. 493–507.

[6] Weertman, J. "Rate of Growth of Fatigue Cracks Calculated from the Theory of Infinitesimal Dislocations Distributed on a Plane," *International Journal of Fracture Mechanics,* Vol. 2, 1966, pp. 460–467.

[7] Lardner, R. W., "A Dislocation Model for Fatigue Crack Growth in Metals," *Philosophy Magazine,* Vol. 17, 1968, pp. 71–82.

[8] Sih, G. C. and Barthelemy, B. M., "Mixed Mode Fatigue Crack Growth Predictions," *Engineering Fracture Mechanics,* Vol. 13, 1980, pp. 439–451.

[9] Lam, Y. C., "Mixed Mode Fatigue Crack Growth and the Strain Energy Density Factor," *Theoretical and Applied Fracture Mechanics,* Vol. 12, 1989, pp. 67–72.

[10] Pustejovsky, M. A., "Fatigue Crack Propagation in Titanium Under General In-plane Loading—I: Experiments," *Engineering Fracture Mechanics,* Vol. 11, 1979, pp. 9–15.

[11] Li, C., "Vector CTD Criterion Applied to Mixed Mode Fatigue Crack Growth," *Fatigue and Fracture of Engineering Materials and Structures,* Vol. 12, No. 1, 1989, pp. 59–65.

[12] Bold, P. E., Brown, M. W. and Allen, R. J., "Shear Mode Crack Growth and Rolling Contact Fatigue," *Wear,* Vol. 144, 1991, pp. 307–317.

[13] Otsuka, A., Tohgo, K., and Matsuyama, H., "Fatigue Crack Initiation and Growth Under Mixed Mode Loading in Aluminum Alloys 2017-T3 and 7075-T6," *Engineering Fracture Mechanics,* Vol. 28, Nos. 5/6, 1987, pp. 721–732.

[14] Otsuka, A., Mori, K., and Tohgo, K., "Mode II Fatigue Crack Growth in Aluminum Alloys," *Current Research on Fatigue Cracks,* 1987, pp. 149–180.

[15] MIL-S-23284, "Steel Forgings, Carbon and Alloy, for Shafts, Sleeves, Propeller Nuts, Couplings and Stocks (Rudders and Diving Planes)," U.S. Military Specification, 28 December 1980.

[16] Richard, H. A. and Benitz, K., "A Loading Device for the Creation of Mixed Mode in Fracture Mechanics," *International Journal of Fracture,* Vol. 22, 1983, pp. R55–R58.

[17] Henn, K. and Richard, H. A., "Some Aspects of Fatigue Crack Growth Under Mixed Mode Loading," *Advances in Fracture Research, ICF7,* Vol. 3, 1989, pp. 2323–2330.

[18] Donald, J. K. and Ruschau, J., "Direct Current Potential Difference Fatigue Crack Measurement Techniques," *Fatigue Crack Measurement: Techniques and Applications,* K. J. Marsh, R. O. Ritchie, and R. A. Smith, Eds., Engineering Materials Advisory Service, Ltd., London, 1990.

[19] Donald, J. K., "A Procedure of Standardizing Crack Closure Levels," *Mechanics of Fatigue Crack Closure, ASTM STP 982,* J. C. Newman, Jr. and W. Elber, Eds., American Society for Testing and Materials, Philadelphia, 1988, pp. 222–229.

[20] Brown, M. W., Liu, H. W., Kfouri, A. P., and Miller, K. J., "An Analysis of Fatigue Crack Growth Under Yielding Conditions," *Proceedings of ICF 5,* Vol. 2, 1980, p. 891.

[21] Gao, H., Brown, M. W., and Miller, K. J., "Mixed-Mode Fatigue Thresholds," *Fatigue of Engineering Materials and Structures,* Vol. 5, No. 1, 1982, pp. 1–17.

Ian M. Fyfe,[1] *Zihong H. Guo,*[1] *and Zhikai K. Guo*[2]

Crack Curvature in Thin Cylinder Failure

REFERENCE: Fyfe, I. M., Guo, Z. H., and Guo, Z. K., **"Crack Curvature in Thin Cylinder Failure,"** *Advances in Multiaxial Fatigue, ASTM STP 1191,* D. L. McDowell and R. Ellis, Eds., American Society for Testing and Materials, Philadelphia, 1993, pp. 359–372.

ABSTRACT: An investigation was conducted on the role played by different factors on the directional stability of cracks in pressurized thin-walled cylinders under fatigue loading conditions. In addition to internal cyclic pressure, the test system was designed to allow axial loads to be applied independently. Fractional factorial design techniques were used to determine the interaction between a number of different parameters which could possibly control the crack path direction.

This statistical analysis shows the importance of the key experimental parameters and the interaction of these parameters on the crack path. It also serves to show that, although crack length and pressure control the bulge characteristics, a symmetric bulge in itself only plays a part in determining the stability of the crack path but not the direction. Another aspect of the study was examining the possible mechanisms which control the direction taken by an inherently unstable crack and the effect these mechanisms could have on the K_{II}/K_I ratio associated with the theoretical models of crack growth direction.

KEY WORDS: fatigue (materials), crack stability, thin cylinder, factorial design, fracture mechanics

With the average age of commercial aircraft steadily increasing, greater attention is being paid to timely inspection and crack growth control. If cracks do escape early detection during in-service inspections, they may reach a critical length during a flight, resulting in fast unstable crack growth with catastrophic results. On the other hand, the curving of a crack limits the extent of the damage to a much smaller portion of the fuselage skin. When a crack curves sufficiently to allow the internal pressure to cause a shell to open in a small area, we have a condition in which controlled decompression occurs by flapping [*1*]. In a cylinder, a phenomenon which causes longitudinal cracks to turn in a circumferential direction may ensure rapid pressure relief with continued structural integrity. In aircraft, this type of crack also makes fuselage pressurization difficult and results in a drop in cabin pressure; thus, an early warning about impending structural failure is built into the system. However, the mechanisms that control crack curving in a thin, pressurized cylinder have not as yet been completely identified, and the research outlined in this paper was mainly concerned with identifying those factors that have the greatest influence on crack growth.

It has been known for sometime that bulging [*2,3*], which occurs when a pressurized cylinder has a longitudinal crack, plays an important role in crack growth. However, this has mainly been considered in relation to growth stability rather than directional stability. Although the number of papers on fatigue crack propagation is very extensive, studies of crack

[1] Professor and graduate student, respectively, Department of Aeronautics and Astronautics, University of Washington, Seattle, WA 98195.

[2] Graduate student, Department of Mechanical Engineering, University of Washington, Seattle, WA 98195.

growth in pressurized thin cylinders is quite limited. This fact is not too surprising since a pressurized cylinder is expected to have a sizeable leak before the fatigue crack has propagated any significant distance. In an aircraft fuselage, where the pressure is quite low, two conditions exist which could allow significant undetected crack growth, these being that air loss is reduced because of insulating blankets and that minor air loss can be compensated for by the air conditioning system. Of the papers on this subject, the work of Catanach and Erdogan [*4*] and Crichlow and Wells [*5*] are typical. Both studies were mainly concerned with crack growth rate, but the latter examined residual strength in cracked titanium cylinders; however, in neither case was the crack curving problem addressed.

It was demonstrated by Kibler and Roberts [*6*] and later by Radon [*7*] that in a flat plate if the ratio of remote stress parallel to the crack to that normal to it, σ_{xx}/σ_{yy}, is less than unity, a stable straight crack growth can be expected. When this ratio, R_A, is greater than 1, crack trajectory becomes increasingly curved into an antisymmetric S-shape centered on the initial straight notch. In cylindrical shells subjected to internal pressure, all elements are normally in equilibrium under tensile hoop stress, σ_{hoop}. However, in the presence of a longitudinal crack of length $2a$, any element along the crack edge has lost one component of σ_{hoop}, as shown in Fig. 1. Since equilibrium of the element must be maintained, the shell bulges and the element is placed in equilibrium along the crack edge by a stress, σ_{bulge}. It was suggested by Swift [*1*] that the axial stress, σ_{bulge}, ahead of the crack could exceed the magnitude of the hoop stresses if the crack length was long enough, and so a quasi-statically pressurized thin cylinder is unstable under these conditions. However, the criterion in Refs *6* and *7* is defined in terms of the far-field stress levels, and the σ_{bulge} quickly decays in value as the distance from the crack tip increases, and so this criterion would be difficult to apply or define as it relates to the cylinder configuration.

Another criterion more closely associated with the crack tip stresses was proposed by Cotterell [*8*] and Streit and Finnie [*9*], where, if a compressive stress parallel to the plane of the crack exists, then the crack propagation will be directionally stable. This latter stability criterion is concerned with the sign of the first nonsingular term of σ_{xx} in the crack tip solution. The appropriate conditions for this type of instability can be more readily reached in a thin

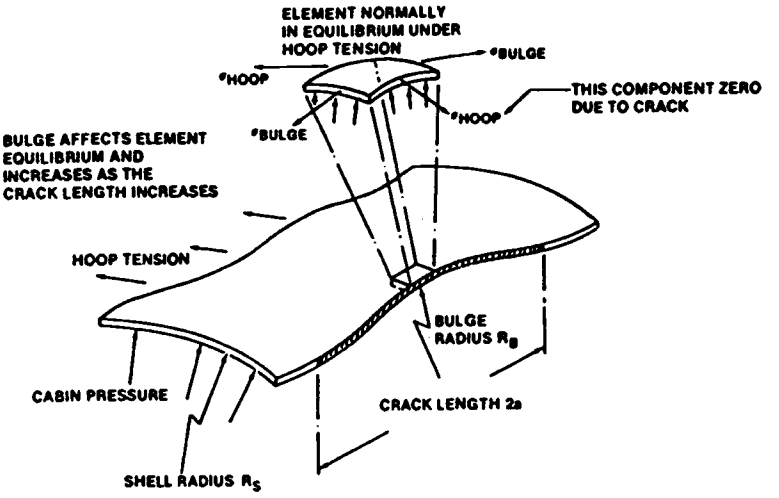

FIG. 1—*Bulging in a cylindrical shell with a crack subjected to internal pressure* [1]

cylinder because, even at relatively small internal pressures and crack lengths, σ_{bulge} will be tensile.

The crack path in the quasi-static burst failure of thin cylinders clearly shows that the crack growth is directionally unstable, but in the fatigue configuration the pressures are usually quite small and bulge stress may not be large enough to allow R_A to exceed 1, even if the ratio is defined as being between the local values of axial and hoop stresses.

The stress conditions ahead of the crack are examined to determine if the conditions that cause the directional instabilities at burst pressure also apply at the pressures associated with fatigue crack growth. The crack curving response to a variety of loading parameters which could contribute to directional instability are statistically analyzed to determine their importance in the crack curving process.

Experimental Equipment and Procedures

The experimental system and procedures described in this section were designed to allow both fatigue and burst tests to be conducted with the same specimen configuration. It was also configured to allow axial stresses to be applied independently of the internal pressure.

Thin Cylinder Testing System

The schematic diagram of the hydraulic system used for direct pressure testing is shown in Fig. 2. The system was designed to have two major load applying components, one to produce the cyclic pressure inside the specimen cylinder and the other to apply the axial load. Pressure is provided by a hydraulic power supply system which, by means of the servovalve, can be directly applied to the cylinder. The electrohydraulic servovalve in turn is controlled by a function generator. The feedback signals from the pressure transducer make this a closed-loop system.

To apply the axial tension or compression to the cylinder, a two-way valve is used to control an actuator, while a regulator is used to reduce the pressure to the proper value for the desired axial loading.

As shown in Fig. 3, the specimen is supported by two holding plates which are used to trans-

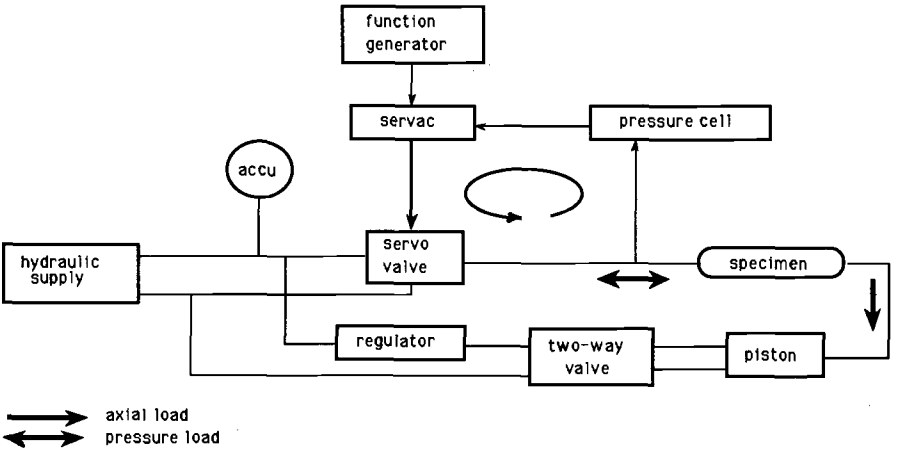

FIG. 2—*MTS direct pressure testing system.*

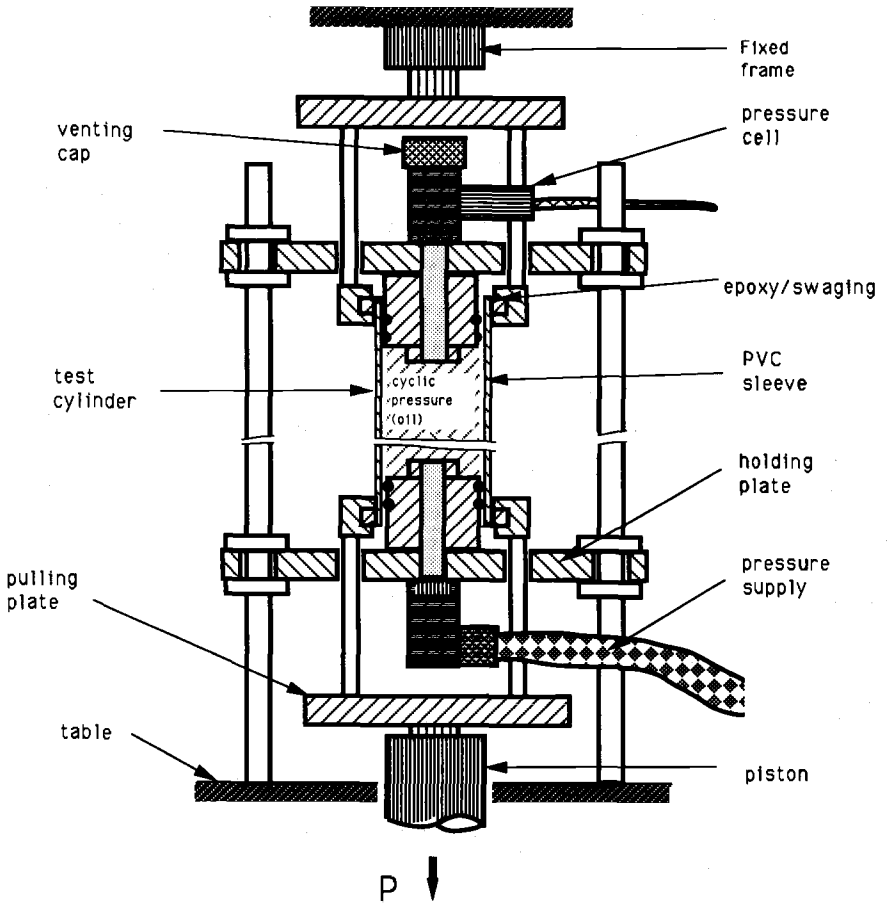

FIG. 3—*The thin cylinder loading frame.*

fer the axial loading caused by internal pressure to external supports, so that the axial load is imposed only by the actuator. Rings attached at each end of the cylinder allow axial tension and compression to be applied independently.

Two different methods are used to prevent leakage from the crack. In one configuration a PVC sleeve inside the specimen is used to contain the oil, while the other is a mylar patch. The PVC sleeve expands naturally with the cylinder, while the mylar patch is folded to allow for expansion.

Crack Path Parameters

As one of the main objectives of this research was to determine the factors responsible for crack curving in thin cylinders, it is particularly desirable to estimate their relative significance, and in this study factorial design techniques were used. A number of parameters or factors were considered to have a possible influence on the direction of crack propagation. These are the radius of the cylinder, thickness of the liner used to prevent leakage through the slot, axial compression which would influence the bulge shape, the frequency, the internal pressure level,

and a combination of two factors, the hoop stress and crack length, $2a$, which for identification purposes is called the stress intensity term $-\sigma_{hoop}\sqrt{(\pi a)}$. As changing one factor at a time is not only costly but also does not give information on the interaction between the factors, a factorial experimental design method, as described by Box, Hunter, and Hunter [*10*], was chosen instead. This technique provides increased precision in the estimation of factor effects by a statistical analysis of the data. Additionally, with this method it is possible to create a design that contains only one half or one quarter of the total number of runs needed to cover all the possible factor combinations. The method also provides an estimate of the interactions among factors.

In the factorial design method used, the factors were studied at two different levels, a high (+) and a low (−) setting. These levels can be quantitative (continuous) or qualitative (discrete), but it is assumed that the effects are linear over the range of the factor levels chosen. Experiments of this type are referred to as 2^k factorial designs, where the 2 indicates the number of levels at which a factor is being studied and the k indicates the number of factors being studied; also, the total number of experiments that need to be performed to fully and conclusively determine the effect of all "main effects" and their interactions is 2^k.

To obtain a relative measure of crack curvature, the deviation from the vertical per unit length of crack was used, but it is essential that the test responses be more or less normally distributed if they are to be plotted on a normal probability plot.

The responses were a measure of the deviation of the upper and lower crack from the initial slot direction and as such are a relative measure of crack curvature. In this study, the larger the response the straighter the curve.

Factorial Design Matrix

The statistical analysis associated with factorial design deals only with the responses to the different levels of the parameters under consideration. Two steps are required to provide input for the analysis program (SQC) used. The first step determines which factor combinations to run, and the second step determines (through randomization) in what order to run them. These data are assembled in matrix format as shown in Table 1. The input is referred to as the design matrix where each row represents a single experimental configuration and gives the factor settings (high or low, i.e., + or −) for each of the three experimental factors being con-

TABLE 1—*Sample fractional factorial design matrix.*

Variable			−	+
Cylinder radius, mm			12.7	19.0
Stress intensity, $MN/m^{3/2}$			10.10	15.14
Stress ratio			0	1
Specimen Number	Cylinder Radius	Stress Intensity	Stress Ratio, R_A	Response
1	−	−	+	0.515
	−	−	+	0.465
2	+	−	−	0.515
	+	−	−	0.515
3	−	+	−	0.375
	−	+	−	0.334
4	+	+	+	0.194
	+	+	+	0.273

sidered, along with the response. The design matrix thus provides a blueprint of the factor combinations and the experimental order. Each combination of factor settings, i.e., each row of the design matrix, was run only once without replication, but by assuming that the path of the upper crack was independent of the lower, it was possible to record the responses of the top and bottom crack tip as two separate sets of data giving a replication of two for each test. This is shown in Table 1 as if each configuration was run twice.

Factorial Analysis

The analysis module of the SQC program performs the statistical operations associated with the full 2^k and fractional design and resolution. A description of the factorial design process is beyond the scope of this paper, and the reader is referred to the many references in this area of which Ref *10* is a classic example. The program gives as output graphs indicating the influence of the main factors, as well as the interactions between different factors. The program also provides numerical estimates of the relative influence of the parameters on crack curving through an analysis of variance (ANOVA) table, and it is this feature that is used in this study. This table is composed of six columns (see Table 2) where the first indicates the factor being considered the next three are statistical information where the "Sum Squares" represent the squared deviations about a mean due to a particular factor, the "DF" is the degrees of Freedom defined by $k - 1$, and the "Mean Square" is an estimate of the variance obtained by dividing the "Sum Squares" by the degrees of freedom "DF." With only one degree of freedom in this two-level study, the "Sum Squares" and "Mean Square" are identical. The two most important columns are the last two, where the larger the "*F* Statistic," or the smaller the "*P* value," the greater the influence of this parameter on the crack path curvature. The *F*-statistic compares the variation in responses due to the effect with the variation due to error and is obtained by dividing the "Mean Square" for each factor by the "Mean Square" error at the bottom of the column. The corresponding "*P* value" is the probability that the "*F* Statistic" is as large as it is simply by chance.

Results and Discussion

The experimental program was conducted in two parts. The first was concerned with the directional stability requirements and the second with the direction taken by an unstable crack. The cylindrical specimens for both experimental phases were identical 6061-T4 aluminum cylinders with a wall thickness of 0.711 mm. The diameter, which was one of the parameters considered, varied between 25.4 and 38.1 mm, and the length parameter varied between 114.3 and 228.6 mm. The pressure varied from zero to the burst pressure, but for the fatigue tests the maximum pressures varied between 0.69 and 1.38 MPa, with the cycle ratio equal to zero.

TABLE 2*a*—*Statistical analysis (ANOVA) by SQC.*

Source	Sum Square	Degrees of Freedom	Mean Square	*F* Statistic	*P* value
Liner thickness	1.33	1	1.33	41.964	0
Axial compression	0.123	1	0.123	3.878	0.0593
Geometric intensity	0.108	1	1.108	3.408	0.0759
Crack tip condition	0.007	1	0.007	0.223	n/s
Error	0.856	27	0.032	...	...

TABLE 2*b*—*Statistical analysis (ANOVA) by SQC.*

Source	Sum Square	Degrees of Freedom	Mean Square	*F* Statistic	*P* value
Stress intensity	1.089	1	1.089	3.667	n/s
Applied stress ratio	5.281	1	5.281	27.779	0.0135
Cylinder radius	1.421	1	1.421	4.785	0.094
Error	1.188	4	0.297		
Corrected total	8.98	7			

Directional Stability

A series of tests were run in which the pressure was increased monotonically, and the hoop and axial strains were measured at discrete pressure intervals, with strain gages located at a distance $r = 2a$ ahead of the crack tip. The pressure was increased until unstable crack growth occurred. The axial and hoop stresses obtained from these measurements are plotted as a function of the internal pressure in Fig. 4*a* where the applied axial stress ratio was $R_A = 0$. With the axial stress due to bulging increasing as the internal pressure increases and exceeding the hoop stress at failure, directional instability is to be expected. At the lower pressures associated with fatigue testing this is not the case, in that the stress ratio requirements for instability suggested in Refs *6* and *7* are not met. However, as the axial stress is tensile, the criterion suggested in Refs *8* and *9* is applicable. If a compressive axial load is applied, the axial stresses ahead of the crack could be compressive, and so, even with the latter criterion, crack directional stability might then be expected. However, in all the fatigue tests run in this study, the crack path was unstable, even with a wide range of axial loads ($-1.5 < R_A < 1.25$). The axial and hoop stresses ahead of a crack, at $r = a$ and $r = 2a$ for $R_A = -1$, are shown in Fig. 4*b*. A comparison of the axial stresses at these two points shows the tendency of the stress to decrease as the crack tip is approached and leads one to believe that even though the axial hoop stress ratio might be less than unity the axial stress is almost certainly in tension in the immediate region of the crack tip. This possibility was reinforced by the results from both a finite element analysis and a Moiré interferometry experiment.

The complexity of conditions at the crack tip are illustrated by the fringe patterns shown in Fig. 5, which illustrates not only the presence of the dimple but also its extent. The out-of-plane displacements obtained from Fig. 5*a*, together with the finite element analysis values obtained using the ABAQUS program, are presented in Fig. 6. The normalizing displacement, C_W, is defined in Ref *3* and has the form

$$C_W = \frac{\sqrt{12(1 - \nu^2)}\, a^2 pR}{2Eh^2}$$

where p is the internal pressure, R is the cylinder radius, and h is the thickness of the cylinder wall.

Figure 5*b* shows the propagation of a slant crack from the corner of a thin, 0.38-mm slot. The fact that this propagation is straight indicates an unusual biaxial stress condition which, according to the results from biaxial loading of plates [*11*], would require an axial loading approximating that of the hoop stress.

These results show that directionally unstable axial crack growth is inherent in the thin cylinder configuration even in cases with axial compressive loads and low pressures.

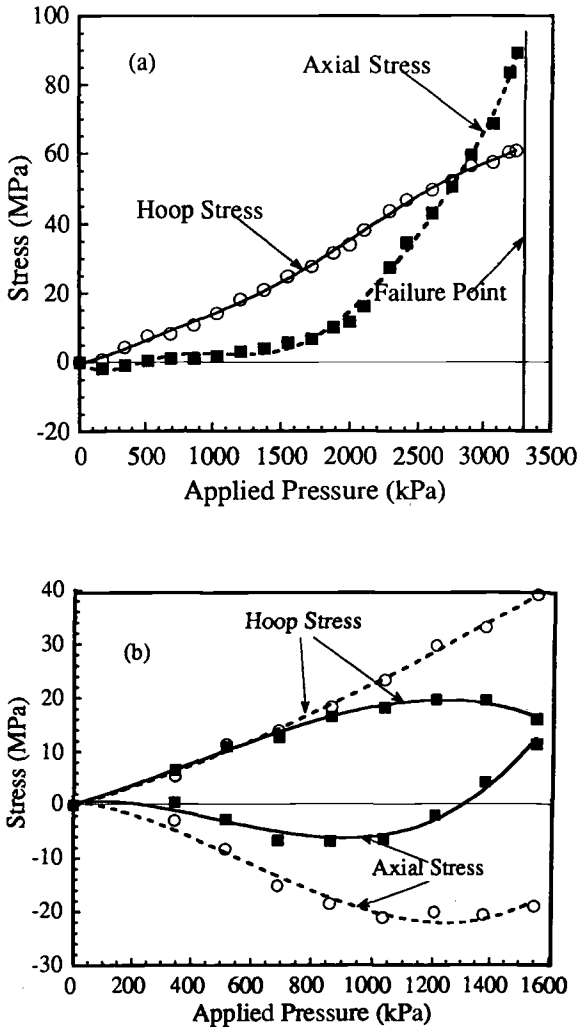

FIG. 4—*Axial and hoop stresses as a function of internal pressure:* (a) r = *2*a, R_A = *0*, (b) —■— r = a, —○— r = *2*a, R_A = *− 1*.

Parameter Variation

The factorial design portion of the study was carried out in four phases, one for a static burst configuration and the other three for fatigue crack growth. In the burst test four factors were examined: liner thickness, axial compression, crack tip condition, and a geometric intensity ($a/\sqrt{(Rh)}$). The ANOVA results are given in Table 2*a*. It can be seen that the cylinder liner was very important in controlling crack curvature, but that the crack tip condition was not. The statistical examination of these results through the "main effect" plots of SQC, which give an average response of a factor at the two levels, determined that the crack path would be much straighter with a thicker liner, a larger radius, and no axial compression. The result, which indicates that the initial crack tip condition was of no significance as far as crack curvature is concerned, must be qualified in that the curvature was very sensitive to any deviation of the initial crack direction from the axial.

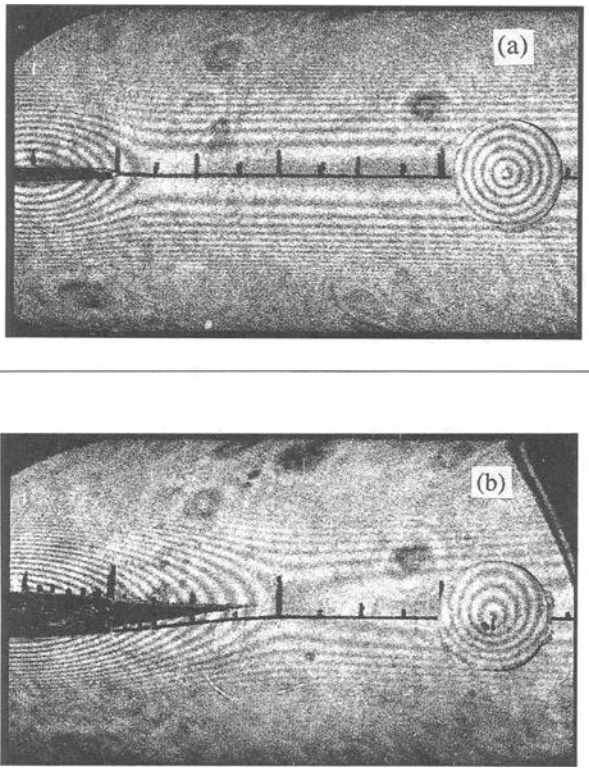

FIG. 5—*Moiré fringe dimple pattern at the crack tip,* f = *2.7 lines/mm,* (a) *straight crack,* (b) *slant crack.*

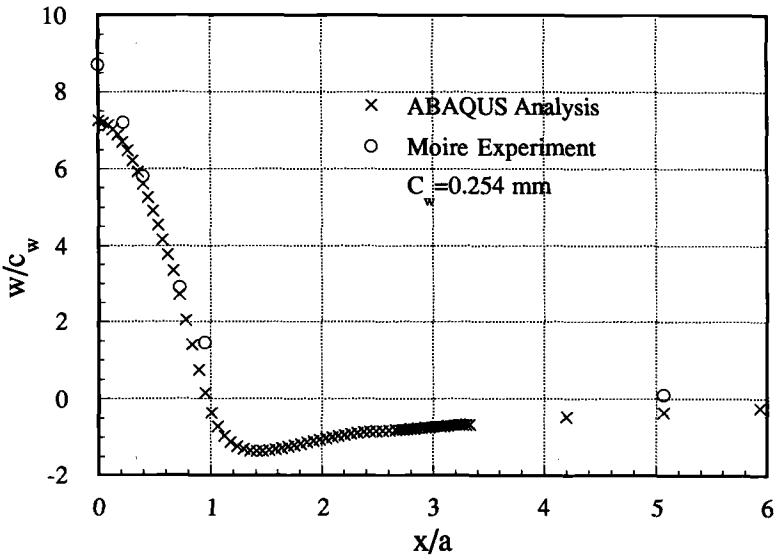

FIG. 6—*Normal displacement of the crack surface.*

In the first of the fatigue tests, five factors were considered: pressure, applied stress ratio, initial crack length, cylinder length, and frequency, where the applied stress ratio is the ratio of applied axial stress to hoop stress. Within the range of levels considered, none of these parameters had a significant effect on the curvature of the crack path. However, there was a significant interaction between the pressure and the crack length, which is not too surprising in that they both control the degree of bulging. The interaction between pressure and initial crack length as calculated by the SQC program is shown in Fig. 7*a*, where the difference of the slopes is a measure of the interaction effect. Figure 7*a* reflects the change in bulge shape controlled by these two factors and the nonlinear aspects introduced by the dimple.

In the second fatigue phase three factors were considered: cylinder radius, stress intensity $[\sigma_{hoop}\sqrt{(\pi a)}]$, and the applied stress ratio. In this phase, the stress ratio range was changed to extend the range of R_A from 0 to 0.5 to 0 to 1. The ANOVA results for a half factorial 2^k with a replicate of 2 are given in Table 2*b*. It can be seen from these results that as far as crack curving is concerned that a change in the intensity, at least in the range considered (10.0 to 15.0 MN/m$^{3/2}$), had little effect on the crack path curvature. The cylinder radius result again

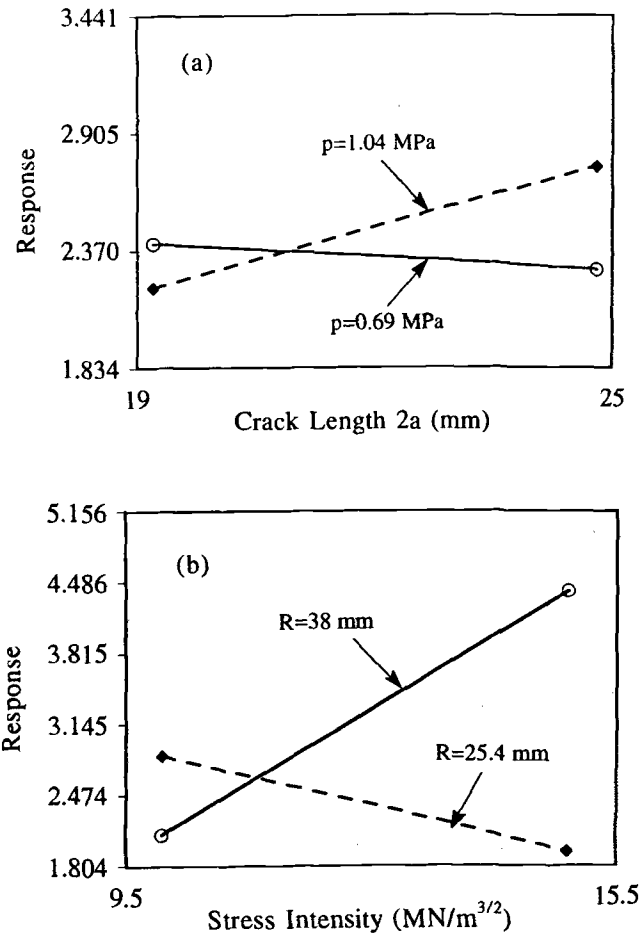

FIG. 7—*Interaction of factors:* (a) *pressure and crack length,* (b) *radius and stress intensity.*

indicated that the larger the radius the straighter the crack path. The stress ratio factor was also found to be significant, indicating that an applied tensile load of $R_A = 1$ would result in a straighter crack.

The final factorial design experiment consisted of the same parameters considered earlier, but in a different mix and over different ranges. The four factors were liner thickness, pressure, applied stress ratio, and frequency. As an example of the changes in this phase, the applied stress ratio was varied only in the range from 0 to 0.5, as it was suspected that over the earlier range the assumption of a linear variation might be invalid. The results for this experiment, again for a full factorial 2^k with a replicate of 2, indicated that none of the parameters over the ranges considered had a significant effect on the crack curvature. In this case both the liners used were thin and flexible, while for the results shown in Table 2*a* one liner was more rigid than the other.

A final series of fatigue tests were run in which the applied stress ration, R_A, alone was varied. The results agreed with the factorial design tests by showing that the axial load effect was indeed nonlinear and that there was a tendency for the crack path to be straighter with the higher applied stress ratios ($R_A \pm 1$). However, the scatter in these results and the lack of interaction with the other variables indicate that some other feature of the failure process is involved. The difficulty in applying a uniform axial load could contribute to the scatter, but the earlier tests indicated that even though the larger axial loads do not change the instability characteristics, they do alter the bulge configuration by reducing either the bulge or its unsymmetric deformations. However, further tests would be required to confirm the importance of the axial load.

Crack Direction Mechanisms

In thin plates, cracks are assumed to change direction under the influence of Mode II deformations or, in fracture mechanics terms, the greater the ratio K_{II}/K_I the greater the change in the crack direction. An expression for this direction change can be obtained from the theory proposed by Erdogan and Sih [*13*] that a crack will propagate in a direction perpendicular to the maximum circumferential stress. This relation has the form

$$\tan\frac{\theta_0}{2} = \frac{1}{4}\frac{K_I}{K_{II}} \pm \frac{1}{4}\sqrt{\left(\frac{K_I}{K_{II}}\right)^2 + 8} \tag{1}$$

where θ_0 is the angle of crack extension. In the tests discussed above, the cracks always curved despite the essential symmetry of the loading conditions. In a thin cylinder, Mode II deformations can be introduced by an unsymmetric bulge, which is to be expected if a constraint such as a stringer is located near the crack. However, the earlier results, which indicate that fatigue crack growth in this configuration is inherently unstable, allows small unsymmetric conditions to grow even though the general loading conditions are symmetric. This type of crack propagation has a built-in lack of symmetry at the crack tip, one due to the shear lip and the other to the location and initial direction of the crack growth.

The conditions that lead to crack curvature initiated by the shear lip are caused by the internal pressure allowing the two sides of the shear lip to move relative to each other, which in turn causes an unsymmetric bulge and a Mode II deformation. This type of deformation is shown schematically in Fig. 8. That the pressure contributes to this lack of symmetry was confirmed by the factorial design experiments, where a thicker liner resulted in a straighter crack, a condition created in part by the inability of the thicker liner to follow the bulge contours. In addition, the larger the radius the less the movement of the two shear lips by virtue of the lower

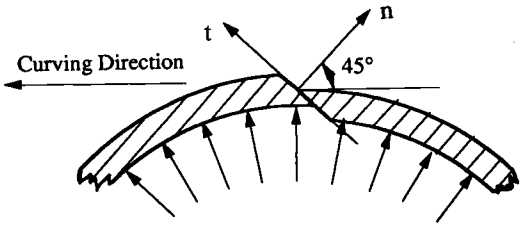

FIG. 8—*Shear lip fracture plane in a pressurized thin cylinder.*

internal pressures. In the factorial design analysis this was reflected in the strong interaction shown between the hoop stress intensity and the cylinder radius, as in Fig. 7*b*.

When a crack originates at the corner of the thin slot, even this small unsymmetric condition quickly leads to the unsymmetric bulge and the attendant Mode II deformations, as seen in Fig. 5*b*. As the shear lip planes and slight deviations in crack direction are essentially a matter of chance, the resultant cracks were thus either S or C shaped depending on these microscopic conditions. Examples of the fatigue crack growth from a thin slot can be seen in the specimens shown in Fig. 9.

The value K_I in Eq 1 could also be affected by the shear lip. In the *Stress Intensity Factors Handbook* [*14*], the definition of K_I in relation to a 45° shear plane is discussed, and it is suggested that such a condition results in a K_I which would be approximately one half of the value were the fracture plane perpendicular to the surface. As K_{II} is not affected to the same extent by this coordinate transformation, greater curvature can result with relatively low values of K_{II}. This correction for the shear lip would greatly improve the experimental results reported in Ref *12*, but it also suggests that the hypotheses used to derive the expression in Ref *13* may not apply in the plane stress ductile case where crack closure is greatly complicated by the motion shown in Fig. 8.

The appropriate theory to calculate the stress intensity factor K_I for the configuration used in this study was developed in Ref *3* and has the form

$$K = (A_m + A_b)(pR/h)\sqrt{\pi a_p} \tag{2}$$

where A_m and A_b are the correction factors for cylinder bulging. Using the above expression, it was possible to compare the value of the critical K for crack growth with results for a similar set of tests conducted in Ref *3*. Using the values appropriate to the burst test of this study (p, R, $2a$, h, A_m, and A_b had values of 3.27 MPa, 14.3 mm, 14.3 mm, 0.711 mm, 2.85, and 0.1, respectively) resulted in a value of $K_c = 44.8$ MN/m$^{3/2}$ for Aluminum 6061-T4, which is in close agreement with the value reported by Erdogan and Ratwani [*3*] for a very similar configuration. Using Eq 2 at the lowest cyclic pressure which produced crack growth, which in this study was 0.69 MPa, results in a threshold stress intensity of $K_T = 9.44$ MN/m$^{3/2}$, considerably above the threshold value given in Ref *3*. If values in the neighborhood of the threshold are used for K_I, then for the crack directions compatible with those shown in Fig. 9 the K_{II} should be on the order of 0.4 MN/m$^{3/2}$ for a 10° change in angle.

Conclusions

The results from this study indicate that the parameters which control the direction of propagation of a longitudinal fatigue crack in a thin-walled pressurized cylinder are those that also apply to a burst test. The crack growth in both cases is inherently directionally unstable, a

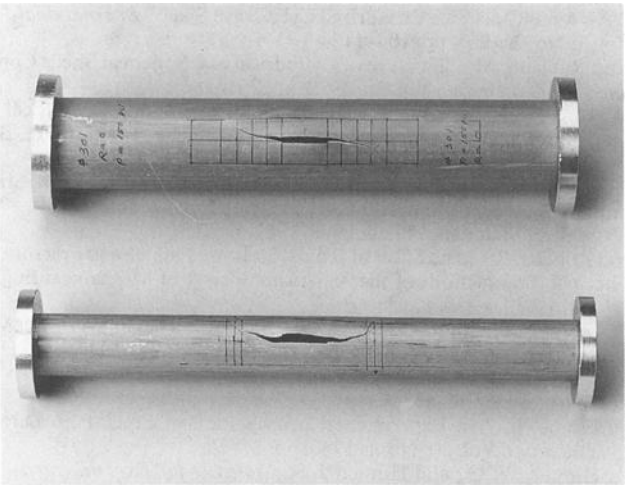

FIG. 9—*Examples of fatigue specimen configuration.*

condition caused by the bulge which results from the presence of the crack, with the bulge causing the tensile axial stress that satisfies the criterion for instability proposed in Ref *9*.

Of the different factors considered, the pressure and crack length both affect the size of the bulge in the region of the crack, but as these parameters did not directly influence the crack path curvature, it appears that the bulge itself does not play a direct role. The tests also confirmed that the larger the cylinder radius, the straighter the crack. It was also shown that a thin liner has little effect on the crack direction, but a lack of flexibility in that liner can result in straighter crack growth. This result could be quite significant in fatigue testing of pressurized cylinders or panels, where a patch is required to reduce leakage. Nonlinear effects were obviously present, and a more sophisticated center point, or 3^k, design should replace the simple two-level design used.

The deformations required to allow the crack to change direction in a cylinder can be a combination of internal pressure acting on the shear lip near the crack tip. As this combination exists in all thin-walled cylinders under internal pressure, the necessary unsymmetrical deformations required for a direction change in a crack are also inherent to the system. External constraints, such as a stringer, also introduce deformations similar to that introduced by the shear lip, but it has yet to be determined how sensitive the crack path is to these two different loading conditions, as each may react differently to crack closure effects and subtle changes in crack direction.

Acknowledgments

This work was supported in part by the Boeing Company. The authors would like to thank Dr. M. Miller and the staff of the Structural Damage Technology Group of Boeing for their helpful discussions.

References

[*1*] Swift, T., "Damage Tolerance in Pressurized Fuselages," *Proceedings,* 11th Plantema Memorial Lecture presented to 14th Symposium of the International Committee on Aeronautical Fatigue (ICAF), Ottawa, Canada, 10–12 June 1987.

[2] Folias, E. S., "An Axial Crack in a Pressurized Cylindrical Shell," *International Journal of Fracture Mechanics,* Vol. 1, No. 2, 1965, pp. 104–113.
[3] Erdogan, F. and Ratwani, M., "Fracture of Cylindrical and Spherical Shells Containing a Crack," *Nuclear Engineering and Design,* Vol. 20, 1972, pp. 265–286.
[4] Cantanach, W. M. and Erdogan, F., "Fatigue Crack Propagation in Cylindrical Shells," *Fracture,* Proceedings of the 2nd International Conference on Fracture, P. L. Pratt, Ed., Brighton, England, 1969, pp. 765–776.
[5] Crichlow, W. J. and Wells, R. H., "Crack Propagation and Residual Static Strength of Fatigue-Cracked Titanium and Steel Cylinders," *Fatigue Crack Propagation, ASTM STP 415,* American Society for Testing and Materials, Philadelphia, 1967, pp. 25–70.
[6] Kibler, J. J. and Roberts, R., "The Effect of Biaxial Stress on Fatigue and Fracture," *Journal of Engineering for Industry,* Transactions of the American Society of Mechanical Engineers, November 1970, pp. 727–734.
[7] Radon, J. C., Leevers, P. S., and Culver, L. E., "Fracture Toughness of PMMA Under Biaxial Stress," *Fracture 1977,* Vol. 3, ICF4, University of Waterloo Press, 1977; pp. 1113–1118.
[8] Cotterell, B., "Notes on the Path and Stability of Cracks," *International Journal of Fracture Mechanics,* Vol. 2, No. 3, 1966, pp. 526–533.
[9] Streit, R. and Finnie, I., "An Experimental Investigation of Crack-Path Directional Stability," *Experimental Mechanics,* Vol. 20, No. 1, 1980, pp. 17–23.
[10] Box, G. E. P., Hunter, W. G., and Hunter, J. S., *Statistics for Experimenters,* Wiley, New York, 1978.
[11] Eftis, J., Jones, D. L., and Liebowitz, "Load Biaxiality and Fracture: Synthesis and Summary," *Engineering Fracture Mechanics,* Vol. 36, No. 4, 1990, pp. 537–574.
[12] Fyfe, I. M. and Sethi, V. "The Role of Thin Cylinder Bulging on Crack Curvature," AIAA Paper No. 91-1086, *Proceedings,* 32nd Structures, Structural Dynamics, and Materials Conference, Baltimore, April 1991, Vol. 2, pp. 1341–1348.
[13] Erdogan, F. and Sih, G. C., "On the Crack Extension in Plates Under Plane Loading and Transverse Shear," *Journal of Basic Engineering,* Transactions of the American Society of Mechanical Engineers, December 1963, pp. 519–527.
[14] *Stress Intensity Factors Handbook,* Vol. 2, K. Murakami, Ed., Pergamon Press, New York, 1987.

Multiaxial Fatigue of Notched Components

Volker B. Köttgen,[1] *Michael Schön,*[1] *and Timm Seeger*[2]

Application of a Multiaxial Load-Notch Strain Approximation Procedure to Autofrettage of Pressurized Components

REFERENCE: Köttgen, V. B., Schön, M., and Seeger, T., **"Application of a Multiaxial Load-Notch Strain Approximation Procedure to Autofrettage of Pressurized Components,"** *Advances in Multiaxial Fatigue, ASTM STP 1191,* D. L. McDowell and R. Ellis, Eds., American Society for Testing and Materials, Philadelphia, 1993, pp. 375–396.

ABSTRACT: Theoretical approaches to predict the effect of autofrettage on the formation of residual stresses have been limited to tubes. This paper presents a new procedure to calculate approximately the residual stresses in pressurized components of any shape—with and without notches. The procedure developed can account very precisely for changes in the deformation behavior of metals during the first load cycles, e.g. the Bauschinger effect. An extension of the constitutive model of Mróz to cyclic hardening and softening was developed to verify the approximation with finite element analyses. Very good agreement between the results of both approaches was found. Through application of the procedure it was found that maximum residual stresses were usually generated by the pressure, producing a fully plastic net section. Only in a special case did the pressure, which gave maximum residual stresses, coincide with the lowest pressure, producing reversed yielding, which in the past often has been regarded as optimal pressure.

KEY WORDS: autofrettage, residual stresses, notch strains, cyclic hardening, cyclic softening, constitutive equations

Nomenclature

A_{bore}	Area of bore
A_{wall}	Area of a cross-section through the wall perpendicular to the bore
E	Young's modulus
$_e$	Subscript denoting "elastic"
K'	Cyclic-hardening coefficient
n'	Cyclic-hardening exponent
p	Pressure
$_p$	Subscript denoting "plastic"
p_{aut}	Maximum pressure during autofrettage
p_p	Pressure at fully plastic limit state
$_q$	Subscript denoting equivalent stress or strain
r	Radial coordinate
R_i	Radius of bore
R_o	Outer radius of tube
$R'_{p0.2}$	Cyclic 0.2% proof stress

[1] Research assistants and [2]professor, T. H. Darmstadt, Werkstoffmechanik, Petersenstrasse 13, D-64287 Darmstadt, Germany.

$\mathbf{s}$ Deviatoric part of stress tensor
$W_k = R_o - R_i$ Smallest wall size of nonuniform components
W_g Largest wall size of nonuniform components
z Longitudinal coordinate
α Translation coefficients of yield surfaces
$\epsilon, \boldsymbol{\epsilon}$ Strain, strain tensor
ν Poisson's ratio
ν' Effective Poisson's ratio in Hencky's equations
φ Circumferential coordinate
$\sigma, \boldsymbol{\sigma}$ Stress, stress tensor
σ^{RS} Residual stress
σ_F Flow stress

Introduction

A process called *autofrettage* can be applied to pressurized components, whereby favorable residual stresses are induced by a single high overpressure. The resulting plastic deformation near the bore will be constrained by the surrounding elastic material, thus leading to compressive residual stresses at the bore after unloading. If the service pressure of the component is significantly smaller than the autofrettage pressure, fatigue cycling will take place under compressive mean stresses at any possible crack initiation location at the bore, thus increasing fatigue life.

Autofrettage has been applied to uniform thick-walled tubes for many years. Suitable autofrettage pressures for this simple system can be chosen with the help of several analytical solutions. Other, more complex-shaped, pressurized components, e.g. injection pumps of diesel engines, could benefit from autofrettage as well. In such nonuniform components, fatigue cracks often start from small notch-like regions, e.g. shoulders, or at cross bores as shown in Fig. 1. In those cases an affordable procedure is needed to determine a relationship between applied autofrettage pressure and resulting residual stresses.

Generally such a procedure is required for three reasons:

1. The plastic collapse load has to be accurately estimated to prevent bursting of the component during autofrettage.
2. It should be possible to determine an "optimal" autofrettage pressure (see section entitled "Optimal Autofrettage Pressure").
3. Fatigue life of the component could be evaluated numerically by the local strain approach provided the relationship between pressure and local stresses and strains could be used for service loading as well as for autofrettage.

As there is only one load component, a single scalar quantity such as the von Mises equivalent residual stress σ_q^{RS} is sufficient to determine the pressure producing maximum compressive residual stresses for a fixed critical location in a given component of a given material. This is regardless of the influence of different mean stress *components* (σ_φ^{RS}, σ_z^{RS}) on fatigue damage because their ratio cannot be individually adjusted. Therefore a function $\sigma_q^{RS} = f(p)$ could be sufficient to determine this pressure.

For application to fatigue calculations, additional quantities are required. If the selection of fatigue damage parameters is not to be restricted, full stress and strain tensors have to be known at possible crack initiation sites, i.e. $\sigma_{ij} = f_{ij}(p)$, $\epsilon_{ij} = h_{ij}(p)$. Also, changes of the material

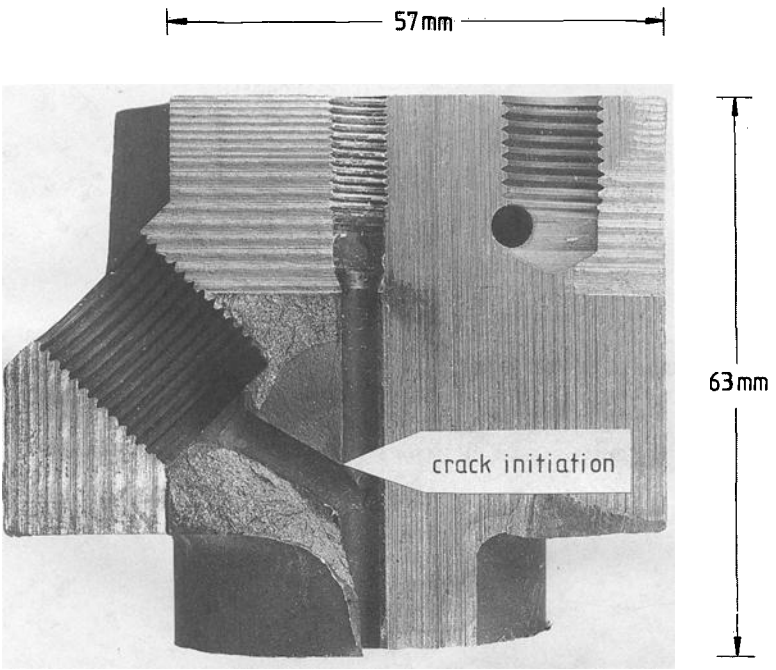

FIG. 1—*Fatigue crack at a cross bore of a fuel injection pump.*

response from the initial (static) to the cyclically stabilized stress-strain curve have to be accounted for and relaxation of the compressive residual stresses has to be considered.

This paper deals only with the determination of plastic limit loads and residual stresses, but the presented method does supply full stress and strain tensors and can therefore be extended to fatigue life calculation. The numerical determination of an "optimal" pressure can greatly reduce the number of experiments needed. It will usually be accompanied by a subsequent experimental determination of fatigue life for a given "optimal" autofrettage pressure to overcome problems with the modeling of the influences of mean stress relaxation, surface roughness, and fatigue damage accumulation.

Analytical Solutions for Uniform Tubes

Assuming linear elastic material, an analytical solution for uniform tubes under internal pressure can be found in many textbooks [*1,2*]. Because it is assumed that the sections of the long tube remain plane during deformation, the radial and hoop stresses across the sections are independent of the end conditions

$$\sigma_r = p \frac{R_i^2}{R_o^2 - R_i^2} \left[1 - \left(\frac{R_o}{r} \right)^2 \right] \tag{1}$$

$$\sigma_\varphi = p \frac{R_i^2}{R_o^2 - R_i^2} \left[\left(\frac{R_o}{r} \right)^2 + 1 \right] \tag{2}$$

whereas the constant longitudinal stress depends on them

$$\sigma_z = p \frac{R_i^2}{R_o^2 - R_i^2} \text{ (closed ends)} \tag{3}$$

$$\sigma_z = 0 \text{ (open ends)} \tag{4}$$

$$\sigma_z = 2\nu\, p \frac{R_i^2}{R_o^2 - R_i^2} \text{ (plane strain)} \tag{5}$$

The largest stresses will always be found at the inner radius R_i. Many analytical solutions exist for tubes of elastic-plastic materials. They differ in their assumptions: type of stress-strain curve (elastic perfectly-plastic, hardening), yield criterion (von Mises, Tresca), compressibility of the material and end conditions [*1–9*]. Most solutions depend on Hencky's flow rule. If the flow rule of Prandtl-Reuss is used, a system of differential equations has to be solved numerically.

The fully plastic limit pressure for an elastic perfectly-plastic material is given by

$$p_p = \sigma_F \frac{2}{\sqrt{3}} \ln\left(\frac{R_o}{R_i}\right) \text{ (VON MISES, plane strain)} \tag{6}$$

$$p_p = \sigma_F \ln\left(\frac{R_o}{R_i}\right) \text{ (TRESCA)} \tag{7}$$

where the solution for the yield criterion of Tresca (Eq 7) is valid for open and closed tubes and for the case of plane strain, but subject to restrictions regarding tube radii (valid for $R_o/R_i \lesssim 5$, see Ref *2*).

In Fig. 2 the maximum stress components at the bore, based on the theory of elasticity (Eqs 1, 2, and 5, and the fully plastic limit load (Eq 6), are depicted for different tube radii. For small ratios $R_o/R_i \rightarrow 1$ the elastic stresses are high, but the limit load is low. A problem with the general applicability of autofrettage can already be seen: for small wall sizes high residual stresses are required, but the autofrettage pressure has to be low to prevent bursting of the component. Several solutions describe the development of residual stresses by purely elastic unloading. Only a few of these also include a way to calculate their limit of applicability, i.e. the occurrence of reversed yielding. Often it is assumed that the maximum residual stress is produced by the lowest pressure, causing reversed yielding [*8*]. While this assumption is true for elastic perfectly-plastic material behavior on unloading, it does not hold for materials exhibiting the Bauschinger effect. The high-strength steels, which are typically used in high-pressure applications, exhibit only a small amount of hardening during first loading. They are cyclically softening in the small strain region and develop a cyclic stress-strain curve much steeper than the one during first loading. This behavior is already significantly present during first unloading, so that the Bauschinger effect cannot simply be modeled by kinematic hardening based on the monotonic σ-ϵ curve. The only published analytical solution known to the authors, which incorporates changes in flow stress σ_F and hardening during first unloading in autofrettage, was obtained by CHEN [*10*]. Most of the recent papers on the subject, e.g. Refs *8,11,12*, however agree that the Bauschinger effect is significant in autofrettage. This is why residual stresses can still increase in spite of reversed yielding. The procedure developed here includes the Bauschinger effect.

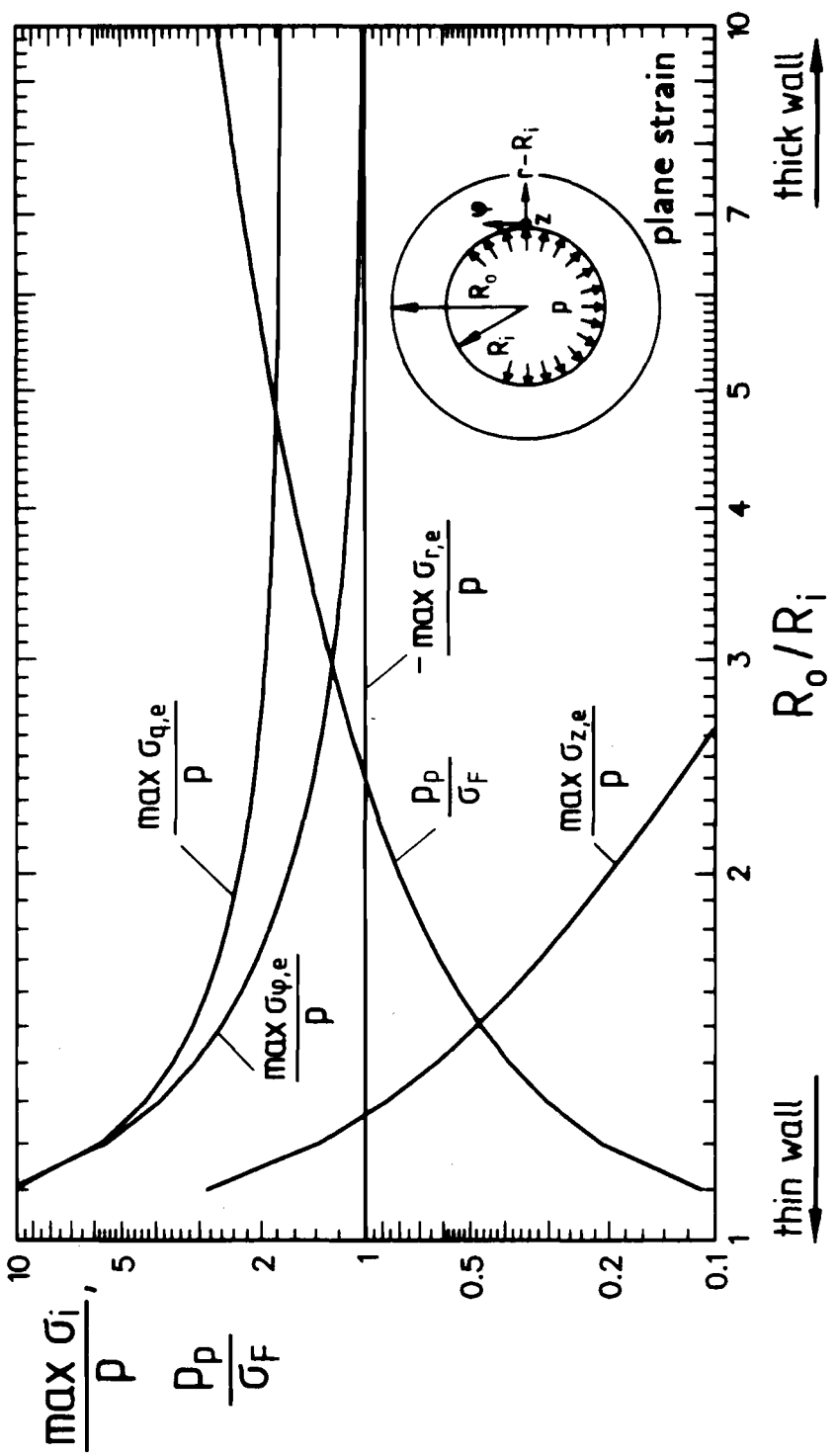

FIG. 2—*Stress components and limit pressure of tubes with different wall sizes.*

Approximation Procedure for Stable Stress-Strain Curves

Hoffmann and Seeger have developed a procedure to estimate multiaxial elastic-plastic notch stresses and strains under proportional loading [*13,14,15*], which can be applied to pressurized components with and without notches. In the following, all equations have been written for locations at the bore. Different from the original papers, the equations include the special boundary conditions of a pressurized notch.

The material's response to deformation is described by a uniaxial stress-strain curve

$$\epsilon = g(\sigma) \tag{8}$$

which is assumed to be stable during the examined time period. It exhibits Masing behavior, i.e. hysteresis path segments can be calculated as

$$\Delta\epsilon = 2 \cdot g(\Delta\sigma/2) \tag{9}$$

and it follows the memory rules [*16,17*]. Multiaxial stress-strain response is based on the uniaxial stress-strain curve for any monotonic proportional loading path by employing equivalent stresses σ_q and strains ϵ_q

$$\epsilon_q = g(\sigma_q) \tag{10}$$

which can be determined by any flow criterion. In the following, the criterion by von Mises is used. As pressurized components are seldom loaded in torsion, existence of a fixed principal stress state at the bore perpendicular to the radial (r), circumferential (φ), and longitudinal (z) directions can be assumed throughout the loading. Therefore the von Mises equivalent stress for a crack initiation location at the pressurized bore is given by

$$\sigma_q = \sqrt{\tfrac{1}{2}\left[(p + \sigma_\varphi)^2 + (\sigma_\varphi - \sigma_z)^2 + (\sigma_z + p)^2\right]} \tag{11}$$

In a second step it is assumed that, for any location where yielding begins, any appropriate conventional load-notch strain approximation formula can be applied if it is written in terms of equivalent stresses and strains. In the following, Neuber's rule in the generalized form [*18*] allowing for nonlinear net section behavior is used

$$E \cdot \sigma_q \cdot \epsilon_q = (\sigma_{e,q})^2 \cdot \frac{E \cdot e^*}{p^*} \quad \text{with} \quad p^* = \frac{p \cdot \sigma_F}{p_p}, \quad e^* = g(p^*) \tag{12}$$

Here $\sigma_{e,q}$ is the local equivalent stress at the examined location based on theory of elasticity, e.g., Eqs 1,2,5 or finite element analysis. It is proportional to the applied pressure p. Note that in order to account for net section yielding the fully plastic limit load for elastic perfectly-plastic material behavior p_p has to be known from Eq 6 or estimated. Combining the stress-strain curve and Neuber's rule as for uniaxial conditions, curves relating pressure to local *elastic-plastic* equivalent strains $\epsilon_q(p)$ and stresses $\sigma_q(p)$ are obtained for a monotonic loading segment starting from zero stresses, strains, and pressure. In the next step those equivalent stresses and strains have to be decomposed into principal stresses and strains. Here, validity of deformation theory is assumed so that plastic strain components are proportional to their deviatoric stress counterparts

$$(\epsilon_p)_{ij} = \frac{3}{2}\frac{\epsilon_{p,q}}{\sigma_q} s_{ij} \tag{13}$$

In total strains Hencky's equations can be written as a generalized form of Hooke's law for the examined location at the bore

$$\epsilon_r = \frac{\epsilon_q}{\sigma_q}(-p - \nu'(\sigma_\varphi + \sigma_z)) \tag{14}$$

$$\epsilon_\varphi = \frac{\epsilon_q}{\sigma_q}(\sigma_\varphi - \nu'(\sigma_z - p)) \tag{15}$$

$$\epsilon_z = \frac{\epsilon_q}{\sigma_q}(\sigma_z - \nu'(\sigma_\varphi - p)) \tag{16}$$

$$\text{where } \nu' = \frac{1}{2} - \left(\frac{1}{2} - \nu\right)\frac{\sigma_q}{E\epsilon_q} \tag{17}$$

There are four equations, 14, 15, 16, and 11, to determine the five unknown quantities ϵ_r, ϵ_φ, ϵ_z, σ_φ, $\sigma_z(\sigma_r = -p)$. The missing equation will in many cases be a boundary condition; sometimes an additional assumption is necessary. For cylindrical tubes with open or closed ends, Eqs 3 and 4, which are based on equilibrium conditions, still apply. For straight cylindrical bores in uniform noncylindrical components, e.g. bores in a rectangular parallelepiped, Eq 4 still describes open end conditions, while closed end conditions have to be formulated more generally than Eq 3

$$\sigma_z = p\frac{A_{\text{bore}}}{A_{\text{wall}}} \tag{18}$$

For cylindrical and noncylindrical components under plane strain conditions, Eq 5, which has been derived by the theory of elasticity, has to be replaced by the more general formulation $\epsilon_z = 0$. If the examined point is located at the intersection of crossing bores, the appropriate boundary condition is

$$\sigma_z = -p \tag{19}$$

If σ_z is known from boundary conditions at the examined location, the decomposed stress components are

$$\sigma_\varphi = \tfrac{1}{2}(\sigma_z - p) + \sqrt{\sigma_q^2 - \tfrac{3}{4}(p + \sigma_z)^2} \qquad \sigma_z \text{ from Eqs 3,4,18, or 19} \tag{20}$$

If the examined location deforms in a state of plane strain, the stress components can be calculated from

$$\sigma_\varphi = \sqrt{\left(\left(\frac{a}{b}\right)^2 - 1\right)p^2 + \frac{2}{b}\sigma_q^2} - \frac{a}{b}p \tag{21}$$

$$\begin{aligned} \sigma_z &= \nu'(\sigma_\varphi - p) \\ \text{with } a &= 1 + 2\nu' - 2\nu'^2 \\ b &= 2(1 - \nu' + \nu'^2) \end{aligned} \tag{22}$$

Still, some notch-like situations at bores remain where none of the boundary conditions described above are valid. Extensive studies have shown that the ratio of $\epsilon_z/\epsilon_\varphi$ remains almost constant in notches throughout plastic deformation, forced by the surrounding elastic material [*13,14*]. Therefore, in the remaining cases it will be assumed that this ratio stays the same as under purely elastic conditions

$$\frac{\epsilon_z}{\epsilon_\varphi} = \frac{\epsilon_{e,z}}{\epsilon_{e,\varphi}} \tag{23}$$

Note that this condition is satisfied exactly in plane strain and that in most thick-walled components ϵ_z remains very small under all kinds of end conditions. The stress components then read as

$$\sigma_\varphi = \sqrt{\left[\left(\frac{m}{2n}\right)^2 - \frac{1+e+e^2}{n}\right] p^2 + \frac{1}{n}\sigma_q^2} - \frac{m}{2n}p \tag{24}$$

$$\sigma_z = d\sigma_\varphi + ep \tag{25}$$

$$\text{with } m = d + 2de - e + 1$$
$$n = 1 - d + d^2$$

$$d = \frac{\epsilon_{e,z}/\epsilon_{e,\varphi} + \nu'}{1 + \nu'\epsilon_{e,z}/\epsilon_{e,\varphi}} \tag{26}$$

$$e = \frac{\nu'(\epsilon_{e,z}/\epsilon_{e,\varphi} - 1)}{1 + \nu'\epsilon_{e,z}/\epsilon_{e,\varphi}}$$

In all three cases the corresponding strain components can then be determined from Eqs 14,15,16.

Now full stress and strain tensors as a function of applied pressure have been determined for a monotonic loading segment starting from zero; $\sigma_{ij}(p)$, $\epsilon_{ij}(p)$. Similarly, curves for unloading can be obtained by this procedure for Masing behavior (Eq 9): $\Delta\sigma_{ij}(\Delta p)$, $\Delta\epsilon_{ij}(\Delta p)$. In a last step these curves are combined following the memory rules [*16,17*], which for a simple loading and unloading sequence as in autofrettage can be reduced to

$$\sigma_{ij}^{RS} = \sigma_{ij}(p = p_{aut}) - \Delta\sigma_{ij}(\Delta p = p_{aut}) \tag{27}$$

$$\epsilon_{ij}^{RS} = \epsilon_{ij}(p = p_{aut}) - \Delta\epsilon_{ij}(\Delta p = p_{aut}) \tag{28}$$

The major assumptions of this approach are

1. Masing behavior of the material.
2. Applicability of Neuber's rule.
3. Hencky's flow rule.
4. Memory rules applied to multiaxial stress and strain *components.*
5. For some cases, lateral constraint at notches ($\epsilon_z/\epsilon_\varphi$ = *constant*).

In Fig. 3 numerical calculations for a relatively thin tube (R_o/R_i = 1.3) under plane strain conditions are shown. The stress-strain curve of the material is of the Ramberg-Osgood type

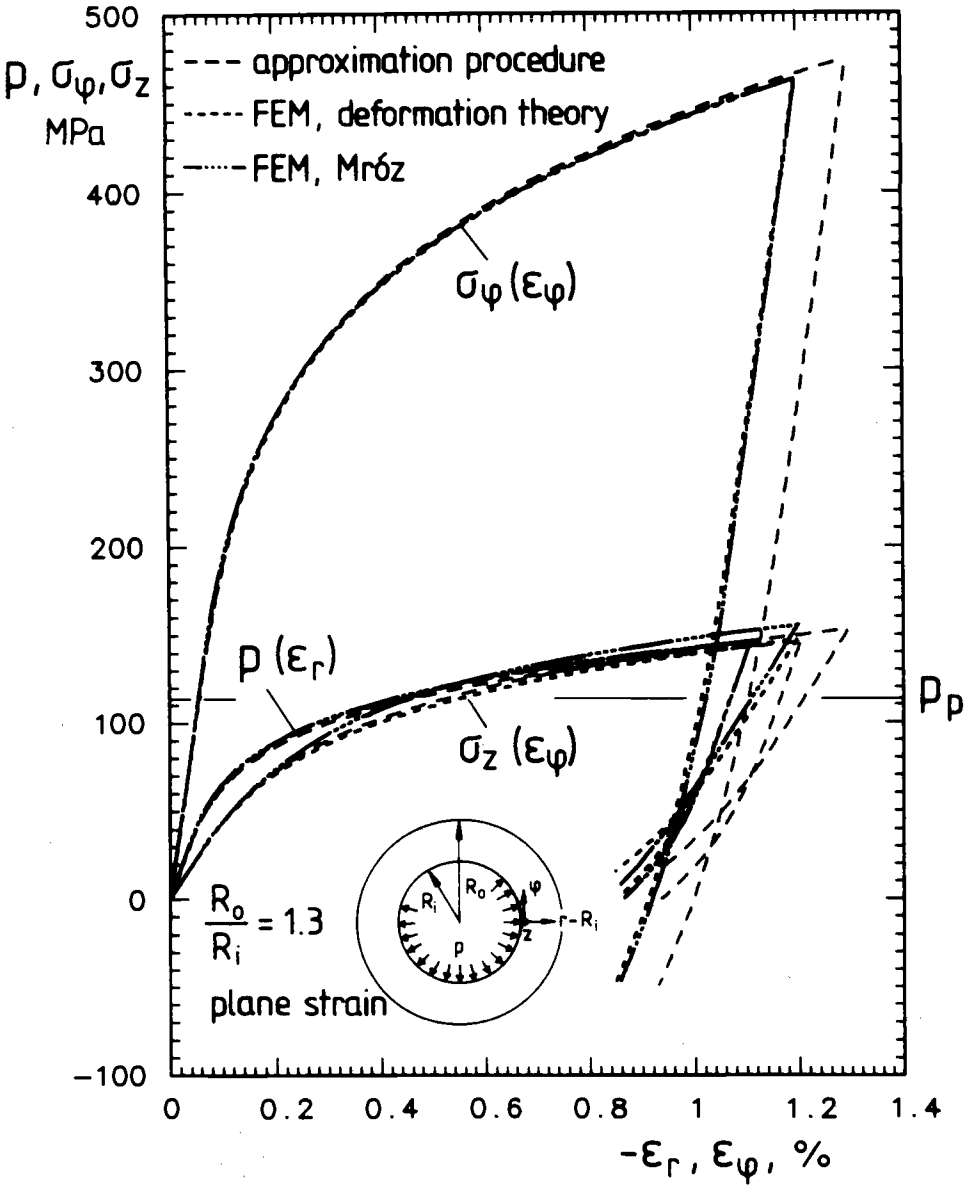

FIG. 3—*Stress-strain path at the bore for stable material behavior.*

$$\epsilon = \frac{\sigma}{E} + \left(\frac{\sigma}{K'}\right)^{1/n'} \tag{29}$$

with $E = 210\,000$ MPa, $K' = 1337$ MPa, $n' = 0.207$

The tube is loaded up to $p = 1.3p_p(R'_{p0.2} = 377$ MPa). In finite element analyses [*19,20*] deformation theory and kinematic hardening modeled by the multi-surface approach of Mróz [*21*]

and by Prandtl-Reuss equations were used. As pure deformation theory cannot be used for unloading, the procedure described by Eqs 27 and 28 was used for the unloading segment of the curves. Comparison of the two finite element analyses clearly shows that Hencky's flow rule and the memory rules applied to components fit very well in this situation. This may be surprising as the ratios of the deviatoric stress components s_φ/s_r and s_z/s_r are not constant during loading (Fig. 4). Integration of the Prandtl-Reuss equations leads to Hencky's flow rule if the ratios of the deviatoric stress components stay constant. This does not necessarily mean that there will be significant deviations between the two theories if the ratios are not constant. This can be seen in Fig. 4, where those ratios change in a similar way for both approaches. The results shown here for one component geometry have been found for others as well, e.g. Figs. 7 and 8. They are in agreement with the results of other investigators [*4*].

Comparison with the approximation procedure shows a slight overestimation of strains. It has to be attributed solely to Neuber's rule, which exhibits this behavior for different geometric situations with relatively smooth notches as well [*22*]. It could be reduced using other load-notch strain approximation formulas [*22,23*], but as almost no deviations exist for the residual stress components, this is thought to be unnecessary for the shown cases. For very large ratios between onset of yielding and fully plastic state, however, Neuber's rule will not be appropriate.

Extension of the Mróz Model to Transient Material Behavior

The Mróz model [*21*] has been found to describe stable cycle behavior of metals well. In uniaxial stress states, identical results to the Masing plus memory approach are obtained. Multiaxial conditions are modeled by a set of discrete yield surfaces, which may move in stress space. These yield surfaces only move during plastic deformation. They never intersect, but can consecutively contact each other. The yield surfaces are concentric about the zero stress state for materials free of residual stresses.

Each yield surface corresponds to a point on the uniaxial cyclic stress-strain curve specifying a flow stress as well as a plastic hardening modulus. If the yield function of von Mises is used, those surfaces are described by

$$\tfrac{3}{2}(\mathbf{s} - \boldsymbol{\alpha}^{(l)}):(\mathbf{s} - \boldsymbol{\alpha}^{(l)}) - (\sigma_0^{(l)})^2 = 0 \tag{30}$$

where $\mathbf{s}$ is the deviatoric stress tensor, $\boldsymbol{\alpha}^{(l)}$ is the center of each yield surface l, and $\sigma_0^{(l)}$ is the stress at point l of the uniaxial σ-ϵ curve.

In the original model of Mróz [*21*], purely kinematic hardening is assumed, i.e. yield surface radii $\sigma_0^{(l)}$, were kept constant. To extend this model to transient material behavior, a very simple approach was used which is analogous to the multilinear description of the σ-ϵ curve in the original model. Experimental data on cyclic hardening or softening can be derived, for example, from plastic strain controlled constant amplitude tests. In these tests the number of cycles N is proportional to the accumulated plastic strain $\int d\epsilon_{p,q} = \int \sqrt{(2/3)(d\epsilon_p : d\epsilon_p)}$. If such tests are conducted with different amplitudes, stress-strain curves corresponding to different accumulated plastic strains can be constructed. These changing σ-ϵ curves can be used to specify the evolution of $\sigma_0^{(l)}$ for $\epsilon_p^{(l)} = \textit{constant}$ as a piecewise linear approximation of experimental data

$$\sigma_0^{(l)} = f(\int d\epsilon_{p,q}) = f(N) \tag{31}$$

These data can also be gathered from single specimen tests by constructing σ-ϵ curves from hysteresis segments through Eqs 8 and 9. Figure 5 gives a sketch of the process.

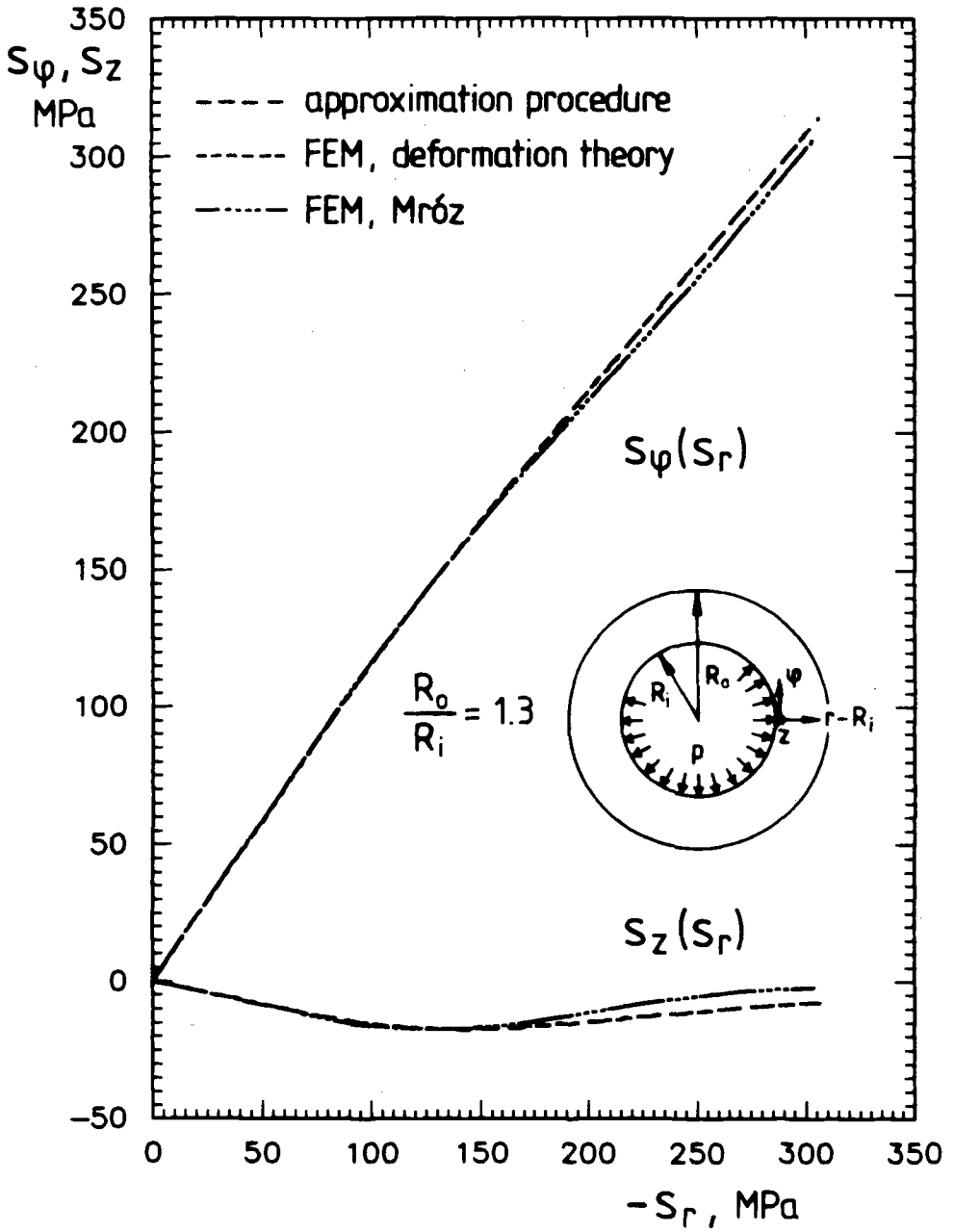

FIG. 4—*Path of deviatoric stress components for stable material behavior.*

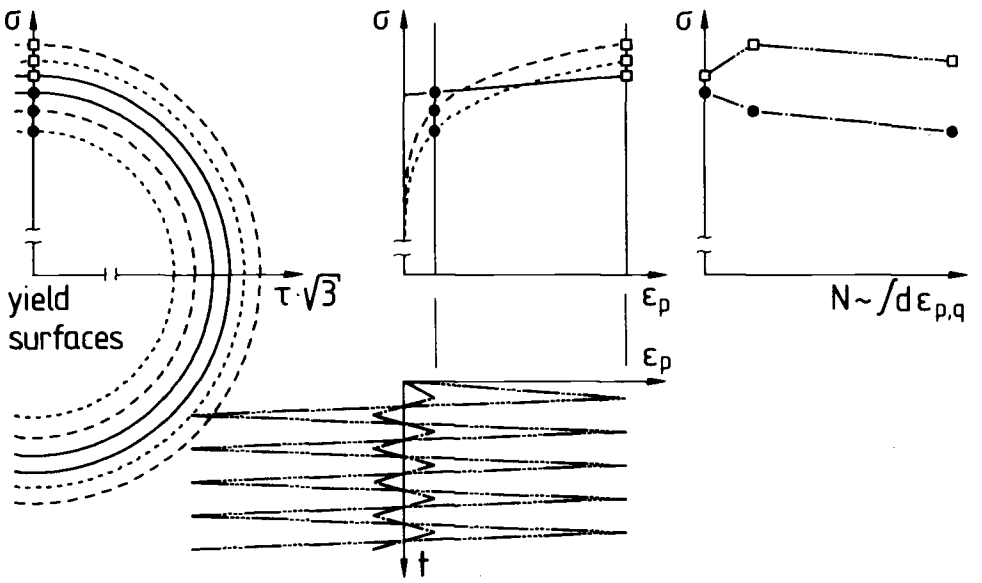

FIG. 5—*Extension of the Mróz model.*

To fulfill the kinematic constraints of the Mróz model, yield surface radii $\sigma_0^{(l)}$ of currently activated surfaces are changed to their interpolated values after finishing the usual Mróz procedure for each incremental load change. Their center points $\alpha^{(l)}$ are moved so that all currently activated surfaces remain in contact at the current stress point, also retaining their normal vectors at that point. Yield surfaces not currently activated are not changed, but after activation they are immediately switched to their current value of $\sigma_0^{(l)} = f(\int d\epsilon_{p,q})$ as if they had been activated throughout the whole process. This means that changes of the σ-ϵ curve do not affect monotonic segments of *proportional* loading, but become obvious immediately after load reversal. Also in proportional loading the stress-strain path will return to the initial (static) curve exceeding prior maximum stresses (Memory 1 or 3), but the ranges of stresses and strains of subsequent cycles with the same amplitude will only be determined by the current σ-ϵ curve. In other words, form and size of hysteresis segments, but not their position, are a function of accumulated plastic strain only, not of the *distribution* or *sequence* of high and low load amplitudes. While this approach may still not model all aspects of cyclic hardening or softening [*24–26*], it is compatible with many approaches in treating accumulated plastic strain as the primary variable to describe changes in stress-strain behavior [*27,28*]. A multilinear approximation of experimental evolution data that is different from other approaches was used here because the mathematical form of the underlying σ-ϵ equation in two-surface models, e.g. Ref *27,* and the evolution equations in both two- and multi-surface models, e.g. Refs *27* and *24,* could not be fitted to data taken from uniaxial tests during the first cycles.

The current model does not include cyclic creep or mean stress relaxation, but it can easily be combined with the respective extension of the multi-surface model of Chu [*29*]. In the context of this paper the extended Mróz model was used for the verification of the developed approximation procedure. For autofrettage the most important feature of the extension of the Mróz model is that the σ-ϵ curves during unloading will depend on the maximum plastic strain during loading just like experimentally obtained curves.

Approximation Procedure for Transient Material Behavior

The procedure of Hoffmann and Seeger [*13,14,15*], which has been described in the section entitled "Approximation Procedure for Stable Stress-Strain Curves," can easily be extended to transient material behavior if the basic stress-strain curve is not kept constant as in the original approach. Different stress-strain curves have to be used for loading by autofrettage $\sigma(\epsilon)$, unloading from autofrettage pressure $\Delta\sigma^{(1)}(\Delta\epsilon^{(1)})$, and for fluctuating service pressure $\Delta\sigma(\Delta\epsilon)$. Here $\sigma(\epsilon)$ is the static stress-strain curve, $\Delta\sigma^{(1)}(\Delta\epsilon^{(1)})$ is the hysteresis segment during first unloading after a static tension test, and $\Delta\sigma(\Delta\epsilon)$ has to be derived from the cyclic σ-ϵ curve assuming MASING behavior (Eq 9).

Starting with these different curves, the rest of the procedure remains as outlined in the section entitled "Appropriate Procedure for Stable Stress-Strain Curves" and as shown in Fig. 6. As autofrettage and subsequent fluctuating service pressure do not provoke the more difficult types of material memory (return on to the static curve), simple superposition of the stress and strain components can still be used (Eqs 27 and 28). In the absence of an experimentally determined σ-ϵ hysteresis segment for first unloading, a conservative estimation of cyclically softening materials is given by the stabilized curve and for cyclically hardening materials by the static curve. Figure 7 shows stress-strain paths calculated by the finite element approach as described in the section entitled "Extension of the Mróz Model to Transient Material Behavior" and by the approximation procedure for a tube ($R_o/R_i = 2$) under plane strain. The autofrettage pressure was $p_{aut} = 0.95\ p_p$. A high-strength steel, 42 Cr Mo 4 (similar to AISI 4140), was modeled using the cyclic σ-ϵ curve for unloading to show the effects more clearly. During loading a bilinear σ-ϵ curve with a yield stress $\sigma_F = 1000$ MPa, Young's modulus $E = 210\,000$ MPa, and a plastic tangent modulus $E_T = 1400$ MPa was used; during unloading for the approximation procedure, a Ramberg-Osgood type of stress-strain curve was used (Eq 29) with $K' = 1370$ MPa and $n' = 0.1$. In the finite element analysis the same unloading curve was used for integration points exceeding accumulated plastic strain $\int d\epsilon_{p,q} = 0.8\%$; for all other points it was linearly interpolated between this curve and the loading segment. Therefore in

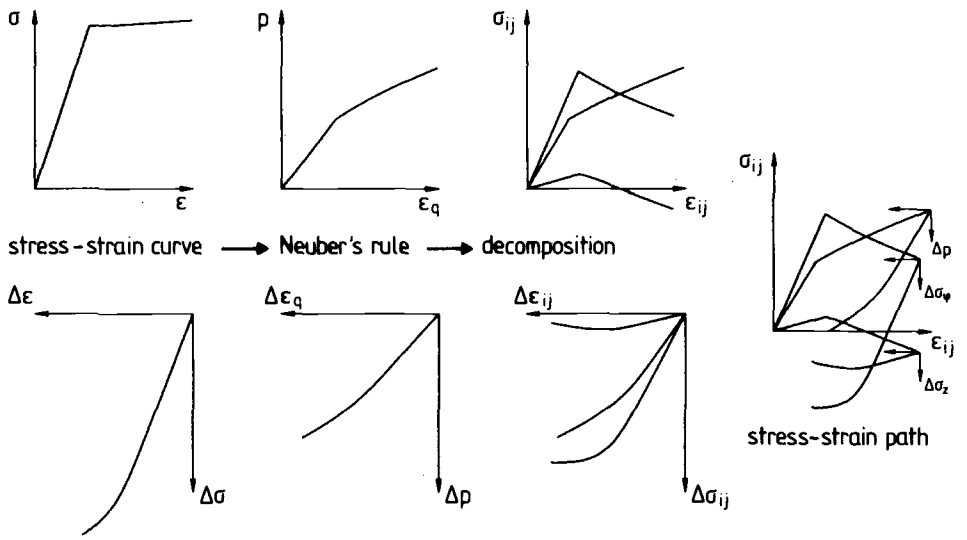

FIG. 6—*Approximation procedure for transient material behavior.*

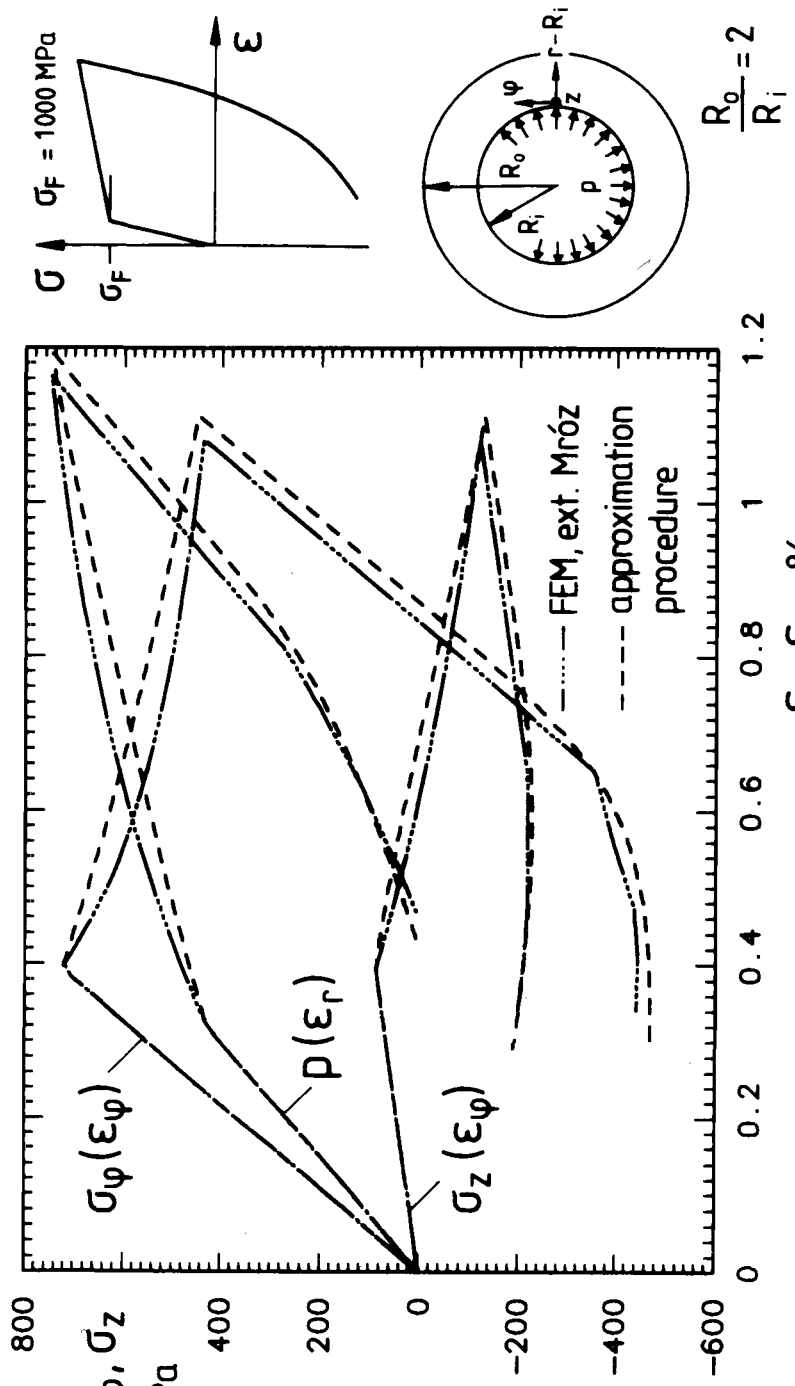

FIG. 7—*Stress-strain path at the bore for transient material behavior.*

the finite element analysis most parts of the structure did not exactly follow the unloading curve of the approximation. Still, the approximation procedure yields very good results. As in the approximation for the stable material behavior, the small deviations in strains have to be attributed to Neuber's rule.

Figure 8 shows the path of the deviatoric stress components for loading as well as for unloading using a $\Delta\sigma_{ij}/2$ coordinate system as in Fig. 6 for the unloading segment. It can be seen that, in spite of significant changes in the deviator ratios, the Prandtl-Reuss equations of the extended Mróz model and Hencky's flow rule as part of the approximation yield similar results.

Although autofrettage pressure had almost reached the limit pressure p_p so that most of the tube's wall had yielded, significant residual stresses were produced.

Optimal Autofrettage Pressure

For components with only one notch, the pressure producing the maximum compressive residual stresses is also the optimal pressure giving the highest fatigue strength because even with mean stress relaxation it produces the lowest mean stresses for service loading. The procedure described above can be used in a straightforward manner to predict influences of autofrettage pressure, component geometry, and material behavior on the formation of residual stresses—the only equations which cannot be solved directly are the set of two nonlinear equations implementing Neuber's rule (Eqs 13 and 8).

In Fig. 9 the influence of four different types of stress-strain curves on resulting residual stresses is shown for a tube with $R_o/R_i = 2$. For the loading segment of the σ-ϵ curve, elastic perfectly-plastic and bilinear hardening materials were assumed. For unloading, a purely elastic and a cyclic stress-strain curve were looked upon. It can be seen in Fig. 9 that regardless of the type of stress-strain curve the residual stress σ_q^{RS} increases monotonically with autofrettage pressure p_{aut} until the fully plastic limit load p_p is reached, assuming elastic perfectly-plastic material. For this type of material, that point marks the collapse load, so these curves stop there. For hardening materials, the other curves show a drastic reduction of residual stresses for $p_{\text{aut}}/p_p > 1$.

To produce high residual stresses it is necessary on one hand to have high plastic *strains* during loading, because otherwise unloading would be almost elastic, but on the other hand to retain a maximum *tensile stress* as low as possible, otherwise the unloading segment will not be able to achieve highly compressive stresses. This explains why the optimal autofrettage pressure occurs at the start of net section yield, producing high plastic strains but not yet high stresses due to hardening. This effect is independent of the type of material examined and of the component geometry as can be seen in Fig. 10. There is only one exception to this rule: if elastic perfectly-plastic behavior is assumed on unloading, the function $\sigma_q^{RS}(p_{\text{aut}})$ remains constant for all pressures, causing reversed yielding. However, even for this material behavior, the fully plastic limit load is reached earlier than reversed yielding for tube radii $R_o/R_i \lesssim 3 \ldots 5$, depending on end conditions and flow criterion (see Fig. 2 for max $\sigma_q = p_p$). Of course, to prevent bursting, p_{aut} will have to be smaller than p_p. Assuming $p_{\text{aut}} = 0.85\, p_p$ the tube wall will have yielded approximately halfway for common tube radii, explaining an often-cited rule of thumb which relates optimal pressure to extending the plastic zone to $R_{\text{opt}} = 0.5(R_o - R_i)$.

Figure 10 also shows that the maximum residual stresses can be quite low for relatively thin-walled tubes due to their low plastic limit load. Here, due to small stress gradients across the tube wall, compressive residual stresses lead to residual stresses of a similar size at the outer radius $r = R_o$, which will be in tension, reducing fatigue strength there. In thick-walled components, the residual stresses at the outside are also in tension, but because of steeper stress gradients residual stresses as well as local stress and strain amplitudes under service pressure are so much smaller and therefore not critical.

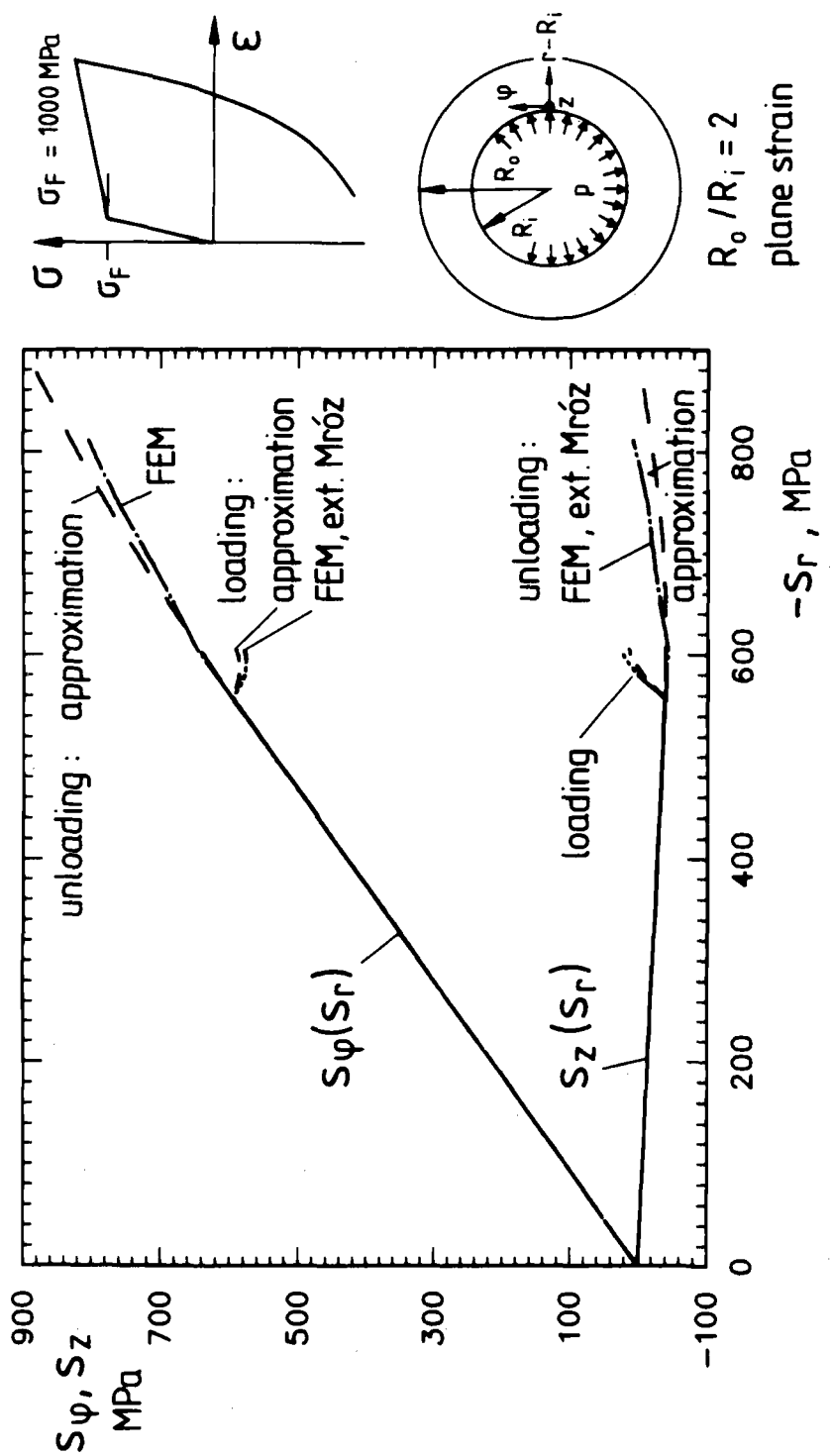

FIG. 8—*Deviatoric stress components on loading and unloading for transient material behavior.*

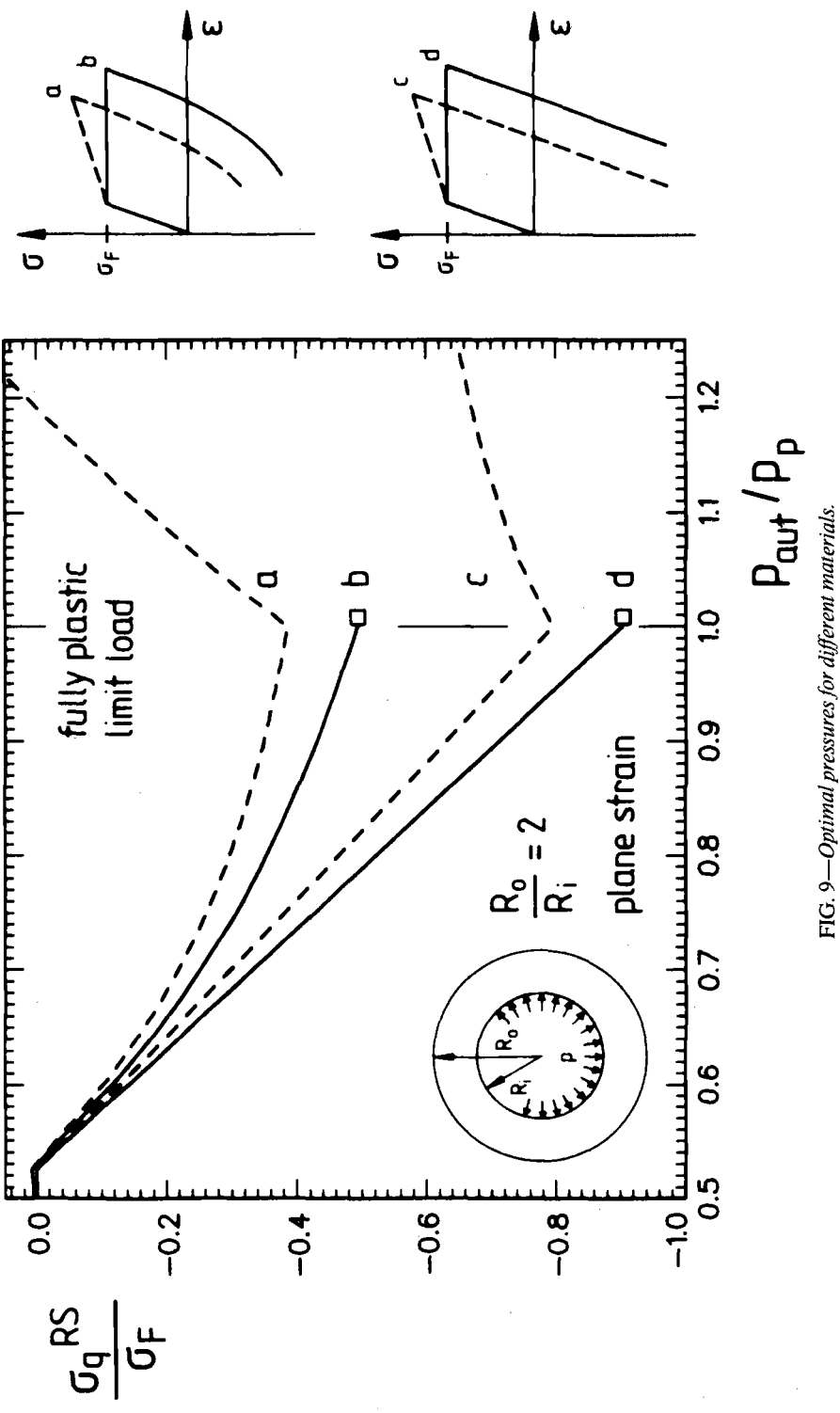

FIG. 9—*Optimal pressures for different materials.*

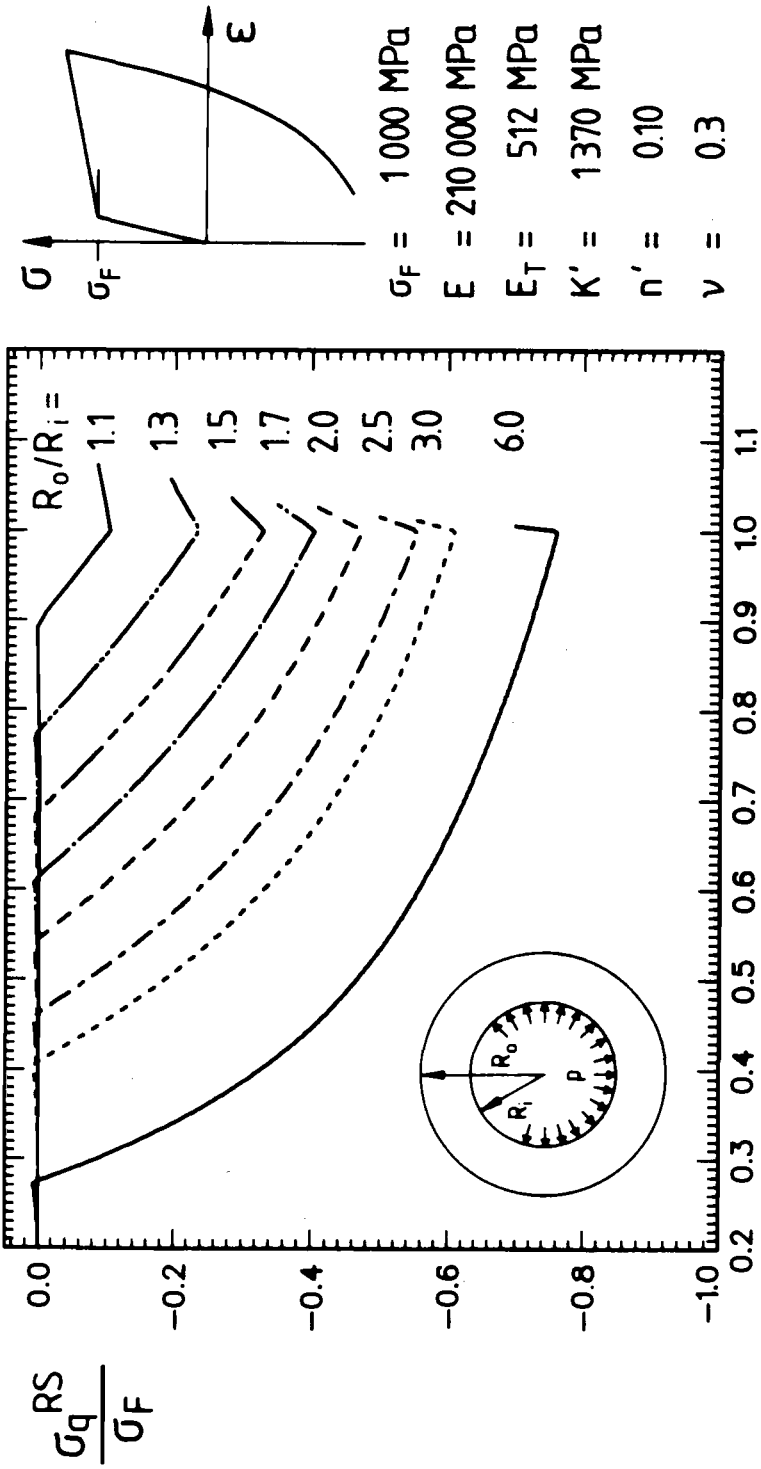

FIG. 10—*Optimal pressures for tubes with different radii.*

Notches on the outer side of a tube, however, might become critical under autofrettage because significant tensile residual stresses may develop if plastic deformation occurs at these notches. Such situations can be checked by the approximation procedure replacing Eqs 20,21,22, or 24,25 with the equations originally developed by Hoffman and Seeger [*13–15*] for pressure-free components

$$\sigma_\varphi = \frac{1}{\sqrt{1 - d + d^2}} \sigma_q \tag{32}$$

$$\sigma_z = d \cdot \sigma_\varphi \tag{33}$$

with d defined in Eq 26. In complex components all locations with a local maximum of equivalent stress will have to be checked with the help of the outlined procedure, adding service loading as the third segment to the calculated stress-strain path. In a few cases it will not be possible to evaluate the influences of different multiaxial mean stresses and multiaxial strain amplitudes under service loading without performing damage calculations for the calculated paths because *in general* the optimal autofrettage pressure for a given component with more than one possible crack initiation site does not have to be the pressure producing the maximum residual stresses.

Application to Components

One problem for the general application of the outlined approximation procedure has not been discussed yet: the knowledge of the fully plastic limit load p_p for a given component. Figure 11 shows the development of plastic zones for four different parallelepipeds with bores. It can be seen that in one case ($R_o/R_i = 1.3$, with wall size ratio $W_g/W_k = 2$, Fig. 12) yielding even starts at the outside. Still it has been found that the plastic limit load can be estimated extremely well by inscribing a tube into the examined component with a wall size equal to the thinnest wall size of the component, p_p can then be determined from Eqs 6 or 7. As sketched in Fig. 12, this approach has been successfully tried for different geometries of parallelepipeds with one bore, parallelepipeds with co-linear rows of bores, tubes with interior shoulders, and for crossbores. The cases in Fig. 11 were analyzed by finite elements for plane strain conditions and von Mises flow criterion. For $R_o/R_i = 1.3$ the estimated $p_p = 0.303$ was only 0.3% off the finite element results, for $R_o/R_i = 2$ (Eq 6) gave $p_p = 0.800$, which was only 2% too low.

There is one common geometry where p_p cannot be estimated this way. It is a closed cylindrical tube yielding through the top instead of the cylinder walls. Dead end bores with thin caps are in the same category. For these cases currently no estimation of p_p can be given.

Conclusion

The multiaxial load-notch strain approximation procedure of Hoffmann and Seeger has been extended to pressurized components exhibiting transient material behavior. It has been shown that the results from this procedure agree very well with finite element analyses; based on deformation theory, the pure Mróz model and a Mróz model extended to transient material behavior. This procedure can predict full residual stress and strain tensors as a function of applied autofrettage pressure for any type of stress-strain curve during loading and unloading and for nonuniform components provided the stress components based on the theory of elasticity at the examined locations are known.

In addition, it was found that deformation theory yields very accurate results when applied to common pressurized components, although the ratios of the deviatoric stress components

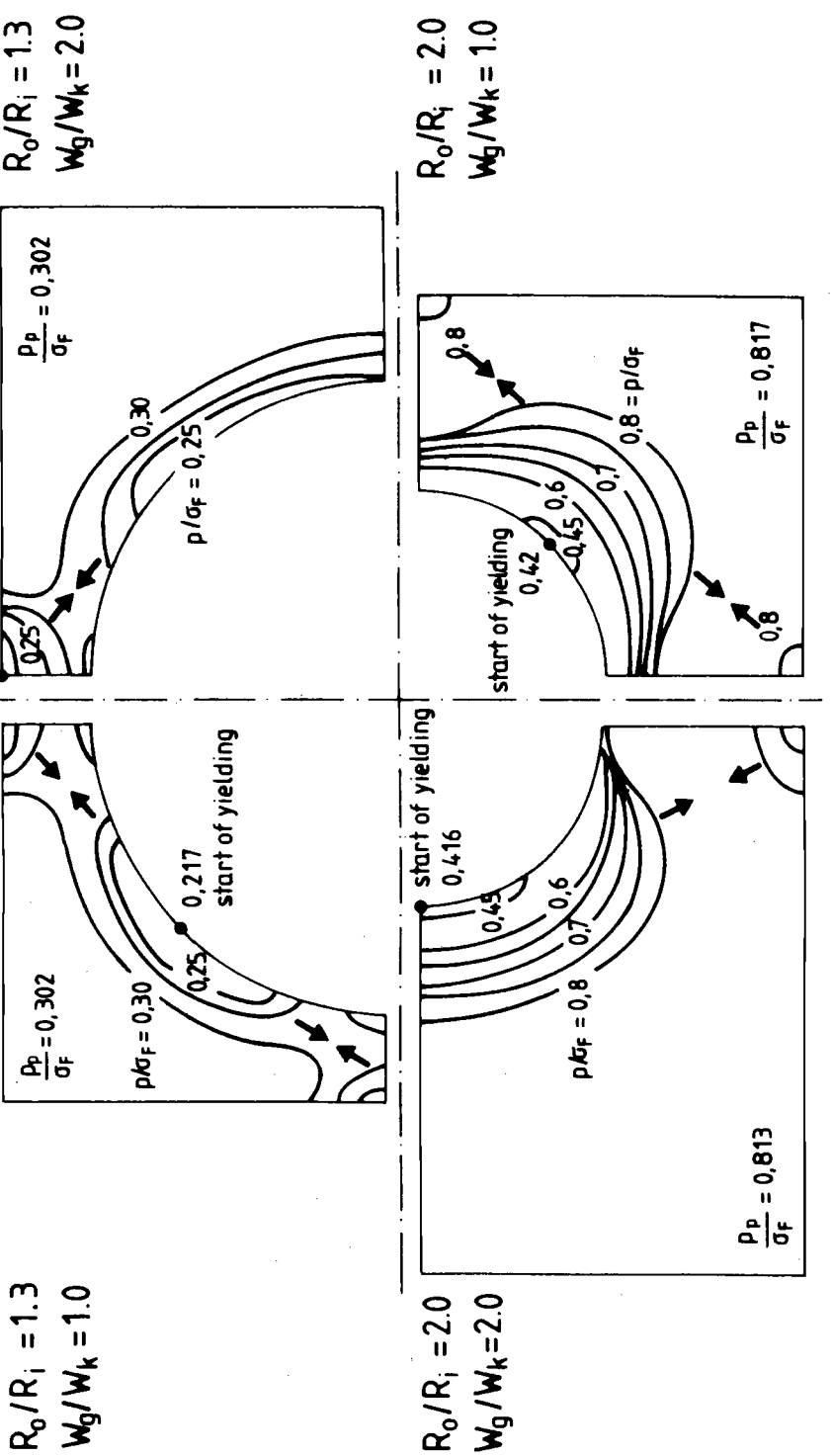

FIG. 11.—*Development of plastic zones in parallelepipeds with one bore.*

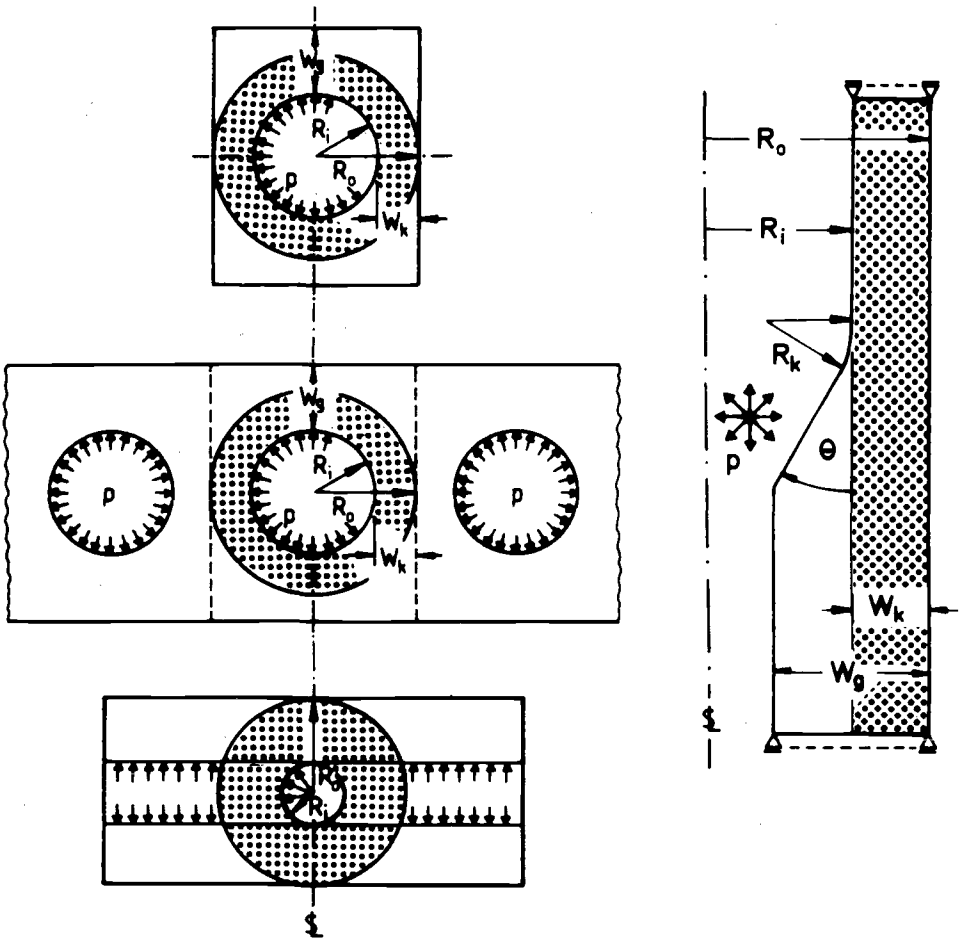

FIG. 12—*Estimation of fully plastic limit loads for different component geometries.*

were found to change during loading. These computations were for proportional loading only, as is typical for autofrettage. This confirms numerically the use of deformation theory in many analytical solutions for tubes and may be exploited for faster finite element analyses of such components.

References

[1] Szabo, I., *Höhere Technische Mechanik,* Springer, Berlin, 1977.
[2] Chakrabarty, J., *Theory of Plasticity,* McGraw-Hill Book Company, New York, 1987.
[3] Hill, R., Lee, E. H., and Tupper, S. J., "The Theory of Combined Plastic and Elastic Deformation," *Proceedings of the Royal Society of London,* Series A, Vol. 191, 1947, pp. 278–303.
[4] Hodge, Jr., P. G. and White, Jr., G. N., "A Quantitative Comparison of Flow and Deformation Theories of Plasticity," *Journal of Applied Mechanics,* June 1950, pp. 180–184.
[5] Bland, D. R., "Elastoplastic Thick-Walled Tubes of Work-Hardening Material Subject to Internal and External Pressures and to Temperature Gradients," *Journal of Mechanics and Physics of Solids,* Vol. 4, 1956, pp. 209–229.

[6] Manning, W. R. D., "The Overstrain of Tubes by Internal Pressure," *Engineering,* Vol. 159, 1945, pp. 83–107.
[7] Crossland, B. and Bones, J. A., Behaviour of Thick-Walled Cylinders Subjected to Internal Pressure," *Proceedings of the Institute of Mechanical Engineers,* Vol. 172, 1958, pp. 777–804.
[8] Rees, D. W. A., "A Theory of Autofrettage with Application to Creep and Fatigue," *International Journal of Pressure Vessels and Piping,* Vol. 30, 1987, pp. 57–76.
[9] Reckling, K. A., *Plastizitätstheorie und ihre Anwendung auf Festigkeitspobleme,* Springer, Berlin, 1967.
[10] Chen, P. C. T., "Bauschinger and Hardening Effect on Residual Stresses in an Autofrettaged Thick-Walled Cylinder," *Journal of Pressure Vessel Technology, Transactions of ASME,* Vol. 108, No. 1, February 1986, pp. 108–112.
[11] Tomita, N. "Analysis of Cyclic Plasticity, Fatigue and Fracture of Thick-Walled Cylinders," Ph.D. thesis, University of Illinois at Urbana-Champaign, 1981.
[12] Stacey, A. and Webster, G. A., "Determination of Residual Stresses in Autofrettaged Tubing," *International Journal of Pressure Vessels Piping,* Vol. 31, No. 3, 1988, pp. 205–220.
[13] Hoffmann, M. and Seeger, T., "A Generalized Method for Estimating Multiaxial Elastic-Plastic Notch Stresses and Strains: Part 1: Theory," *Journal of Engineering Materials and Technology,* Vol. 107, 1985, pp. 250–254.
[14] Hoffmann, M. and Seeger, T., "A Generalized Method for Estimating Multiaxial Elastic-Plastic Notch Stresses and Strains: Part 2: Application and General Discussion," *Journal of Engineering Materials and Technology,* Vol. 107, 1985, pp. 255–260.
[15] Hoffmann, M. and Seeger, T., "Stress-Strain Analysis and Life Predictions of a Notched Shaft Under Multiaxial Loading," SAE AE-14, G. E. Leese and D. Socie, Eds., *Multiaxial Fatigue—Analysis and Experiments,* Chap. 6, Society of Automotive Engineers, Warrendale, PA, 1989, pp. 81–101.
[16] Matsuishi, M. and Endo, T., "Fatigue of Metals Subjected to Varying Stress," *Proceedings of the Kyushu Branch of Japan Society of Mechanical Engineers,* 1968, pp. 37–40.
[17] Clormann, U. H. and Seeger, T., "RAINFLOW-HCM, Ein Zählverfahren für Betriebsfestigkeitsnachweise auf werkstoffmechanischer Grundlage," *Stahlbau,* Vol. 55, No. 3, 1986, pp. 65–71.
[18] Seeger, T. and Heuler, P., "Generalized Application of Neuber's Rule," *Journal of Testing and Evaluation,* Vol. 8, No. 4, 1980, pp. 199–204.
[19] *ABAQUS Theory Manual, Version 4.8,* Hibbit, Karlsson and Sorensen, Inc., Providence, RI, 1990.
[20] Köttgen, V. B., Anthes, R. J., and Seeger, T. "Implementation of the Mróz Model into the Finite Element Program ABAQUS," Technical Reports FF-7/1991, FW-8/1991, Technische Hochschule Darmstadt, Fachgebiet Werkstoffmechanik, 1991. Part 1: Theory; Part 2: source code on floppy disk and examples (in German).
[21] Mróz, Z., "On the Description of Anisotropic Workhardening," *Journal of Mechanics and Physics of Solids,* Vol. 15, 1967, pp. 163–175.
[22] Seeger, T., Beste, A., and Amstutz, H., "Elastic-Plastic Stress Strain Behaviour of Monotonic and Cyclic Loaded Notched Plates," *Fracture 1977, Proceedings of the International Conference on Fracture,* University of Waterloo, Waterloo, Canada, D. M. R. Taplin, Ed., 1977, pp. 943–952.
[23] Glinka, G., "Energy Density Approach to Calculation of Inelastic Strain-Stress Near Notches and Cracks," *Engineering Fracture Mechanics,* Vol. 22, 1985, pp. 485–508.
[24] Mröz, Z., "Hardening and Degradation Rules for Metals Under Monotonic and Cyclic Loading," *Journal of Engineering Materials and Technology,* Vol. 105, 1983, pp. 113–118.
[25] Scheibe, H.-J., "Zum zyklischen Materialverhalten von Baustahl und dessen Berücksichtigung in Konstruktionsberechnungen," Technical Report 6314, TU Braunschweig, Institut für Stahlbau, Germany, 1990.
[26] Chaboche, J. L., "Viscoplastic Constitutive Equations for the Description of Cyclic and Anisotropic Behaviour of Metals," Technical Report Serie des Sciences Techniques, Vol. XXV, No. 1, l'Academie des Sciences, Paris, 1977.
[27] McDowell, D. L., "A Two Surface Model for Transient Nonproportional Cyclic Plasticity—Part 1 and 2, *Journal of Applied Mechanics, Transactions of ASME,* Vol. 52, 1985, pp. 298–308.
[28] Krempl, E. and Yao, D., "The Viscoplastic Theory Based on Overstress Applied to Ratchetting and Cyclic Hardening," K.-T. Rie, Ed., *Low Cycle Fatigue and Elasto-Plastic Behaviour of Materials,* Elsevier Applied Science, London, 1987, pp. 137–148.
[29] Chu, C.-C., "A Constitutive Model for Cyclic Creep/Relaxation," F. Jinghong and S. Murakami, Eds., *Proceedings International Conference on Constitutive Laws for Engineering Materials,* Vol. II, August 1989, Bejing, China, 1989, pp. 709–713.

Rangaswamy Seshadri[1] *and Revi K. Kizhatil*[2]

Notch Root Inelastic Strain Estimates Using GLOSS Analysis

REFERENCE: Seshadri, R. and Kizhatil, R. K., **"Notch Root Inelastic Strain Estimates Using GLOSS Analysis,"** *Advances in Multiaxial Fatigue, ASTM STP 1191,* D. L. McDowell and R. Ellis, Eds., American Society for Testing and Materials, Philadelphia, 1993, pp. 397–411.

ABSTRACT: Inelastic strains in notched mechanical components and structures can be predicted with reasonable accuracy using the generalized local stress strain (GLOSS) method of analysis. The GLOSS diagram is essentially a normalized stress-strain plot of a "local" region that is subjected to greater inelastic strains as compared to the "remaining" region. Inelastic response of the local region due to plasticity and creep is simulated by artificially lowering the stiffness of the nominally inelastic region. Thus, inelastic strains at the root of a notch can be estimated on the basis of two linear elastic finite element analyses per point on the load-notch strain curve.

The theory underlying GLOSS analysis essentially relates the inelastic multiaxial stress redistribution in the local region to the uniaxial stress relaxation process. The varying degrees of interaction between the local and remaining regions, which are characterized by the "constraint parameter," enable the determination of inelastic strains when used in conjunction with the cyclic stress strain curve.

The GLOSS method of analysis can be used to estimate inelastic effects for realistic notch geometries and component loadings. The method can be applied in a routine manner to a range of inelastic zone sizes. The incorporation of an Irwin's type of correction to the plastic zone enables reasonably accurate determination of the inelastic notch strains for the purpose of low-cycle-fatigue evaluations. The GLOSS method is applied in this paper to several geometric configurations of practical interest.

KEY WORDS: low-cycle fatigue, strain concentration, relaxation modulus, constraint parameter, follow-up

Nomenclature

- A_k Area of the kth element in a finite element discretization scheme
- E_0 Modulus of elasticity of local region
- E_s' Secant modulus of softened elements in the second linear elastic finite element analysis
- E_s'' Secant modulus of the softened elements in the second linear elastic finite element analysis with plasticity correction
- $E_{s,n}$ Secant modulus of a point on the Neuber locus
- E_r Relaxation modulus
- K' Cyclic strength coefficient
- $2N_f$ Reversals to failure
- n' Cyclic strain-hardening exponent
- ϵ_c Creep strain
- ϵ_{el} Elastic strain

[1] Professor and dean, and [2]graduate student, Faculty of Engineering, University of Regina, Regina S4S 0A2, Canada.

ϵ_t Total strain
ϵ'_f Fatigue ductility coefficient
τ Time
σ_e Equivalent stress (von Mises)
σ_{ei} Equivalent initial stress
σ'_f Fatigue strength coefficient
σ_m Mean stress
σ_y Yield stress
σ'_y Modified yield stress
$\overline{\sigma}_y$ Normalized yield stress ($= \sigma_y/\sigma_{ei}$)
$\Delta\epsilon_t^0$ Total local strain range
$\Delta\sigma$ Local stress range
θ Follow-up angle
$\overline{\gamma}$ Constraint parameter

Superscripts

o Local region
r Remainder region

Introduction

The strain-life approach has been used widely in evaluations pertaining to fatigue crack initiation and related life estimation. Fatigue life estimates of notched mechanical components and structures can be performed on the basis of a knowledge of the notch root strain history and smooth specimen fatigue data for fully reversed constant amplitude loading [*1,2*]. Total fatigue life of notched components can be estimated by procedures which combine the strain-life approach with fracture mechanics methods [*3,4*]. The total life is assumed to be made up of the initiation and propagation phases.

Central to the strain-life approach is the determination of the notch root inelastic strains. The common techniques that have been used in this regard are strain gage measurements, inelastic finite element analyses, and approximate analytical methods. While strain gaging and inelastic finite element modeling can be implemented in principle, they can be time consuming and expensive. Approximate analytical methods such as the Neuber rule [*5*], its variations [*6,7*], and the energy-based methods [*8,9*], while useful and simple to implement, generally lead to an overestimation or an underestimation of the notch root inelastic strains. Quite understandably, it would be difficult to accurately predict notch root strain fields using the approximate methods for a wide range of geometric configurations and material behavior.

The GLOSS method of analysis, which is the subject of this paper [*10,11*], is a practical compromise between the elaborate methods (such as the inelastic finite element technique and strain gaging) and the approximate analytical techniques. The GLOSS method offers useful insights into the nature of the local deformation field and constraints. The method possesses an aspect of "robustness," i.e., an ability to provide acceptable results on the basis of a conceptual insight and the availability of a less than ideal material data.

The GLOSS method of analysis is applied to several notched component configurations in this paper. Specifically, examples of a plate with a circular hole subjected to a tensile load, a Bridgman notch specimen in tension, and a pressurized cylinder with an internal circumferential notch are considered. The results obtained by GLOSS analysis are compared with inelastic finite element results and predictions made by the use of the Neuber rule.

The Generalized Local Stress Strain (GLOSS) Analysis

In the GLOSS method, described by Seshadri [*10*], the mechanical component or structure is divided into the local and remainder regions (Fig. 1). The local region typically experiences the largest inelastic effect and is often of interest from a design standpoint. The size of the local element, such as the notch root, would depend on the finite element discretization scheme used in the analysis. The GLOSS theory essentially relates the multiaxial stress distribution in the local region to the uniaxial redistribution process. The varying degrees of interaction between the local and remainder regions are characterized by a "constraint parameter" which can be used in conjunction with the uniaxial model to generate inelastic results.

Key to GLOSS evaluations is the determination of the local region relaxation modulus. This can be accomplished by studying the relaxation locus on the GLOSS diagram, which is essentially a plot of the normalized equivalent stress and the normalized equivalent strain. For small-to-moderate plastic zone sizes, the relaxation locus is almost linear in many practical component configurations. In other words, the local region relaxation modulus is dependent, to a first approximation, on the response of the remainder region. The local region response would therefore appear to be insensitive to the precise nature of the local region nonlinearity and the material constitutive relationship. The implication is quite significant in that the relax-

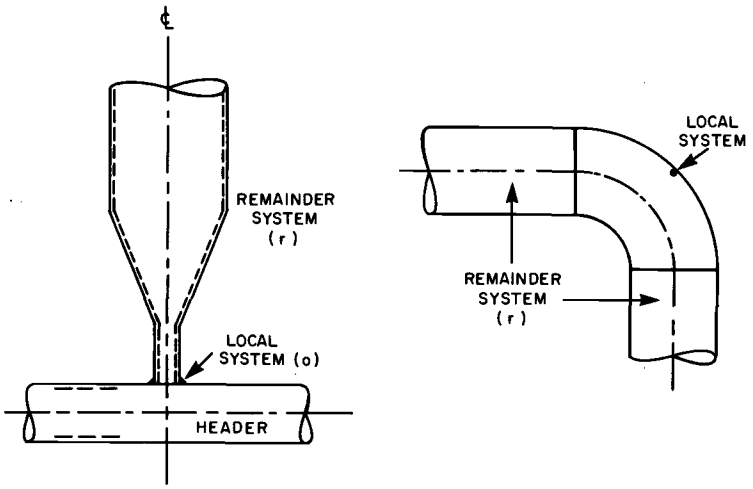

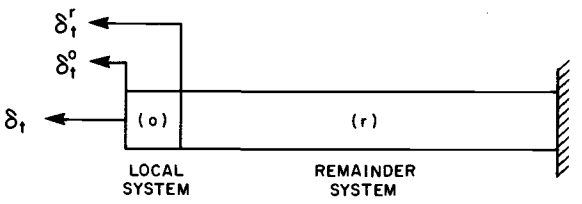

FIG. 1—*One-dimensional idealization of systems experiencing follow-up.*

ation modulus can be determined using any convenient constitutive relationship that allows progressive relative softening of the local region. Therefore, GLOSS analysis can be used to predict inelastic response whether the inelasticity arises due to first stage creep, steady state creep, or even time-independent plasticity. Local region softening by systematically reducing the elastic modulus, for instance, is therefore an attractive prospect.

On account of the foregoing aspect of the approximate dependence of the behavior of the local region on the response of the remainder system, which for small-to-moderate plasticity is almost linear, it is possible to theoretically derive the local region relaxation modulus on the basis of creep constitutive equations, which can then be used to determine plastic strains, say at the notch root.

The theory of GLOSS analysis is developed next on the basis of a comparison between multiaxial and uniaxial stress relaxation processes. The equivalent uniaxial strain distribution of the local region, which actually represents a multiaxial strain distribution, can be expressed as [*10*]

$$\dot{\epsilon}^o_{el} + \bar{\gamma}\dot{\epsilon}^o_c = 0 \tag{1}$$

where $\bar{\gamma}$ is the constraint parameter. Since the total local strain $\dot{\epsilon}^o_t$ is the sum of elastic, plastic, and creep contributions, and if the plastic strains are time invariant, then

$$\dot{\epsilon}^o_t = \dot{\epsilon}^o_{el} + \dot{\epsilon}^o_c \tag{2}$$

Combining Eqs 1 and 2

$$\dot{\epsilon}^o_{el} = \left(\frac{\bar{\gamma}}{\bar{\gamma} - 1}\right)\dot{\epsilon}^o_t \tag{3}$$

Recognizing that $\dot{\epsilon}^o_{el} = (1/E_0)(d\sigma_e/d\tau)$, the relaxation-modulus (E_r) can be defined as

$$E_r = \frac{d\sigma_e}{d\epsilon^o_t} = \frac{1}{\dot{\epsilon}^o_t}\left(\frac{d\sigma_e}{d\tau}\right) = \left(\frac{\bar{\gamma}}{\bar{\gamma} - 1}\right)E_0 \tag{4}$$

The relaxation modulus is the slope of the stress relaxation locus in the local region σ_e versus ϵ^o_t plot, i.e., the GLOSS diagram.

Introducing the nondimensional quantities,

$$\bar{\sigma} = \frac{\sigma_e}{\sigma_{ei}}, \bar{\epsilon}^o_t = \frac{\epsilon^o_t}{(\sigma_{ei}/E_0)}, \bar{E}_r = \frac{E_r}{E_0} \tag{5}$$

the normalized relaxation modulus can be expressed as

$$\bar{E}_r = \frac{\bar{\gamma}}{\bar{\gamma} - 1} \tag{6}$$

or

$$\bar{\gamma} = \frac{\bar{E}_r}{\bar{E}_r - 1} \tag{7}$$

The constraint parameter $\bar{\gamma}$ can therefore be expressed in terms of the relaxation modulus, $\bar{E}_r$.

Equation 1 can now be written as

$$(\bar{E}_r - 1)\dot{\epsilon}^o_{el} + \bar{E}_r\dot{\epsilon}^o_c = 0 \tag{8}$$

The above equation expresses the strain redistribution process in the local region in terms of the relaxation modulus.

Determination of Relaxation Modulus, $\bar{\mathrm{E}}_\mathrm{r}$

The insensitivity of the local region response to the precise nature of the local region nonlinearity and material constitutive relationship enables the determination of the relaxation modulus by systematically adjusting the modulus of elasticity in the inelastic region. The softening of the local region is relative to the remainder region; the actual material is not necessarily undergoing a cyclic softening process. This aspect of insensitivity of the local region response offers considerable simplifications.

The GLOSS diagram is a plot of the normalized equivalent stress versus the normalized local equivalent total strain that can be generated on the basis of two linear elastic finite element analyses. The first finite element analysis is carried out for a component configuration with the various mechanical and thermal loadings prescribed. The entire component is assumed to be linear elastic. The second finite element analysis is carried out next after artificially reducing the elastic modulii of all elements that exceed the yield stress as follows

$$E'_s = \left(\frac{\sigma_y}{\sigma_e}\right) E_0 \tag{9}$$

It is assumed that the redistribution is deformation controlled and that the material is elastic-perfectly plastic, although the foregoing softening process can be carried out for any other material constitutive relationship. The elastic properties of all other elements are left unchanged in the second finite element analysis. On the basis of the two finite element analyses, the relaxation line AC (Fig. 2) can be located.

The relaxation modulus ($\bar{E}_r$) can be expressed as

$$\bar{E}_r = \frac{d\bar{\sigma}}{d\bar{\epsilon}^o_t} \simeq \frac{\Delta\bar{\sigma}}{\Delta\bar{\epsilon}^o_t} \tag{10}$$

The angle θ is a measure of the extent of the multiaxiality and local follow-up. The term *follow-up* refers to the inability of the remainder system to force the local region response along $\theta = 0$ (the uniaxial reference case). In other words, follow-up is the deviation from pure deformation control action.

The triaxiality factor (TF) is defined as [*12*]

$$TF = \frac{3\sigma_m}{\sigma_e} \tag{11}$$

Positive θ is indicative of a stress state that has a larger triaxiality factor than the uniaxial case for which $TF = 1$, and a negative θ implies a state of stress with a smaller triaxiality factor.

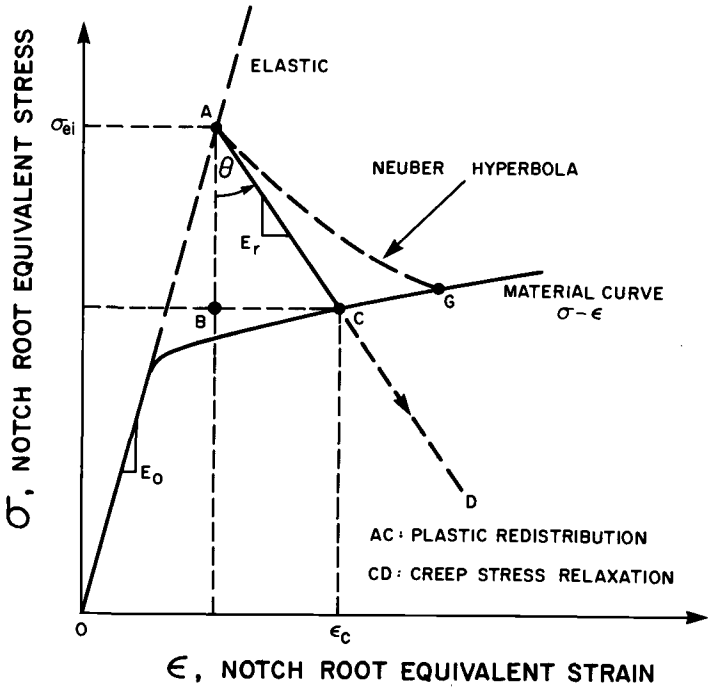

FIG. 2—*Determination of notch root inelastic response.*

For constitutive relationships other than elastic-perfectly plastic, E_s' can be obtained by locating the point of intersection of the relaxation line with the material stress-strain curve either graphically or analytically.

Plastic Zone Correction Factors

In the foregoing section, the elastic modulus of all elements in which the equivalent stress exceeded the yield stress was artificially reduced in a systematic manner. With reference to Fig. 3, this would correspond to a plastic zone (R_p) that lies within the contour Γ_1. The portion of the stress distribution that is in excess of the yield stress is not accounted for in the determination of the plastic zone size, i.e., the actual size of the plastic zone (R_p') which lies within the contour Γ_2 is larger than R_p. An approximate estimate of actual plastic zone size can be obtained by invoking a procedure similar to Irwin's crack-tip plastic zone correction technique [*13*]. The larger plastic zone will essentially increase the inelastic strains at the notch location.

With reference to the finite element discretization shown in Fig. 4, a typical element (k) of area A_k is considered. The unbalanced force due to the stresses in excess of yield is given by

$$F_{\text{unbalanced}} = \sum_{k=1}^{N} (\sigma_e - \sigma_y)_k \bar{A}_k \tag{12}$$

where N is the number of elements in the finite element mesh that exceed yield and $\bar{A}_k$ is some fictitious area over which the equivalent stress acts. It would be awkward in the present computational scheme to make adjustments to the size of the plastic zone. Instead of attempting

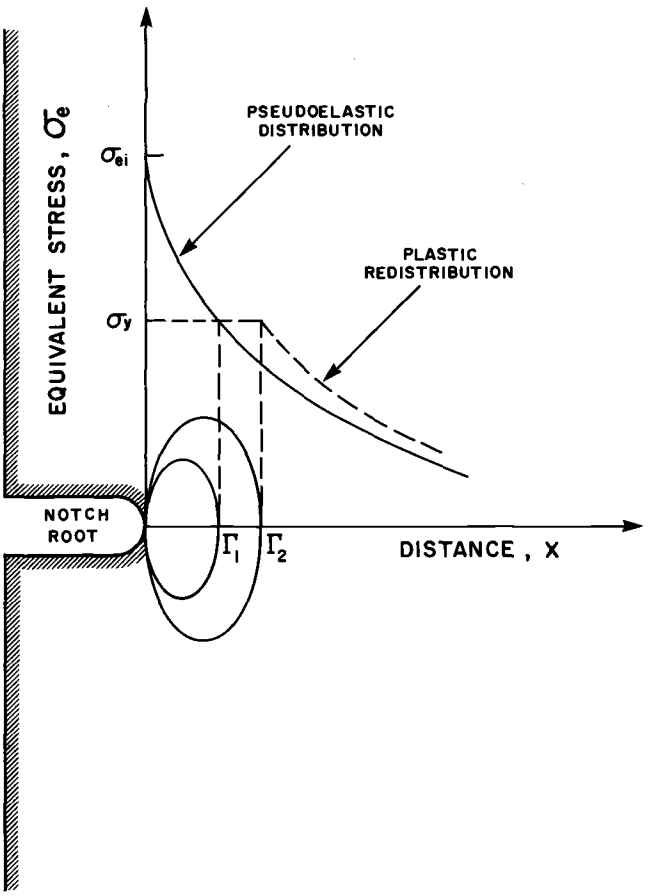

FIG. 3—*Plastic zone redistribution around a notch.*

to determine the actual size of the plastic zone (R_p'), the yield stress of each element within the nominal plastic zone (R_p) can be lowered artificially for the purpose of inelastic strain concentration estimates so that additional inelastic strains can be induced at the notch root. Therefore, for every individual element in which the equivalent stress exceeds the yield stress

$$(\sigma_e - \sigma_y)_k \overline{A}_k = (\sigma_y - \sigma_y')_k \overline{A}_k \tag{13}$$

leading to

$$\sigma_y' = 2\sigma_y - \sigma_e \tag{14}$$

The above equation can also be obtained on the basis of energy considerations. For well-designed components and structures, $\sigma_y' > 0$. However, for acute notches or larger plastic zone sizes σ_e could be greater than $2\sigma_y$. In such cases it would suffice if σ_y' is specified as a small quantity, say $E_0/1000$, without loss of accuracy in strain-concentration estimates. The secant modulus for the second linear elastic analysis can be expressed as

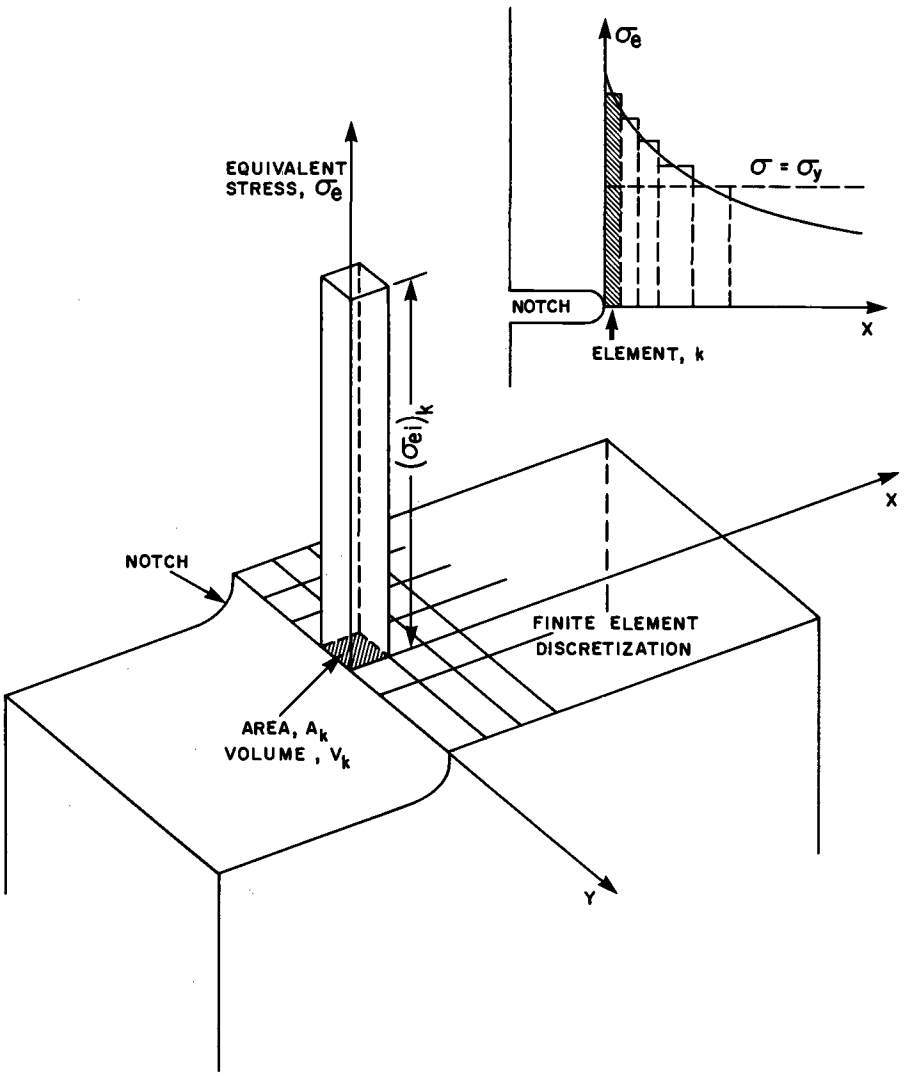

FIG. 4—*Notch stress distribution.*

$$E_s'' = \left[2\left(\frac{\sigma_y}{\sigma_e}\right) - 1\right] E_0 \tag{15}$$

For small to medium amounts of follow-up ($\theta < 60$), for which the proportional loading assumption is not seriously violated, the inelastic strain estimates would constitute an upper bound [*14*] which from the standpoint of low cycle fatigue assessment is conservative. Although a rigorous method for estimating the proximity of the bound to the exact solution is required, the several GLOSS-based analyses of common component configurations have repeatedly shown the estimates to be reasonably good for small to medium amounts of follow-

up. However, without plasticity correction the inelastic strains would be underestimated, and the correct value would lie between the foregoing estimate and the upper bound estimate of inelastic strains based on plasticity corrections. In this sense, the magnitude of error bounds on the estimate can be obtained.

The method can be extended to include creep effects by invoking the concept of "isochronous yield surfaces [*15*]." In effect, the creep active zone is used instead of the plastic zone by identifying all elements that exceed the time-dependent allowable stress $S_m(\tau)$. This allowable stress for isothermal components and structures can be established on the basis of specified creep deformation in a given time or the rupture life. The secant modulus of all the elements in the creep-active zone can be modified as

$$E_s'' = \left[2\left(\frac{S_m(\tau)}{\sigma_e}\right) - 1 \right] E_0 \tag{16}$$

Marriott [*16*] has proposed a similar adjustment procedure in a different context.

Multiaxial Constraints and Local Region Follow-up

Load and Deformation Control

The concepts of load and deformation control can be illustrated on the GLOSS diagram. For deformation control action, the angle θ is zero, $TF = 1$, and the constraint parameter $\bar{\gamma} = 1$. The implication is that a highly localized inelastic zone is surrounded by an entirely elastic remainder. It is precisely due to this reason that "shakedown" action occurs in mechanical components and structures. For the load control action, the angle θ is 90° and $\bar{\gamma} = 0$. This situation is usually associated with a statically determinate action such as incipient collapse or net section yielding.

Local region yielding in most components involve both load and deformation control actions in varying proportions. The angle θ for such situations is less than 90°. Incidentally, an angle θ of 45° on the GLOSS diagram corresponds to the initial slope of the Neuber locus. For the more general component configurations, the angle θ can be calculated by the following expression (Fig. 2)

$$\theta = \frac{\pi}{2} - \arctan\left(-\bar{E}_r\right) \tag{17}$$

Positive θ is indicative of a triaxial state of stress at the notch root which is greater than the uniaxial reference case ($\theta = 0$), whereas negative θ implies a lower triaxiality. The smooth specimen configuration would then correspond to the "reference case" of $\theta = 0$ degrees.

A constant value of $\bar{\gamma}$ implies that the principal stress ratios are invariant along the relaxation line. For small to medium amounts of follow-up, the stress ratio changes are not significant. The assumption of proportional loading is implied along a relaxation line for which $\bar{\gamma}$ is constant, although in reality some departure from this is expected.

The Neuber Locus on the GLOSS Diagram

Neuber's rule states that the theoretical stress concentration factor is the geometric mean of the actual stress and strain concentration factors. Although this approximation holds only for a specific notch and component geometry, it is commonly used as an analytical approximation for a variety of configurations.

The Neuber locus can be described by the normalized equation

$$\bar{\sigma}\bar{\epsilon}_t^0 = 1 \tag{18}$$

With respect to Fig. 2, the strain at point G is given by

$$\bar{\epsilon}_t^0|_G = \frac{\bar{\sigma}_i \bar{\epsilon}_{ti}^0}{\bar{\sigma}_y} \tag{19}$$

i.e., the relaxation-modulus ($\bar{E}_r$) can be obtained as

$$\bar{E}_r = -\frac{\bar{\sigma}}{\bar{\epsilon}_t^0} \tag{20}$$

The relaxation modulus has the same magnitude as the secant modulus ($\bar{E}_{s,n}$) of a given point on the Neuber locus, but is of the opposite sign. Using Eq 7, the constraint parameter, $\bar{\gamma}$, which characterizes the interaction between the local and remainder regions, can be expressed as

$$\bar{\gamma} = \frac{\bar{E}_{s,n}}{1 + \bar{E}_{s,n}} \tag{21}$$

It can be seen that the constraint parameter varies along the Neuber locus.

Inelastic Strain Concentration Factors—The Critical Location Method (Fig. 5)

Monotonic stress-strain curves have been commonly used to obtain design parameters for limiting stresses in mechanical components and structures that are subjected to static loading. For repeated loadings, however, cyclic stress-strain curves are relevant for assessing the design adequacy.

On the basis of the knowledge of the cyclic stress-strain curve, estimation of the stabilized hysteresis loop for materials that exhibit symmetric behavior in tension and compression is possible by using Massing's hypothesis [*17*]. By doubling the stress and strain values from the stabilized cyclic stress-strain curve, a corresponding point on the hysteresis loop can be obtained. The general hysteresis curve is given by the equation

$$\Delta\epsilon_t^o = \frac{\Delta\sigma}{E_0} + 2\left(\frac{\Delta\sigma}{2K'}\right)^{(1/n')} \tag{22}$$

The strain-life relationship is commonly expressed as

$$\frac{\Delta\epsilon_t^o}{2} = \frac{\sigma_f'}{E_0}(2N_f)^b + \epsilon_f'(2N_f)^c \tag{23}$$

$\Delta\epsilon_t^o$ can be obtained by the GLOSS method of analysis described in this paper, and the fatigue life can be obtained from Eq 23. While an elastic-perfectly plastic constitutive equation is assumed for the numerical examples presented in this paper, the GLOSS method is not necessarily restricted to this type of material behavior. For strain-hardening materials, $\Delta\epsilon_t^o$ is obtained by simply locating the intersection of the relaxation line with the prescribed material stress-strain curve.

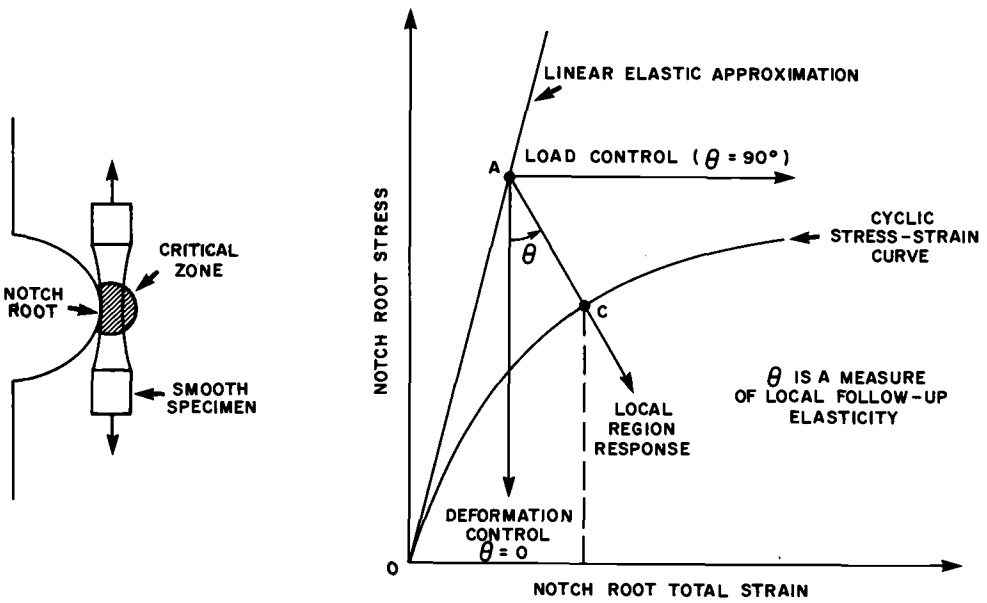

FIG. 5—*The critical location method.*

The effect of mean stress can be introduced by modifying the elastic term in the strain-life equation, i.e.,

$$\frac{\Delta\epsilon_t^o}{2} = \frac{\sigma_f' - \sigma_m}{E_0}(2N_f)^b + \epsilon_f'(2N_f)^c \tag{24}$$

Other forms of equations have been reported in the literature [*18,19*] which also take into account the effect of mean stress.

Numerical Examples

Inelastic strains at the notch root are evaluated by the GLOSS method, without and with plastic zone corrections, for the following assuming an elastic-perfectly plastic material.

Plate with a Circular Hole Subjected to a Tensile Load (Fig. 6)

Material: 24S-T3 Aluminum alloy
Radius of the hole = 0.6375×10^{-2} m
Width of the plate = 0.3819×10^{-1} m
Length of the plate = 0.7620×10^{-1} m
Yield stress, σ_y = 363.20 MPa
Modulus of elasticity, $E_0 = 7.2368 \times 10^4$ MPa

Bridgman Notch Bar in Tension (Fig. 7)

Material: Cr-Mo Steel
Maximum diameter = 2.6416×10^{-2} m

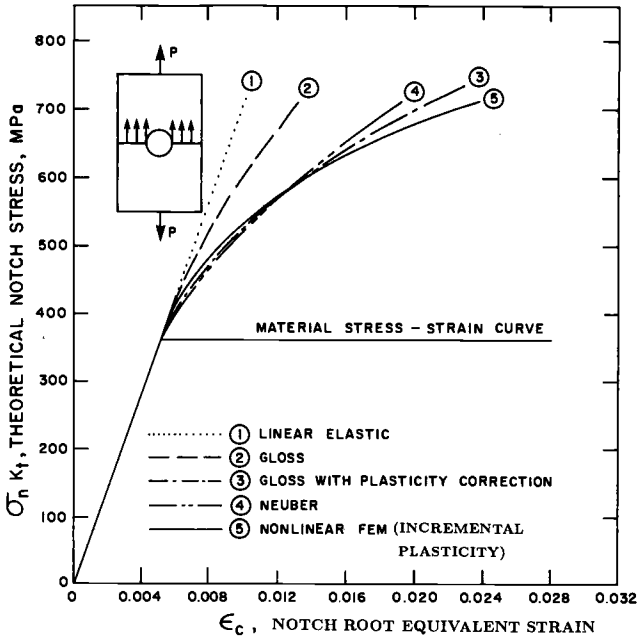

FIG. 6—*Plastic strain concentration in a plate with a circular hole.*

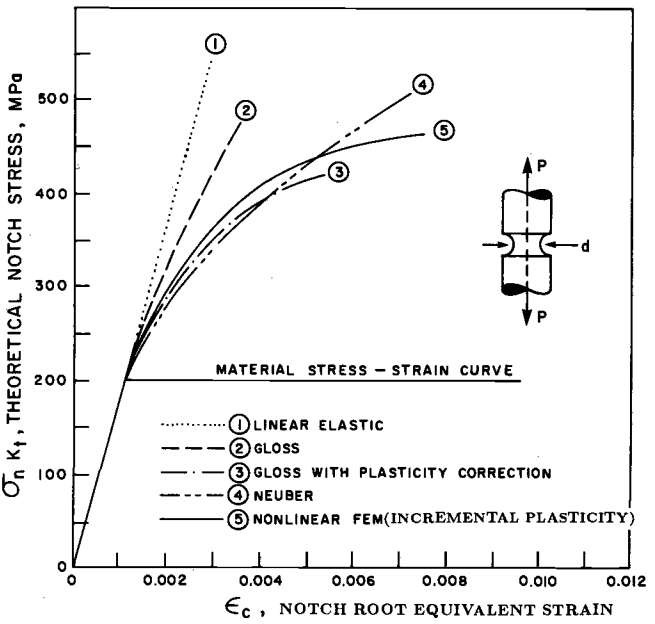

FIG. 7—*Plastic strain concentration for a Bridgman notch.*

Minimum diameter = 2.1082×10^{-2} m
Notch radius = 0.6858×10^{-2} m
Yield stress, σ_y = 200.00 MPa
Modulus of elasticity, $E_0 = 1.90 \times 10^5$ MPa

Pressurized Cylinder with a Circumferential Notch on the Inside Surface (Fig. 8)

Material: Stainless steel
Outer radius = 0.6350 m
Inner radius = 0.4064 m
Notch radius = 0.0254 m
Yield stress, σ_y = 200.00 MPa
Modulus of elasticity, $E_0 = 1.896 \times 10^5$ MPa

It can be seen from the figure that the GLOSS method without plasticity correction consistently underestimates the magnitude of notch root inelastic strains. The incorporation of plastic zone corrections improves the estimate considerably as can be seen from the comparisons with inelastic finite element analysis results.

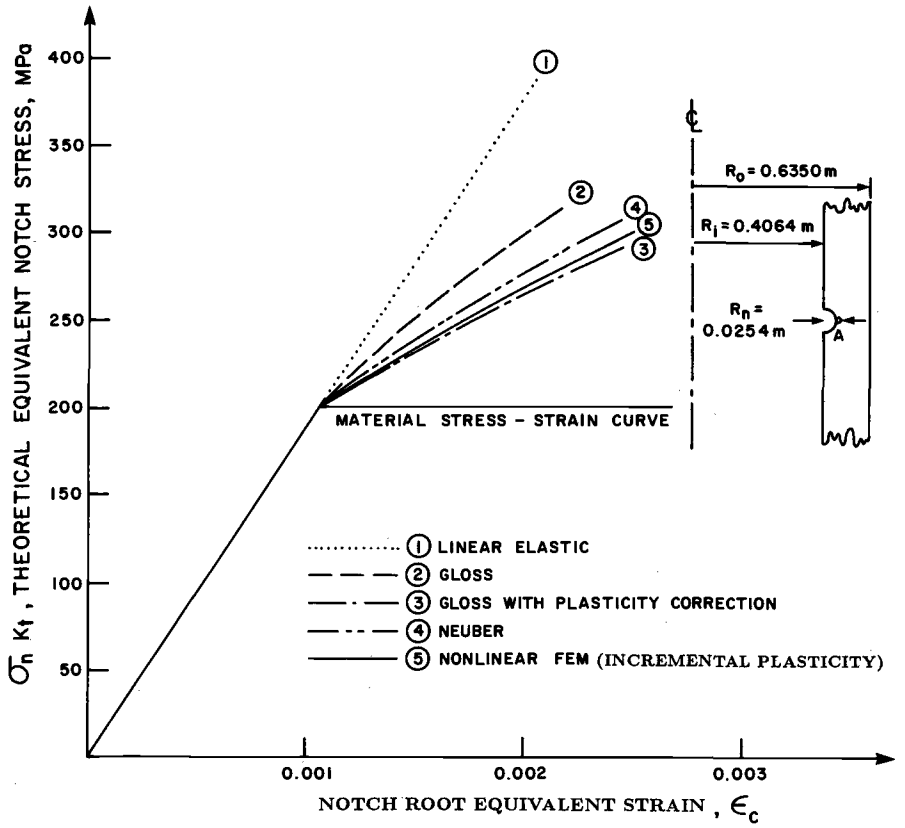

FIG. 8—*Plastic strain concentration in a closed cylinder with a circumferential circular notch.*

The inelastic strain estimates using Neuber's rule are also plotted in Figs. 6, 7, and 8. It can be seen that the Neuber-type inelastic strain estimates depend on the type of constraint, i.e., the predictions are better for plane stress geometric configurations.

For small to moderate amounts of plasticity, i.e., follow-up angles below 60°, the GLOSS method with plasticity corrections leads to accurate to marginally conservative values of inelastic strains at the notch root that would underestimate low cycle fatigue life predictions.

Conclusions

The GLOSS method of analysis that incorporates plastic zone corrections provides reasonably good estimates of the notch root inelastic strains. The relaxation modulus of the notch root, which characterizes the constraint effect, can be obtained on the basis of two linear elastic finite element analysis per point on the load-notch strain curve. The inelastic strains at the notch root can be computed for any given component configuration, loading description, and material stress-strain relationship.

The GLOSS method has been applied in this paper to several geometric configurations, and the inelastic strain estimates compare favorably with the results of inelastic finite element analysis. The method can be extended to problems involving notch creep strain concentrations in mechanical components and structures.

Acknowledgment

The authors acknowledge the financial support provided by the Natural Sciences and Engineering Research Council of Canada, which made it possible to carry out the research reported in this paper.

References

[1] Crews, J. H. Jr. and Hardrath, H. F., "A Study of Cyclic Plastic Stresses at a Notch Root," *Experimental Mechanics,* Vol. 6, No. 6, 1966, pp. 313–320.

[2] Topper, T. H., Wetzel, R. M., and Morrow, J. D., "Neuber's Rule Applied to Fatigue of Notched Specimens," *Journal of Materials,* Vol. 4, No. 1, 1969.

[3] Dowling, N. E., "Fatigue at Notches and the Local Strain and Fracture Mechanics Approaches," *Fracture Mechanics, ASTM STP 677,* C. W. Smith, Ed., American Society for Testing and Materials, Philadelphia, 1979, pp. 247–273.

[4] Socie, D. F., Dowling, N. E., and Kurath, P., "Fatigue Life Estimation of Notched Members," *Fracture Mechanics (Fifteenth Symposium), ASTM STP 833,* R. J. Sanford, Ed., American Society for Testing and Materials, Philadelphia, 1984, pp. 284–299.

[5] Neuber, H., "Theory of Stress Concentration for Shear-Strained Prismatical Bodies with Arbitrary Nonlinear Stress-Strain Laws," *Journal of Applied Mechanics, Transactions of ASME,* Vol. E28, 1961, p. 544.

[6] Seeger, T. and Heuler, P., "Generalized Application of Neuber's Rule," *Journal of Testing and Evaluation,* Vol. 8, No. 4, 1980, pp. 199–204.

[7] Dowling, N. E., "A Discussion of Methods for Estimating Fatigue Life," Proceedings of the SAE Fatigue Conference, Society of Automotive Engineers, Warrendale, PA, 1982, p. 109.

[8] Ellyin, F. and Kujawski, D., "Notch Root Stress/Strain Prediction for Elastic-Plastic Loading," *Res Mechanica,* Vol. 20, 1987, pp. 177–190.

[9] Molski, K. and Glinka, G., "A Method of Elastic-Plastic Stress and Strain Calculation at a Notch Root," *Material Science Engineering,* Vol. 50, 1981, pp. 93–100.

[10] Seshadri, R., "The Generalized Local Stress Strain (GLOSS) Analysis-Theory and Applications," *Journal of Pressure Vessel Technology,* Vol. 113, May 1991, pp. 113–119.

[11] Seshadri, R. and Kizhatil, R. K., "Inelastic Analysis of Pressure Components using the GLOSS Diagram," *Transactions of CSME,* Vol. 14, No. 3, 1990.

[12] Davis, E. A. and Connelly, F. M., "Stress Distribution and Plastic Deformation in Rotating Cylin-

ders of Strain-Hardening Material," *ASME Journal of Applied Mechanics,* Vol. 26, Series E, March 1959, pp. 25–30.

[*13*] Ewalds, H. L. and Wanhill, R. J. H., *Fracture Mechanics,* Arnold, Delftse Uitgeuers Maatschappij, 1986.

[*14*] Burgreen, D., *Design Methods for Power Plant Structures,* C. P. Press, Jamaica, NY, 1975, pp. 82–86.

[*15*] Goodall, I. W., Leckie, F. A., Ponter, A. R. S., and Townley, C. H. A., "The Development of High Temperature Design Methods Based on Reference Stress and Bounding Theorems," *ASME Journal of Engineering Materials and Technology,* 1979, pp. 349–355.

[*16*] Marriott, D. L., "Evaluation of Deformation or Load-Control of Stresses under Inelastic Conditions Using Elastic Finite Element Analysis," ASME PVP-Vol. 136, ASME, New York, 1988.

[*17*] Bannantine, J. A., Comer, J. J., and Handrock, J. L., *Fundamentals of Metal Fatigue Analysis,* Prentice Hall, Inc., Englewood Cliffs, NJ, 1990.

[*18*] Morrow, J., *Fatigue Design Handbook, Advances in Engineering,* Vol. 4, Sec. 3.2, Society of Automotive Engineers, Warrendale, Pa., 1968, pp. 21–29.

[*19*] Manson, S. S. and Halford, G. R., "Practical Implementation of the Double Linear Damage Rule and Damage Curve Approach for Treating Cumulative Fatigue Damage," *International Journal of Fracture,* Vol. 17, No. 2, 1981, pp. 169–172.

DISCUSSION

R. J. DiMelfi[1] *(written discussion)*—As I understand your analysis, you artificially lower the elastic stiffness in the local region of a notch to account for inelastic flow in this region. During fatigue cycling, when you reverse load, do you allow the local region to unload in accordance with this lower stiffness or do you have it change back to be compatible with the stiffness of the "remaining" region? Also, regardless of the artifice that you use to model cyclic hardening, is there a physical justification in this alloy for the consequent hardening that you show for the local region while the remaining region flows perfectly plastically?

R. Seshadri and R. K. Kizhatil (authors' closure)—The GLOSS method discussed in this paper, intended for use in conjunction with the strain-life method, enables determination of the equivalent total strain range on the basis of two linear elastic finite element analyses. The artificial stiffness adjustment of the nominally plastic region is carried out in order to assess inelastic action in the local region.

The equivalent total strain range can be determined by locating the intersection of the relaxation line and the cyclic stress-strain curve (obtained from stable hysteresis loops for a family of constant strain amplitudes). In the context of the method outlined in this paper, no further adjustments to the stiffness are prescribed for dealing with fatigue load reversals.

During the unloading part of the fatigue cycle, the remainder region will still control the response of the local region for small to medium amounts of follow-up. The authors do wish to point out that further refinements to the method are indeed possible.

[1] Argonne National Laboratory, RE-207, Argonne, IL 60439.

Somnath Chattopadhyay[1]

Multiaxial Low-Cycle Fatigue Evaluations of Pressure Vessel Components

REFERENCE: Chattopadhyay, S., **"Multiaxial Low-Cycle Fatigue Evaluations of Pressure Vessel Components,"** *Advances in Multiaxial Fatigue, ASTM STP 1191,* D. L. McDowell and R. Ellis, Eds., American Society for Testing and Materials, Philadelphia, 1993, pp. 412–428.

ABSTRACT: In this paper analytical methods to evaluate multiaxial low-cycle fatigue lives for pressure vessel components have been appraised and the sources of conservatism highlighted. For this purpose, a sample design problem involving a pressure vessel component fabricated from a coded structural alloy subjected to a specified set of loading conditions has been evaluated for fatigue. The local strain approach has been used as a basis for assessing two methods of fatigue evaluation in the low-cycle fatigue regime: (1) the ASME Code, and (2) the Japanese MITI Code. A possible extension of the code procedures to include hydrostatic effects has been recommended.

KEY WORDS: low-cycle fatigue, ASME code, MITI code, multiaxiality, elastic plastic analysis, strain concentration factor, peak stresses, linearized stresses

Nomenclature

A_0	Material parameter (MITI code)
b	Fatigue strength exponent
c	Fatigue ductility exponent
E	Young's modulus, MPa
Δe	Nominal stress range
K	Ratio of Young's moduli
K'	Cyclic strength coefficient
K_e	Low-cycle fatigue strain enhancement factor
K_t	Elastic stress concentration factor (Neuber)
K_{pe}	Surface strain concentration in mathematical model
m	Material parameter in the code expression of K_e factor
n	Strain-hardening exponent in the code expression of K_e
n_i	Actual number of cycles for ith combination
n'	Cyclic strain-hardening exponent
N_i	Allowable number of cycles for ith combination
N_f	Number of cycles to failure
S_e	Effective stress, MPa
S_m	Code design value of the stress intensity, MPa
S_n	Linearized stress over the thickness, MPa
S_p	Surface peak stress, MPa
ΔS	Nominal stress range, MPa
TF	Triaxiality factor

[1] Department of Mechanical Engineering, The University of Vermont, Burlington, VT 05405-0156.

U Cumulative fatigue usage factor
ϵ_f Uniaxial strain
ϵ_{fm} Multiaxial strain
ϵ'_f Fatigue ductility coefficient
$\Delta\epsilon$ Local total strain range
$\Delta\epsilon_e$ Local elastic strain range
$\Delta\epsilon_p$ Local plastic strain range
σ_i Principal stresses, $i = 1,2,3$
σ'_f Fatigue strength coefficient
ρ Ratio of the linearized stress to the peak stress

Introduction

Simplified inelastic analyses are used in fatigue evaluations during inelastic strain cycling. Both the Japanese Code MITI Modification 501 [*1*] as well as the ASME Boiler and Pressure Vessel Code Section III [*2*] contain rules for simplified elastic-plastic analyses. These evaluations are based on applying fatigue enhancement factors to the elastically computed strain range when the stress range exceeds a certain limiting value, usually twice the nominal yield strength (low-cycle fatigue region). These low-cycle fatigue enhancement factors have been computed for a structural alloy using the cyclic stress-strain characteristics and Neuber's rule. The computed values of these enhancement factors have been compared with the corresponding values in the various code procedures [*1,2*].

Furthermore, the conservatism of a typical code procedure, namely the ASME Code, has been assessed by comparing the fatigue evaluations using the code as well as the local strain approach. The local strain approach is based on crack initiation as the criterion for service life. This method requires loading history imposed on the component in service as well as the material property data. Additionally, local plastic deformation is assumed at stress concentrations. This method has been used extensively in the automotive industry [*3*].

For the purpose of comparison of the fatigue evaluation by the two procedures, an example problem involving a typical pressure vessel component subjected to a specified set of loading conditions has been analyzed. For the ASME Code evaluation, the stress ranges for different loading conditions have been used to obtain the allowable number of cycles from the code design fatigue curve. For the evaluation using the local strain procedure, the stress ranges have been converted to strain ranges and allowable number of cycles determined from the continuous cycling fatigue curve for the material. For both methods, the cumulative fatigue usage, U, is determined using Miner's rule, $U = \Sigma \frac{n_i}{N_i}$, where n_i and N_i are the actual number of cycles and the allowable number of cycles, respectively.

Implication of the K_e Factor

As defined by the ASME Code [*2*], primary stress is any stress developed which is necessary to satisfy the laws of equilibrium. Should a stress of this type exceed the yield strength of the material by a substantial amount, gross distortion and possible failure of the component will result. A secondary stress, as defined by the ASME Code [*2*], is a stress developed by the constraint of adjacent material or by the self-constraint of the structure. The basic characteristic of the secondary stress is that it is self-limiting. The stress intensity (not to be confused with the stress intensity factor in fracture mechanics) is defined by the ASME Code [*2*] as the largest absolute magnitude of the difference of the principal stresses. The design value of the stress intensity is denoted by S_m, which typically gives a design factor of safety of 1.5 with respect to

the nominal yield strength. When the primary plus the secondary stress intensity range (linearized through the section) is close to $3S_m$ (typically twice the nominal yield strength), there will be small plastic zones well contained by the remainder of the structure, which is assumed to stay elastic. The ASME Code then ignores the contribution of the localized plastic zone as long as the range of the stress intensity is less or equal to $3S_m$. But even when the stress intensity is linearized through the section, S_n equal to $3S_m$, the surface peak stress intensity, S_p, can exceed $3S_m$, thus enhancing the potential to initiate surface cracks. This aspect is apparently recognized by the MITI Code [*1*] where a correction is introduced at $S_n = 3S_m$ to account for plastic strain, especially when S_p exceeds S_n. This correction is extended beyond $3S_m$ to a slightly greater stress.

When the stress intensity range, S_n, exceeds $3S_m$, the strict shakedown limit is exhausted and there will be cycles of alternating yielding in the zones of stress concentration. Therefore it is necessary to perform a low-cycle fatigue analysis. For such situations, the elastic-plastic strain range must be calculated because it is an important parameter in the initiation of low-cycle fatigue cracks. The K_e factor essentially gives the elastic-plastic strain ranges from the strain ranges calculated by purely elastic means. Alternatively, it can be stated that the equation for K_e in both the ASME and the MITI codes provides for decay in fatigue lives when cycling in the plastic range. The MITI Code applies the strain enhancement factor at $S_n = 3S_m$, where values typically exceed unity and progressively increase with increasing ratios of S_p/S_n.

Code Expressions for K_e

The equations for K_e in both the MITI as well as the ASME codes are provided in three different regions of stress intensity ranges: (1) $S_n \leq 3S_m$, (2) $3S_m \leq S_n \leq 3mS_m$, and (3) $S_n \geq 3mS_m$, where m is a material parameter. The expression of the K_e factor in the MITI and the ASME codes are essentially identical in Regions 1 and 3. For Region 1, the K_e factor is unity, and for Region 3, the factor is $1/n$ where n is the strain-hardening exponent. In Region 2 there is a significant difference between the two codes as outlined below

$$K_e = 1 + A_0\left(\frac{S_n}{3S_m} - \frac{S_n}{S_p}\right) \tag{1a}$$

$$K_e = 1 + \frac{1-n}{n(m-1)}\left(\frac{S_n}{3S_m} - 1\right) \tag{1b}$$

In Eqs 1*a* and 1*b*, A_0 is a material parameter. The greater of the two expressions, Eqs 1*a* and 1*b*, is used for determining K_e in the region of stress intensities, $3S_m \leq S_n \leq 3mS_m$ in the MITI Code.

For the ASME Code there is only one expression for K_e in the region of stress intensities, $3S_m \leq S_n \leq 3mS_m$, which reads

$$K_e = 1 + \frac{1-n}{n(m-1)}\left(\frac{S_n}{3S_m} - 1\right) \tag{2}$$

Note that Eqs 1*b* and 2 are identical. Equation 1*a* introduces the parameter, S_n/S_p, which causes a discontinuous behavior of K_e at S_n equal to $3S_m$ for situations where the peak stress, S_p, exceeds the linearized stress, S_n.

When the peak stress is below the linearized stress, the ASME and the MITI codes provide

identical expressions for K_e. Figure 1 shows the variation of K_e as a function of $S_n/3S_m$ for both the ASME and the MITI codes. For comparison purposes, the K_e expressions for austenitic stainless steels and high nickel alloys in Ref *2* have been used. The material parameters in Eqs 1 and 2 are: $m = 1.7$, $n = 0.3$, and $A_0 = 0.7$. Figure 1 shows the region from S_n/S_m equal to unity to a higher value where the MITI Code is different from the ASME Code. Table 1 highlights the difference between the two codes.

Proposed Technique to Address Peak Stresses

Figure 2 illustrates a typical stress distribution through a vessel wall. Only one stress component, namely a radial, circumferential, or axial component, has been considered. This stress distribution could be a result of internal pressure or temperature gradients or a combination of both. From this stress distribution, an equivalent linear distribution is calculated which gives the same bending moment as the actual distribution. The actual peak stresses at the inside and outside surfaces are used for fatigue evaluation. The K_e factors in the ASME Code

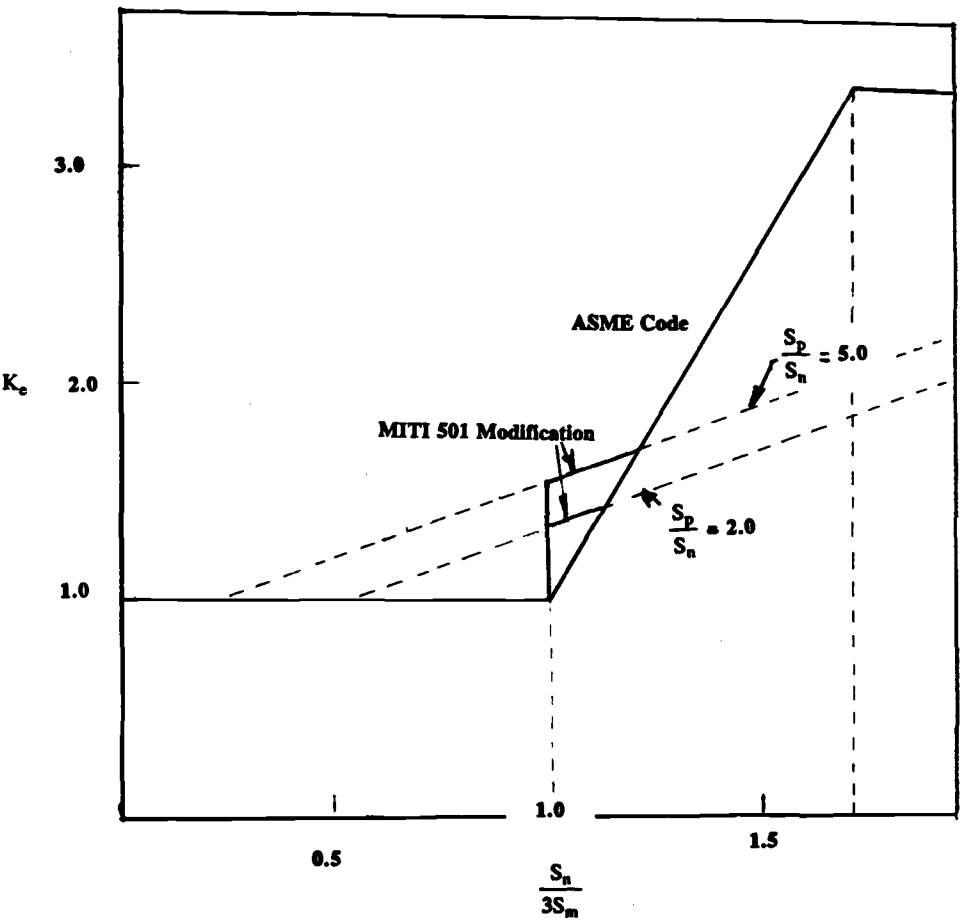

FIG. 1—*Variation of the* K_e *factor in the ASME and MITI codes.*

TABLE 1—*Comparison of* K_e *factors.*

Region	MITI 501, Article 14	ASME NB3228.3
$S_n \leq 3S_m$	$K_e = 1.0$	$K_e = 1.0$
$3S_m \leq S_n \leq 3mS_m$	The greater of $K_e = 1 + \frac{1-n}{n(m-1)}\left(\frac{S_n}{3S_m} - 1\right)$ and $K_e = 1 + A_0\left(\frac{S_n}{3S_m} - \frac{S_n}{S_p}\right)$	$K_e = 1 + \frac{1-n}{n(m-1)}\left(\frac{S_m}{3S_m} - 1\right)$
$S_n > 3mS_m$	$K_e = 1/n$	$K_e = 1/n$

are based solely on the range of stress intensity, S_n, obtained for the equivalent linear distribution. For the MITI Code, however, the K_e factor depends on S_n as well as the peak stress intensity range, S_p.

As long as the linearized stress intensity range, S_n, is within the $3S_m$ limit of the material, it is implicitly assumed that there is no plastic action. For S_n above the $3S_m$ limit, a plasticity correction needs to be introduced. The ASME Code provides the enhancement factor, K_e, which increases linearly with the linearized stress intensity range, S_n (see Fig. 1), up to a certain value. However, when the surface peak stress range, S_p, exceeds S_n, an additional strain concentrator is introduced at the surface. Denoting K_{pe} as the strain concentration at the surface for computing the local strain, or

$$K_{pe} = \frac{S_p}{S_n} \tag{3}$$

From Neuber [*4*] the corresponding elastic stress concentration, K_t, is given by using Eq 3

$$K_t^2 = \frac{S_p}{S_n} \tag{4}$$

Here the local stress concentration factor has been assumed to be unity. For situations where S_p exceeds S_n, the K_e factors are calculated using the local strain approach by simulating the situation with that of a notched member having a stress concentration factor, K_t, as given by Eq 4. This idealization is depicted in Fig. 3.

Computation of the K_e Factors

The application of this procedure requires the knowledge of the local stress-strain behavior. Since these data are based on uniaxial tests, the elastic stresses intensified by K_t will be used for the computation of the K_e factors.

If ΔS represents the nominal stress range, with a value of $K_t S_n$, then the nominal elastic strain range, Δe will be given by

$$\Delta e = \frac{K_t S_n}{E} \tag{5}$$

where E is Young's modulus, and the elastic stress concentration factor, K_t, is given by Eq 4.

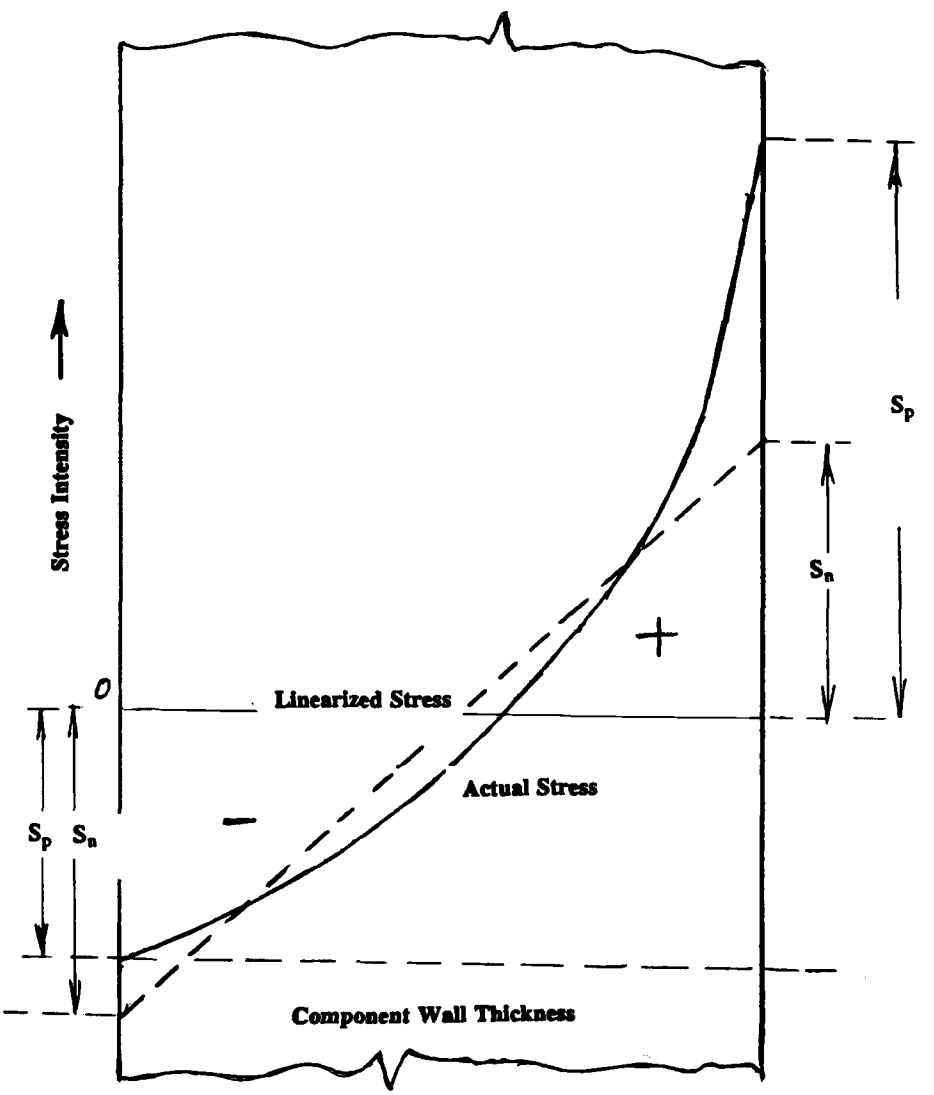

FIG. 2—*Categorization of stresses.*

To determine the local strain range, the cyclic stress-strain curve is used since under the influence of cyclic loads, the material will soon approach the stable cyclic condition. The cyclic stress-strain curve can be computed by calculating $\Delta\sigma/2$ from the ASTM Recommended Practice for Constant-Amplitude Low-Cycle Fatigue Testing (E 606)

$$\Delta\sigma/2 = K'(\Delta\epsilon_p/2)^{n'} \tag{6}$$

where

$\Delta\sigma$ = true stress range,
$\Delta\epsilon_p$ = true plastic strain range,

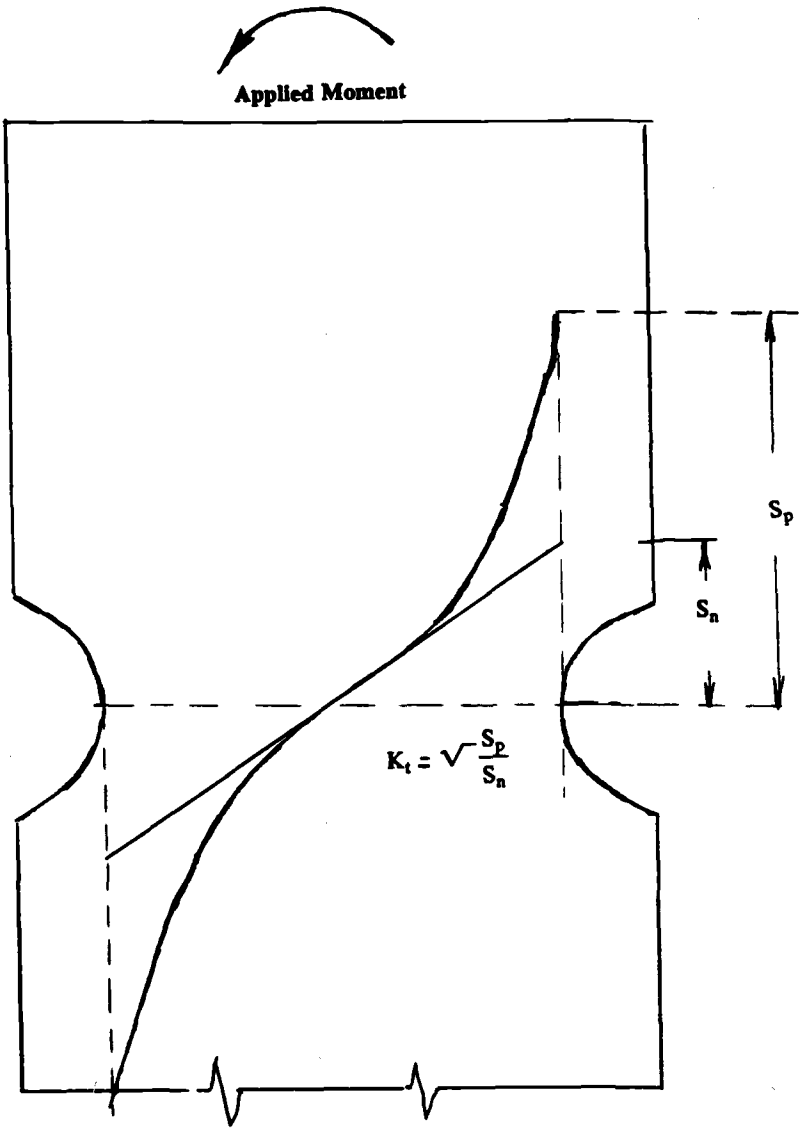

FIG. 3—*Notch idealization of the peak stress effects.*

K' = cyclic strength coefficient, and
n' = cyclic strain hardening exponent.

The true elastic strain range, $\Delta\epsilon_e$, is

$$\frac{\Delta\epsilon_e}{2} = \frac{\Delta\sigma}{2E} \tag{7}$$

and the total strain range, $\Delta\epsilon$, can be calculated from

$$\Delta\epsilon = \Delta\epsilon_e + \Delta\epsilon_p \tag{8}$$

According to Neuber's rule [*4*] and using Eq 5

$$\Delta\sigma\Delta\epsilon = K_t^2 S_n^2 E \tag{9}$$

From Eqs 4, 5, and 6

$$\Delta\epsilon = \frac{\Delta\sigma}{2E} + \left(\frac{\Delta\sigma}{2^{1-n'}K'}\right)^{1/n'} \tag{10}$$

Substituting $\Delta\sigma$ in Eq 8

$$\Delta\epsilon = \frac{K_t^2 S_n^2}{E^2\Delta\epsilon} + \left(\frac{K_t^2 S_n^2}{2^{1-n'}K'E}\right)^{1/n'} \tag{11}$$

Therefore the true strain range, $\Delta\epsilon$, is related to the nominal stress range, S_n, by Eq 11. Equation 11 requires an iterative solution to obtain $\Delta\epsilon$.

The cyclic stress-strain data (Eq 6) for Ni-Cr-Fe Alloy 600 are obtained from Ref *5* as

0.2% offset yield = 236 MPa

Young's modulus, E = 214 GPa

K' = 766 MPa

n' = 0.1323

The cyclic stress strain curve for Alloy 600 is shown in Fig. 4, which is obtained from ASTM E 606. With these numerical values, Eq 11 becomes

$$\Delta\epsilon = \frac{K_t^2 S_n^2}{E^2\Delta\epsilon} + \left(\frac{K_t^2 S_n^2}{1398E\Delta\epsilon}\right)^{1/0.1323} \tag{12}$$

For different values of S_n, the inelastic strain ranges, $\Delta\epsilon$, are computed using Eq 12. The low-cycle fatigue strain enhancement factor, K_e, is defined as

$$K_e = \frac{\text{Inelasticity computed strain}}{\text{Elastically computed strain}} \tag{13}$$

which gives

$$K_e = \frac{\Delta\epsilon}{\Delta e} \tag{14}$$

with Δe and $\Delta\epsilon$ obtained from Eqs 5 and 12, respectively.

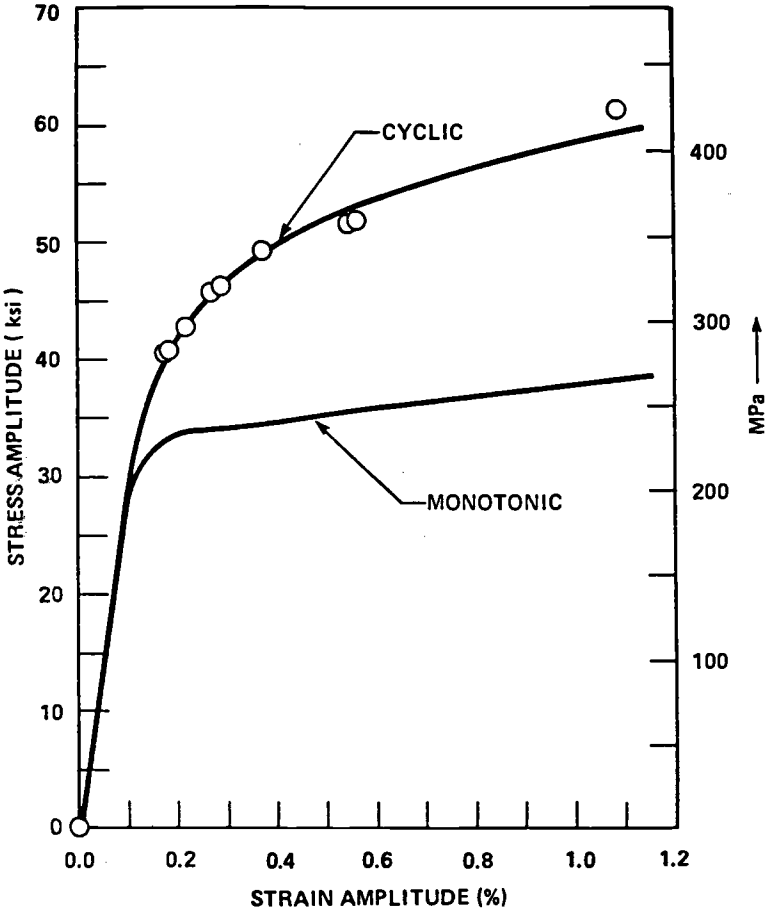

FIG. 4—*Cyclic stress-strain curve for Alloy 600* [5].

Figure 5 shows the values of K_e for Alloy 600 computed using Eq 14 for two values of the ratio S_p/S_n. The corresponding values as recommended by the MITI Code are shown as two parallel lines. The variation of K_e as given by the ASME Code is also indicated in the same figure. The computed values of the K_e factors seem to follow the same trend as the ones specified by the Japanese Code [*1*].

Fatigue Evaluation Using the Local Strain Procedure

The approach pursued in this paper for evaluation of fatigue life makes use of the elastically computed stresses for a pressure vessel structural component subjected to a specified set of loadings. Generally the evaluation using the Code approach involves working with the stress intensity which is the largest absolute magnitude of the difference of the principal stresses. An equivalent procedure could involve the use of the effective stress, S_e, which is defined as

$$S_e = \frac{1}{\sqrt{2}} \sqrt{[(\sigma_1 - \sigma_2)^2 + (\sigma_2 - \sigma_3)^2 + (\sigma_3 - \sigma_1)^2]} \tag{15}$$

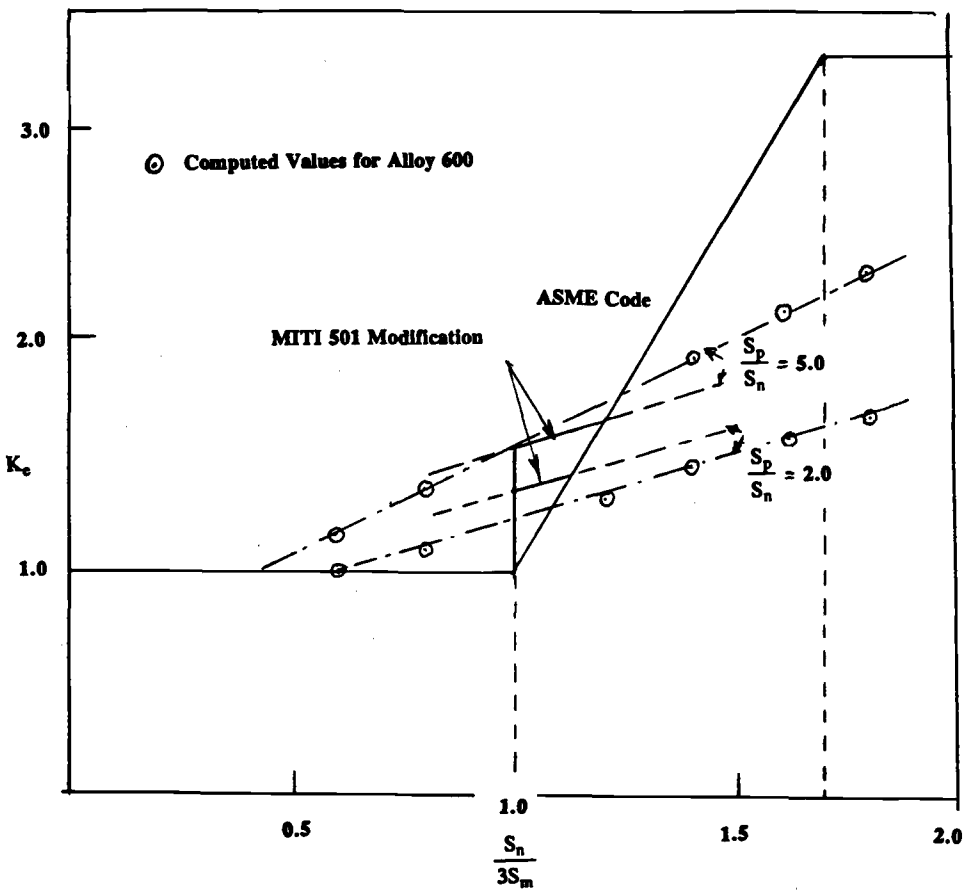

FIG. 5—*Comparison of the* K_e *factors for Alloy 600.*

where σ_1, σ_2, σ_3 are the principal stresses. In most situations, the stress intensities and the effective stresses are not too different from each other.

For various loading conditions, the stress ranges measured in terms of the stress intensities (or alternatively effective stresses), S_n, are assumed to be known by elastic calculations. Based on the values of S_n, the local true strain ranges, $\Delta\epsilon$, are obtained from Eq 11. From the local strain range, the number of cycles to failure, N_f, is obtained using ASTM E 606.

$$\frac{\Delta\epsilon}{2} = \frac{\sigma_f'}{E}(2N_f)^b + \epsilon_f'(2N_f)^c \tag{16}$$

where

σ_f' = fatigue strength coefficient,
ϵ_f' = fatigue ductility coefficient,
b = fatigue strength exponent, and
c = fatigue ductility exponent.

Equation 16 effectively divides the total strain range into elastic and plastic parts. An iterative solution is required to obtain N_f from $\Delta\epsilon$ in Eq 16.

The low-cycle fatigue data for Alloy 600 are obtained from Ref *5* as follows

$$\sigma'_f = 819 \text{ MPa}$$

$$\epsilon'_f = 1.655$$

$$b = -0.0841$$

$$c = -0.6356$$

The cyclic stress-strain curve for Alloy 600 is shown in Fig. 4, and the strain range versus life curve is shown in Fig. 6, both obtained from Ref *5*. With these numerical values, Eq 16 transforms to

$$\frac{\Delta\epsilon}{2} = 0.0038(2N_f)^{-0.0841} + 1.655(2N_f)^{-0.6356} \tag{17}$$

The procedure of fatigue evaluation using the local strain approach involves finding the number of cycles to failure by first converting the stress ranges for different pairs of loading conditions to local strain ranges using Eq 12 and then finding the number of cycles to failure from Eq 17. The cumulative fatigue usage, U, is then determined by Miner's rule.

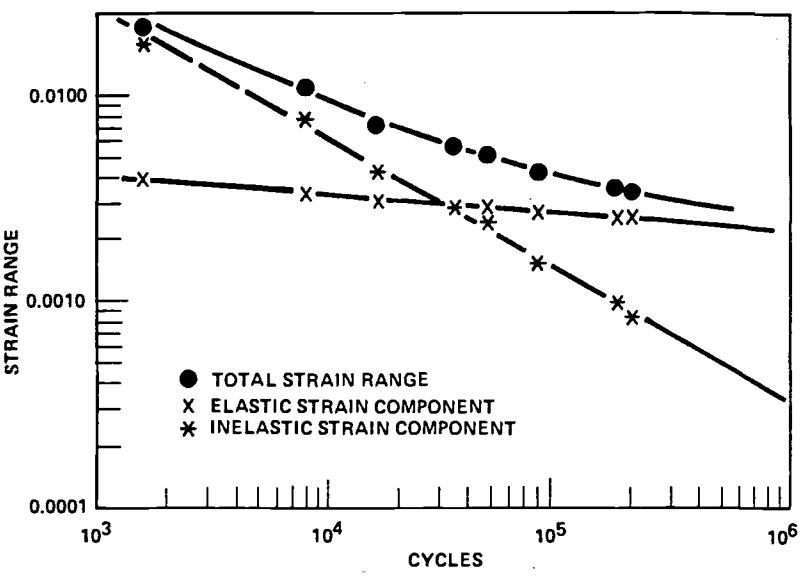

FIG. 6—*Strain range versus life plot for Alloy 600* [5].

Recommendation for the Incorporation of Hydrostatic Effects

As a result of the thermomechanical loads, the state of stress may be hydrostatic sensitive. The role of the state of stress on ductility can be represented by the triaxiality factor [6] defined as

$$TF = \frac{\sigma_1 + \sigma_2 + \sigma_3}{S_e} \tag{18}$$

where S_e is the effective stress as defined in Eq 15. The strains for the multiaxial (ϵ_{fm}) and uniaxial (ϵ_f) situations can be related as a ratio given by Ref 7 as

$$\frac{\epsilon_{fm}}{\epsilon_f} = 2^{(1-TF)} \tag{19}$$

This approximate relationship was obtained in Ref 7 based on experimental results for $TF > 0$. For cases involving extrusion of ductile metals under high compressive fields, the ratio goes to unity for $TF = -1$. The ratio monotically decreases from unity for larger negative values than $TF = -1$ [6].

However, if the loadings are such that $-1 < TF < +1$, then it is possible to write

$$\frac{\epsilon_{fm}}{\epsilon_f} = 2^{1-|TF|} \tag{20}$$

Conceptually the hydrostatic effects could influence the elastically calculated stresses which are used to compute the local strain range in Eq 11 as well as the strain-life relationship given by Eq 17. For a conservative assessment, it seems worthwhile to use an intensifier, K_{ma}, to be applied on the elastically calculated stress intensity ranges, S_n, in Eq 11 to account for multiaxiality as

$$K_{ma} = 2^{(1-|TF|)n'} \tag{21}$$

where n' is the cyclic strain-hardening exponent, as in Eq 6. The elastically calculated stress intensity ranges, S_n, are to be multiplied by the intensifier, K_{ma}, to reflect multiaxiality. The stress intensity ranges so intensified that $K_{ma} S_n$ should be used in place of S_n in Eq 11 to determine the local strain ranges. The revised strain ranges, $\Delta\epsilon$, should be used in the modified strain-life relationship (modified Eq 16) as

$$\frac{\Delta\epsilon}{2} = \frac{\sigma_f'}{E}(2N_f)^b + \epsilon_f' 2^{1-|TF|}(2N_f)^c \tag{22}$$

The rest of the fatigue evaluation remains the same as outlined before.

Numerical Example of a Design Problem

In order to determine the conservatism of the ASME Code procedure for fatigue evaluation, a sample design problem was studied as shown in Fig. 7. This shows a thermal liner welded to a nozzle. The loading conditions for the nozzle-to-liner weld are characterized by internal pres-

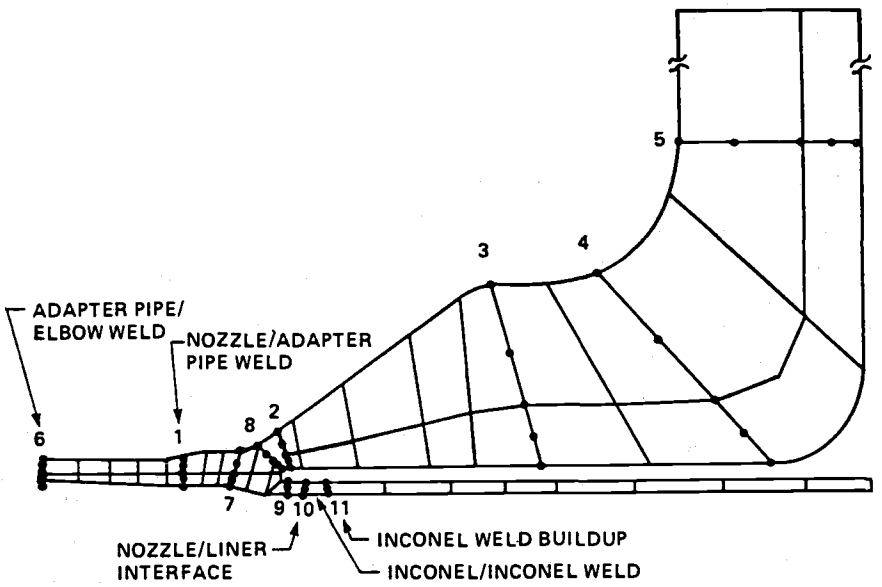

FIG. 7—*Pressure vessel nozzle fatigue analysis section locations.*

sure, as well as temperature and flow excursions of the fluid entering the nozzle. The temperature distribution through the thickness of the weld has been calculated using a finite element model for a number of loading transients. The transient analyses involve specification of appropriate heat transfer coefficients at the fluid-solid interface. In order to provide peak stress conditions for fatigue evaluations, the times during the transient analysis have been identified by investigating the conditions when the shock and bending stresses are maximized. The thermal solutions at these instants of time have been used for subsequent finite element elastic stress analyses. The calculated stresses at the outside surface of the Analysis Section 11 (Fig. 7) associated with various loading conditions are listed in Table 2.

Based on the principal stresses reported in Table 2, the stress intensities and the effective stresses are computed. The stress intensity is the largest absolute magnitude of the difference of the principal stresses, while the effective stresses are given by Eq 15. Although the ASME Code procedure [*2*] does not require the effective stresses for fatigue evaluation, these have been nonetheless calculated for comparison purposes. The stress intensities and the effective stresses are listed in Table 3 for all included loading conditions. A sign has been applied to

TABLE 2—*Loading condition and principal stresses.*

Condition	Transient	Number of Cycles	Principal Stress 1, MPA	Principal Stress 2, MPA	Principal Stress 3, MPA
1	Load	500	194	−126	−122
2	Normal	200	203	−105	−97
3	Upset 1	770	−190	−20	−32
4	Upset 2	20	249	−171	−163
5	Upset 3	30	364	−134	−123
6	Upset 4	30	265	−195	−185

TABLE 3—*Stress intensities and effective stresses.*

Condition	Stress Intensity, MPA	Effective Stress, MPA
1	319	318
2	308	304
3	−170	−165
4	420	416
5	498	492
6	461	456

each of the stresses based on an inspection of the state of stress associated with the particular loading condition in Table 2. From Table 3, it can be noted that the stress intensities and the effective stresses are nearly the same for all loading conditions considered in the problem.

The material for the thermal liner as well as the liner to nozzle weld is Inconel 600, with the following material properties obtained from the Code [*2*].

$$S_m = 160 \text{ MPa}$$

$$\text{Yield strength} = 1.5S_m = 240 \text{ MPa}$$

$$\text{Young's modulus, } E = 207 \text{ GPa}$$

The design fatigue curve for the material is obtained from Ref *2* and is shown in Fig 8. This figure is based on an elastic modulus of 180 MPa. Therefore the alternating stresses have to be multiplied by the factor $K = 180/207 = 0.87$ to perform the fatigue evaluation.

Table 4 shows the fatigue evaluation using the ASME Code procedure. A cumulative fatigue usage factor of 0.303 results from this evaluation.

For the purpose of fatigue evaluation by the local strain approach, a distinction needs to be made regarding the surface and the linearized stresses. The ASME Code employs the linearized stresses to evaluate the enhancement factors, K_e, when the linearized stress ranges exceed the $3S_m$ limit. For the particular problem under consideration, the ratio, ρ, of the linearized stress, S_n, to the surface peak stress, S_p, is greater than unity (typically 1.4, see Table 3). Therefore for

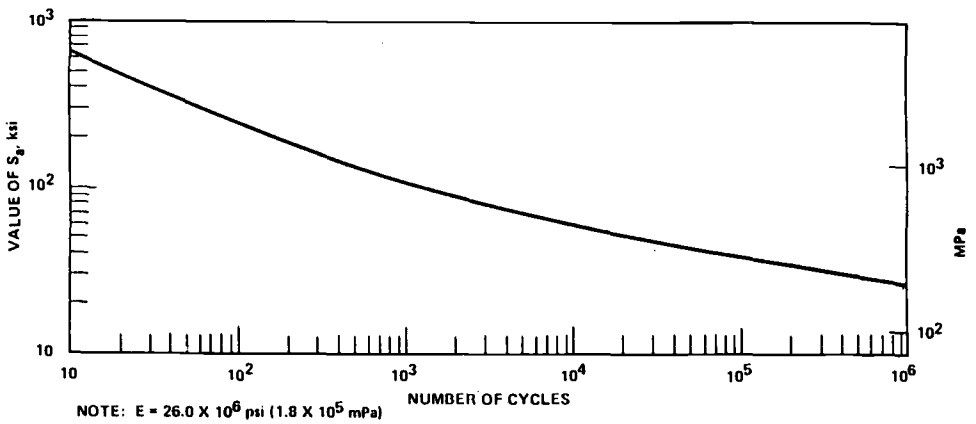

FIG. 8—*ASME Code design fatigue curve for Alloy 600.*

TABLE 4—*Fatigue evaluation using the ASME Code.*

Combo	Stress Intensity Range, MPA	Ratio[a]	K_e[b]	Cycles	Stress Amplitude[c], MPA	All Cycles	Usage
5–3	668	1.41	3.33	30	971	450	0.067
6–3	632	1.35	3.33	30	918	534	0.056
4–3	591	1.36	3.20	20	825	747	0.027
1–3	490	1.37	2.32	500	501	4345	0.115
2–3	479	1.40	2.31	190	483	4994	0.038
							0.303

[a] The ratio of the linearized stress intensity over the outside surface stress intensity.
[b] K_e factors are based on stress intensity ranges linearized through the section thickness.
[c] Stress amplitude = 1/2 (stress intensity range) $K K_e$, where $K = 0.87$.

comparing the ASME Code and the local strain approaches, the plastic strains for the local strain method should be based on the peak stresses which are obtained by multiplying the linearized stress intensity ranges by the ratio, ρ. From Neuber's rule, this corresponds to an amplification of $\sqrt{\rho}$ on elastically computed stress. For the example problem, the local strain ranges, $\Delta\epsilon$, have been iteratively computed using Eq 12 with the stress intensity ranges amplified by $\sqrt{\rho}$. The cycles to failure have been calculated by iteratively solving Eq 17. The fatigue evaluation results, using the local strain method, are shown in Table 5. A cumulative fatigue usage of 0.0023 results from this evaluation. However, there are sources of conservatism in the ASME Code design fatigue curve. To account for the conservatism involved in the fatigue evaluation alone, the ASME Code fatigue usage calculation must be based on identical fatigue curve as in Ref *5*. Such an evaluation is shown in Table 6. A cumulative fatigue usage of 0.019 is then obtained which is greater than the 0.0023 calculated using the local strain approach.

Conclusions

Analytical methods for evaluating multiaxial low-cycle fatigue life exist in various design codes. The low-cycle fatigue evaluation is performed by multiplying the elastically calculated stresses by enhancement factors in both the ASME and MITI Codes. The MITI Code prescribes a low-cycle fatigue enhancement factor, K_e, which is somewhat different than what appears in the ASME Code.

The singular behavior of the K_e factor in the MITI Code has been appraised for a structural

TABLE 5—*Fatigue evaluation using local strain approach.*

Combo	Effective Stress, MPA	Peak Stress[a], MPA	Strain Range	Cycles	All Cycles	Usage
5–3	657	780	0.0047	30	66 182	0.0005
6–3	620	721	0.0041	30	101 442	0.0003
4–3	580	689	0.0039	20	131 889	0.0002
1–3	482	564	0.0029	500	500 870	0.0010
2–3	469	555	0.0028	190	571 250	0.0003
						0.0023

[a] For each load combination, the peak stress range is obtained by applying a factor (equal to the square root of the ratio obtained from Table 4) to the effective stress range.

TABLE 6—*ASME fatigue evaluation using Ref* 5 *curve.*

Combo	Stress Amplitude[a], MPA	Strain Range[b]	Cycles	All Cycles	Usage
5–3	971	0.0094	30	10 102	0.003
6–3	918	0.0089	30	11 500	0.003
4–3	825	0.0080	20	14 808	0.002
1–3	501	0.0048	500	58 872	0.008
2–3	483	0.0047	190	66 370	0.003
					0.019

[a] Obtained from Table 4.
[b] Calculated as 2 (stress amplitude)/E; E is the Young's modulus taken as 207 GPa.

material using the local strain approach. The ratio of the peak stress to the linearized stress has been introduced as a strain concentration in a mathematical model. The resulting computed values of the K_e factors follow the same trend as the ones prescribed in the MITI Code, as shown in Fig. 5. However, for different ratios of the peak stress to the linearized stress, the mathematical model proposed in this paper predicts K_e factor to increase linearly at different rates (Fig. 5). The K_e factors given in the MITI Code (Fig. 5) increase linearly with the stress level at the same rate for all ratios of the peak stresses to the linearized stresses.

Nevertheless, there seems to be some justification in the Japanese approach, which accounts for additional strain concentration caused by surface peak stress exceeding the linear stress as developed in this paper. The singular behavior of the K_e factor in the MITI Code needs further clarification. However, this singularity stems from the fact that for values of linearized stress ranges, S_n, less than the $3S_m$ limit, the structure is assumed to shake down to an elastic condition and K_e reduces to unity. The multiaxiality is incorporated in the ASME and MITI codes through stress intensity which addresses the three-dimensional state of stress without specifically addressing the hydrostatic effects.

In this paper recommendations have been provided to incorporate the hydrostatic effects through the triaxiality factor. The triaxiality factor is shown to introduce additional strain concentration to that already present due to inelasticity. Furthermore, the triaxiality is shown to modify the strain-life relationship. Both effects must be adequately addressed in the fatigue design procedures.

A numerical example of a sample design problem demonstrates the conservatism of the code procedure for fatigue evaluation when compared with the local strain approach. This conservatism stems partly from the safety factors in the code design fatigue curves and partly from the estimation of low-cycle fatigue enhancement factors as shown in Fig. 5. Although the example problem shows the code approach to be fairly conservative, for stress ranges in the vicinity of $3S_m$ (typically twice the nominal yield), nonconservative evaluations could result. For those loading situations, the MITI Code seems to be more conservative than the ASME Code. Further research is needed in the low-cycle fatigue evaluations which employ only elastic analysis. Research is also needed to properly address hydrostatic effects.

References

[1] MITI Notification 501, Structural Design Rules for Nuclear Power Plant Components, Ministry of International Trades and Industry, Japan, 1980.
[2] ASME Boiler and Pressure Vessel Code, Section III, Subsection NB, Class I Components, American Society of Mechanical Engineers, New York, 1989.

[3] Fatigue Design Handbook, AE-10, Society of Automotive Engineers, Inc., Warrendale, PA, 1988.
[4] Neuber, H., "Theory of Stress Concentration for Shear Strained Prismatic Bodies with Arbitrary Nonlinear Stress-Strain Law," *Journal of Applied Mechanics,* Vol. 28, 1961, pp. 544–550.
[5] EPRI-NP-2957, RPS 110-1, Fatigue Performance of Ni-Cr-Fe Alloy Under Typical PWR Steam Generator Conditions, Electric Power Research Institute, Palo Alto, CA, March 1983.
[6] Davis, E. A. and Connelly, F. M., "Stress Distribution and Plastic Deformation in Rotating Cylinders of Strain-Hardening Materials," *Journal of Applied Mechanics,* Vol. 21, 1959, pp. 25–30.
[7] Manjoine, M. J., "Ductility Indices at Elevated Temperature," *Journal of Engineering Materials and Technology,* Vol. 97, 1975, pp. 156–161.

Kin Liao[1] *and Kenneth L. Reifsnider*[1]

Multiaxial Fatigue and Life Prediction of Composite Hip Prostheses

REFERENCE: Liao, K. and Reifsnider, K. L., **"Multiaxial Fatigue and Life Prediction of Composite Hip Prostheses,"** *Advances in Multiaxial Fatigue, ASTM STP 1191*, D. L. McDowell and R. Ellis, Eds., American Society for Testing and Materials, Philadelphia, 1993, pp. 429–449.

ABSTRACT: The fatigue behavior of hip prostheses made from laminated fiber-reinforced polymeric composite material under biaxial loading was investigated. Two types of prototype specimens with different layups were cyclically tested at several different load levels. X-ray radiography and surface replication were used to record fatigue damage development in the specimens tested. Internal damage features were also examined after sectioning of selected specimens. Damage mechanisms in the composite prostheses are discussed in association with results of the nondestructive and destructive tests. A life prediction model that is capable of predicting the residual strength and life of a composite prosthesis was developed based on a critical-element model for composite laminates. An example is provided to illustrate the application of the life prediction model.

KEY WORDS: composite material, hip prosthesis, biaxial loading, compression-compression fatigue, fatigue damage, critical-element model, life prediction

The metallic hip prosthesis now used in hip arthroplasty has at least two disadvantages. First, the stiffness of the implant material is relatively high compared to the cortical bone (load-carrying tissue of the human femur). This mismatch in mechanical properties causes a stress shielding effect, resulting in bone loosening and fracture of the prosthesis [*1*]. Second, patients may experience hypersensitivity as a result of the release of metallic ions from the prosthesis caused by wear [*2*]. With advances in materials science, hip prostheses made of fiber-reinforced polymeric composite materials are under development. Such prostheses possess some advantageous characteristics that their metallic counterparts do not: the stiffness of polymeric composite materials is more compatible to the cortical bone compared to materials such as titanium alloys and stainless steel, which are widely used for making hip prostheses; the strength and stiffness of a composite prosthesis can be tailored according to service loads, and they are inert to harsh human body environments [*1–4*]. A plot of the stiffness of the cortical bone of the human femur and three implant materials is shown in Fig. 1. It is seen that the stiffness of the quasi-isotropic composite laminate made from C/PEEK [carbon fiber reinforced poly(ether ether ketone)] is much closer to that of the cortical bone than the other two implant materials, namely, 316L stainless steel and Ti-6Al-4V ELI.

Since composite hip prosthesis is still in its developmental stage, many problems need to be well studied before clinical application become a reality. Among many performance-related concerns, the fatigue behavior of the implant structure is a fundamental one. Although a large amount of fatigue data have been obtained on many types of filamentary composite materials,

[1] Graduate student and Alexander Giacco professor, respectively, Materials Response Group, Engineering Science and Mechanics Department, Virginia Polytechnic Institute and State University, Blacksburg, VA 24061-0219.

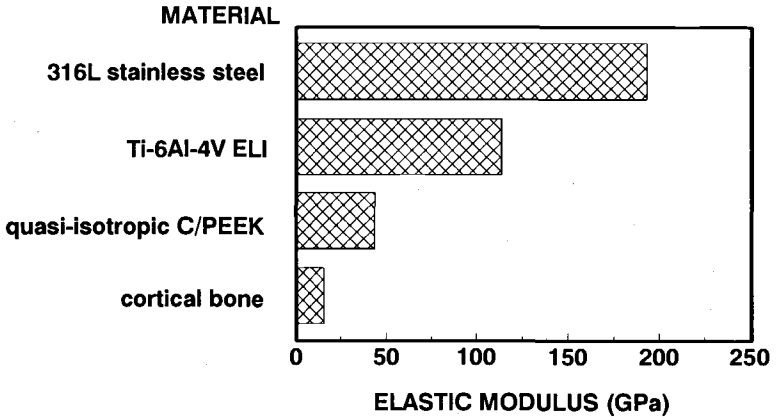

FIG. 1—*A comparison of the elastic modulus between the cortical bone and three implant materials.*

to the authors' knowledge, investigation of the compression-compression fatigue behavior of thick-sectioned, complex-shaped structures under biaxial loading is rare, if not nonexistent, in the literature to date. In this paper, results of an investigation on the fatigue behavior of composite hip prostheses under biaxial mechanical loading condition are presented. Fatigue damage process is discussed in association with results of several nondestructive and destructive tests. A life prediction model for the composite prosthesis was developed based on a mechanistic, cumulative damage model for composite laminates.

Experimental

Specimens

The prototype composite prostheses used in this investigation were manufactured from C/PEEK prepreg by a plate-cut process wherein a prosthesis was cut from a cured composite laminate and its contour machined according to design (Fig. 2). Nomenclatures of the hip prosthesis are shown in Fig. 3. The laminate consisted of approximately a hundred individual plies at its thickest section (shoulder). The head of the prosthesis is a hollow stainless steel ball inserted on the neck of the prosthesis.

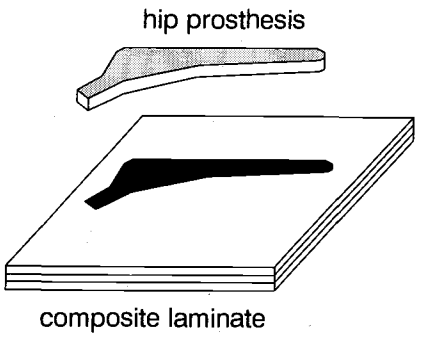

FIG. 2—*Schematic diagram of the plate cut process.*

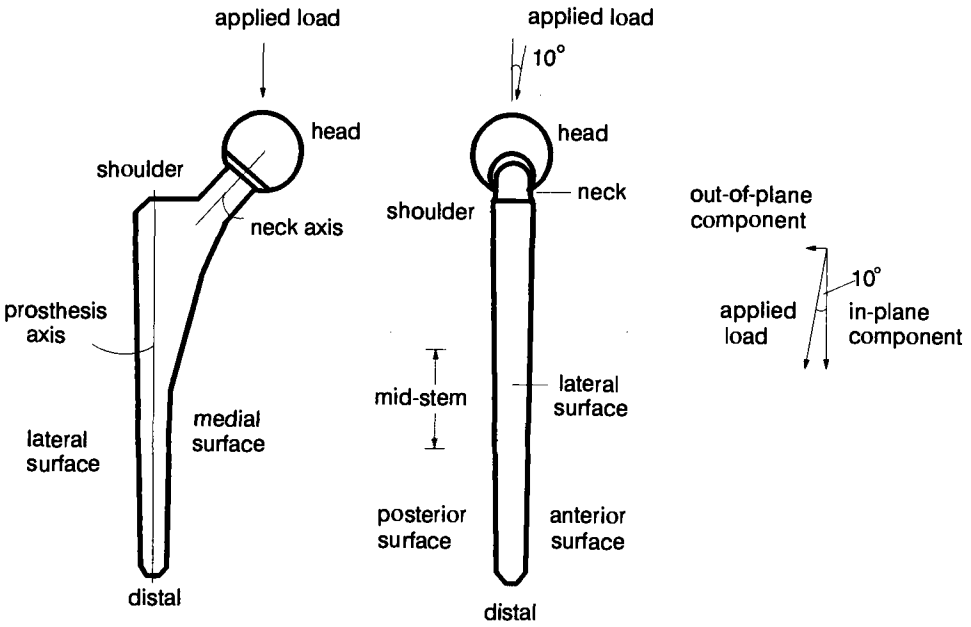

FIG. 3—*Nomenclatures of a hip prosthesis.*

Three specimen groups consisting of a total of nine specimens were cyclically tested in compression-compression. Group 1 consisted of three specimens with a stacking sequence hereafter referred to as the L1 layup. Groups 2 and 3 each consisted of three specimens with a different stacking sequence from the L1 layup, hereafter referred to as the L2 layup. Due to the proprietary nature of these layups, they will not be reported here. To facilitate subsequent discussion, individual plies are identified according to the following scheme (Fig. 4):

L1 layup:

A1—Plies with lowest positive angle of incident (PAI) to the prosthesis axis (first quadrant).

B1—Plies with second lowest PAI to the prosthesis axis (first quadrant).

C1—Plies with highest PAI to the prosthesis axis (second quadrant).

L2 layup:

A2—Plies with lowest PAI to the prosthesis axis (first quadrant).

B2—Plies with second lowest PAI to the prosthesis axis (first quadrant).

C2—Plies with third lowest PAI to the prosthesis axis (second quadrant).

D2—Plies with highest PAI to the prosthesis axis (second quadrant).

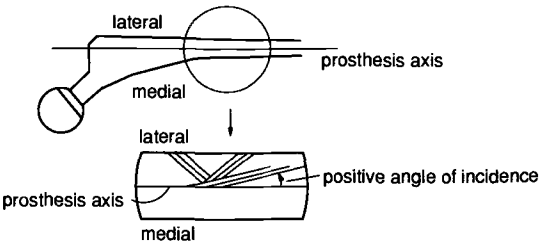

FIG. 4—*Ply identification scheme for a composite hip prosthesis.*

Loading and Test Fixture

Hip loading usually occurs in two planes of the prosthesis (that is, the anterior/posterior and the medial/lateral plane) during various activities. By inclusion of the abductor muscle forces, Gavens et al. [5] found that peak amplitude of hip loading during gait can be reproduced with a 0° in-plane and 10° out-of-plane load, as shown in Fig. 3. Here, in-plane force (moment) refers to force (moment) parallel to the anterior/posterior plane, and out-of-plane force (moment) refers to force (moment) perpendicular to the anterior/posterior plane. This kind of loading imposes in-plane and out-of-plane bending, compression, and torsion on the prosthesis. The aforementioned load angles were used in all the cyclic tests performed.

A test fixture was designed to perform cyclic tests on the prostheses under a simulated *in vivo* mechanical loading condition, as illustrated in Fig. 5. The fixture consists of a thick-walled, metallic sleeve (with two small circular holes at the bottom) sitting on an 10° inclined metallic platform. The inclined platform produces out-of-plane moment and force on the prosthesis. This structure (the sleeve and the platform) is adjustable in position to a supporting ball-and-socket-type structure, which is gripped in the lower grip of the servohydraulic testing frame. The sleeve is filled with a solid insert made from a polymeric material reinforced by chopped short fibers. The stiffness of the reinforced polymeric insert is close to that of the human bone structure. The hip prosthesis is secured in the polymeric insert by hammering on its shoulder using a plastic hammer. A small metallic bar with two knobs is placed between the bottom of the insert and the metallic sleeve to prevent rotation of the prosthesis. During a cyclic test, the polymeric insert was replaced several times as a result of damage and deformation. The upper load fixture consists of a metallic cylinder with a acetabular cup to apply load to the head of the prosthesis.

Fatigue Tests

Group 1 specimens (L1 layup) were cyclically loaded to failure at maximum applied loads (R = 10) of 53, 61, and 75% of the mean ultimate quasi-static load of the L1 specimens (at the same load angles), respectively. Group 2 specimens (L2 layup) were cyclically loaded to failure at maximum applied loads of 59, 69, and 84% of the mean ultimate quasi-static load of the L2 specimens, respectively. All Group 3 specimens (L2 layup) were cyclically tested at maximum applied load of 47% of the mean ultimate quasi-static load of the L2 specimens. The quasi-static data were obtained from a separate investigation [6]. For all the Group 3 specimens, tests were stopped at the end of 6E6, 10E6, and 15E6 cycles. It should be mentioned

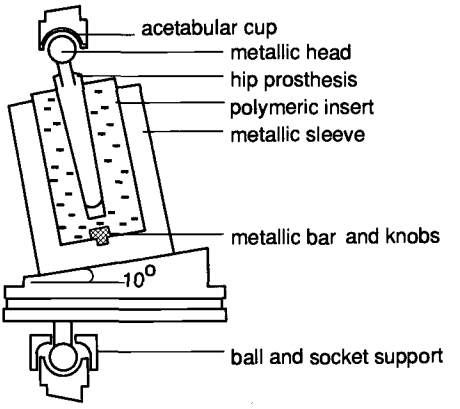

FIG. 5—*Schematic diagram of the test fixture.*

TABLE 1—*Test matrix and results.*

Group	Specimen	Maximum Load, % GSS[a]	Frequency, Hz	Life, Cycles	Failure Site
1 (L1 layup)	3Q	53	2	265E3	Midstem
	5G	61	1	9.4E3	Midstem
	2N	75	1	1.2E3	Midstem
2 (L2 layup)	BD	59	2	398E3	Midstem
	BB	69	1	10.4E3	Neck
	BF	84	1	0.6E3	Neck
3 (L2 layup)	FA	47	6	15E6	N/A
	FB	47	6	10E6	N/A
	FC	47	6	6E6	N/A

[a] Quasi-static strength.

here that the lowest chosen load levels (53% ultimate load for L1 specimen, 47% ultimate load for L2 specimen) well exceeded expected peak joint load during gait, which is about six times body weight [*3*]. All the cyclic tests were carried out in an MTS 880 servohydraulic testing frame using a load-controlled mode wherein a specimen was loaded by a sinusoidal load of constant amplitude. The loading frequency was determined by the magnitude of the applied load. As a result of high compliance of the polymeric insert, only lower frequencies can be used to achieve the required load amplitude. The test matrix is shown in Table 1.

X-Ray Radiography

X-ray radiography was used at intervals to examine all nine specimens tested using a Hewlett Packard 43805N cabinet X-ray system. The energy level and exposure time were set at 50 kV and 2.3 min, respectively. Zinc iodide penetrant was applied to the medial surface of the specimen for about an hour before taking the radiograph. When taking the X-ray, the prosthesis was positioned with its posterior/anterior side parallel to the horizontal lead plate underneath. The target-specimen distance was about 100 cm.

Surface Replication

A surface replication technique was used to record surface-related damage development in all of the specimens tested. Replications of the medial neck surface and medial midstem surface of each of the nine specimens was made at intervals throughout the cyclic test using acetone and acetyl cellulose film.

Destructive Tests

Two Group 1 specimens (3Q and 5G) were sectioned at the neck region after failure (in the midstem) to examine internal damage features. All Group 3 specimens were sectioned at the same location at the end of their cyclic tests. The sectioned necks were polished and examined under a Nikon EPIPHOT inverted microscope.

Results and Discussion

Results of the cyclic tests are summarized in Table 1 and Fig. 6. In general, damage and failure modes depend on the layups of the specimens.

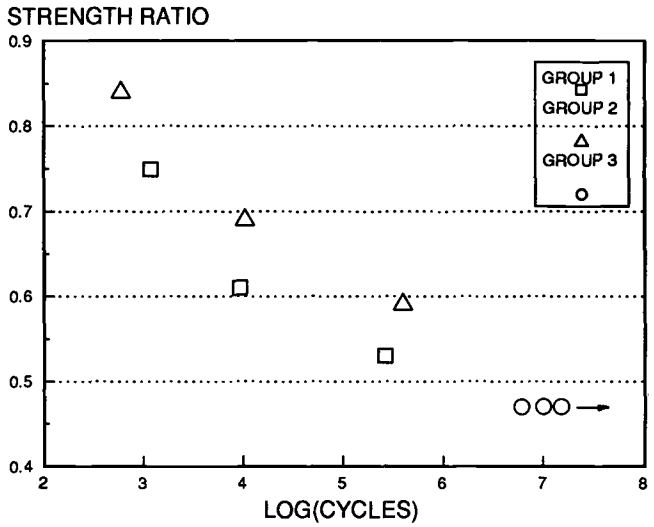

FIG. 6—*Fatigue test results.*

X-Ray Radiography

Selected results of the X-ray radiography of specimens 2N (L1 layup) and BD (L2 layup) are shown schematically in Fig. 7. These drawings represent damage development in a portion of the medial neck and medial midstem region of the prosthesis and are typical of the L1- and L2-type specimens. For all three groups of specimens, thin penetrant lines in fiber directions were observed in the neck region, which are believed to be caused by matrix cracking along fiber directions. These penetrant lines all initiated from the medial surface and extend to the lateral side. The density and area covered by these thin penetrant lines both increased with an increase in applied cycles, indicating damage progression. For Group 1 specimens, more penetrant lines were seen in A1 and B1 plies than other plies. The orientation of A1 and B1 plies were closest to the neck axis. For specimens with L2 layup, most of the neck damage occurred in A2 plies and B2 plies. There were also plies with orientations closest to the neck axis. Only a few penetrant lines were seen in other plies in specimens with either L1 or L2 layups. A few delaminations were also observed.

In the midstem region, thin penetrant lines along fiber directions initiated from the medial surface for both types of specimens. They later developed into thick penetrant lines (though fewer in number), extending to the lateral side. These thick penetrant lines joined to form a wide penetrant band at late life. Within the penetrant band, thin penetrant lines in fiber directions were not recognizable. This is an indication of severe damage. For Group 1 specimens, these penetrant bands were about 135° (or −45°) to the prosthesis axis (Fig. 7*a*). For Group 2 specimens, the penetrant bands were more or less perpendicular to the prosthesis axis (Fig. 7*b*). For Group 3 specimens, only a few penetrant lines were observed in the medial midstem region at the end of each cyclic test.

Surface Replication

Selected results of surface replication are shown in Fig. 8. A detailed discussion for each of the Group 1 and 2 specimens can be found in Ref *4*. In general, in the neck region of all three

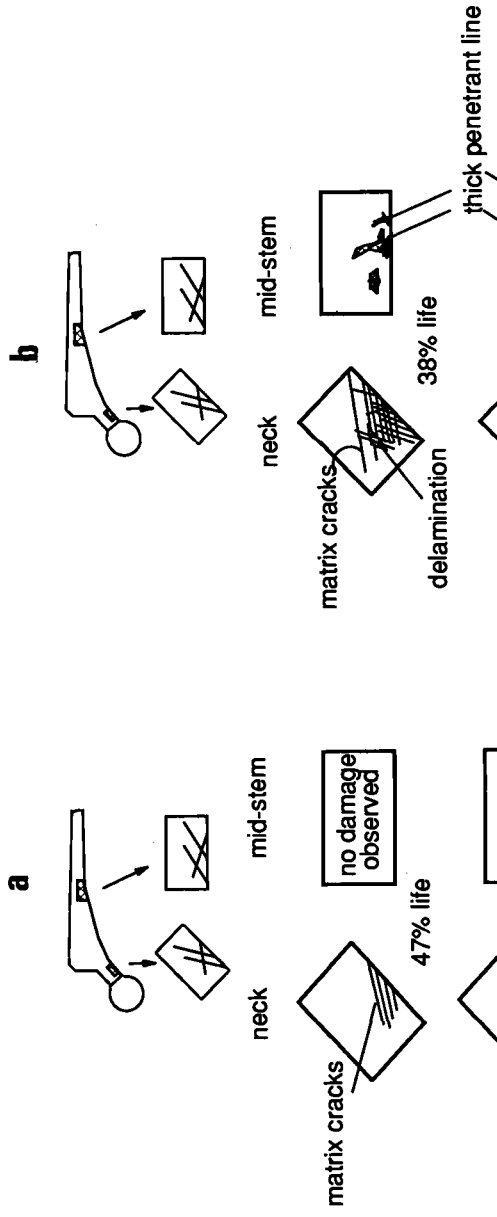

FIG. 7—(a) *Schematic diagram of results of X-ray radiography for specimen 2N;* (b) *schematic diagram of results of X-ray radiography for specimen BD.*

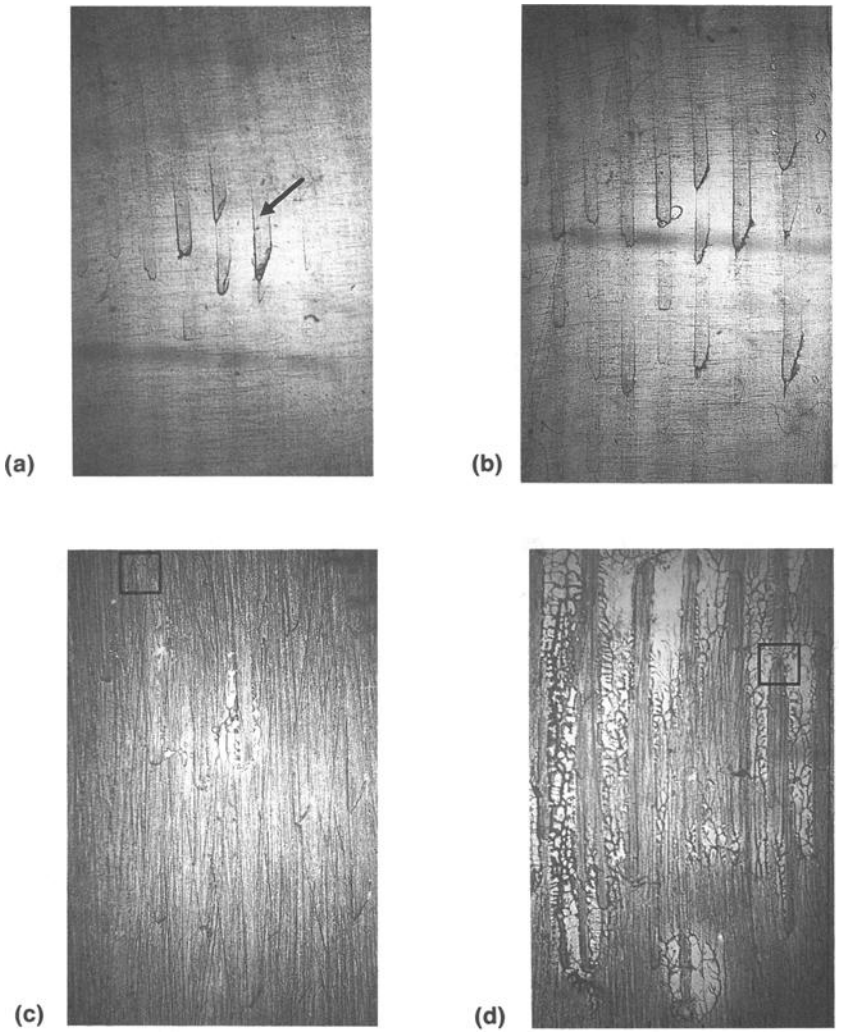

FIG. 8*a*—*Surface replica of medial neck region of specimen 5G at 53% life. Arrow indicates an downward pop-out ply.*

FIG. 8*b*—*Surface replica of medial neck region of specimen 5G at 88% life.*

FIG. 8*c*—*Surface replica of medial neck region of specimen BB at 50% life. Square indicates an upward pop-out ply.*

FIG. 8d—*Surface replica of medial neck region of specimen BB at 96% life. Square indicates an upward pop-out ply.*

groups of specimens, damage was observed in form of pop-out plies. These damaged plies may protrude from the surface in two directions, downward (that is, toward the distal end) and upward (that is, toward the head). Only downward pop-out plies were observed in Group 1 specimens (Figs. 8*a* and 8*b*), while both downward and upward pop-out plies were observed in both Group 2 and 3 specimens (Figs. 8*c* and 8*d*). Aided by X-ray radiographs, the down-

FIG. 8*e*—*Surface replica of medial midstem region of specimen 3Q at 25% life.*

FIG. 8*f*—*Surface replica of medial midstem region of specimen BD at 4% life. Arrows indicate in-plane microbuckling damages; filled triangle indicates an out-of-plane microbuckling damage.*

ward pop-out plies in the neck region for Group 1 and Groups 2 and 3 specimens were identified to be A1 and A2 plies, respectively. These were plies with orientations closest to the neck axis. The upward pop-out plies in Groups 2 and 3 specimens were identified to be the plies with the next closest orientation to the neck axis. Pop-out plies first appeared in medial-posterior corner, extending their distribution toward the anterior side and along the medial surface with an increase of applied cycles. Pop-out plies were also observed in the midstem region of all three groups of specimens, as shown in Figs. 8*e* and 8*f*. In addition, some microbuckling-type damages were observed in Group 2 specimens (Fig. 8*f*).

Destructive Tests

Results from sectioning of specimen 3Q (L1 layup) are shown in Fig. 9. Similar results were found in other specimens subjected to sectioning [*7*]. Figures 9*a* and 9*b* were taken near the medial surface and center of the cross section, respectively. Matrix cracks like those shown in Fig. 9*a* were observed near both the medial and the lateral surface. More such cracks were observed near the posterior-medial surface since this region sustained highest compressive stress. For Group 1 specimens, these matrix cracks mainly occurred in A1 plies, which are the plies with lowest angle of incidence to the neck axis. It is seen from Fig. 9*a* that a piece of damaged ply was separated from the medial surface by a through-the-thickness lamina matrix crack, forming a pop-out ply. Some delaminations were also developed in the neck region, although only a few were observed, such as the one shown in Fig. 9*b*. It was verified by the

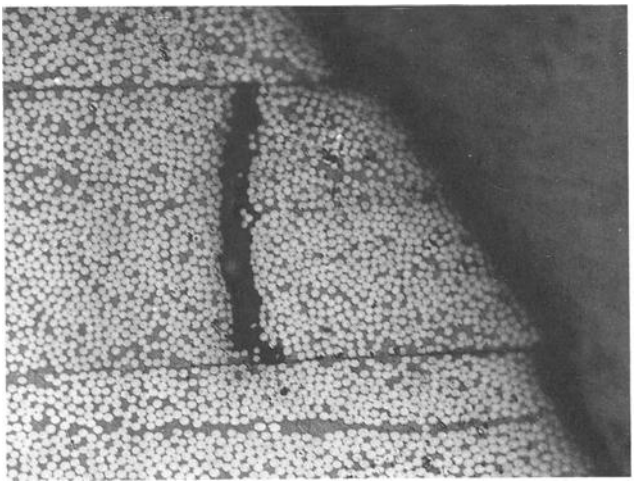

FIG. 9*a*—*Micrograph of a section of neck region of specimen 3Q near medial surface.*

destructive tests that the penetrant lines observed in the X-ray radiographs indeed resulted from matrix cracking, and delaminations did occur in the neck region.

Based on the results of X-ray radiography, surface replication, and destructive tests, a brief discussion of the fatigue damage process in the prostheses is presented as follows. For the two types of prostheses tested, L1 and L2 specimens, damage occurred exclusively in both the neck and the midstem region. Subsequently, failure occurred in either of the two regions, depending on the layup. The medial-posterior corner of the mid-neck region is under the highest local compressive stress as a result of a combination of in-plane and out-of-plane bending moment, as well as axial compressive force normal to the neck axis. Under applied cyclic load, a gap

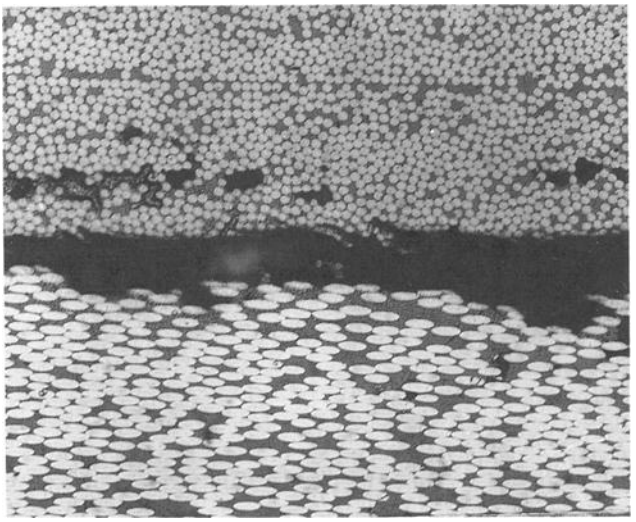

FIG. 9*b*—*Micrograph of a section of neck region of specimen 3Q near the middle of the cross section.*

was gradually developed between the prosthesis and the polymeric insert as a result of damage and deformation of the latter. This causes the initially fully supported portion of the specimen to gradually recede to its midstem region, resulting in higher bending moments and thus higher compressive stress on the medial side of the midstem region. Usually, initiation of neck damage precedes that of the midstem damage. This is evident from the fact that for specimen 2N no midstem damage was seen from either X-ray radiographs or surface replication images at 47% life, while some neck damage was observed (Fig. 7*a*). Damage process in the neck and the midstem region are discussed separately in the following.

Damage Development in the Neck Region

Damage in the neck region initiated from the medial-posterior corner, a region under highest compressive stress, in the form of matrix cracking along the fiber directions. This kind of damage first occurred in plies with orientations closest to the neck axis, sometimes as early as 4% life (specimen BD), followed by plies next closely oriented to the neck axis, and so on. Plies with other orientations were also subjected to damage, but usually after midlife or in late life. Delaminations may also develop in some of the specimens. In one of the specimens (specimen BD), a delamination was detected at 10% life; in other specimens delaminations were detected after midlife. The damaged region expanded with an increase of applied cycles. Matrix cracks were found distributing from the posterior surface toward the anterior side. At the same time, these cracks also extended (in length) toward the lateral side of the prosthesis, as indicated schematically in Fig. 10*a*.

From surface replication, it is seen that the transverse section of the pop-out plies were angled, as illustrated in Fig. 10*b* (see also Figs. 8*a* through 8*d*). Those plies close to the anterior side popped out at an angle of about 120°, those close to the posterior side popped out at an angle around 55°, and those close to the middle of the laminate were V-shaped or blunted. This phenomenon was observed in all of the specimens tested, with the effect more pronounced (that is, a more recognizable pattern of angled pop-out plies) in the L1 specimens. It is believed that this pattern of pop-out plies is an indication of the effect of the biaxial stress state.

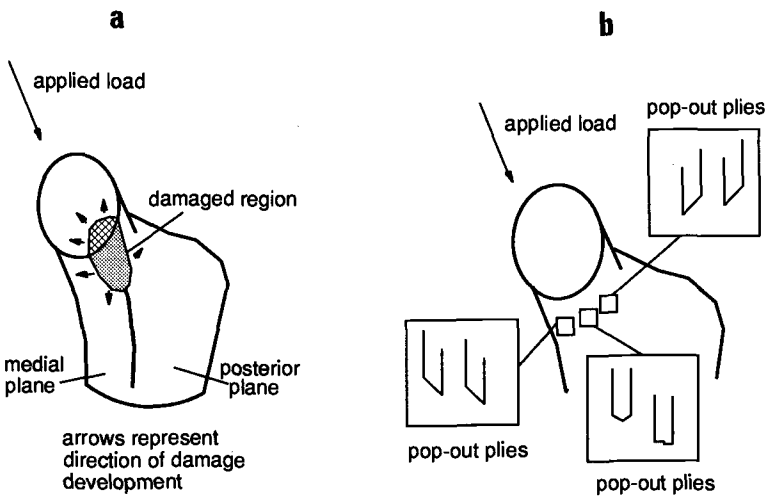

FIG. 10—(a) *Schematic diagram of damage progression in the neck region;* (b) *schematic diagram of patterns of damaged plies in the neck region.*

Schematic drawings of the six failed specimens are shown in Fig. 11. Two out of three of the Group 2 specimens (specimens BB and BF) failed at the neck region, one (specimen BD) failed at the midstem region. Specimens BB and BF were loaded at higher load levels than specimen BD. The failure surface of BB and BF, when viewed from either the medial or the lateral side, both showed a similar V-shaped cross section. When viewed from the top of the failure surfaces, a crushed region around the medial-posterior side was seen, with the one under higher load level (BF) more recognizable than the one under lower load level (BB), but smaller in size. These crushed regions are indications of compressive failure. When one examines the lateral side of specimen BB and BF, through-the-ply matrix cracks in D2 plies were seen. These cracks were all more or less separated from each other, indicating tensile failure. The cracks in specimen BB (under lower load level) were more dispersed through the thickness of the specimen than those in specimen BF (which was under higher load level). This indicates that more damage had been introduced to the specimen under lower load level than the one under higher load level at the time of failure. A similar phenomenon was reported previously on notched composite laminates by Razvan et al. [*8*]. In general, the failure process in the neck initiated from the medial-posterior corner due to compression, leaving a crushed compressive failure surface. The lateral side failed by tension, as indicated by matrix cracks in D2 plies in L2 specimens. The overall inverted V-shaped failure surface suggests a dominant shear-type failure due to compression.

Damage Development in the Midstem Region

For Group 1 specimens, damage initiated in the medial-posterior corner of the midstem region, first in the form of matrix cracks along fiber directions in all plies. Between midlife and late life, local failures involving several plies occurred, as indicated by several thick penetrant lines. They extended into the lateral side and joined together to form a larger local failure zone, as indicated by even thicker penetrant band, where all midstem failures had occurred. All the

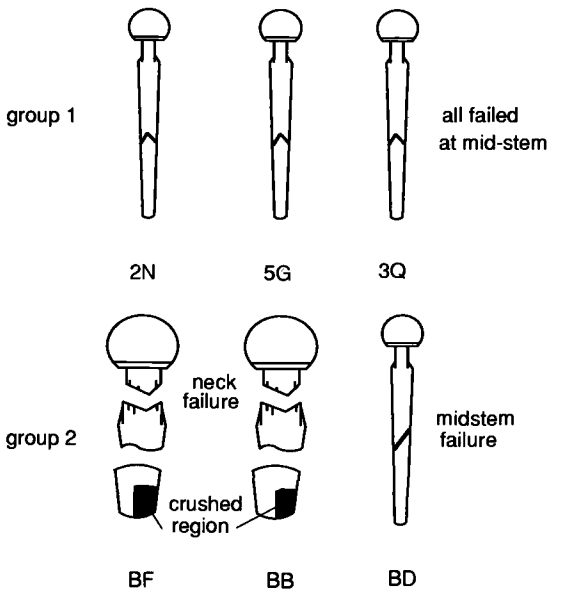

FIG. 11—*Schematic diagram of failure patterns of Group 1 and 2 specimens.*

Group 1 specimens failed at the midstem region at about 9 cm from the distal end of the prosthesis. The inverted V-shaped failure surface suggested that these specimens failed by shear (Fig. 11).

All of the Group 2 specimens showed midstem damage, although only one of them (specimen BD) failed in that region. Matrix cracks along fiber directions initiated from the medial surface and extended toward the lateral side. Local microbuckling-type damage was developed within a distance of 8.9 to 10.2 cm from the distal end in the major load-carrying plies. These microbuckling-type damages gradually developed into a global shear failure zone (as indicated by a wide penetrant band), causing structural failure in specimen BD (Fig. 11).

The apparent inconsistency of the failure mode of the L2 specimens can be explained by the difference in applied load levels. Specimen BD was tested at the lowest load level among Group 2 specimens, which implies that a substantial amount of damage had been developed in the specimen before it failed. The residual strength in the midstem region was exceeded by the applied load while the residual strength of the neck still exceeded that of the local applied load, resulting in midstem failure.

Life Prediction Model

In developing the composite prosthesis, it is almost impossible to produce a complete phenomenological database of stress and life, associated with such factors as complex loading conditions, required testing time, as well as cost. Hence, a life prediction model is desirable in making inquiry predictions for the long-term behavior for various designs. Such a model should represent, mechanistically and physically, property evolution in the composite prosthesis. A life prediction model for the composite prosthesis is developed based on a mechanistic, cumulative damage model for composite laminates known as the critical-element model [*9*]. A brief discussion of the model is presented as follows.

Stress Analysis

A stress analysis model for the composite prosthesis was first developed using a strength of materials approach. The structure of the composite prosthesis, which consists of more than a hundred individual plies with different ply orientations, is highly anisotropic. Large computation times would be required to analyze such a structure if a finite element method (FEM) was used to evaluate the stress state of each individual ply along the prosthesis. This is a major obstacle to the use of the FEM as an effective design tool. For this reason, a strength of materials approach was chosen.

The general approach for the stress analysis model is shown in Fig. 12. The basic assumption of this model is that the prosthesis is simply supported at its distal end, a worst case scenario compared to expected loadings. The geometry of the structure is first defined. This includes description of the longitudinal profile of the prosthesis by polynomial equations and calculation of cross-sectional geometric properties such as the area moment of inertia. In-plane and out-of-plane applied loads are defined next. Under the applied loads, global stress and moment distributions on each arbitrary chosen section along the prosthesis are determined. The curved beam theory is used in this model to account for curved geometry of the prosthesis. Global stress and moment components determined are then transformed into the laminate coordinate system at three locations of a section, namely, an element on the lateral, center, and medial curve. Laminate analysis is performed at each of these three locations to determine stress components of each individual ply at that particular location. General failure functions (Tsai-Hill, maximum stress, and maximum strain) are computed in association with the stress state of each individual ply to predict the strength of the structure by means of a first ply failure

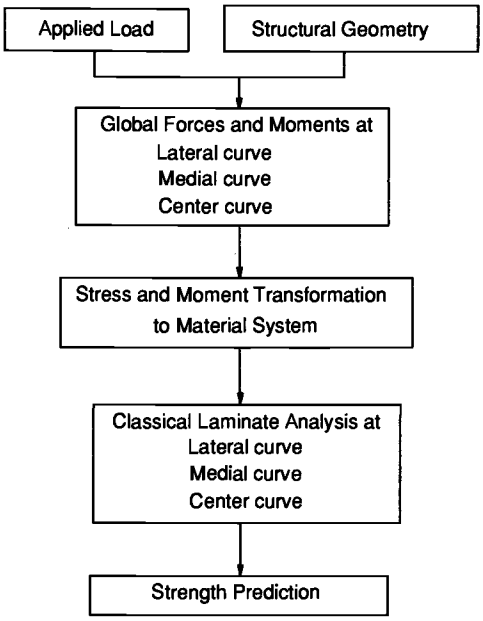

FIG. 12—*Flow chart of the stress analysis model.*

scheme, meaning the failure of the structure is defined when the failure function of any ply exceeds unity. The quasi-static strength predictions of the model are in very good agreement with experimental results. A detailed discussion of the stress analysis model can be found in Ref *4*.

The Critical Element Model

A life prediction model for the composite prosthesis was developed based on the concept of the critical-element model, a mechanistic, cumulative damage model for predicting the residual strength and life of composite laminates subjected to arbitrary cyclic loading [*9*]. A conceptual chart of the model is shown in Fig. 13. The failure mode of a component is first established. Based on the failure mode and the associated damage mechanisms, a representative volume that controls damage and failure and hence the life of the laminate or component is identified. It is often assumed that the mechanical response of the representative volume is the same as the bulk material, such as in the case of unnotched coupons. In some cases, the representative volume depends on the structural geometry and the stacking sequence, for instance, in notched coupons where the representative volume is around the notch. For a composite prosthesis, the representative volume is identified experimentally to be within either the medial neck or medial midstem region where structural failure usually occurred. Analytically, the location of the representative volume is at a point on the medial surface under maximum compressive stress as determined by the stress analysis model discussed previously. It is the process of continuous property degradation to this representative volume (as a function of applied cycles) which causes reduction of strength and eventually the structural failure that is to be described in the model.

Once the representative volume is established, it is subdivided into two types of elements, critical and subcritical. Critical elements are defined as those parts of the representative volume whose failure causes failure of the component. Since critical elements are the last part of

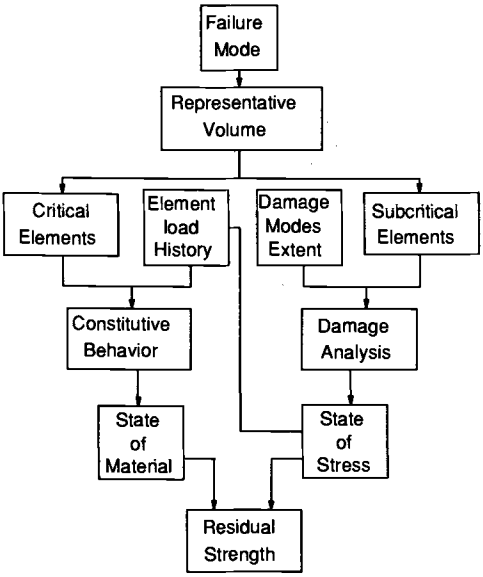

FIG. 13—*Flow chart of the critical-element model.*

a component to fail (after the failure of subcritical elements), the strength of a component is dominated by the response of the critical element to applied stress. Subcritical elements are defined as those parts of a component or laminate which sustain damage during the fatigue loading process, but only cause redistribution of internal stress because of fatigue damage (such as matrix cracking). The response of subcritical elements is determined by mechanics analysis, while the response of the critical elements is represented by phenomenological information and constitutive equations. As shown in Fig. 13, once the subcritical elements are defined and information regarding the damage modes and the extent of damage is obtained, a damage analysis can be conducted to establish the state of stress in the interior of the component, i.e., the stress state in both the critical and the subcritical elements as functions of the number of applied cycles. Damage modes and damage mechanisms can be accessed using NDE and destructive test methods. The local state of stress in the critical element, the element load history, obtained at a given number of applied cycles, may be used to determine the constitutive behavior of the element in some cases, that is, the state of the material. If the state of stress and the state of the material have been determined for the critical elements, then one should be able to use some phenomenological strength philosophy (such as Tsai-Hill) to determine the residual strength of the critical elements and therefore of the component. Detailed derivation of the associated equations can be found in Ref 9. The resulting general residual strength equation is

$$S_r(n) = 1 - \int_0^{\gamma} (1 - F_L(n))i \left(\frac{n}{N(n)}\right)^{i-1} d\left(\frac{n}{N(n)}\right) \tag{1}$$

where

S_r = residual strength of the critical element,
n = applied cycles,
F_L = failure function,

i = nonlinearity parameter, and
N = life of the critical element at current applied stress.

The residual strength, $S_r(n)$, can be evaluated at any applied cycle by numerically integrating Eq 1. Note that S_r, F_L, and N are all functions of applied cycles, n. Detailed computational procedures for a composite hip prosthesis are described in the following section.

Application to a Composite Prosthesis

The ultimate goal of the modeling effort is to transform the critical-element model concept into an operating computer code for design purpose. A flow chart of the computer model is shown in Fig. 14. To begin, global stress state in the prosthesis is first determined. The global stresses are then transformed into local stresses at the ply level using laminate analysis. These computations are accomplished using the stress analysis model. After the stress state in each individual ply at each chosen point along the prosthesis has been determined, the stresses are compared so that the location of the critical element and the subcritical elements can be identified: a ply with the highest stress in the fiber direction, σ_{11}, is identified as the critical element; all the other plies are identified as subcritical elements. Since it is known from experimental results that the prosthesis failed by compression, only the stress state and residual strength in the medial surface are evaluated.

As the number of applied load cycles (mechanical and environmental) increases, damage development in the subcritical elements results in degradation of material properties. For instance, creep and moisture effects cause reduction in transverse and shear modulus [*10–20*]; matrix cracking due to mechanical loading produces the same consequence [*21–25*].

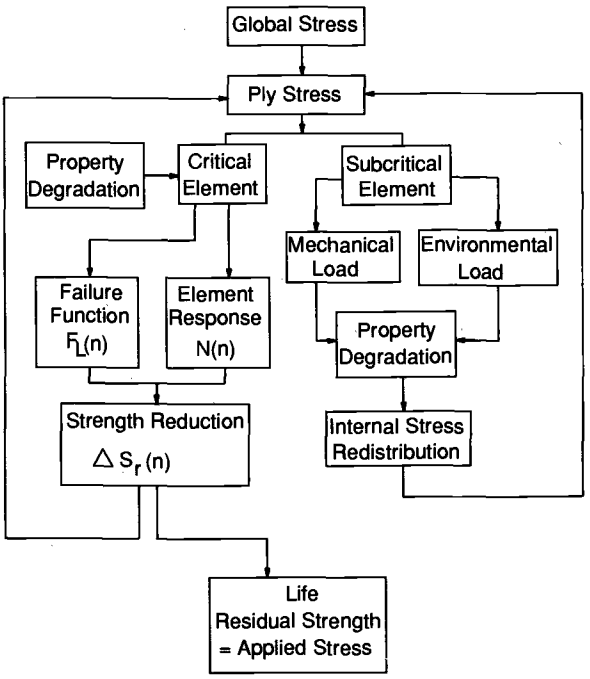

FIG. 14—*Flow chart of the life prediction model for composite hip prosthesis.*

Property degradation in the material is determined by damage analysis, wherein evolution of material properties is represented as functions of applied cycles.

Characterization of fatigue damage in composite materials has been the subject of numerous investigations [*21–25*]. In general, fatigue damage in composite materials consists of various combinations of matrix cracking, fiber-matrix debonding, delamination, void growth, and local fiber breakage. These damage mechanisms are complex and very difficult to describe in a general way. Reifsnider et al. [*23*] suggested the characteristic damage states (CDS) for matrix cracking in composite laminates having off-axis plies during long-term fatigue loading. These matrix cracks play an important role in controlling the life and residual strength of the laminate. Indeed, it has been found that matrix cracking is a dominant damage mode in the neck region of the prosthesis, as discussed in the experimental section. To represent transverse cracking in the matrix material during fatigue, it is required that the ply transverse and shear moduli, F_2 and G_{12}, decrease as transverse crack density increases with the number of applied cycles. Such a stiffness reduction relation may be represented in terms of applied cycles, n, in polynomial form

$$\frac{E_2}{E_2^0} = \sum c_m \left(\frac{n}{N}\right)^m \tag{2}$$

where c_m are coefficients, E_2^0 and E_2 are initial and current ply transverse stiffness, respectively, n and N are the same as in Eq 1. The same type of equation also applies for ply shear modulus, G_{12}. The effects of creep and moisture on stiffness changes of the material are also considered in the model. Detailed analysis can be found in Ref *4*.

As discussed earlier, damage in the subcritical element causes internal stress redistribution. Assume that the initial transverse modulus of the subcritical element is E_2^0. At some applied cycle, n, the transverse modulus becomes E_2, such that $E_2^0 > E_2$ as a result of damage development caused by either mechanical, or environmental, or both types of loadings. Analytically, from laminate theory, this reduction in transverse stiffness causes alternations in the A, B, and D matrices of the laminate, which in turn causes alternations in the stress state of all plies.

For the critical element at 0 applied cycles, no degradation in strength and stiffness has taken place. At this moment, the failure function $F_L(n) = F_L(0)$. The element response is determined by phenomenological data, which may be represented by a *S-N* curve

$$\frac{\sigma_{11}}{X_c} = a + b \log (N) \tag{3}$$

or

$$N = \log^{-1}\left[\frac{(\sigma_{11}/X_c - a)}{b}\right] \tag{4}$$

where

σ_{11} = instantaneous compressive stress in the fiber direction,
X_c = unidirectional compressive strength,
a, b = constants, and
N = life of the critical element at σ_{11}.

Note that σ_{11} and X_c are both functions of the number of applied cycles, n, so that life, N, is also a function of n.

Having calculated the failure function $F_L(0)$ and element response $N(0)$, we skip the step "strength reduction" for now and go back to the step "ply stress" in Fig. 14, as no damage is introduced to the element initially. Assuming that the number of applied cycles is increased to n, stress redistribution occurs in the interior of the laminate as a result of damage development in the subcritical elements. Usually this suggests that the critical elements are under higher stress than before. Moreover, environmental effects may cause a reduction in the compressive strength, X_c, of the critical element. Increase in applied stress, σ_{11}, and reduction in strength, X_c, of the critical element cause an increase in the failure function, such that $F_L(n) > F_L(0)$. The element response is also changed by the stress redistribution. Since σ_{11},X_c is no longer the same at n cycles when compared to 0 cycle, $N(n)$ is different from $N(0)$. Usually, $N(n) < N(0)$. Now $F_L(0)$, $F_L(n)$, $N(0)$, $N(n)$, and n are all known. These quantities enter the residual strength equation (Eq 1), and the equation is evaluated by numerical integration. For each increment of applied cycles, ply stresses, failure functions, and element response are recalculated and enter the strength reduction equation so that the reduction in strength and residual strength can be evaluated.

Example

A sample calculation obtained from the life prediction model is provided here for illustration. The result is shown in Fig. 15, where the residual strength (represented by Eq 1) of a L2 prosthesis under a load of 0.77 *Nl* and 0.63 *Nl*, and at load angles of 0° in-plane and 10° out-of-plane, is plotted against log of applied cycles. Here *Nl* is a normalization force unit such that the quasi-static ultimate load of the L1 specimens is 1.05 *Nl*. The calculation is based on a 16-ply laminate with thickness the same as the prototype specimens. The representative volume, a point under highest compressive stress, is found to be located on the medial surface at the middle of the neck region. The critical element is the ply with the lowest angle of incidence to the neck axis. For simplicity, the failure function, $F_L(n)$, is represented by the maximum strain ratio

$$F_L(n) = \frac{\varepsilon_{11}(n)}{\varepsilon_F} \tag{5}$$

where

$\varepsilon_{11}(n)$ = strain in the fiber direction (a function of applied cycles), and
ε_F = failure strain in the fiber direction.

The residual strength is calculated based on the maximum strain ratio since the local failure function, F_L, is represented by that ratio. Hence, failure of the prosthesis occurs when the residual strength of this point is exceeded by the instantaneous maximum strain ratio. The unidirectional *S-N* curve used is

$$\frac{\sigma_{11}}{X_c} = 1.0 - 0.12 \log N \tag{6}$$

The coefficient 0.12 is typical of polymeric matrix unidirectional material. This value is obtained by adjusting the residual strength curve to Data 1. Damage due to mechanical loading is represented by a linear degradation functions for the ply transverse and shear modulus. The ordinates of the experimental data points are taken to be the maximum strain ratio of the critical element at their respective load levels, as determined by the stress analysis model. It should be mentioned that the linear degradation functions for the ply transverse moduli and

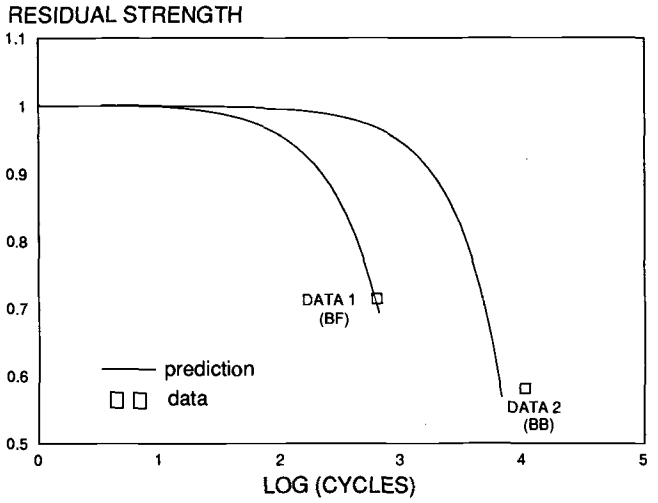

FIG. 15—*Example of application of the life prediction model.*

the unidirectional *S-N* curve were chosen for their simplicity, and that more exact representations of these functions are not available for the particular material system used for the prosthesis at present.

Summary

Two types of composite hip prostheses with different layups were cyclically tested under biaxial loading conditions. Fatigue damage was studied using X-ray radiography, a surface replication technique, and sectioning of the specimens. Damage in the neck region is predominantly in the form of matrix cracking along fiber directions. These cracks initiated from the medial-posterior corner, extended to the lateral side, and distributed toward the anterior side. Damage in the midstem region of Group 1 specimens was predominantly in form of matrix cracking. Damage in the midstem region of Group 2 specimens was in form of microbuckling following some matrix cracking at the medial surface. Structural failure in these specimens was caused by accumulation of local failures. In general, failure modes of the two types of specimens tested depend on their stacking sequence.

A life prediction model for a composite prosthesis was developed based on a critical-element model for composite laminates. Due to a lack of supporting data, however, it is recognized that some of the damage analyses presented here are still in an incomplete form. However, the present results suggest that the model can be used to make inquiry predictions for the remaining strength and life of various designs of a composite prosthesis.

Acknowledgment

This work was supported by Smith and Nephew Richards, Inc., Memphis, TN.

References

[*1*] Chang, F. K., Perez, J., and Davidson, J. A., "Design of a Composite Hip Prosthesis," *Proceedings*, American Society for Composites Fourth Technical Conference, Technomic Publishing Co., Inc., Warrendale, PA, 1989.

[2] Davidson, J. A., "The Challenge and Opportunity for Composites in Structural Orthopedic Applications," *Journal of Composites Technology and Research,* Vol. 9, No. 4, 1987, pp. 151–161.
[3] Reifsnider, K. L., Jamison, R. D., Gavens, A. J., and Maharaj, G. R., "Long Term Behavior of Biomedical Composites," *Proceedings,* American Society for Composites Fourth Technical Conference, Technomic Publishing Co., Inc., Warrendale, PA, 1989.
[4] Liao, K., "Performance Simulation of a Composite Orthopedic Implant Device," *Masters thesis,* Virginia Polytechnic Institute and State University, Blacksburg, VA, 1991.
[5] Gavens, A. J. and Locke, L. L., "Influence of the Abductor Muscle Force on Femoral Prosthesis Strain," *Proceedings,* American Society of Biomechanics 13th Annual Meeting, Burlington, VT, 23–25 August 1989.
[6] Gavens, A. J., Materials Research Report ML-89-44, Smith and Nephew Richards Inc., Memphis, TN, July, 1989.
[7] Gavens, A. J., Liao, K., Maharaj, G. R., Jamison, R. D., and Reifsnider, K. L., "Evaluation of Damage Progression in a Composite Material Hip Implant During Long-Term Biaxial Fatigue," *Damage Detection in Composite Materials, ASTM STP 1128,* J. E. Masters, Ed., American Society for Testing and Materials, Philadelphia pp. 256–271.
[8] Razvan, A., Bakis, C. E., and Reifsnider, K. L., "Influence of Load Levels on Damage Growth Mechanisms of Notched Composite Materials," *Composite Materials: Testing and Design (Ninth Volume), ASTM STP 1059,* S. P. Garbo, Ed., American Society for Testing and Materials, Philadelphia, 1990, pp. 371–389.
[9] Reifsnider, K. L. and Stinchcomb, W. W., "A Critical-Element Model of the Residual Strength and Life of Fatigue-Loaded Composite Coupons," *Composite Materials: Fatigue and Fracture, ASTM STP 907,* H. T. Hahn, Ed., American Society for Testing and Materials, Philadelphia, 1986, pp. 298–313.
[10] Yeow, Y. T., Morris, D. H., and Brinson, H. F., "Time-Temperature Behavior of a Unidirectional Graphite/Epoxy Composite," *Composite Materials: Testing and Design (Fifth Conference), ASTM STP 674,* S. W. Tsai, Ed., American Society for Testing and Materials, Philadelphia, 1979, pp. 263–281.
[11] Shen, C. H. and Springer, G. S., "Moisture Absorption and Desorption of Composite Materials," *Journal of Composite Materials,* Vol. 10, January 1976, p. 2.
[12] Gillat, O. and Broutman, L. J., "Effect of an External Stress on Moisture Diffusion and Degradation in a Graphite-Reinforced Epoxy Laminate," *Advanced Composite Materials—Environmental Effects, ASTM STP 658,* J. R. Vinson, Ed., American Society for Testing and Materials, Philadelphia, 1978, pp. 61–83.
[13] Whitney, J. M. and Browning, C. E., "Some Anomalies Associated with Moisture Diffusion in Epoxy Matrix Composite Materials," *Advanced Composite Materials—Environmental Effects, ASTM STP 658,* J. R. Vinson, Ed., American Society for Testing and Materials, Philadelphia, 1978, pp. 43–60.
[14] Chang, F., Shahid, I., and Engdahl, R. A., "Predicting Moduli and Strengths Reduction of Unidirectional Graphite/Epoxy Composites Due to Hygrothermal Effects," *Journal of Reinforced Plastics and Composites,* Vol. 8, March 1989.
[15] Chamis, C. C., Lark, R. F., and Sinclair, J. H., "Integral Theory for Predicting the Hygrothermomechanical Response of Advanced Composite Structural Components," *Advanced Composite Materials—Environmental Effects, ASTM STP 658,* American Society for Testing and Materials, Philadelphia, 1978, pp. 160–192.
[16] Loos, A. C. and Springer, G. S., "Moisture Absorption of Graphite-Epoxy Composites Immersed in Liquids and in Humid Air," *Journal of Composite Materials,* Vol. 13, April 1979, p. 131.
[17] Garley, G. L. and Herakovich, C. T., "Two-Dimensional Hygrothermal Diffusions into a Finite Width Composite Laminate," VPI-E-77-20, College of Engineering, Virginia Polytechnic Institute and State University, Blacksburg, VA, 1977.
[18] Shirrell, C. D., "Diffusion of Water Vapor in Graphite/Epoxy Composites," *Advanced Composite Materials—Environmental Effects, ASTM STP 658,* J. R. Vinson, Ed., American Society for Testing and Materials, Philadelphia, 1978, pp. 21–42.
[19] Hofer, K. E., Skaper, G. N., Bennet, L. C., and Rao, N., "Effect of Moisture on Fatigue and Residual Strength Losses for Various Composites," *Journal of Reinforced Plastics and Composites,* Vol. 6, January 1987.
[20] Sumsion, H. T. and Williams, D. P., "Effects of Environment on the Fatigue of Graphite-Epoxy Composites," *Fatigue of Composite Materials, ASTM STP 569,* J. R. Hancock, Ed., American Society for Testing and Materials, Philadelphia, 1975, pp. 226–247.
[21] Stinchcomb, W. W. and Reifsnider, K. L., "Fatigue Damage Mechanisms in Composite Materials: A Review," *Fatigue Mechanisms, ASTM STP 675,* J. T. Fong, Ed., American Society for Testing and Materials, Philadelphia, 1979, pp. 762–787.

[22] Charewicz, A. and Daniel, I. M., "Damage Mechanisms and Accumulation in Graphite/Epoxy Laminates," *Composite Materials: Fatigue and Fracture, ASTM STP 907,* H. T. Hahn, Ed., American Society for Testing and Materials, Philadelphia, 1986, pp. 274–297.

[23] Reifsnider, K. L., Schulte, K., and Duke, J. C., "Long-Term Fatigue Behavior of Composite Materials," *Long-Term Behavior of Composites, ASTM STP 813,* T. K. O'Brien, Ed., American Society for Testing and Materials, Philadelphia, 1983, pp. 136–159.

[24] Highsmith, A. L. and Reifsnider, K. L., "Internal Load Distribution Effects During Fatigue Loading of Composite Laminates," *Composite Materials: Fatigue and Fracture, ASTM STP 907,* H. T. Hahn, Ed., American Society for Testing and Materials, Philadelphia, 1986, pp. 233–251.

[25] Bakis, C. E. and Stinchcomb, W. W., "Response of Thick, Notched Laminates Subjected to Tension-Compression Cyclic Loads," *Composite Materials: Fatigue and Fracture, ASTM STP 907,* H. T. Hahn, Ed., American Society for Testing and Materials, Philadelphia, 1986, pp. 314–334.

Author Index

Subject Index

ISBN 0-8031-1862-7